Search for $2\nu\beta\beta$ Excited State Transitions and HPGe Characterization for Surface Events in GERDA Phase II

DISSERTATION

zur Erlangung des akademischen Grades
Doctor rerum naturalium
(Dr. rer. nat.)

vorgelegt der
Fakultät Mathematik und Naturwissenschaften
der Technischen Universität Dresden

von
Björn Lehnert
geboren am 07. 09. 1982 in Halle-Saale

Gutachter: Prof. Dr. Kai Zuber	**Datum der Einreichung:** 30. 10. 2015
Prof. Dr. Stefan Schönert	**Datum der Disputation:** 01. 03. 2016

Abstract

The search for the neutrinoless double beta ($0\nu\beta\beta$) decay is one of the most active fields in modern particle physics. This process is not allowed within the Standard Model and its observation would imply lepton number violation and would lead to the Majorana nature of neutrinos. The experimentally observed quantity is the half-life of the decay, which can be connected to the effective Majorana neutrino mass via nuclear matrix elements. The latter can only be determined theoretically and are currently affected by large uncertainties. To reduce these uncertainties one can investigate the well established two-neutrino double beta ($2\nu\beta\beta$) decay into the ground and excited states of the daughter isotope. These similar processes are allowed within the Standard Model.

In this dissertation, the search for $2\nu\beta\beta$ decays into excited states is performed in ^{110}Pd, ^{102}Pd and ^{76}Ge. Three gamma spectroscopy setups at the Felsenkeller (Germany), HADES (Belgium) and LNGS (Italy) underground laboratories are used to search for the transitions in ^{110}Pd and ^{102}Pd. No signal is observed leading to lower half-live bounds (90 % C.I.) of $2.9 \cdot 10^{20}$ yr, $3.9 \cdot 10^{20}$ yr and $2.9 \cdot 10^{20}$ yr for the $0/2\nu\beta\beta$ 2_1^+, 0_1^+ and 2_2^+ transitions in ^{110}Pd and $7.9 \cdot 10^{18}$ yr, $9.2 \cdot 10^{18}$ yr and $1.5 \cdot 10^{19}$ yr for the $0/2\nu\beta\beta$ 2_1^+, 0_1^+ and 2_2^+ transitions in ^{102}Pd, respectively. This is a factor of 1.3 to 3 improvement compared to previous limits. The data of PHASE I (Nov 2011 - May 2013) of the $0\nu\beta\beta$ decay experiment GERDA at LNGS is used to search for excited state transitions in ^{76}Ge. The analysis is based on coincidences between two detectors and finds no signal. Lower half-life limits (90 % C.L.) of $1.6 \cdot 10^{23}$ yr, $3.7 \cdot 10^{23}$ yr and $2.3 \cdot 10^{23}$ yr are obtained for the $2\nu\beta\beta$ 2_1^+, 0_1^+ and 2_2^+ transitions, respectively. These limits are more than two orders of magnitude larger than previous ones and could exclude many old matrix element calculations.

In addition to the excited state searches, important measurements and improvements for GERDA PHASE II upgrades are performed within this dissertation. 30 new BEGe detectors are characterized for their surface and active volume properties which is an essential ingredient for all future physics analyses in GERDA. These precision measurements reduce the systematic uncertainty of the active volume to a subdominant level. In extension to this, a new model for simulating pulse shapes of n$^+$ electrode surface events is developed. With this model it is demonstrated that the dominant background of ^{42}K on the detector surfaces can be suppressed by a factor of 145 with an A/E pulse shape cut in PHASE II. A further suppression of background is obtained by a liquid argon scintillation light veto. With newly developed Monte Carlo simulations, including the optical scintillation photons, it is demonstrated that ^{208}Tl in the detectors holders can be suppressed by a factor of 134. ^{42}K homogeneously distributed in the LAr can be suppressed with this veto in combination with pulse shape cuts by a factor of 170 for BEGe detectors. The characterization measurements and the developed simulation tools presented within this dissertation will help to enhance the sensitivity for all $0/2\nu\beta\beta$ decay modes and will allow to construct an improved background model in GERDA PHASE II.

Autorenreferat

Die Suche nach dem neutrinolosen Doppelbetazerfall ($0\nu\beta\beta$) ist eines der aktivsten Felder der modernen Teilchenphysik. Der Zerfall setzt die Verletzung der Leptonenzahl voraus und hätte die Majorananatur des Neutrinos zur Folge. Die durch eine Beobachtung bestimmbare Halbwertszeit des Zerfalls ermöglicht, über ein nukleares Matrixelement, Zugang zur effektiven Majorananeutrinomasse. Die größten Unsicherheiten gehen dabei auf das Matrixelement zurück, welches nur durch verschiedene, teilweise stark voneinander abweichende theoretische Modelle zugänglich ist. Eine Möglichkeit diese Unsicherheiten zu reduzieren bieten genaue Studien des im Standardmodell erlaubten neutrinobegleiteten Doppelbetazerfalls ($2\nu\beta\beta$) in angeregte Zustände des Tochterkerns.

In dieser Dissertation wird der $2\nu\beta\beta$-Zerfall der Nuklide ^{110}Pd, ^{102}Pd und ^{76}Ge in angeregte Zustände untersucht. Die Untersuchungen von ^{110}Pd und ^{102}Pd wurden in drei umfangreichen Gammaspektroskopie-Experimenten in den Untergrundlaboren Felsenkeller (Deutschland), HADES (Belgien) und LNGS (Italien) durchgefürt. Es wurde kein Signal beobachtet und damit die weltweit besten unteren Grenzen für die Halbwertszeit dieser Zerfälle festgesetzt: $2{,}9 \cdot 10^{20}$ yr, $3{,}9 \cdot 10^{20}$ yr und $2{,}9 \cdot 10^{20}$ yr für die $0/2\nu\beta\beta$ 2^+_1, 0^+_1 und 2^+_2 Übergänge in ^{110}Pd and $7{,}9 \cdot 10^{18}$ yr, $9{,}2 \cdot 10^{18}$ yr und $1{,}5 \cdot 10^{19}$ yr für die $0/2\nu\beta\beta$ 2^+_1, 0^+_1 und 2^+_2 Übergänge in ^{102}Pd (90 % C.I.). Dies ist eine 1,3 bis 3-fache Verbesserung gegenüber den vorher bekannten Grenzen. Die Untersuchung des $2\nu\beta\beta$-Zerfalls in ^{76}Ge basiert auf Daten aus PHASE I (Nov. 2011 - Mai 2013) des $0\nu\beta\beta$-Zerfall Experiments GERDA. Mit der auf koinzidenten Ereignissen basierten Analyse konnte kein Signal beobachtet werden und folgende untere Grenzen für die Halbwertszeit der $2\nu\beta\beta$ 2^+_1, 0^+_1 und 2^+_2 Übergänge wurden festgelegt: $1{,}6 \cdot 10^{23}$ yr, $3{,}7 \cdot 10^{23}$ yr und $2{,}3 \cdot 10^{23}$ yr (90 % C.L.). Diese 100-fache Verbesserung gegenüber den bisher bekannten Grenzen widerlegt eine Vielzahl älterer, zur Verfügung stehender Matrixelemente.

Zusätzlich wurden im Rahmen dieser Dissertation für die Erweiterungen des GERDA Experiments zur PHASE II wichtige Messungen durgeführt und Verbesserungen entwickelt. 30 neu produzierte BEGe Detektoren wurden hinsichtlich ihrer Oberflächeneigenschaften sowie ihrer aktiven Volumina charakterisiert. Diese Präzisisionsmessungen sind für alle zukünftigen Analysen in GERDA notwendig und erlauben die entsprechenden systematischen Unsicherheiten auf ein subdominantes Niveau zu reduzieren. Erweiternd wurde ein neues Model zur Beschreibung der n$^+$-Elektrode entwickelt, welches erstmals erlaubt die Pulsform von Oberflächeninteraktionen zu simulieren. Mithilfe dieses Models konnte demonstriert werden, dass der in Oberflächeninteraktionen begründete und in GERDA dominante Messuntergrund von ^{42}K auf der Detektoroberfläche durch Pulsformanalyse um das 145-fache unterdrückt werden kann. Eine weitere Untergrundreduzierung wird durch ein Flüssigargon Szintillationsveto erreicht. Im Rahmen dieser Arbeit wurden vorhandene Monte Carlo Simulationen um den Transport von optischen Photonen erweitert und die 134-fache Unterdrückung des ^{208}Tl Untergrundes demonstriert. Die Ergebnisse dieser Arbeit helfen eine deutliche Sensitivitätsverbesserung für die zükünftige Suche nach dem $0/2\nu\beta\beta$-Zerfall zu erzielen und erlauben die Erstellung eines präziseren Untergrundmodels in GERDA PHASE II.

Contents

Chapter 1

Introduction

The focus of particle physics today is the search for phenomena beyond its well established Standard Model (SM). The neutrino is the least understood elementary particle in the SM because of its extremely low cross section with other particles which requires an enormous experimental effort to study it. 50 years after its discovery, the absolute neutrino mass is still unknown, it is unclear whether the mass ordering of its three known eigenstates is normal or inverted, whether there are additional sterile flavor eigenstates and whether it may be its own antiparticle, i.e. of Majorana nature. Especially the Majorana nature of the neutrino would imply lepton number violation which could explain the asymmetry between matter and antimatter in the universe and thus the very existence of matter itself. Thus, the investigation of neutrinos is an important frontier in the search for new physics with implications reaching beyond the simple properties of a particle.

The study of neutrinoless double beta ($0\nu\beta\beta$) decay can shed light on neutrino properties and particle physics in general. The second order weak nuclear decay is only possible if the lepton number is violated and if the neutrino is its own anti-particle. $0\nu\beta\beta$ decay has not been observed so far but is predicted by many theories extending the SM. The easiest mechanism to describe the decay is the exchange of a virtual light Majorana neutrino which would connect the decay half-life with the neutrino mass. This conversion of an experimentally measured half-life into an effective Majorana neutrino mass requires a phase space factor and a nuclear matrix element (NME). Both quantities can only be determined with theoretical calculations of which especially the NME is heavily dependent on nuclear models and subject to their uncertainties. The search for $0\nu\beta\beta$ decay is currently pursued by about a dozen experiments worldwide using different isotopes and different experimental techniques. The current limits on the half-life exceed 10^{25} yr which translates into upper bounds of $< 0.2 - 0.4\,\text{eV}$ for the effective Majorana neutrino mass. The largest uncertainty for the conversion are the NMEs which are specific to the double beta decay isotope under study. Their theoretical calculation can be tested and constrained with the process of two-neutrino double beta ($2\nu\beta\beta$) decay which is allowed in the SM. To add even more tests and constrains into the picture, also the $2\nu\beta\beta$ decay into excited states of the daughter isotope can be examined. Especially the observation of multiple $2\nu\beta\beta$ decay modes in the same isotope is valuable experimental input for the theory community, disentangling model inherent uncertainties and isotope specific uncertainties in the calculation. So far the $2\nu\beta\beta$ decay into the ground state has been experimentally measured in more than 10 isotopes whereas the $2\nu\beta\beta$ decay into an excited state has only been observed in two isotopes.

In this dissertation, three searches for $2\nu\beta\beta$ decay transition into excited states are performed in isotopes in which the decay has not yet been discovered: ^{76}Ge, ^{110}Pd, and

^{102}Pd. The search in ^{76}Ge is performed with the GERmanium Detector Array (GERDA) experiment located underneath the Apennine mountains in the Laboratori Nazionali del Gran Sasso (LNGS), Italy. The GERDA experiment is designed to search for the ground state transition of $0\nu\beta\beta$ decay at an energy of $2039\,\mathrm{keV}$ with an array of High Purity Germanium (HPGe) detectors isotopically enriched in ^{76}Ge. The tight configuration of the detectors provides an excellent possibility to also search for de-excitation γ-ray cascades from excited state transitions. The experiment was planned in two stages. PHASE I was running from November 2011 to May 2013 using $18\,\mathrm{kg}$ of enriched semi-coaxial HPGe detectors refurbished from predecessor experiments. This dataset is used for the search of excited state transitions. GERDA PHASE II includes a number of major upgrades which are currently (fall 2015) being commissioned. Another focus of this dissertation is the preparation of some of these upgrades which will significantly increase the sensitivity for all previously achieved measurements.

One of the major upgrades are 30 newly produced enriched Broad Energy Germanium (BEGe) detectors which double the target mass of ^{76}Ge and will reduce the background by superior pulse shape discrimination. The characterization of the surface layer and active volume of the new BEGe detectors is performed in this thesis. The n$^+$ electrode of the p-type semi-conducting detectors is produced via lithium diffusion with thicknesses in the order of $1\,\mathrm{mm}$ which are, however, notoriously different for each detector. The precise measurement of the n$^+$ electrode thickness and the fiducial active volume is imperative for every physics analysis in PHASE II. The aim is a high precision measurement which will reduce systematic uncertainties in the determination of the $0\nu\beta\beta$ decay and all other decay modes.

The HPGe detectors in GERDA are immersed in liquid argon (LAr) which features an ultra pure high density passive shielding along with the necessary cryogenic cooling for the detectors. A prototype set of PHASE II BEGe detectors was already deployed in PHASE I to investigate the performances of the new detectors. It was found that $60\,\%$ of the total background for these detectors is originating from the beta decay of ^{42}K which is collected on the detector surface. Charged ^{42}K is produced by ^{42}Ar, a radioactive trace element inside argon, and is then attracted by the E-field of the operational high voltage. The beta particles have an energy up to $3525\,\mathrm{keV}$, large enough to mimic the signal of $0\nu\beta\beta$ decay at $2039\,\mathrm{keV}$. However, they have to traverse the detector surface creating particular slow pulses with long rise time. The pulse shape of surface events can be used for a strong discrimination against events from the detector bulk such as the major part of $0\nu\beta\beta$ decays. A new model describing the surface pulse shapes along with Monte Carlo (MC) simulations of surface events are developed in this thesis. The model is tuned to calibration data from a unique characterization setup featuring an enriched PHASE II BEGe detector mounted upside-down without passivation layer in a vacuum cryostat. This allows to investigate the p$^+$ electrode and n$^+$ electrode simultaneously. Predictions are made for the quantitative suppression of the dominant ^{42}K background along with other implications for particle interactions in the detector surface layer.

Another major improvement in GERDA PHASE II is the instrumentation of the LAr as an active scintillation veto. Radioactive background in the LAr as well as in the surrounding material can deposit energy inside the germanium detectors and the LAr simultaneously. Those background events can be discriminated with the LAr veto, further lowering the overall background level. The event topologies of such background components are investigated in this thesis. MC simulations of optical scintillation photons are developed and

applied to key background components. Quantitative predictions are made for the background suppression capabilities in PHASE II.

This thesis is organized with an initial introduction, followed by the developments for the GERDA PHASE II upgrades and ending with the physics analyses of excited state transitions in ^{76}Ge and ^{110}Pd / ^{102}Pd. The introduction is separated into four chapters: Chap. 2 introduces neutrino physics as an approach to search for physics beyond the SM. Chap. 3 introduces the various forms of double beta decay including an overview of current experiments and experimental techniques. Chap. 4 summarizes the necessary methodology for this thesis including particle interactions with matter, germanium and LAr based detector systems as well as the origin and mitigation techniques for major background sources. Chap. 5 briefly introduces the GERDA experiment and its most important achievements. The characterization of PHASE II BEGe detectors is separated into three chapters starting with the description of the experimental setups and results from the upside-down measurement campaign in Chap. 6. The precision measurement of the n$^+$ electrode thickness and the active volume of all BEGe detectors is described in detail in the dedicated Chap. 7. The successive development of a new n$^+$ electrode model to describe the semi-active part of the n$^+$ electrode is presented in Chap. 8. The development of MC simulations for the LAr scintillation veto and their application to predict the suppression of key background components in PHASE II is described in Chap. 9. The most important achievement of this dissertations is presented in Chap. 10 with the analysis of $2\nu\beta\beta$ excited state transitions in ^{76}Ge using GERDA PHASE I data. The results and tools obtained in the previous chapters are used for a sensitivity study of such an analysis in PHASE II. Finally, the search for excited state transitions in ^{110}Pd and ^{102}Pd, performed with three measurements in smaller gamma spectroscopy setups, is presented in Chap. 11.

The nuclear data relevant for this thesis is collected in appendix Chap. A. Each chapter with original work has its own detailed conclusion and outlook in the end of the chapter as well as its own appendix. An integrated conclusion of the entire thesis is given in Chap. 12. Acronyms are extensively used throughout this thesis and the reader is advised to refer to the appendix Chap. H as a dictionary. The definition of acronyms is occasionally repeated throughout the text to increase readability. References to figures, tables, sections, chapters, citations and acronyms are hyperlinks in the pdf document indicated by color coding.

Chapter 2

Neutrino Physics

Neutrinos are an essential part in the SM of particle physics providing the uncharged counterpart to the charged leptons. They are the lightest fundamental particle by far, do not carry an electric or color charge and interact only weakly. Their low cross section with other particles made them elusive for many years. Large neutrino fluxes, huge volume detectors and ultra low background environments are needed to observe neutrinos and investigate their properties. Only recently, neutrino physics is providing groundbreaking new discoveries starting with neutrino oscillation and successively measuring the oscillation parameters with ever more precision. The great challenges for the next generation of neutrino experiments are the measurement the leptonic CP violation and neutrino mass hierarchy. The neutrino mass will be constrained by multiple approaches. One of these is $0\nu\beta\beta$ decay with the additional possibility to investigate lepton number violation and the Majorana nature of neutrinos.

This chapter is organized as follows: A brief theoretical introduction of neutrinos in the SM (Sec. 2.1) is followed by two beyond the SM sections: Neutrino oscillations (Sec. 2.2) and neutrino masses (Sec. 2.3). The last section (Sec. 2.4) discusses the three experimental approaches to constrain the neutrino mass. This chapter has the focus on general neutrinos physics and the interplay of different experimental approaches. The double beta decay is discussed in detail in the dedicated following chapter.

2.1 Standard Model and Neutrinos

In 1930 Wolfgang Pauli postulated a very light, charge-less particle to explain the continuous energy spectrum of electrons in beta decays. This problem had troubled the scientific world since the first spectral electron measurements by Lise Meitner and Otto Hahn in 1911. Pauli was in a dilemma to either abandon energy conservation or to postulate a particle that, as he foresaw, might never be discovered. This particle was later coined neutrino by Enrico Fermi in 1933 to avoid a naming conflict with the newly discovered neutron. Its discovery took 26 years until 1956 when Frederick Reines and Clyde L. Cowan performed a nuclear reactor experiment observing electron antineutrinos [1, 2]. As foreseen by Pauli, the measured cross section was extraordinary small and well in agreement with the prediction of $6.3 \cdot 10^{-44}\,\mathrm{cm}^2$.

In 1933 Enrico Fermi was the first who developed a theory for weak interactions, motivated by the beta decay observations [3]. He suggested 4-fermion vertices which could describe weak decays and weak interactions rather well. Later with the advent of a complete electroweak theory and the SM, it became clear that the Fermi theory is an effective theory with

good approximation for particle decays and interactions with energies much smaller than the mass of the W boson $\approx 100\,\text{GeV}$.

Only two years after its discovery, Goldhaber measured the helicity of the neutrino in 1957 [4]. The experiment showed that neutrinos are only realized left-handed and antineutrinos right-handed. This experiment was in agreement with the Wu experiment which showed parity violation in weak interaction just one year earlier [5]. Additionally, beta decay experiments at the time showed that the neutrino mass is smaller than $0.5\,\text{keV}$ [6].

These experiments led to the conclusion that neutrinos are mass-less fermions[1] that occur in nature only as left-handed neutinos ν or right-handed antineutrinos $\bar{\nu}$. With these properties neutrinos are included in the SM as part of the electroweak theory which was developed by Glashow, Salam and Weinberg in 1961 [7]. Now it became clear that Fermi's 4-fermion interactions are in fact driven by the underlying exchange of vector bosons. The calculation of electroweak matrix elements considers a propagator term with the heavy Z^0 ($91.1876 \pm 0.0021\,\text{GeV}$) and $W^\pm$ ($80.385 \pm 0.015\,\text{GeV}$) bosons [8] in its denominator. Thus the interactions appear point-like for energies smaller than the vector boson mass and with extremely small cross sections.

Neutrinos are only subject to the weak interaction which does not act upon right-handed fermions and left-handed antifermions since there are only left-handed weak charge currents[2] (V-A structure). If fermions have zero rest mass, their helicity is conserved and has the same eigenvalues as chirality[3]. This means that right-handed fermions or left-handed antifermions cannot be created by weak interactions in the SM and that the fermionic and antifermionic spin projections are always negative and positive respectively.

Fermions are grouped into left-handed doublets and right-handed singlets[4] as shown in Tab. 2.1. The same is true for antifermions with opposite chirality.

Table 2.1 Fermionic doublets and singlets in the electroweak theory.

Quarks			Leptons		
$\binom{u}{d'}_L$	$\binom{c}{s'}_L$	$\binom{t}{b'}_L$	$\binom{e}{\nu_e}_L$	$\binom{\mu}{\nu_\mu}_L$	$\binom{\tau}{\nu_\tau}_L$
$(u)_R,\ (d)_R$	$(c)_R,\ (s)_R$	$(t)_R,\ (b)_R$	$(e)_R$	$(\mu)_R$	$(\tau)_R$

The three quarks d', s' and b' are weak flavor eigenstates mixed out of the quark mass eigenstates d and u, s respectively according to the Cabibbo-Kobayashi-Maskawa (CKM) matrix. This mixing violates the baryon flavor and breaks the charge conjugation parity

---

[1]Spin $\frac{1}{2}$ particles.

[2]The handiness or chirality is the chiral projection of a spinor ψ by the projection operators: $\psi_{L/R} = (1 \mp \gamma^5)\psi$. The weak interaction includes a projection operator, which is a consequence of maximal parity violation, and hence, does not act upon a particle spinor $\psi_R = (1 + \gamma^5)\psi$ or on antiparticle spinor $\psi_L = (1 - \gamma^5)\psi$.

[3]Helicity is the sign of the projection of the spin vector, $\boldsymbol{\sigma}$, onto the direction of momentum, $\frac{\mathbf{P}}{|\mathbf{P}|}$: $\mathcal{H} = \frac{\boldsymbol{\sigma} \cdot \mathbf{P}}{|\mathbf{P}|}$. Helicity is only conserved for massless particles when there is no reference frame in which the direction of momentum can turn around. Then, helicity is identical to chirality.

[4]The quantum number of the weak interaction is the weak isospin, T, which is $1/2$ for left-handed fermions and groups them into doublets with $T_3 = \pm 1/2$. Right-handed fermions have no weak isospin charge ($T = 0$) and are thus singlets. T_3 together with the weak hypercharge Y_W relate to the electric charge Q with $Q = T_3 + \frac{1}{2}Y_W$.

(CP) symmetry. The right-handed singlets do not mix since they do not couple to the weak interaction. For leptons there is only one right-handed singlet per family because right-handed neutrinos cannot interact weakly, therefore cannot interact at all and are not present as particles in the SM. The lepton flavor is accidentally conserved in the SM in contrast to baryon flavor; however, the total baryon and lepton number seem to be conserved with the best experimental constraints coming from proton decay and $0\nu\beta\beta$ decay experiments respectively[5].

The amount of three light neutrino flavors according to the three lepton families was established in 1989 by measurements of the Z^0 boson width at the LEP collider [9]. The Z^0 boson width does not exclude additional heavy neutrinos (larger than half of the Z^0 mass) or sterile neutrinos that do not couple via the weak interaction.

2.2   Neutrino Oscillations

The idea of neutrino mixing, analogous to the quark sector, was introduced by Maki, Nakagawa and Sakata in 1962 [10], but the first connection to possible neutrino flavor oscillations was not until seven years later by Gribov and Pontecorvo in 1969 [11]. They introduced the idea of massive neutrinos that allows for neutrino flavor oscillation and thus flavor violation analogously to quark flavor oscillation with the CKM matrix. The basic assumption for neutrino oscillation is that the weak flavor eigenstates are not identical to the mass eigenstates. The flavor and mass eigenstates are a superposition of each other which can be mathematically described as

$$|\nu_\alpha\rangle = \sum_i U_{\alpha i}^* |\nu_i\rangle \quad \text{and} \quad |\nu_i\rangle = \sum_\alpha U_{\alpha i} |\nu_\alpha\rangle \tag{2.1}$$

in which $\alpha = e, \mu, \tau$ are the weak flavor eigenstates, $i = 1, 2, 3$ are the mass eigenstates and $U_{\alpha i}$ are the matrix elements of the Pontecorvo-Maki-Nakagawa-Sakata (PMNS) matrix. In its most general form the PMNS matrix can be parametrized as

$$U = \begin{pmatrix} 1 & 0 & 0 \\ 0 & c_{23} & s_{23} \\ 0 & -s_{23} & c_{23} \end{pmatrix} \cdot \begin{pmatrix} c_{13} & 0 & s_{13}e^{-i\delta} \\ 0 & 1 & 0 \\ -s_{13}e^{i\delta} & 0 & c_{13} \end{pmatrix} \tag{2.2}$$

$$\cdot \begin{pmatrix} c_{12} & s_{12} & 0 \\ -s_{12} & c_{12} & 0 \\ 0 & 0 & 1 \end{pmatrix} \cdot \begin{pmatrix} e^{i\alpha_1/2} & 0 & 0 \\ 0 & e^{i\alpha_2/2} & 0 \\ 0 & 0 & 1 \end{pmatrix} \tag{2.3}$$

in which s and c denote sine and cosine of the mixing angles ij respectively and δ, α_1 and α_2 are CP violating phases. Specifically α_1 and α_2 are Majorana phases which are present only if neutrinos are Majorana particles[6]. The observable oscillation, however, does not depend on these phases.

Neutrino oscillation can be illustrated as follows: A neutrino is produced in its respective flavor eigenstate which is a quantum mechanical superposition of mass eigenstates. One of the mass eigenstates is realized with the chance given by the PMNS matrix. The mass eigenstate then propagates through space according to kinematic laws. The mass eigenstate is again a superposition of flavor eigenstates of which one is realized upon interaction, i.e.

---

[5]There is no theoretical reason, i.e. no symmetry according to the Noether's-theorem, that imposes baryon and lepton flavor conservation, as well as their number conservation in the SM.

[6]The two degrees of freedom of the Majorana phases are traded with two additional Dirac mass states.

detection. Thus the detected neutrino flavor can be different from the produced neutrino flavor. The probability that a neutrino created with flavor α is detected with a flavor β, also known as transition probability, is

$$
\begin{aligned}
P_{\alpha \to \beta} &= |\langle \nu_\beta(t) | \nu_\alpha \rangle|^2 \\
&= \left| \sum_i U_{\alpha i}^* U_{\beta i} \cdot e^{-i m_i^2 L / 2E} \right|^2 \\
&= \delta_{\alpha \beta} - 4 \sum_{i=1}^2 \sum_{j=i+1}^3 \mathcal{R}e \left(U_{\alpha i}^* U_{\beta i} U_{\alpha j} U_{\beta j}^* \right) \sin^2 \left(\Delta m_{ij}^2 \frac{L}{4E} \right) \\
&\quad + 2 \sum_{i=1}^2 \sum_{j=i+1}^3 \mathcal{I}m \left(U_{\alpha i}^* U_{\beta i} U_{\alpha j} U_{\beta j}^* \right) \sin \left(\Delta m_{ij}^2 \frac{L}{2E} \right).
\end{aligned}
\tag{2.4}
$$

Here, Δm_{ij}^2 is the squared mass difference between the mass eigenstates i and j as $\Delta m_{ij}^2 = m_j^2 - m_i^2$, E is the energy of massless neutrinos and L is the propagated distance of the neutrino between source and detector. It can be seen that the oscillation wavelength depends on E, L and Δm_{ij}^2 whereas the oscillation maximum $\sin^2 \left(\Delta m_{ij}^2 \frac{L}{4E} \right) = 1$ depends only on the mixing angles encoded in the PMNS matrix. In order to determine the unknown Δm_{ij}^2, an experiment has to know precisely E and L of the neutrinos.

Figure 2.1 Two different scenarios of neutrino mass patterns deduced from oscillation experiments. Left: normal mass hierarchy ($\nu_1 < \nu_2 < \nu_3$); right: inverted mass hierarchy ($\nu_3 < \nu_1 < \nu_2$). The flavor composition of neutrino mass eigenstates is illustrated with red for the e part, with yellow for the μ part and with blue for the τ part. From [12].

In general, the Δm_{ij}^2 can be positive or negative. The sign of Δm_{12}^2 has been fixed by solar neutrino experiments explaining the MSW effect[7] [13]. The remaining uncertainty of the sign of Δm_{23}^2 leads to two possible scenarios referred to as normal and inverted mass hierarchy which are illustrated in Fig. 2.1. The flavor composition of each neutrino mass eigenstate is shown. The hierarchy scenario cannot be easily decided by neutrino oscillation experiments and the absolute mass scale remains unfathomed since Δm_{ij}^2 denotes only the mass difference. Future oscillation experiments might be able to determine the hierarchy using matter effects in oscillations.

As a conclusion for neutrino masses, we know from oscillation experiments that at least two neutrino mass eigenstates are different from zero and with the knowledge about mixing, that all neutrino flavor eigenstates have an effective non zero rest mass. Two mass hierarchies remain possible which could also be degenerated in case of $\nu_1 \sim \nu_2 \sim \nu_3 > \Delta m_{23}$.

---

[7] MikheyevSmirnovWolfenstein effect describing neutrino oscillation in matter.

2.3 Neutrino Masses

2.3.1 Dirac versus Majorana Masses

Particles $|\psi\rangle$ and antiparticles $|\bar{\psi}\rangle$ are connected by the charge-conjugation operator C with $\mathcal{C}|\psi\rangle = |\bar{\psi}\rangle$. The charge-conjugation changes the sign of all additive quantum numbers. Fermions are called Dirac particles if the particle and antiparticle are different states: $|\psi\rangle \neq |\bar{\psi}\rangle$; they are called Majorana particles if the particle and the antiparticle are identical: $|\psi\rangle \equiv |\bar{\psi}\rangle$. In the latter case, all their additive quantum numbers, e.g. electric charge, baryon number, lepton number etc., have to be neutral which is only possible for neutrinos among the elementary particles in Tab. 2.1 [8]. With this argument, Dirac neutrinos could have a static magnetic and electric dipole moment whereas Majorana neutrinos cannot. Neutrinos are embedded in the SM as Dirac particles which can be described as four-component spinors by the Dirac equation in quantum field theory. Their spin of $1/2$ allows for two chiral projection for each particle and antiparticle respectively: ν_L^D, ν_R^D, $\bar{\nu}_L^D$ and $\bar{\nu}_R^D$. The Majorana spinor only needs two components in contrast: $\nu_L^M = \bar{\nu}_L^M$ and $\bar{\nu}_R^M = \nu_R^M$. The two remaining degrees of freedom manifest in two additional Majorana phases. The different Dirac and Majorana states are summarized in Tab. 2.2 including their interaction probability with charged fermions. The massless Dirac (anti-)neutrino only interacts with negatively charged fermions if it is left-handed and with positively charged anti-fermions if it is right-handend. Hence, only two Dirac states are experimentally accessible and the distinction between Dirac and Majorana neutrinos is impossible. The right-handed projection of a massive Dirac neutrino can, however, also interact with negatively charged fermions with the probability ([14])

$$p = \frac{1}{2}\left(1 - \frac{v}{c}\right) \approx \left(\frac{m_\nu}{2E}\right)^2.\tag{2.5}$$

Equally, massless left-handed Majorana neutrinos cannot interact with anti-fermions whereas massive Majorana neutrinos can interact with the probability p.

Table 2.2 States of Dirac and Majorana Neutrinos. $p(l^-)$ and $p(l^+)$ denote the probability to produce a lepton of the respective charge. For $m_\nu \to 0$ the difference between Dirac and Majorana neutrino disappears.

	notation	chirality	$p(l^-)$	$p(l^+)$
Dirac ν	ν_L^D	L	$1 - \left(\frac{m_\nu}{2E}\right)^2$	0
	ν_R^D	R	$\left(\frac{m_\nu}{2E}\right)^2$	0
Dirac $\bar{\nu}$	$\bar{\nu}_L^D$	L	0	$\left(\frac{m_\nu}{2E}\right)^2$
	$\bar{\nu}_R^D$	R	0	$1 - \left(\frac{m_\nu}{2E}\right)^2$
Majorana ν	$\nu_L^M = \bar{\nu}_L^M$	L	$1 - \left(\frac{m_\nu}{2E}\right)^2$	$\left(\frac{m_\nu}{2E}\right)^2$
Majorana $\bar{\nu}$	$\bar{\nu}_R^M = \nu_R^M$	R	$\left(\frac{m_\nu}{2E}\right)^2$	$1 - \left(\frac{m_\nu}{2E}\right)^2$

For massive neutrinos, all four Dirac states can interact with charged fermions and a distinction between the Dirac and Majorana nature is possible; however, with neutrino masses converting towards zero, the distinction becomes continuously smaller and experimentally more difficult to measure.

---

[8] A meson's example for a Majorana particle is e.g. the π^0

2.3.2   Neutrino Mass Description

The observation of neutrino oscillation requires the neutrino to have a non-zero rest mass which has to be inserted in the SM. Consequently, also neutrino singlets, $(\nu_e)_R$, $(\nu_\mu)_R$ and $(\nu_\tau)_R$, which are not present in the definition of the SM[9] have to be inserted to create Dirac masses (see Tab. 2.1).

A straight forward approach is the introduction of a Dirac mass term into the Lagrangian with which leptons acquire mass by coupling to the Higgs field:

$$\mathcal{L}^D = -\mathcal{M}_D \nu \bar{\nu} = -\mathcal{M}_D \left[\bar{\nu}_R \nu_L + \bar{\nu}_L \nu_R \right]. \tag{2.6}$$

In this equation, $\mathcal{M}_D$ is the coupling strength of the neutrino spinor to the Higgs field, i.e. the neutrino mass. ν and $\bar{\nu}$ are the four-component neutrino spinors that can be separated into their chiral projections ν_R and ν_L. It becomes clear that there cannot be a Dirac mass term without right-handed neutrinos, ν_R, and left-handed antineutrinos, $\bar{\nu}_L$.

The ν and $\bar{\nu}$ can be seen as creation and annihilation operators that have to come in pairs on order to conserve quantum numbers e.g. electric charge or lepton number. The electric charge is conserved since neutrinos are neutral and with abandoning the lepton number conservation, in principle there can be two more mass terms which are precisely the Majorana mass terms:

$$\mathcal{L}^M = -\frac{1}{2}\mathcal{M}_{M_L} \left[(\bar{\nu}_L)^c \nu_L + \bar{\nu}_L \nu_L^c \right] - \frac{1}{2}\mathcal{M}_{M_R} \left[(\bar{\nu}_R)^c \nu_R + \bar{\nu}_R \nu_R^c \right]. \tag{2.7}$$

Here, the mass is created with the coupling of a field to its charge conjugated field which is denoted by the superscript c. Generally all three mass terms, $\mathcal{M}_D$, $\mathcal{M}_{M_L}$ and $\mathcal{M}_{M_R}$, could coexist and can be rewritten in form of a 2×2-matrix $\mathcal{M}$:

$$\mathcal{L}^M = -\frac{1}{2} \cdot ((\bar{\nu}_L)^c, \bar{\nu}_R) \cdot \mathcal{M} \cdot \begin{pmatrix} \nu_L \\ \nu_R^c \end{pmatrix} \quad , \quad \mathcal{M} = \begin{pmatrix} \mathcal{M}_{M_L} & \mathcal{M}_D^T \\ \mathcal{M}_D & \mathcal{M}_{M_R} \end{pmatrix}. \tag{2.8}$$

The eigenvalues of $\mathcal{M}$ may give an intuitive way to create very light and very heavy neutrinos.

2.3.3   See-Saw Mechanisms

The mass matrix, $\mathcal{M}$, can be diagonalized resulting in generally two non-degenerated eigenvalues, $\mathcal{M}_1$ and $\mathcal{M}_2$. With the simplifying assumptions that $\mathcal{M}_{M_R} \gg m_e$, $\mathcal{M}_{M_L} \approx 0$ and $\mathcal{M}_D \approx m_e$ the equation solves to

$$\mathcal{M}_1 = \frac{\mathcal{M}_D^2}{\mathcal{M}_{M_R}} \ll \mathcal{M}_D \tag{2.9}$$

$$\mathcal{M}_2 = \mathcal{M}_{M_R} \left(1 + \frac{\mathcal{M}_D}{\mathcal{M}_{M_R}} \right) \approx \mathcal{M}_{M_R} \gg \mathcal{M}_D, \tag{2.10}$$

which is called type I see-saw mechanism. This mechanism provides an elegant way of explaining a light neutrino mass, $\mathcal{M}_1$, assuming a Dirac neutrino coupling to the Higgs field, $\mathcal{M}_D$, similar to the one of the other Dirac leptons e, μ or τ. Additionally, a heavy

---

[9]Depending on how one defines the Standard Model, massive neutrinos can be described by it or not. If by definition the SM is merely the combination of the $U(1) \times SU(2) \times SU(3)$ gauge symmetry groups, then new particles can be incorporated i.e. neutrino singlets. If the SM is defined by the symmetry group and the fermions in Tab. 2.1, then massive neutrinos are physics beyond the standard model.

neutrino, $\mathcal{M}_2$, is postulated that could potentially serve as a dark matter candidate or a relict particle leading to leptogenesis. In the see-saw type I mechanism, the lightness of $\mathcal{M}_1$ is connected with the predominance of the V-A structure; the heaviness of $\mathcal{M}_2$ is connected with the scale of how much parity breaking is violated.

Assuming a GUT scale $\mathcal{M}_{M_R} \approx 10^{15} \, \text{GeV}$ and an electroweak scale $\mathcal{M}_D \approx 100 \, \text{GeV}$ then $\mathcal{M}_1$ would be $\mathcal{O}(0.01 \, \text{eV})$ and $\mathcal{M}_2 \, \mathcal{O}(10^{15} \, \text{GeV})$.

In the see-saw type I mechanism the mass operator is created by a fermion singlet. There are also other types of the see-saw mechanism where the mass is created by a scalar Higgs triplet (see-saw type II) or a fermion triplet (see-saw type III). See e.g. [12] for more detail.

2.4   Neutrino Mass Experiments

The definition of an observable neutrino mass is rather complex including all three neutrino mass eigenstates, the flavor eigenstates, their mixing and up to three complex phases. There are three fundamentally different experimental approaches to access the neutrino mass and they all measure a different mass observable:

$$m_\beta = \sqrt{\sum_i m_i^2 |U_{ei}|^2} \tag{2.11}$$

$$m_{\text{cosm}} = \sum_i m_i \tag{2.12}$$

$$m_{\beta\beta} = \left| \sum_i m_i U_{ei}^2 \right| \tag{2.13}$$

m_β is the mass of the electron neutrino and hence the incoherent sum of its mass eigenstates. This is typically measured with β-decays in which a $\bar{\nu}_e$ is produced.

m_{cosm} is measured when fitting cosmological models to observational astrophysical data. The neutrino influence on cosmological parameters is typically not dependent on the flavor eigenstate and the inferred neutrino mass is the simple sum of mass eigenstates.

$m_{\beta\beta}$ is the effective Majorana neutrino mass which may trigger neutrinoless double beta decay. In contrast to the other neutrino masses, the virtual nature of the neutrino propagator makes $m_{\beta\beta}$ a coherent sum of the electron neutrino mass eigenstates and dependent on the complex phases.

A brief overview of the experimental status and challenges is given below.

2.4.1   Beta Decay

Beta decay experiments investigate the endpoint of a beta spectrum in order to see a distortion due to massive neutrinos. The spectral form of allowed beta decays is well described. The maximum beta energy reaches up to the Q-value[10] of the decay in case of massless neutrinos. For a non-zero neutrino mass eigenstate m_1, the endpoint is reduced to $Q_\beta - m_1 c$. In case of multiple non-zero mass eigenstates, the measured beta spectrum is a weighted superposition of all the electron neutrino mass eigenstate spectra $Q_\beta - m_i$. This

---

[10]The energy available for the transition.

manifests in a steplike structure around the endpoint. However, the resolution of present experiments is far from resolving energy differences around the Δm_{ij}^2 and the analysis is reduced to a search for spectral distortions.

A distortion around the endpoint by neutrino masses is more easily visible with lower endpoints i.e. with beta decay isotopes that have a small Q-value. Past experiments based on ^{3}H with a Q-value of 18.59 keV are MAINZ and TROITSK using large electromagnetic spectrometers to separate the electron energies close to the endpoint. Up to date MAINZ and TROITSK yield the best upper limit for the electron neutrino mass of $m_\beta < 2.3$ eV (95% C.L.) [15] and $m_\beta < 2.05$ eV (95% C.L.) [16]. A new ^{3}H experiment is KATRIN [17, 18] with an expected sensitivity of 350 meV for discovery ($5\,\sigma$) and 200 meV for an upper limit (90% C.L.). The size of the spectrometer and the intensity of the ^{3}H source pose severe logistical limits on a future increase of sensitivity with this approach.

A novel approach to measure m_β is pursued by ECHO [19] and HOLMS [20] using a $^{163}_{67}$Ho electron capture source with an endpoint of 2.8 keV. The source material is implanted directly onto Si detectors. Claimed sensitivity estimations go down to 100 meV. Yet another approach is the precise determination of ^{3}H decay electron energies with frequency measurements as proposed by Project8 [21]. Claimed sensitivity estimation go down to 50 meV.

These experiments are also sensitive to other neutrino mass eigenstates as e.g. a fourth sterile neutrino. Another recent idea [22] is the investigation of the cosmic neutrino background (CNB) which could accelerate endpoint electrons to $Q_\beta + m_{\mathrm{CNB}}$. However, this is not feasible with the sensitivity of current beta decay experiments.

Other kinematic limits on m_β can be obtained from time of flight (TOF) measurements. The best neutrino mass measurement from TOF comes from the supernova (SN) explosion SN1987a on February 23, 1987, which was seen by several neutrino detectors on earth. The distance of SN1987a is roughly 50 kpc or $1.65 \cdot 10^5$ lyr. For a sharp neutrino emission the different mass eigenstates are expected to arrive at different times. A time dependence was not observed and a SN model dependent upper limit of $5.7 - 5.8$ eV (95% C.L.) [23, 24] was set.

2.4.2 Cosmology

Neutrino masses affected the evolution of the universe in a variety of ways. They had an influence during the time of the photon decoupling from matter which can be observed in the cosmic microwave background (CMB) radiation. The temperature power spectrum of the CMB would show a larger main peak and shifted smaller peaks for larger neutrino masses. In the later evolution of the universe, the formation of large scale structures (LSS) was influences by trapping neutrinos in the gravitational wells of the LSS. The neutrinos free-streaming length decreases with increasing neutrino of mass. A small free-streaming length favors smaller structures which would otherwise be washed out by neutrinos that carry matter and energy outside the gravitational wells. The effect of the neutrino mass on the formation of LSS can be investigated by looking for baryonic acoustic oscillations (BAO), a typical length scale of structures in the universe. The observational data is based on large sky surveys. Future data will also include weak gravitational lensing as a probe of matter distribution in the universe.

The effect on the CMB and LSS is mainly independent on the individual mass eigenstates

and only the integral neutrino mass is considered in m_{cosm}. This cosmological sum is already constrained to $0.06\,\mathrm{eV} < m_{\mathrm{cosm}} < 7\,\mathrm{eV}$ by other arguments: Neutrino oscillation requires at least two mass eigenstates to be non-zero and sets the lower bound. Beta decay experiments find $m_\beta < 2.3\,\mathrm{eV}$ and set the upper bound for the maximum sum of all mass eigenstates. Cosmological fits reach bounds with $m_{\mathrm{cosm}} \leq 1.08\,\mathrm{eV}$ with Plank data and $m_{\mathrm{cosm}} \leq 0.32\,\mathrm{eV}$ with Plank and BAO data [25]. Neutrino properties are typically extracted from cosmological models via the neutrino density $\Omega_\nu h^2$ which is correlated with other model parameters. The neutrino mass limits dependent on the specific cosmological model.

Additional to the neutrino mass, also the number of neutrino flavors N_ν can be constrained by cosmology. Especially sensitive is the investigation of elemental abundancies in the Universe today which is dependent on the ratio of neutrons and protons after the big bang nucleosynthesis (BBN). The freeze out of the neutron-proton equilibrium and hence the following BBN dependents on the electron neutrino flavor.

2.4.3 Neutrinoless Double Beta Decay

The mass observable of neutrinoless double beta ($0\nu\beta\beta$) decay experiments is the mass of the light Majorana neutrino propagator $m_{\beta\beta}$. It should be noted that $0\nu\beta\beta$ decay requires lepton number violation (LNV) which may or may not be triggered by the Majorana neutrino propagator. If the decay is not dominantly triggered by Majorana neutrinos, it has in fact little to no sensitivity to the neutrino mass. Here only the mass observable is discussed. More information about double beta decays and other possible LNV processes is presented in the next chapter.

The light Majorana neutrino mass is the coherent sum of the electron neutrino mass eigenstates and can be unfolded as:

$$
\begin{aligned}
m_{\beta\beta} &= \left| \sum_i m_i U_{ei}^2 \right| \\
&= \left| m_1 |U_{e1}|^2 + m_2 |U_{e2}|^2 e^{i(\alpha_2 - \alpha_1)} + m_3 |U_{e3}|^2 e^{-i(\alpha_1 + 2\delta)} \right|.
\end{aligned}
\tag{2.14}
$$

$m_{\beta\beta}$ depends on the three complex phases δ, α_1 and α_2. In case of the normal mass ordering (see Fig. 2.1), the largest component of the electron neutrino is the smallest mass eigenstate m_1. In this case, a certain combination of the phases can cancel $m_{\beta\beta}$ to zero. In the inverted mass ordering the largest component of the electron neutrino is heavy and cannot be canceled by any combination of the complex phases. The complex sum of Eq. 2.14 is illustrated in Fig. 2.2 (left).

From Eq. 2.14 one can plot $m_{\beta\beta}$ versus the lightest mass eigenstates m_1. This parameter space is constrained by the mixing matrix U_{ei} and the Δm^2. The allowed regions are illustrated in Fig. 2.2 (right) for the inverse hierarchy (green) and the normal hierarchy (red). The solid lines denote the best fit values for U_{ei} and Δm^2. The shaded regions are the $3\,\sigma$ ranges of the oscillation parameters. The area between the solid lines are left unconstrained by the unknown complex phases. As mentioned, $m_{\beta\beta}$ is non-zero in all cases for the inverse ordering, whereas $m_{\beta\beta}$ can cancel to zero in case of the normal ordering.

Experimental results on $m_{\beta\beta}$ rely on the assumption that light Majorana neutrino exchange is the dominant process in $0\nu\beta\beta$. Furthermore the conversion from a measured half-life
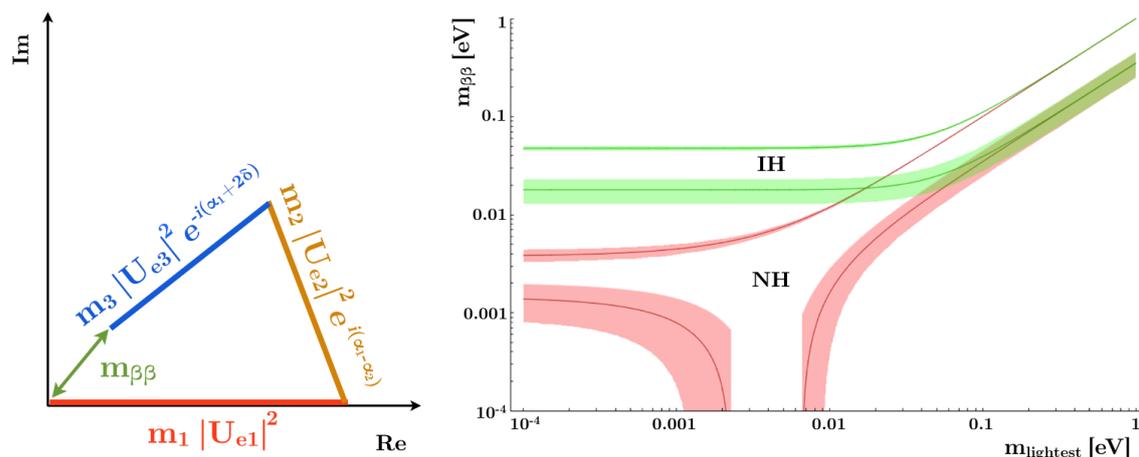
Figure 2.2 Left: Illustration of the terms in the definition of the light Majorana neutrino mass (Eq. 2.14) in the complex plane. The summation of the terms results in $m_{\beta\beta}$. In case of the inverse hierarchy structure, the ν_1 component (red) is large and the remaining terms cannot cancel to zero. In case of the normal hierarchy structure, the ν_1 component is small and for a certain combination of complex phases the terms can cancel to zero. Right: Parameter space of light Majorana neutrino mass versus lightest mass eigenstate. The allowed area for the inverse hierarchy is confined by the green solid lines whereas the allowed area in case of the normal hierarchy is confined by the red solid lines. The extended areas are created by the complex phases. The green and red shaded area illustrates the uncertainty of the allowed regions due to uncertainties of oscillation parameters. Right plot adopted from [26].

to $m_{\beta\beta}$ requires nuclear model calculations which introduce large theoretical uncertainties. The best constrains come from $0\nu\beta\beta$ experiments investigating ^{76}Ge and ^{136}Xe and combined limits for theses isotopes reach $m_{\beta\beta} < 200 - 400\,\text{meV}$ depending on the nuclear model [27, 28].

2.4.4 Combined Information of Neutrino Mass Observables

A summary of current limits for the three accessible neutrino masses is shown in Tab. 2.3. Also shown are expectations for near future and far future sensitivities of such experiments.

Table 2.3 Current limits and future sensitivities of neutrino mass experiments. Also shown are the advantages and disadvantages of each approach.

neutrino mass	current eV	near future eV	far future eV	pro / con
m_β	< 2.3	< 0.2	< 0.1	model independent experimental limits
m_{cosm}	< 0.7	< 0.3	< 0.05	best hierarchy disrimination model dependent
$m_{\beta\beta}$	< 0.3	< 0.1	< 0.05	testing Majorana nature model and nuclear theory dependent

These three neutrino masses are correlated via Eq. 2.11 - 2.13. The correlations are shown in Fig. 2.3 for (a) $m_{\beta\beta}$ versus m_1, (b) $m_{\beta\beta}$ versus m_{cosm} and (c) $m_{\beta\beta}$ versus m_β. Plot (a) is a similar illustration as Fig. 2.2, here in a consistent set with (b) and (c). The dark regions
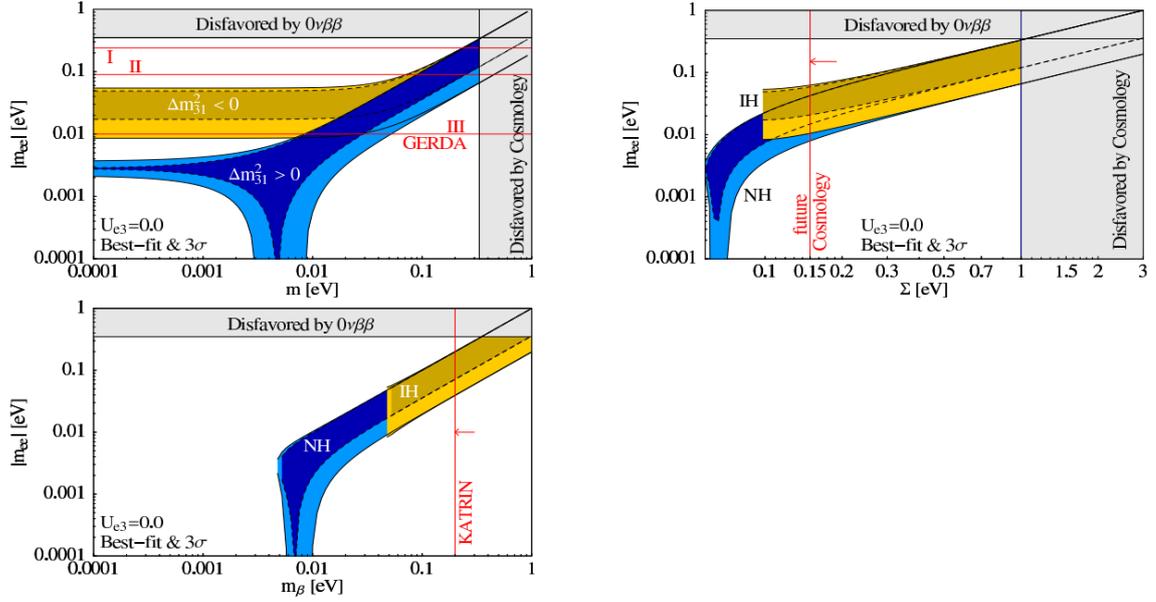
Figure 2.3 Complementarity of neutrino mass measurement. Shown is $m_{\beta\beta}$ versus m_1 (top left), $m_{\beta\beta}$ versus m_{cosm} (top right) and $m_{\beta\beta}$ versus m_β (bottom left). Yellow regions are allowed for the inverse and blue regions are allowed for the normal mass ordering. Dark colored regions are unconstrained by complex phases; light colored regions denote uncertainties from oscillation parameters. From [29].

are unconstrained by the complex phases whereas the light regions are uncertainties in the oscillation parameters. Yellow denotes the inverted mass ordering and blue the normal mass ordering. The following conclusions can be drawn:

- Parameter space (a) is constrained by m_{cosm} and m_β from the right via m_1. Currently stronger constrains come from cosmology. At a certain value of m_1 the inverse and normal ordering are completely separated for double beta decay (DBD) experiments.

- There is a minimal value for m_{cosm} and m_β due to the known mass splitting. $m_{\beta\beta}$ on the other hand can add up to zero due to the complex phases.

- m_{cosm} and m_β can directly exclude the inverse hierarchy scenario (plot (b) and (c) respectively). The required sensitivity is around $m_{\text{cosm}} = 0.1\,\text{eV}$ and $m_\beta = 0.05\,\text{eV}$,

- DBD experiments can exclude the inverted hierarchy at around $m_{\beta\beta} = 0.01\,\text{eV}$ but only if the $0\nu\beta\beta$ decay exists and the light Majorana neutrino mechanism are assumed. The strongest statement can be made if the manifestation of inverted hierarchy is determined beforehand and DBD experiments do not see a signal within the allowed range. Then the neutrino is very likely a Dirac particle.

The combination of these three experimental approaches together with input from neutrino oscillation experiments can disentangle all relevant neutrino parameters. In the current situation it is likely that oscillation experiments using matter effects will determine the hierarchy before neutrino mass experiments.

Chapter 3

Double Beta Decay

Double beta decays (DBD) are the rarest measured nuclear decays. The SM process of $2\nu\beta\beta$ decay is measured in more than 10 different isotopes with half-lives up to 10^{24} yr. The beyond SM process of $0\nu\beta\beta$ decay is a promising possibility to investigate lepton number violation (LNV) and the Majorana nature of neutrinos but is not discovered so far. Many DBD experiment are searching for this rare decay using a variety of experimental methods and isotopes in ultra low background environments.

This chapter is organized as follows: It starts with the nuclear physics conditions for DBD in Sec. 3.1 and then introduces the $2\nu\beta\beta$ decay in Sec. 3.2 and the $0\nu\beta\beta$ decay in Sec. 3.3. The LNV physics which can trigger $0\nu\beta\beta$ decay is discussed in Sec. 3.4 and the difficulties for calculating $2\nu\beta\beta$ and $0\nu\beta\beta$ half-lives in Sec. 3.5. Excited state transitions in DBD isotopes are the major focus of this thesis and are discussed in Sec. 3.6. Finally, an experimental overview is given in Sec. 3.7 including recently measured half-life limits for $0\nu\beta\beta$ decay, the current experiments and different experimental techniques.

3.1   Nuclear Physics Conditions

DBD is a second order weak nuclear decay process with extremely long half-lives. It can be experimentally observed in nuclear configurations in which two consecutive single beta decays are (1) energetically forbidden or (2) strongly suppressed. Condition (1) is illustrated in Fig. 3.1 for the $A = 76$ isobar. The binding energy is largest for the nuclide ^{76}Se with 34 protons and 42 neutrons. Other configurations with $A = 76$ have less binding energy. The alternating sequence of odd-odd and even-even proton and neutron numbers create two mass parabolas in which the odd-odd configurations are less strongly bound. For this reason ^{76}Ge cannot directly decay into ^{76}As and the observation of DBD in ^{76}Ge is experimentally possible. For condition (2) the single beta decay is strongly suppressed by spin configurations as e.g. in ^{48}Ca (0^+) and ^{48}Sc (6^+). Here the DBD of ^{48}Ca into ^{48}Ti (0^+) is more likely than the highly forbidden $0^+ \rightarrow 6^+$ single beta transition.

Conditions (1) and (2) are not strictly necessary for DBD to occur and merely prevent the experimental saturation by single beta decays. See for example [31] for searches in other isotopes without single beta decay suppression.
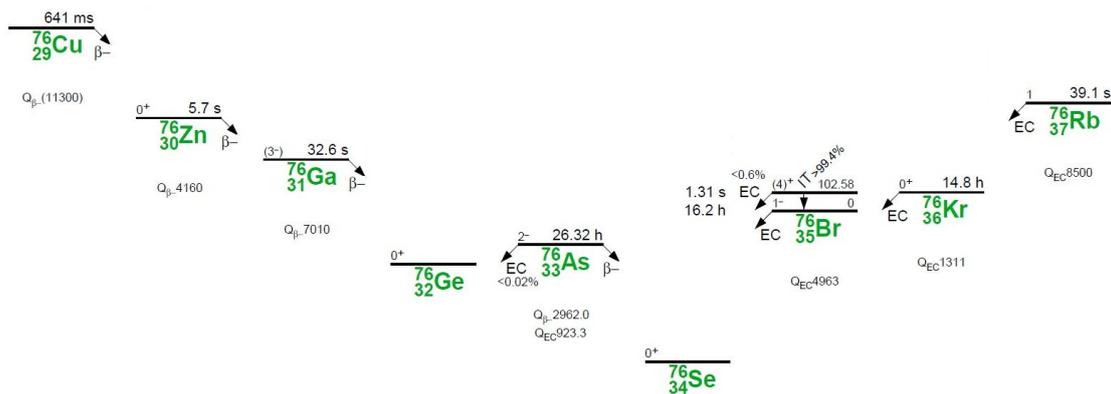
Figure 3.1 Mass parabola for isobar $A = 76$. The specific configuration of ^{76}Ge, ^{76}As and ^{76}Se prevents the single beta decay of ^{76}Ge and enables the observation of double beta decay. From [30].

3.2 $2\nu\beta\beta$: Two Neutrino Double Beta Decay

The $2\nu\beta\beta$ decay is described within the framework of the SM. The following decay modes are possible:

$$2\nu\beta^-\beta^- : \qquad\qquad (Z, A) \rightarrow (Z + 2, A) + e_1^- + e_2^- + \bar{\nu}_{e_1} + \bar{\nu}_{e_2}, \qquad (3.1)$$

$$2\nu\text{ECEC} : \qquad (Z, A) + e_1^- + e_2^- \rightarrow (Z - 2, A) + \nu_{e_1} + \nu_{e_2}, \qquad (3.2)$$

$$2\nu\text{EC}\beta^+ : \qquad\qquad (Z, A) + e^- \rightarrow (Z - 2, A) + e^+ + \nu_{e_1} + \nu_{e_2}, \qquad (3.3)$$

$$2\nu\beta^+\beta^+ : \qquad\qquad (Z, A) \rightarrow (Z - 2, A) + e_1^+ + e_2^+ + \nu_{e_1} + \nu_{e_2}, \qquad (3.4)$$

in which EC stands for electron capture. The experimental signature of the $2\nu\beta^-\beta^-$ decay mode is the energy deposition of the two electrons. The spectral shape of the sum electron energy can be approximated by [32]:

$$\frac{dN}{dE} \approx E(Q - E)^5[E^4 + 10E^3 + 40E^2 + 60E + 30]. \qquad (3.5)$$

(a) single and sum electron spectra

(b) angular correlation
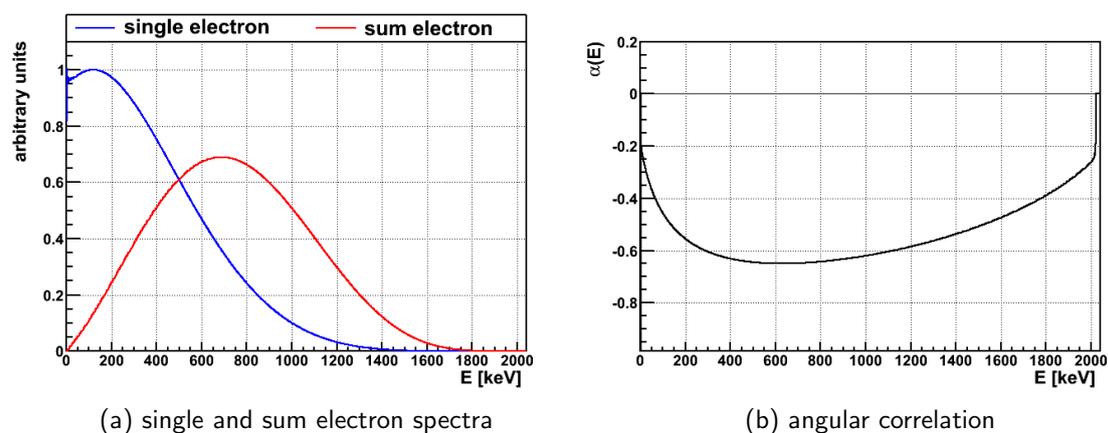
Figure 3.2 Decay properties of $2\nu\beta\beta$ in ^{76}Ge. Left: Energy spectra of single electron and sum of electrons. Right: Angular correlation $\alpha(E)$ between electrons. Plots created with data from [33, 34].

E is the electron energy and Q the Q-value of the decay. The rate is dominated by the highest order term in the polynomial and is therefore roughly proportional to E^{11}. More

detailed calculations of the single and sum energy spectra are performed by e.g. [33, 34] and illustrated in Fig. 3.2a. The electron sum energy peaks roughly at 1/3 of the Q-value. For a given single electron energy, the emission probability is proportional to $p \propto (1 + \alpha(E) \cdot \cos \theta)$ and is largest for an emission angle of $\theta = 180 \deg$. The angular correlation $\alpha(E)$ between the electrons is energy dependent and plotted in Fig. 3.2b. The correlation is weakest for small and large single electron energies and strongest for about $600 \, \mathrm{keV}$ in ^{76}Ge.

A total of 35 nuclides can decay via $2\nu\beta^-\beta^-$ in which the single beta decays are highly suppressed or forbidden (see Tab. A.1 in the appendix for a list). The decay has been directly observed in 9 nuclides (^{48}Ca, ^{76}Ge, ^{82}Se, ^{96}Zr, ^{100}Mo, ^{116}Cd, ^{130}Te, ^{136}Xe, ^{150}Nd) with half-lives between $10^{18} - 10^{24}$ yr [35, 36]. Additionally, two indirect observations have been made with geochemical experiments (^{128}Te, ^{238}U).

The 2νECEC, 2νECβ^+ and $2\nu\beta^+\beta^+$ decays are experimentally more difficult to detect. For the EC processes the major part of the released energy is taken by the neutrino and lost from the experimental setup. The capture of an electron is accompanied by atomic shell de-excitations and X-rays or Auger electrons of the daughter nucleus are emitted. For the 2νECEC process the decay energy is completely taken by the neutrinos and only the emission of X-rays can be detected directly. A total of 34 nuclides can decay via 2νECEC. The decay has only been observed indirectly[1] in two nuclides (^{130}Ba and ^{64}Zn). For the e^+ processes the available Q-value is reduced by $1022 \, \mathrm{keV}$ per e^+. This results in a reduced rate compared to the competing EC process and leaves 19 out of 34 nuclides with a large enough Q-value for 0νECβ^+. However, there are additionally two $511 \, \mathrm{keV}$ γ-rays per e^+ in the final state after annihilation which provide an experimental tag. For $2\nu\beta^+\beta^+$ the Q-value is reduced by $2044 \, \mathrm{keV}$ leaving only six known isotopes with sufficiently high decay energy for this mode (see Tab. A.3 in the appendix for a list).

3.3 0νββ: Neutrinoless Double Beta Decay

The neutrinoless mode of DBD requires LNV and has not yet been observed. The decay is triggered by a LNV propagator such that no neutrinos are present in the final state. The same decay modes as for $2\nu\beta\beta$ are possible:

$$0\nu\beta^-\beta^- : \qquad\qquad (Z, A) \to (Z + 2, A) + e_1^- + e_2^-, \qquad (3.6)$$

$$0\nu\text{ECEC} : \qquad (Z, A) + e_1^- + e_2^- \to (Z - 2, A), \qquad (3.7)$$

$$0\nu\text{EC}\beta^+ : \qquad (Z, A) + e^- \to (Z - 2, A) + e^+, \qquad (3.8)$$

$$0\nu\beta^+\beta^+ : \qquad\qquad (Z, A) \to (Z - 2, A) + e_1^+ + e_2^+. \qquad (3.9)$$

For $0\nu\beta^-\beta^-$, both final state electrons together carry the total energy released in the decay. Measuring these electrons together would result in a peak in the sum energy spectrum at the Q-value of the decay. Both electrons separately have an energy distribution that peaks at half the Q-value (Fig. 3.3a). Both electrons are most likely to be emitted back to back with the strongest angular correlations at also half the Q-value energy (Fig. 3.3b).

In the case of 0νECEC, there are no final state particles apart from the daughter nucleus and the two X-rays. There exist various theoretical models which describe the energy release in 0νECEC with e.g. e^+e^- pair emission, internal conversion or emissions of one or two γ-rays [6]. The latter two models are the so called radiative 0νECEC decay where

---

[1] The indirect observations with geochemical experiments are often disputed.

(a) single electron spectrum

(b) angular correlation
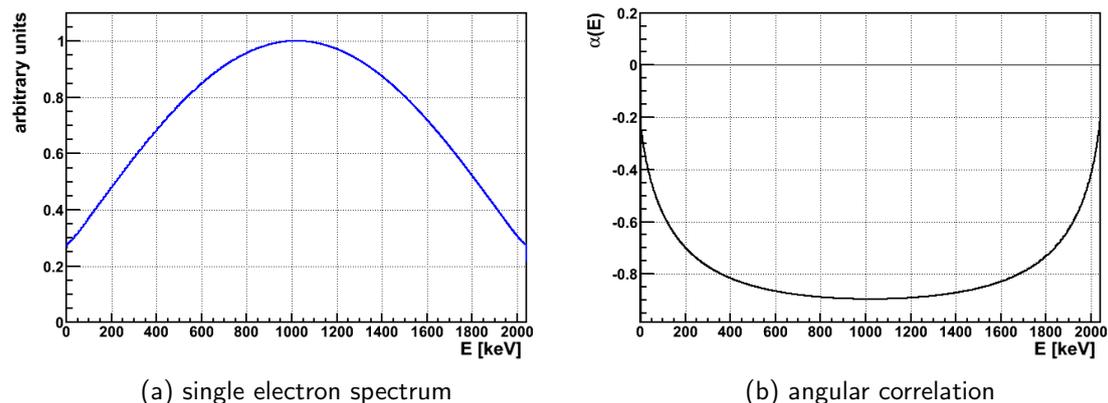
Figure 3.3 Decay properties of $0\nu\beta\beta$ in ^{76}Ge. Left: Energy spectra of single electron. Right: Angular correlation $\alpha(E)$ between electrons. Plots created with data from [33, 34].

the γ-rays results from Bremsstrahlung of the captured electron. The experimentally most accessible decay mode is the single γ-ray emission. In this case the emitted X-ray photons have to originate from different shells since in total three photons need to account for angular momentum conservation in the $0^+ \to 0^+$ transition. Thus the most probable signal for this decay will consist of three photons, one with a K-shell energy, one with an L-shell energy and one with $E_\gamma = Q - E_K - E_L$.

Another aspect of 0νECEC is a potential resonance enhancement of the decay rate if the ground state of the 0νECEC isotope is sufficiently equal in energy $\mathcal{O}(< 1\,\text{keV})$ to an excited state of the daughter isotope. The resonance enhancement could decreases the 0νECEC half-life by multiple orders of magnitude. Candidate isotopes are ^{124}Xe, ^{152}Gd, ^{156}Dy, ^{164}Er and ^{180}W. See e.g. [37] for more information.

3.4   Lepton Number Violation

Many LNV processes are proposed that could trigger the $0\nu\beta\beta$ decay. The standard interpretation is the exchange of a virtual light Majorana neutrino in which case the rate of $0\nu\beta\beta$ is proportional to the neutrino mass $m_{\beta\beta}$ as defined in Eq. 2.13. This is often called long-range mechanism.

Other Mechanisms of DBD   Beyond the standard interpretation are typically short-range mechanisms in which heavy particles are exchanged. These can be SUSY particles e.g. gluinos or squarks as well as right handed currents with heavy neutrinos or scalar fields as e.g. some form of Higgs particle. See Fig. 3.4 for Feynman diagrams of some processes. In the case of multiple mechanisms that compete on the same level of strength, the half-life of the decay is not anymore dominated by one process alone. It can be described as:

$$\left[T_{1/2}^{0\nu}\right]^{-1} = G^{0\nu}(Q, Z) \cdot \left| \sum_{\text{mech. } i} \mathcal{M}_i \cdot \eta_i \right|^2 . \tag{3.10}$$

Here $\mathcal{M}_i$ is the NME of the specific mechanism i and η_i the lepton number violating parameter. The sum over all mechanisms is a coherent sum so that in principle different mechanisms can interfere with each other.
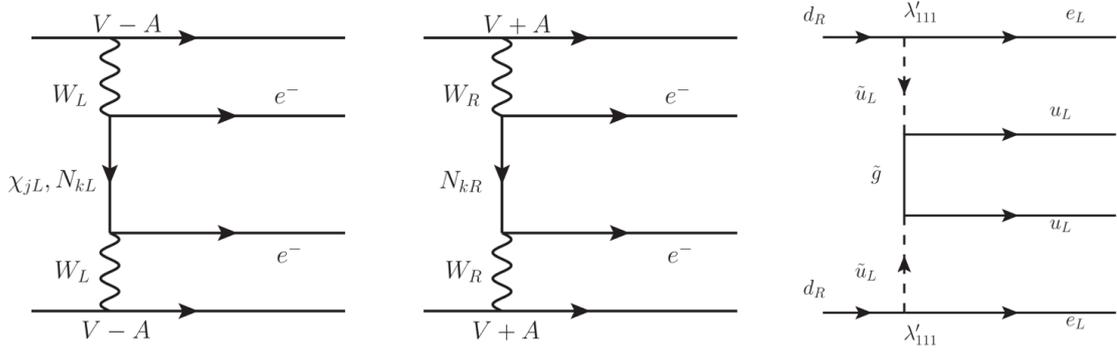
Figure 3.4 Example of possible processes contributing to $0\nu\beta\beta$ decay. Left: The exchange of a light Majorana neutrino χ_{jL} (standard process) or a heavy Majorana neutrino N_{kL}. Center: Heavy Majorana neutrino exchange with right handed charged currents W_R. Right: Gluino exchange and R-parity violation. From [38].

If a $0\nu\beta\beta$ half-life is measured it is not a priori clear which mechanism is responsible. However, a disentanglement can be perceived in two ways: (1) The measurement of $0\nu\beta\beta$ half-lives in multiple DBD isotopes or (2) constrains on other LNV processes using different experimental approaches. The first way is based on the difference of $\mathcal{M}_i$ and η_i for different DBD isotopes. Assuming good knowledge of the $\mathcal{M}_i$, Eq. 3.10 can be constrained with measurements of the half-life on i isotopes. Respectively more experimental information is needed in case the η_i are interfering. See [38] for a recent review. In the second way other particle physics experiments provide constrains on LNV. Chief among these is the LHC. Some authors argue that if $0\nu\beta\beta$ is discovered with half-lives around 10^{26-27} yr then a signal should be found at LHC for dominant short-range mechanisms [39]. In this case the dominating $0\nu\beta\beta$ mechanisms could be identified. This implies vice versa: If no signal is found at the LHC, then the dominant $0\nu\beta\beta$ process around these half-lives is likely not a short-range mechanisms. See e.g. [40] for a review.

Schechter Valle Theorem   Schechter and Valle showed in 1982 that the existence of $0\nu\beta\beta$ decay always implies a Majorana mass term for neutrinos. This is independent of the dominating LNV process triggering the decay. The argumentation is illustrated in Fig. 3.5. It can be understood as a rewriting of the $0\nu\beta\beta$ Feynman diagram in a way that creates a neutrino self interaction via the LNV process in the black box. However, other authors argue that if $0\nu\beta\beta$ decay is triggered by new LNV physics other than Majorana neutrino masses, then the induced Majorana masses by the Schechter Valle Theorem may be numerically extremely small [41]. The Majorana mass component could be orders of magnitude below the observed neutrino mass splitting and practically not contribute to the neutrino mass. De jure the neutrino would be a Majorana particle but de facto it would have a Dirac mass. If on the other hand the neutrino mass is dominantly of Majorana nature, the $0\nu\beta\beta$ rate would be dominated by light Majorana neutrino exchange [41].

In conclusion: The inference of a neutrino mass via $0\nu\beta\beta$ decay is not necessarily possible. Whether it is possible or not cannot be answered by $0\nu\beta\beta$ decay experiments alone. The major implication in case of discovery will be lepton number violation and new physics beyond the SM.
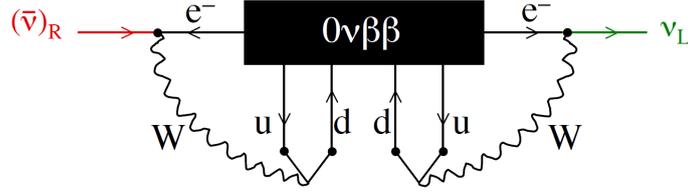
Figure 3.5 Illustration of the Schechter-Valle theorem: The existence of the $0\nu\beta\beta$ process implies the existence of Majorana mass terms for neutrinos.

3.5 Nuclear Matrix Elements and Phase Space Factors

The half-life $\left(T_{1/2}\right)$ or rate (Γ) of DBD decay modes can be calculated with Fermi's golden rule. This requires a matrix element describing the perturbation of the Hamilton operator between initial and final state and the density of final states. In the case of DBD, the matrix element is typically called nuclear matrix element (NME, $\mathcal{M}$) and the final state density is called phase space factor (PSF, F). The partial half-life of $2\nu\beta\beta$ can be directly calculated whereas the partial half-life of $0\nu\beta\beta$ requires the strength of an LNV parameter which is typically factored out of $\mathcal{M}$. In case of light Majorana neutrino exchange the LNV parameter is $m_{\beta\beta}$ and the half-lives are calculated as follows:

$$2\nu\beta\beta: \qquad \left[T_{1/2}^{2\nu}\right]^{-1} \ = \ \tfrac{1}{\ln 2}\Gamma^{2\nu} = \quad F^{2\nu} \cdot \left|\mathcal{M}^{2\nu}\right|^2 \qquad\qquad (3.11)$$

$$0\nu\beta\beta: \qquad \left[T_{1/2}^{0\nu}\right]^{-1} \ = \ \tfrac{1}{\ln 2}\Gamma^{0\nu} = \quad F^{0\nu} \cdot \left|\mathcal{M}^{0\nu}\right|^2 \cdot |m_{\beta\beta}|^2 \qquad (3.12)$$

Note that $\ln 2$ is condensed into F by convention.

3.5.1 Nuclear Matrix Elements

The NME for DBD can be described as usual matrix elements with $\langle f|H(p)|i\rangle$ in which $|i\rangle$ is the initial state wave function (ground state of the parent), $\langle f|$ the final state wave function (ground state of the daughter) and $H(p)$ the Hamiltonian which includes all possible excited states of the intermediate nucleus. The NME can be separated into a Fermi and a Gamow-Teller contribution[2].

$$\mathcal{M}^{0\nu} = g_A{}^2 \cdot \left(\mathcal{M}_{GT}^{0\nu} - \frac{g_V^2}{g_A^2}\mathcal{M}_F^{0\nu}\right). \qquad\qquad (3.13)$$

The Gamow-Teller term, $\mathcal{M}_{GT}^{0\nu}$, includes transitions over multiple excited states in the intermediate nucleus whereas the Fermi term, $\mathcal{M}_F^{0\nu}$, only includes 0^+ states. $2\nu\beta\beta$ decays have only a Gamow-Teller contribution since only the 1^+ states are allowed in the intermediate nucleus[3].

The Gamow-Teller strength of the individual legs of a DBD reaction (e.g. $^{76}_{32}\text{Ge}-^{76}_{33}\text{As}$ and $^{76}_{34}\text{Se}-^{76}_{33}\text{As}$) can be studied with charge-exchange reactions. The first leg transforms a

---

[2]A Fermi transition denotes a vector coupling without the exchange of spin; a Gamow-Teller transition denotes an axial-vector coupling with the exchange of spin ($\sigma\tau$-operator).

[3]Similar to a simple beta decay, the e^- and $\bar\nu$ carry away a total spin of 1. This spin is used in the 0^+ ground state of the parent to turn the spin of an initial proton into the opposite spin of the final neutron, leaving the final nucleus in a 1^+ state.

neutron into a proton, e.g. $^{76}Ge(p,n)^{76}As$, which is experimentally feasible with a $(^3He,t)$ reaction. The second leg transforms a proton into a neutron, e.g. $^{76}Se(n,p)^{76}As$, which is experimentally feasible with a $(d,^2He)$ reaction. This enables the experimental determination of the $2\nu\beta\beta$ decay NMEs. See e.g. [42] for more information.

The wave functions of DBD nuclides are composed of many nucleons $\mathcal{O}(100)$. They are too complex to be calculated exactly and various approximations have to be applied. Different approximations of nuclear structure and effective interactions are used in different nuclear models. The main approaches for DBD calculations are QRPA (Quasiparticle Random Phase Approximation) with its derivates RQRPA and pnQRPA, the ShM (Shell Model) and the IBM-2 (Interacting Boson Model). Other models are the HFB (Hartree-Fock Bogoljubov) model, the GCM (Generating Coordinate Method) and the EDF (Energy Density Functional). The QRPA is a collective model based on particle-hole and particle-particle interactions to which effective interactions strengths are applied. The ShM on the other hand is a microscopic model based on nuclear shells where each nucleon is bound by strong fields. Above complete shells, denoting magic numbers, the nucleon orbits are described by two body interactions. The ShM is limited to isotopes with small numbers of nucleons due to an increase of complexity solving the diagonalization problem for larger valence nucleon bases. The IBM-2 is based on nucleon pairs forming bosonic quasi particles similar to Cooper pairs in solid states. The particle interaction is bosonic and only applied for valence particles above closed shells. See e.g. [43] for a recent review.
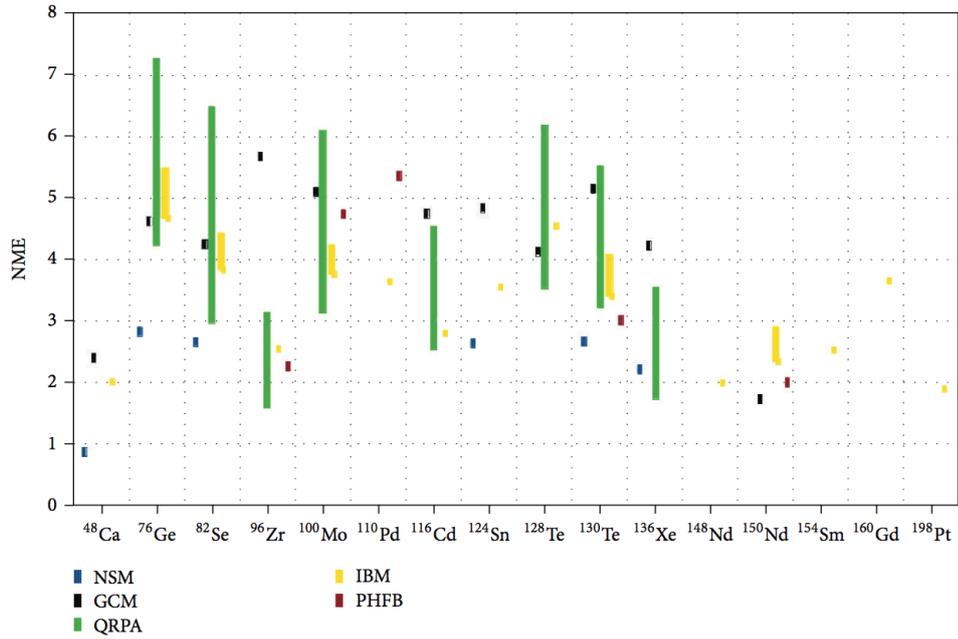
Figure 3.6 $0\nu\beta\beta$ decay nuclear matrix elements for major nuclear models and various DBD isotopes. See [43] for details on nuclear models and references therein.

The NME values for a given DBD isotope can vary strongly between the nuclear models. Fig. 3.6 shows a recent comparison of various models for different isotopes with differences up to a factor of 2. Note that the NME enters squared in Eq. 3.12 and hence changes the half-life prediction by up to a factor of 4. The differences in theoretical NME values are the largest uncertainty to convert a measured half-life into an effective Majorana neutrino mass.

Yet another source of uncertainty is the axial nucleon coupling, g_A, which is measured as $g_A = 1.25$ in vacuum but could as well be as different as $g_A \approx 1$ or even less in nuclear matter (see e.g. [44]). The g_A has a large impact on the half-life prediction entering to the power of 4. Comparisons between nuclear models should be done for the same values of g_A.

The $\mathcal{M}^{2\nu}$ and $\mathcal{M}^{0\nu}$ in the system of Eq. 3.11 and 3.12 are intrinsically and numerically different. However, the different nuclear model calculations are based on the same approximations and effective interactions in both cases. Experimental input on $2\nu\beta\beta$ can help to check and tune calculations for $0\nu\beta\beta$. Furthermore the correct prediction of the $2\nu\beta\beta$ rate increases confidence for $0\nu\beta\beta$ predictions.

3.5.2 Phase Space Factors

The PSF contains the available final state density and depends mainly on the Q-value of the decay. In first order $F^{0\nu}$ scales with E^5 whereas $F^{2\nu}$ scales with E^{11} with E being the total energy of rest mass (2x511 keV) and kinetic energy of the final state electrons (Q-value).

Recent calculations in [34] consider the exact Dirac wave functions, finite nuclear size, electron screening and electron angular correlation corrections. Fig. 3.7 shows the PSF for $2\nu\beta\beta$ and $0\nu\beta\beta$ for different isotopes.

(a) $2\nu\beta\beta$ decay (b) $0\nu\beta\beta$ decay
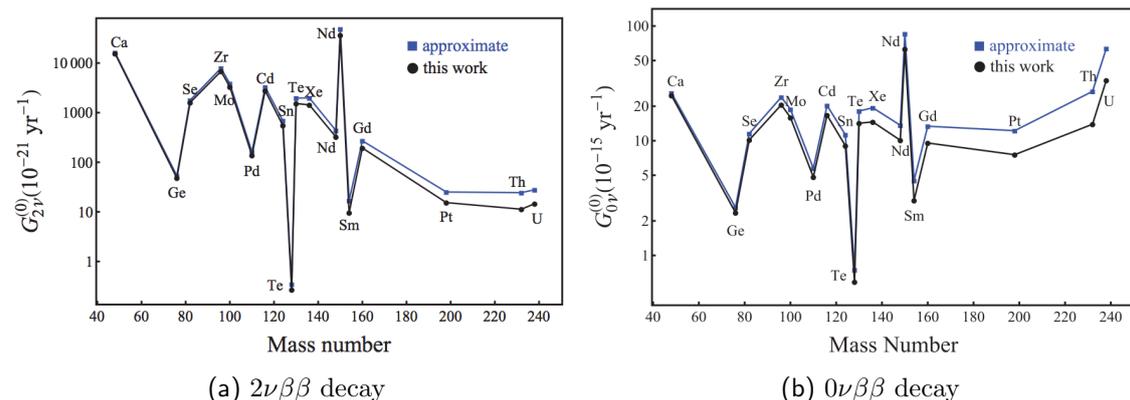
Figure 3.7 Phase space factors for different DBD isotopes. The two curves denote a calculation with an approximate wave function (blue squared markers) and with the exact Dirac electron wave function (black circular markers). From [34]; the label "this work" in the legends refers to the reference.

3.6 Excited State Transitions

Double beta decays can also occur into excited states of the daughter nucleus. In this case, the two electrons of the final state are accompanied by the prompt relaxation of the daughter with a γ-ray cascade. This provides an excellent experimental signature for searches. However, these decay modes have a significantly slower rate due to a smaller phase space. Furthermore, final states other than 0^+ are suppressed by spin combinations. The transition to the 0_1^+ excited state is typically expected to have the largest rate after the ground state transition and is thus experimentally the most interesting. In the specific nuclear configuration of DBD isotopes, the ground states of the mother and daughter isotope are 0^+ states. Typically, the first excited state in the daughter is a 2^+ state. Excited 0^+ states cannot directly relax into the $0_{g.s.}^+$ and must cascade via the 2^+ state while emitting two γ-rays. If there are more than one 2^+ state below the first 0^+ state, multiple decay

branches exist for the same decay mode. This segments the experimental signature and reduces the sensitivity for detection. The energy level for the 0_1^+ and 2_1^+ states in selected DBD isotope daughters is shown in Tab. A.4 in the appendix. Illustration of the final states relevant for this thesis are shown in Fig. 10.1 for ^{76}Ge, in Fig. 11.1 for ^{110}Pd and in Fig. 11.2 for ^{102}Pd.

Excited state transitions can in principle occur in the $2\nu\beta\beta$ and the $0\nu\beta\beta$ domain with a difference only in the residual electron energy. $2\nu\beta\beta$ excited state transitions can provide valuable experimental input for NME calculations extending the system of Eq. (3.11,3.12). The $2\nu\beta\beta$ 0_1^+ excited state transition has been observed within ^{100}Mo in 1995 [45] and within ^{150}Nd in 2004 [46]. The latest half-life values are $T_{1/2} = (7.5 \pm 1.2) \cdot 10^{20}$ yr [47] and $T_{1/2} = (1.33^{+0.63}_{-0.36}) \cdot 10^{20}$ yr [48], respectively.

The half-life for $2\nu\beta\beta$ excited state transitions can be calculated directly via Eq. 3.11. Various direct calculations have been performed in the past which are, however, largely older than 10 years. An alternative is to use the ratio of NMEs and PSFs for the excited state (e.s.) and ground state (g.s.) transition and scale that ratio with the measured $2\nu\beta\beta$ ground state half-life:

$$T_{1/2}^{\text{e.s.}} = \frac{[\mathcal{M}_{\text{g.s.}}]^2 \cdot F_{\text{g.s.}}}{[\mathcal{M}_{\text{e.s.}}]^2 \cdot F_{\text{e.s.}}} \cdot T_{1/2}^{\text{g.s.}} \,. \tag{3.14}$$

The ratio of NMEs has the advantage that some theoretical uncertainty cancel out and the excited state half-life prediction becomes more reliable. Especially the strong dependance on g_A is removed in the ratio. This approach can be used with a systematical and intra-comparable calculation of NMEs as is e.g. performed with IBM-2 model in [49].

Tab. 3.1 shows the current situation of measured $2\nu\beta\beta$ decay excited state half-lives and selected prediction for prominent DBD isotopes. The second and third column show the measured values and limits for the $2\nu\beta\beta$ $0_{\text{g.s.}}^+$ and 0_1^+ transitions. The third and fourth column show a list of direct calculations for the 0_1^+ transition using QRPA. The predictions in the last column are calculated using the ratio in Eq. 3.14 with NMEs from [49], PSFs from [34] and $T_{1/2}^{\text{g.s.}}$ from column 2. The theoretical predictions from QRPA and IBM-2 often disagree strongly. The tendency is that IBM-2 predicts longer half-lives. Many of the older QRPA predictions are ruled out by recent experimental limits. Most IBM-2 predictions are still beyond the current experimental sensitivity.

It is particular interesting to look at the two cases of ^{100}Mo and ^{150}Nd in which the measured $0_{\text{g.s.}}^+$ and 0_1^+ half-life values can be directly compared to the models. The IBM-2 half-lives do not describe the experimental observation. In fact the predictions for the 0_1^+ transitions are a factor of 37 and 14 larger than the observed half-life in ^{100}Mo and ^{150}Nd, respectively. This would suggest that experimental observations could be feasible below the larger IBM-2 predictions. A recent idea to explain this deficiency are intermediate scissor states which could potentially increase the rate of 0_1^+ compared the $0_{\text{g.s.}}^+$ transitions. The argument is based on the deformation of the nucleus during the decay which can be larger for the ground state transition due to the larger energy transfer compared to the excited state transitions. Such a behavior has been shown for ^{154}Gd in [67] and further conclusions are expected for ^{150}Nd.

Table 3.1 Current data for excited state transitions. Shown are observed half-lives or half-life limits of the ground state and 0_1^+ transitions. The last two columns show selected theoretical predictions from the QRPA and the IBM-2 models. The selection is not exhaustive and based on publications quoting predictions for multiple isotopes such that the values are comparable. In the case of IBM-2, the ratio of NMEs and PSFs for the $0_{g.s.}^+$ and 0_1^+ transitions [34, 49] are scaled with the observed half-life $0_{g.s.}^+$ quoted in column 2 to obtain the half-life for 0_1^+ as described in the text.

Transition $2\nu\beta\beta$	$0_{g.s.}^+$ exp $T_{1/2}$ [yr]	0_1^+ exp $T_{1/2}$ [yr]	0_1^+ QRPA $T_{1/2}$ [yr]	0_1^+ IBM-2 $T_{1/2}$ [yr]
$^{48}_{20}\text{Ca} \to {}^{48}_{20}\text{Ti}$	$4.4^{+0.6}_{-0.5} \cdot 10^{19}$ ^{a} [50]	$> 1.5 \cdot 10^{20}$ [51]	—	$1.8 \cdot 10^{23}$
$^{76}_{32}\text{Ge} \to {}^{76}_{34}\text{Se}$	$1.926 \pm 0.094 \cdot 10^{21}$ [52]	$> 6.2 \cdot 10^{21}$ [53]	$(7.5 - 310) \cdot 10^{21}$ [54, 55, 56]	$6.0 \cdot 10^{24}$
$^{82}_{34}\text{Se} \to {}^{82}_{36}\text{Kr}$	$9.2 \pm 0.7 \cdot 10^{19}$ [50]^a	$> 3.0 \cdot 10^{21}$ [57]	$(1.5 - 3.3) \cdot 10^{21}$ [54, 55]	—
$^{96}_{40}\text{Zr} \to {}^{96}_{42}\text{Mo}$	$2.3 \pm 0.2 \cdot 10^{19}$ [50]^a	$> 6.8 \cdot 10^{19}$ [58]	$(2.4 - 3.8) \cdot 10^{21}$ [55, 56]	$2.8 \cdot 10^{24}$
$^{100}_{42}\text{Mo} \to {}^{100}_{44}\text{Ru}$	$7.1 \pm 0.4 \cdot 10^{18}$ [50]^a	$= 5.9^{+0.8}_{-0.6} \cdot 10^{20}$ [50]^a	$1.6 - 2.1 \cdot 10^{21}$ [59, 56]	$2.2 \cdot 10^{22}$
$^{110}_{46}\text{Pd} \to {}^{110}_{48}\text{Cd}$	$> 1 \cdot 10^{17}$ [60]	$> 2.0 \cdot 10^{20}$ [61]	$(4.2 - 9.1) \cdot 10^{23}$ [62]	$> 1.1 \cdot 10^{22}$
$^{116}_{48}\text{Cd} \to {}^{116}_{50}\text{Sn}$	$2.8 \pm 0.2 \cdot 10^{19}$ [50]^a	$> 2.0 \cdot 10^{21}$ [63]	$(1.1 - 11) \cdot 10^{21}$ [54, 56]	$6.4 \cdot 10^{23}$
$^{130}_{52}\text{Te} \to {}^{130}_{54}\text{Xe}$	$6.8^{+1.2}_{-1.1} \cdot 10^{20}$ [50]^a	$> 1.3 \cdot 10^{23}$ [64]	$(3.3 - 7.1) \cdot 10^{20}$ [54, 55] ^{b}	$2.2 \cdot 10^{25}$
$^{136}_{54}\text{Xe} \to {}^{136}_{56}\text{Ba}$	$2.29 \pm 0.08 \cdot 10^{21}$ ^{b}	$> 1.2 \cdot 10^{23}$ [65]	$(2.5 - 6.3) \cdot 10^{21}$ [54, 56]	$2.6 \cdot 10^{25}$
$^{150}_{60}\text{Nd} \to {}^{150}_{62}\text{Sm}$	$8.2 \pm 0.9 \cdot 10^{18}$ [50]^a	$= 1.33^{+0.45}_{-0.26} \cdot 10^{20}$ [50]^a	—	$1.9 \cdot 10^{21}$

^{a} world average values
^{b} corrected in [66]

3.7 Experimental Overview

3.7.1 Recent Results

The most competitive recent results on $0\nu\beta\beta$ decay come from the KamLAND-Zen, EXO-200 and GERDA experiments. The achieved half-live limits (90 % C.L.) and neutrino mass limits according to IBM-2 [49] are listed below.

- KamLAND-Zen (^{136}Xe): $T_{1/2} > 1.9 \cdot 10^{25}$ yr corresponding to $m_{\beta\beta} < 0.18$ eV [68]

- EXO-200 (^{136}Xe): $T_{1/2} > 1.1 \cdot 10^{25}$ yr corresponding to $m_{\beta\beta} < 0.24$ eV [28]

- GERDA (^{76}Ge): $T_{1/2} > 2.1 \cdot 10^{25}$ yr corresponding to $m_{\beta\beta} < 0.26$ eV [27]

3.7.2 Claim of Discovery

In 2002 a claim of evidence for $0\nu\beta\beta$ decay in ^{76}Ge was made by a subgroup of the Heidelberg-Moscow (HdM) experiment [69]. The claim was strengthened in 2004 with $4.2\,\sigma$ confidence level reporting a half-live of $T_{1/2}^{0\nu} = 1.19^{+0.37}_{-0.23} \cdot 10^{25}$ yr [70]. A later publication in 2006 [71], further strengthening the claim, has methodical inconsistencies as argued in [72]; hence the 2004 value is taken as reference.

The claim of evidence was recently scrutinized by the GERDA experiment and rejected with > 99 % probability. The combination with data from other ^{76}Ge experiments results in an even stronger rejection. The scrutinization by GERDA and other ^{76}Ge experiments is independent of theoretical assumptions and done on the half-life level of ^{76}Ge (see Sec. 5.5.3 for detailed results).

Results from the ^{136}Xe based experiments EXO-200 and KamLAND-ZEN also disfavor the claim for most NME calculations going via the neutrino mass level and assuming light Majorana neutrino exchange. This is illustrated in Fig. 3.8. The half-lives for ^{136}Xe and ^{76}Ge are shown on the x and y axes, respectively. The conversion is performed via the

lines for different NME calculations. The half-life values for 0.2, 0.3 and 0.4 eV effective Majorana neutrino mass are shown as blue, magenta and red markers respectively. The claim [70] is shown as a green band. The combined ^{136}Xe half-live is excluding the claim with $> 97.5\,\%$ C.I. even for the most unfavorable NME calculation [73].
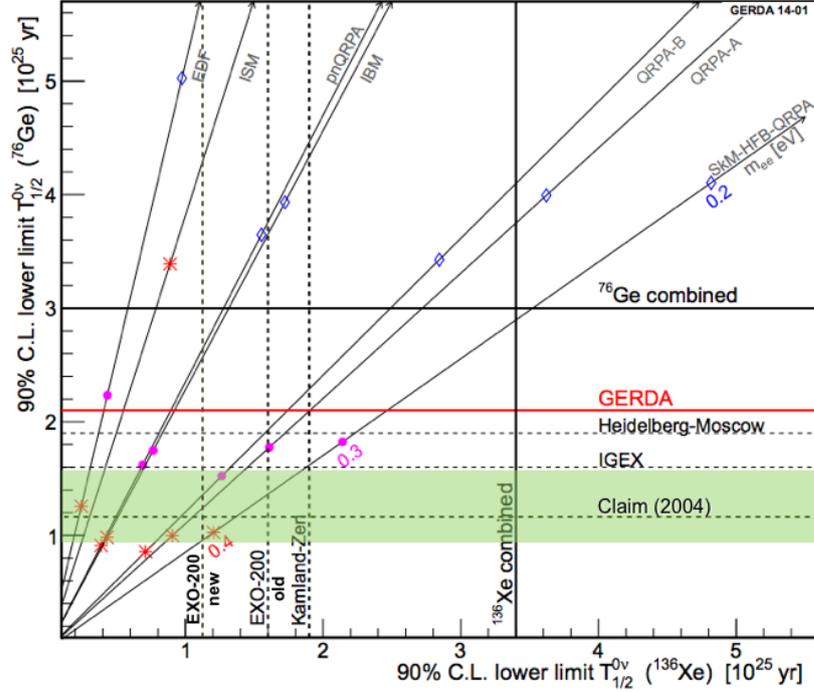
Figure 3.8 Comparison of recent results in ^{136}Xe [73] [74] [75] and ^{76}Ge [27]. The diagonal lines show half-life conversions for various NME calculations: EDF [76], ISM [77], IBM [49], pnQRPA [78], QRPA [79] and SkM-HFB-QRPA [80]. The markers denote the calculated half-lives for a Majorana neutrino mass of 0.2, 0.3 and 0.4 eV in blue diamonds, magenta points and red stars respectively. The green band shows the 2004 claim [70] with 68 % C.L. error band. From [81].

3.7.3 Experimental Sensitivity

The sensitivity of DBD experiments is often used to compare different experiments and techniques. It is typically determined by the expected number of DBD events (n_s), the efficiency to detect them (ε) and the expected number of background events (n_b). The measuring time (T) is much shorter than the DBD half-life $T << T_{1/2}$ and n_s is given by:

$$n_s = \varepsilon \cdot \frac{f \cdot M \cdot N_A}{m_A} \cdot \frac{\ln 2 \cdot T}{T_{1/2}}. \tag{3.15}$$

Here, f is the isotopic abundance and m_A is the molar mass of the DBD isotope. M is the mass of the target material and N_A is the Avogadro number. In the **regime of no background** the half-life is given by

$$T_{1/2} = \varepsilon \cdot \frac{f \cdot M \cdot N_A}{m_A} \cdot \ln 2 \cdot T \cdot \frac{1}{N_s} \tag{3.16}$$

and scales linear with M and T and inverse with the number of observed events N_s. The background in DBD experiments can be quantified with a background index (BI) defined

in units of $\text{cts}/(\text{kg} \cdot \text{yr} \cdot \text{keV})$. The background counts are often simply assumed to follow a flat distribution and scale with M and T

$$n_B = \text{BI} \cdot M \cdot T \cdot \Delta E, \tag{3.17}$$

with the energy resolution ΔE to account for the definition of BI^4. In the **regime of Gaussian background** (> 10 events), the sensitivity is then defined as a $1\,\sigma$ upwards fluctuation of n_B that would be interpreted as a signal $N_s = \sqrt{N_b}$. The $1\,\sigma$ half-life sensitivity is then given by

$$T_{1/2} = \varepsilon \cdot \frac{f \cdot N_A}{m_A} \cdot \ln 2 \cdot \sqrt{\frac{M \cdot T}{\text{BI} \cdot \Delta E}}. \tag{3.18}$$

Current DBD experiments typically operate in a Poisson background regime in which the approximations in Eq. 3.18 do not hold. However, Eq. 3.18 contains many important parameters that can be used to compare DBD experiments. Economic considerations can be applied to some of the physical properties.

Detection efficiency ε It scales linearly with $T_{1/2}$ and depends strongly on the experimental technique. Typically it can be further separated into an active or fiducial volume fraction, and into individual cut efficiencies.

Isotopic abundance f The DBD isotopes of major interest have natural abundancies between $0.2\,\%$ for ^{48}Ca and $34\,\%$ for ^{130}Te. The background typically scales with the elemental target mass and a higher abundance results in more isotopic target for the same background. Isotopic enrichment is often used to increase the abundance but comes at large costs that is strongly dependent on the isotope.

Target mass M An increase in target mass typically comes with a similar increase in cost. Very large masses of rare elements are also constrained by world production. With increasing target mass the background can be further reduced due to self-shielding in single volume experiments or anti-coincidences in modular experiments.

Measuring time T Experimental time scales are often constrained by funding. The largest increase in sensitivity occurs in the beginning of an experiment due to the square root dependence in Eq. 3.18. Another important temporal aspect is the crossing of the no background regime (linear increase of sensitivity) into a Poisson or Gaussian background regime (square root increase of sensitivity).

Background index BI The background level of an experiment is paramount for its sensitivity. In the Gaussian regime of Eq. 3.18, a factor of 2 improvement in BI is equivalent to a factor 2 reduction in target mass which is typically the dominating economical cost. The BI strongly depends on the experimental technique. Typically the BI can be improved with a reduction of the detection efficiency by additional cuts or by selecting a smaller fiducial volume in the center of the detector which is screened from outside radiation. This trade off can be optimized to the experimental situation. The various sources of background radiation are described in Sec. 4.4. The further reduction of background levels in future experiments will enter new background domains with potentially yet unknown background contributions. A natural irreducible background limit for $0\nu\beta\beta$ decay experiments are solar neutrinos at an estimated BI of $10^{-7}\,\text{cts}/(\text{kg} \cdot \text{yr} \cdot \text{keV})$ [82].

---

[4] The ΔE typically covers only a fraction of the Gaussian peak as e.g. a full width at half maximum (FWHM) or $\pm\sigma_E$. In this case the efficiency should be reduced by this fraction which is however often ignored.

Energy resolution ΔE A larger size of the energy window for $0\nu\beta\beta$ events increases the total background assuming the same BI. So BI and ΔE ought to be compared together. A poor energy resolution introduces the issue of $2\nu\beta\beta$ events leaking into the peak region of $0\nu\beta\beta$. This becomes an irreducible background for some experiments. An epistemological argument is the discovery credibility of experiments with poor energy resolution: If an excess of events is visible in the $0\nu\beta\beta$ peak region it is more difficult to exclude the possibility of unknown background contributions with poor resolution than with good resolution. Experiments with poor energy resolution strongly depend on the correctness of their background model which is difficult to achieve given the fact of unprecedented low background levels and potentially unknown contributions. This aspect is difficult to quantify for comparison.

The above aspects are experimental parameters that are optimizing the half-life sensitivity of an experiment. However, the $0\nu\beta\beta$ process is trigged by underlying LNV physics with different strength in different isotopes. The expected half-life is thus also depending on the NME and the PSF (see Sec. 3.5).

3.7.4 Overview of Current Experiments and Techniques
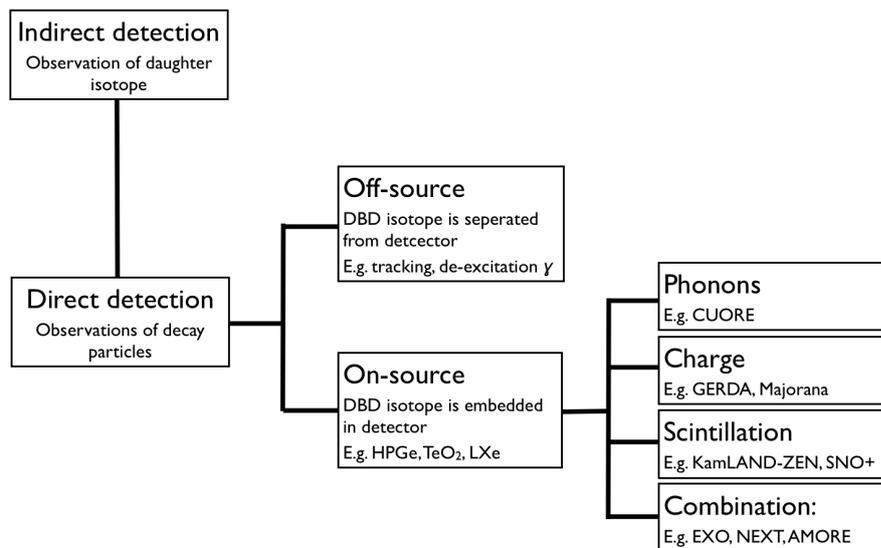
Figure 3.9 Taxonomy of DBD experiments. The major part of current experiments aim for direct observation of the decay from an isotope that is embedded in the detector material. The detection principle is based on charge, phonons, scintillation or a combination of these.

Various experimental techniques are utilized to investigate DBD. A possible taxonomy of DBD experiments is shown in Fig. 3.9. A first distinction is made between **direct and indirect** approaches. The first observation[5] of DBD was done with an indirect measurement of ^{130}Te in 1950 [83]. The isotopic abundance of the daughter isotope ^{130}Xe is significantly altered in a geological samples due to DBD. The samples not only have to be well chosen and understood, but also have to exist for a long enough time so that an effect can be observed. No information on the decay mode can be obtained such as $2\nu\beta\beta$ or $0\nu\beta\beta$ and ground state or excited state transitions. The inferred half-life is the combination of all

---

[5]The first measurement of a DBD isotope in which the quoted half-life was in agreement with later results. Earlier measurements were performed with claimed observation but the results could not be confirmed.

modes. Direct searches, on the other hand, aim to see the decay products of the DBD in real time. This is the most common approach used nowadays to search for DBD.

Direct detections can be further divided into the **on-source and off-source** approaches. In the on-source experiments the DBD target isotope is embedded into the detector material. This can be in the form of a naturally occurring isotope in a detector material such as ^{76}Ge in HPGe detectors or ^{136}Xe in LXe scintillation detectors. It can also be achieved artificially while mixing a DBD isotope / element into a solid or liquid scintillator. The energy of the two electrons is measured by calorimetry inside the detector material. The main advantage is a large possible target volume and a good detection efficiency. In the off-source approach the DBD electrons are detected externally to the source material. This can be done by tracking and allows to determine the angle between the electrons. The main advantage of this approach is a good topological distinction between DBD and background events and allows for large background suppression.
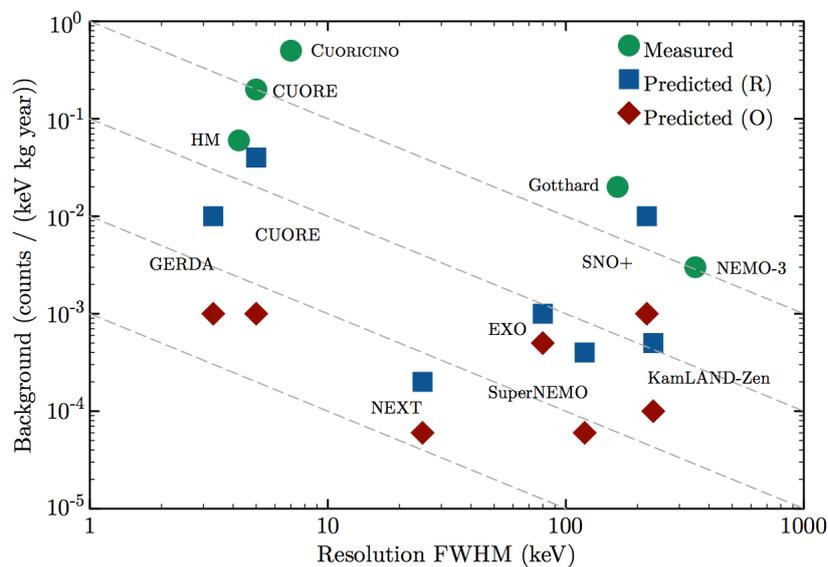
Figure 3.10 Comparisons of experiments with BI versus ΔE. Off-diagonal lines denote equal sensitivity for BI $\cdot \Delta E$. Two populations of experiments are visible: Solid state detectors with high energy resolution and larger BI and large volume detectors with poorer energy resolution but smaller BI. Green circles denote past experiments as of 2012. Current experiments are depicted in blue squares for realistic predictions and in red diamonds for optimistic prediction. From [84].

The calorimetric energy measurement of the DBD electrons in the on-source detectors can be done in various ways: Measurement of **phonons, charge, scintillation light or a combination of them**. The advantage of measuring ionization or phonons in solid state detectors is a good energy resolution since almost all information is collected. In scintillating materials, a significant amount of photons can be lost which typically results in reduced energy resolution. A combination of different signals can be used to differentiate certain forms of radiation. Such a combination of signals is state of the art in dark matter experiments and is currently pioneered with AMORE [85] and LUCIFER [86] for DBD. Here the idea is to use scintillating bolometric crystals and acquire simultaneously phonon and light information. A different combination of charge and scintillation is already used with a LXe TPC in EXO and will be used in a GXe TPC in NEXT.

Apart from achieving a large target mass, the major benchmark of technological approaches are the background index and the energy resolution. The product of both is a figure of merit for the sensitivity[6] (see Eq. 3.18). Both parameters are plotted against each other in Fig. 3.10 for past and current DBD experiments. The off-diagonal dashed lines show equal sensitivity if all other secondary parameters in Eq. 3.18 are kept similar. Two population of DBD experiments are visible: (1) Solid state detectors with high energy resolution but larger BI as e.g. GERDA and CUORE and (2) large volume detectors with poor energy resolution but smaller BI as e.g. SNO+ and KamLAND-Zen. Note that the advantage of a large target mass is not represented in this plot.

Table 3.2 Major current and near future DBD experiments. Information taken from [43, 85], references therein and the experimental websites. The columns denote the experiment, the DBD nuclide, the experimental technique, the effectively used isotopic mass of the DBD nuclide, the energy resolution in FWHM at the Q-value, the background index in $\mathrm{cts}/(\mathrm{kg}\cdot\mathrm{yr}\cdot\mathrm{keV})$ and the location of the experiment. The underground laboratories are presented in Tab. 4.2.

experiment	DBD isotope	method	isotopic mass [kg]	ΔE FWHM [keV]	BI $10^{-3}\,\mathrm{cts}/(\mathrm{kg}\cdot\mathrm{yr}\cdot\mathrm{keV})$	location
			Running experiments			
KamLAND-ZEN	^{136}Xe	scint.	179 kg	240	0.15	Kamioka
EXO-200	^{136}Xe	LXe TPC	79 kg	96	1.1	WIPP
GERDA I/II	^{76}Ge	ioni.	11/30 kg	4	10/1	LNGS
			Experiments in construction			
CUORE	^{130}Te	bolom.	206 kg	5	10	LNGS
Majorana	^{76}Ge	ioni.	26 kg	4	0.8	SURF
SNO+	^{130}Te	scint.	163 kg	240	0.3	SNOlab
NEXT-100	^{136}Xe	GXe TPC	90 kg	12.5	0.8	Canfranc
AMORE	^{100}Mo	bolom./scint.	50 kg	5	0.4	YangYang
SuperNemo	^{82}Se/^{150}Nd	track.	100 kg	120	0.5	LSM
CANDLES	^{48}Ca	scint.	350 g	N/A	N/A	Kamioka

A list of major current DBD experiments is given in Tab. 3.2. The list is separated into currently running experiments and experiments in construction. The table shows the target isotopes, the detection method, the usable isotopic mass, the energy resolution, the background level and the underground location. DBD experiments in the R&D phase are not listed.

3.7.5 Techniques for DBD Excited State Detection

The event topology with additional de-excitation γ-rays permits different experimental strategies. The three major approaches are illustrated in Fig. 3.11. Standard gamma spectroscopy with a HPGe detector (a) can be used to investigate a DBD sample. This approach is independent of the target isotope and the technology is well established for decades. In fact, gamma spectroscopy has been used for the only two observations of excited state transitions in ^{100}Mo and ^{150}Nd. The principle is the equivalent of an off-source experiment where only the γ-rays can be detected. Information on the $0\nu\beta\beta$ or $2\nu\beta\beta$ regime is lost with the electrons remaining in the source material. Quoted half-life limits are valid for both regimes. Gamma spectroscopy is used to investigate DBD excited state transitions in ^{102}Pd and ^{110}Pd in Chap. 11 of this work.

---

[6]This is valid in a Gaussian background regime and for an exclusion limit.

The physics case for excited state transitions in $2\nu\beta\beta$ decays does not create sufficient interest to construct larger dedicated experiments. The other two approaches (b) and (c) are using the target mass, detector system and infrastructure of larger scale $0\nu\beta\beta$ decay experiments. Those are often constructed with detector segmentation as e.g. in the case of GERDA and CUORE (b) or with large scale homogeneous detectors as in the case of e.g. EXO and NEXT (c). In case of (b) the segmentation can be used to tag real coincidences between detectors. This is e.g. done in CUORICINO [64] and in GERDA (Chap. 10 in this work). In combination with good energy resolution this allows for larger background discrimination. For homogeneous experiments (c) the multi-site topology has to be selected with pulse shape information which adds complexity to the analysis and typically does not allow for strong background discrimination. On the other hand, the target mass and detection efficiency is typically larger in homogeneous experiments. An analysis is performed for instance with EXO-200 data [65].
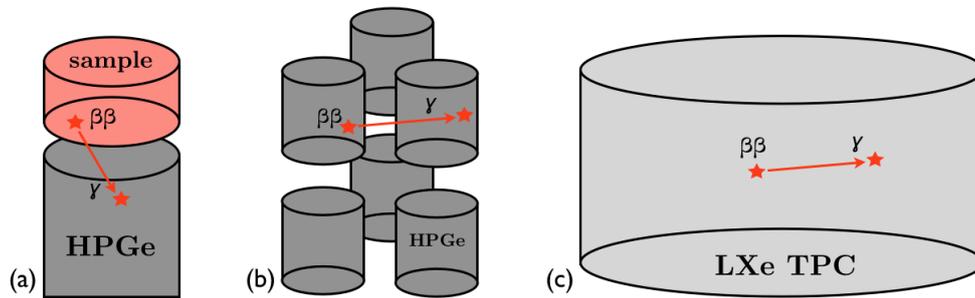
Figure 3.11 Three approaches for investigating excited state transitions. (a) Gamma spectroscopy of a DBD sample with a HPGe detector. Only the de-excitation γ-rays are detected and $2\nu\beta\beta$ and $0\nu\beta\beta$ modes cannot be distinguished. (b) Utilization of the detector segmentation of a large scale DBD experiment as e.g. GERDA. The electron and gamma components are measured in separate detectors and $2\nu\beta\beta$ and $0\nu\beta\beta$ modes can be distinguished. (c) Utilization of a large single volume DBD experiment as e.g. EXO-200. The separation between electron and gamma interaction is fuzzy and has to be done via pulse shapes.

Chapter 4

Particle Detection

The detection and precise energy measurement of elementary particles is essential for DBD experiments. Equally important is an ultra low background environment avoiding various sources of natural and anthropogenic radioactivity. Such an environment can only be realized in underground laboratories using a natural overburden for shielding against cosmic radiation.

This chapter is organized as follows: The fundamentally different interactions of α, β and γ radiation with matter are described in Sec. 4.1. The energy deposition of the particles can be measured with different detector technologies. The relevant detector systems for this work are germanium semiconductors and liquid argon (LAr) which are introduced in Sec. 4.2 and Sec. 4.3, respectively. The different forms of radioactive background are described in Sec. 4.4 and the relevant underground facilities in Sec. 4.5.

4.1 Interactions with Matter

Particle interactions with matter are important to understand for radiation detection and radiation shielding. The main interaction mechanism for γ-ray, electron, positron and alpha particles is the electromagnetic force acting on these particles. A measurable signal is created by charge separation in the case of HPGe detectors or the creation of optical scintillation photons in LAr.

Gamma interactions: γ-rays interact with matter by three main processes: (1) photoelectric effect, (2) incoherent scattering (Compton scattering) and (3) pair production. These processes have different energy dependencies and dominate the γ-ray interaction at different energies. This is illustrated in Fig. 4.1 for germanium. Fig. 4.1a shows the energy dependent mass attenuation coefficient μ for the three interaction processes. Fig. 4.1b shows the attenuation length d_0 for each process, which is defined as the distance after which the γ-ray interacted with a probability $p = 1 - \frac{1}{e}$. This is e.g. $1\,\text{mm}$ for $60\,\text{keV}$, $38\,\text{mm}$ for $1333\,\text{keV}$ and $51\,\text{mm}$ for $2614\,\text{keV}$ in germanium. The intensity loss of a γ-ray flux after a certain distance d can be calculated with the mass attenuation coefficient μ and the density of the material ρ:

$$\frac{I}{I_0} = e^{-\mu \cdot \rho \cdot d} \tag{4.1}$$

μ is mainly dependent on the atomic shell structure for low energies. The attenuation length is additionally dependent on the density of the material. Both quantities are shown

in Fig. 4.2 for various materials relevant in this work.

In all cases the initial γ-ray is transferring its energy to a fast electron which is then creating the measurable effect i.e. charge separation or scintillation. Thus, the γ-ray is a secondary ionizing particle. The individual interaction process are described in the following:

(a) mass attenuation versus energy

(b) attenuation length versus energy
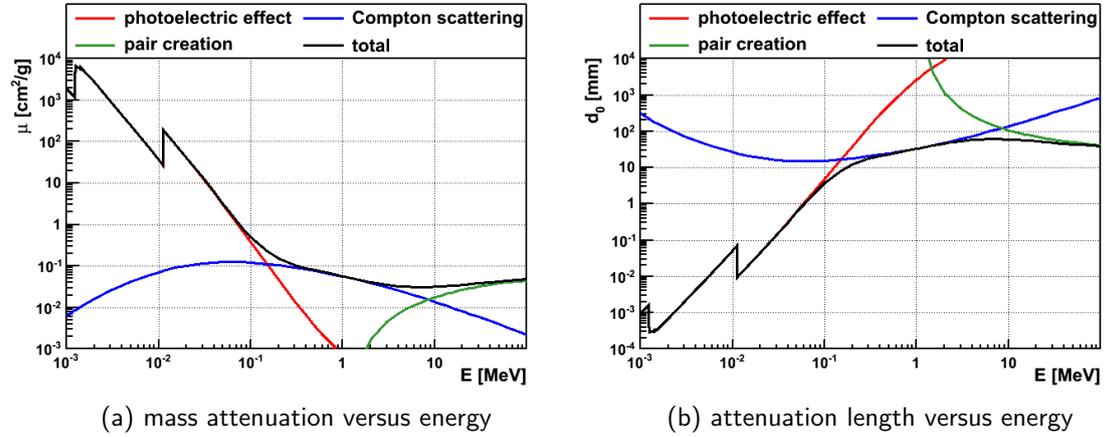
Figure 4.1 Left: Energy dependent γ-ray mass attenuation in germanium for different interaction processes. Right: Attenuation length in germanium and the contribution of different interaction processes. Plots created with data from [87].

(a) mass attenuation versus energy

(b) attenuation length versus energy
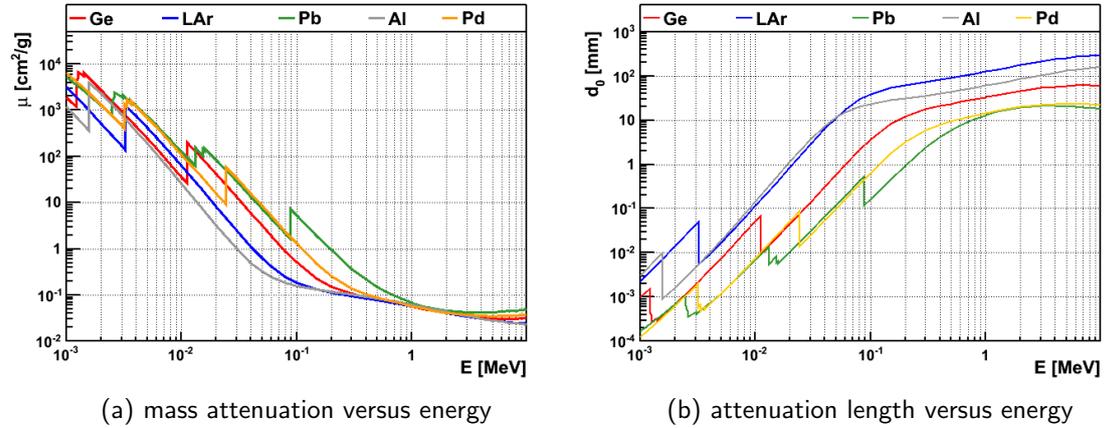
Figure 4.2 Left: Energy dependent total mass attenuation for γ-rays in different materials. Right: Attenuation length of the same materials in standard densities (natural elemental abundance; LAr at boiling point). Plots created with data from [87].

The photoelectric effect is a process in which the entire γ-ray energy E_γ is transferred to an electron. The process is dominating for small energies below $\approx 150\,\mathrm{keV}$ in germanium with an energy dependence of $\approx E^{-3.5}$. The dependence on the nuclear charge of different materials is $\approx Z^{4-5}$. The energy of the emitted electron E_e depends on the binding energy of the original electron in the atomic shell E_shell with $E_e = E_\gamma - E_\mathrm{shell}$. Interactions occur predominantly with the stronger bound K and L-shell electrons. The energy transfer creates holes at these shells which are rearranged by the emission of X-ray photons or Auger electrons. X-ray photons in germanium have energies of around $E_\mathrm{shell} = (9.9 - 11.0)\,\mathrm{keV}$ for the K-shell and $1.2\,\mathrm{keV}$ for the

L-shell and are subsequently absorbed via the photoelectric effect with lower bound shell electrons.

The incoherent scattering is the inelastic scattering of a γ-ray on an unbound electron. If there are no free electrons in the material, the scattering is mainly occurring on the loosely bound outer shell electrons. The energy dependence is $\approx E^{-2}$ and Compton scattering is dominating at energies between $\approx 150\,\text{keV}$ and $\approx 8\,\text{MeV}$ in germanium. The dependence on the nuclear charge is proportional to Z. The energy transfer and the interaction probability depend on the scattering angle between the incident and scattered photon. The energy transfer is largest for backscattering at $180\,\text{deg}$ and approaches zero for forward scattering at $0\,\text{deg}$. The angular distribution for a given incident γ-ray energy is described by the Klein-Nishina formula [88] and illustrated in Fig. 4.3. This polar plot of the angular distribution illustrates the high probability of forward scattering for larger γ-ray energies. Also visible is the suppression at $90\,\text{deg}$ scattering angles. A higher energetic γ-ray typically scatters once or multiple times until it is fully absorbed by the photoelectric effect. Thus, parts of the energy are deposited on multiple sites.
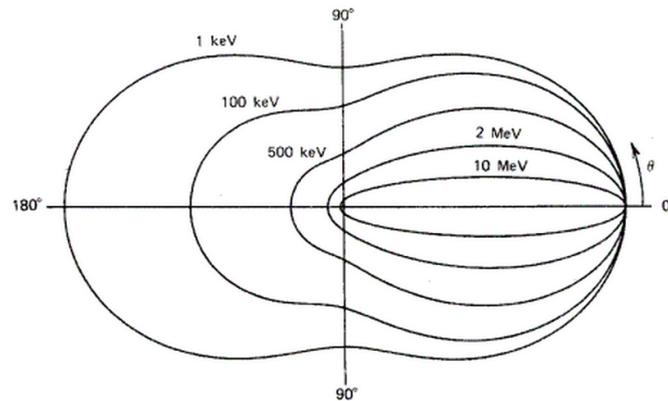
Figure 4.3 Polar plot of the angular distribution of incoherent scattering. The incident γ-ray with the indicated energy enters from the left. The distance from the plot center shows the relative number of scattered photons into a unit solid angle at polar angle Θ. From [89].

Pair production occurs in the Coulomb field of a nucleus if E_γ is larger than the rest mass of the e^+-e^--pair i.e. $E_{\text{pair}} = 1022\,\text{keV}$. The subsequent e^+ and e^- share the remaining energy $E_{e^+} + E_{e^-} = E_\gamma - E_{\text{pair}}$. The positron annihilates within $\mathcal{O}(1\,\text{ns})$ into two γ-rays of $511\,\text{keV}$. Pair production becomes dominant for higher energetic γ-rays $> 8\,\text{MeV}$ in Ge. The energy dependence is $\approx \log E$ and the dependence on the nuclear charge is $\approx Z^2$. The production of the two annihilation γ-rays creates two common event topologies: The singe escape peak (SEP) and the double escape peak (DEP). SEP events occur if one of the γ-rays escapes the detector volume and have an energy of $E_\gamma - 511\,\text{keV}$ in the energy spectrum. DEP events occur if the two γ-rays escape the detector volume and have an energy of $E_\gamma - 1022\,\text{keV}$.

A summary of the atomic charge and γ-ray energy dependence of the interaction probability can be found below. The dependencies often cannot be described analytically and are based on empirical approximations [89].

process	atomic charge	γ-ray energy
Photoeffect	Z^{4-5}	$E^{-3.5}$
Compton scattering	Z	E^{-2}
Pair production	Z^2	$\log E$

Beta interactions: Different to point-like γ-ray interactions, electrons and positrons interact continuously along their trajectory. With respect to particle detection, the interaction of direct electrons is identical to the one of γ-rays which always produce secondary electrons.

Electrons and positrons have a nearly identical energy loss via (1) ionization or (2) Bremsstrahlung. Ionization occurs when the electron scatters with other electrons in the material. The scattering partners have equal mass which enables large deviations from the initial electron path and produces random trajectories. Bremsstrahlung is created by an abrupt change of momentum which predominantly occurs when the electron scatters in the strong Coulomb field of a nucleus. The emitted Bremsstrahlung γ-rays have a continuous energy spectrum reaching up to the initial electron energy. The fraction of energy loss due to Bremsstrahlung is proportional to Z and E. Therefore, Bremsstrahlung dominantly occurs for higher energetic electrons in large Z materials. The fraction of energy loss by Bremsstrahlung in germanium (natural isotopic abundance) and liquid argon is plotted in Fig. 4.4a. A 2 MeV electron loses on average roughly 4 % of its energy due to Bremsstrahlung in germanium whereas only 2 % in LAr.

(a) Bremsstrahlung fraction   (b) electron range
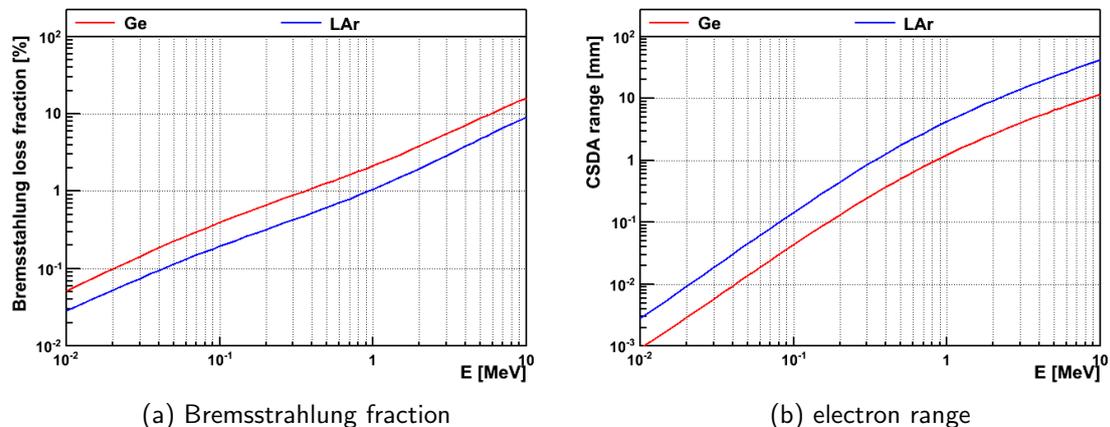
Figure 4.4 Left: Average fraction of energy that is lost via Bremsstrahlung for electron interactions in germanium (natural isotopic abundance density) and liquid argon. Right: Range of electrons as defined with the continuous-slowing-down approximation. Plots created with data from [90].

The electron range is difficult to describe due to the randomness of the electron path. The range definition for the continuous-slowing-down approximation (CSDA) is roughly equivalent to the average path length. The CSDA range in dependence of the electron energy is plotted for germanium and liquid argon in Fig. 4.4b. The CSDA range for a 2 MeV electron is roughly 2 mm in germanium and 10 mm in LAr. Other examples are the range of a 3.5 MeV electron (e.g. ^{42}K) of up to 20 mm in LAr and 5 mm in germanium or the range of a 500 keV electron (e.g. ^{39}Ar) with up to 2 mm in LAr and 0.5 mm in germanium. However, the typical penetration depth into a material may be considerably shorter than the average path length. The CSDA ranges can be considered as a maximal

penetration depth if the path is straight.

Alpha interactions: Alpha energy loss can be described by the Bethe-Bloch formula. Their mass is considerably larger than for electrons which results in faster energy loss. Ranges for alpha particles of different energies in germanium (natural abundance) and liquid argon are shown in Fig. 4.5. The CSDA range of a 5 MeV alpha particle is $\approx 15\,\mu$m in germanium and $\approx 50\,\mu$m in LAr. The Bremsstrahlung creation by alpha interactions is negligible.
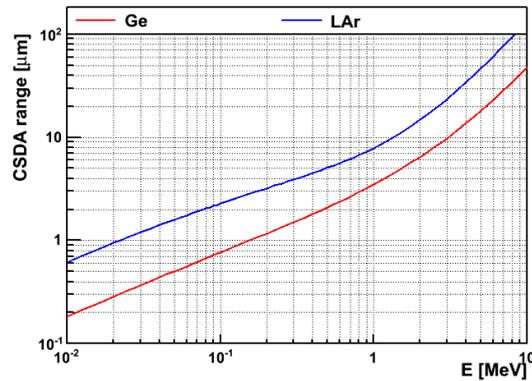
Figure 4.5 Ranges of alpha particles in germanium (natural abundance density) and liquid argon as defined by the continuous-slowing-down approximation. Plot created with data from [90].

4.2 Germanium Detectors

In semiconducting germanium detectors, all previously described interactions result in the excitation of a large amount of electrons. These electrons and their vacancies (holes) can be separated with a HV potential creating an induced current which can be measured.

4.2.1 Semiconductor Detectors

Semiconductors Solid materials have typically two separated energy bands which can be populated by electrons: The valence band and the energetically higher conduction band. Depending on the occupation of these bands and their separation, called band gap, solids can be distinguished into insulators, conductors and semiconductors. In insulators the valence band is fully occupied by electrons and the separation energy between the conductive band is typically $\mathcal{O}(10\,\text{eV})$. Thermal excitation cannot overcome the separating barrier between the bands and no free charge carries are present; thus no electric charge transport is possible. In conductors the conductive band is partly occupied and thus charges can be transported in presence of an electric field.

Semiconducting materials have a fully occupied valence band similar to insulators; however, the band gap is typically smaller $\mathcal{O}(1\,\text{eV})$ and can be overcome by thermal excitation. At sufficiently large temperatures, a certain amount of electrons is excited to the conductive band and provides free charge carriers for conduction. The number of electrons that is excited to the conduction band, and thus the conductivity, is dependent on the temperature and band gap of the semiconductor. For the application of particle detection the thermal conductivity of semiconducting detectors is a nuisance and many semiconducting materials

have to be cooled for operation. The small band gap in semiconducting materials is used for particle detection. The comparably high energy $1\,\mathrm{keV} - 1\,\mathrm{MeV}$ of a primary electron, either directly from a beta decay or after a γ-ray interaction, can excite many valence electrons into the conductive band. The number of excited electrons in the conduction band n is directly proportional to the energy of the primary electron which is absorbed E_{abs}

$$n = \frac{E_{\mathrm{abs}}}{\epsilon} \tag{4.2}$$

with ϵ being the energy needed for the excitation. For n electrons in the conduction band there are also n vacancies in the valence band. These vacancies are referred to as *holes* which behave like positively charged particles. The combination with an excited electron is called electron-hole pair. These electrons and holes are free charge carriers that move inside the semiconductor e.g. in the presence of an electric field: The electrons will drift toward the anode and the holes towards the cathode.

In an ideal situation all n charges are measured on the electrodes of the detector. The creation of n free charge carriers is a statistical process and its uncertainty would follow Poisson statistics ($\sqrt{n}$) if the formation of electron-hole pairs were independent. However, energy depositions can also create phonon excitations which are bound together with the electron-hole pair creation by total energy conservation and thus making the process non-independent. The difference in variance of n compared to the Poisson case is described by the Fano factor and can significantly enhance the energy resolution of semiconductor detectors. In general, semiconductor materials with a smaller band gap create more free charge carries for a certain E_{abs} and thus have a smaller relative uncertainty of n. Those semiconductors have a better intrinsic resolution.

In practice the lifetime of electron-hole pairs is limited in semiconductors due to impurities disturbing the crystal lattice or other lattice defects coming e.g. from radiation damage. The collection of the charges must be sufficiently fast in order to keep a linear relation between measured charge and E_{abs}.

Diodes   The ideal semiconductor has no conductivity at zero temperature and behaves like described above. This is called an intrinsic semiconductor. In practice there are always impurities creating a small conductivity. Impurities can be electrically separated into acceptor and donor impurities, providing additional holes or electrons, respectively. In germanium with four valence electrons, an acceptor impurity is e.g. boron with three valence electrons which creates an additional valence state i.e. a hole (p-type germanium); a donor impurity provides additional free conductive states i.e. electrons (n-type) germanium.

Combining n-type and p-type materials create an electrostatic system called diode. At the junction between the n-type and p-type region, the free electrons and holes diffuse into the opposite materials and leave a region depleted of free charge carriers. This region is called depletion zone and is used as the active volume of a semiconductor detector in which particle interaction create electron-hole pairs that can be collected. The depletion zone extends until the electrostatic system is in equilibrium and is typically very small. However, it can be significantly extended with a HV potential. A positive HV applied to the n-type side further depletes electrons from this region; equally a negative HV applied to the p-type side depletes holes from the p-type region.

In summary, a semiconductor detector for γ-ray energy measurements needs to fulfill certain criteria: (1) A small ϵ for good energy resolution, (2) good electron and hole mobility to avoid charge trapping, (3) large Z material and density to effectively contain γ-rays and (4) cost effective production of large crystals with low impurity concentrations to maximize the active detector volume. Tab. 4.1 compares some of these properties for commonly used silicon, germanium and CdZnTe detectors.

Table 4.1 Comparison of semiconductor materials for particle detection. Columns show the atomic charge Z, the density ρ, the band gap energy E_g, the energy required to create an electron-hole pair ϵ and the electron and hole mobility. Values of ϵ are given for the operation temperature of 300 K for Si and CdZnTe and 77 K for Ge. Data from [91].

material	Z	ρ [g/cm^3]	E_g [eV]	ϵ [eV]	electron mobility [cm^2/V/s]	hole mobility [cm^2/V/s]
silicon	14	2.33	1.106	3.62	1350	480
germanium	32	5.32 (5.54)^a	0.67	2.96	$3.6 \cdot 10^4$	$4.2 \cdot 10^4$
CdZnTe	48,30,52	5.78	1.57	4.64	1000	$50 - 80$

^{a} Germanium enriched in ^{76}Ge

4.2.2 High Purity Germanium Detectors

High Purity Germanium detectors are produced in various configurations. Fig. 4.6 shows the shape of selected p-type detectors: (a) a semi-coaxial detector, (b) a BEGe detector and a (c) p$^+$ point contact (PPC) detector. (a) and (b) are used in the GERDA experiment and (c) in the Majorana experiment. The volume, shape and contact size are typically constrained by compromises between the detector size, the depletion voltage and the capacity (resolution).
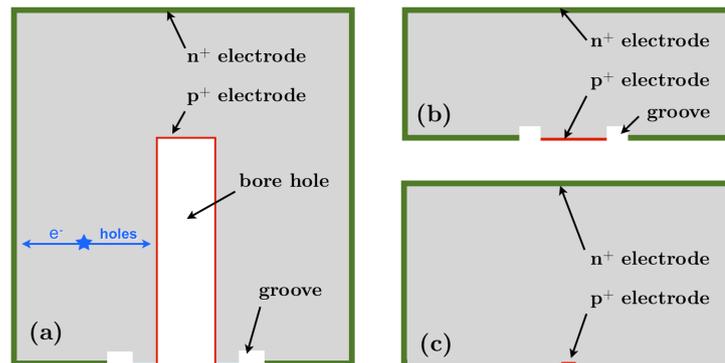
Figure 4.6 Various designs of HPGe detectors: (a) semi-coaxial detector, (b) BEGe detector, (c) PPC detector. Illustrated are the schematics (not to scale) with the n$^+$ electrode and p$^+$ electrode. The electric separation of both electrodes is achieved with a groove and / or an electrically passivated surface treatment over a larger area around the p$^+$ electrode.

The detectors are manufactured from a single crystal of p-type material. The p$^+$ electrode is created by implantation of boron atoms with an ion beam. The implanted concentration follows a distribution with maximum depth at $\mathcal{O}(1\,\mu\text{m})$. The additional implantation of a

p$^+$ electrode on top of the p-type bulk material is needed as a blocking or non-injecting contact. Without this contact some of the electrons which are collected on the n$^+$ electrode would be replaced via the p$^+$ electrode and cause leakage current. The p$^+$ electrode is typically small for p-type HPGe detectors to create a large electric field and reduce the capacity. In semi-coaxial detectors it fills out the bore-hole which enables the depletion of a large volume. For BEGes the p$^+$ electrode is a concentrical disk of 7.5 mm radius. For PPC detectors the contact is even further point-like.

The n$^+$ electrode is created with thermal diffusion of lithium atoms. The time and temperature of the annealing process determines the thickness of the n$^+$ electrode layer and is typically around $0.3 - 2.0$ mm. This thickness can slowly increase in time by thermal diffusion at room temperature. The n$^+$ electrode extends around the outer surface of the detectors. With its macroscopic thickness it reduces the active volume of the detector compared to the total volume by typically $5 - 15\%$. The two contacts must be electrically separated on the surface. This is done for the GERDA BEGe and semi-coaxial detectors with the groove, a ditch-like ring engraved around the p$^+$ electrode. Additionally, a larger area around the p$^+$ electrode can be passivated to reduce surface leakage currents.

Charge collection   The free charge carriers inside a HPGe detector can be transported by two processes: (1) drift inside an electric field along the field lines and (2) diffusion. The saturated drift velocity is typically $\approx 10^7$ cm/s whereas the diffusion velocity is significantly slower [89]. Charge drift is the dominating process in the bulk. Holes are drifting toward the p$^+$ electrode and electrons towards the n$^+$ electrode. Charge diffusion becomes only important in regions with no or very small electric field as e.g. inside to the n$^+$ electrode.

A HPGe detector with applied HV can be considered as an electrostatic system. Its electric potential and electric field can be modeled using the Poisson equation with boundary conditions. This is e.g. presented in [92] for a typical BEGe detector. The potential $\phi(\vec{r})$ can be divided into two parts: (1) an intrinsic potential created by the presence of p-type impurities in the depleted region (also called space charge) $\phi_\rho(\vec{r})$ and (2) a potential created by the HV applied on the electrodes $\phi_0(\vec{r})$. The potential as well as the electric field is a superposition of its components and can be described separately:

$$\phi(\vec{r}) = \phi_0(\vec{r}) + \phi_\rho(\vec{r}) \qquad \text{and} \qquad \vec{E}(\vec{r}) = \vec{E}_0(\vec{r}) + \vec{E}_\rho(\vec{r}). \qquad (4.3)$$

The HV and the intrinsic components of the potential and the electric field as well as their superpositions are illustrated in Fig. 4.7. The specific electric field configuration in a BEGe collects charges from almost all initial locations first into the detector center; then they are funneled towards the p$^+$ electrode sharing the same trajectory path in the end. This feature creates similar pulse shapes for pulses with different starting position.

The measured current on the electrode is induced by moving charges close to the electrodes rather than actual charges arriving at the electrodes (Shockley-Ramo theorem [93, 94]). The instantaneous current i on the electrode depends on the charge q, the velocity v and the weighting field $\vec{E}_w$ as $i = q \cdot \vec{v} \cdot \vec{E}_w$. The weighting field and potential can be calculated with the Laplace equation in certain boundary conditions. The total charge induced in the electrode is then simply the difference in weighting potential which is crossed by the charges. The weighting potential for a typical BEGe is shown in Fig. 4.8. It is practically zero throughout the detector volume and has significant values only around the p$^+$ electrode. Consequently, if incident radiation creates electron-hole pairs in the bulk volume, there is an immediate current induced in the electrodes which is, however, very
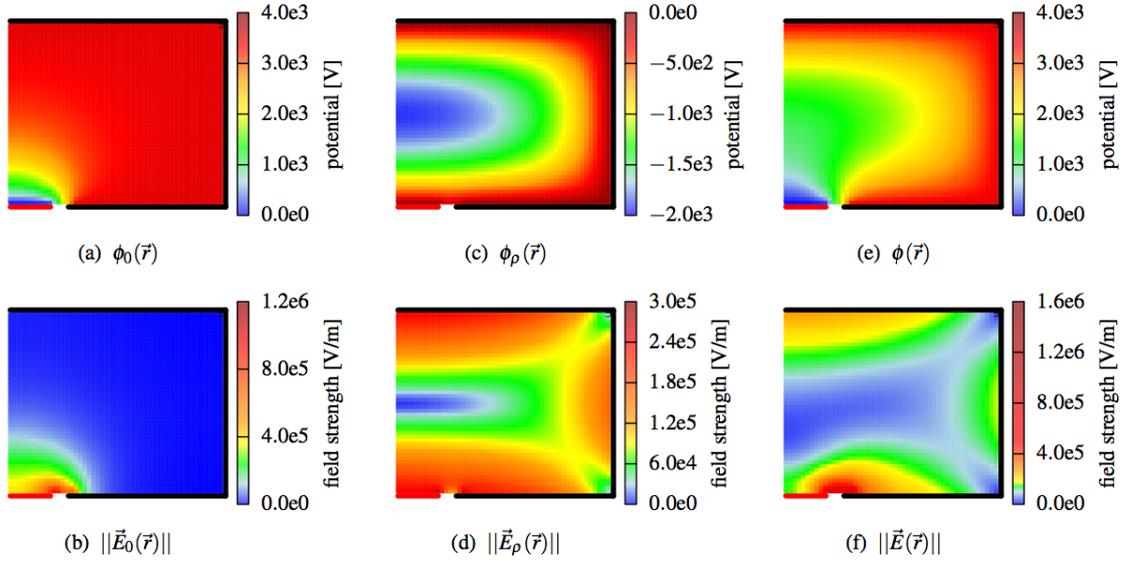
Figure 4.7 Potential and electric field inside a modeled BEGe detector (71 mm diameter, 32 mm height, 3500 V, 10^{10} atoms/cm^3 impurities). (a) and (b) show the potential and field created by the HV, (c) and (d) show the potential and field created by the space charge distribution and (e) and (f) show the sum of both components. The spatial field configuration collects bulk charges first in the detector center which then move along similar trajectories towards the p$^+$ electrode. From [92].

small. This current becomes only large when the holes have drifted into the large weighting potential around the p$^+$ electrode. The similarity of trajectories inside the large weighting potential is the reason for the similar pulse shapes for bulk events.
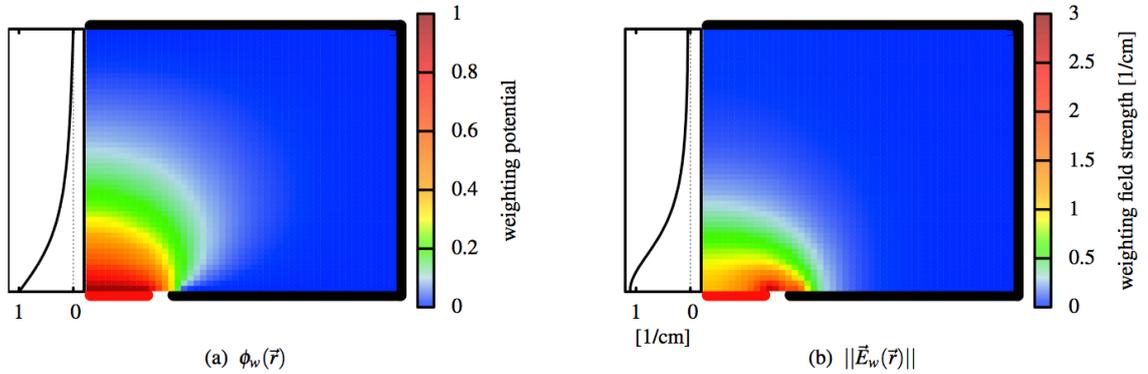
Figure 4.8 Computed weighting potential (a) and weighting field strength (b) inside a BEGe detector. Color maps show half of a vertical section. Side plots show the profile along the symmetry axis of the detector. From [92].

If the electron-hole pairs are produced close to the p$^+$ electrode, the induces current is immediately large; hence they are called "fast pulses". Their maximum current is also increased since now holes and electrons move in the weighting potential at the same time. This can induce up to twice the current that only holes can induce in case of bulk events. If the electron-hole pairs are produced inside the n$^+$ electrode they have to diffuse first into the electric field. This takes a considerable time and they are thus called "slow pulses".

The diffusion process results in charge loss and a reduced energy measurement for those events.

Additionally, charges can be trapped or lost during transport. Charge trapping can cause a slower signal formation if they are released within the integration time; if they are trapped longer than the integration time they are lost from the signal which results in a smaller energy measurement, typically seen as low energy peak tails.

4.2.3   Signal Processing

The fist stage of a typical readout system of a HPGe detector is a combination of a charge sensitive preamplifier and a feedback circuit. The illustration of the readout scheme is shown in Fig. 4.9a. The separated charges in the detector are amplified by the preamplifier (A) and charge the feedback capacitor (C_f). The capacitor is then discharged by the feedback resistor (R_f). This is creating a fast charge signal and slow discharge tail shown in Fig. 4.9b. In GERDA, the typical rise time is $0.5 - 1.5\,\mu$s. The RC component has a time constant $\tau = 150\,\mu$s with $C_f = \approx 0.3\,$pF and $R_f = 500\,$MΩ [95].

(a) readout electronics   (b) charge pulse
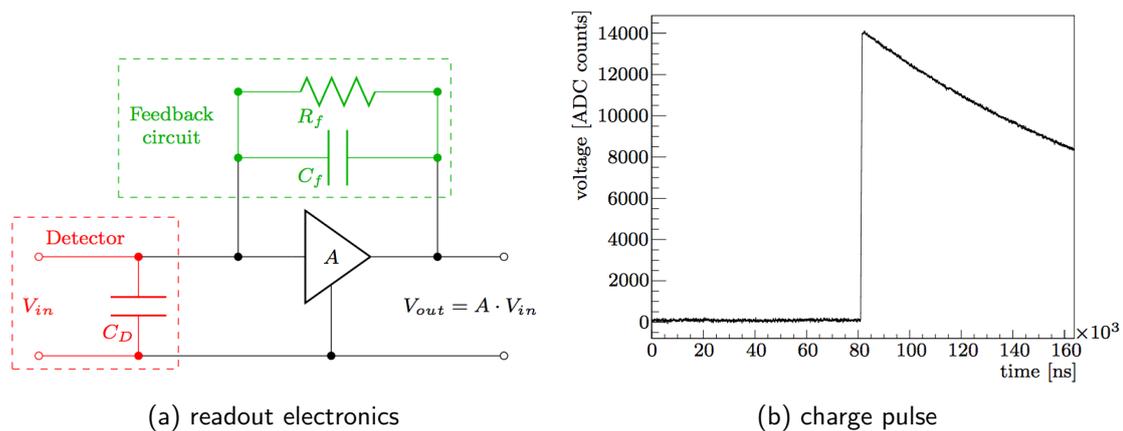
Figure 4.9   Readout scheme of a HPGe detector (left) and corresponding waveform (right). Charges which are separated in the HPGe detector (C_D) are amplified (A) and collected in the feedback capacitor (C_f). The capacitor is slowly discharged via the feedback resistor (R_f). This creates a fast charge rise with an exponential tail (right). Figures from [96].

There are two main principles to further process the charge signal: (1) Direct online analogue shaping to reconstruct the energy which is then recorded with an analog-to-digital converter (ADC); (2) Digitization of the full charge waveform with a fast ADC (FADC) and digital reconstruction of the energy offline. The online shaping relies on the choice of signal processing at runtime and does not need additional processing and computing power. The recording of the waveform with an FADC allows to use the full event information which comes at the price of storage.

In GERDA, the data acquisition (DAQ) samples the waveforms with a 14 bit FADC at 100 MHz. The traces consist of 16384 samples of 10 ns each. A 80 μs segment of the baseline is recorded prior to the trigger, followed by the rise of the charge signal in $\approx 1\,\mu$s, followed by the discharge with an exponential tail for the remaining $\approx 80\,\mu s$ (see also Fig. 4.9b).

The standard GERDA energy reconstruction is done with a pseudo-Gaussian filter. First the charge waveform is differentiated to create a current pulse according to the algorithm

$$x_0[t] \rightarrow x_1[t] = x_0[t] - x_0[t - \delta] \tag{4.4}$$

where $x_0[t]$ is the charge and $x_1[t]$ the current at time t and δ is set to $5\,\mu$s. Then the current pulse is shaped 25 times with a moving window average (MWA) algorithm:

$$x_i[t] \rightarrow x_{i+1}[t] = \frac{1}{\delta} \sum_{t'=t-\delta}^{t} x_i[t'] \qquad i = 1..25 \ . \tag{4.5}$$

After this pseudo-Gaussian filter, the pulse has close to Gaussian shape. The height of the shaped pulse is taken as the energy E. Note that originally the energy information is encoded in the integral of the current pulse. The Gaussian shaping connects the pulse integral to the pulse height.

Additional information is contained in the shape of the current pulse. The amplitude A of the current pulse is taken to construct the pulse shape quantifier A/E. For the extraction of A the current pulse is typically shaped 3 times with a MWA of $\delta = 50$ ns window size. After this mild shaping, A is still dependent on the charge collection time; on the other hand, E is largely independent on the charge collection time due to the stronger shaping.

The shape of the waveforms and the A/E are different depending on the initial location of the charge cloud and the collecting process. Fig. 4.10 shows measured charge pulses (red) and the current pulses (blue) for four different types of interactions in a BEGe detector. The energy of the pulses is the same for all cases. The top left panel shows a single-site event SSE in the bulk. Here the charge cloud is created within a small volume e.g. due to a single Compton scattering, a DEP event or a $0\nu\beta\beta$ event. As discussed above, the induced charge on the electrodes starts immediately after the interaction (Shockley-Ramo theorem). The largest charge induction occurs later when the charge cloud is traversing the large weighing field close to p^+ electrode. The drift path in the high weighting field is the same such that the illustrated pulse has a representative shape for all SSE in the bulk with the same A/E. Experimentally the difference in total drift time disappears due to triggering at the same pulse height.

In case of a multi-site event MSE in the top right panel, in which the energy is deposited at different locations inside the detector, the charge and current pulses are superpositions of the individual charge collections. These event types occur e.g. due to multiple Compton scatterings, SEP events or beta interactions with a hard Bremsstrahlung component. Due to the different drift times for charge clouds starting at different locations, the current maxima may be separated and A is taken as the amplitude of the largest charge cloud. However, the stronger shaping for the energy reconstruction will measure the sum of the charge clouds. Hence the A/E is reduced for MSE which is a powerful tool to discriminated scattering γ-ray background.

The charge collection for events in a small volume of $3 - 6\,\%$ around the p^+ electrode is immediately large requiring no previous drift (Fig. 4.10 bottom left panel). The amplitude can be twice as high as for bulk interactions with the same energy deposition. Hence for p^+ electrode events the A/E is larger than for bulk events and they can be discriminated.
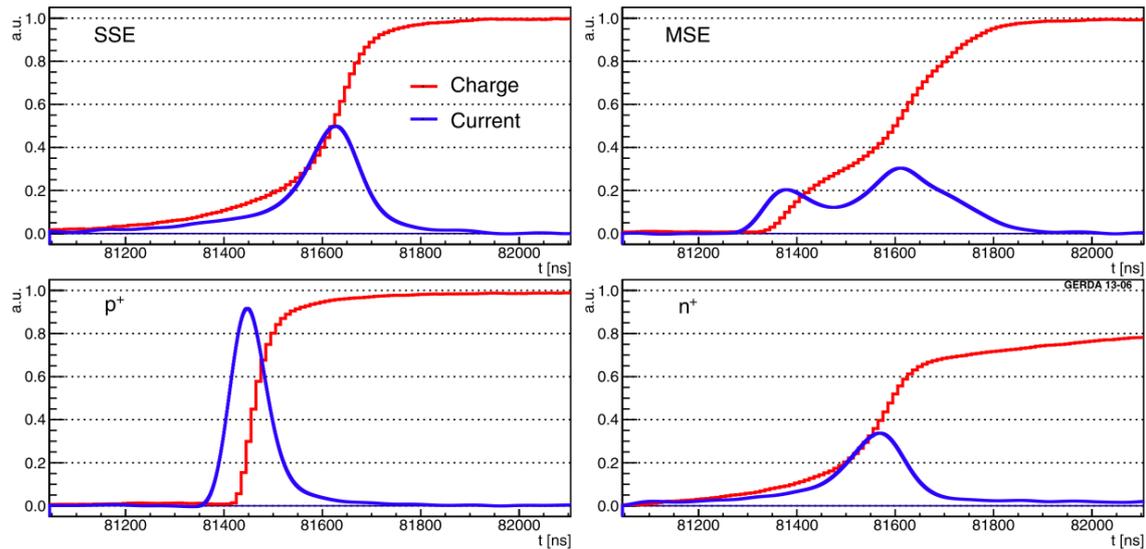
Figure 4.10 Measured charge pulse shapes (red) and current pulse shapes (right) for various event types: A DBD-like single-site event in the detector bulk (top left). A multi-site event in the bulk (top right). A fast event in the small volume around the p^+ electrode (bottom left). A slow event in the n^+ electrode (bottom right). The maximal charge pulse amplitudes are set to one and the current pulses have equal integrals. From [97].

For slow pulses originating at the n^+ electrode (bottom right), the A/E is reduced because the charges first have to diffuse slowly into the drift region. The n^+ electrode is covering $96-98\,\%$ of a typical BEGe surface making those type of interactions one of the dominating contribution to surface backgrounds. The modeling and discrimination capabilities of such events is the subject of a study in Chap. 8.

4.3   Liquid Argon as Particle Detector

Noble gases such as argon are scintillators which can be utilized as particle detectors. The interaction medium is the argon which has a density of $1.40\,\mathrm{g/cm^3}$. The scintillation light can be read out by a photomultiplier tube (PMT) or semiconductor detectors such as a silicon photomultiplier (SiPM) or an avalanche photo diode (APD) .

4.3.1   Scintillation in Argon

Interactions of ionizing particles in argon excite or ionize argon atoms which then recombine under the emission of 128 nm UV light. The scintillation process occurs in gaseous and liquid argon with different properties. Fig. 4.11 illustrates the two different processes of excitation and ionization. If an argon atom is excited Ar^* it collides with a neighboring argon atom forming a neutral excited dimer or excimer[1] Ar_2^* within $\mathcal{O}(1-10\,\mathrm{ps})$. This excimer decays into two argon atoms under emission of scintillation photons. If an argon atom is ionized, it combines with another Ar atom to a charged excimer Ar_2^+. The Ar_2^+ recombines with a thermalized electron within $\mathcal{O}(100\,\mathrm{ps})$ leading to a neutral excimer under emission of recombination luminescence. The neutral excimer then decays with scintillation light emission as for the excitation process. The excitation process is dominant in gaseous argon (GAr) at room temperature and atmospheric pressure. In LAr the ionization process

---

[1]Dimer: di-, "two" + -mer, "parts". An excimer is an excited dimer.

dominates with an excitation-ionization ratio Ar*/Ar$^+$ of 0.21 [98]. Both processes are density dependent. A more detailed description of the processes can be found in [98, 99, 100].
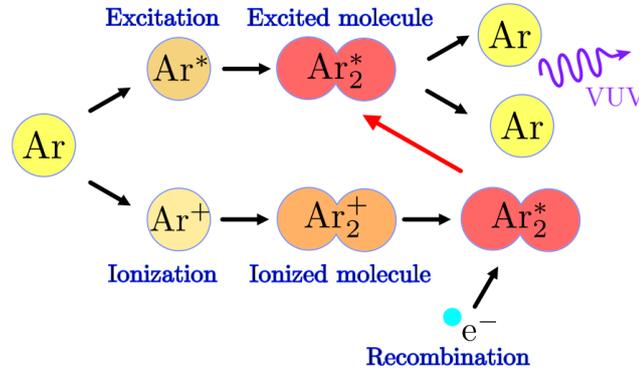
Figure 4.11 Two mechanisms for scintillation in argon. The excitation channel dominates for GAr whereas the ionization channel dominates for LAr. From [99].

Argon excimers can be produced in a singlet or a triplet state. The population of these states depends on the linear energy transfer (LET) or stopping power of the ionizing particle and is different for e, p, n, α particles and nuclear recoils. The ratios between singlet and triplet state population increases with the LET and is 0.3, 1.3 and 3 for electrons, alphas and nuclear recoils respectively [101]. The lifetime of the two states is different and independent of the LET: The de-excitation of the singlet state is an allowed transition with a lifetime of $2-6$ ns whereas the de-excitation of the triplet state is forbidden with a lifetime of $1100-1600$ ns [102, 103]. This is referred to as the fast and the slow component of the scintillation light. The difference in lifetime is uniquely large for argon scintillation and can be utilized to distinguish different types of particle interactions. E.g. electron interaction show a larger slow component than alpha interactions.

The emission of argon scintillation light peaks at 128 nm with $\approx$ 6 nm FWHM [102]. An emission spectrum for LAr is shown in the bottom panel of Fig. 4.12. Most light detectors are encased in glass which is opaque for hard UV light. Therefore the scintillation photons have to be shifted to higher wavelength before detection. The light yield of XUV photons per MeV is roughly $40.000\,\gamma/\mathrm{MeV}$ in pure LAr for interacting electrons with 1 MeV energy. The light yield is dependent on the LET and is quenched for alpha interactions by 11 % [98].

The attenuation of scintillation light in LAr is influenced by scattering and absorption which have to be distinguished. In the application of a large volume detector such as the GERDA cryostat, the absorption will result in light loss whereas the scattering merely changes the direction. In fact the scattering of light may even enhance the light detection from certain locations with circumventing shadowing effects. On the other hand, small scale experiments measuring LAr properties are often long thin tubes in which scattering of light is almost equivalent to losing the light on the vessel walls. Special care has to be taken to interpret literature values of attenuation. The Rayleigh scattering length in LAr is theoretically calculated as 90 cm [105] and measured as 66 cm [106][2]. The absorption

---

[2]Note that reference [105] is interpreting the attenuation value of 66 cm in [106] as a measurement of
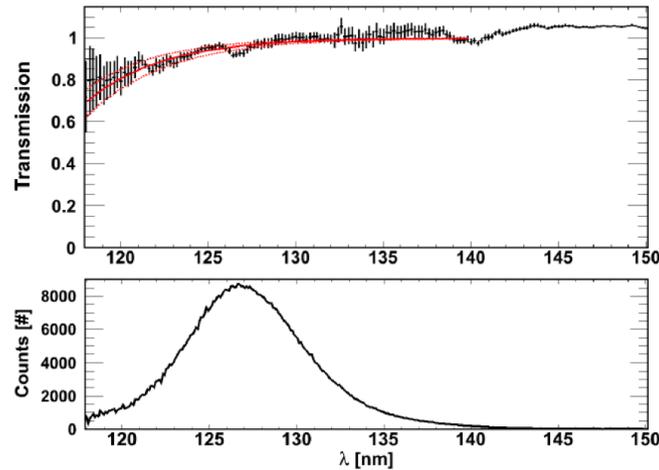
Figure 4.12 Top: Transmission spectrum of pure LAr. Bottom: Emission spectrum with the dominant peak at 128 nm. From [104].

length varies largely with the type and concentration of impurities and has to be measured in-situ of the specific setup. Measurements with an artificial light source showed that the attenuation is strongly wavelength dependent for XUV light [104]. A transmission spectrum for XUV light is shown in the top panel of Fig. 4.12. For optical photons e.g. after wavelength shifting of the XUV photons, the LAr is practically transparent.

Impurities in the LAr such as N_2, O_2, H_2O or CO_2 can significantly alter the light yield, the triplet lifetime and the attenuation length. Changes in scintillation properties are mainly caused by increasing non-radiative de-excitation of the triplet state and by absorbing the 128 nm scintillation light after production. The effects depend on the impurity concentration and the chemical properties. Investigations have been performed in e.g. in [100, 107], [108] and [99] for nitrogen, oxygen and air respectively.

4.3.2   Single Photon Detection

Photomultiplier tubes (PMT) are evacuated glass tubes for the detection of single photons. If a photon hits the photocathode it knocks out an electron via the photoelectric effect. The probability for this process is the quantum efficiency which depends on the cathode material and the photon wavelength. The photo electron is accelerated in an electric field towards the first dynode where it knocks out multiple secondary electrons. The secondary electrons are accelerated towards the next dynode in an successively increasing electric field until they reach the anode. The number of electrons collected at the anode for a single incident photon is called the gain factor of the PMT. The amplified measured signal is called the single photo electron (spe) signal. Multiple initial photons scale the spe signal linearly. The gain and the spe signal are dependent on the number and type of dynodes and the operational voltage. A typical operational voltage is $1000 - 2000\,\mathrm{V}$ with a gain between 10^6 and 10^7 and an spe signal around $1 - 10\,\mathrm{mV}$.

A signal can also be created by thermal electron emission, cosmic rays or radioactive decays inside the PMT. The frequency of those events is called dark rate. Specific design concepts are necessary for PMT operation at cryogenic temperatures and in a low background

---

the scattering length.

environment which is an ongoing technical challenge.

Avalanche photo diodes (APD) are the semiconductor equivalent to a PMT. A photo sensitive diode is operated with typically $100 - 200\,\text{V}$. If an incident photon knocks out an electron in the semiconductor lattice, an avalanche multiplication is triggered. Typical gains are around 100.

Silicon photo multipliers (SiPM) are arrays of several APD pixels per mm^2. Each APD is operated in Geiger mode and read out in parallel with the other APDs in the array. Multiple photons can be discriminated by signals from multiple pixels. The operational voltage depends on the individual APDs and rages from $20 - 100\,\text{V}$. The gain is around 10^6.

4.4 Background Sources

The low expected count rate in $0\nu\beta\beta$ decay experiments requires an ultra low background environment in which the understanding and mitigation of the remaining background sources is imperative. Furthermore, the construction of Monte Carlo background models for data analysis demands a good knowledge of the remaining background composition.

The GERDA experiment achieved a background level of $0.02\,\text{cts}/(\text{kg} \cdot \text{yr} \cdot \text{keV})$ around the region of interest in PHASE I [27][3]. In PHASE II the goal is a background index of $0.001\,\text{cts}/(\text{kg}\cdot\text{yr}\cdot\text{keV})$ in the ROI. This can be compared to typical values of an unshielded HPGe detector on the surface in which one would see $10^{4-5}\,\text{cts}/(\text{kg} \cdot \text{yr} \cdot \text{keV})$ in the same energy region. The most radioactively pure environment in a large volume detector was achieved by the Borexino experiment [109]. The contamination of ^{238}U and ^{232}Th are $5 \cdot 10^{-18}\,\text{g/g}$ and $4 \cdot 10^{-18}\,\text{g/g}$ respectively compared to e.g. the concentrations in typical dust of around $10^{-5}\,\text{g/g}$ for both isotopes [110].

Low background environments are almost exclusively created in underground locations to reduce the background induced by cosmic radiation. They are described in the dedicated next section. The main background contributions in low background environments can be separated into direct cosmic radiation, cosmic activated radionuclides, primordial radioactive isotopes and anthropogenic radioactivity. An exhaustive review of background influences is given in [111]. In the following, values are taken from there if not marked differently.

4.4.1 Direct Cosmic Radiation

Primary cosmic radiation can be separated in a low energy flux from solar winds and a high energy flux from galactic sources. Solar winds with typical particle energies up to $100\,\text{keV}$ have only a small influence on sea level in normal weather condition. Primary particles from galactic sources hit the atmosphere with an approximate flux of $100{,}000\,\text{m}^{-2}\text{s}^{-1}$ and are composed of 92% protons, 6% alphas and 2% heavy nuclei [112]. These primary particles interact with atmospheric nuclei and produce showers of secondary particles that result in an average composition of 0.6% protons, 15.1% electrons, 21.3% neutrons and 63.0% muons at sea-level. This composition highly depends on local parameters such as the magnetic field, the atmospheric density and humidity, i.e. the weather conditions and

---

[3]This background index is before pulse shape analysis

on building material in the vicinity; especially the proton and neutron fluxes are highly variable. Primary cosmic γ-ray radiation contributes less than 1% to the overall γ-ray flux which is dominated by primordial decay chain isotopes.

The μ-flux is the largest and most stable cosmic flux on sea-level with $1.27 \cdot 10^2 \, \mathrm{m}^{-2}\mathrm{s}^{-1}$ ($\geq 0.35 \, \mathrm{GeV}$) [113] and can penetrate into multiple kilometers of rock. For flat overburdens, the flux scales approximately exponentially with the depth. The shape of the muon spectrum shifts towards higher energies with increasing depth due to the more effective absorption of low energy muons via ionization. Tab. 4.2 shows an overview of underground laboratories including the remaining μ-flux among other key parameters.
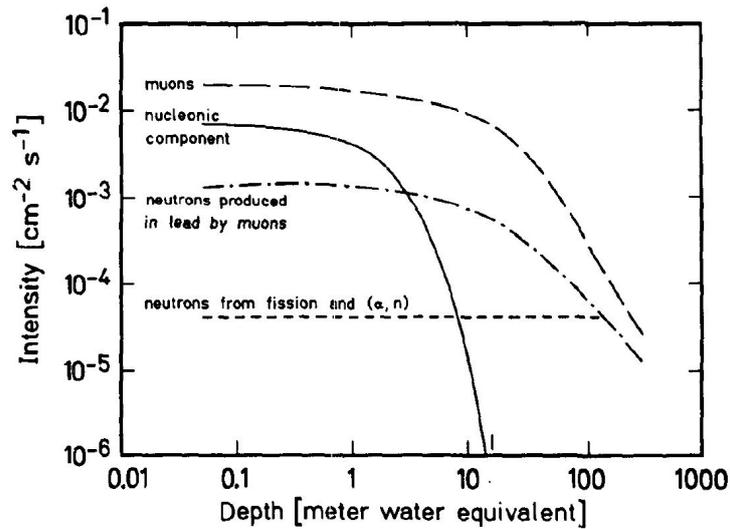
Figure 4.13 Fluxes of different secondary cosmic particles as a function of depth in m.w.e. From [111].

The intensity of different cosmic radiation components for different overburdens is shown in Fig. 4.13. The overburden is scaled to meters of water equivalent (m.w.e.) in order to compare different underground sites with different rock composition; a water column of 1000 m has roughly the same attenuation as 300 m of standard rock [111]. The atmospheric μ-flux is compared to the nucleonic flux of protons and neutrons and to the flux of muon induced secondary neutrons. The depth independent flux of neutrons from fission and (α, n) reactions in primordial decay chains is also shown. It can be seen that after 20 m.w.e. the primary nucleonic component becomes insignificant and secondary neutrons and neutrons from primordial decay chains dominate. After a depth of approximately 100 m.w.e., the constant contribution of neutrons from primordial decay chains becomes the dominant element.

4.4.2   Cosmic Activation

The neutron and proton radiation on sea-level activates materials for detector and assembly components producing unstable radioactive nuclides internally. Especially the long lived isotopes represent a serious issue, as they can remain in the detector throughout construction and decay during run time. The direct approach to reduce cosmic activation is to limit the exposure to cosmic radiation. This is done by reducing transport ways, transport times, avoiding the transportation at high altitudes, shielding the material during trans-

port, storing material underground or even producing material underground.

For the GERDA detectors the activated radionuclides ^{68}Ge/^{68}Ga ($T_{1/2} = 270.8$ d / Q-value $= 2.92$ MeV)[4] and ^{60}Co ($T_{1/2} = 5.27$ yr, Q-value $= 2.82$ MeV) are a potential background. During the transport and production of the detectors a large effort was made to reduce the exposure to cosmic radiation [114]. Cosmogenic activated isotopes are also present in the LAr as ^{39}Ar ($T_{1/2} = 269$ yr, Q-Value $= 565$ keV) and ^{42}Ar/^{42}K ($T_{1/2} = 32.9$ yr / Q-Value $= 3.52$ MeV). The latter is mainly being produced by the ^{40}Ar($\alpha, 2p$)^{42}Ar reaction of cosmic alphas with the argon in the outer atmosphere. Especially ^{42}K, the daughter nuclide of ^{42}Ar, with a Q-value up to 3.52 MeV is a major background contribution that requires strong mitigation (see also Chap. 5 and Chap. 8).

4.4.3 Primordial Decay Chains

Primordial decay chains include a variety of radioactive nuclides undergoing mainly alpha and beta decays with accompanying γ-ray emission. Apart from short ranged alpha and beta particles with energies up to 10 MeV, the most energetic of the prominent γ-rays is 2614.5 keV from the ^{208}Tl decay. All decay chain nuclides are fed by four long living nuclides, ^{238}U, ^{232}Th, ^{235}U and ^{40}K, that have been produced in supernovae explosions and remain at significant quantities today. A list of all associated nuclides with their decay characteristics is given in Tab. A.6 and illustrated in Fig. A.1 in the appendix. Typical activities in the continental upper crust are 850 Bq/kg for ^{40}K, 44 Bq/kg for the ^{232}Th chain and 36 Bq/kg for the ^{238}U chain[5] which together accounts for a sea-level γ-ray flux of 10^5 m^{-2}s^{-1} and renders all other primordial isotopes insignificant [111].

In modern experiments, it is rather easy to shield against α, β and γ-rays from the surrounding rock. The difficulties lie in primordial decay chain impurities in materials close to the detectors and in the detectors itself. In GERDA PHASE I, the background from the detector assembly has a strong contribution from these decay chains, with ^{228}Th (^{232}Th chain) and ^{214}Bi (^{238}U chain) contributing, each, approximately 25 % to the overall background budget of the experiment [115].

Radon is another major issue with the isotopes ^{222}Rn ($T_{1/2} = 3.82$ d) and ^{220}Rn ($T_{1/2} = 55.6$ s) being volatile noble gas nuclides in the ^{238}U and ^{232}Th chain, respectively. ^{222}Rn is emitted from surfaces containing primordial decay chains so that 1300 Bq/(m^2 · d) accumulates in the air coming from the continental crust [111]; this accounts for an activity of around $10 - 20$ Bq/m^3 in the atmosphere [116]. In confined cavities as underground laboratories this concentration can get larger by two orders of magnitude. Typical radon activities in underground facilities can be seen in Tab. 4.2 where ventilation already reduces the activity compared to standing air. If radon can propagate freely, its often charged decay products can stick to surfaces and induce high energy background through alpha and beta particles. Approaches to reduce this background are the physical hindrance of air movements, sealing experiments from the common mine air, flushing experimental interiors with e.g. nitrogen, reducing decay chains containing material inside the experiments and avoiding airborne impurities to come close to the detectors with cleanrooms. In GERDA PHASE I the background from alpha emitting radon daughters accounted for 5 % of the

---

[4]The isotope ^{68}Ge is produced with a long half-life decaying into ^{68}Ga with a large Q-value. The half-life refers to ^{68}Ge and the Q-value to ^{68}Ga.

[5]Note also the useful conversions factors of 1 Bq/kg(^{238}U) $\widehat{=} 81 \cdot 10^{-9}$ g/g; 1 Bq/kg(^{232}Th)$\widehat{=} 246 \cdot 10^{-9}$ g/g and 1 Bq/kg(^{40}K) $\widehat{=} 32.3 \cdot 10^{-6}$ g/g.

total background in the ROI.

4.4.4 Anthropogenic Radioactivity

The main origins of anthropogenic radioactivity are nuclear bomb tests, the Chernobyl and the Fukushima Daiichi accident and nuclear fuel reprocessing which mainly increase the concentration of ^{3}H ($T_{1/2} = 12.33\,\text{yr}$), ^{14}C ($T_{1/2} = 5730\,\text{yr}$), ^{85}Kr ($T_{1/2} = 10.76\,\text{yr}$), ^{90}Sr ($T_{1/2} = 28.79\,\text{yr}$) and ^{137}Cs ($T_{1/2} = 30.07\,\text{yr}$) in the atmosphere. The concentrations vary significantly and are location dependent. A danger for low background experiments exists when these nuclides get into production chains and find their way into the experiment. A more direct anthropogenic impurity in e.g. stainless steel results from ^{60}Co ($T_{1/2} = 5.27\,\text{yr}$) which is used in steel works to measure and control the attrition of walls.

Another specific danger originates from less concentrated anthropogenic radioactive nuclides in the atmosphere as e.g. ^{42}Ar in GERDA which, besides the ^{40}Ar($\alpha, 2p$)^{42}Ar process, can also be produced by double neutron capture ^{40}Ar(n, γ)^{41}Ar(n, γ)^{42}Ar in atmospheric nuclear explosions [117].

4.5 Underground Facilities

Table 4.2 Overview of worldwide underground facilities with data taken from [116]. Name acronyms and abbreviations denote: LNGS - Laboratory Nationali del Gran Sasso, HADES - High Activity Disposal Experimental Site, BNO - Baksan Neutrino Observatory, BUL - Boulby Palmer Laboratory, CJPL - China JinPing Deep Underground Laboratory, CuPP - Centre for Underground Physics at Pyhäsalmi, LSC - Laboratorio Subterráneo de Canfranc, LSM - Laboratoire Subterrain de Modane, SUL - Solotvia Underground Laboratory, Kamioka - Kamioka Observatory, OTO - OTO-Cosmo Observatory, Y2L - Yang Yang Underground Laboratory, SNOlab - VALE's Creighton Inc. mine, SUL - Soudan Underground Laboratory, and DUSEL - Deep Underground Science and Engineering Laboratory. The values for n and μ are total fluxes unless an energy range is given in parentheses, the values for radon activities are at experimental sites and include counter measures as e.g. ventilation.

name	country	depth [m.w.e.]	n-flux (ΔE) [m^{-2}s^{-1}] (MeV)	μ-flux [m^{-2}s^{-1}]	Rn in air [Bq/m^3]
LNGS	Italy	3200	$3.78 \cdot 10^{-2}$	$3 \cdot 10^{-4}$	$50 - 120$
HADES	Belgium	500	N/A	0.1	$6 - 43$
Felsenkeller	Germany	110	$< 1.4 \cdot 10^{-4}$	6	$50 - 60$
BNO	Russia	4700	$1.4 \cdot 10^{-3} (> 1)$	$(3.03 \pm 0.19) \cdot 10^{-5}$	40
BUL	UK	2800	$1.7 \cdot 10^{-2} (> 0.5)$	N/A	N/A
CJPL	China	2500 rock	N/A	N/A	N/A
CUPP	Finland	1400 rock	N/A	N/A	N/A
LSC	Spain	2400	$2 \cdot 10^{-2}$	$(2 - 4) \cdot 10^{-3}$	$50 - 80$
LSM	France	4800	$5.6 \cdot 10^{-2}$	$4.7 \cdot 10^{-5}$	15
SUL	Ukraine	1000	$< 2.7 \cdot 10^{-2}$	$1.7 \cdot 10^{-2}$	33
Kamioka	Japan	2700	$2 \cdot 10^{-1}$	$3 \cdot 10^{-3}$	N/A
OTO-Cosmo	Japan	1400	$4 \cdot 10^{-2}$	$4 \cdot 10^{-3}$	10
Y2L	Korea	2000	$8 \cdot 10^{-3} (1.5 - 6)$	$2.7 \cdot 10^{-3}$	$40 - 80$
INO	India	3500	N/A	N/A	N/A
SNOlab	Canada	6010	$9.3 \cdot 10^{-2}$	$3 \cdot 10^{-6}$	120
SUL	USA	2000	N/A	$2 \cdot 10^{-3}$	$300 - 700$
DUSEL	USA	7200	N/A	N/A	N/A

A variety of underground laboratories exists worldwide of which most are the remains of abandoned mines or mine galleries and only few were built specifically for scientific

purposes. The main underground sites are listed in Tab. 4.2 with data from [116]. The table lists the location, overburden, neutron and muon fluxes as well the radon content in the air. The relevant underground laboratories for this work are LNGS (Italy), HADES (Belgium) and the Felsenkeller (Germany) which are described below.

4.5.1 Laboratori Nazionali del Gran Sasso (LNGS)

The LNGS [118] is part of the Italian Instituto Nazionale di Fisica Nucleare (INFN) and is one of the largest underground facility worldwide. It was proposed in 1979 as a cost efficient side gallery to a highway tunnel crossing the Apennine mountains close to L'Aquila. LNGS was approved in 1982, completed in 1987 and operated as an international laboratory since then. Three main halls and ancillary tunnels provide a space of $17300\,\mathrm{m}^2$ or $180000\,\mathrm{m}^3$ for experiments (see Fig. 4.14) that are recommended by an international Scientific Committee [116]. Experiments include the main physics topics of dark matter, double beta decay, solar neutrinos, supernova neutrinos, nuclear astrophysics and neutrino oscillation, amongst other. $1400\,\mathrm{m}$ of overburden ($3200\,\mathrm{m.w.e.}$) reduce the μ-flux to $3 \cdot 10^{-4}\,\mathrm{m}^{-2}\mathrm{s}^{-1}$. The total n-flux is measured to be $3.78 \cdot 10^{-2}\,\mathrm{m}^{-2}\mathrm{s}^{-1}$ and the radon activity in the air is $50 - 120\,\mathrm{Bq/m}^3$ [116].

Figure 4.14 Illustration of the LNGS underground laboratory and the surrounding landscape.

Both the GERDA and LArGe setups are located at LNGS. GERDA data is used in Chap. 10. A dedicated BEGe characterization measurement was set up at LNGS which is described in Chap. 6 and data from this setup is used in (Chap. 8). Furthermore, a palladium sample was measured in the screening facility at LNGS (Chap. 11).

4.5.2 High Activity Disposal Experimental Site (HADES)

The HADES facility is located in Mol, Belgium, and was built as a research facility for storage of high activity nuclear waste in a clay layer (Fig. 4.15). The facility is part of the Belgian Nuclear Research Center SCK·CEN (Studie Centrum voor Kernenergie Centre d'Etude de l'Energie Nucléaire) and managed by EURIDICE (European Underground Research Infrastructure for Disposal of nuclear waste In Clay Environment) since 1997 [119]. HADES is $223\,\mathrm{m}$ deep inside the "Boom clay" layer that spans northern Belgium and the Netherlands. The overburden accounts for $\approx 500\,\mathrm{m.w.e.}$ and reduces the μ-flux by three orders of magnitude to $\approx 0.1\,\mathrm{m}^{-2}\mathrm{s}^{-1}$. The radon content was measured to be

$6 - 43\,\mathrm{Bq/m^3}$ which is comparatively low due to the small uranium concentration in the clay [120]. An Ultra Low-level Gamma-ray Spectrometry (ULGS) facility with 9 HPGe detectors is operated by the Institute for Reference Material and Measurements (IRMM) which is part of the European Commissions Joint Research Centre (JRC) [120].
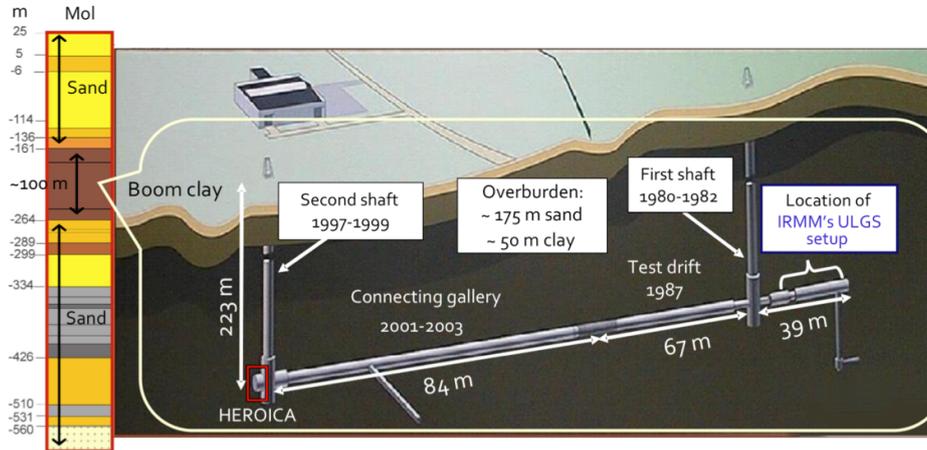
Figure 4.15 Illustration of the HADES underground facility. Highlighted are the ULGS and the HEROICA lab. From [121].

The HADES Experimental Research Of Intrinsic Crystal Appliances (HEROICA) facility was constructed in 2011 on the far side of the ULGS (Fig. 4.15). The main purpose of the $152\,\mathrm{m^2}$ new lab space was the characterization of the GERDA PHASE II BEGe detectors in an underground location and in close vicinity of the germanium detector manufacturer Canberra in Olen (see Chap. 6 and 7). A measurement of the palladium sample described in Chap. 11 was also performed at ULGS.

4.5.3   Niederniveaumesslabor Felsenkeller

The Niederniveaumesslabor[6] Felsenkeller [122] was built in 1982 and is run by the Verein für Kernverfahrenstechnik und Analytik (VKTA) Rossendorf e.V. since 1991. The main purposes is the decommissioning of the old nuclear facilities in Rossendorf, fissile material and waste management, environmental and radiation protection and commercial analytical services. The laboratory is situated outside Dresden and is easily accessible in the storage gallery of an old brewery with $47\,\mathrm{m}$ of Monzonite rock overburden ($110\,\mathrm{m.w.e.}$). Up to ten experimental setups are placed inside two chambers which are reinforced with up to $35\,\mathrm{cm}$ of composite shielding. A n-flux of smaller than $1.4 \cdot 10^{-4}\,\mathrm{m^{-2}s^{-1}}$ and a μ-flux of $6\,\mathrm{m^{-2}s^{-1}}$ is present inside the chambers. The radon activity is roughly $150\,\mathrm{Bq/m^3}$ in the gallery and $50 - 60\,\mathrm{Bq/m^3}$ inside the measuring chambers.

The palladium sample also measured at LNGS and HADES was initially measured at Felsenkeller (Chap. 11).

---

[6]German: Laboratory for low level background measurements.

Chapter 5

The GERDA Experiment

The GERmanium Detector Array (GERDA) is a state-of-the-art experiment designed to investigate the $0\nu\beta\beta$ decay of ^{76}Ge. An array of high purity germanium detectors is operated directly inside liquid argon (LAr) at the Laboratori Nazionali del Gran Sasso (Sec. 4.5.1). PHASE I of the experiment resulted in the worldwide most stringent limits on $0\nu\beta\beta$ decay in ^{76}Ge as well as for other $0\nu\beta\beta$ and $2\nu\beta\beta$ decay modes. PHASE II of the experiment is currently (fall 2015) being commissioned and features major upgrades which further increase the sensitivity for $0\nu\beta\beta$ decay and all other decay modes.

This chapter is organized as follows: The physics goals of GERDA are presented in Sec. 5.1 followed by the experimental setup in Sec. 5.2 and the GERDA specific software in Sec. 5.3. The PHASE I commissioning is briefly described in Sec. 5.4 followed by the achievements of the full PHASE I background run in Sec. 5.5. The upgrades and outlook for PHASE II are presented in Sec. 5.6. Especially the PHASE I dataset and the PHASE II developments are further discussed in the next chapters.

5.1 Physics Goals

The GERDA experiment was proposed in March 2004 [123] with the new concept of operating an array of bare HPGe detectors directly inside a large volume of cryogenic liquid as suggested in [111]. This approach combines the advantages of a radioactively ultra pure passive shielding, a scintillation based active shielding while providing the cryogenic cooling for the operation of the detectors. The construction in Hall A of LNGS was completed in November 2009 and followed by an extensive commissioning phase where the setup was optimized against an unexpected large background contribution from LAr born ^{42}K.

The physics program is divided into two phases. PHASE I was running from November 2011 until May 2013. It was designed to have a total mass of $18\,$kg with semi-coaxial HPGe detectors and a BI of $10^{-2}\,$cts/(kg · yr · keV). The detectors were refurbished from predecessor experiments of which 8 detectors had been isotopically enriched to $87\,\%\ ^{76}$Ge. With a planed total exposure of $20\,$kg · yr, the main purpose of PHASE I was to scrutinize the claim of $0\nu\beta\beta$ decay observation by a subgroup of the Heidelberg-Moscow (HdM) experiment (see Sec. 3.7). At this time only GERDA had the unique ability to test the claim through direct comparison on the half-live level. This avoids NME related uncertainties and assumptions when testing with another isotope. Additionally, 5 out of the 8 enriched detectors were originally used in the HdM experiment providing the possibility of scrutinization with the same detectors.

PHASE II is planned with additional $20\,\mathrm{kg}$ of BEGe detectors enriched in $^{76}\mathrm{Ge}$, a BI goal of $10^{-3}\,\mathrm{cts/(kg \cdot yr \cdot keV)}$ and a minimum exposure of $100\,\mathrm{kg \cdot yr}$. The goal for PHASE II is a half-life sensitivity of $1.4 \cdot 10^{26}\,\mathrm{yr}$ for $0\nu\beta\beta$ decay, corresponding to an effective Majorana neutrino mass of approximately $100\,\mathrm{meV}$, depending on the NME.

5.2   Detector Description

The experimental setup is described in [95] and illustrated in Fig. 5.1a. The shielding concept follows a graded approach. This includes a $650\,\mathrm{m}^3$ water tank, $16\,\mathrm{t}$ of copper lining and $64\,\mathrm{m}^3$ of LAr. Additionally, the water tank is instrumented as an active Cherenkov muon veto. The LAr will be instrumented as an active scintillation veto for muons and close radioactive sources in PHASE II. A brief descriptions of all components is given below.

(a) GERDA setup	(b) cryostat
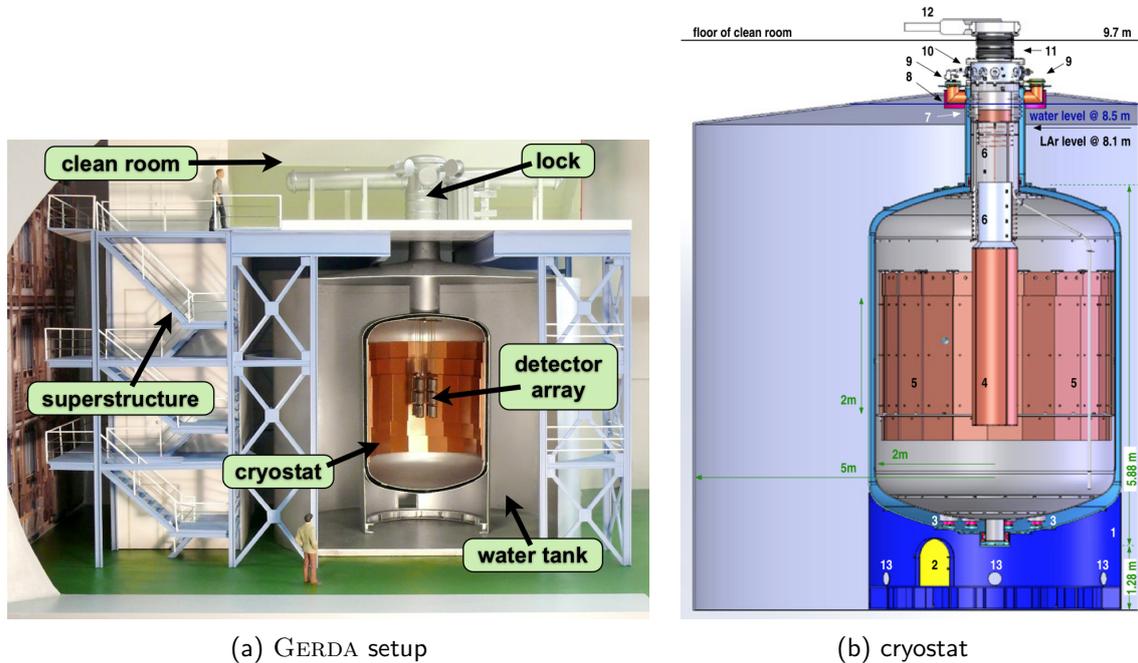
Figure 5.1 Left: GERDA illustration with main features (detector array not to scale). Right: Cross section of cryostat and water tank with dimensions. Relevant components: (4) Radon shroud, (5) inner Cu shield and (6) heat exchanger. From [95].

Water Tank and Muon Veto: The $650\,\mathrm{m}^3$ stainless steel water tank contains $590\,\mathrm{m}^3$ of $> 0.17\,\mathrm{M\Omega m}$ purified water. The $10\,\mathrm{m}$ diameter and $8.9\,\mathrm{m}$ high tank is lined with VM2000 reflective foil and equipped with 66 PMTs. Together with five $200\,\mathrm{cm}$ x $50\,\mathrm{cm}$ x $3\,\mathrm{cm}$ scintillator panels on top of the clean room they serve as the muon veto. The $3500\,\mathrm{m.w.e.}$ overburden at LNGS reduces the cosmic muon flux by a factor of 10^6 to $1.2\,(\mathrm{hr \cdot m}^2)^{-1}$. The muon veto works with more than $99.9\,\%$ efficiency. The muon component of the BI is $3.2 \pm 0.8 \cdot 10^{-3}\,\mathrm{cts/(kg \cdot yr \cdot keV)}$ without and $2.9 \pm 0.8 \cdot 10^{-5}\,\mathrm{cts/(kg \cdot yr \cdot keV)}$ with muon veto after anti-coincidence and before pulse shape cuts [124].

Cryostat: The double-walled stainless steel cryostat measures $5.9\,\mathrm{m}$ from bottom to neck and contains $64\,\mathrm{m}^3$ ($89.2\,\mathrm{t}$) of grade 5 LAr (Fig. 5.1b). $16\,\mathrm{t}$ of copper plates are lining the

inside of the wall for additional passive shielding with a thickness of $3 - 6$ cm. The central 75 cm diameter LAr volume around the detector array is separated with a $30\,\mu$m thin Cu foil. This so called Rn shroud prevents convection of LAr with higher radon content from the cryostat walls towards the detector array.

Superstructure and Cleanroom: The four level superstructure in Hall A contains room for a workshop, the DAQ and storage. On top of the superstructure is a class 10,000 clean room. The air inside is constantly monitored for radon concentrations. Inside the clean room is a glove box for detector string assembly in nitrogen atmosphere.

Lock System: Inside the clean room is a lock system which enables the submersion of the detector array into the cryostat through its neck. The cryostat neck has a height of 1.8 m and a diameter of 79 cm. The lock system is based on a deflection pulley due to height constrains in Hall A (about 18 m high). It contains mechanical support for the array as well as signal and HV cables. The lock system for PHASE I was composed of two individual arms: A 1-string arm and a 3-string arm supporting one and three detector strings respectively. During the commissioning only the 1-string arm was used. For PHASE II a new system is installed supporting a total of 7 strings on a single 7-string arm without modularization.

HPGe Detectors & Array Configurations: The detector array is composed of strings of one to five detectors each. For PHASE I, each string was surrounded with a $60\,\mu$m thin copper foil called Mini-Shroud (MS) to prevent ^{42}K migration (see Fig. 5.2a). The detectors were supported by low mass Cu holders that provided a modular assembly of multiple detectors into strings (see Fig. 5.2b). The electrical connection to the detectors was realized with copper screws and a pressure contact. The PHASE I holders needed to be solid enough to support this force. For PHASE II the electrical contacts are made with wire bonding which permits the use of cleaner and lighter Si detector holders. The PHASE I copper MS is incompatible with the LAr veto, blocking the scinitalltion light from inside the array, and the a transparent nylon MS will be used in PHASE II.

(a) detector string mounting in copper Mini-Shroud   (b) PHASE I low mass copper holders
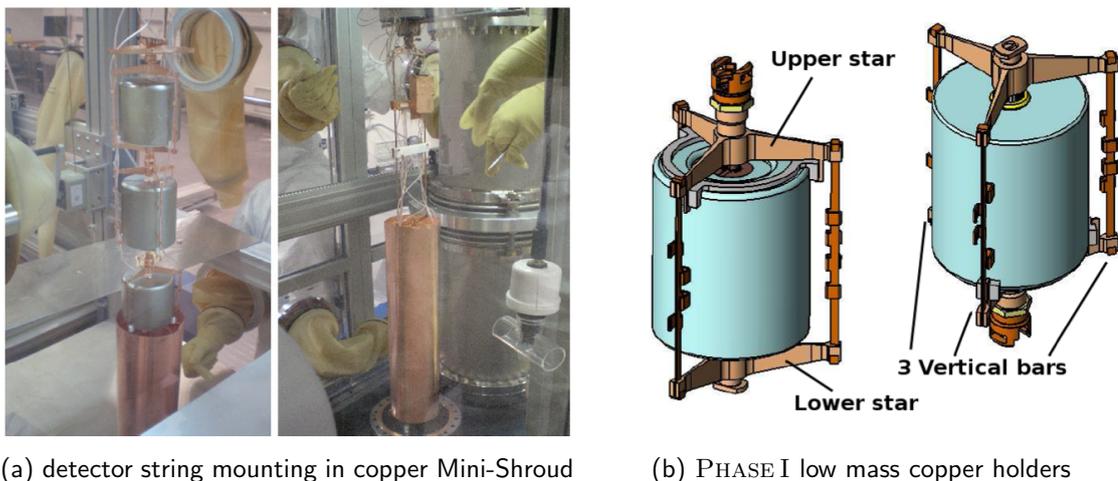
Figure 5.2 Detector string assembly in clove box (left). In PHASE I each detector string was surrounded by a thin copper Mini-Shroud. The detector holders consisted of three main parts: The upper star, the lower star and three vertical bars (right). From [95].

Two detector types are used in GERDA (see also Fig. 4.6): Semi-coaxial detectors refur-

bished from previous experiments provided the major exposure for PHASE I. Newly produced BEGe detectors will provide a comparable exposure as the semi-coaxial detectors for PHASE II. However, they will have a higher sensitivity due to better background rejection. Five of the new BEGe detectors were already deployed in the end of PHASE I. Tab. 5.1 lists the detectors that were deployed during the commissioning phase and PHASE I. The 5 $^{\text{enr}}$Ge semi-coaxial detectors ANG1-5 had been produced for the HdM experiment [125], the 3 $^{\text{enr}}$Ge semi-coaxial detectors RG1-3 had been produced for the IGEX experiment [126] and the 6 $^{\text{nat}}$Ge semi-coaxial detectors GTF(x) had been produced for the GENIUS test facility [127].

Table 5.1 Basic properties of PHASE I detectors. The columns denote from left to right: Detector name, the total mass, the ^{76}Ge abundance, the active volume (AV) fraction, the $0\nu\beta\beta$ decay detection efficiency, the detector origin (HdM: Heidelberg-Moscow, IGEX: International Germanium EXperiment and GTF: GENIUS Test Facility) and the deployment in GERDA (CS: commissioning string, PIa: first configuration of PHASE I, PIb: intermediate configuration of PHASE I without 1-string arm, PIc: last configuration of PHASE I). Values taken from [95] for semi-coaxial detectors. AV fraction and $0\nu\beta\beta$ detection efficiency for BEGe detectors are quoted as used in PHASE I analysis. Revised values in Chap. 7 may slightly differ.

working name	mass [g]	^{76}Ge abun. [%]	AV fraction [%]	$0\nu\beta\beta$ det. eff. [%]	det. origin	deployment
ANG1	958	85.9	83.0 ± 5.2	88.9 ± 1.8	HdM	PIa, PIb, PIc
ANG2	2833	86.4	87.1 ± 5.1	91.8 ± 1.8	HdM	PIa, PIb, PIc
ANG3	2391	88.2	86.6 ± 5.7	91.6 ± 1.8	HdM	PIa, PIb, PIc
ANG4	2372	86.3	90.1 ± 5.7	91.6 ± 1.8	HdM	PIa, PIb, PIc
ANG5	2746	85.6	83.1 ± 4.8	91.8 ± 1.8	HdM	PIa, PIb, PIc
RG1	2110	87.4	90.4 ± 5.9	91.5 ± 1.8	IGEX	PIa, PIb, PIc
RG2	2166	87.4	83.1 ± 5.3	91.2 ± 1.8	IGEX	PIa, PIb, PIc
RG3	2087	87.4	89.5 ± 5.4	91.4 ± 1.8	IGEX	PIa, PIb, PIc
GTF32	2321	7.8	97 ± 5	N/A	GTF	CS, PIa
GTF42	2467	7.8	N/A	N/A	GTF	
GTF44	2465	7.8	N/A	N/A	GTF	
GTF45	2332	7.8	N/A	N/A	GTF	CS, PIa
GTF110	3046	7.8	N/A	N/A	GTF	
GTF112	2965	7.8	N/A	N/A	GTF	CS, PIa
GD32B	717	87.7	89.0 ± 2.7	89.9 ± 1.8	new	PIc
GD32C	743	87.7	91.1 ± 3.0	90.1 ± 1.8	new	PIc
GD32D	723	87.7	92.3 ± 2.6	89.9 ± 1.8	new	PIc
GD35B	812	87.7	91.4 ± 2.9	90.1 ± 1.8	new	PIc
GD35C	635	87.7	90.6 ± 3.2	89.2 ± 1.8	new	PIc

The PHASE I array was deployed in three different sub configurations. The 3-string arm was continuously deployed with all 8 $^{\text{enr}}$Ge semi-coaxial detectors and GTF112. The 1-string arm was initially equipped with the $^{\text{nat}}$Ge semi-coaxial detectors GTF32 and GTF45. This period from November 2011 to June 2012 is called PHASE Ia. In June 2012 the 1-string arm was removed and reconfigured with 5 $^{\text{enr}}$Ge BEGe detectors. In an intermediate period of 3 weeks only the 3-string arm was deployed (PHASE Ib). The final period with the 5 BEGe detectors in the 1-string arm from July 2012 to the end of PHASE I on May 2013 is called PHASE Ic. The array configurations and dimensions are illustrated in Fig. 5.3.
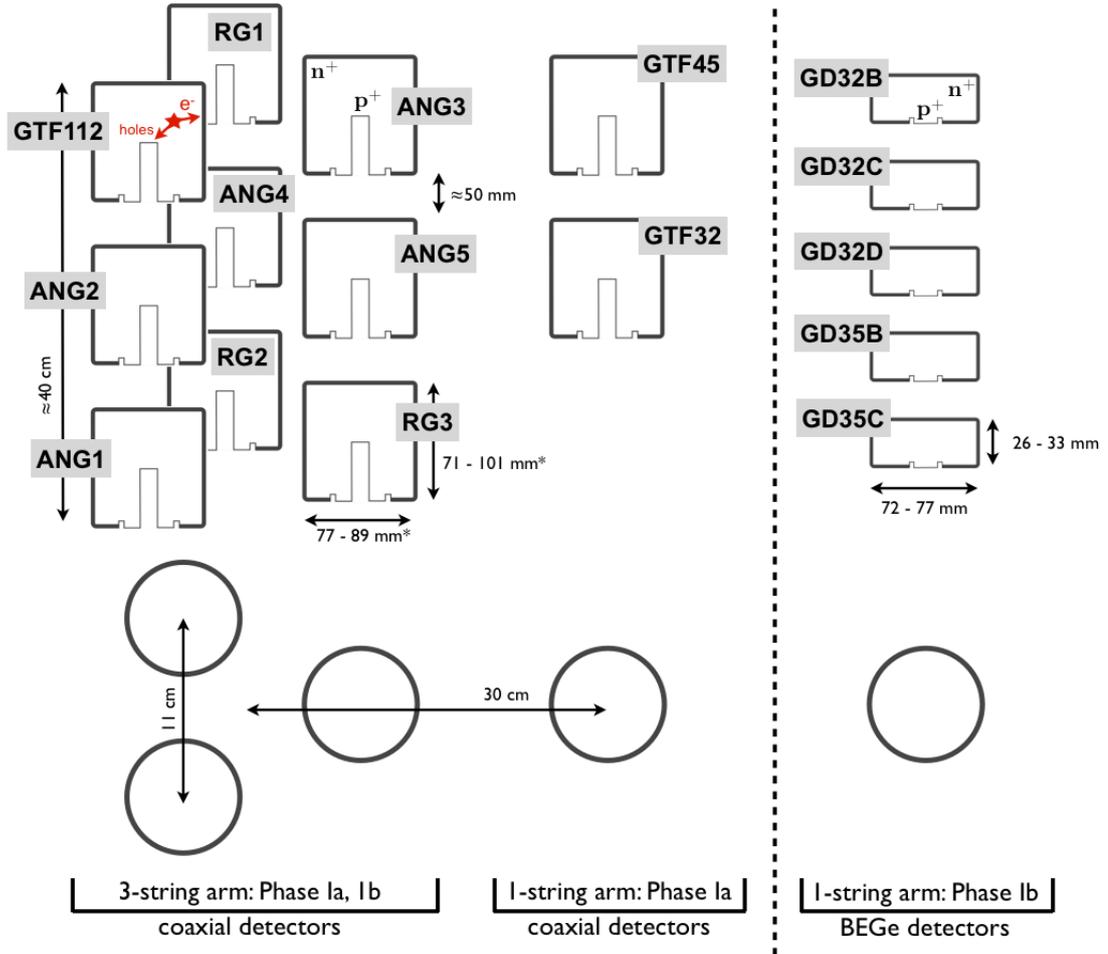
Figure 5.3 Illustration of the GERDA PHASE I array configurations. PHASE Ia contains strings 1-3 and 4a, PHASE Ib contains string 1-3 and PHASE Ic contains strings 1-3 and 4b.

Electronics: The PHASE I front-end electronics consists of custom made charge sensitive preamplifiers placed inside the LAr at ≈ 40 cm above the top detector of each string. This optimizes the electronic noise level which prefers short cable length versus the radioactive background contribution which is reduced with distance. The charge signal is sampled with an FADC as described in Sec. 4.2.3. For PHASE II the front-end electronics are separated into two stages to further optimize the noise mitigation without sacrificing in background. The first stage focus on high radioactive purity and consists of a JFET, a capacitor and a resistor sitting on top of the silicon wafer that holds the detector. A second, less radioactively pure, stage contains a preamplifier and is located 80 cm above the top of the detector assembly.

Calibration: The energy calibration is performed with three ^{228}Th sources which are lowered from the top of the cryostat in-between the detector array for about 1 h calibration per week. In PHASE I the energy shift between consecutive calibrations was typically smaller than 1 keV at $Q_{\beta\beta}$. The deviation of reconstructed peak positions from the calibration curves was smaller than 0.3 keV. The calibrations are also used to monitor the energy resolution which was stable over the entire time of PHASE I data taking. A comparison of the energy resolution of the 1524.6 keV ^{42}K γ-line in the background spectrum shows a 10 %

larger resolution than calculated from the calibration curves. This small variation illustrates the good stability of the energy scale between calibrations. The exposure-averaged energy resolutions are $4.8 \pm 0.2\,\mathrm{keV}$ and $3.2 \pm 0.2\,\mathrm{keV}$ FWHM at $Q_{\beta\beta}$ for the semi-coaxial detectors and the BEGe detectors, respectively.

5.3   Software Description

Two dedicated software frameworks are used in GERDA. The GELATIO framework is used for processing the FADC raw data providing various modular tools for event reconstruction. The MaGe framework is used for Monte Carlo (MC) simulations.

5.3.1   GELATIO: HPGe Detector Signal Processing

The GELATIO (GErda LAyouT for Input/Output) framework [128] is a tool for analysis and digital signal processing of FADC data. It is designed to support the full analysis chain from reading charge traces to calibration. It can incorporate various veto channels coming from the muon veto and the LAr veto. GELATIO is based on MGDO (Majorana Gerda Data Objects) [129] which is a joint development between the GERDA and Majorana collaborations. MGDO is providing various waveform transformations and data containers.

5.3.2   MaGe: Monte Carlo Simulations

MaGe (MAjorana-GErda) [130] is a common development of the GERDA and Majorana collaborations. It is based on GEANT4 [131, 132] providing dedicated physics lists for the simulation of low energy processes. MaGe includes the geometries of various experimental setups including the full GERDA geometry. Additionally, it includes tools such as interfaces to commonly used event generators (e.g. DECAY0), random sampling of events in bulk volumes or on surfaces, decay chain simulation and an out-of-the-box simulations of simple geometries without hardcoded implementation.

Depending on the simulated particles and energies, various physics realms are defined. They differ strongly in the maximum stepping length during particle propagation and CPU requirements:

DarkMatter: Used for very low energies with high stepping precision. γ-ray steps are smaller than $0.005\,\mathrm{mm}$ and beta tracks smaller than $0.0005\,\mathrm{mm}$.

BBDecay: Used for DBD simulations and most background simulations at medium energies of $\mathcal{O}(1\,\mathrm{MeV})$. γ-ray and beta track steps are smaller than $0.1\,\mathrm{mm}$.

CosmicRay: Used for cosmic muons at higher energies. γ-ray steps are smaller than $5\,\mathrm{cm}$ and beta tracks smaller than $1\,\mathrm{cm}$.

DeadLayer: A dedicated realm is introduced for investigating the n^+ electrode in Chap. 7 and Chap. 8. The stepping length is reduced to $1\,\mathrm{micron}$ for γ-rays and betas inside the germanium detector. Additionally, the secondary production threshold[1] is lowered to $250\,\mathrm{eV}$. Outside the germanium volume the tracking is equal to the BBDecay realm saving computing time. See also Sec. 7.1.2 for application and comparison with other realms.

---

[1]The secondary production threshold defines an energy above which the secondary particles are further propagated. Below this energy the particle energy is deposited at the location of the interaction.

The typical use of MaGe at run time is via a macro file or a command line user interface. The major components of a MaGe simulation which need to be specified are: (1) geometry definition, (2) physics list definition, (3) event generation, (4) event sampling, (5) output scheme and filename and (6) a simulation run. Along this way the simulation can be tuned and adjusted in manifold flexible ways. MaGe is heavily used throughout this work and analysis specific details are given in the respective chapters.

5.4   Commissioning Phase

The commissioning of GERDA started November 2009 and lasted until the start of PHASE I in November 2011. An unexpected large background contribution of ^{42}Ar$-^{42}$K was found which was not compatible with a homogeneous distribution of ^{42}K in the LAr. This triggered an extensive investigation of mitigation strategies. See e.g. [133] for a summary. As a consequence the MS (Fig. 5.2a) was introduced in PHASE I to mechanically block each detector string from ^{42}K.

5.5   Phase I

5.5.1   Phase I Datasets

For the GERDA PHASE I $0\nu\beta\beta$ analysis [27] the data is separated in BEGe and semi-coaxial detectors due to their different properties. The semi-coaxial dataset is further divided into a *golden* and *silver* dataset due to a short increase in the background level at the time of detector operation in July 2012 for the BEGe insertion. The three datasets amount to a total live-time of 492.3 d and 21.6 kg · yr of enriched germanium[2]. A summary of the datasets is shown in Table 5.3.

In order to perform an unbiased analysis of $0\nu\beta\beta$ decay, a blinding procedure was applied on the raw data conversion. Events in the energy window $Q_{\beta\beta}\pm20$ keV were not initially processed and remained hidden during the analysis preparations.

5.5.2   Background in Phase I

A fraction of 18.5 kg · yr of the PHASE I dataset[3] is analyzed and decomposed into individual background contributions in [115]. The energy spectrum for BEGe and semi-coaxial detectors is shown in Fig. 5.4. Additionally, the spectrum of the ^{nat}Ge semi-coaxial detector GTF112 is shown. The dominating features is the ^{39}Ar beta decay at low energies, the $2\nu\beta\beta$ decay of ^{76}Ge and the 1524.6 keV ^{42}K γ-line at intermediate energies and an alpha component at higher energies. Additional γ-lines from ^{40}K, ^{214}Bi, ^{214}Pb and ^{228}Th can be identified.

^{39}Ar is a pure beta emitter with an endpoint of 565 keV. It is the dominant background at low energies but has no influence on the $0\nu\beta\beta$ region of interest (ROI). The ^{76}Ge $2\nu\beta\beta$ component is clearly visible above 600 keV and stronger pronounced in the isotopically enriched detectors than in the natural one. A dedicated analysis of the $2\nu\beta\beta$ decay was performed with 17.9 kg · d of PHASE I data which is reported in [52]. The signal p.d.f. was fitted together with the background model in a range of $570 - 7500$ keV. The analysis is

---

[2]The exposure refers to the elemental mass of germanium enriched to 87 % in ^{76}Ge.
[3]The background model was fixed prior to the end of the data taking.
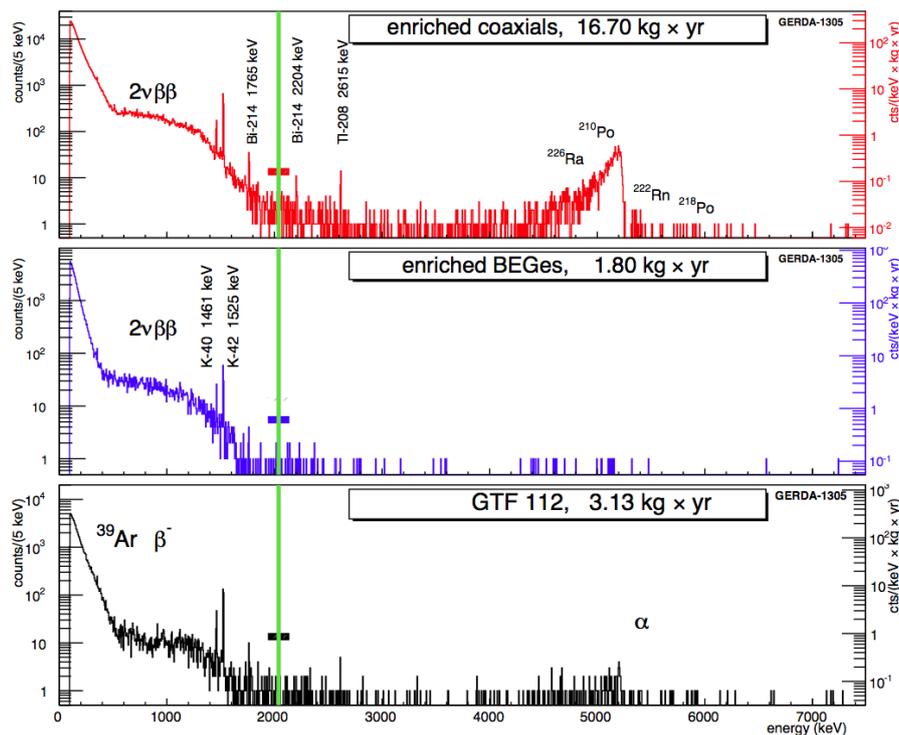
Figure 5.4 GERDA PHASE I energy spectrum from the $^{\mathrm{enr}}$Ge semi-coaxial detectors (top), the $^{\mathrm{enr}}$Ge BEGe detectors (center) and a $^{\mathrm{nat}}$Ge semi-coaxial detector (bottom). From [115].

based on a Bayesian maximum posterior likelihood fit and yields a $2\nu\beta\beta$ decay half-life of

$$T_{1/2}^{2\nu} = \left[1.926^{+0.025}_{-0.022}\,(\mathrm{stat})\,^{+0.091}_{-0.091}\,(\mathrm{syst}) \right] \cdot 10^{21}\,\mathrm{yr}\,. \tag{5.1}$$

The most prominent γ-line originates from ^{42}K which is part of a decay chain starting from ^{42}Ar, a radioactive low natural abundance isotope in argon which is produced via cosmic activation. ^{42}K can be ionized after the preceding ^{42}Ar decay and drift in the LAr towards the crystals due to the electric field created by the HV applied to the detector. This results in an increased background component in the measured data, which is not consistent with an homogeneous distribution. ^{42}K has a Q-value of 3525.4 keV and beta-decays with 81.9 % probability into the ground state (see Fig. A.4 in the appendix for the decay scheme). In 17.6 % of the cases the decay is followed by the emission of a 1524.6 keV γ-ray. Especially for decays into the ground state, the resulting high energy betas have the potential to penetrate the n$^+$ electrode layer of HPGe detectors which are in the range of 2 mm for the semi-coaxial detectors and $0.5 - 1.0$ mm for the BEGe detectors. For the thin dead layer BEGe detectors, around 60 % of the background in the ROI is attributed to ^{42}K surface event. The detailed decomposition of the BEGe background model in PHASE I is shown in Tab. 5.2.

The events at higher energy originate from alpha decays on the p$^+$ electrode surface which has a dead layer thickness of $\mathcal{O}(\mu\mathrm{m})$. The p$^+$ area is larger in the semi-coaxial detectors including the bore hole and thus making this detector type more prone to significant alpha contribution to the background. The main alpha component was identified as ^{210}Po with a fit of the count rate over time matching the ^{210}Po half-life of 138.4 d. The alpha background contribution in the ROI was estimated to be $10 - 15$ % for semi-coaxial detectors.

Table 5.2 Background model for Phase I BEGe dataset before pulse shape cuts as described in [115]. Shown is the background contribution and the location. The background index contribution is shown as the global mode of the Bayesian fit. The uncertainties in brackets are the smallest 68 % interval of the marginalized distributions of each contribution. The last columns shows the fraction of the contributions.

nuclide	location	BI $[10^{-3}\,\mathrm{cts}/(\mathrm{kg}\cdot\mathrm{yr}\cdot\mathrm{keV})]$	fraction
^{42}K	LAr homogeneous	2.0 [1.8,2.3]	0.06
^{42}K	n$^+$ electrode	20.8 [6.8,23.7]	0.59
^{60}Co	germanium	1.0 [0.3,1.0]	0.04
^{214}Bi	det. assembly	5.1 [3.1,6.9]	0.14
^{214}Bi	p$^+$ electrode	0.7 [0.1,1.3]	0.02
^{228}Th	det. assembly	4.2 [1.8,8.4]	0.12
α model	p$^+$ electrode and close by LAr	1.5 [1.2,1.8]	0.03

Other major background contributions where identified as ^{214}Bi and ^{208}Tl in the detector assembly.

The ultimate conclusion of the background decomposition of Phase I data is the validation of a flat continuous background assumption in the energy window of $\approx 200\,\mathrm{keV}$ around $Q_{\beta\beta}$ and the absence of known γ-lines in the ROI of $0\nu\beta\beta$.

5.5.3   Analysis of $0\nu\beta\beta$ Decay with Phase I Data

The event topology of $0\nu\beta\beta$ decays are two electrons that deposit their energy almost always inside a small volume inside a single detector. Events with energy depositions in more than one detector and events within a muon veto trigger window of $8\,\mu s$ are removed from the dataset. These cuts reject roughly $40\,\%$ of events around $Q_{\beta\beta}$. A coincidence cut for events within $1\,\mathrm{ms}$, designed to remove the ^{214}Bi$-^{214}$Po chain, rejects two events. These cuts practically do not reduce the detection efficiency for $0\nu\beta\beta$ events nor introduce a dead time.

A pulse shape discrimination (PSD) cut is applied to reject surface and γ-ray background events in the surviving event sample [97]. The PSD method for the BEGe detectors is based on an A/E cut (Sec. 4.2.3). The A/E versus E values for the Phase I BEGe events are shown in Fig. 5.5. The red lines illustrate the low and high A/E cut selecting single site bulk events. The green region shows the blinding window. It can be seen that the majority of events around $Q_{\beta\beta}$ has a reduced A/E value which is in line with the background model identifying ^{42}K on the n$^+$ electrode as the major background component. Those events are largely removed by the cut. Also high energy events can be seen with large A/E values which are attributed to alpha decays on the p$^+$ electrode and inside the groove; also these events are removed. After the cut, with a $0\nu\beta\beta$ event survival efficiency of 0.92 ± 0.02, more than $80\,\%$ of the counts in the BI window are removed.

The PSD methods for semi-coaxial detectors are significantly less effective due to a larger variety of pulse shapes for single-site events (SSE). A neutral network is used to separate SSE and MSE. With a fixed SSE survival efficiency of 0.90, about $45\,\%$ of counts in the BI window are removed. The PSD cut performance is cross checked with two independent PSD methods and with $2\nu\beta\beta$ events in the data [97].
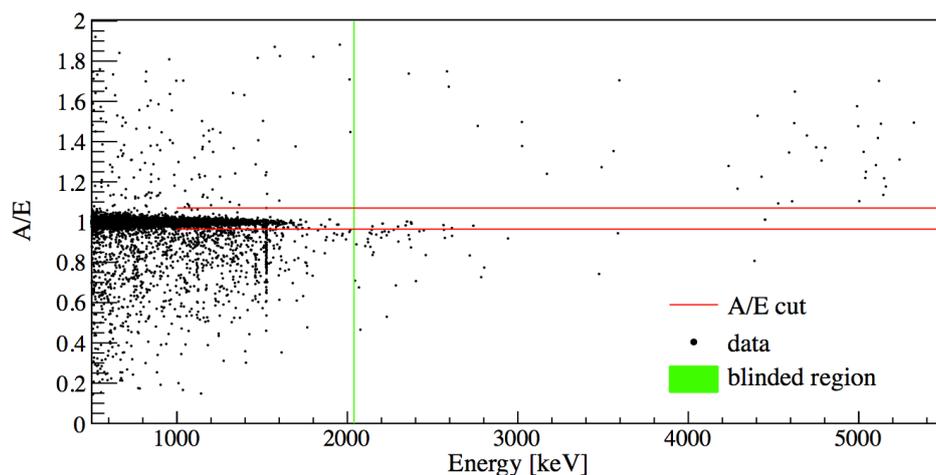
Figure 5.5 A/E values of events in the GERDA PHASE I BEGe dataset. The solid red lines denote the high and low A/E cut to select single site bulk events. The green region denotes the blinding window. From [97].

The unblinding of the $Q_{\beta\beta}\pm20\,\text{keV}$ window was performed in two steps: In a first step the 15 keV wings of the window were unblinded to cross check the understanding of the background. Then, the dataset, all cuts and the statistical analysis were fixed prior to the second step: the processing of the events inside the remaining window of $Q_{\beta\beta}\pm5\,\text{keV}$. After the full unblinding, 7 events were found before PSD and 3 events after PSD in $Q_{\beta\beta}\pm5\,\text{keV}$. This can be compared to 5.1 and 2.5 expected background events, respectively. The observed number of counts in the ROI is consistent with the background expectation and no signal is found. See also Tab. 5.3 for the results of the individual datasets.

Table 5.3 Summary of exposure and counts in the PHASE I datasets for $0\nu\beta\beta$ analysis.

dataset	exposure [kg·yr]	background level [10^{-2} cts /(keV·kg·yr)]		expected counts $Q_{\beta\beta}\pm5\,\text{keV}$		observed counts $Q_{\beta\beta}\pm5\,\text{keV}$	
		w PSD	w/o PSD	w PSD	w/o PSD	w PSD	w/o PSD
Golden	17.9	1.8 ± 0.2	1.1 ± 0.2	3.3	2.0	5	2
Silver	1.3	$6.3^{+1.6}_{-1.4}$	$3.0^{+1.1}_{-0.9}$	0.8	0.4	1	1
BEGe	2.4	$4.2^{+1.0}_{-0.8}$	$0.5^{+0.4}_{-0.3}$	1.0	0.1	1	0
Sum	21.6			5.1	2.5	7	3

A profile likelihood fit is used to extract a lower half-life limit. The fit function is a Gaussian peak with a constant background. It is used on each dataset with $1/\text{T}^{0\nu}_{1/2}$ as a common parameter. The width of the Gaussian is fixed to the known energy resolution of each dataset. The mean is centered around $Q_{\beta\beta}\pm0.2\,\text{keV}$. The background is left unconstrained for each set in a 240 keV window from 1930 keV to 2190 keV. Excluded are $\pm5\,\text{keV}$ windows around known γ-lines of 2104 keV from ^{208}Tl and 2119 keV from ^{214}Bi. The signal strength is not allowed to be negative: $1/\text{T}^{0\nu}_{1/2} \geq 0$. Systematic uncertainties (such as the peak position, the resolution and all efficiencies) are folded into the analysis a posteriori by toy MC. The result is taken as the average limit of 10,000 simulated experiments with randomly

generated sets of parameters in the allowed space of the systematic uncertainties. The best fit yields 0 counts and the 90 % quantile yields a lower half-life limit of

$$T_{1/2}^{0\nu} \geq 2.1 \cdot 10^{25} \, \text{yr} \quad (90 \, \% \, \text{C.L.}).$$

Without systematic uncertainties the limit improves by 1.5 %. The sensitivity, defined as the median value of a set of 10,000 toy MC experiments with the background only assumption, is $T_{1/2}^{0\nu} \geq 2.4 \cdot 10^{25} \, \text{yr}$ (90 % C.L.).

The results from the IGEX [126] and HdM [125] experiments can be included in this analysis as a 4th and a 5th dataset. The likelihood of the combined GERDA datasets, the IGEX and HdM datasets as well as their combination is shown in Fig. 5.6. A combined lower half-life limit for ^{76}Ge is set to:

$$T_{1/2}^{0\nu} \geq 3.0 \cdot 10^{25} \, \text{yr} \quad (90 \, \% \, \text{C.L.}).$$

The 2004 claim [70] is tested with the GERDA PHASE I data. Two hypotheses are compared: The H_1 hypothesis with the $0\nu\beta\beta$ decay half-life claim of $1.19^{+0.37}_{-0.23} \cdot 10^{25}$ yr and the H_0 hypothesis with the background only assumption. 5.9 signal and 2.0 background events are expected in $Q_{\beta\beta} \pm 2\sigma_E$ for H_1 in the GERDA dataset after PSD. In total, three events are observed and the spectral fit yields 0 signal events. The probability to observe no event assuming H_1 is $p(\text{data}|H_1) = 0.01$; hence the claim is strongly disfavored. The Bayes factor defined as $B = p(\text{data}|H_1)/p(\text{data}|H_0)$ is $B = 0.024$. The combined result for ^{76}Ge, including IGEX and HdM data, yields $B = 2 \cdot 10^{-4}$. In conclusion, GERDA PHASE I could confute the HdM claim with large probability.
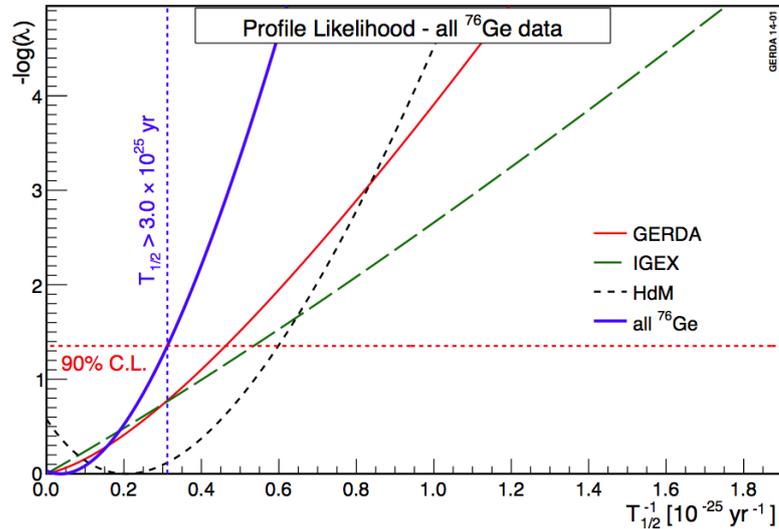
Figure 5.6 Likelihoods of $1/T_{1/2}^{0\nu}$ for the combined GERDA datasets, the IGEX dataset, the HdM dataset and their combination. From [81].

Assuming light Majorana neutrino masses as the dominating DBD process, also the EXO-200 and Kamland-ZEN experiments confute the claim for most NMEs. See Sec. 3.7.1 for the general status of DBD results and Fig. 3.8 for a comparison between ^{136}Xe and ^{76}Ge.

5.6   Phase II

The main upgrades for GERDA PHASE II are the procurement of 20 kg additional enriched BEGe detectors and a scintillation veto in the LAr. Additional background reduction is achieved with new silicon plate detector holders and radioactively purer two stage front-end electronics. The energy resolution is improved by the front-end electronics and the BEGe detector design. Additionally the background discrimination via PSD is improved with BEGe detectors.

The active volume and n^+ electrode surface of the new PHASE II BEGe detectors are characterized in this work and described in Chap. 7. The rejection of the dominating surface background of ^{42}K is investigated with newly developed pulse shape simulations in Chap. 8. The LAr scintillation veto is also crucial for reaching the PHASE II background goals. The design of the LAr veto was accompanied with extensive MC studies in order to optimize the suppression of various background contributions. A part of this MC study is presented in Chap. 9.

The deployment scheme of the PHASE II detector array was not fixed at the writing. The studies in this work are based on a tentative array of 30 BEGe detectors and 9 semi-coaxial detectors arranged in 4 and 3 strings, respectively. A GEANT4 visualization of this array is shown in Fig. 5.7. The three center strings are populated with semi-coaxial detectors and the four flanking strings with BEGe detectors. The semi-coaxial detectors are implemented with the dead layer properties in Tab. 5.1. The BEGe detectors are implemented with the n^+ electrode dead layer values from the characterization presented in Chap. 7 (Tab. 7.3).

(a) array top view   (b) array side view   (c) BEGe pair with holder
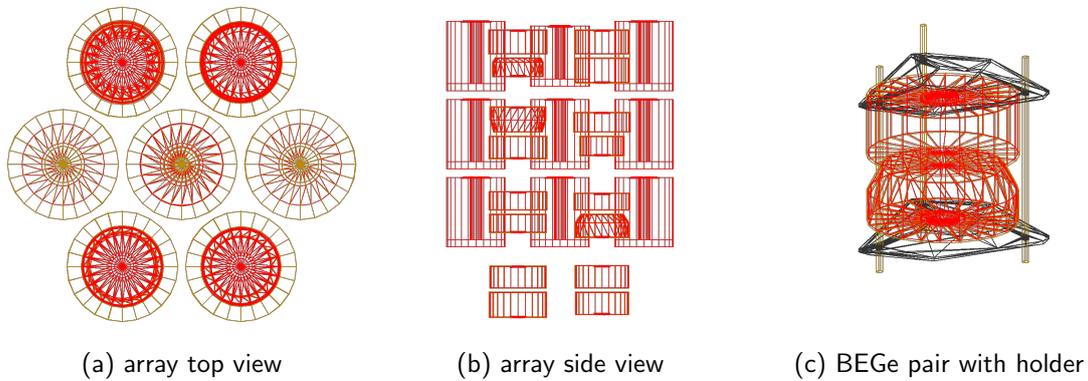
Figure 5.7 Illustration of the tentative PHASE II array configuration. In the top view (a), the two upper and two lower strings are composed of BEGe detectors and the three center strings of semi-coaxial detectors. The nylon MS around each string are shown in orange. In the side view (b), only two out of four BEGe strings are shown for visibility. A BEGe pair (c) is shown with silicon holders in gray.

The silicon holders of the detectors are implemented in the MC geometry and shown in Fig. 5.7c. The cabling and electronic components around the detectors are not yet implemented. The arrangement of the detectors inside the strings is chosen randomly and will not be further specified. However, a different arrangement has only a small effect on the overall results since the detectors have similar dimensions within their type.

Chapter 6

Phase II BEGe Production and Characterization Setups

30 new BEGe detectors were produced and characterized for GERDA PHASE II. The production of the detectors required a significant amount of logistics in order to reduce the exposure to cosmic radiation. The main characterization campaign was performed in the HADES underground facility in Mol, Belgium. Within this project called HEROICA (Hades Experimental Research Of Intrinsic Crystal Appliances), a dedicated laboratory was set up. The results of the main characterization campaign were inconclusive or insufficient for some detector properties. To further investigate these properties, a single enriched BEGe detector (GD91C) was mounted upside-down without passivation in a vacuum cryostat at LNGS.

This chapter is organized as follows: A brief summary of the BEGe production line is given in Sec. 6.1. The geometrical dimensions and operational parameters of the detectors are listed in Sec. 6.2. The characterization facility in HADES is described in Sec. 6.3 and the mounting, operation and measurements with the upside-down setup are described in Sec. 6.4. A few selected results are given in Sec. 6.5.

6.1   Production of 30 BEGe detectors

Prior to the production of BEGe detectors from enriched material, the full production chain was tested and optimized with residual depleted material from the enrichment process. The procedures and results from the depleted BEGe detectors is described in [134].

The production of enriched BEGe detectors relevant for this work is described in [114]. Starting from the crystal pulling, the production proceeded in two batches. A first batch of 7 BEGe detectors was processed and characterized first. 5 of these detectors were already deployed in GERDA PHASE I. In brief, the production steps are:

Enrichment: Natural germanium is fluorinated to $^{nat}GeF_4$. The $^{nat}GeF_4$ is heated until it becomes gaseous and is then enriched in centrifuges to $^{enr}GeF_4$. This is in turn converted with hydrolysis to $^{enr}GeO_2$. The enrichment process was performed at Production Association Electrochemical Plant (ECP) in Zelenogorsk, Russia. $53.4\,kg$ of $^{enr}GeO_2$ powder was produced.

Purification: The $^{enr}GeO_2$ was reduced to metallic germanium under H_2 atmosphere. The metallic germanium was then zone-refined in perpetual steps until 6N purity

(99.9999 %) was reached. The purification was performed at PPM Pure Metals GmbH in Langelsheim, Germany. The yield was 94.5 % leaving 35.5 kg of 6N ^{enr}Ge.

Crystal growth: Prior to crystal growth, the 6N ^{enr}Ge is further zone refined to 11N material. Two batches of ingots were produced from this material with 2 and 7 ingots respectively. From each ingot 2-4 crystal slices were cut out. The first batch consists of 7 slices and the second batch of 23 slices. The crystal growth was performed at Canberra Industries Inc., Oak Ridge (TN), USA. The total mass yield in crystal slices is 20.0 kg ^{enr}Ge.

Diode production: HPGe semiconductor diodes (Sec. 4.2.2) were produced from the crystal slices at Canberra Semiconductors N.V., Olen, Belgium. The major steps are surface grinding, groove drilling and the implantation of the p$^+$ electrode with a boron beam. The n$^+$ electrode was created with diffusion of lithium into the surface during one or two annealing cycles. The diodes were mounted in vacuum cryostats and basic operational parameters were tested by the company. Requirements for delivery were (1) an energy resolution < 2.3 keV FWHM at 1333 keV, (2) the stable operation at ≤ 4 kV and (3) a leakage current < 50 pA at depletion voltage.

The information provided by Canberra on the detector datasheets is summarized in Tab. B.1 in the appendix. The name of the BEGe detectors was different at each production step. Tab. B.2 in the appendix shows the translation of identifiers for future reference including the Canberra Oak Ridge name, the Canberra Olen name, the acceptance test working name and the final GERDA name. In this work, the final name attributed by GERDA shall be used.

6.2 BEGe Geometry and Dimensions

The diodes are distinguished according to their position in the ingot whereas the slice closes to the seed is refereed to as AA. The consecutive slices are called BB, CC and DD. An ingot and its separation into four slices is illustrated in Fig. 6.1.

(a) germanium ingot   (b) detector slice separation
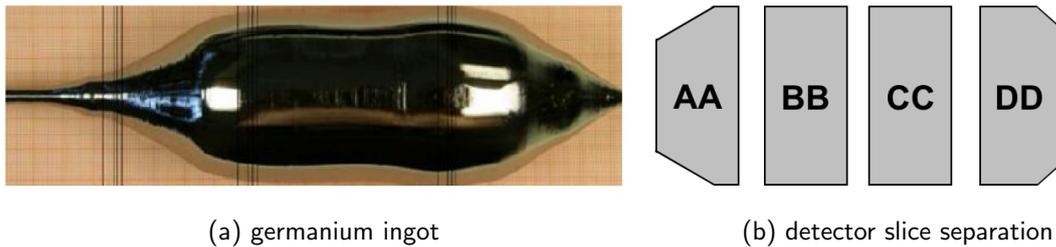
Figure 6.1 Germanium ingot after crystal pulling (left) and its separation into detector slices (right). Note that not all ingots yield four slices and not all slices are suitable for detector fabrication.

Two different ideal BEGe geometries are considered: (1) A cylindrical diode and (2) a conical diode. These geometries are illustrated in Fig. 6.2. The conical diodes are the result of maximizing the ^{enr}Ge yield during production. They are typically the slices at the ends of the ingot AA or DD. Among the 30 BEGe detectors are 7 conical AA slices and 1 conical DD slice.
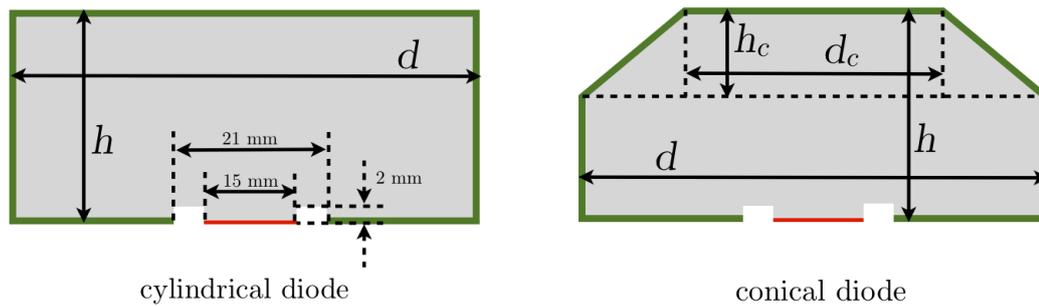
Figure 6.2 Shapes of BEGe detectors as implemented in the analysis. The n^+ electrode is illustrated in green, the p^+ electrode in red. The groove separating the n^+ electrode and p^+ electrode has the same dimensions for all detectors.

The diodes were grinded manually and variations from the ideal shapes can occur. The diode dimensions were measured by GERDA[1] and are documented in Tab. 6.1 according to the definitions in Fig. 6.2. Each dimension was measured at 4 to 5 different positions to estimate a potential tilt or eccentricity of the diodes. The uncertainties given in Tab. 6.1 are the standard deviations of these measurements under the assumption of ideal shape. A large uncertainty is an indication for large deviations from the ideal dimensions. Another cross-check is the calculation of the diode mass from the diode volume assuming the measured dimensions, ideal shape and the density of $^{\mathrm{enr}}$Ge of $5.54\,\mathrm{g/cm^3}$. This "MC mass" m_{MC} can be compared to the measured mass m_{scale}. The mass difference $\Delta m = m_{\mathrm{MC}} - m_{\mathrm{scale}}$ can be positive or negative and is shown in the last two columns of Tab. 6.1 in absolute and relative units.

Some diodes have especially strong variations and are marked in Tab. 6.1. A mass discrepancy $> 1\,\%$ is found for diodes GD32A, GD32D, GD79B, GD89D, GD91D, GD00A and GD00C. The geometric MC model in these cases may be inadequate for the determination of the active volume (Chap. 7) and can yield incorrect results. Some diodes show other known anomalies and require special attention. They are also marked in Tab. 6.1. The pictures of some of these diodes are shown in Fig. B.1 in the appendix. GD91C is a regular cylindrical diode without anomalies and is used as an example throughout this work. It is shown in Fig. B.1a as a crystal slice before diode production. Fig. B.1d and B.1e show GD00A as an irregular conical detector before and after diode production. The change of surface texture is clearly visible. Also visible is the convex surface on the cone part. The remaining pictures show other irregular cases which are listed below.

GD61A, GD91A, GD00A Conical diodes which have a non-regular cone. Typically, the cone part is convex or double coned. This feature decreases the ideal m_{MC} over the measured mass m_{scale}. Examples are shown in Fig. B.1b, B.1d, B.1e and B.1f.

GD89D A part of the corner is chopped off. See Fig. B.1g.

GD61B This diode is classified as cylindrical but shows a small decrease of diameter towards the top.

---

[1]The dimensions provided by the manufacturer did not have the necessary precision and were often erroneous.

Table 6.1 BEGe dimensions and mass. Distances are measured with a caliber on multiple positions. The uncertainties are the standard deviation of the measurements. The mass is weighted with a scale. The mass difference $\Delta m = m_{\mathrm{MC}} - m_{\mathrm{scale}}$ is the difference between the calculated mass assuming a volume with ideal shape and the measured mass. The last three rows show the minimum, maximum and average value of the dimensions.

detector	h [mm]	d [mm]	h_c [mm]	d_c [mm]	m [g]	Δm [g]	Δm [%]
GD32A^e	24.90 ± 0.03	66.26 ± 0.07	5.50 ± 0.50	60.00 ± 0.50	458 ± 1	6.2	1.3
GD32B	32.16 ± 0.12	71.89 ± 0.04			716 ± 1	5.3	0.7
GD32C	33.15 ± 0.06	71.99 ± 0.01			743 ± 1	2.6	0.4
GD32D^e	32.12 ± 0.09	72.29 ± 0.02			720 ± 1	8.5	1.2
GD35A	35.34 ± 0.08	73.54 ± 0.06	12.75 ± 0.25	58.25 ± 0.25	768 ± 1	3.7	0.5
GD35B	32.10 ± 0.11	76.33 ± 0.03			810 ± 1	1.9	0.2
GD35C	26.32 ± 0.18	74.84 ± 0.06			634 ± 1	5.6	0.9
GD61A^c	33.57 ± 0.46	73.48 ± 0.03	16.13 ± 0.36	63.51 ± 0.54	731 ± 1	6.7	0.9
GD61B^a	30.21 ± 0.10	75.95 ± 0.03			751 ± 1	5.4	0.7
GD61C	26.45 ± 0.10	74.56 ± 0.02			634 ± 1	3.9	0.6
GD76B^f	26.29 ± 0.06	58.27 ± 0.13			384 ± 1	2.5	0.7
GD76C	33.18 ± 0.12	75.84 ± 0.04			824 ± 1	4.5	0.5
GD79B^e	29.04 ± 0.03	76.84 ± 0.14			736 ± 1	8.2	1.1
GD79C	30.22 ± 0.01	78.95 ± 0.06			812 ± 1	5.7	0.7
GD89A	28.34 ± 0.47	68.63 ± 0.10	12.00 ± 1.00	50.50 ± 0.71	524 ± 1	-4.3	-0.8
GD89B	24.85 ± 0.02	76.05 ± 0.02			620 ± 1	3.5	0.6
GD89C	24.75 ± 0.09	74.70 ± 0.05			595 ± 1	4.0	0.7
GD89D^{b,e}	22.89 ± 0.19	73.43 ± 0.05			526 ± 1	9.1	1.7
GD91A^c	31.18 ± 0.11	70.53 ± 0.01	11.50 ± 0.58	56.00 ± 0.50	627 ± 1	-1.8	-0.3
GD91B	30.26 ± 0.08	70.58 ± 0.13			650 ± 1	4.0	0.6
GD91C	29.79 ± 0.02	69.91 ± 0.00			627 ± 1	4.6	0.7
GD91D^e	31.88 ± 0.09	71.29 ± 0.04			693 ± 1	10.1	1.4
GD00A^{c,e}	26.41 ± 0.11	70.33 ± 0.01	14.35 ± 0.51	46.50 ± 0.71	496 ± 1	-22.3	-4.7
GD00B	29.46 ± 0.01	73.96 ± 0.02			697 ± 1	2.3	0.3
GD00C^e	33.64 ± 0.48	75.52 ± 0.01			815 ± 1	17.9	2.2
GD00D	32.28 ± 0.04	76.39 ± 0.03			813 ± 1	4.7	0.6
GD02A	27.55 ± 0.50	70.46 ± 0.06	12.36 ± 0.61	57.50 ± 0.58	545 ± 1	2.1	0.4
GD02B	28.66 ± 0.02	71.01 ± 0.01			625 ± 1	1.9	0.3
GD02C	32.59 ± 0.13	74.88 ± 0.03			788 ± 1	5.2	0.7
GD02D^d	27.91 ± 0.01	74.59 ± 0.10	6.83 ± 1.04	68.50 ± 0.01	662 ± 1	-1.4	-0.2
minimum	22.89	58.27			384	-22.3	-4.7
maximum	35.34	78.95			824	17.9	2.2
average	29.6	72.8			667.5		0.6
sum					20024.0	110.4	

^{a}Irregular: Slightly conical

^{b}Irregular: Part chopped of on corner.

^{c}Irregular: Double coned.

^{d}Impurity concentration changes from p-type to n-type within the bulk. Not fully depleted at operational voltage.

^{f}Strong rework and mass loss.

^{e}Otherwise large mass discrepancies.

GD76B This diode showed micro scratches after production and had to be reworked. The height and diameter was significantly decreased and a mass of 377 g was lost in the process.

GD02D The impurity concentration changes from p-type to n-type within the bulk. Parts of the detector are not fully depleted at operational voltage. The cone is on the tail side for this BEGe. See Fig. B.1c.

With the dimensions in Tab. 6.1 the n^+ electrode surface area is calculated and reported in Tab. B.3 in the appendix. Also shown is the n^+ electrode surface fraction and the surface to volume ratio. The surface area is between $98 - 170 \, cm^2$ and $96 - 98 \, \%$ are covered by the n^+ electrodefor the different detectors.

6.3 Characterization Facility in HADES

The acceptance tests were performed in the HADES underground facility (Sec. 4.5.2). The setup and measurement protocol are documented in [121] and will be briefly summarized here.

The test setup consists of two static measurement tables and three scanning tables whose pictures are shown in Fig. 6.3. The static tables have a bay to enter the detector cryostat. A lead castle is constructed on top of each table with 5 cm shielding on the lateral sides. Additionally, the interior is lined with three layers of 1 cm thick copper plates to reduce lead X-rays interfering with low energy calibration measurements. The static tables are used for uncollimated source measurements on the top surface up to a source-endcap distance of 20 cm.

static table   scanning tables

Figure 6.3 Pictures of the measurement setup. Left: Static table with lead shield and copper inlay. Right: Three scanning tables.

The scanning tables are equipped with a $\approx 5 \, MBq$ ^{241}Am source on a movable arm. The source is placed inside a $3 \, cm$ x $3 \, cm$ x $6.5 \, cm$ copper collimator with a $22.5 \, mm$ long hole of $1 \, mm$ diameter. Four different sets of scanning schemes are possible: (1) Linear scans on

the top surface, (2) circular scans on the top surface, (3) linear scan on the lateral surface and (4) circular scans on the lateral surface. The movements are illustrated in Fig. 6.4 and have a reproducible precision of $< 1\,\mathrm{deg}$ and $< 1\,\mathrm{mm}$ depending on the measurement type. An analysis of these scanning measurements is shown in Sec. 7.2.
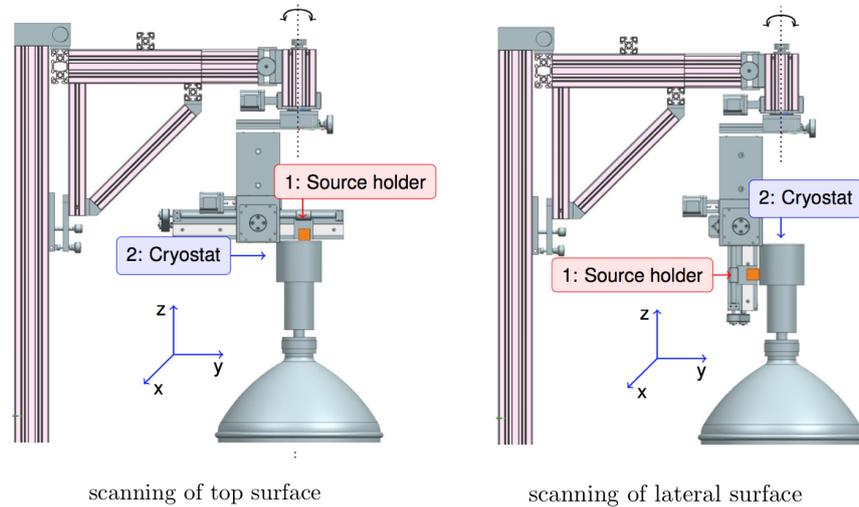
Figure 6.4 Automated measuring setup for surface scans. Left: Position for scanning the top surface. The arm with the source holder can rotate (circular top surface scan) or the source holder can be moved along the arm (linear top surface scan). Right: Position for scanning the lateral surface. The arm can rotate (circular lateral scan) or the source holder can be moved along the arm (linear lateral scan). From [121].

The data acquisition is composed of multi channel analyzer (MCAs) and FADCs. Two MCA systems are used: CanberraMultiport II NIM for the static tables and ORTEC926 and ORTEC927 for the scanning tables. Additionally two Struck SIS3301 VME FADCs with 8 input channels are used. The FADCs record samples with $100\,\mathrm{MHz}$ and 14 bit resolution and are the same as used in the GERDA DAQ. MCA and FADC were operated in parallel when necessary.

6.3.1 Test Protocol

A complete set of tests is composed of the following measurements (table and source used are identified):

1. Depletion voltage (static, ^{60}Co)

2. Energy resolution (static, ^{60}Co)

3. Leakage current (static, no source)

4. Dead layer thickness (static, ^{241}Am, ^{133}Ba)

5. Active volume (static, ^{60}Co)

6. Dead layer inhomogeneity (scan, ^{241}Am)

7. Pulse shape properties (static, scan, ^{228}Th, ^{241}Am)

Depletion voltage and energy resolution are provided on the Canberra data sheets (Tab. B.1 in the appendix). Measuring these properties is relatively fast and simple and was therefore performed as a verification of the detector performance. The dead layer thickness is not provided on the standard datasheet but on a separate technical drawing or through private communication. The dead layer is determined at Canberra with an ^{241}Am calibration source and tabulated values. The precision of the values is limited to $\mathcal{O}(0.1)$ mm without uncertainties and a more precise measurement is needed to reduce systematic uncertainties in GERDA analyses. The measurement of the dead layer thickness and active volume it described in detail in Sec. 7.1. The homogeneity of the dead layer is an important assumption to infer the active volume of the detector. The measurement is described in Sec. 7.2. The pulse shape properties of the detectors are of no concern for standard gamma spectroscopy and not provided by the manufacturer. The BEGe detectors are mounted in the vacuum cryostats with a passivation layer covering the groove and part of the n^+ electrode on the bottom surface. In vacuum cryostats the passivation layer is necessary to prevent leakage current on the detector surface when the detector is handled in normal atmosphere. For operation in LAr the passivation layer potentially favors the collection of charges on its surface and induces an increased leakage current. Test have shown that this can be prevented without a passivation layer, which, however, also influences the pulse shape properties. Testing the pulse shape performances in vacuum cryostats are not representative for future application in LAr. The energy resolution depends on the front-end electronics and cable length. The 5 deployed BEGe detectors in the GERDA environment with passivation layer and PHASE I electronics showed a 30 % larger energy resolution than in vacuum cryostats [114].

6.4   Upside-Down Mounting of GD91C in Vacuum Cryostat

After the characterization of all enriched BEGe detector in HADES some questions remained. For this purpose one of the detectors was mounted without passivation layer in a vacuum cryostat at LNGS (Sec. 4.5.1) in an upside-down configuration. This project combines a threefold unique situation:

- A BEGe detector without passivation layer in a vacuum cryostat. This requires the mounting operation in a protective atmosphere inside a glove box to prevent condensation of airborne impurities onto the groove. The BEGe detectors with passivation layer in HADES showed significant artifacts in the PSD performance. A characterization without passivation layer is closer to the situation in GERDA PHASE II.

- Upside down mounting with the p^+ electrode pointing towards the cryostat endcap. This requires the modification of a standard Canberra vacuum cryostat such that the p^+ electrode pin and signal cable is placed between the detector and the endcap. The thin carbon window of the cryostat endcap enables the direct investigation of the p^+ electrode and groove region with low energy γ-rays and electrons.

- Enriched GERDA PHASE II detector. Various investigations have been previously performed with BEGe detectors with natural germanium abundance ([135]) or isotopically depleted in ^{76}Ge [134]. Differences in performance are observed for different BEGe production charges (see [134] and [114]). Additional tests with one of the GERDA PHASE II detectors allows to investigate potential performance differences from different productions. Furthermore, it may be possible to extrapolate properties from a single well characterized BEGe to all detectors with less extensive standard characterization.

6.4.1 Mounting and Operation

The mounting of GD91C was performed at LNGS in October 2013. A standard Canberra 7500SL Vertical Slimline Dipstick Cryostat was modified at TU Munich to support the upside-down configuration. Fig. 6.5 shows some of the cryostat components: The electronic base (a), the detector holder with an additional teflon piece (b) and the carbon endcap (c). The teflon piece is designed to support the p^+ electrode contact pin on top of the BEGe and to guide the signal cable down to the side.
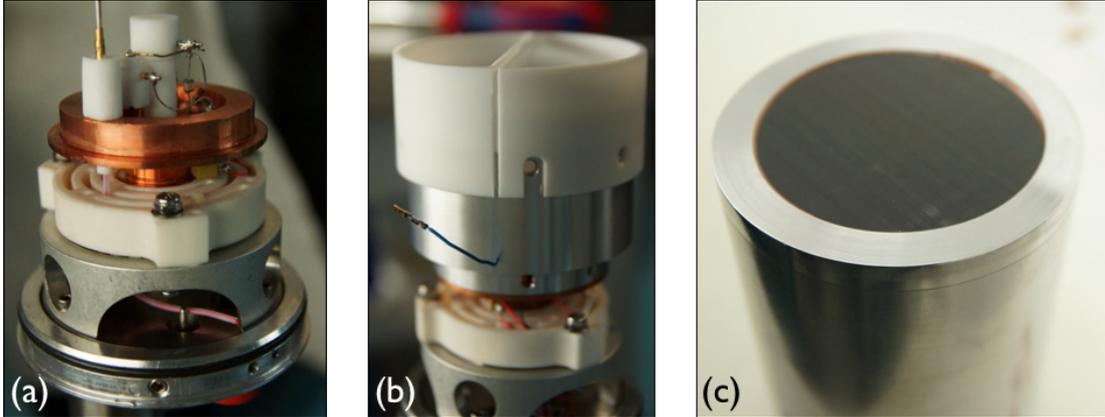
Figure 6.5 Vacuum cryostat components: (a) The electronic base, (b) the aluminum detector holder with teflon add-on to hold the p^+ electrode contact pin and (c) the cryostat shell with carbon window.

The mounting procedure inside the glove box of the GERDA clean room is shown in Fig. 6.6. After the detector was placed inside the holder (a), it was wrapped with mylar foil for thermal insulation (b). The wrapping was tightened with teflon tape in order to prevent physical contact and thermal conductivity to the cryostat endcap. The detector was mounted onto the electronic base (c) with the n^+ electrode resting on a teflon pedestal being connected to a flexible pin (Fig. 6.5 a). Finally the cryostat was evacuated after closing (d). The additional large amount of teflon and mylar increased the outgassing rate and required extensive vacuum pumping. After 10 d of ≈ 2 h pumping per day, a pressure of $5 \cdot 10^{-6}$ mbar was reached. The cryostat was immediately cooled down to prevent further outgassing.

The detector was placed into the GERDA electronic cabinet and connected to the standard GERDA DAQ (Sec. 5.2). The data is processed with GELATIO tools (Sec. 5.3.1). The data was taken in calibration mode recording $40\,\mu$s long traces. During the initial HV ramp up the baseline and the leakage current (LC) were monitored with an oscilloscope and on the test point[2]. The LC and baseline voltage plotted against HV is shown in Fig. B.2 in the appendix. GD91C depletes at 3500 V and is recommended to be operated at 4000 V according to the manufacturer. This is consistent with results from the HADES characterization. In this setup the LC strongly increased above 3000 V and reached 650 pA at 3800 V. Thus, to prevent a larger LC the operational voltage was chosen as 3800 V.

An improvised table with a hole was used as a pedestal to support calibration sources and

---

[2]The test point is a pin connected to the second stage of the pre-amplifier and encodes the LC.
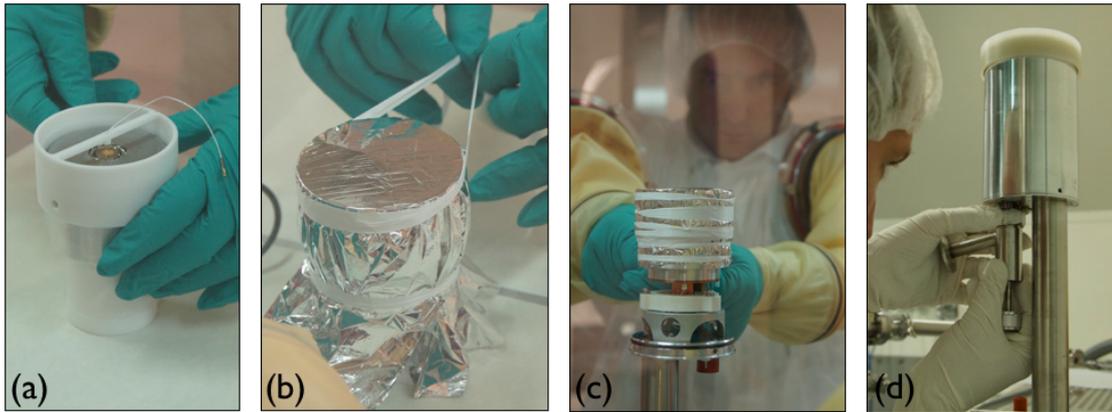
Figure 6.6 Mounting of the detector in the glove box under nitrogen atmosphere: (a) Fixation of detector in holder and mounting of teflon add-on with p$^+$ electrode pin, (b) wrapping in mylar foil, (c) mounting onto electronic base and (d) closing and pumping of cryostat.

a lead castle. The lead castle was constructed from 20x10x5 cm^3 lead bricks in different configurations which are illustrated in Fig. 6.7. The background levels for the three configurations, without lead castle, with open lead castle and with closed lead castle are shown in Fig. 6.8.
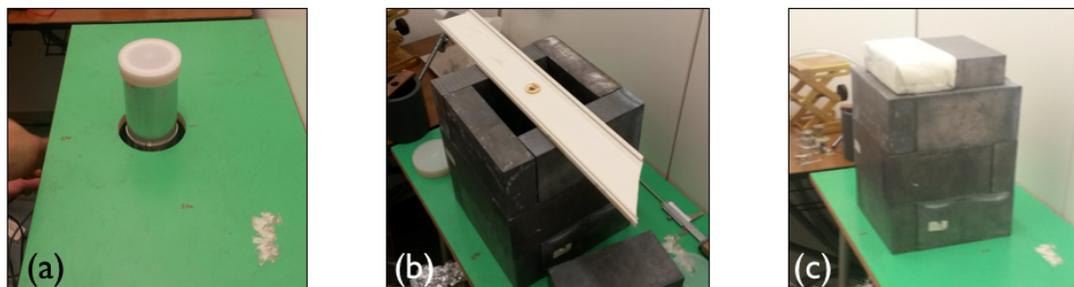
Figure 6.7 Lead castle configurations: (a) Without lead castle, (b) lead castle open and (c) lead castle closed.

The calibration is performed with various radioactive sources. The energy scale is calibrated with the ^{241}Am 59.5 keV and the ^{208}Tl 2614.5 keV γ-lines and assumed linear. The energy resolution is calibrated with the γ-lines at 59.5 keV, 356.5 keV, 583.7 keV, 1173.2 keV, 1332.5 keV and 2614.5 keV and Gaussian fits. It is shown with a square root parametrization in Fig. 6.9a. The A/E resolution is calibrated with the SSE components of the 59.5 keV, 356.5 keV, 1173.2 keV, 1332.5 keV and 2614.5 keV γ-lines and the DEP at 1592.5 keV. Manual Gaussian fits are performed using only the high A/E tail of the SSE band to avoid MSE contributions. The calibration with a square root function is shown in Fig. 6.9b.

A peculiar behavior was observed when exposing the p$^+$ electrode side to a ^{90}Sr beta source; the LC increased in strong incremental steps until the beta source was removed. The baseline level as read out with the FADC is illustrated in Fig. 6.10a for a ^{90}Sr measurement
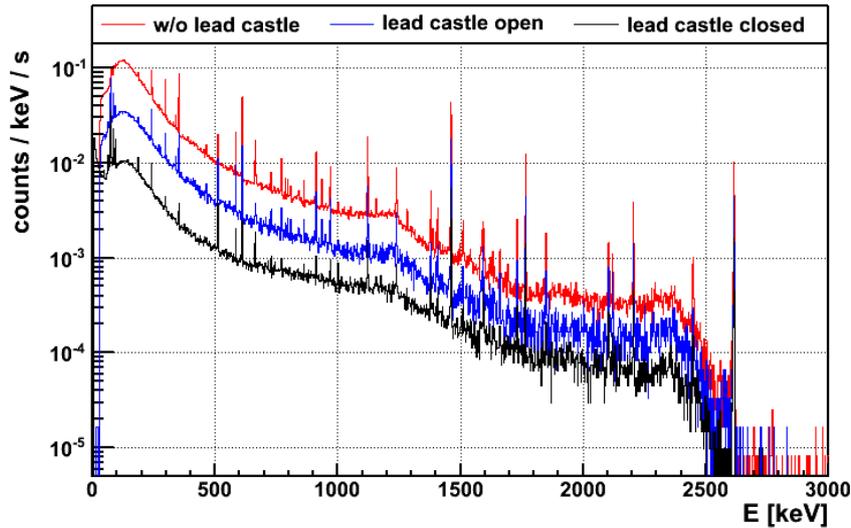
Figure 6.8 Background spectrum for different lead castle configurations.

and in Fig. 6.10b for an ^{241}Am measurement for comparison. The following observations are made.

- Increase in LC occurs predominantly with the beta source and not with a gamma source at comparable rate.

- The increase in LC is larger when exposing the p^+ electrode directly. When collimated on the n^+ electrode next to the p^+ electrode the effect is reduced but still visible.

- The increase in LC does not alter energy or A/E calibration.

- The LC decreases immediately after source removal.

- The LC restores to normal values after $\mathcal{O}(\min)$.

One hypothesis to explain this phenomenon is the collection of charges on the groove changing its conductivity. Another hypothesis is the ionization and polarization of the surrounding mylar foil changing the electrostatic environment close to the p^+ electrode. The LC effect did not change the pulse shape performance in a visible way and was not further investigated. None of the hypotheses is concluded.

6.4.2 Test Protocol and Measurement Overview

The measurement protocol was adapted to the missing conclusions from the HADES standard characterizations. A focus is put on the bottom side of the BEGe including p^+ electrode, groove and n^+ electrode pulses. The individual goals are:

1. PSD performance w/o passivation layer in vacuum cryostat (^{228}Th, uncollimated source)

2. p^+ electrode pulses (^{241}Am, small collimated scan)

3. Groove pulses (^{241}Am, small collimated scan; ^{90}Sr scattered electrons)

(a) energy resolution
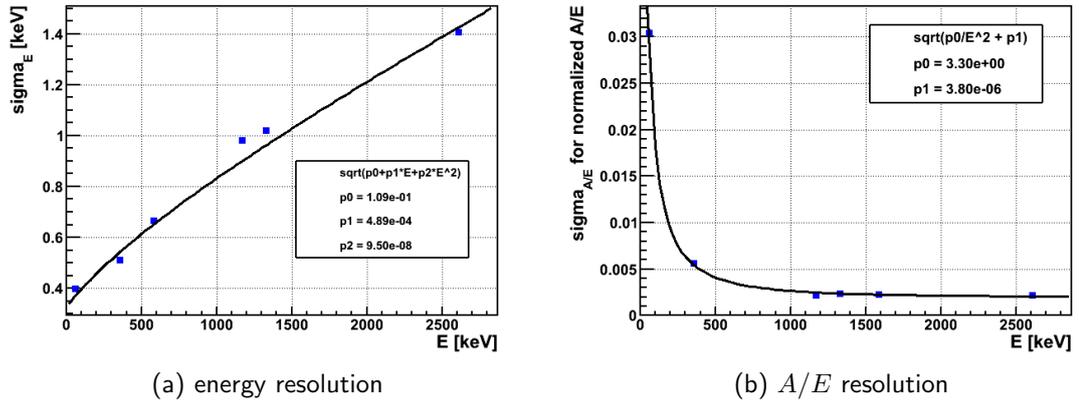
(b) A/E resolution

Figure 6.9 Calibration of the upside-down BEGe mounting of GD91C. Left: Calibration of the energy resolution with selected γ-lines. Right: Calibration of the resolution of the A/E normalized to the DEP with selected γ-lines. The resolution was retrieved with a one-sided fit of the high A/E side ignoring MSE features on the low A/E tail.
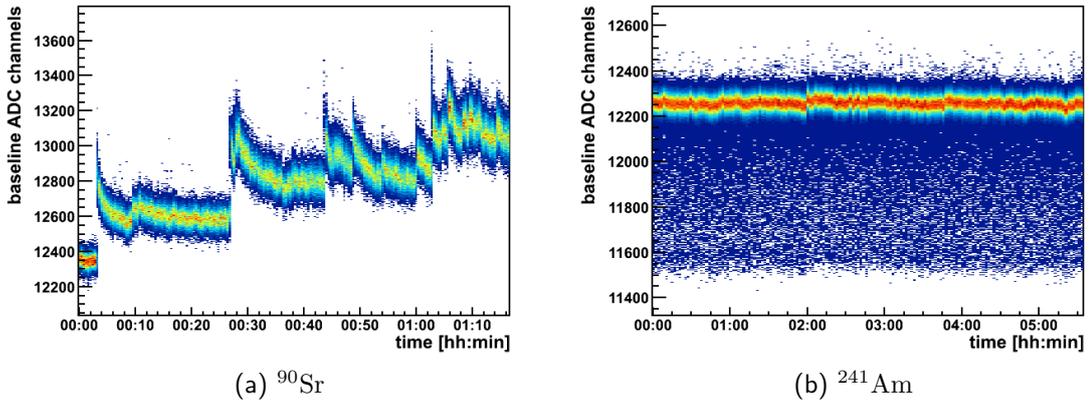
(a) ^{90}Sr

(b) ^{241}Am

Figure 6.10 Baseline ADC counts versus time stamp. Left: A ^{90}Sr source measurement shows the leakage current anomaly. Right: An ^{241}Am source measurement with same setup shows a stable baseline over a longer time. The baseline is plotted for events with a baseline resolution < 5 channels.

4. n^+ electrode pulses (^{90}Sr and ^{241}Am, wide collimated)

5. Dead layer on bottom side[3] (^{241}Am, ^{133}Ba, wide collimated)

6. Active volume (^{60}Co, uncollimated source)

7. Dead layer homogeneity on lateral and bottom side (^{241}Am, small collimated)

The measurement setup is illustrated in Fig. 6.11. Shown are the dimensions of the BEGe overlaid on a picture of the cryostat endcap. Also shown are the beam sizes on the detector surface for the scanning measurements with three types of collimators, named *2mm Copper*, *1mm Brass* and *Beta2000*. The collimators are described in the following:

- *2mm Copper*: A 30 mm long and 2 mm wide copper collimator resulting in 5 mm beam diameter on the detector surface. It was used for a rough scan with ^{241}Am. A picture is shown in Fig. 6.12a.

---

[3] Bottom side refers to the p^+ electrode side.
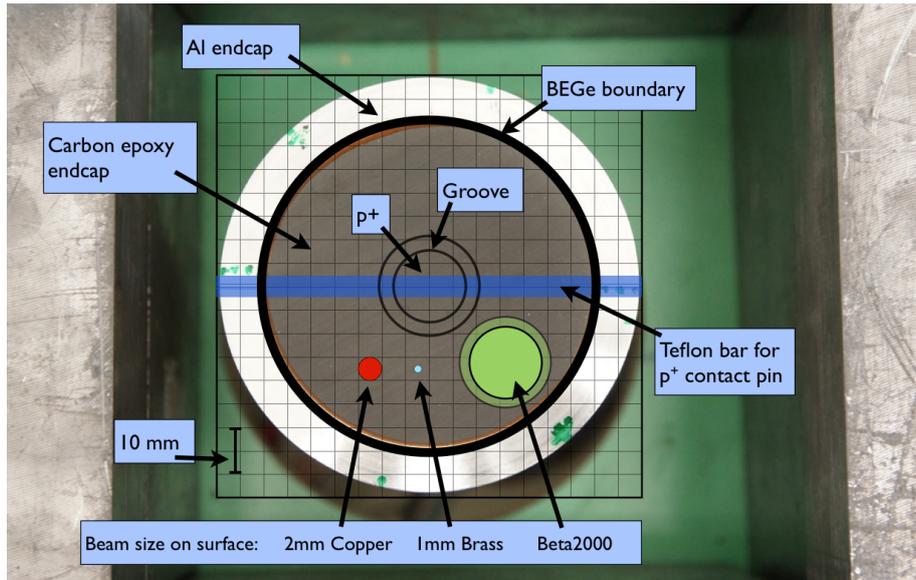
Figure 6.11 Overview of the measurement dimensions overlaid on a picture of the setup. Illustrated is the detector outline underneath the carbon epoxy endcap including the groove and the p$^+$ electrode. Also shown is the position of the teflon bar (blue) holding the p$^+$ electrode pin which attenuates radiations at these positions. The three beam sizes are illustrated for the three different collimators used for scanning measurements: *2mm Copper, 1mm Brass* and *Beta2000*. For scans with the extended ^{90}Sr source with the *Beta2000*, the solid surface denotes the umbra and the translucent surface denotes the penumbra. The overlaid grid is to scale and illustrates the dimensions.

- *1mm Brass*: A 10 cm long and 1 mm wide brass collimator resulting in 1.5 mm beam diameter on the detector surface. It was used for an ^{241}Am scan with finer sampling of positions inside the groove and on the p$^+$ electrode. The smaller beam size comes at a cost of longer measuring times and larger background contribution. A picture is shown in Fig. 6.12b.

- *Beta2000*: A wide composite collimator designed to reduce the Bremsstrahlung contribution. The collimator includes a 15 cm thick polyethylene (PE) layer with 12 mm hole diameter and two 8 mm thick copper layers with 14 mm and 16 mm hole diameter. A picture is shown in Fig. 6.13a along with the MC implementation in Fig. 6.13b. The *Beta2000* was used for a rough scan with a ^{90}Sr source and large statistic measurements on the n$^+$ electrode with an ^{241}Am source. The ^{90}Sr beta source is extended and results in an umbra of roughly 16 mm and a penumbra of roughly 19 mm on the BEGe surface. Both, umbra and penumbra are illustrated in Fig. 6.11. The low Z PE material attenuates the betas without creating hard Bremsstrahlung. The remaining Bremsstrahlung is largely attenuated by the copper plates. The wider collimator holes of the copper prevent direct scattering of betas on the plates; however, the multiple scattering nature of betas creates some exposure of a wider range on the BEGe surface. Also the Bremsstrahlung created in the PE may have a larger cone on the BEGe surface than the illustrated penumbra. The beam size of the ^{241}Am point source is identical to the umbra for the ^{90}Sr scan.
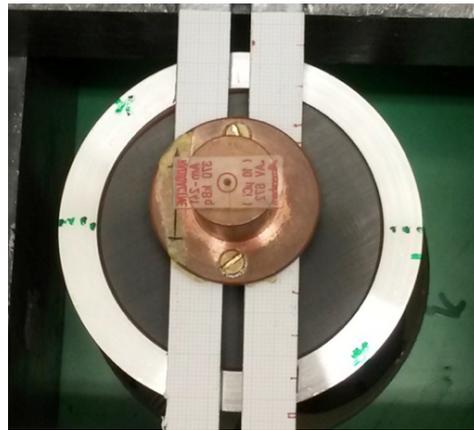
(a) *2mm Copper* collimator
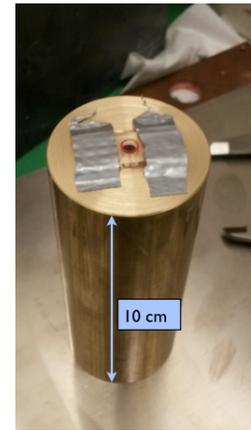
(b) *1mm Brass* collimator

Figure 6.12 Collimators with ^{241}Am source. The *2mm Copper* collimator creates a beam size of 5 mm and the *1mm Brass* collimator a beam size of 1.5 mm on the detector surface.
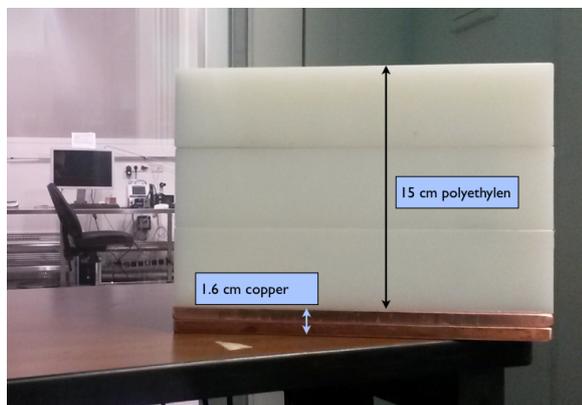
(a) ^{90}Sr scan collimator
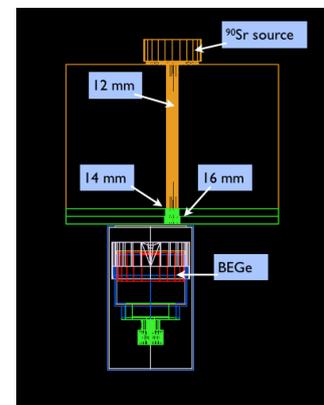
(b) MC implementation

Figure 6.13 Collimator *Beta2000* designed for ^{90}Sr source measurements with small Bremsstrahlung component. The polyethylene layers for blocking beta particles with a soft Bremsstrahlung spectrum and the copper layers for shielding the remaining Bremsstrahlung are shown on the left. A sketch of the MC implementation showing the collimator holes with increasing width along with the source and the cryostat interior is shown on the right.

6.5   Immediate Characterization Results

The data taken with the upside-down mounting of GD91C will be used in the following chapters. In Sec. 7.3 the dead layer of this detector will be compared between the top, the bottom and the lateral side. In Chap. 8, the data is used to develop a more comprehensive model for the n$^+$ electrode. Here, a few important conclusions are presented that are not connected with the rest of this thesis.

6.5.1   PSD in Vacuum Cryostat with and without Passivation Layer

The HADES characterization of the PSD performance found large anomalies in the A/E distributions. A poor A/E resolution at ^{208}Tl DEP energies was observed along with occasional double peak structures. A previous characterization of depleted BEGe detectors

that followed the same general production line[4] did not show anomalies. In both cases the groove was covered with a passivation layer.

One hypothesis for the anomaly assumes that charges are collected on the passivation layer which then distort the electric potential inside the BEGe. Pulse shape simulations with an asymmetric charge in the groove could qualitatively reproduce double peak structures in the A/E spectra [136]. This hypothesis can be cross-checked with the upside-down mounting of GD91C without passivation layer.

(a) ^{208}Tl DEP with and without PL   (b) ^{56}Co DEPs
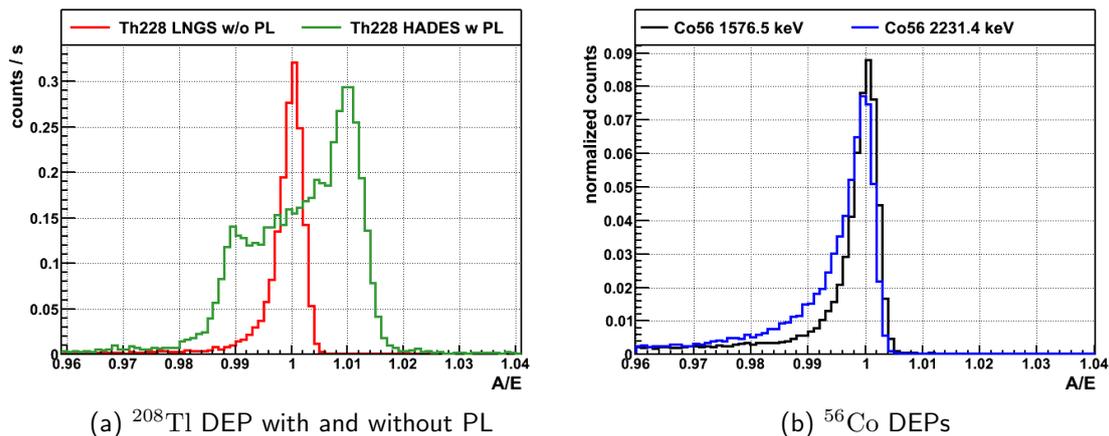
Figure 6.14 Comparison of DEPs as proxy for single-site $0\nu\beta\beta$ events. Left: ^{208}Tl DEP comparison with and without passivation later in HADES and LNGS, respectively. Right: Two DEPs from ^{56}Co.

Fig. 6.14a shows the A/E spectra for ^{208}Tl DEP events in GD91C from HADES (green) and from the upside-down mounting (red). The double peak structure in the HADES measurement is not present after removal of the passivation layer. The FWHM determined in the histogram is 2.5 % with passivation layer and 0.45 % without.

An additional measurement was performed with a ^{56}Co source which has multiple DEPs e.g. at 2231.4 keV and 1576.5 keV compared to 1592.5 keV for ^{208}Tl. The source was produced at TU Munich to cross-check the PSD performances in LAr in GERDA with a DEP closer to $Q_{\beta\beta}$ at 2039 keV. Fig. 6.14b shows the A/E spectra for the two ^{56}Co DEPs measured with GD91C in the vacuum cryostat. The histograms are normalized to the counts in the peak window and the A/E values are calibrated to the 1576.5 keV peak. The 2231.4 keV peak shows a larger low A/E tail due to Bremsstrahlung. The higher energetic Bremsstrahlung created by a larger electron / positron energy can deposit energies further away from the primary interaction point and create MSE features.

6.5.2   Pulse Shapes on the p$^+$ Electrode and the Groove

Circular ^{241}Am Scan

The groove has been scanned on the outer edge with the *1mm Brass* collimator at different positions. The scan was performed to test the assumption that the pulse shapes are consistent throughout the groove. The measurement positions are illustrated in Fig. 6.15a with the red labels in terms of angular coordinates. It was found that the groove was slightly

---

[4]The diode production of depleted and enriched detectors lies several years apart and small changes in the production procedure cannot be excluded by the manufacturer.

misaligned with respect to the endcap center and the groove illustration in the picture. The measurement points were chosen accordingly. The resulting A/E spectra within the 59.5 keV peak window are shown in Fig. 6.15b. The fraction of the beam hitting the groove was estimated with the peak count rate and is shown in the legend.
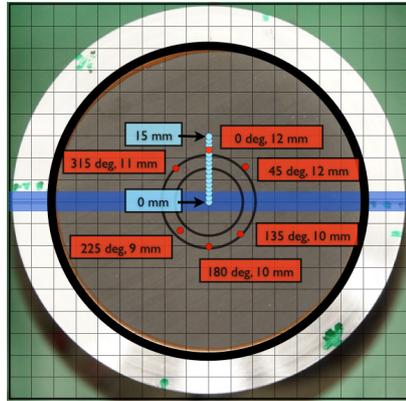
(a) *1mm Brass* collimator scan positions   (b) ^{241}Am A/E $55-65$ keV
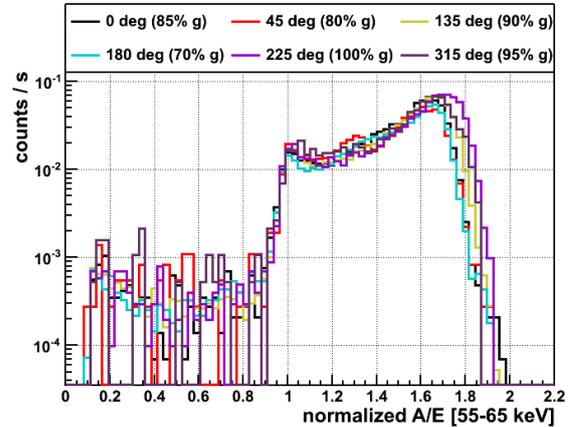
Figure 6.15 Left: Illustration of the scanning points for ^{241}Am circular (red) and radial measurement (light blue). Right: A/E spectrum for 59.5 keV events for all circular points. The legend shows the measurement position along with the estimated covering fraction of the groove.

The A/E spectra show small differences in the high A/E maxima and in the count rate which can be correlated with the coverage of the groove: A larger groove coverage implies more events close to the p$^+$ electrode which increase the A/E maximum as will become clear later. It also implies less events on the n$^+$ electrode resulting in less attenuation and a larger count rate. Otherwise, there is no evidence that the A/E reconstruction of groove events is dependent of the angular position inside the groove for this detector.

Radial ^{241}Am Scan

A radial scan has been performed with the *1mm Brass* collimator from the n$^+$ electrode over the groove onto the p$^+$ electrode. The measurement points are illustrated in Fig. 6.15a with the light blue labels. Fig. 6.16a is showing the energy spectra of selected measurement points and Fig. 6.16b shows the corresponding A/E spectra for the 59.5 keV peak region. The legends show the distance from the endcap center. The circular scan suggest a slight misalignment of ≈ 1 mm so that the p$^+$ electrode reaches up to roughly 8.5 mm followed by the groove reaching up to 11.5 mm.

The furthest 14 mm point is fully collimated on the n$^+$ electrode surface which can be seen in a large fraction of slow pulses and missing high A/E events in Fig. 6.16b. Additionally the low energy γ-lines of ^{241}Am and X-rays are not visible for this point in Fig. 6.16a suggesting a thicker layer of dead germanium starting just outside the groove. For all other measurement points the low energy γ-lines are visible. They are highly sensitive to attenuating material. Qualitatively, the count rate for those peaks does not appear significantly different between the groove and p$^+$ electrode positions; however, note that the center point at 1 mm is shadowed by the teflon bar and an attenuation is visible.

The A/E value is strongly depending on the precise interaction position as can be seen in

(a) ^{241}Am energy spectra   (b) ^{241}Am A/E $55-65$ keV
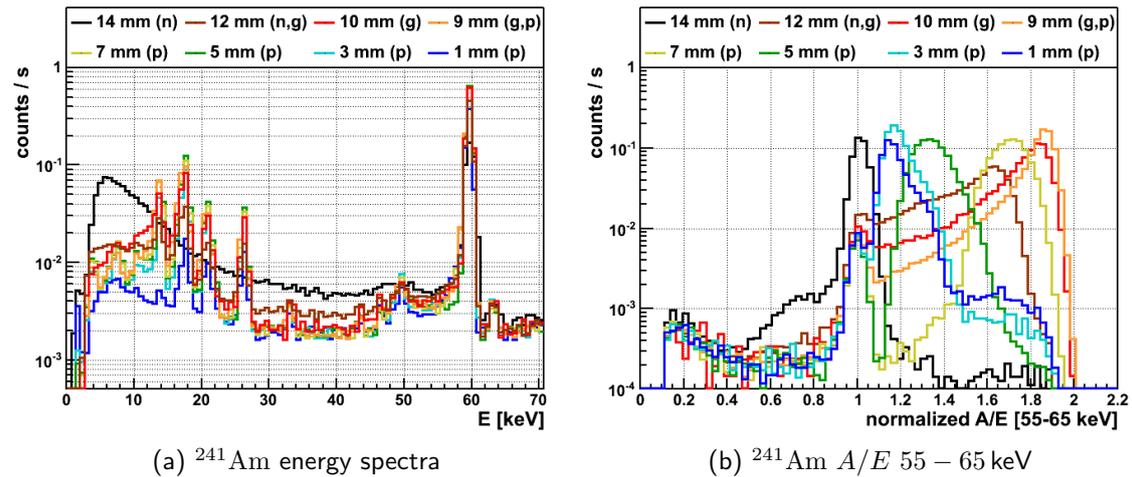
Figure 6.16 Selected positions of the radial ^{241}Am scan with *1mm Brass* collimator from n$^+$ electrode (n) over the groove (g) onto the p$^+$ electrode (p) in 1 mm steps. The beam size is 1.5 mm. The positions denote the radial distance from the endcap center. The p$^+$ electrode reaches up to roughly 8.5 mm followed by the groove up to 11.5 mm.

Fig. 6.16b. The full set of A/E vs E scatter plots is shown in Fig. B.3 and B.4 in the appendix. Interactions on the inside edge of the groove at 9 mm show the largest A/E values of up to 1.9 when normalized to the 59.5 keV bulk events. Towards the outer edge of the groove the A/E distribution shifts to smaller values. Towards the p$^+$ electrode the A/E values are also decreasing. This is consistent with the calculated strength of the weighting field shown in Fig. 4.8 which is strongest at the inner edge of the groove. The largest A/E values are created when holes and electrons drift simultaneously in the largest weighting field. Towards the center of the p$^+$ electrode the A/E distribution shifts to lower values. At the center position at roughly 1 mm the A/E values are smallest but still significantly larger than bulk events.

The dependence of A/E values on the interaction position around the p$^+$ electrode potentially allows to determine the position for point-like events. This may give a handle to pin-point background contributions on the thin dead layer surfaces such as alpha emitters: Larger A/E-values would indicate a position inside the groove whereas smaller A/E-values would indicate a position more centered on the p$^+$ electrode. Qualitatively comparing the A/E values of alpha events above 3 MeV in the GERDA PHASE I BEGe dataset (Fig. 5.5) with the measured A/E distributions in the scan (Fig. 6.16b) suggest that the alpha events originate from the p$^+$ electrode and not from the groove[5].

Wide circular ^{90}Sr and ^{241}Am Scan

A wider area of the n$^+$ electrode surface has been scanned with *Beta2000* collimator using a ^{90}Sr and an ^{241}Am source. The scan positions are illustrated in Fig. 6.17a. The energy spectra of the ^{90}Sr source on the 0 deg position and the p$^+$ electrode position along with a background and Bremsstrahlung measurement are shown in Fig. 6.17b. The Bremsstrahlung measurement was performed with the ^{90}Sr source placed misaligned with respect to the collimator hole. Thus, this spectrum only accounts for the Bremsstrahlung contribu-

---

[5]Note that this is only an indication. The number of alpha events in the PHASE I BEGe dataset is limited. Also the difference in electronics between the GERDA setup and the vacuum cryostat potentially introduces a bias for maximum A/E values.

tion going through the collimator material and not for the contribution being created inside the germanium or along the collimator hole. It can be seen that the ^{90}Sr spectra contain a large fraction of beta interactions up to $2\,\mathrm{MeV}$ which is enhanced for the p$^+$ electrode spectrum. The energy range below $600\,\mathrm{keV}$ is dominated by Bremsstrahlung.
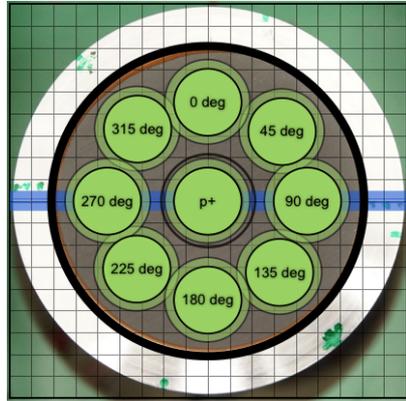
(a) *Beta2000* collimator scan positions   (b) ^{90}Sr energy spectra
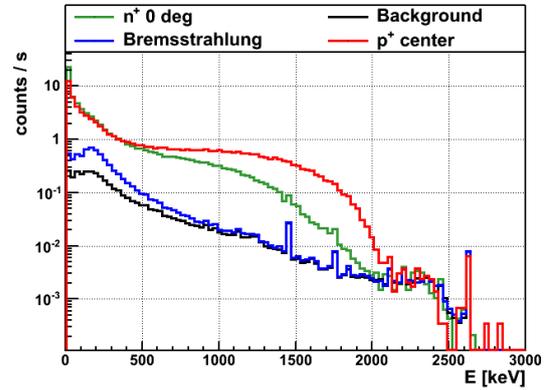
Figure 6.17 Left: Illustration of scanning points for ^{90}Sr and ^{241}Am circular scans with the *Beta2000* collimator. Right: Energy spectra for the ^{90}Sr source at the n$^+$ electrode and p$^+$ electrode position as well as for a background and Bremsstrahlung measurement.

A/E spectra are shown for the energy ranges of $650 - 1000\,\mathrm{keV}$ and $1000 - 1450\,\mathrm{keV}$ in Fig. 6.18a and 6.18b respectively for all measurements. Due to the scattering of electrons the n$^+$ electrode measurements contain some p$^+$ electrode events and vice versa. The A/E distribution are qualitatively equal for all n$^+$ electrode points suggesting a homogeneous n$^+$ electrode surface on the bottom of the BEGe. Note that the measurements at $90\,\mathrm{deg}$ and $270\,\mathrm{deg}$ are partly shadowed by the teflon bar and show a reduced rate. In all ^{90}Sr spectra two gaps can be seen between low A/E values, $A/E{=}1$ and high A/E values enabling a strong separation between those event types.
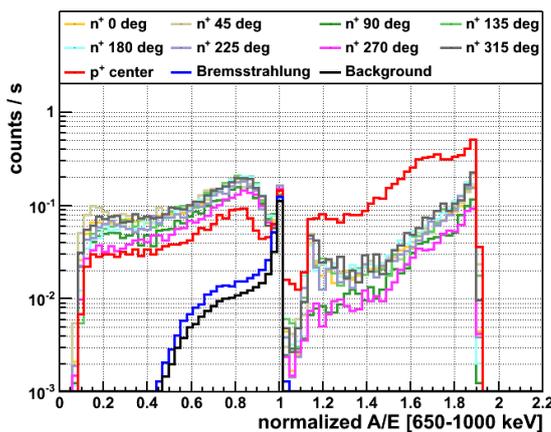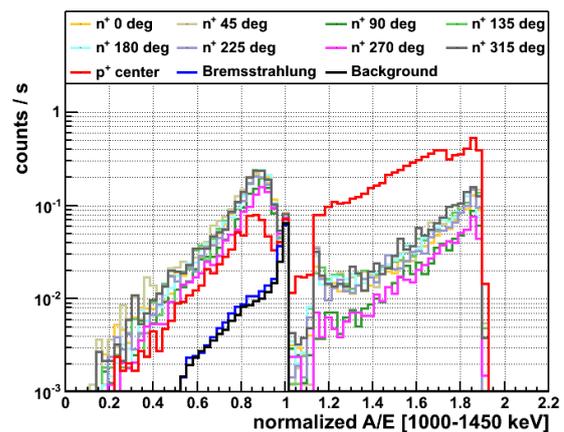
(a) ^{90}Sr $650 - 1000\,\mathrm{keV}$ (b) ^{90}Sr A/E $1000 - 1450\,\mathrm{keV}$

Figure 6.18 A/E spectra for the ^{90}Sr circular scan points in two different energy regions.

The ^{241}Am scan measurements, obtained with the same collimator and a subset of the same n$^+$ electrode positions as the ^{90}Sr measurements, are shown in Fig. 6.19a (energy spectra)

(a) ^{241}Am energy spectra

(b) ^{241}Am A/E $55 - 65$ keV
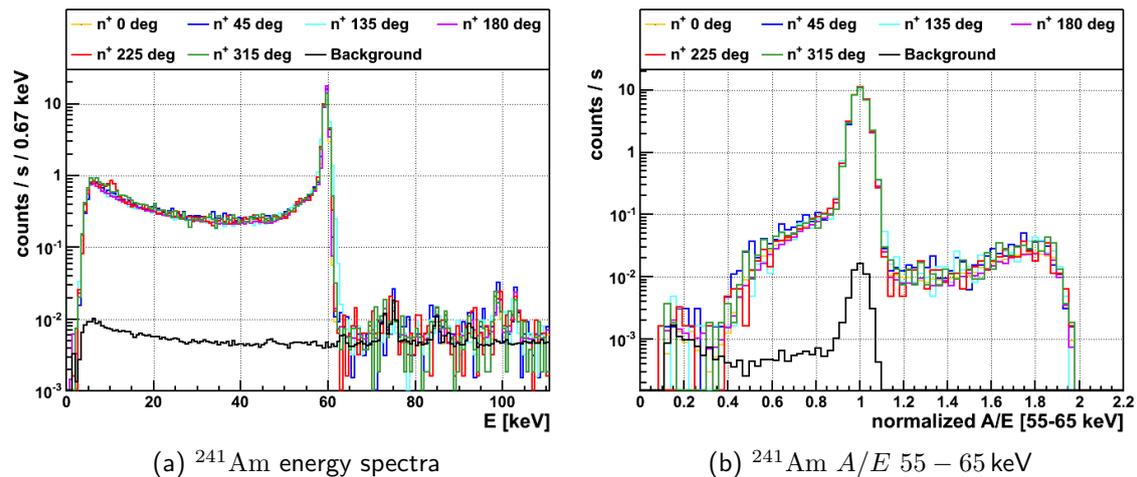
Figure 6.19 ^{241}Am energy spectra (left) and A/E spectra for peak events (right) for circular scan measurements on the n$^+$ electrode.

and Fig. 6.19b (A/E distribution for peak energies). No difference for the n$^+$ electrode contact surface section is observed either in the energy spectra nor in the A/E distribution. Both ^{90}Sr and ^{241}Am measurements strengthen the conclusion that the n$^+$ electrode surface is homogeneous on the bottom side of GD91C.

6.6   Conclusion

30 new BEGe detectors have been produced for GERDA PHASE II and characterized. The main characterization campaign was performed in a dedicated laboratory in HADES. Afterwards a more detail characterization was performed for a single detector (GD91C) at LNGS in an unique upside-down mounting.

The geometry of the BEGe detectors is parametrized with two ideal shapes. The dimensions of all detectors were measured and are listed in Tab. 6.1. The mass calculated with the ideal parametrization is compared with the measured mass and discrepancies are reported along with other particularities of individual detectors.

The measurement of GD91C in the upside-down mounting without passivation later showed no peculiarities of the A/E in contrast to the measurements at HADES with passivation layer. The investigation of the bottom surface indicates a homogeneous n$^+$ electrode surface with no angular dependence. Also the pulse shapes inside the groove showed no dependence on ϕ. Pulse shapes and A/E distributions were recorded for different distances from the center of the p$^+$ electrode and show a strong dependence on the radial position. A/E-values are largest for interactions at the inner edge of the groove and decrease towards the p$^+$ electrode center and the outer edge of the groove. The measurements suggest that the thick n$^+$ electrode layer starts immediately at the outer edge of the groove.

Chapter 7

Dead Layer and Active Volume Characterization of BEGe Detectors

The n$^+$ electrode thickness of BEGe detectors can vary strongly between different detectors in the same production batch and needs to be characterized after production. The n$^+$ electrode layer does not contribute to the fully active volume of the detector and a high precision measurement is needed to reduce its systematic uncertainty for all analyses in GERDA PHASE II.

This chapter presents a first step of the characterization in which the full charge collection depth, or dead layer thickness for $0\nu\beta\beta$ decay, is determined. In a second step in Chap. 8, the semi-active part of the n$^+$ electrode and the pulse shape properties of surface events are studied and characterized.

This chapter is organized as follows: The dead layer and active volume analysis of all BEGe detectors is presented in Sec. 7.1. An investigation of the surface homogeneity on the top and lateral detector sides is shown for a large set of detectors in Sec. 7.2 and for the bottom side of a single representative detector (GD91C) in Sec. 7.3. The main result of this chapter is the active detector volume connected with the detection efficiency for $0\nu\beta\beta$ decay which is presented in a consistent picture in Sec. 7.4.

7.1 Dead Layer and Active Volume Determination

The dead layer (DL) thickness is connected with the active volume (AV) through three model assumptions: (1) The DL has a homogeneous thickness covering the full n$^+$ electrode surface. (2) The DL is a completely dead (inactive) volume. (3) The DL is the only dead volume in the detector. Hence, the active volume is calculated as

$$\text{active volume} = \text{total volume} - \text{dead layer volume}. \tag{7.1}$$

The detailed geometrical calculation of Eq. 7.1 for cylindrical and conical diodes is reported in Sec. C.1 in the appendix. The three assumptions combine into a simplified model which is often used in past literature. The model assumptions hold reasonably well for efficiencies of discreet energy depositions such as full energy peaks (FEPs) from γ-rays or $0\nu\beta\beta$ decay. However, these assumptions fail for continuous energy depositions such as in $2\nu\beta\beta$ decays, for electrons penetrating the detector surface and continuous features in gamma spectra

such as the Compton continuum. In order to accurately describe these interaction types, an advanced model is discussed in Chap. 8 assuming a semi-active transition layer. In this context the terminology of the dead layer thickness is misleading and will be replaced by the full charge collection depth (FCCD)[1] from here on. The FCCD is the depth at which separated charges are fully collected and can be understood as the thickness of the n^+ electrode. γ-rays fully contained below this depth contribute to FEP events. The long tradition of gamma spectroscopy focuses on γ-lines or FEP events for which surface events above the FCCD are practically dead. Here the DL and the FCCD are fully equivalent. In this chapter the FCCD is determined with gamma spectroscopy for which the model Eq. 7.1 is used. In Chap. 8 the DL and FCCD are no longer equivalent. Following this argument, the concept of the AV is revised. Previously the AV was the volume remaining when subtracting the DL as in Eq. 7.1 ignoring the semi-active volume above the FCCD. From here on the volume in Eq. 7.1 is referred to as fully active volume (FAV) which is equivalent to the old concept of AV for the investigation of γ-rays and $0\nu\beta\beta$ decays.

The basic idea of this analysis is to compare the gamma spectrum of a calibration source with MC simulations of the measurement in which the FCCD of the BEGe is varied. The FCCD in the MC spectrum which describes best the measured spectrum is the inferred FCCD of the detector. The observable in the gamma spectrum needs to be easily obtainable, comparable between measurement and simulation and highly sensitive to the FCCD. Two methods based on peak count ratios and absolute peak counts are used and further described below (Sec. 7.1.1).

The analysis flow is designed for a fast analysis of many detectors and is illustrated in Fig. 7.1. After the measurement the gamma spectrum is calibrated for energy and resolution. Along with this step the setup is simulated. The simulated spectrum is smeared with the energy resolution. At the same time the MC is post processed with a volume cut to create a set of MC spectra with increasing FCCD (Sec. 7.1.2). At this point the observable is compared between the experimental spectrum and the MC spectra and the best fitting FCCD is inferred. Finally, the FAV is calculated with the measured FCCD and the BEGe dimensions based on Eq. 7.1. The statistical uncertainties in the measured spectrum and systematical uncertainties in the MC spectrum are jointly propagated through this analysis flow (Sec. 7.1.4).

7.1.1 Experimental Signatures

The FCCD and the FAV are measured with two fundamentally different methods: (1) Measuring the attenuation of the top surface FCCD with a surface probe and (2) measuring the active volume of the detector with a volume probe. The two methods are connected with the model assumption Eq. 7.1. The ratio of low energy γ-lines from ^{241}Am and ^{133}Ba are used as two independent surface probes. The high energetic γ-lines from ^{60}Co are used as volume probes. The observables which are compared with MC simulations are defined as follows:

^{241}Am Surface probe   The ^{241}Am method uses the count ratio of the prominent 59.5 keV γ-line and two low probability γ-lines at around 100 keV:

$$O_{241\text{Am}} = \frac{C_{59.5\,\text{keV}}}{C_{99.0\,\text{keV}} + C_{103.0\,\text{keV}}}. \tag{7.2}$$

---

[1]In accordance to the terminology in [137].
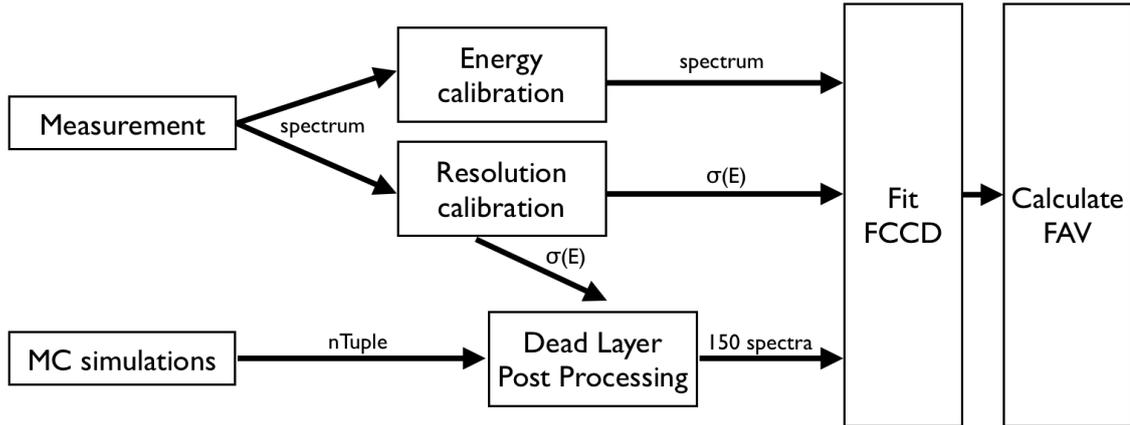
Figure 7.1 Analysis flow for the FCCD/FAV analysis. The inferred geometrical parameter is the homogeneous FCCD. The absolute FAV and FAV fractions are calculated from the FCCD.

The decay scheme of ^{241}Am is shown in Fig. A.5a in the appendix. The emission probabilities are p(59.5 keV) = 35.9 (4) %, p(99.0 keV) = 0.0203 (4) % and p(103.0 keV) = 0.0195 (4) % [138]. The γ-ray emission ratio corresponding to O_{241Am} is 902 ± 10. The uncertainties on the emission probabilities are a systematic uncertainty on the observables and are discussed later in more detail. A few peculiarities have to be considered for the ^{241}Am method. Directly below the 59.5 keV γ-line are dominant Compton features of scatterings at the source holders which can influence the background estimation (see Fig. 7.2a). Additionally this region is populated by degraded energy events (slow pulses) from interactions shallower than the FCCD (see Sec. 4.2 and a more detailed discussion in Chap. 8). Between the low probability γ-lines in the second peak window is the $K_{\alpha 1}$ X-ray line at 101.1 keV associated with the ^{241}Am decay. The emission probability is 0.0018 % and the influence on the peak ratio is ≈ 5 % if counted together with the two other γ-lines. It is not suitable to include this peak in the analysis[2]; however it must be considered as a background.

^{133}Ba Surface probe   The ^{133}Ba method uses the count ratio of the double peak around 80 keV and the γ-line at 356.0 keV as an observable:

$$O_{133Ba} = \frac{C_{79.6\,keV} + C_{81.0\,keV}}{C_{356.0\,keV}}. \tag{7.3}$$

The decay scheme is shown in Fig. A.5b in the appendix. The probability of the γ-emissions are p(79.6 keV) = 2.65 (5) %, p(81.0 keV) = 32.9 (3) % and p(356.0 keV) = 62.05 % [138]. The γ-ray emission ratio corresponding to O_{133Ba} is 0.573 ± 0.005. Also here some peculiarities need to be considered. For measurements without the copper lining in the lead castle[3], the window around the 80 keV double peak is populated by lead X-ray lines which need to be considered in the background estimation. Additionally there are Compton and slow pulse features below the 80 keV γ-lines which complicate the background estimation in this region (Fig. 7.2b). The 356.0 keV γ-lines is a single peak with the 351.9 keV ^{214}Pb background γ-line in the vicinity. Coincidences between the 79.6 keV and 80.0 keV γ-rays and between the 81.0 keV and 356.0 keV γ-rays can occur and need to be considered in the MC simulations.

---

[2]The low probability of this peaks makes it difficult to be constrained in a fit.
[3]The copper lining was installed during the characterization campaign and not present for the early measurements.

^{60}Co Volume probe   The ^{60}Co method uses two prominent γ-lines for direct comparison with MC simulations. The counts of each peak are a separate observable:

$$O_{60\mathrm{Co}\,1} = R_{1173.2\,\mathrm{keV}} \tag{7.4}$$

$$O_{60\mathrm{Co}\,2} = R_{1332.5\,\mathrm{keV}} \tag{7.5}$$

The decay scheme is shown in Fig. A.5c. The emission probability is p(1173.2 keV) = 99.85 (3) % and p(1332.5 keV) = 99.9826 (6) % [138]. The two γ-rays are emitted practically simultaneously and can create coincidences. The angular correlation in the $4^+ \to 2^+ \to 0^+$ cascade is $p(\theta) \propto 1 + \frac{1}{8}\cos^2\theta + \frac{1}{24}\cos^4\theta$ with the angle θ between the two γ-rays. This has to be included in the MC simulations.

The calibration sources are not collimated and typically placed 19.8 cm above the cryostat endcap. Fig. 7.2 shows the energy spectra of representative measurements with the three calibration sources with illustration of the peak regions.

(a) ^{241}Am   (b) ^{133}Ba   (c) ^{60}Co
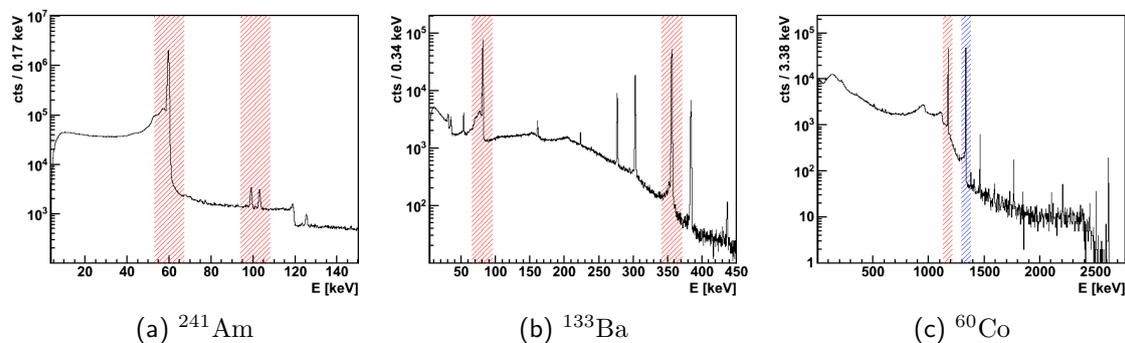
Figure 7.2   Typical spectra of calibration sources for flood source measurements on the static tables with 198 mm source-cryostat distance. The color shaded area denote the ROIs for the observables.

MC simulations can be used for a better understanding of the position of the γ-ray interaction inside a BEGe that lead to an FEP event. A larger sensitivity to the FCCD is reached if a large number of interactions occur close to the detector surface. Fig. 7.3 shows the energy distribution for different FEP energies of the calibration sources. The histograms are filled with the absolute position of all GEANT4 hits in the $z-r^2$ plane for events within the FEP. Each MC hit is weighted with its energy deposition. The absolute scale of the histogram is adjusted to the total number of events in the respective peak. Thus, the histogram scale can be considered as energy per event per voxel bin. The r-coordinate is plotted in r^2 to normalize the counts to a common voxel size. The color scale in the plots can be directly compared in-between each plot[4]. A similar plot illustrating the interactions in the $x-y$ plane is shown in Fig. C.3 in the appendix.

The plots show that interactions of events in the ^{241}Am γ-lines occur only on the detector top surface. The ^{60}Co γ-line events are distributed throughout the full detector instead. A statistically larger energy fraction of ^{60}Co events is deposited in the BEGe center. This is due to the finite detector volume and the high probability of Compton interaction for ^{60}Co γ-ray energies[5]. A γ-ray is more likely to be contained and result in a FEP measurement if it initially interacts in the center of the detector than if it initially interacts close to the

---

[4]Note that on the fringes of the BEGe illustration, binning effects may jeopardize the color scale.

[5]The probability for Compton interaction at these energies is more than two orders of magnitude more likely than interactions with the photoelectric effect or pair production. See also Fig. 4.2b.

(a) ^{241}Am 59.5 keV events

(b) ^{133}Ba 80.5 ± 1.0 keV events

(c) ^{60}Co 1173.2 keV events

(d) ^{241}Am 101 ± 4 keV events

(e) ^{133}Ba 356.2 keV events

(f) ^{60}Co 1332.5 keV events.
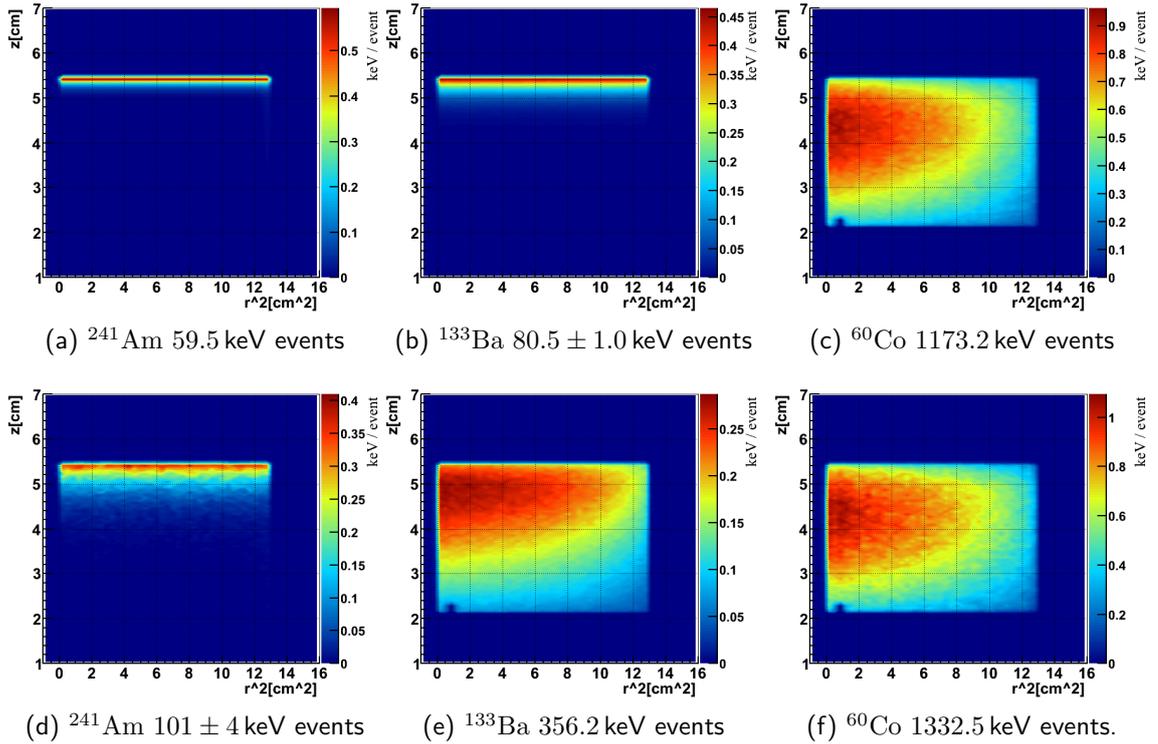
Figure 7.3 Localization of energy deposition in a typical BEGe detector for γ-ray energies in the FCCD/FAV measurements. Shown are the MC hit positions weighted with the energy deposition in the projected $r - z$ plane. r is plotted in quadrature to achieve uniform voxel size and a comparable color scale throughout the BEGe. Visible on the bottom is the groove at $r = 7.5 - 10.5$ mm in case of higher γ-ray energies that illuminate the full detector volume.

surface. This has ramification for the sensitivity of the volume probes for FCCD inference. A variation of the FCCD on the surface, results in a significantly reduced effect on the ^{60}Co γ-line intensity than expected with a homogeneous energy distribution of the events. This reduces the sensitivity of high energy volume probes to FCCD inferences. The ^{133}Ba 356.2 keV γ-line shows an energy distribution throughout the full volume with preference to the top volume.

In conclusion, the ^{241}Am methods probes attenuation versus attenuation with the peak ratio observable. The ^{133}Ba method probes attenuation versus part of the volume and the ^{60}Co methods probes the volume only. However, the analysis is always based on the measurement of the FCCD which is then used to calculate the FAV.

7.1.2 Monte Carlo Simulations

MC simulations are used to obtain a set of simulated spectra with different FCCD. This set of MC spectra is compared to the experimental spectra. The best fitting MC spectrum is used to infer the FCCD of the detector. To reduce systematic uncertainties and achieve a high precision measurement, a significant amount of effort was put into the development of MC simulations starting from precise geometry and material implementations to a CPU efficient post processing of the FCCD boundary. The simulations were performed on the computing cluster ATLAS at TU Dresden with the MaGe framework (Sec. 5.3.2). The underlying version of GEANT4 is 9.4p02 with CLHEP 2.1.0.1. A new project was set up

in order to quickly and flexibly simulate new measurements.

Geometry Implementation

The important components for the geometry are separated in (1) BEGe detector, (2) vacuum cryostat and interior, (3) calibration sources (4) source holder and (5) lead castle. Especially the material in the line-of-sight between the source material and the detector needs precise consideration since any additional material or attenuation would be interpreted as a reduction of FCCD by the analysis.

BEGe detector The BEGe detectors are implemented as defined in Sec. 6.2 with two ideal shapes: cylindrical and conical. Small deviations from the ideal shapes are considered as systematic uncertainties.

Vacuum cryostat and interior The BEGe detectors were mounted in 9 different equal sized 7500SL Vertical Slimline Dipstick Canberra cryostats during the acceptance test. In addition a different sized cryostat from Tübingen University was used which is referred to as "Tuebingen Cryostat"[6]. The outer aluminum shell of the cryostats consists of the endcap and the lateral walls. The relevant interior components include an insulating high density polyethylene (HDPE) cup surrounding the BEGe, an aluminum detector holder with screws for detector fixation and a copper base. The interior is shown in Fig. 7.4. The dimensions of the cryostat components have been obtained from data sheets and confirmed with dedicated measurements. They are summarized in Tab. C.1 in the appendix. The MC geometry includes all mentioned components.
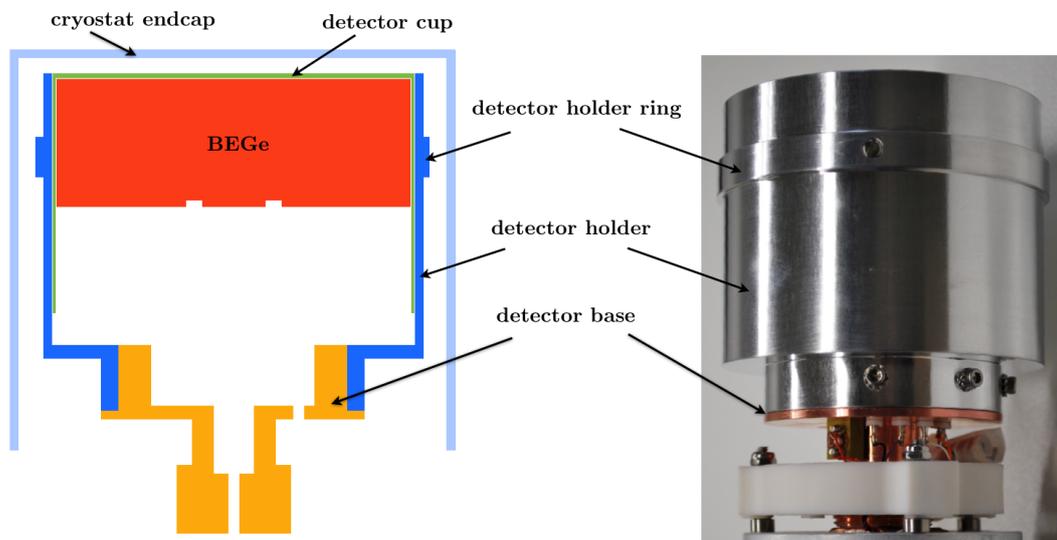
Figure 7.4 Interior of the vacuum cryostat holding the BEGe detectors. Left: Illustration of implementation in MC simulation. Right: Picture of detector holder and base.

Calibration sources Various forms of calibration sources were used. The detailed MC implementation of these sources is important since the housing material is in the direct line-of-sight between the active source material and the detector. The various source geometries are illustrated in Fig. C.4 in the appendix. The source activities are reported in Tab. C.2.

---

[6]Only GD02A was mounted in this cryostat.

Source holder   The source holders are made from cylindrical plexiglas segments that can be combined to create various source-endcap distances. The cylindrical bottom segments fit to the cryostat housing. The flat top segments hold the various forms of calibration sources. A picture can be seen in Fig. C.5 in the appendix. The typical source distance used for these measurements is 198 mm. There is no material from the source holders in line-of-sight between the source and the detector. However, Compton scatterings of low-energy γ-rays, as e.g. 59.5 keV from ^{241}Am, create spectral features closely below the FEP which interfere with the background estimation. The source holder is implemented in the MC geometry and the mentioned scattering features can be modeled. The effect of the source holder on the low energy part of the ^{241}Am spectrum is later explored in Sec. D.1 (Fig. D.2b) in the appendix.

Lead castle   The lead castle geometry is implemented as shown in Fig. 6.3.

MC Event Sampling

The radioactive decays of the three calibration sources are sampled by three different event generators:

- ^{241}Am: The 59.5 keV, 99.0 keV and 103.0 keV γ-rays are sampled with the GEANT4 General Particle Source (GPS) according to their emission probability. Typically 10^{10} γ-rays are sampled to account for sufficiently high statistics in the low probability γ-lines. The direction is limited to the hemisphere pointing toward the detector.

- ^{133}Ba: The full ^{133}Ba decay is generated with the GEANT4 G4ParticleGun using the `PhotonEvaporation` and `RadioactiveDecay` data bases. This event generator considers γ-ray coincidences which correctly describe summation effects in the spectra. Inconsistencies were found [139] in the branching ratios for some ^{133}Ba γ-rays in the present version of GEANT4 compared to the ENSDF database [138]. The simulated emission ratio for Eq. 7.3 was found to be 0.601 ± 0.001 whereas the expected ratio from [138] is 0.573 ± 0.005 (see also [140] for a bug report of the same issue). A correction factor is applied to the MC peak ratio observable as $C_{\text{corr}} = \text{ENSDF ratio}/\text{GEANT4 ratio} = 0.954$ to use the latest branching ratios for ^{133}Ba. Typically 10^9 ^{133}Ba decays are generated per detector.

- ^{60}Co: DECAY0 [141] is used as an external event generator for ^{60}Co. 100 ASCII files are generated with different random seed containing 10^7 individual decays each. A total sample of 10^9 events is simulated. DECAY0 accounts for the angular correlation of the two γ-rays in the cascade. This was cross-checked with the ^{60}Co summation peak which could be well reproduced by DECAY0 but shows a $\approx 10\%$ difference in rate when the γ-rays are sampled isotropically with the G4ParticleGun.

Dead Layer Post Processing (DLPP)

The set of MC spectra consists of spectra with increasing FCCD but with otherwise unchanged geometry. In order to efficiently use the computing resources, the setup is simulated only once without a hardcoded FCCD boundary. The simulations are performed with a small particle step length and a large sample of events. Additionally, the distance of each MC hit to every BEGe surface is recorded (see Fig. C.6b in appendix). In a second step the FCCD effect is calculated with a posterior volume cut on the individual hits of an event. This dead layer post processing (DLPP) reduces the energy of an event if some

MC hits are in the dead volume above the FCCD.

Statistically, the MC spectra in the set are not independent. An increasing thickness of the FCCD will cut more and more events out of the same sample. The FCCD is increased from $0 - 1.5\,\mathrm{mm}$ in steps of $10\,\mathrm{micron}$. The effect on the event topology is illustrated in Fig. 7.3: If the hit distribution is closely concentrated on the surface (e.g. $^{241}\mathrm{Am}$), the DLPP has a strong effect on the FEP and total number of events in the spectrum. If the hit distribution is spread out throughout the detector the DLPP effect is small and mainly limited to degrading the energy of FEP events.

An investigation is performed to tune the GEANT4 stepping parameters to be sufficiently small for the DLPP method and FCCD values of around $0.5 - 1.0\,\mathrm{mm}$. Fig. 7.5 shows the number of hit distribution for a typical $^{241}\mathrm{Am}$ event with $59.5\,\mathrm{keV}$ energy deposition and a $^{133}\mathrm{Ba}$ event with $356.2\,\mathrm{keV}$. The hit distribution is shown for the different predefined realms in MaGe (Sec. 5.3.2) and a newly defined DL realm. In the DL realm the GEANT4 step length is reduced to $1\,\mathrm{micron}$ for electrons and γ-rays inside the detector. Outside the detector the particles are tracked with the less precise BB realm settings. Additionally the secondary production threshold is set to $250\,\mathrm{eV}$.

(a) $^{241}\mathrm{Am}$ $59.5\,\mathrm{keV}$ events   (b) $^{133}\mathrm{Ba}$ $356.2\,\mathrm{keV}$ events
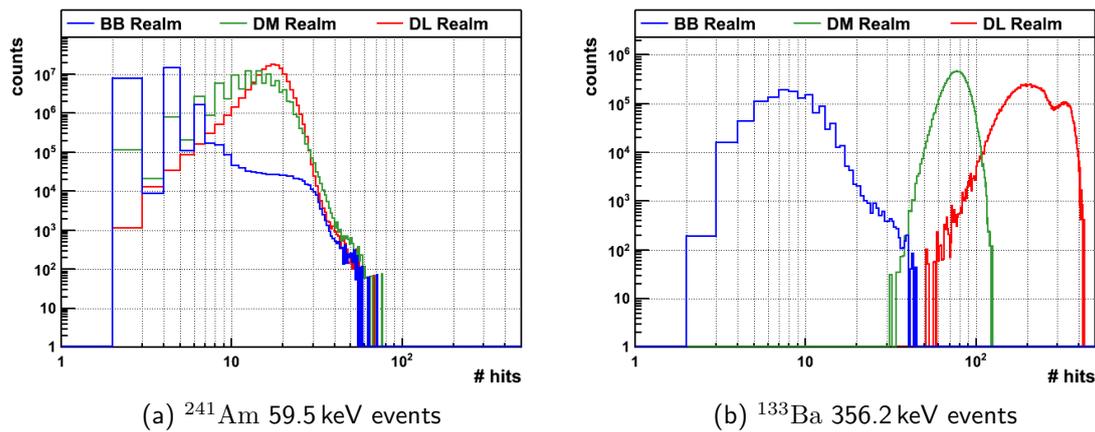
Figure 7.5 Hit number distribution for different simulation realms (precisions) as defined in Sec. 5.3.2 for two selected γ-ray energies.

It can be seen that the predefined BB and DM realms show hit number artifacts for events with few hits summing up to the FEP[7]. For very large hit numbers the artifacts are smeared by a multitude of possible tracking topologies. In all cases, the finer particle propagation shows smoother hit distributions and is used in the following MC simulations to avoid potential biases.

The number of hits at a certain distance to the top surface is shown for $^{241}\mathrm{Am}$, $^{133}\mathrm{Ba}$ and $^{60}\mathrm{Co}$ FEP events in Fig. 7.6 in logarithmic and double logarithmic scale. This is similar to the representation of the hit distribution in Fig. 7.3 summed over all radii. The plot illustrates the interaction depth of a certain γ-ray with FEP deposition. $60\,\mathrm{keV}$, $80\,\mathrm{keV}$ and $100\,\mathrm{keV}$ show exponential attenuation throughout the BEGe thickness. Higher energetic γ-rays are detected in the whole volume with a preference to the detector center. Inside

---

[7]One of these hits is always attributed to crossing the volume boundary of the detector; another for the main energy deposition. Multiples of two hits are preferred for larger hit numbers due to the production of two particles in case of secondary production.
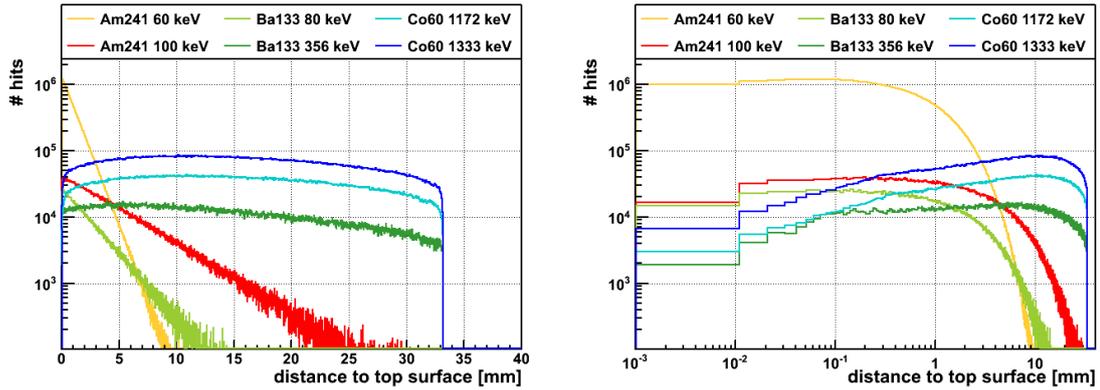
Figure 7.6 Distance to top detector surface for MC hits in events with an energy deposition in the respective FEP of the calibration sources. The plot on the right shows the same content in double logarithmic scale such that the FCCD cut region can be seen: The FCCD cut is varied from 0 to 1.5 mm in steps of 10 micron. Typical FCCD values are 0.5 to 1.0 mm.

the investigated surface layer of 0 to 1.5 mm with steps of 10 micron, an increase of MC hits can be seen towards larger depth. This is expected due to escaping energy at shallow depth even for low energy depositions.

The MC event energies are smeared with the energy resolution of the detector. The resolution is determined with the function $\sigma(E) = p_0 + p_1 \cdot E + p_2 \cdot E^2$ for compatibility with GammaVision [142]. The parameters p_i are obtained in-situ from the measured calibration source spectrum and a Gaussian fit of the peaks of interest. In this way the resolution is correct for the peaks of interest independent of the parametrization.

The effect of different FCCD values in the DLPP is shown in Fig. 7.7 for the different peak regions. As expected the spectral differences are strongest for low energy γ-lines which are affected by attenuation.

7.1.3 Analysis

In this section the final part of the analysis flow (Fig. 7.1) is presented: The fitting of the experimental spectrum to a spectrum in the MC set[8]. In a first step the observables are extracted from the spectra which is essentially a problem of determining the peak counts with high precision. In a second step the observables are compared, the best FCCD value is inferred and the uncertainties are propagated.

Data Selection

The analysis is performed on binned spectra in histograms from the MCA systems. The binning is roughly equal for all histograms with a bin width of $\approx 0.3\,\mathrm{keV/bin}$. In some cases multiple measurements were taken for the same detector with the same source type. Especially in the beginning of the characterization campaign many different sources and combinations were tested to investigate systematics. For the final results of the ^{241}Am and ^{133}Ba methods only one measurement per method and detector is selected[9]. The selection is unbiased and prefers measurements that were taken under the same condition

---

[8]In reality the observables from the MC spectra are interpolated.

[9]The combination of multiple measurements of the same kind was omitted due to simplicity and the fact that statistical uncertainties are not dominant.
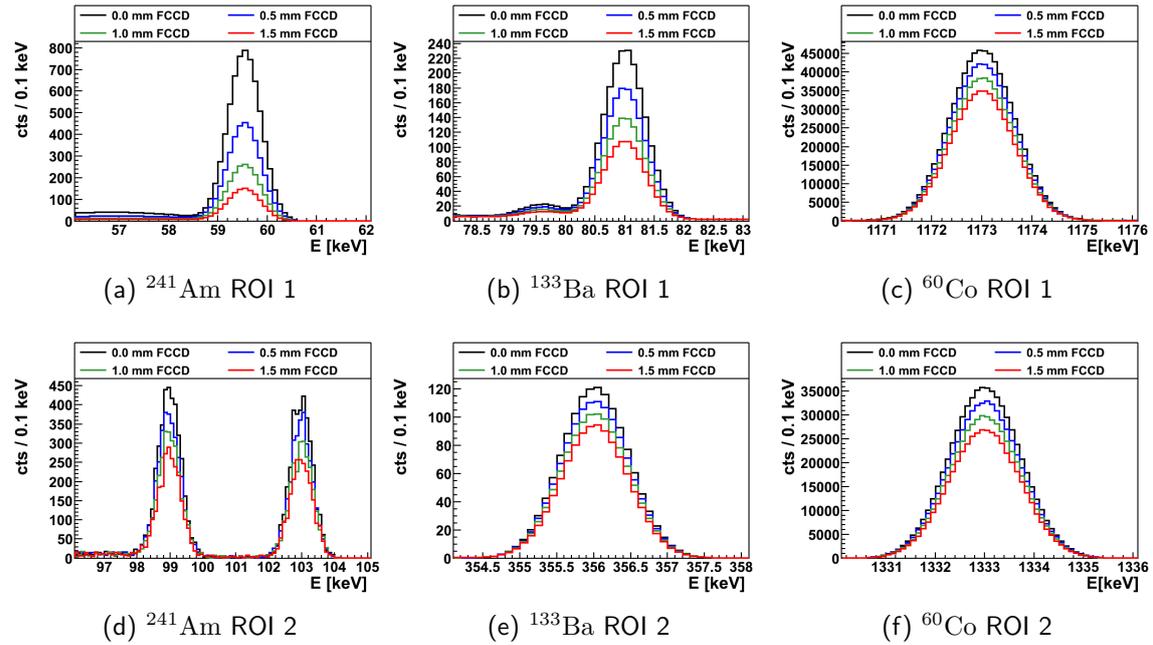
Figure 7.7 Variation of peak regions for different FCCD values. Stronger peak count variations are observed for smaller γ-line energies. Simulated spectra are for GD91C.

(source geometry, distance, etc). In the case of ^{60}Co there are additional systematics uncertainties which are uncorrelated between different measurements of the same detector (e.g. the activity of different ^{60}Co source). Here, multiple measurements of the same detector are combined with a weighted average. The MC spectra are convolved with the energy resolution and binned and treated in exactly the same way as the experimental spectra[10].

Methods for Peak Count Determination

The peak counts are determined with two different methods: (1) A counting method with background estimation from side bands and (2) a fitting method. The counting method implies a linear background assumption. If this assumption is justified both methods should give the same result. The fitting methods may include a complex background p.d.f. and deviations from Gaussian shape for the signal p.d.f. which is used to investigate peal tails. The counting and fitting algorithms for each calibration source are described in detail in the appendix Sec. C.2. Here only the selected algorithms are briefly outlined and illustrated. For ^{241}Am and ^{133}Ba the validity of a flat background assumption is limited due to the previously described peculiarities in the ROIs. Here the fitting method is chosen for the final analysis and the counting method used as a cross-check.

The two ROIs of ^{241}Am are illustrated in Fig. 7.8 for an experimental spectrum of GD91C and the MC spectrum with the best fitting FCCD. The fit function is constructed with Gaussian peaks and constant background section below and above the peaks. The background sections are connected with a Gaussian commutative distribution function (c.d.f.) set to the same width as the peak. In the second peak window around 100 keV the branching ratios of the two signal peaks and the background peak are tightly constrained. The measured spectra of all other detectors are shown in Fig. C.10 to C.13 in the appendix.

---

[10]In some situations background peaks or peak tails are omitted in the fit of the MC spectra.

(a) ^{241}Am measured

(b) ^{241}Am simulated
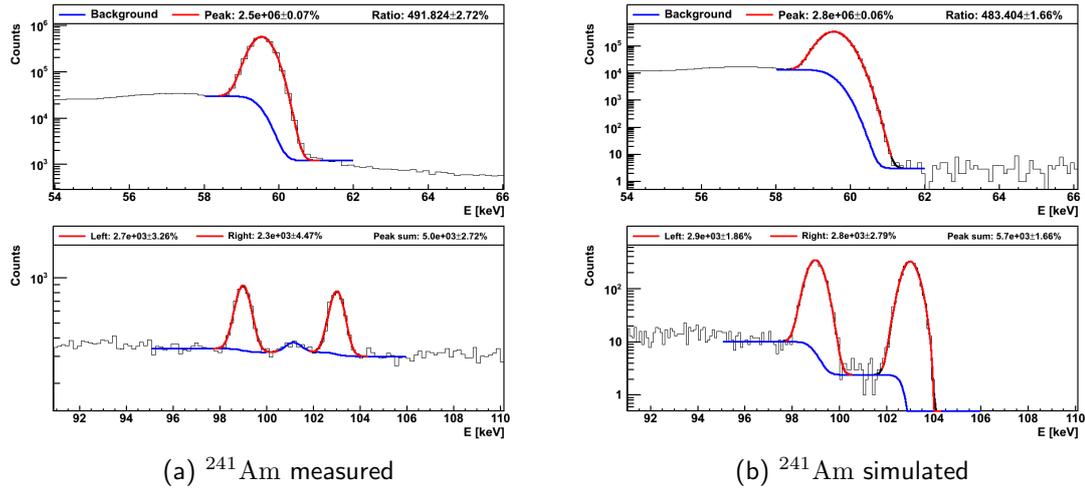
Figure 7.8 Determination of peak counts in the two ROIs of ^{241}Am. The histogram contains data taken with GD91C (left) and the corresponding MC simulation (right). The fit function is shown separated into the signal (red) and background (blue) components. The legends show the counts in the respective peaks and the ratio defined as observable.

(a) ^{133}Ba measured

(b) ^{133}Ba simulated
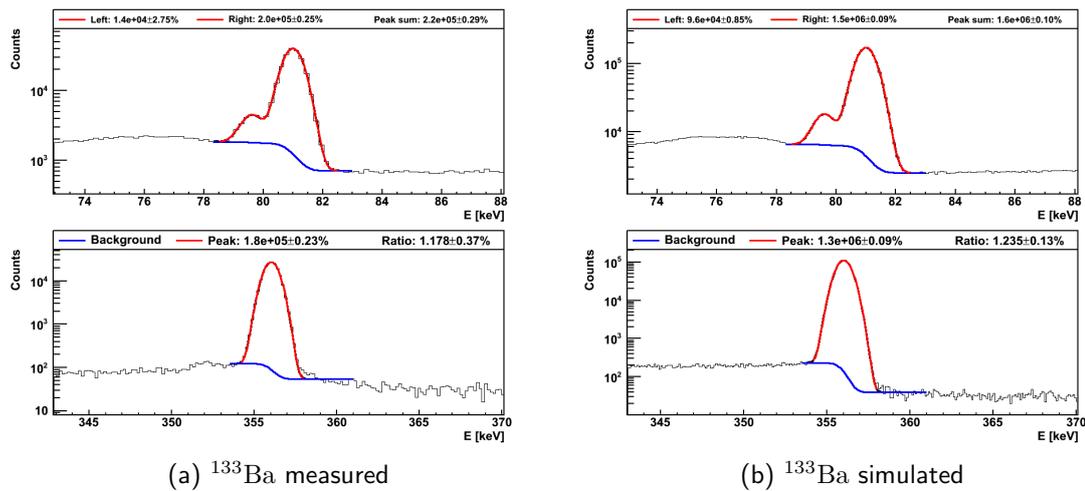
Figure 7.9 Determination of peak counts in the two ROIs of ^{133}Ba. The histogram contains data taken with GD91C (left) and the corresponding MC simulation (right). The fit function is shown separated into the signal (red) and background (blue) components. The legends show the counts in the respective peaks and the ratio defined as observable.

The two ROIs of ^{133}Ba are presented in Fig. 7.9. The signal peaks and background functions are constructed similar to those of ^{241}Am. The double peak structure in the first peak window requires strong constrains on the branching ratio and energy resolution of the peaks. The ROIs for all other detectors are shown in Fig. C.14 to C.17 in the appendix.

The two ROIs for ^{60}Co are shown in Fig. 7.10 for an experimental spectrum of GD91C. The ^{60}Co peaks are single peaks with flat background regions below and above. Here the counting and fitting method yield practically identical results. The fitting method includes a low energy peak tail in the fit which is illustrated as the green function in Fig. 7.10b. A low energy tail could be a potential indication for charge collection deficiencies inside

(a) ^{60}Co 1173.2 keV   (b) ^{60}Co 1332.5 keV
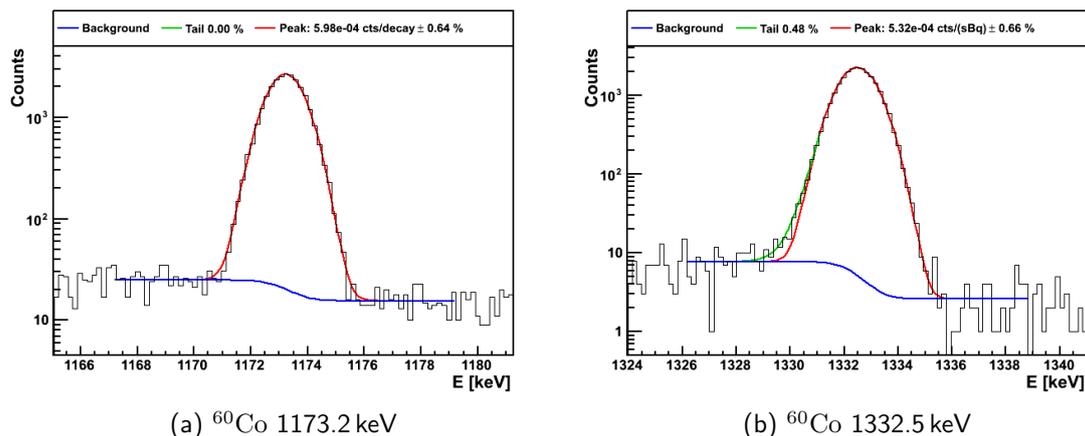
Figure 7.10   Determination of the ^{60}Co peak counts for as independent observables for 1173.2 keV (left) and 1332.5 keV (right). The histograms show the experimental spectrum of one of three ^{60}Co measurements with GD91C. The legends show the peak count rate (red) and the event fraction in the low energy tail (green). The peak count rate is normalized to counts per second and Bq source activity.

the detector. The tail information is extracted for all detectors and the fitting method is chosen as reference for the ^{60}Co analysis.

The ^{60}Co peak counts are obtained by integrating the fit function without background. To estimate the peak asymmetry due to the tail, the peak counts are separated into a left side (N_{left}) and right side (N_{right}) with respect to the mean value,. The asymmetry information is converted into the fraction of events that are in the tail f_{tail}:

$$f_{\text{tail}} = \frac{N_{\text{left}} - N_{\text{right}}}{N_{\text{left}} + N_{\text{right}}}. \tag{7.6}$$

The presented choices of the fitting functions, their parameters, and their constrains, are the result of a long fine-tuning process. The challenge of the fitting methods is to construct an algorithm that can fit many experimental and MC spectra from different detectors and measurements without manual input. The number of individual fits sums up to $150 + 1$ fits for each detector and method. The fit methods are constructed robust and occurrences of non-convergence are identified and flagged. Detailed tuning of individual spectral features have to be omitted in this automated approach. It was found that the selection choices of parameters do slightly influence the final results but do so for all detectors in a systematic way. The variations with different parameter choices are typically much smaller than the systematic uncertainty budget.

Fitting the FCCD   After extracting the observable from the measured spectrum and from the set of MC spectra, both values are compared. The observable is plotted in Fig. 7.11a for the ^{241}Am method ($O_{241\text{Am}}$ Eq. 7.2) for GD91C. The 150 observable values from the MC simulation are plotted in a histogram over the range of 0 to 1.5 mm FCCD. The histogram is interpolated with an empirical spline function such that the FCCD dependence of the observable in the MC is well described. The underlying physical dependence for the ^{241}Am methods is an exponential function since the dominating effect is attenuation. The underlying physical dependence for ^{60}Co observables ($O_{60\text{Co}\,1/2}$ Eq. 7.4 and 7.5), shown in Fig. 7.11c and 7.11d, is a cubic function since increasing the FCCD is decreasing the active volume. For the ^{133}Ba observable ($O_{133\text{Ba}}$ Eq. 7.3), shown in Fig. 7.11b, it is a combination of both. In all cases the conical diodes add an additional contribution from

sloped surfaces and more complex volume description to the dependence. Especially for ^{241}Am it was found that the simulation of a limited number of MC FCCD values interpolated with a simple exponential function introduces a bias, especially for conical diodes. This was often done in the past. The control of this effect, along with saving computing time, is a strong advantage of the DLPP approach developed for this work.
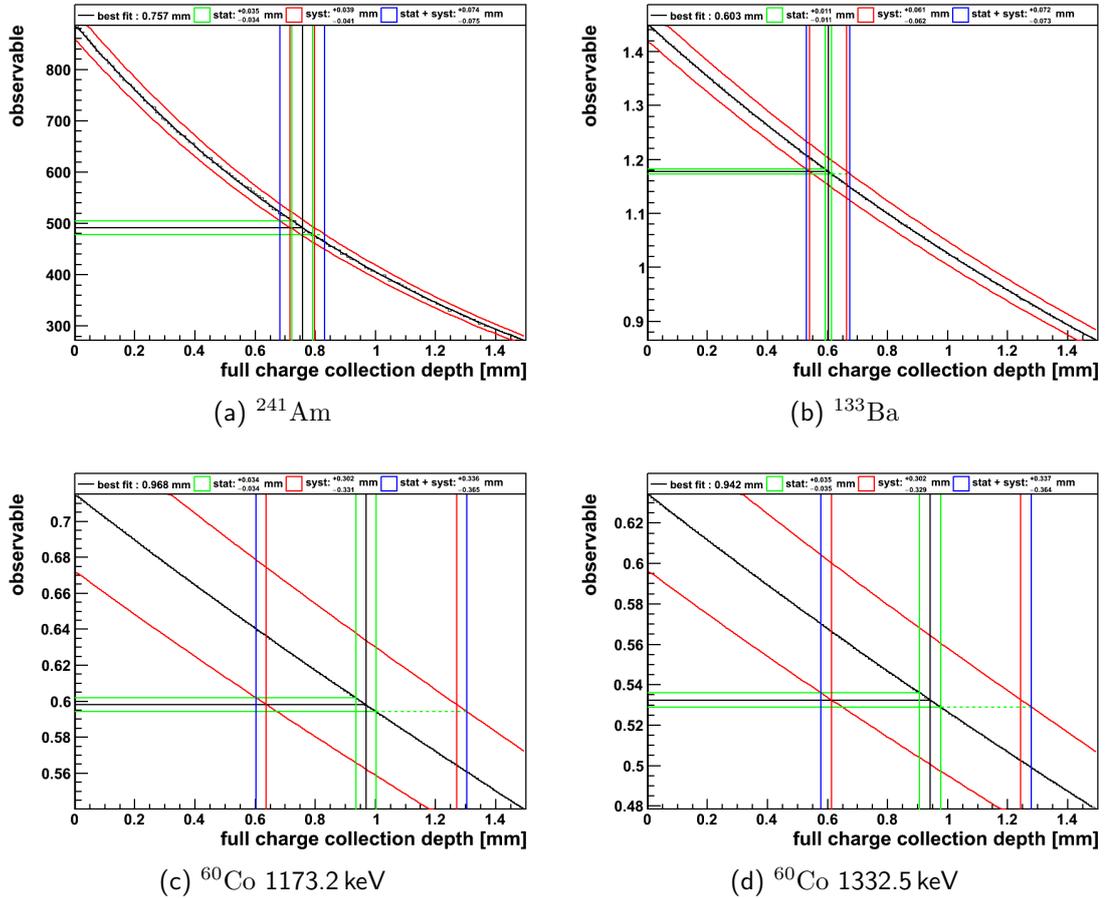
Figure 7.11 Finding the FCCD with fitting the experimental observable to the set of MC observables for GD91C. The histogram entries are the MC observable values for each FCCD step. They are interpolated with a spline function (black). The MC uncertainties are shown in the band around this function (red). The horizontal line is the experimental observable value (black) with its statistical uncertainty (green). The vertical lines illustrate the best fit FCCD value (black), its statistical uncertaintiy (green), its systematic uncertaintiy (red) and their non-linear combination (blue). Note that lines may overlap in the plots.

The value of the measured observable is shown as a horizontal black line. Its $1\,\sigma$ statistical uncertainty is plotted as green horizontal lines below and above this value. The intersection of the experimental value with the MC curve is the best fit FCCD. The intersections of the experimental uncertainty values with the MC curve are the propagated statistical uncertainties on the FCCD. This uncertainty propagation naturally transforms symmetric uncertainties on the observable level into asymmetric uncertainties on the FCCD level. All uncertainties are treated asymmetrically in the following.

The statistical uncertainties in the MC simulation result in a band along the MC curve. This uncertainty is taken as the $1\,\sigma$ uncertainty on each MC point. Due to the DLPP the

uncertainties of different points on the MC curve are correlated. The uncertainty of each individual FCCD value is taken as an approximation. All other systematic uncertainties are also applied to the MC curve. The individual systematic uncertainties are assumed to be uncorrelated with each other and added in quadrature. The total systematic uncertainty including the MC statistical component is plotted as the red band around the MC curve. A detailed description of the systematic uncertainties is given in the next section.

The combined statistical and systematic uncertainty is determined from the intersection of the horizontal green lines with the red MC error band. The resulting total uncertainty on the FCCD is illustrated as blue vertical lines. Due to the non-linearity of the observable dependence, the statistical and systematic uncertainties on the FCCD cannot be simply distinguished. To separate the uncertainties, the following definition is used:

$$\Delta\mathrm{FCCD}_{\mathrm{syst}} = \Delta\mathrm{FCCD}_{\mathrm{total}} - \Delta\mathrm{FCCD}_{\mathrm{stat}}. \tag{7.7}$$

As described above, $\Delta\mathrm{FCCD}_{\mathrm{total}}$ is obtained with the propagation of statistical and systematic uncertainties (blue) whereas $\Delta\mathrm{FCCD}_{\mathrm{stat}}$ is obtained with the propagation of only the statistical uncertainty (green). Note that with this definition the simple sum of statistical and systematic uncertainty results in the total uncertainty.

The general sensitivity of the ^{241}Am, ^{133}Ba and ^{60}Co methods can be estimated with the relative change of the observable within a given range of FCCD values, e.g. for ^{241}Am in Fig. 7.11a the observable is ≈ 880 at FCCD=0 mm and ≈ 290 at FCCD=1.5 mm. Hence the relative change is $\approx 67\%$. In contrast, the relative change of the observable is $\approx 40\%$ for ^{133}Ba and only $\approx 27\%$ for ^{60}Co within this FCCD range. A given uncertainty on the observable level will propagate stronger on the FCCD level for ^{60}Co than for ^{241}Am or ^{133}Ba. The poor sensitivity to the FCCD for the ^{60}Co methods has two reasons: (1) ^{60}Co probes the volume of the detector and the dead volume is only a small fraction $\mathcal{O}(10\%)$ of the total volume. (2) The energy depositions for ^{60}Co FEP events is not distributed homogeneously in the detector volume and is preferring the detector center over the detector surfaces (see argumentation around Fig. 7.3). Hence, the FEP counts in the ^{60}Co γ-lines change only little with changing FCCD, making this method subject to strong influences from uncertainties in the peak counts.

For an unbiased comparison of experimental and MC spectra, the peak counts need to be determined in the same way and as precise as possible. This creates various difficulties:

(1) The MC spectra include only the background created by the calibration source. The background in the experimental spectra includes additional background from natural radioactivity. This issue was addressed with the fitting methods that only use a small section of the spectrum in which the absences of prominent background γ-lines is confirmed.

(2) The peak shapes in the MC are exactly Gaussian with the width of the energy resolution. Peaks in the experimental spectra may be slightly distorted due to DAQ effects or degraded energy reconstruction in small parts of the detector. This issue was investigated for ^{241}Am and ^{133}Ba including a tail to the fit function. No significant effect on the FCCD result was observed after reprocessing the entire analysis chain. The peak tails - although clearly visible in log scale - contain only an insignificant small number of events. An additional argument is the presence of tails in all peaks which should cancel the effect to some extent in the ratio methods. For ^{60}Co the peak tails are included in the fit.

(3) The MC spectra include coincidences from γ-rays originating in the same nuclear decay. The experimental spectra additionally include random coincidences from γ-rays originating in separate decays. Random coincidences are clearly visible for the stronger ^{241}Am sources in e.g. Fig. 7.2a at 120 keV. Time and hardware constrains did not allow for a larger source distance. However, the probability for a random coincidence with a second γ-ray arriving at the same time is similar for any γ-ray energy; hence, it is canceled by the peak ratio. For the lower activity sources of ^{60}Co and ^{133}Ba no random coincidences are visible in the spectra.

7.1.4 Systematic Uncertainties

A thorough investigation of the systematic uncertainties is performed in order to understand the remaining uncertainty budget such that it can be included in the GERDA PHASE II physics analyses. The various systematic contributions can be roughly divided into the following categories: (1) MC simulation, (2) calibration source, (3) BEGe geometry, (4) cryostat interior and (5) DAQ.

The initial uncertainties on the input parameters are propagated to the FCCD and FAV uncertainty. In a first step the effect on the observable is determined. This is typically straight forward and can be analytically calculated in many cases. In a second step the systematic variation of the observable is translated into the uncertainty of the FCCD. This step is dependent on the actual FCCD and performed for each BEGe individually. The propagation to the uncertainty in the FAV depends on the BEGe geometry and is calculated according to the assumption in Eq. 7.1 for each BEGe individually as well.

The uncertainties on the observable, i.e. the peak ratio for ^{241}Am and ^{133}Ba and the peak count rate for ^{60}Co are summarized in Tab. 7.1. The following assumptions are made:

Gamma line emission Uncertainties on the γ-ray emission probabilities are taken from nuclear data sheets [138] and combined into the uncertainty of the peak ratio with Gaussian error propagation. For the ^{60}Co γ-lines, the uncertainty of the emission probabilities translate directly to the observable level.

General Geant4 uncertainty This uncertainty accounts for the physics processes and implemented cross sections in GEANT4. Several MC comparisons are performed in e.g. [143, 144]. A conservative uncertainty is taken as 4 % for direct comparison between MC and data (^{60}Co) and 2 % for a relative spectral comparison (^{241}Am, ^{133}Ba) [145]. This is the largest systematic uncertainty and intrinsically poorly understood. The effect is correlated between all detectors.

MC statistics Uncertainty from limited statistics in MC simulations. The value is individual for each detector and simulations and retrieved by Gaussian error propagation from the uncertainty in the peak fitting methods. The number of simulated events is chosen such that this uncertainty is subdominant.

Source distance to endcap Uncertainty in the source distance above the endcap. The uncertainty of ± 1 mm is negligible for the ratio methods but has an influence on the solid angle for ^{60}Co. This uncertainty is assumed to be independent for each detector.

Source thickness The uncertainty on the thickness of the calibration sources affects the attenuation in the source material and is different for each source type. This uncertainty also includes the size of the active material.

Source material Same as as above. Uncertainty comes from variations in density of the source material e.g. HDPE.

Source activity The uncertainty on the activity has a direct influence on peak count rate in ^{60}Co method. The ^{60}Co source activities were remeasured and found to be consistent within $1\,\%$ $(1\,\sigma)$ uncertainty with each other. The source activity cancels out in ratio methods.

BEGe distance to endcap Same effect as source distance to endcap. The uncertainty in the mounting procedure was given as $\pm 1\,\text{mm}$ by the manufacturer.

BEGe dimensions The uncertainty on the BEGe dimensions affects the FAV measurement of ^{60}Co. E.g. a $1\,\text{mm}$ change of all dimensions would also change the FCCD inference by $1\,\text{mm}$. Tab. 6.1 shows the BEGe dimensions and uncertainties created by deviations from ideal shapes. The discrepancy in mass (last columns) is an indication for this uncertainty. An average of $3\,\%$ is assumed which is independent for each detector. This uncertainty is attributed for the determination of the FCCD[11]. For the ratio methods probing mainly the top surface, the dimension uncertainties are negligible.

Endcap thickness Taken as $\pm 0.1\,\text{mm}$ uncertainty on the aluminum alloy thickness of the endcap.

Detector cup thickness Taken as $\pm 0.1\,\text{mm}$ uncertainty on the HDPE thickness of the detector cup.

Detector cup material Taken as variations in density for HDPE types similar to the source material.

MCA dead time Taken as $10\,\%$ uncertainty in the dead time of a measurement. This affects only the ^{60}Co values.

The influence on the FCCD is illustrated in Fig. C.9 in the appendix which is a zoomed version of Fig. 7.11a. Here, the systematic contributions are unfolded in the various colors of the dashed lines. The combined systematic uncertainty is illustrated in red.

Uncertainty Correlations

In the final application of the FAV in GERDA it is useful to distinguish correlated and uncorrelated uncertainties between the detectors. The uncorrelated part of the uncertainty includes the statistical uncertainty and is individual for each detector. It can be simply combined with Gaussian error propagation and decreases relatively with more detectors in the dataset. The correlated part of the uncertainty is intrinsic in the method of determining the FAV. It is the same for all BEGe detectors and does not decrease with more detectors in the dataset. The correlated or uncorrelated nature of an uncertainty is indicated in the last column of Tab. 7.1. Correlated and uncorrelated uncertainties are separated similarly to statistical and systematic uncertainties in Eq. 7.7. The following definition is made:

$$\Delta\text{FCCD}_{\text{corr}} = \Delta\text{FCCD}_{\text{total}} - \Delta\text{FCCD}_{\text{uncorr}}. \tag{7.8}$$

---

[11]The uncertainty of the ^{60}Co method due to the detector dimensions might be reduced when directly investigating the FAV of the detector. This can be interpreted as ignoring the precise dimensions of the full detector and matching the MC to the dimensions of the FAV instead. The uncertainty of the dimension or the FCCD shell would then only contribute via attenuation; however, the reduced uncertainty budget is more complicated to determine and this approach was not followed. The final FAV uncertainty contribution from the BEGe dimensions can be considered conservative when propagated through the FCCD.

Table 7.1 Systematic uncertainties on the observable level separated into (1) MC simulation, (2) calibration source, (3) BEGe geometry, (4) cryostat interior and (5) DAQ. Shown for comparison are typical statistical uncertainties and typical values of correlated and uncorrelated uncertainties. Numbers are given ±% on the observable and need to be further propagated into uncertainties on the FCCD and FAV. See text for more description.

systematic	uncertainty	^{241}Am ΔO [±%]	^{133}Ba ΔO [±%]	^{60}Co ΔO [±%]	detector correlation
γ-line probability	nuclear data	1.81	0.69	0.03	yes
general GEANT4 uncertainty	inter comparisons	2	2	4	yes
MC statistics	individual	$1 - 2$	$0.1 - 0.2$	≈ 0.2	no
source distance to endcap	±1 mm	-	-	1.2	no
source thickness	various	0.02	0.02	0.02	yes
source material	HDPE variations	0.01	0.01	0.01	yes
source activity	±1 %	-	-	1	no
BEGe distance to endcap	±1 mm	-	-	1.2	no
BEGe dimensions	mass discrepancy	-	-	3	no
endcap thickness	±0.1 mm	0.31	0.28	0.15	yes
detector cup thickness	±0.1 mm	0.03	0.07	0.06	yes
detector cup material	HDPE variations	0.01	0.03	0.03	yes
MCA dead time	±10 %	-	-	< 0.1	no
sum systematics		$2.9 - 3.4$	≈ 2.2	≈ 5.4	
typical statistical uncertainty		$2 - 4$	$0.2 - 0.5$	≈ 0.2	no
sum correlated uncertainties		≈ 2.7	≈ 2.4	≈ 4.1	
sum uncorrelated uncertainties		$2.2 - 4.5$	$0.2 - 0.5$	≈ 3.4	

The $\Delta FCCD_{total}$ is the same total uncertainty as defined in Eq. 7.7. $\Delta FCCD_{uncorr}$ is the value obtained from adding all uncorrelated uncertainties in quadrature and propagating them into an FCCD value. The influence of the uncertainty budget onto the FCCD and FAV level is individual for each detector; even for detectors with similar budgets on the observable level. In the following it is exemplified for GD91C. A collection of all results is given in the next section.

7.1.5 Example Analysis with Diode GD91C

For the ^{241}Am measurement of GD91C the measured peak ratio is 491.9 (Fig. 7.8a). The statistical uncertainty on this observable is ±2.7 %. The combined systematic uncertainty on the MC observables is ±3.2 % with a correlated part of ±2.7 % (compare with average values in Tab. 7.1).

The comparison of experimental and MC observables yields a best fit FCCD of 0.76 mm (Fig. 7.11a). On the FCCD level the statistical uncertainty results in $^{+0.04}_{-0.03}$ mm and the systematic uncertainty (Eq. 7.7) in $^{+0.04}_{-0.04}$ mm. The separation in correlated and uncorrelated uncertainty (Eq. 7.8) is $^{+0.04}_{-0.03}$ mm and $^{+0.04}_{-0.04}$ mm respectively.

The calculated FAV is 103.7 cm^3 compared to a total volume of 114.0 cm^3. This can be expressed in a FAV fraction as f_{FAV}=90.9 %. The maximum and minimum FAV bound is calculated with the minimum and maximum FCCD bound, respectively. The separation into correlated and uncorrelated uncertainties is $\Delta f_{FAV} = ^{+0.4}_{-0.4}$ % and $\Delta f_{FAV} = ^{+0.5}_{-0.5}$ %,

respectively. In summary the two forms of presentation can be written as:

$$FCCD = 0.76^{+0.04}_{-0.03}(\text{corr.})^{+0.04}_{-0.04}(\text{uncorr.}) \text{ mm} \tag{7.9}$$

$$f_{FAV} = 90.9^{+0.4}_{-0.4}(\text{corr.})^{+0.5}_{-0.5}(\text{uncorr.}) \% \tag{7.10}$$

For the ^{133}Ba measurement of GD91C the measured peak ratio is 1.178 (Fig. 7.9a). The statistical uncertainty on this observable is $\pm 0.4\%$. The combined systematic uncertainty on the MC observable is $\pm 2.1\%$ with a strongly dominating correlated part of also $\pm 2.1\%$ (compare with average values in Tab. 7.1).

The comparison of experimental and MC observables yields a best fit FCCD of 0.60 mm (Fig. 7.11b). On the FCCD level the statistical uncertainty results in $^{+0.01}_{-0.01}$ mm and the systematic uncertainty (Eq. 7.7) in $^{+0.06}_{-0.06}$ mm. The separation in correlated and uncorrelated uncertainty (Eq. 7.8) is $^{+0.06}_{-0.06}$ mm and $^{+0.01}_{-0.01}$ mm, respectively.

The calculated FAV fraction is 92.7%. The separation into correlated and uncorrelated uncertainties is $\Delta f_{FAV} = ^{+0.7}_{-0.7}\%$ and $\Delta f_{FAV} = ^{+0.1}_{-0.1}\%$, respectively. In summary the two forms of presentation can be written as:

$$FCCD = 0.60^{+0.07}_{-0.07}(\text{corr.})^{+0.01}_{-0.01}(\text{uncorr.}) \text{ mm} \tag{7.11}$$

$$f_{FAV} = 92.7^{+0.7}_{-0.7}(\text{corr.})^{+0.1}_{-0.1}(\text{uncorr.}) \% \tag{7.12}$$

For the ^{60}Co method multiple measurements per detector are analyzed and combined with a weighted average according to the uncorrelated uncertainty budget of the measurement[12]. For the measurement of GD91C in Fig. 7.10 the observable is shown as the FEP counts per decay and found to be $5.98 \cdot 10^{-4}$ and $5.32 \cdot 10^{-4}$ for the 1173.2 keV and the 1332.5 keV peak, respectively. This corresponds to a FCCD of 0.97 mm or 0.94 mm respectively. Combining this measurement with two other ^{60}Co measurements for FD91C results in

$$1173.2 \text{ keV}: FCCD = 1.01^{+0.25}_{-0.27}(\text{corr.})^{+0.07}_{-0.08}(\text{uncorr.}) \text{ mm} \tag{7.13}$$

$$f_{FAV} = 88.1^{+3.1}_{-3.1}(\text{corr.})^{+1.0}_{-1.0}(\text{uncorr.}) \% \tag{7.14}$$

$$1332.5 \text{ keV}: FCCD = 1.00^{+0.25}_{-0.27}(\text{corr.})^{+0.08}_{-0.08}(\text{uncorr.}) \text{ mm} \tag{7.15}$$

$$f_{FAV} = 88.3^{+3.1}_{-3.0}(\text{corr.})^{+1.0}_{-1.0}(\text{uncorr.}) \% \tag{7.16}$$

with uncertainties separated into a correlated and uncorrelated part. The combination of multiple measurements is not used to reduce the uncertainty budget but to average the central value between the uncorrelated systematic uncertainties[13]. The uncertainties are combined with the same weights as the central value.

7.1.6 Results

In this section the FCCD results are presented, first as individual results from the different methods (^{241}Am, ^{133}Ba, the two ^{60}Co peaks and fitting and counting methods) and then their combination.

---

[12]The set of systematics used for the weights is based on the correlation between different detectors as shown in the last columns of Tab. 7.1. In principle it is more correct to use a different set of systematics which is uncorrelated between different measurements of the same detector (e.g. not including the BEGe geometry). However, the effect on the final combined number is negligible and the existing set of systematics was used for simplicity.

[13]E.g. the activity of different ^{60}Co sources.

Individual Results for ^{241}Am and ^{133}Ba Methods

The individual results of the fitting methods for ^{241}Am and ^{133}Ba are shown in Tab. 7.2. For ^{241}Am, the measurement of GD32C was performed with a weaker source such that a number of background γ-lines influence the peak region around $100\,\mathrm{keV}$ (see Fig. C.10 in the appendix). The quoted ^{241}Am result for this detector is not fully reliable. GD02D is not completely depleted on one side such that the assumption of a homogeneous FCCD does not hold. The analysis for this detector is performed straight forwards as described above. The ^{133}Ba method does not yield a finite result for this detector. The ^{241}Am results may be interpreted as an average FCCD on the top surface.

Table 7.2 ^{241}Am and ^{133}Ba FCCD results for the fitting method. Also the FCCD value reported by the manufacturer is given. The uncertainties are separated in correlated and uncorrelated components. Particularities of some detectors are listed in the footnotes.

detector	^{241}Am [mm]	^{133}Ba [mm]	man. [mm]	detector	^{241}Am [mm]	^{133}Ba [mm]	man. [mm]
GD32A	$0.59^{+0.03+0.02}_{-0.03-0.02}$	$0.53^{+0.06+0.01}_{-0.06-0.01}$	0.60	GD89B	$0.85^{+0.03+0.02}_{-0.04-0.02}$	$0.75^{+0.06+0.01}_{-0.06-0.01}$	0.80
GD32B[a]	$0.84^{+0.03+0.02}_{-0.03-0.02}$	$0.73^{+0.06+0.00}_{-0.06-0.01}$	0.90	GD89C	$0.71^{+0.03+0.03}_{-0.03-0.03}$	$0.66^{+0.06+0.01}_{-0.07-0.01}$	0.85
GD32C[c]	$0.81^{+0.03+0.02}_{-0.04-0.02}$	$0.54^{+0.06+0.01}_{-0.06-0.01}$	0.70	GD89D	$0.83^{+0.03+0.03}_{-0.03-0.02}$	$0.62^{+0.07+0.01}_{-0.07-0.01}$	0.76
GD32D[ab]	$0.61^{+0.03+0.03}_{-0.04-0.03}$	$0.41^{+0.06+0.01}_{-0.06-0.01}$	0.70	GD91A	$0.75^{+0.03+0.04}_{-0.03-0.03}$	$0.65^{+0.05+0.01}_{-0.05-0.01}$	0.80
GD35A	$0.62^{+0.03+0.01}_{-0.03-0.01}$	$0.58^{+0.05+0.01}_{-0.04-0.01}$	0.70	GD91B	$0.73^{+0.03+0.03}_{-0.04-0.03}$	$0.60^{+0.06+0.01}_{-0.06-0.01}$	0.80
GD35B[a]	$0.58^{+0.03+0.06}_{-0.04-0.05}$	$0.53^{+0.06+0.01}_{-0.06-0.01}$	0.70	GD91C	$0.76^{+0.03+0.04}_{-0.04-0.04}$	$0.60^{+0.06+0.01}_{-0.06-0.01}$	0.76
GD35C	$0.58^{+0.03+0.02}_{-0.03-0.02}$	$0.50^{+0.06+0.01}_{-0.06-0.01}$	0.60	GD91D	$0.72^{+0.03+0.04}_{-0.03-0.04}$	$0.64^{+0.06+0.01}_{-0.06-0.01}$	0.80
GD61A	$0.84^{+0.04+0.05}_{-0.04-0.04}$	$0.65^{+0.05+0.01}_{-0.05-0.01}$	0.76	GD00A	$0.62^{+0.03+0.04}_{-0.03-0.03}$	$0.64^{+0.05+0.01}_{-0.05-0.01}$	0.75
GD61B	$0.75^{+0.03+0.04}_{-0.04-0.04}$	$0.69^{+0.06+0.01}_{-0.06-0.01}$	0.80	GD00B	$0.81^{+0.03+0.04}_{-0.04-0.04}$	$0.71^{+0.06+0.01}_{-0.06-0.01}$	0.76
GD61C	$0.70^{+0.03+0.04}_{-0.03-0.04}$	$0.67^{+0.06+0.01}_{-0.07-0.01}$	0.76	GD00C	$0.75^{+0.03+0.02}_{-0.04-0.02}$	$0.62^{+0.06+0.01}_{-0.06-0.01}$	0.76
GD76B	$0.93^{+0.03+0.03}_{-0.04-0.03}$	$0.76^{+0.06+0.01}_{-0.07-0.01}$	1.00	GD00D	$0.77^{+0.03+0.02}_{-0.03-0.02}$	$0.68^{+0.06+0.01}_{-0.06-0.01}$	0.80
GD76C	$0.89^{+0.03+0.03}_{-0.03-0.03}$	$0.81^{+0.06+0.01}_{-0.06-0.01}$	0.92	GD02A[d]	$0.75^{+0.03+0.03}_{-0.03-0.03}$	$0.52^{+0.05+0.01}_{-0.05-0.01}$	0.75
GD79B	$0.76^{+0.03+0.03}_{-0.04-0.03}$	$0.68^{+0.06+0.01}_{-0.06-0.01}$	0.85	GD02B	$0.77^{+0.03+0.04}_{-0.03-0.04}$	$0.63^{+0.06+0.01}_{-0.06-0.01}$	0.80
GD79C	$0.90^{+0.03+0.03}_{-0.04-0.03}$	$0.78^{+0.06+0.01}_{-0.06-0.01}$	0.90	GD02C	$0.79^{+0.03+0.04}_{-0.04-0.04}$	$0.71^{+0.06+0.01}_{-0.06-0.01}$	0.76
GD89A	$0.72^{+0.03+0.04}_{-0.03-0.03}$	$0.64^{+0.05+0.01}_{-0.05-0.01}$	0.80	GD02D[be]	$1.17^{+0.03+0.06}_{-0.03-0.06}$	0.00	N/A

[a] Lead X-ray lines. ^{133}Ba counting method not reliable. Fitting method (this table) not effected
[b] Strong low energy tail at $356\,\mathrm{keV}$. ^{133}Ba methods not reliable
[c] Weak ^{241}Am source. ^{241}Am methods not reliable
[d] Mounted in different cryostat
[e] Not fully depleted. Homogeneous FCCD assumption does not hold. Results not reliable

The results of the counting methods are considered as a cross-check. The values are reported in Tab. C.8 in the appendix. Correlation plots between fitting and counting values are shown in Fig. 7.12a for ^{241}Am and in Fig. 7.12b for ^{133}Ba with error bars denoting the statistical uncertainty. A difference between the fitting and counting method can be seen as a distance from the diagonal line in the plots and indicates a problematic measurement. GD76B shows a significant difference for the ^{241}Am methods whereas GD32D, GD35B and GD32B show large discrepancies for the ^{133}Ba methods.

The observed discrepancy for GD76B (Fig. 7.12a) cannot be explained by the spectral analysis; however, this diode was initially not functional and was heavily reworked. The ^{133}Ba measurements of GD32B, GD32D and GD35B show lead X-rays in the vicinity of the analysis peaks. Here the counting method does not correctly handle the background estimation. GD02D exhibits a large low energy tail for the $356\,\mathrm{keV}$ peak of ^{133}Ba. Also GD32D exhibits a relatively large low energy tail (see Fig. C.14 in the appendix).

(a) ^{241}Am   (b) ^{133}Ba
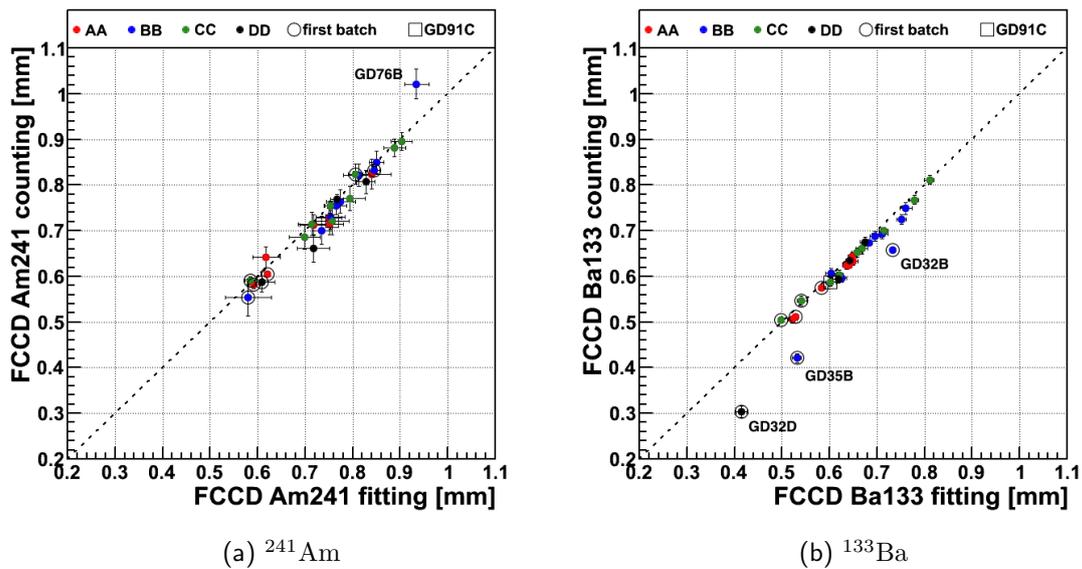
Figure 7.12 Comparison of the fitting and counting method for peak count extraction. The measured and simulated spectra are identical; only the method for the peak count determination is different. The error bars denote statistical uncertainties. The fitting methods handles better the background situation in all cases and is preferred. Highlighted are the original ingot positions of the crystal slices as AA, BB, CC and DD positions, the first and second batch distinction and GD91C as example detector.

In conclusion, ^{241}Am results are considered not reliable for GD32C and GD02D. ^{133}Ba results are considered not reliable for GD32D and GD02D. GD76B is flagged for special caution. For all other detectors, the individual ^{241}Am and ^{133}Ba measurements of the FCCD could be performed with good precision.

Fig. 7.13 shows the correlation plots of the ^{241}Am and ^{133}Ba FCCD results from this work with those values given by the manufacturer. The latter are quoted without uncertainty and seem to be limited to discrete steps. The method employed by the manufacturer for determining the FCCD is based on a ^{241}Am source in which the 59.5 keV count rate is compared to tabulated values [146]. Those values appear to be more in agreement with the ^{241}Am results than with the ^{133}Ba results of this work; however, being based on the same type of calibration source suggests a similar set of systematic uncertainties for the ^{241}Am methods.

Individual Results for ^{60}Co Method

The FCCD values determined from each ^{60}Co peak are shown in Tab. C.9 in the appendix. The values are the combined weighted average over all measurements for an individual detector. The number of measurements used for the combination is shown in the second column. The correlation of the FCCD values from the two ^{60}Co peaks is shown in Fig. 7.14a. A strong correlation is observed and the FCCD values determined from both peaks are practically the same. This is a strong indication that there is no energy dependence on the FCCD analysis between 1173.2 keV and 1332.5 keV.

The results for GD02D are determined straight forwards with the analysis method as described above. The non-depleted volume is interpreted as a homogeneous FCCD of > 7 mm and would correspond to a FAV fraction of about 30 %. These numbers should only be

(a) manufacturer vs. ^{241}Am   (b) manufacturer vs. ^{133}Ba
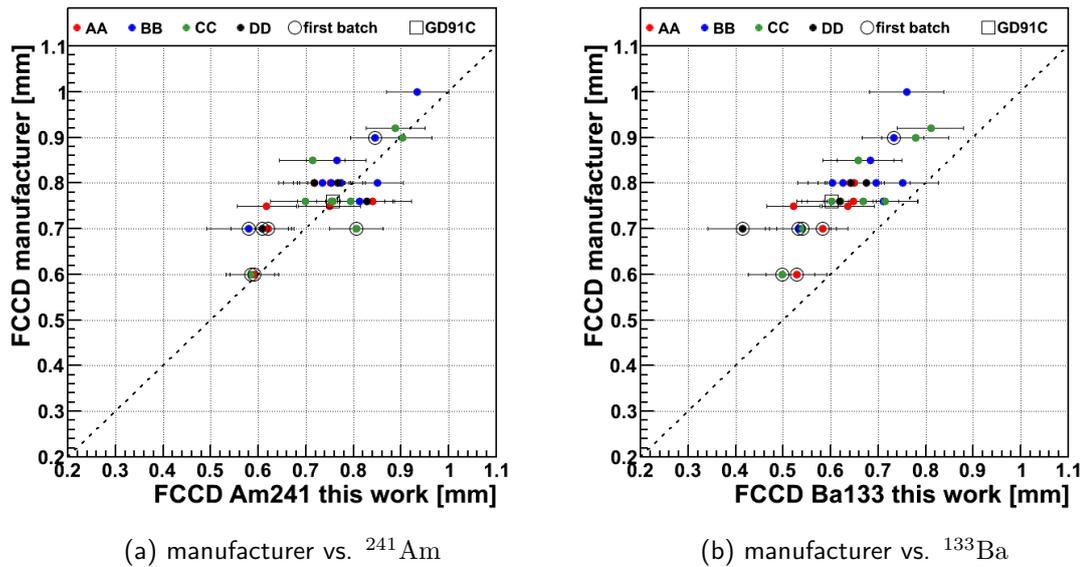
Figure 7.13 Comparison of ^{241}Am FCCD results (left) and ^{133}Ba results (right) with those given by the manufacturer Canberra. The error bars of the FCCD values from this work show the total uncertainty. No uncertainties are quoted by the manufacturer. Highlighted are the original ingot positions of the crystal slices as AA, BB, CC and DD positions, the first and second batch distinction and GD91C as example detector.

understood as an order of magnitude of the FAV and not taken at face value since the conditions for Eq. 7.1 are not fulfilled.

The fraction of events in the peak tail (Eq. 7.6) are also shown in Tab. C.9. This number is the weighted average tail fraction over all measurements for a single detector, taking the same weight as for the FCCD values based on the uncorrelated uncertainty budget. The tail fraction is quoted without uncertainty[14]; however, the significance of potential peak tails is illustrated with the correlation of the tail fractions between the 1173.2 keV and 1332.5 keV peak. This is shown in Fig. 7.14b. Detectors with strong tails on both peaks have potential charge collection deficiencies. This is especially observed for GD02D ($\approx 3\,\%$) and GD35B $\approx 0.7\,\%$[15]. Other detectors with minor peak tails are GD91B, GD00A, GD76C and GD61B. Here the tail fraction is however smaller than 0.3 %. On the other hand, the low energy tail observed for GD32D with the ^{133}Ba measurements could not be observed in the ^{60}Co spectrum. Some ^{60}Co peak regions for selected detectors with visible tails (GD35B, GD02C and GD02D) are shown in Fig. C.18 in the appendix.

FCCD Combination from Surface Probes

The results for the surface probing methods ^{241}Am and ^{133}Ba are combined to get a single number for the FCCD. The correlation of ^{241}Am and ^{133}Ba FCCD values are shown in Fig. 7.15a. The error bars denote the total uncertainty. The ^{133}Ba method exhibits systematically reduced FCCD values compared to the ^{241}Am method. This indicates a

---

[14]The uncertainty from the peak counting is typically larger than the fraction of tail events. Hence, the formal propagation of this uncertainties is consistent with no tail for all detectors but GD35B.

[15]Note that only an FADC measurement exists with ^{60}Co for GD35B. It is likely that the strong peak tail is created by non-optimal DAQ settings in this measurement. The ^{133}Ba measurement does not show a visible tail for this detector. In any case the tail fraction for this detector should not be compared with those of other detectors.

(a) ^{60}Co FCCD

(b) ^{60}Co peak tails
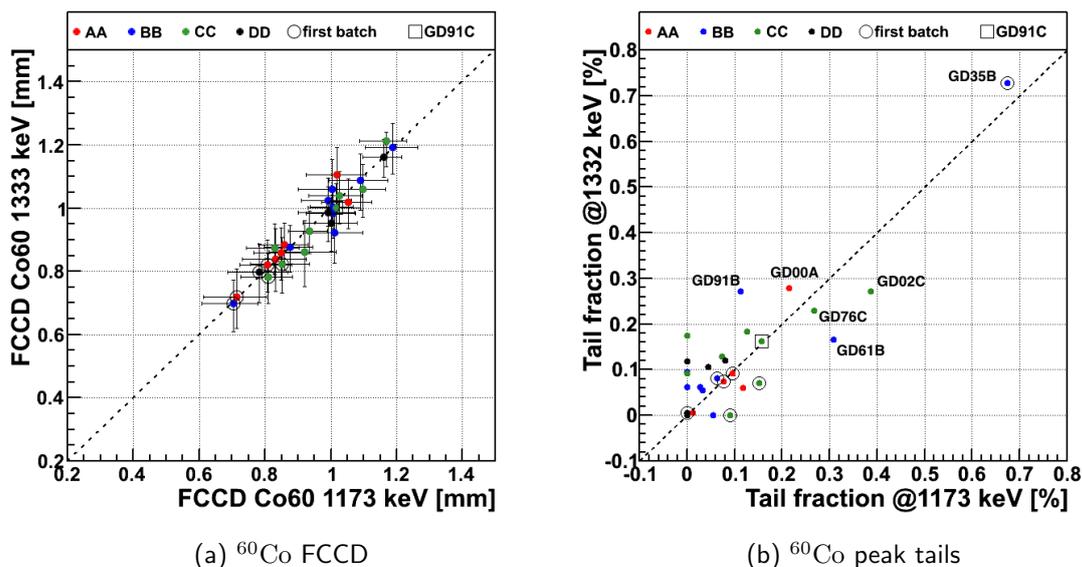
Figure 7.14 Comparison of the two ^{60}Co peaks. Left: FCCD value averaged over all measurements. Right: Fraction of events in low energy tail. Highlighted are the original ingot positions of the crystal slices as AA, BB, CC and DD positions, the first and second batch distinction and GD91C as example detector. Detector GD02D is out of scale in this plot.

systematic shift for all BEGe detectors with a similar magnitude as the individual FCCD uncertainty. This shift may be either due to ^{241}Am or ^{133}Ba or both. The same correlation is shown in Fig. 7.15b with error bars based in the uncorrelated uncertainties, i.e. based on uncertainties subject to individual detectors and not to the whole ensemble. A linear function is fitted to the data points of selected detectors with reliable results for both methods[16]. The constant term is fixed to zero and the linear term is found to be 0.880 ± 0.002. Thus the average systematic shift between ^{241}Am and ^{133}Ba FCCD values is about 12 %.

Both methods show a similar total uncertainty budget. However, typical ^{241}Am value exhibit less correlated uncertainty and more uncorrelated uncertainty than ^{133}Ba. In other words, a systematic shift of the FCCD values for all GERDA detectors is potentially larger for the ^{133}Ba values whereas the individual spread of single detectors is larger for the ^{241}Am values. The combination of the two values is done with a weighted average

$$\hat{\mu} = \frac{1}{w} \cdot \sum_{i=1}^{n} w_i \cdot x_i, \qquad (7.17)$$

in which the two mean values are $x_{i=1,2}$ and the weights w_i are constructed with the variance σ_i^2 as $w_i = \sigma_i^{-2}$ and $w = \sum_i w_i$. The σ_i are taken as the total uncertainty which gives roughly equal weight to both methods. The variance for the combined value can be calculated as $\hat{\sigma} = \frac{1}{\sqrt{w}}$; however, this would destroy the information of the correlated and uncorrelated uncertainty component which can later be included in a full GERDA PHASE II analysis. Therefore, the uncorrelated components of both methods are added in quadrature for the combined value. Due to the systematic shift, the correlated component of the combined value is not reduced: It is taken asymmetrically as the correlated component

---

[16]GD32A, GD32C, GD32D, GD61A, GD76B, GD89D, GD91A, GD00A, GD00C, GD02A and GD02D are excluded due to geometry inconsistencies or issues with one of the measurements.

(a) total uncertainties   (b) uncorrelated uncertainties
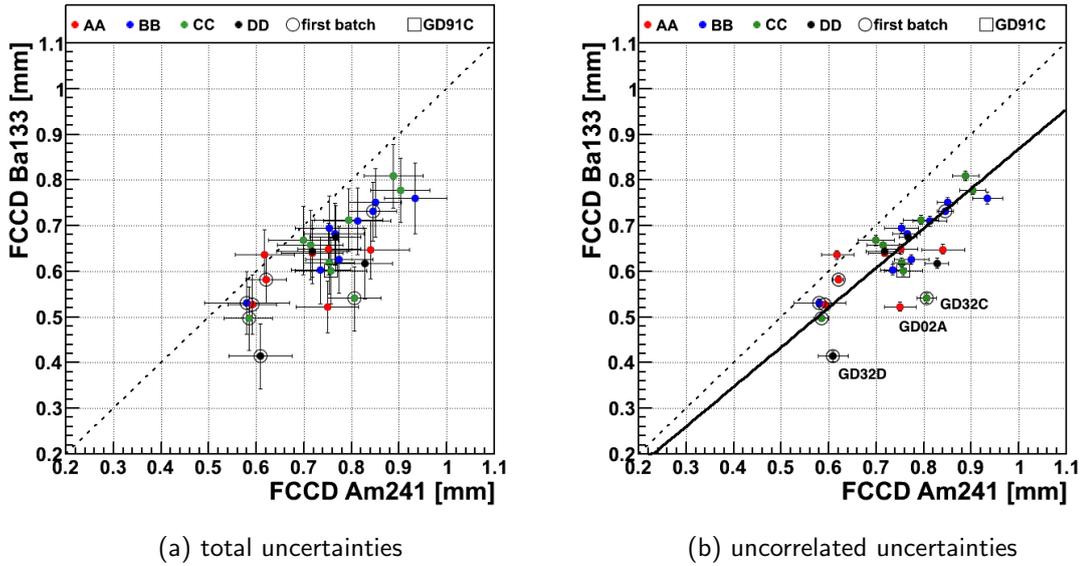
Figure 7.15 Correlation between ^{241}Am and ^{133}Ba FCCD results. Left: The error bars are based on the total uncertainty. Right: The error bars are based on the uncorrelated uncertainties. A linear function is fit to the data points of detectors with reliable results (solid line). Highlighted are the original ingot positions of the crystal slices as AA, BB, CC and DD positions, the first and second batch distinction and GD91C as example detector.

from the ^{133}Ba result for the lower bound and as the correlated component from the ^{241}Am result as the upper bound[17]. As an example for GD91C this results in

$$\text{FCCD} = 0.68^{+0.03}_{-0.06}(\text{corr})^{+0.04}_{-0.04}(\text{uncorr})\,\text{mm}, \tag{7.18}$$

$$f_{\text{FAV}} = 92.0^{+0.7}_{-0.4}(\text{corr})^{+0.5}_{-0.5}(\text{uncorr})\,\%. \tag{7.19}$$

The diodes with the largest discrepancy between the ^{241}Am and ^{133}Ba method are highlighted in Fig. 7.15b. For GD32C the ^{241}Am results were flagged as not being reliable, which might explain also the large difference with respect to the ^{133}Ba results. GD02A was mounted in a different type of cryostat which might result in a bias[18]. For GD32D, strong peak tails were observed in the ^{133}Ba ROI and those results are flagged as not reliable which may explain the observed discrepancy compared to ^{241}Am.

The combination of surface FCCD values is strictly performed according to the methods described above using the fitting methods for ^{241}Am and ^{133}Ba. The results are reported in Tab. 7.3 in a consistent picture. In case of known experimental issues, abnormal spectral features or strong inconsistencies, the diode is marked for suspicious behavior. In case of only one method yielding an unreliable result, the FCCD can be taken from Tab. 7.2 using

---

[17] There is no easy way to combine two systematically different values. This procedure is somewhat constructed and based on the observation that the ^{133}Ba values are typically smaller than the ^{241}Am values. Without further information no preference can be given to either method and they have to be treated equally. The weights based on the total uncertainty of each method ensures this. The correlated and uncorrelated components of the uncertainty are useful for further analysis and need to be separated also for the combined value. The asymmetrical treatment of the correlated uncertainties ensures that the larger component of the ^{133}Ba is better covered in the combined result. This procedure was designed to be the best compromise between the requirements and information at hand and is necessarily an approximation.

[18] The different dimensions of the Tübingen cryostat were considered in the MC; however, some additional systematic uncertainties, e.g. cryostat thickness and material, may contribute which are not accounted in the uncertainty budget.

Table 7.3 Combined FCCD and FAV fraction (f_{FAV}) from surface probes (^{241}Am and ^{133}Ba). The uncertainties are separated in correlated and uncorrelated components. Particularities of some detectors are listed in the footnotes.

detector	FCCD [mm]	f_{FAV} [%]	detector	FCCD [mm]	f_{FAV} [%]
GD32A[a]	$0.57^{+0.03+0.02}_{-0.06-0.02}$	$92.7^{+0.7+0.2}_{-0.4-0.2}$	GD89B	$0.82^{+0.03+0.02}_{-0.06-0.02}$	$89.7^{+0.8+0.3}_{-0.4-0.3}$
GD32B	$0.80^{+0.03+0.02}_{-0.06-0.02}$	$91.0^{+0.7+0.2}_{-0.4-0.2}$	GD89C	$0.69^{+0.03+0.04}_{-0.07-0.04}$	$91.2^{+0.8+0.4}_{-0.4-0.5}$
GD32C[c]	$0.70^{+0.03+0.02}_{-0.06-0.02}$	$92.2^{+0.7+0.2}_{-0.4-0.2}$	GD89D[a]	$0.75^{+0.03+0.03}_{-0.07-0.03}$	$89.8^{+0.9+0.4}_{-0.4-0.4}$
GD32D[abd]	$0.52^{+0.03+0.03}_{-0.06-0.03}$	$94.1^{+0.7+0.4}_{-0.4-0.4}$	GD91A[a]	$0.69^{+0.03+0.04}_{-0.05-0.03}$	$92.3^{+0.5+0.4}_{-0.3-0.4}$
GD35A	$0.61^{+0.03+0.01}_{-0.04-0.01}$	$93.7^{+0.5+0.1}_{-0.3-0.1}$	GD91B	$0.68^{+0.03+0.03}_{-0.06-0.03}$	$92.0^{+0.7+0.3}_{-0.4-0.3}$
GD35B	$0.55^{+0.03+0.06}_{-0.06-0.05}$	$93.9^{+0.7+0.6}_{-0.4-0.6}$	GD91C	$0.68^{+0.03+0.04}_{-0.06-0.04}$	$92.0^{+0.7+0.5}_{-0.4-0.5}$
GD35C	$0.55^{+0.03+0.02}_{-0.06-0.02}$	$93.1^{+0.8+0.2}_{-0.4-0.2}$	GD91D[a]	$0.68^{+0.03+0.04}_{-0.06-0.04}$	$92.3^{+0.7+0.4}_{-0.4-0.5}$
GD61A[a]	$0.72^{+0.04+0.05}_{-0.05-0.05}$	$92.3^{+0.6+0.5}_{-0.4-0.5}$	GD00A[a]	$0.63^{+0.03+0.04}_{-0.05-0.03}$	$92.2^{+0.6+0.4}_{-0.3-0.4}$
GD61B[a]	$0.72^{+0.03+0.04}_{-0.06-0.04}$	$91.8^{+0.7+0.4}_{-0.4-0.4}$	GD00B	$0.76^{+0.03+0.04}_{-0.06-0.04}$	$91.1^{+0.7+0.4}_{-0.4-0.4}$
GD61C	$0.68^{+0.03+0.04}_{-0.07-0.04}$	$91.6^{+0.8+0.5}_{-0.4-0.5}$	GD00C[a]	$0.70^{+0.03+0.02}_{-0.06-0.02}$	$92.4^{+0.6+0.2}_{-0.4-0.2}$
GD76B[a]	$0.86^{+0.03+0.03}_{-0.07-0.03}$	$88.3^{+0.9+0.4}_{-0.4-0.4}$	GD00D	$0.73^{+0.03+0.02}_{-0.06-0.02}$	$92.0^{+0.7+0.2}_{-0.4-0.2}$
GD76C	$0.85^{+0.03+0.03}_{-0.06-0.03}$	$90.8^{+0.6+0.3}_{-0.4-0.3}$	GD02A[cd]	$0.62^{+0.03+0.03}_{-0.05-0.03}$	$92.6^{+0.6+0.4}_{-0.4-0.4}$
GD79B[a]	$0.73^{+0.03+0.03}_{-0.06-0.03}$	$91.6^{+0.7+0.3}_{-0.4-0.3}$	GD02B	$0.70^{+0.03+0.04}_{-0.06-0.04}$	$91.6^{+0.7+0.4}_{-0.4-0.4}$
GD79C	$0.85^{+0.03+0.03}_{-0.06-0.03}$	$90.6^{+0.7+0.3}_{-0.4-0.3}$	GD02C	$0.75^{+0.03+0.04}_{-0.06-0.04}$	$91.7^{+0.7+0.4}_{-0.4-0.4}$
GD89A	$0.67^{+0.03+0.04}_{-0.05-0.03}$	$92.1^{+0.5+0.4}_{-0.3-0.4}$	GD02D[bcd]	$0.02^{+0.03+0.06}_{-0.00-0.06}$	$99.7^{+0.0+0.6}_{-0.4-0.7}$

[a] Issue or potential issue with BEGe geometry
[b] Issue or potential issue with BEGe performance
[c] Issue with ^{241}Am measurement
[d] Issue with ^{133}Ba measurement

the alternative method. However, due to the common systematic shift of ^{241}Am and ^{133}Ba values, this will result in a bias.

FCCD Combination from Volume Probes

The ^{60}Co results from using the two different γ-lines are practically the same. The FCCD results from both peaks are combined into a single number by extending the weighted average between multiple measurements by the results from the two peaks. A single FCCD and FAV value for the ^{60}Co volume probe is reported in Tab. 7.4.

A correlation plot between the FCCD determined with the volume probe and the surface probes is shown in Fig. 7.16a. The error bars denote the combined correlated and uncorrelated uncertainty. The volume probe results in larger FCCD values in all cases. The systematic difference between the values is estimated in Fig. 7.16b showing the same correlation plot with uncorrelated uncertainties as error bars. A linear fit is performed on selected detectors similar as for the comparison between ^{241}Am and ^{133}Ba. A systematic difference of $31 \pm 3\,\%$ FCCD is found.

The strong discrepancy between surface and volume probes was thoroughly investigated. Dedicated measurements were taken with an independent DAQ recording the full pulse information with FADC. The energy reconstruction and the integration time was varied in the analysis to investigate an influence. Long term measurement and HV changes were performed. The detector dimensions were remeasured. The source activities were

Table 7.4 Combined volume probes (both ^{60}Co peaks) results for FCCD and FAV fraction (f_{FAV}). The uncertainties are separated in correlated and uncorrelated components. Particularities of some detectors are listed in the footnotes.

detector	FCCD [mm]	f_{FAV} [%]	detector	FCCD [mm]	f_{FAV} [%]
GD32A[a]	$0.81^{+0.23+0.08}_{-0.25-0.08}$	$89.53^{+3.10+1.06}_{-3.03-1.06}$	GD89B	$1.01^{+0.23+0.07}_{-0.24-0.08}$	$87.36^{+2.96+0.98}_{-2.90-0.97}$
GD32B	$1.00^{+0.27+0.06}_{-0.29-0.07}$	$88.82^{+3.12+0.75}_{-3.05-0.75}$	GD89C	$0.93^{+0.23+0.06}_{-0.24-0.07}$	$88.17^{+2.99+0.80}_{-2.93-0.79}$
GD32C	$0.84^{+0.28+0.08}_{-0.30-0.09}$	$90.79^{+3.20+1.00}_{-3.13-0.99}$	GD89D[a]	$1.16^{+0.21+0.05}_{-0.22-0.06}$	$84.62^{+2.84+0.80}_{-2.79-0.79}$
GD32D[a]	$0.79^{+0.27+0.09}_{-0.29-0.10}$	$91.15^{+3.22+1.05}_{-3.15-1.04}$	GD91A[a]	$0.87^{+0.26+0.07}_{-0.28-0.08}$	$90.37^{+3.05+0.85}_{-2.99-0.84}$
GD35A	$0.72^{+0.29+0.09}_{-0.31-0.10}$	$92.66^{+3.15+1.00}_{-3.08-1.00}$	GD91B	$0.97^{+0.26+0.09}_{-0.27-0.09}$	$88.80^{+3.09+1.06}_{-3.02-1.06}$
GD35B[c]	$0.70^{+0.29+0.07}_{-0.31-0.09}$	$92.30^{+3.40+1.00}_{-3.33-0.99}$	GD91C	$1.01^{+0.25+0.08}_{-0.27-0.08}$	$88.19^{+3.10+0.96}_{-3.04-0.95}$
GD35C	$0.80^{+0.24+0.07}_{-0.26-0.08}$	$90.21^{+3.10+0.99}_{-3.04-0.99}$	GD91D[a]	$0.99^{+0.27+0.08}_{-0.29-0.09}$	$88.90^{+3.12+0.99}_{-3.06-0.98}$
GD61A[a]	$1.06^{+0.28+0.09}_{-0.30-0.09}$	$88.75^{+3.08+0.96}_{-3.01-0.95}$	GD00A[a]	$0.84^{+0.23+0.09}_{-0.24-0.10}$	$89.68^{+2.95+1.22}_{-2.90-1.21}$
GD61B[a]	$1.09^{+0.26+0.06}_{-0.28-0.10}$	$87.78^{+3.07+1.04}_{-3.00-1.03}$	GD00B	$1.03^{+0.26+0.09}_{-0.27-0.10}$	$88.14^{+3.07+1.15}_{-3.01-1.15}$
GD61C	$0.85^{+0.24+0.08}_{-0.26-0.08}$	$89.58^{+3.09+1.01}_{-3.03-1.00}$	GD00C	$1.08^{+0.27+0.07}_{-0.30-0.09}$	$88.51^{+3.14+0.93}_{-3.07-0.93}$
GD76B[a]	$1.19^{+0.22+0.07}_{-0.24-0.08}$	$84.17^{+3.04+1.06}_{-2.97-1.05}$	GD00D	$0.98^{+0.28+0.08}_{-0.30-0.09}$	$89.39^{+3.13+0.92}_{-3.06-0.92}$
GD76C	$1.03^{+0.27+0.07}_{-0.31-0.09}$	$88.96^{+3.19+0.94}_{-3.12-0.93}$	GD02A[a]	$1.04^{+0.24+0.07}_{-0.26-0.08}$	$87.74^{+2.94+0.93}_{-2.88-0.93}$
GD79B	$0.88^{+0.26+0.07}_{-0.28-0.08}$	$89.93^{+3.11+0.87}_{-3.05-0.87}$	GD02B	$0.99^{+0.25+0.07}_{-0.27-0.08}$	$88.18^{+3.07+0.92}_{-3.00-0.91}$
GD79C	$1.19^{+0.26+0.05}_{-0.28-0.08}$	$86.90^{+3.00+0.87}_{-2.94-0.86}$	GD02C	$0.89^{+0.28+0.10}_{-0.30-0.11}$	$90.28^{+3.17+1.13}_{-3.10-1.13}$
GD89A	$0.85^{+0.24+0.08}_{-0.26-0.09}$	$89.95^{+2.99+0.99}_{-2.93-0.99}$	GD02D[bc]	$7.33^{+0.21+0.08}_{-0.22-0.08}$	$33.21^{+1.46+0.54}_{-1.43-0.53}$

[a] Issue with BEGe geometry
[b] Issue with BEGe performance
[c] Issue with ^{60}Co measurement

reevaluated and the dead time dependence on the source activity and source distance was investigated. None of these investigations could explain the large discrepancy between surface and volume probes. Finally, the assumption of a homogeneous FCCD needed for Eq. 7.1 was questioned. Potential charge collection deficiencies in the detector corners, FCCD inhomogeneities and FCCD differences between the top, lateral and bottom side of the detector were investigated. Those analyses are reported in the next two sections.

Finally, it should be noted that the systematic uncertainty budget for the ^{60}Co FCCD values is large due to the direct comparison of MC with data. The correlated uncertainty is around 30 % and thus in the same ballpark as the systematic shift. Hence, technically the surface and volume probes agree within uncertainties.

Conclusion and Outlook

The FCCD values from all three methods (^{241}Am, ^{133}Ba and ^{60}Co both peaks combined) are shown in Fig. 7.17. The error bars denote the uncorrelated uncertainties. The detectors are ordered according to their diode production sequence at the manufacturer. This representation allows to investigate a change of FCCD values due to a potential change of the production process over time. In Fig. C.19 in the appendix the same plots is shown with total uncertainties and no consecutive ordering for comparison.

A clear systematic shift was found between the three methods. The shift between ^{241}Am and ^{133}Ba is about ≈ 12 % FCCD and the two methods were combined into a single value

(a) total uncertainties   (b) uncorrelated uncertainties
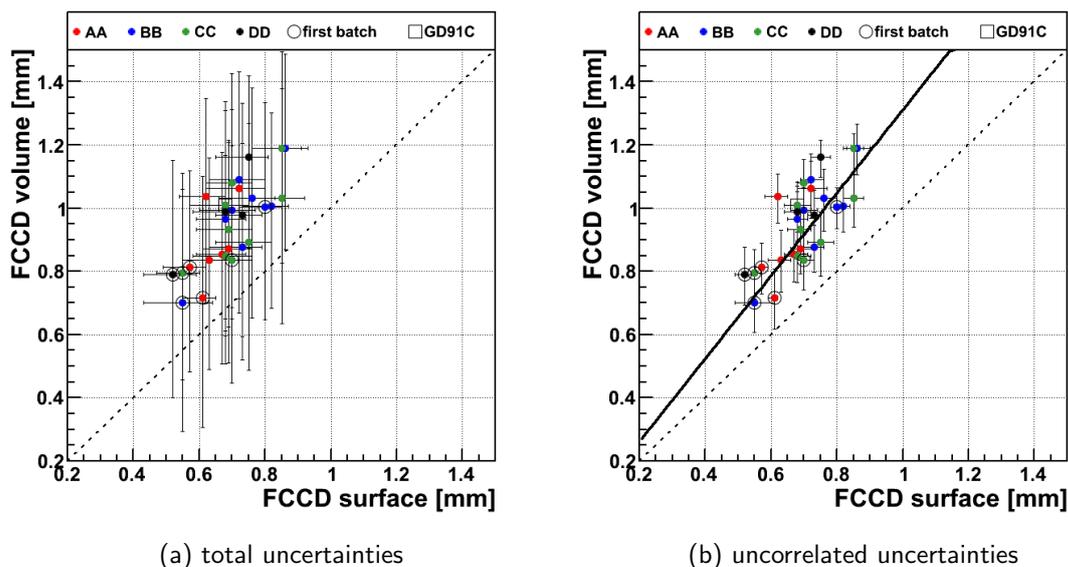
Figure 7.16 Correlation between surface average (^{241}Am and ^{133}Ba) and volume average (both ^{60}Co peaks) FCCD values. Left: The error bars are based on the total uncertainty. Right: The error bars are based on the uncorrelated uncertainties. A linear function is fit to the data points of detectors with reliable results (solid line). Highlighted are the original ingot positions of the crystal slices as AA, BB, CC and DD positions, the first and second batch distinction and GD91C as example detector.

describing the top surface FCCD. The combination gives roughly equal weight to both methods. The shift between the surface FCCD value and the effective ^{60}Co FCCD value probing the full volume is about 31 % FCCD. It remains unclear if the discrepancy is due to unfavorable realizations of systematic uncertainties or due to a physical effect which is not considered in the MC simulations.

A suggested explanation is connected with the size of the charge cloud formed by charge carrier separation in the semiconductor which may be dependent on the amount of energy deposition. The charge cloud size is not the size of the electron track which is extended for higher electron energies and precisely modeled by the MC tracking. It would have to be a faster or stronger expansion of the charges around the electron track in case of larger energy depositions or larger energy densities. This might lead to the escape of charges into the dead or semi-active volume which is not described in the MC. Such an effect would be seen in the analysis as a smaller active volume for full charge collection at higher energies and hence a larger effective FCCD for ^{60}Co Compton electrons. Detailed pulse shape simulations are necessary to investigate this effect which is beyond the scope of this work.

If the suggested explanation should prove correct, then the FAV of $0\nu\beta\beta$ with 2 MeV electron energy deposition is closer to the FAV values obtained with ^{60}Co than the one from the low energy surface probes. However, such an effect should be attributed to the detection efficiency of a process, rather than to a detector property as the FAV. Strong topological differences still exist between the two electron energy distributions of $0\nu\beta\beta$ and ^{60}Co Compton interactions. It would be prudent to investigate and model such an effect and extrapolate it to the $0\nu\beta\beta$ process via pulse shape simulations rather than naively adopt the potentially closer but more uncertain ^{60}Co result as the FCCD value of the detector. The extrapolation should start from the well defined and more precisely known low energy
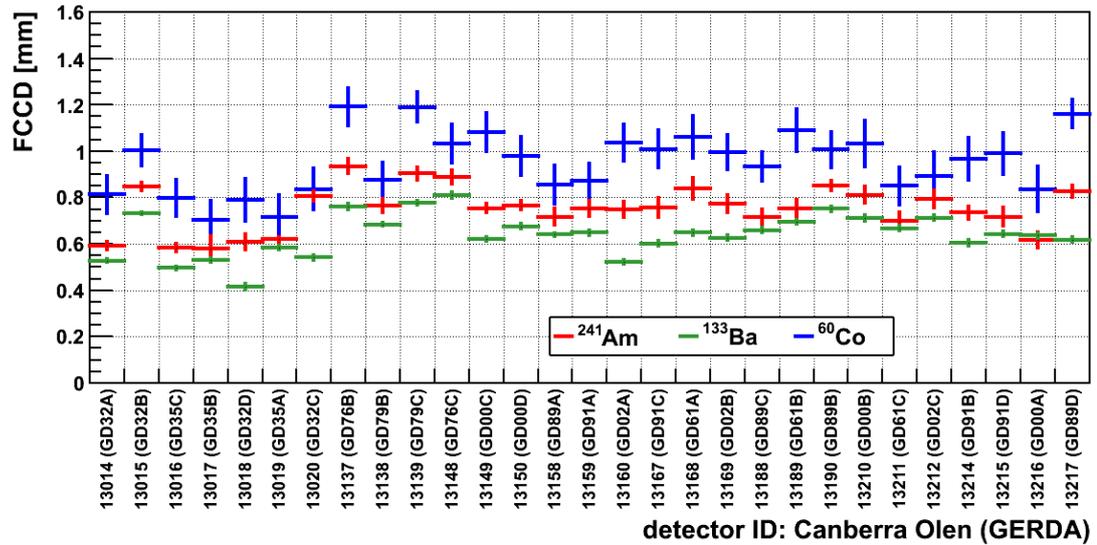
Figure 7.17 FCCD values for all three methods ^{241}Am, ^{133}Ba and ^{60}Co ordered according to production sequence. The error bars denote uncorrelated uncertainties such that the values of a given method can be compared between all detectors.

point-like surface FCCD. However, so far there is no compelling evidence to support an energy dependence in the measurement of the FCCD or the FAV.

As a conclusion, the FCCD and corresponding FAV values for the GERDA PHASE II BEGe detectors are taken from the combined surface probes of ^{241}Am and ^{133}Ba. The ^{60}Co values are not used in the combination. The majority of detectors could be characterized with good precision. Some detectors which showed peculiar performances during the characterization were identified and highlighted for future reference.

7.2   Homogeneity of the FCCD

The homogeneity of the FCCD over the whole n$^+$ electrode surface is an important assumption for the FAV determination (Eq. 7.1). It is investigated with ^{241}Am surface scans using the three scanning tables with a movable collimated ^{241}Am source (Sec. 6.3 and Fig. 6.4).

Some reasons for potential FCCD inhomogeneities on different surfaces are listed below. They are based on qualitative statements derived from first principles or from previous observations.

- Lithium diffusion depends on the orientation of the crystal axis. The magnitude of this effect on the FCCD remains unknown. Variations would be expected to be observed in circular lateral scans.

- Lithium diffusion depends on the impurity concentration. BEGe diodes are constructed such that an impurity gradient goes from lower concentrations on the top to higher concentrations on the bottom. Higher impurity concentrations inhibit the diffusion of lithium and a potential effect could be expected as a larger FCCD on the bottom than on the top side of a diode e.g. visible in a lateral linear scan.

- A reduced charge collection efficiency and hence larger FCCD on the corners of a detector.

- Previously observed inhomogeneities on the top surface of a detector.

In addition, the surface scans can be used as a sensitive cross-check of the FCCD differences between detectors. The scanning measurements are performed under similar conditions for all detectors such that count rate differences between detectors directly depend on FCCD differences.

7.2.1 Measurements

The surface scans are performed for each BEGe detector along the top and lateral surface. This analysis omits AA slices due to the conical shapes[19]. Typically four types of scans are performed: (1) A top linear scan along the diameter of the detector. Typically there exist measurements at various angular coordinates for a single diode. (2) A top circular scan following a concentric path on the top surface. Multiple measurements at different radii are taken. (3) A lateral linear scan moving from the top to the bottom of one side of the detector. Typically there exist multiple measurements at different sides (angular coordinates). (4) A lateral circular scan circling the detector at a given height. Multiple measurements are performed at different heights. The different types of measurements are illustrated in Fig. 7.18a and Fig. 7.20.

(a) source movements   (b) energy spectrum
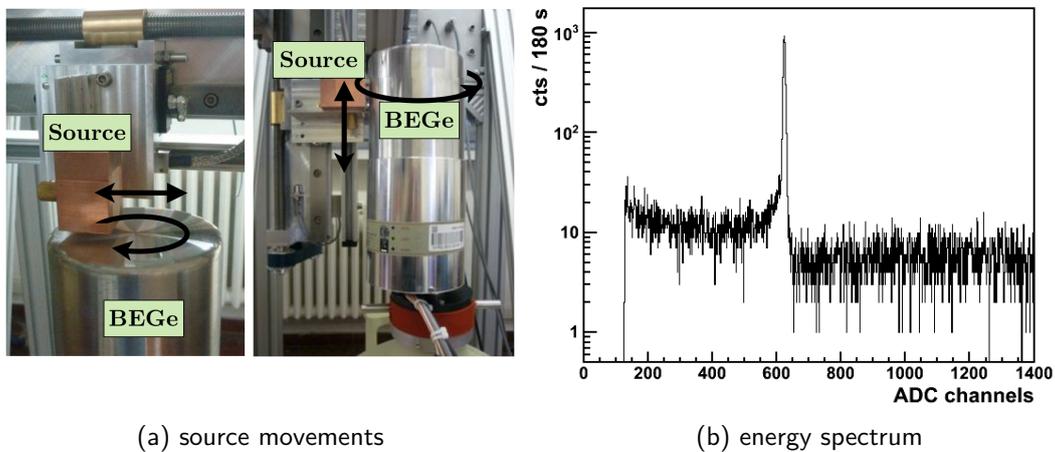
Figure 7.18 Left: Source positions and movements of collimated ^{241}Am source along the top and lateral cryostat surface. Linear and circular scans are possible on each surface. Right: Typical spectrum of a single measurement point for 180 s with the ≈ 5 MBq ^{241}Am source. Clearly visible is the $^{keV}59.5$ γ-line.

The scanning step length along a path is typically between 0.5 and 2 mm resulting in around 140 to 35 measuring positions respectively on the 70 mm top surface diagonal of a standard BEGe. The collimator distance to the cryostat surface is kept small < 1 cm (Fig. 7.18a). This results in a 59.5 keV beam size of ≈ 1.5 mm diameter on the detector surface. The data is taken with the MCA system (Sec. 6.3). The measuring time for a single position is between 30 s and 180 s. A typical spectrum for a 180 s measurement is

---

[19]GD02A which was mounted in a different cryostat is not included in this selection. Hence all investigated detectors are mounted in the same type of cryostat.

shown in Fig. 7.18b. The scanning measurements were planed to acquire only sufficient statistics in the 59.5 keV peak and such spectra do not allow for an investigation of peak ratios with the low probability γ-lines around 100 keV or slow pulses[20].

The ^{241}Am spectra of each scan are treated the same way to automatically extract the 59.5 keV peak counts. First, a spectrum in the middle of the scan is taken to determine the ROI searching for the largest peak in the spectrum. The peak is fitted with a Gaussian and the ROI is defined as the mean $\pm 4.5\,\sigma$. The low and high energy side bands are taken as $4.5\,\sigma$ wide regions, 5 ADC channels below and above the peak region, respectively. The peak counts are determined with the integral counts in the ROI minus the integral counts in the side bands.

7.2.2   Analysis

The ^{241}Am 59.5 keV peak counts are plotted versus the beam position. This is exemplified for a linear top surface scan of GD91C in Fig. 7.19a and for a lateral linear surface scan in Fig. 7.19b. The top scan region is fitted with a constant function from corner to corner. The range is selected manually for each scan such that beam size effects (≈ 2 mm)[21] are omitted but corner effects due to detector deficiencies (up to 10 mm) are included. The lateral linear scan region is separated in three parts according to different detector holder thicknesses inside the cryostat. The ranges are selected manually such that beam size influences on the region boundaries are omitted. The legend in the plots shows the fit results including the mean counts C, their uncertainty σ_C and the quality of the fit for each segment. The circular top and lateral scans are performed from $0 - 360$ deg and analyzed with a constant fit on a single segment similar to the top linear scans.

(a) top scan   (b) lateral scan
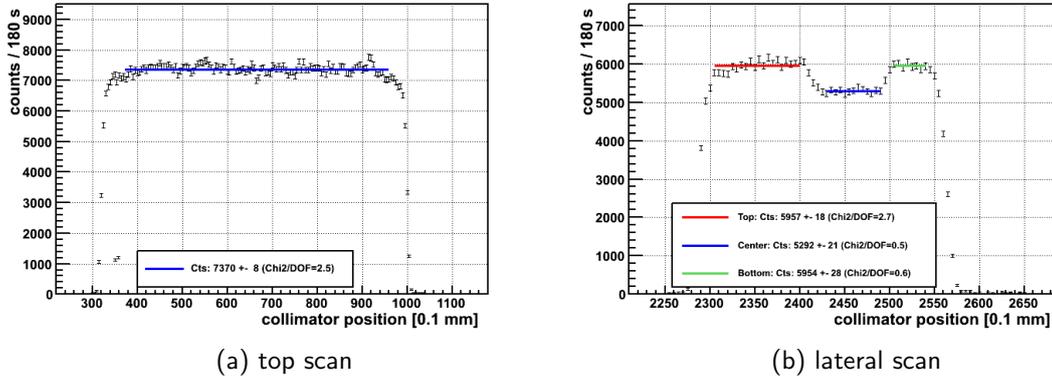
Figure 7.19   Top and lateral surface scans of GD91C. The surface regions are fitted with a constant. The fit result including uncertainty and quality are shown in the legend.

The peak counts are transformed into a count rate R normalized to the measurement livetime T, the source activity $A \pm \sigma_A$ and to the attenuation on the top side of the detector with the attenuation correction factor $f_{CF} \pm \sigma_{f_{CF}}$. The uncertainty of R is determined with

---

[20]For these type of analysis as presented in the next chapter a significantly longer measuring time, a larger collimator and a background shielding would be required.

[21]The beam size can be estimated from e.g. the lateral linear scan when the beam passes from the thin to the thick holder piece. The width of the transition is ≈ 2 mm.

Gaussian error propagation.

$$R = \frac{1}{T \cdot A} \cdot f_{\text{CF}} \cdot C \tag{7.20}$$

$$\sigma_R = \frac{1}{T} \cdot \sqrt{\left(\frac{C}{A} \cdot \sigma_{f_{\text{CF}}}\right)^2 + \left(\frac{f_{\text{CF}}}{A} \cdot \sigma_C\right)^2 + \left(\frac{f_{\text{CF}} \cdot C}{A^2} \cdot \sigma_A\right)^2}. \tag{7.21}$$

The activity of the three sources is shown in Tab. C.10 in the appendix. The uncertainty on the absolute activity is quoted as 8 % by the manufacturer; however, for this work only the activity difference between the sources enters into the analysis. A relative calibration between the sources showed that the activity differences are $< 0.2\,\%$. This uncertainty is taken as σ_A [22].

Correction for Attenuation

For the top and lateral scans of the detectors, the ^{241}Am 59.5 keV beam passes different materials as e.g. the aluminum alloy holders of the detector. The difference in attenuation has to be corrected between the beam path on the top and lateral side to deduce the difference in FCCD in germanium; this is done with normalizing the lateral count rate to the top surface count rate with the factor f_{CF}. There are three different paths for the 59.5 keV beam in the surface scans which are illustrated in Fig. 7.20: The path on the top side (A) and the paths on the lateral side on the height of the thin (B) and the thick (C) holder parts, respectively. Path A crosses the cryostat endcap and the detector cup. The endcap has the same material and thickness of 1.5 mm aluminum alloy AL 6061 T6 on the top and lateral side. The detector cup has a top thickness of 1 mm and a side thickness of 0.5 mm of HDPE. On the lateral side, the beam has to pass an additional 1.5 mm thick aluminum alloy EN AW-2011 AL Cu6BiPB detector holder (path B). The thick part of the holder has a thickness of 3 mm (path C). See also Tab. C.1 in the appendix for all dimensions and materials.

The attenuation for the material layers f_{att} is calculated according to Eq. 4.1 with values from [87]. The materials along with their attenuation are summarized in Tab. C.11 in the appendix. Uncertainties are considered for thicknesses (detector cup and holder), densities (detector cup) and material compositions (detector holder). The cryostat endcap material is stamped in the same production process for the top and lateral side. Since the thickness is equal for the top and the lateral side, the uncertainty of the endcap thickness is not considered in the systematic budget. The uncertainties are assumed to be uncorrelated and propagated as Gaussian errors.

The combined attenuation is calculated for paths A, B and C and reported in Tab. 7.5. Also shown are the normalization factors f_{CF1} and f_{CF2} for the thin and thick holder path respectively.

Combination of Measurements

Multiple scanning results for a given surface are combined with a weighted average estimator as in Eq. 7.17. The weights are based on the fit error σ_{R_i} of the constant fit in an

---

[22]In principle this uncertainty is only needed for comparison of measurements on different scanning tables with different ^{241}Am sources. Mostly, however, scans are performed only on one table for a given detector. Nevertheless, σ_A is small compared to other systematic sources and conservatively applied to all measurements.

(a) top scan
(b) lateral scan
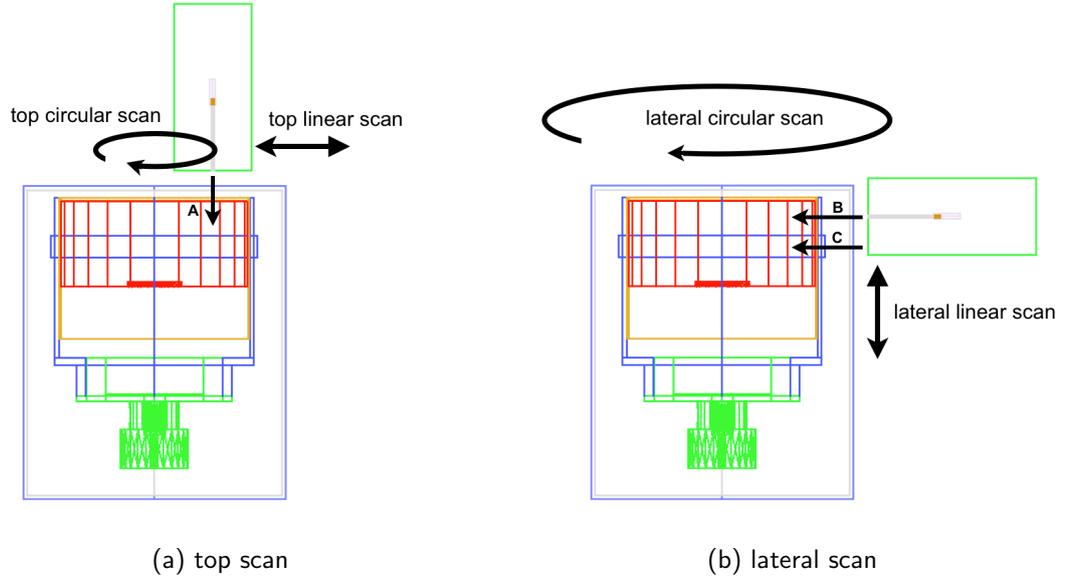
Figure 7.20 Illustration of top surface scans (left) and lateral surface scans (right). The materials between collimated source and detector are different for the three paths A, B and C.

Table 7.5 Attenuation for different beam paths and attenuation correction factors normalized to the top side.

beam path	$f_{\mathrm{att}} \pm \sigma_{f_{\mathrm{att}}}$
TOP (A)	0.8746 ± 0.0016
LAT thin (B)	0.7440 ± 0.0090
LAT thick (C)	0.6271 ± 0.0150
correction	
f_{CF1}: LAT thin / TOP	0.8508 ± 0.0104
f_{CF2}: LAT thick / TOP	0.7171 ± 0.0172

individual scanning measurements i. After this step there is a single average normalized count rate value for each BEGe for the top side ($\hat{R}_{\mathrm{TOP}}$) and the lateral side ($\hat{R}_{\mathrm{LAT}}$). The uncertainties of $\hat{R}_{\mathrm{TOP}}$ and $\hat{R}_{\mathrm{LAT}}$ are calculated twofold:

$$\left(\sigma_{\hat{R}}^{(I)}\right)^2 = \left(\sum_i \frac{1}{\sigma_{R_i}^2}\right)^{-1} \qquad \left(\sigma_{\hat{R}}^{(II)}\right)^2 = \frac{1}{N} \cdot \sum_i (\hat{R} - R_i)^2 \ . \qquad (7.22)$$

The type (I) variance estimator $\left(\sigma_{\hat{R}}^{(I)}\right)^2$ is based on the weighted average which assumes a single true FCCD value on a given BEGe side and decreases with increasing number of measurements. The type (II) variance estimator $\left(\sigma_{\hat{R}}^{(II)}\right)^2$ is based on the population variance of the individual scans compared to the known mean $\hat{R}$ [23]. It ignores the uncertainty of the individual scans and does not decrease with additional measurements. $\sigma_{\hat{R}}^{(I)}$ is used

---

[23]Note that in this case the variance is calculated compared to an assumed known sample mean. n degrees of freedom are taken by the variances and none by the sample mean. Hence Bessel's correction of $\frac{N}{N-1}$ as factor in Eq. 7.22 is not needed.

to compare the top and lateral sides with each other. $\sigma_{\hat{R}}^{(II)}$ is used as an indication of the surface variations on a given detector side.

With this contracted information it is possible to calculate the count rate ratio r between lateral and top side:

$$r = \frac{\hat{R}_{\mathrm{LAT}}}{\hat{R}_{\mathrm{TOP}}} \qquad\qquad \sigma_r = \sqrt{\left(\frac{\sigma_{\hat{R}_{\mathrm{LAT}}}^{(I)}}{\hat{R}_{\mathrm{TOP}}}\right)^2 + \left(\frac{\hat{R}_{\mathrm{LAT}}}{\hat{R}_{\mathrm{TOP}}^2} \cdot \sigma_{\hat{R}_{\mathrm{TOP}}}^{(I)}\right)^2}, \qquad (7.23)$$

with σ_r based on $\sigma_{\hat{R}}^{(I)}$. Successively the difference in FCCD between top and lateral surface (ΔFCCD) is calculated with the count rate ratio:

$$\Delta\mathrm{FCCD} = \frac{-1}{\mu \cdot \rho} \cdot \ln r \qquad\qquad \sigma_{\Delta\mathrm{FCCD}} = \frac{1}{\mu \cdot \rho} \cdot \frac{\sigma_r}{r}, \qquad (7.24)$$

with the attenuation in germanium $\mu = 2.12\,\mathrm{cm}^2/\mathrm{g}$ and the density for $^{\mathrm{enr}}$Ge $\rho = 5.54\,\mathrm{g/cm}^3$. The variation of FCCD on a given surface (δFCCD) can be estimated with $\sigma_{\hat{R}}^{(II)}$:

$$\delta\mathrm{FCCD} = \frac{-1}{\mu \cdot \rho} \cdot \ln\left(\frac{\hat{\mathrm{R}} - \sigma_{\hat{\mathrm{R}}}^{(\mathrm{II})}}{\hat{\mathrm{R}}}\right). \qquad (7.25)$$

7.2.3 Quantitative Results

A total of 474 surface scans are analyzed for 22 detectors and treated as described in the previous section. This includes measurements for all BB, CC and DD diodes except GD02D. The individual results are written in an SQL database including all the measurement information. Next, a subset of measurements and surface segments is selected based on quality requirements:

- Measuring time per position $> 50\,\mathrm{s}$

- Number of degrees of freedom (DOF) in a surface segment fit > 9. This is equivalent to require at least 10 measuring points

- $\chi^2/\mathrm{DOF} < 5$

A total number of 469 surface sections are selected[24] and shown in Tab. C.12 in the appendix. The table shows the measurement name with encoded detector ID, scan type (lateral or top and linear or circular) and the date. Also shown is the segment ID, the fitted counts C_i, the number of DOF of the fit, the fit quality χ^2/DOF, the measuring time, the ^{241}Am source ID and the normalized count rate R_i. The R_i in Tab. C.12 are used to combine top and lateral surface values to $\hat{R}_{\mathrm{TOP}}$ and $\hat{R}_{\mathrm{LAT}}$ as described above. N_{TOP} and N_{LAT} scan segments are used for the combination for a particular BEGe. These numbers along with $\hat{R}_{\mathrm{TOP}}$ and $\hat{R}_{\mathrm{LAT}}$ and their two uncertainties $\sigma_{\hat{R}}^{(I)}$ and $\sigma_{\hat{R}}^{(II)}$ are shown in Tab. 7.6 for all selected BEGe detectors. Also listed is the count rate ratio in the last column.

---

[24]Note that the lateral linear scans consist of 3 surface segments per scan. Hence the total number of segments is larger that the total number of scans. However, the selection criteria largely remove the small segments of the lateral linear scans.

Table 7.6 Results from the combination of surface scans separated into top and lateral surface. Shown from left to right are the detector name, the number of surface segments N_{TOP} used for the combined value, the combined average count rate on the top surface $\hat{R}_{\mathrm{TOP}}$ and the two uncertainty estimators as defined in the test. The next four columns show the same information for the lateral count rate. The last column shows the count rate ratio r.

detector	N_{TOP}	$\hat{R}_{\mathrm{TOP}}$	$\sigma_{\hat{R}_{\mathrm{TOP}}}^{(I)}$	$\sigma_{\hat{R}_{\mathrm{TOP}}}^{(II)}$	N_{LAT}	$\hat{R}_{\mathrm{LAT}}$	$\sigma_{\hat{R}_{\mathrm{LAT}}}^{(I)}$	$\sigma_{\hat{R}_{\mathrm{LAT}}}^{(II)}$	r
GD32B	10	8.40	± 0.01	± 0.33	4	7.76	± 0.06	± 0.17	0.924 ± 0.007
GD32C	9	9.91	± 0.01	± 0.25	2	9.66	± 0.09	± 0.06	0.974 ± 0.009
GD32D	14	10.30	± 0.00	± 0.27	7	9.99	± 0.05	± 0.11	0.970 ± 0.005
GD35B	9	10.42	± 0.01	± 0.09	4	10.11	± 0.06	± 0.05	0.970 ± 0.006
GD35C	11	10.07	± 0.01	± 0.18	4	9.93	± 0.06	± 0.19	0.986 ± 0.006
GD61B	26	8.88	± 0.00	± 0.43	14	8.50	± 0.03	± 0.55	0.957 ± 0.004
GD61C	28	8.87	± 0.00	± 0.17	13	8.67	± 0.03	± 0.48	0.978 ± 0.004
GD76B	8	7.81	± 0.01	± 0.21	3	9.96	± 0.07	± 0.15	1.276 ± 0.009
GD76C	8	8.23	± 0.01	± 0.12	4	8.22	± 0.06	± 0.12	0.999 ± 0.007
GD79B	7	9.28	± 0.01	± 0.15	5	9.03	± 0.06	± 0.13	0.973 ± 0.007
GD79C	6	7.97	± 0.01	± 0.07	6	7.88	± 0.05	± 0.15	0.989 ± 0.006
GD89B	22	8.27	± 0.00	± 0.36	9	7.90	± 0.04	± 0.40	0.955 ± 0.005
GD89C	20	9.13	± 0.00	± 0.12	11	8.99	± 0.04	± 0.14	0.984 ± 0.004
GD89D	9	8.36	± 0.01	± 0.09	2	9.08	± 0.08	± 0.04	1.086 ± 0.010
GD91B	12	9.35	± 0.01	± 0.17	9	9.10	± 0.04	± 0.34	0.973 ± 0.005
GD91C	2	9.71	± 0.01	± 0.01	4	9.34	± 0.07	± 0.21	0.962 ± 0.008
GD91D	6	9.53	± 0.01	± 0.13	7	9.33	± 0.05	± 0.18	0.979 ± 0.005
GD00B	21	8.72	± 0.00	± 0.34	17	8.58	± 0.03	± 0.46	0.984 ± 0.003
GD00C	21	9.34	± 0.00	± 0.43	24	9.10	± 0.03	± 0.62	0.974 ± 0.003
GD00D	10	9.11	± 0.01	± 0.27	12	9.02	± 0.04	± 0.26	0.991 ± 0.004
GD02B	13	9.06	± 0.00	± 0.31	9	8.77	± 0.04	± 0.28	0.968 ± 0.005
GD02C	15	9.07	± 0.00	± 0.14	13	9.09	± 0.03	± 0.34	1.002 ± 0.004

The following observations are made: The count rates are correlated with the absolute FCCD values of the detectors as determined with the ratio methods. BEGe detectors from the first batch show a larger $\hat{R}$ and hence a smaller FCCD as expected. The type (I) uncertainties, based on the variance of the weighted mean, are small whereas $\sigma_{\hat{R}_{\mathrm{TOP}}}^{(I)}$ is smaller than $\sigma_{\hat{R}_{\mathrm{LAT}}}^{(I)}$ because the latter additionally contains the systematic uncertainty from the normalization factors f_{CF}. The count rate ratio r is systematically slightly smaller than 1 for most detectors. This systematic shift is not covered by the type I uncertainties which would underestimate any correlated systematic contribution. The type (II) uncertainties $\sigma_{\hat{R}}^{(II)}$ based on the variance in the scan measurement population are larger. When comparing with the σ_{R_i} of the individual scans (last column of Tab. C.12 in the appendix), the combined $\sigma_{\hat{R}}^{(II)}$ are up to a factor of 10 larger than the σ_{R_i} of the top surface scans and up to a factor of 5 larger than the σ_{R_i} of the lateral surface scans. This indicates that the overall detector surface seen by all scans is typically less homogeneous than seen by an individual scan.

The results in Tab. 7.6 are illustrated with correlation plots. The correlation of $\hat{R}_{\mathrm{TOP}}$ with the FCCD values from the ^{241}Am ratio method is show in Fig. 7.21a and with the ^{133}Ba ratio method in Fig. 7.21b. In general a strong correlation can be observed between the FCCD values and the count rate. Comparing with the ^{241}Am FCCD values, GD32C is identified as an outlier from the general BEGe population. This could be explained by experimental difficulties in the ^{241}Am FCCD determination (see Sec. 7.1.6) since no such effect is observed comparing with ^{133}Ba. A clear outlier in the comparison with the

(a) $\hat{R}_{\mathrm{TOP}}$ vs FCCD ^{241}Am   (b) $\hat{R}_{\mathrm{TOP}}$ vs FCCD ^{133}Ba
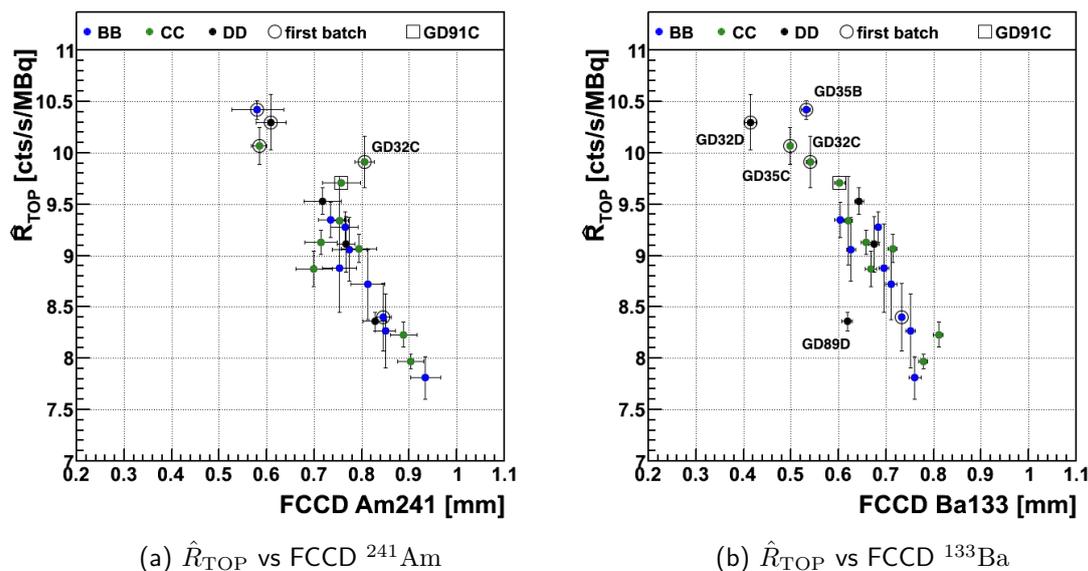
Figure 7.21 Correlation between averaged top count rate from surface scans with FCCD values from ratio measurements. Error bars are $\sigma_{\hat{R}}^{(II)}$ for the count rate and the uncorrelated uncertainties for the FCCD values. Highlighted are the original ingot positions of the crystal slices as BB, CC and DD positions, the first and second batch distinction and GD91C as example detector.

^{133}Ba FCCD values is GD89D which has an irregular shape and a large mass discrepancy (Tab. 6.1). An irregular shape would affect the ^{133}Ba FCCD inference more than the ^{241}Am FCCD inference since the ^{133}Ba method is partly sensitive to the detector volume.

The correlation of the combined surface FCCD values with the top and lateral count rates is shown in Fig. 7.22. Here, the previous outliers for the individual FCCD methods are somewhat mitigated by the FCCD combination and the overall correlation is consistent for the investigated BB, CC and DD detectors. GD76B shows still a large discrepancy and is discussed later. Apart from this detector, the top and lateral surface count rates are well in agreement with the inferred FCCD values for the selected BEGe population, thus strengthening the absolute FCCD results of the surface probing ratio methods ^{241}Am and ^{133}Ba.

The direct comparison of $\hat{R}_{\mathrm{TOP}}$ and $\hat{R}_{\mathrm{LAT}}$ is graphically shown in Fig. 7.23 once with the error bars based on $\sigma_{\hat{R}}^{(I)}$ (left) and once with error bars based on $\sigma_{\hat{R}}^{(II)}$ (right). A larger lateral count rate is observed for GD76B and GD89D resulting in a smaller FCCD on the lateral side. A slightly smaller lateral count rate is observed for GD32B resulting in a larger lateral FCCD.

The FCCD difference between top and lateral side (ΔFCCD) as calculated from the count rate ratio r is shown in Tab. 7.7. GD76B shows a 0.21 ± 0.01 mm smaller FCCD on the lateral side than on the top side. Since the absolute FCCD is measured predominantly on the top side by the ratio methods[25] and $\hat{R}_{\mathrm{TOP}}$ is well within the FCCD correlation whereas $\hat{R}_{\mathrm{LAT}}$ is not (Fig. 7.22), it can be concluded that the lateral FCCD value is 0.52 mm compared to the top FCCD value of 0.73 mm. The differences in FCCD between top and lateral

---

[25]The ^{241}Am sensitivity is exclusively measuring the top surface whereas the ^{133}Ba method is slightly influenced by the volume and hence by the lateral FCCD. See Fig. 7.3.

(a) $\hat{R}_{\mathrm{TOP}}$ vs FCCD combined

(b) $\hat{R}_{\mathrm{LAT}}$ vs FCCD combined
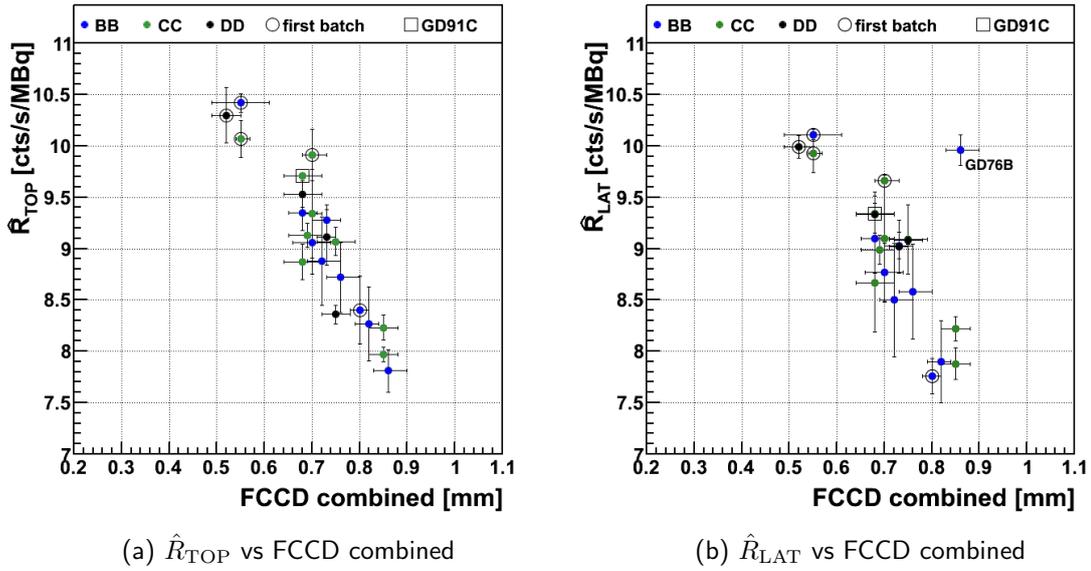
Figure 7.22 Correlation between averaged top (left) and lateral (right) count rate from surface scans with combined FCCD values from ratio measurements. Error bars are $\sigma_{\hat{R}}^{(II)}$ for the count rate and the uncorrelated uncertainties for the FCCD values. Highlighted are the original ingot positions of the crystal slices as BB, CC and DD positions, the first and second batch distinction and GD91C as example detector.

side are potentially connected to the initial problems of GD76B due to which the diode was reworked and lost a substantial mass fraction.

Table 7.7 Surface FCCD variations from scanning measurements. Shown is the BEGe name, the FCCD difference between top and lateral surface ΔFCCD and the FCCD variations on either surface δFCCD$_{\mathrm{TOP}}$ and δFCCD$_{\mathrm{LAT}}$ as defined in the text. Negative ΔFCCD values denote a larger FCCD on the top side.

det.	ΔFCCD [mm]	δFCCD$_{\mathrm{TOP}}$ [mm]	δFCCD$_{\mathrm{LAT}}$ [mm]	det.	ΔFCCD [mm]	δFCCD$_{\mathrm{TOP}}$ [mm]	δFCCD$_{\mathrm{LAT}}$ [mm]
GD32B	0.07 ± 0.01	0.03	0.02	GD89B	0.04 ± 0.00	0.04	0.04
GD32C	0.02 ± 0.01	0.02	0.01	GD89C	0.01 ± 0.00	0.01	0.01
GD32D	0.03 ± 0.00	0.02	0.01	GD89D	-0.07 ± 0.01	0.01	0.00
GD35B	0.03 ± 0.01	0.01	0.00	GD91B	0.02 ± 0.00	0.02	0.03
GD35C	0.01 ± 0.01	0.02	0.02	GD91C	0.03 ± 0.01	0.00	0.02
GD61B	0.04 ± 0.00	0.04	0.06	GD91D	0.02 ± 0.00	0.01	0.02
GD61C	0.02 ± 0.00	0.02	0.05	GD00B	0.01 ± 0.00	0.03	0.05
GD76B	-0.21 ± 0.01	0.02	0.01	GD00C	0.02 ± 0.00	0.04	0.06
GD76C	0.00 ± 0.01	0.01	0.01	GD00D	0.01 ± 0.00	0.03	0.02
GD79B	0.02 ± 0.01	0.01	0.01	GD02B	0.03 ± 0.00	0.03	0.03
GD79C	0.01 ± 0.01	0.01	0.02	GD02C	-0.00 ± 0.00	0.01	0.03

For GD89D, the lateral FCCD is found to be 0.07 mm smaller than the top FCCD which is, however, within the uncertainties for the absolute FCCD value. Additionally, the diode is outside the general detector population for the correlation between the ^{133}Ba FCCD value and $\hat{R}_{\mathrm{TOP}}$ as can be seen in Fig. 7.21b. This is not observed in the correlation between the ^{241}Am FCCD value and $\hat{R}_{\mathrm{TOP}}$. A small part of the lateral surface is chopped off which could have influenced the FCCD determination with ^{133}Ba and may also influence the lat-

(a) $\sigma_{\hat{R}}^{(I)}$ (b) $\sigma_{\hat{R}}^{(II)}$
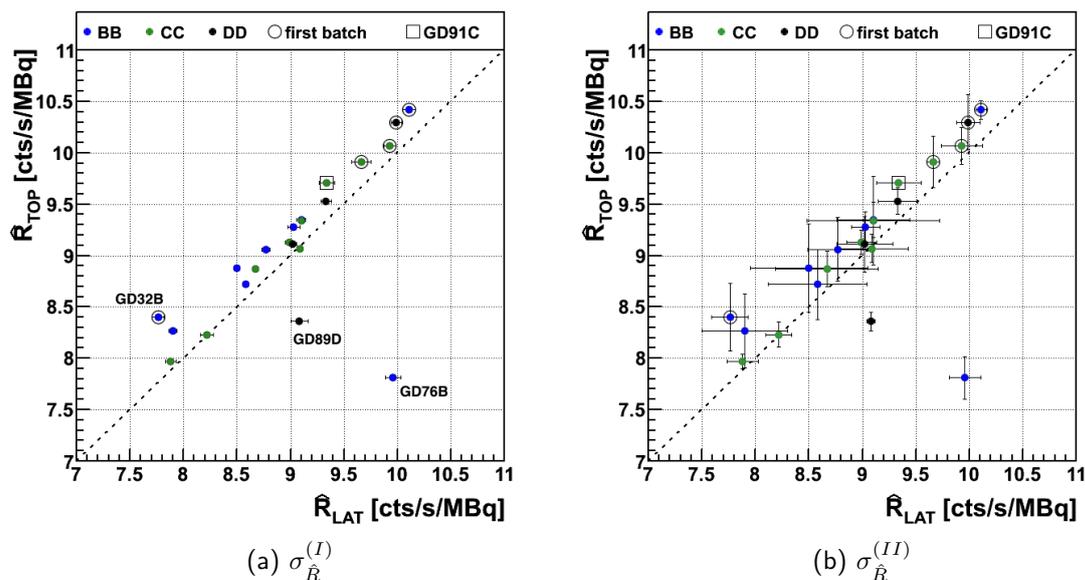
Figure 7.23 Correlation of $\hat{R}_{\mathrm{TOP}}$ vs $\hat{R}_{\mathrm{LAT}}$ for the two uncertainty estimators $\sigma_{\hat{R}}^{(I)}$ and $\sigma_{\hat{R}}^{(II)}$. Highlighted are the original ingot positions of the crystal slices as BB, CC and DD positions, the first and second batch distinction and GD91C as example detector.

eral count rate.

For GD32B a 0.07 mm larger lateral FCCD is observed which is, however, also within the uncertainties of the FCCD values. Apart from X-ray lines in the ^{133}Ba ROI no other indication of anomaly is found for this diode.

The type (II) count rate variation is translated into a variation of FCCD (δFCCD) over the BEGe surface which is also shown in Tab. 7.7. It can be seen that the FCCD surface variation on a given top or lateral surface is typically smaller than 0.05 mm and hence smaller than the absolute uncertainties on the inferred FCCD values with the ratio methods.

Fig. 7.24 illustrates the top and lateral count rate for each BEGe. The detectors are ordered in the sequence of manufacturing and a potential change in the production process can be investigated. The detectors from the first batch (first 5 detectors in the plot) were intentionally produced with a smaller FCCD which is clearly visible in the larger count rates. The n$^+$ electrode of the other detectors were produced with the same procedure according to the manufacturer. The change between consecutively produced detectors is however rather small compared to the overall variation between the detectors. This indicates that the FCCD is dependent on a variable in the production process which can change over time and which might not be fully controlled by the manufacturer.

7.2.4   Qualitative Results

The visible inspection of all 474 surface scans gave the overall impression of a rather homogeneous FCCD surface. This is given the fact that a count rate difference of 10 % results in roughly 0.1 mm difference in FCCD. Hence a significant difference in count rate results only in a small change in FCCD compared to the average FCCD uncertainties from the ratio method. Nevertheless a few peculiarities are observed and are listed in the following.
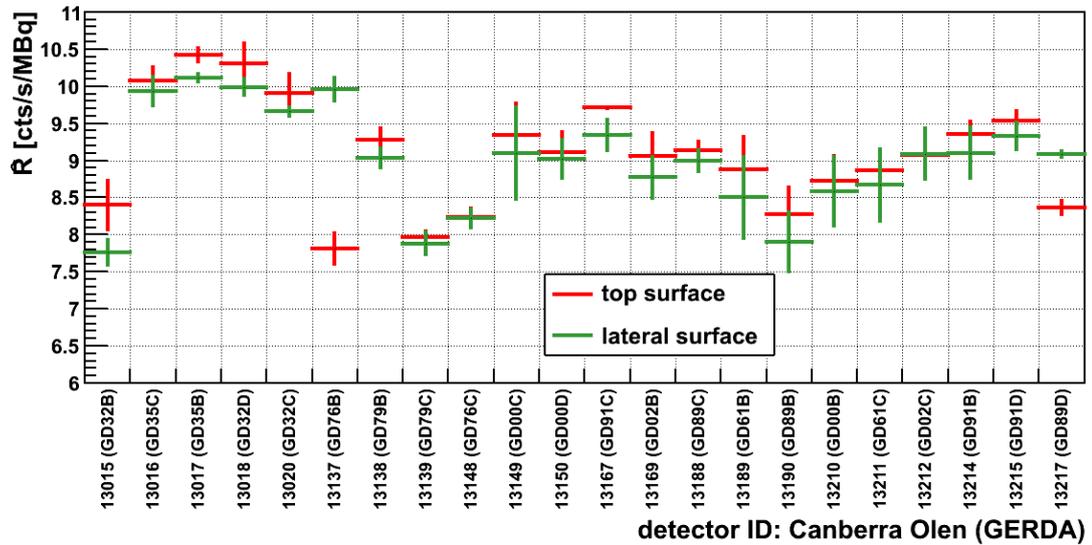
Figure 7.24 Top and lateral normalized count rates for 22 BEGe detectors. The detectors are ordered according to their production sequence.

- Spikes of count rate in small areas on the top surface indicating a localized reduction of the FCCD. This can be seen exemplified in Fig. C.20a and Fig. C.20b in the appendix. Especially for GD00C a strong localized reduction in FCCD is observed. The spot is traced back to a thin supporting holder on which the detector is resting during the electrolytic bath in which lithium is put onto the n^+ electrode surface. The strongest variations are $< 20\%$ in count rate and very localized such that the average FCCD is not strongly influenced. Given the fact that all detectors are resting on a holder during the lithium bath, there will be always localized spots with reduced FCCD. In the top circular measurement of GD00D (Fig. C.21a) on the other hand, a localized increase in FCCD is observed. The localization seems wider than those in which a FCCD decrease is observed. No explanation is found.

- Symmetric FCCD structures on the top surface have been observed and can be distinguished into two types: (1) A decrease in FCCD at around 1/2 the radius which is exemplified in Fig. C.20c in the appendix. Due to the peculiar shape of the count rate plots, such a feature was coined "Mickey Mouse Effect". This behavior is observed for GD32C, GD32D, GD61C and GD02C. Another feature (2) shows the opposite behavior: An increase in count rate at roughly 1/2 of the radius. This is shown in Fig. C.20d for GD76B which is the only detector with this feature.

- Lateral FCCD increases towards the top of the detector have been observed. This can be seen in Fig. C.21c and C.21d in the appendix for GD76C and GD02B with the lateral linear scan. Also GD32B, GD61B and GD00C are showing such a behavior; however, not always a good and conclusive lateral linear scan is available for each detector such that this selection is not complete.

- Small FCCD structures on the circular scan on the lateral side as e.g. shown in Fig. C.21b for GD02C are rare and not very pronounced.

7.2.5   Investigation of Corner Effects

In the detector corners the electric fields are weaker which potentially leads to charge collection deficiencies which would be interpreted as dead volume by the FCCD/FAV analysis. Interactions in the corner regions would not contribute to the FEP and might cause a discrepancy between the surface and volume probes as observed.

An extreme example within the GERDA PHASE II BEGe population of corners deficiencies can be seen in the count rate of the top linear scan of GD61C in Fig. C.20c. In this case a reduced count rate can be seen up to $\approx 10\,\mathrm{mm}$ inside from the edge of the detector. The maximum reduction in count rate on the edge is $\approx 15\,\%$ translating into a roughly $0.14\,\mathrm{mm}$ larger FCCD. If an average reduction of $0.07\,\mathrm{mm}$ FCCD is assumed over $10\,\mathrm{mm}$ of the largest radii, then the total effected volume would be $\approx 0.07\,\mathrm{cm}^3$ or $0.07\,\%$ of the FAV for a typical BEGe with $35\,\mathrm{mm}$ radius and $600\,\mathrm{g}$ mass.

Another extreme example of the same effect on the lateral side of the corner can be seen in Fig. C.21c with the lateral linear scan. A similar estimation results in $\approx 0.15\,\mathrm{cm}^3$ or $0.14\,\%$ of the FAV. Assuming the same corner effects for the bottom edge, a total of $0.4\,\%$ of the volume could be affected by charge collection deficiencies in the corners. The lateral side of the top edge and the bottom edge are not seen by the surface probes (^{241}Am, ^{133}Ba) but by the volume probe (^{60}Co). However, the estimated extreme case of $0.4\,\%$ of the volume cannot explain the large discrepancy between surface and volume probes which is in the order of $4\,\%$ of the volume.

7.2.6   Conclusions

A quantitative and qualitative analysis of surface scans on the top and the lateral sides has been performed. The quantitative analysis finds that FCCD differences between the top and the lateral surface ΔFCCD is negligible for the majority of PHASE II detectors. This partly validates the assumption in Eq. 7.1 to calculate the FAV of the detectors from measurements of the top surface FCCD with the ratio methods. It remains to be tested if the FCCD on the bottom side has similar values compared to the top and lateral side. This is done in the next section with data from the upside-down mounting of GD91C at LNGS.

Detectors in which the assumption for Eq. 7.1 does not hold are GD76B, GD89D and in a smaller extent GD32B. The FAV calculation for these detectors should not be fully trusted. Additionally, the comparisons of count rates with peak ratios finds inconsistencies for GD32C measured with ^{241}Am and GD35B and GD89D measured with ^{133}Ba. These inconsistencies were known from the ratio analysis but have now been verified with additional data. The quantitative analysis also finds that the individual surface FCCD variations δFCCD are small ($< 0.05\,\mathrm{mm}$) and in the same order of magnitude as the differences between top and lateral side. The variations are typically smaller than the FCCD uncertainties from the ratio methods and hence negligible in calculating the FAV. The assumption of a homogeneous FCCD on the top and lateral surface holds true.

For some diodes, small features of FCCD variations have been identified in a qualitative analysis from localized spots to larger structures covering the full surface. They are only visible in the scanning measurements but do not influence the average FCCD values or FAV in a significant way. However, it should be noted that the amount of surface which is covered by the scans varies strongly between different detectors.

Finally, the dead volume in the detector corners was estimated with the surface scans. Even in extreme cases, the reduction of FAV in the corners is less than 0.4 % of the volume and cannot explain the discrepancy between surface and volume probes. The surface scans provide a very precise cross-check of the absolute FCCD values obtained with the ratio method. Previously observed discrepancies for some detectors could be confirmed and better understood. Apart from these few exceptions, the surface scans complement the overall consistent picture of the n$^+$ electrode characterization and thus strengthen the results.

7.3   Bottom Surface FCCD of GD91C

A potential difference of the FCCD between the bottom (p$^+$ electrode) side and the lateral side is investigated with the upside-down mounted GD91C at LNGS (Sec. 6.4) and follows the analysis in the previous section.

The *1mm Brass* collimator (Fig. 6.13a) is used to measure an ^{241}Am calibration source on the bottom and lateral side. The narrow beam size reduces the effect of surface curvature on the lateral side but requires an extended measurement time. The bottom measurement was placed 25 mm off-center and taken for 18 h. The lateral measurement was taken for 21 h and the collimator was placed radial towards the BEGe axis at a height in which the beam traverses the thin aluminum holder part and the thick teflon support. An illustration of the setup and measurement is shown in Fig. 7.25a and the resulting ^{241}Am spectra are shown in Fig. 7.25b.

(a) setup illustration   (b) ^{241}Am spectra
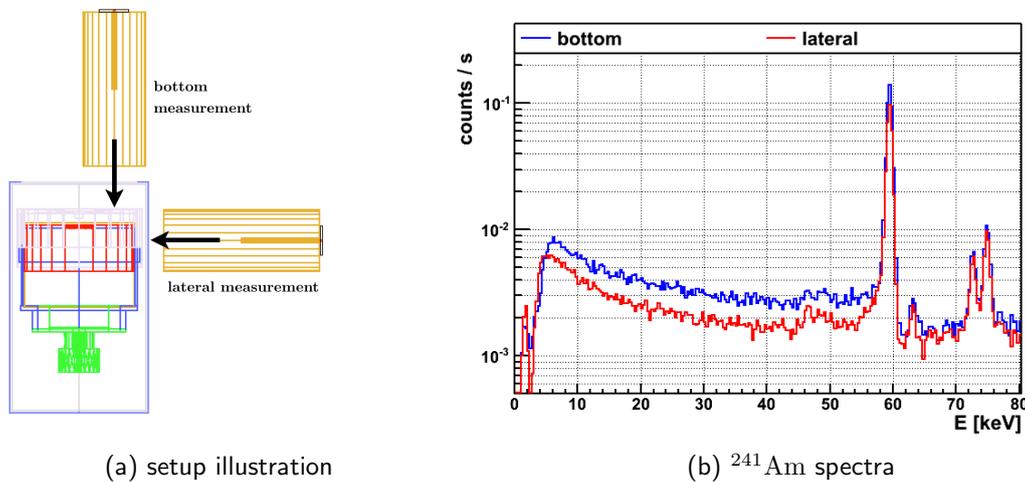
Figure 7.25 Comparison of the FCCD on the bottom and lateral side of GD91C. Left: The setup and the scan positions are illustrated. Right: ^{241}Am spectra of the two measurements are shown.

The attenuation of the 59.5 keV beam on the bottom side is dominated by the 0.6 mm carbon-epoxy window and reduces the intensity to 0.981. The attenuation on the lateral side is dominated by the 1.5 mm thick AL 6061 T6 endcap, the 1.5 mm thick AW-2011 AL detector holder, the 0.5 mm thick HDPE detector cup and the 2.9 mm thick teflon support. The teflon support is additional material unique to the upside-down mounting and accounts for an attenuation of 0.886. All other attenuation are the same as in Tab. C.11 in the appendix. The total attenuation on the lateral side accounts to 0.66 ± 0.04. The uncer-

tainty includes a potentially 0.5 mm thick layer of teflon tape which was wrapped around the detector side (see Fig. 6.6). Hence the expected count rate ratio between lateral side and bottom side is 0.67 ± 0.04.

The 59.5 keV peak in the two spectra was fitted as described in Sec. 7.1.3 for the fitting method of ^{241}Am. The peak count rate ratio was found to be 0.69 ± 0.01. Correcting this ratio with the calculated ratio of attenuations results in $r = 1.03 \pm 0.06$ as defined in Eq. 7.23. The difference in n$^+$ electrode thickness is calculated with Eq. 7.24 and found as ΔFCCD $= 0.03 \pm 0.05$ mm. Hence, no difference in FCCD was found between the bottom and the lateral side of GD91C. The test is based only on a small surface sample of a circular area with 1.5 mm diameter. However, the lateral surface was extensively scanned as shown in the previous section and no significant variation was found for GD91C and the majority of the other detectors. The bottom side of GD91C was scanned with a wide range collimator (see Fig. 6.19a) and no inhomogeneity was found at various angular positions. This strengthens the assumption that the small sample area used in this analysis is representative for the full lateral and bottom surface. Thus, the FCCD of GD91C can be concluded homogeneous on the top, lateral and bottom side. During the extensive characterization there is no evidence that GD91C is different from other BEGe detectors and hence the conclusion is reasonably valid for all Gerda Phase II detectors.

7.4   Detection Efficiencies for $0\nu\beta\beta$ in Gerda Phase II

The detection efficiency of $0\nu\beta\beta$ decays is smaller than 100 % due to the finite volume of the detectors. If not all energy is contained inside the FAV, the event energy is reconstructed outside the full energy peak and the $0\nu\beta\beta$ event is not detected with the peak search. The energy of a $0\nu\beta\beta$ decay can escape the FAV if the electron track is partly leaking inside the n$^+$ electrode or if the electrons generate Bremsstrahlung which then escapes. The single electron energy has a maximum probability at 1 MeV (see Fig. 3.3a) at which the Bremsstrahlung fraction of energy loss is around 2 % (see Fig. 4.4a).

The energy window for the peak search of $0\nu\beta\beta$ is at 2039 ± 5 keV and thus, less than 0.25 % of the energy of an $0\nu\beta\beta$ decay event is allowed to escape such that the event is still inside this window. This argument practically excludes the possibility of detecting $0\nu\beta\beta$ events that occur inside the dead or semi-active part of the n$^+$ electrode. Thus, the FCCD is a clear boundary between DL and AV for $0\nu\beta\beta$ events.

The detection efficiencies in the BEGe detectors were determined with MC simulation in MaGe and the dead layer post processing as described in Sec. 7.1.2. For each detector 10^7 primary $0\nu\beta\beta$ decays are sampled with Decay0 inside the total detector volume described by a single Geant4 physical volume. No FCCD is implemented as a separate volume. The particles are propagated in the BBDecay realm (Sec. 5.3.2). Each Geant4 hit coordinate is recorded in the output and a posterior volume cut is used to determine the spectrum in the FAV.

The following efficiency definitions are made:

- Detection efficiency (f_{det}):
  ($0\nu\beta\beta$ peak counts) / (events sampled in FAV)

- Active volume fraction ($f_{\mathrm{FAV}}^{\mathrm{MC}}$):
  (events sampled in FAV) / (events sampled in total volume)

- Total efficiency (f_{tot}):
  ($0\nu\beta\beta$ peak counts) / (events sampled in total volume)

The $0\nu\beta\beta$ decay peak counts are determined in the raw MC spectrum[26] in a window of $\pm 5\,\text{keV}$ around $Q_{\beta\beta}$. The DLPP cut is based on the FCCD reported in Tab. 7.3. The uncertainties are dominated by the FCCD uncertainties and separated in a correlated and uncorrelated contribution as quoted in Tab. 7.3 and described in Sec. 7.1.6. The statistical uncertainties of the simulation are $< 0.1\,\%$ and uncorrelated between the detectors. The systematic uncertainty on f_{det} are due to the MaGe MC simulation and include the uncertainties on the knowledge of the single electron spectrum, accuracy of the MC tracking and precision of the MC geometry model. This uncertainty is correlated between the detectors and estimated to be about $2\,\%$. It can be assumed that $0\nu\beta\beta$ decay events inside the bulk are fully detected in all cases; thus, the systematic uncertainty is only applied to the fraction of events not reconstructed in the peak reducing the effect to around $0.2\,\%$ compared to all events.

The results are presented in Tab. 7.8 for all BEGe detectors listing f_{det}, $f_{\text{FAV}}^{\text{MC}}$ and their combination f_{tot}. The detection efficiency is similar for all detectors and ranges from 0.88 to 0.90. The difference of detection efficiency is mainly due to the detector volume which can be up to a factor of two different between the GERDA PHASE II detectors. Hence, the small uncertainties of the FAV does not influence the detection efficiency and their uncertainties are practically uncorrelated.

The active volume fraction $f_{\text{FAV}}^{\text{MC}}$ is in principle the same as f_{FAV} quoted in Tab. 7.3. The difference is that $f_{\text{FAV}}^{\text{MC}}$ is obtained by randomly sampling events in the total volume and then applying a volume cut whereas f_{FAV} is calculated analytically by subtracting the dead volume (FCCD) from the total volume. Both methods are equivalent and form a cross-check of the calculation. The results are identical apart from the numerical precision in the last digit for some detectors. The total efficiency f_{tot} is the combination of the two fractions. The uncertainties are separated into correlated and uncorrelated parts and propagated from the uncertainties of f_{det} and $f_{\text{FAV}}^{\text{MC}}$ with Gaussian errors. Tab. 7.8 also summarizes the proposed status of the detectors separated into:

Not usable (o): Not fully depleted and no quantitive statement can be made about FAV or detection efficiency.

Known major issue (x): Not recommended to be used in analysis unless further investigated.

Known minor issue (y): FCCD and FAV values have known discrepancies which are however not expected to be larger than the uncertainty budget. Recommended to be used in analysis but not as reference detector.

Suspected minor issue (z): E.g. minor variation from the ideal shape ($> 1\,\%$) which is not clear how it influences the FCCD and FAV inference. Observed peak tails in one of the spectra which are not clear if they are due to the specific measurement or intrinsic to the detector. Recommended to be used in analysis but not as reference detector.

Especially GD76B, GD89D, GD00A and GD02D show strong issues in the FCCD / FAV analysis and the results are not trusted for these detectors. GD76B shows strong differences

---

[26]Spectrum without convoluted energy resolution of the detector

Table 7.8 Efficiencies for BEGe detectors. Shown are the detection efficiency (f_{det}), the FAV fraction ($f_{\text{FAV}}^{\text{MC}}$) and the combination of both (f_{tot}). Uncertainties are shown in correlated and uncorrelated components. Comments on some detectors are listed as footnotes in the table.

detector	$f_{\text{det}} \pm$ corr $\pm$ uncorr	$f_{\text{FAV}}^{\text{MC}} \pm$ corr $\pm$ uncorr	$f_{\text{tot}} \pm$ corr $\pm$ uncorr
GD32A^z	$0.888 \pm 0.002 \pm 0.001$	$0.926^{+0.008+0.002}_{-0.004-0.003}$	$0.822^{+0.008+0.002}_{-0.004-0.003}$
GD32B^y	$0.900 \pm 0.002 \pm 0.001$	$0.911^{+0.006+0.002}_{-0.005-0.002}$	$0.819^{+0.006+0.002}_{-0.005-0.002}$
GD32C^y	$0.901 \pm 0.002 \pm 0.001$	$0.923^{+0.007+0.002}_{-0.004-0.003}$	$0.831^{+0.007+0.002}_{-0.004-0.003}$
GD32D^y	$0.900 \pm 0.002 \pm 0.001$	$0.942^{+0.006+0.004}_{-0.004-0.004}$	$0.847^{+0.006+0.004}_{-0.004-0.004}$
GD35A	$0.904 \pm 0.002 \pm 0.001$	$0.936^{+0.005+0.002}_{-0.003-0.001}$	$0.846^{+0.005+0.002}_{-0.004-0.001}$
GD35B^z	$0.902 \pm 0.002 \pm 0.001$	$0.940^{+0.006+0.006}_{-0.003-0.006}$	$0.847^{+0.006+0.006}_{-0.004-0.006}$
GD35C	$0.893 \pm 0.002 \pm 0.001$	$0.932^{+0.008+0.001}_{-0.005-0.002}$	$0.832^{+0.008+0.001}_{-0.005-0.002}$
GD61A^z	$0.902 \pm 0.002 \pm 0.001$	$0.923^{+0.005+0.005}_{-0.004-0.005}$	$0.832^{+0.005+0.005}_{-0.004-0.005}$
GD61B^z	$0.899 \pm 0.002 \pm 0.001$	$0.919^{+0.006+0.003}_{-0.005-0.005}$	$0.825^{+0.006+0.003}_{-0.005-0.005}$
GD61C	$0.892 \pm 0.002 \pm 0.001$	$0.917^{+0.007+0.004}_{-0.005-0.005}$	$0.818^{+0.007+0.004}_{-0.005-0.005}$
GD76B^x	$0.883 \pm 0.002 \pm 0.001$	$0.884^{+0.008+0.004}_{-0.005-0.005}$	$0.781^{+0.008+0.004}_{-0.005-0.005}$
GD76C^z	$0.902 \pm 0.002 \pm 0.001$	$0.909^{+0.006+0.003}_{-0.004-0.003}$	$0.820^{+0.006+0.003}_{-0.004-0.003}$
GD79B^z	$0.897 \pm 0.002 \pm 0.001$	$0.916^{+0.008+0.004}_{-0.003-0.002}$	$0.822^{+0.008+0.004}_{-0.004-0.002}$
GD79C	$0.900 \pm 0.002 \pm 0.001$	$0.906^{+0.006+0.003}_{-0.004-0.004}$	$0.815^{+0.006+0.003}_{-0.004-0.004}$
GD89A	$0.893 \pm 0.002 \pm 0.001$	$0.919^{+0.006+0.004}_{-0.003-0.005}$	$0.820^{+0.006+0.004}_{-0.004-0.005}$
GD89B	$0.890 \pm 0.002 \pm 0.001$	$0.897^{+0.009+0.004}_{-0.004-0.003}$	$0.798^{+0.009+0.004}_{-0.004-0.003}$
GD89C	$0.889 \pm 0.002 \pm 0.001$	$0.912^{+0.008+0.005}_{-0.004-0.004}$	$0.811^{+0.008+0.005}_{-0.004-0.004}$
GD89D^x	$0.884 \pm 0.002 \pm 0.001$	$0.899^{+0.009+0.004}_{-0.004-0.004}$	$0.795^{+0.009+0.004}_{-0.004-0.004}$
GD91A^z	$0.898 \pm 0.002 \pm 0.001$	$0.922^{+0.006+0.004}_{-0.003-0.004}$	$0.828^{+0.006+0.004}_{-0.004-0.004}$
GD91B^z	$0.897 \pm 0.002 \pm 0.001$	$0.921^{+0.007+0.003}_{-0.004-0.004}$	$0.825^{+0.007+0.003}_{-0.004-0.004}$
GD91C	$0.896 \pm 0.002 \pm 0.001$	$0.920^{+0.007+0.005}_{-0.003-0.005}$	$0.824^{+0.007+0.005}_{-0.004-0.005}$
GD91D^z	$0.899 \pm 0.002 \pm 0.001$	$0.923^{+0.007+0.005}_{-0.003-0.004}$	$0.830^{+0.007+0.005}_{-0.004-0.004}$
GD00A^x	$0.888 \pm 0.002 \pm 0.001$	$0.919^{+0.006+0.005}_{-0.004-0.004}$	$0.816^{+0.006+0.005}_{-0.004-0.004}$
GD00B	$0.897 \pm 0.002 \pm 0.001$	$0.912^{+0.007+0.005}_{-0.004-0.004}$	$0.818^{+0.007+0.005}_{-0.004-0.004}$
GD00C^z	$0.903 \pm 0.002 \pm 0.001$	$0.925^{+0.006+0.002}_{-0.004-0.002}$	$0.835^{+0.006+0.002}_{-0.004-0.002}$
GD00D	$0.902 \pm 0.002 \pm 0.001$	$0.921^{+0.006+0.002}_{-0.005-0.003}$	$0.830^{+0.006+0.002}_{-0.005-0.003}$
GD02A^z	$0.893 \pm 0.002 \pm 0.001$	$0.925^{+0.006+0.005}_{-0.004-0.004}$	$0.826^{+0.006+0.005}_{-0.004-0.004}$
GD02B	$0.895 \pm 0.002 \pm 0.001$	$0.917^{+0.007+0.004}_{-0.005-0.005}$	$0.820^{+0.007+0.004}_{-0.005-0.005}$
GD02C^z	$0.901 \pm 0.002 \pm 0.001$	$0.918^{+0.007+0.005}_{-0.004-0.004}$	$0.827^{+0.007+0.005}_{-0.004-0.004}$
GD02D^o	N/A	≈ 0.3	N/A

^{o} Not usable

^{x} Known major issue

^{y} Known minor issue

^{z} Suspected minor issue

(0.2 mm or 30 %) between the lateral and top FCCD. GD89D has a visibly chopped-off corner and is not described by the standard shape. GD00A shows 5 % mass discrepancy when described by the standard shape in the MC. A conservative approach to use these detectors in the analysis would be an ad-hoc increase of the FAV uncertainty. GD02D on the other hand is not fully depleted at operational HV and no FAV could be determined.

Known minor issues are identified for GD32C which is measured with a low activity ^{241}Am and whose surface scan shows a discrepancy for the ^{241}Am FCCD value. This is expected to be reduced by the combination with ^{133}Ba [27]. GD32B shows a small (0.07 mm) difference between the lateral and top FCCD in the surface scans. In total 11 detectors are analyzed without known or suspected issues and could be used as reference detectors for a potential future in-situ FAV calibration with the $2\nu\beta\beta$ decay of ^{76}Ge.

Feasibility of an In-situ FAV Calibration with $2\nu\beta\beta$ Decay

The $2\nu\beta\beta$ counts of the 11 reference detectors with strongly trusted FAV values can be compared to those with less trusted FAV values. The full uncertainty of the FCCD thickness is about 10 % which translates into roughly 1 % uncertainty of the FAV fraction. At least 10,000 $2\nu\beta\beta$ counts are required to achieve a measurement with 1 % statistical uncertainty. This is ignoring the systematic uncertainties created by extracting this number with a fit to a complex background model. To count 10,000 $2\nu\beta\beta$ events in an energy window of $600 - 1800$ keV as done in [147], with a typical detection efficiency in BEGe detectors of 90 % and with a typical FAV fraction of 90 %, roughly 20,000 $2\nu\beta\beta$ decays are required to occur in a single detector. Assuming the measured ^{76}Ge $2\nu\beta\beta$ decay half-life of $T_{1/2} = 1.84 \cdot 10^{21}$ yr [147] and a typical enriched BEGe with 600 g mass, this requires roughly 12 yr of operation.

Hence, a potential in-situ calibration on the 1 % level is not feasible in the near future[28]. Additional complications are systematic uncertainties in the background model between the individual detectors and the additional semi-active volume seen by $2\nu\beta\beta$ decay which increases the active volume for $2\nu\beta\beta$ compared to the FAV.

Combined Efficiency in the Gerda Phase II Array

The total mass of the 29 normal working GERDA PHASE II BEGe detectors is 19.362 ± 0.029 kg [29]. The uncertainty on the total mass originates from the conservative estimate of a 1 g correlated scale uncertainty for the mass measurement of each detector (see Tab. 6.1). The combined FAV fraction of all BEGe detectors f_{FAV} is taken as the mass weighted average[30] of the FAV fractions f_{FAV}^i for detector i:

$$f_{\text{FAV}} = \frac{\sum_i m_i \cdot f_{\text{FAV}}^i}{\sum_i m_i} \ . \tag{7.26}$$

The correlated FAV uncertainty is not reduced when considering multiple detectors and is taken as the mass weighted average of the individual correlated uncertainties. The

---

[27]Taking only the trusted ^{133}Ba FCCD value for this detector would result in a bias compared to the other detectors due to the systematic difference between the two methods.

[28]Within a timeframe of 3 yr of operation a calibration on the 2 % level might be possible.

[29]GD02D is not fully depleted and the FAV fraction cannot be determined reliably. The mass of all 30 BEGe detectors is 20.024 ± 0.030 kg.

[30]Here, the detectors are assumed to be all operational at the same time. If only subsets of the detectors are operational at a given time, the weights should be based on the exposure.

uncorrelated uncertainty is reduced with multiple detectors and treated with Gaussian error propagation and weights based on the detector mass:

$$\sigma_{f_{\mathrm{FAV}}}^{\mathrm{uncorr}} = \sqrt{\frac{\sum_i m_i \cdot \left(\sigma_{f_{\mathrm{FAV}},i}^{\mathrm{uncorr}}\right)^2}{\sum_i m_i}} \tag{7.27}$$

The average FAV fraction of the BEGe array is

$$f_{\mathrm{FAV}} = 0.919^{+0.007}_{-0.004}(\mathrm{corr.})^{+0.004}_{-0.004}(\mathrm{uncorr.}) \,, \tag{7.28}$$

which translates into the total active mass of 17.794 kg with 29 detectors. The combination of the detection efficiencies is treated in the same way as the FAV fraction. The average detection efficiency for the 29 working detectors is

$$f_{\mathrm{det}} = 0.897 \pm 0.002(\mathrm{corr.}) \pm 0.001(\mathrm{uncorr.}) \,. \tag{7.29}$$

7.4.1 Energy Resolution of BEGe Detectors

As a side product of the peak fitting for the FCCD/FAV analysis, the energy resolution is obtained for all analysis peaks. Fig. 7.26 shows the energy resolution at 59.5 keV, 356.0 keV and 1332.5 keV FWHM for each detector. The resolution at the 1332.5 keV peak is taken as the FWHM from the Gaussian component of the fit; the low energy peak tail is not included in this number. All detectors apart from GD02D are well below a resolution of 2 keV FWHM at 1332.5 keV. Note, however, that the resolution is dependent on the amplifier electronics and the energy reconstruction algorithms. The obtained values are not representative for the energy resolution in GERDA PHASE II inside LAr.
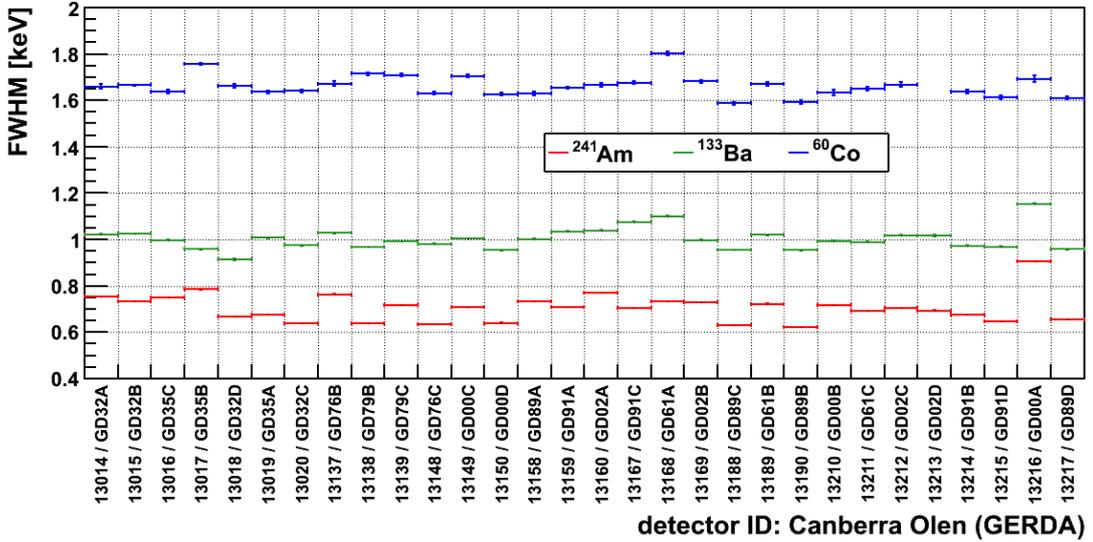
Figure 7.26 Energy resolution in FWHM at three different γ-lines of 59.5 keV, 356.0 keV and 1332.5 keV. The 1332.5 keV γ-line was fitted with an exponential low energy tail which is not included in the FWHM. The detectors are ordered in sequence of diode production at the manufacturer. Note that the ^{60}Co measurement of GD35B was taken with an FADC and is not comparable with the other detectors.

The energy resolution can be correlated to the detector mass influencing the capacitance of the diode and the length of the charge trajectories. A correlation plot of the FWHM at the 1332.5 keV ^{60}Co line with the detector mass is shown in Fig. 7.27a. However, no strong correlation is observed.
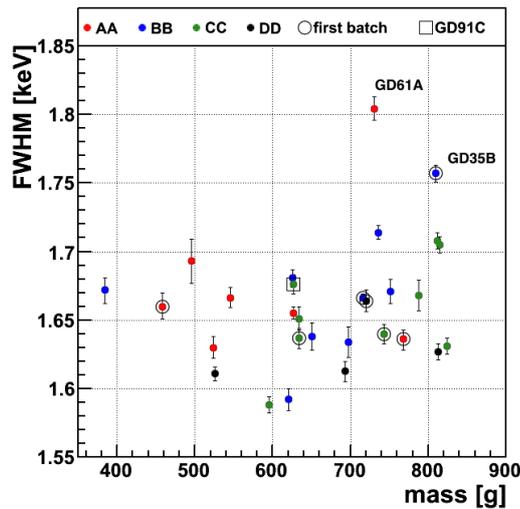
(a) FWHM vs mass

Figure 7.27 Correlations between energy resolution and detector mass. Note that the ^{60}Co measurement of GD35B was taken with an FADC and is not comparable with the other detectors.

7.5   Conclusions

The fully active volume (FAV) and the full charge collection depth (FCCD) has been determined for the GERDA PHASE II BEGe detectors. The FAV is the active volume for processes that involve discrete spectral energies such as $0\nu\beta\beta$ decay and FEPs from γ-ray interactions. The FCCD can be interpreted as the dead layer thickness for these processes using the same terminology as in older literature. The FAV determined in this chapter is underestimating the active volume for processes involving continuous spectral energies such as $2\nu\beta\beta$ decay or $0\nu\beta\beta$ decay with Majoron emission. The FCCD should not be interpreted as a dead layer thickness for these processes. Especially for surface interactions such as beta particles penetrating the n^+ electrode, an additional transition layer is required for an accurate description. A study of these cases is presented in the next chapter.

Three methods based on ^{241}Am, ^{133}Ba and ^{60}Co were applied to obtain first the FCCD and then calculate the FAV under the assumption of a homogeneous FCCD. The ^{241}Am and ^{133}Ba methods probe the top surface FCCD with high precision. The ^{60}Co method probes the full volume of the detector but is less sensitive to FCCD changes and influenced by large systematic uncertainties. The FCCD values determined with the three methods agree within uncertainties. However, systematic shifts were observed between the methods indicating a strong correlated uncertainty common to all detectors. For the final results, the ^{241}Am and ^{133}Ba values were combined into a single FCCD value for each detector. Due to a much larger uncertainty budget of the ^{60}Co method, the results from the volume probe were not considered in the combination.

The assumption of homogeneity for the FCCD over the n^+ electrode was extensively tested with collimated ^{241}Am scans. The top and lateral surface was scanned for a subset of 22 detectors and no significant inhomogeneity was observed for all but two detectors (GD76B and GD89D). The FCCD difference between the lateral and bottom surface was tested for GD91C in the upside-down mount. Also here no significant difference was observed, thus strengthening the assumption of a homogeneous FCCD over the full detector surface.

Charge collection deficiencies in the corners were estimated with the surface scans to be smaller than 0.4% of the total volume which cannot explain the observed FCCD difference between surface and volume probes.

The ^{241}Am scanning measurements were also used as a sensitive crosscheck of FCCD values between the detectors using the $59.5\,\mathrm{keV}$ peak count rate. This very precise method is only sensitive to the FCCD difference between the detectors which can be compared to the difference obtained with the ratio methods. A strong correlation was found for 19 of 22 detectors strengthening the final FCCD results from the ratio methods.

The top surface FCCD measurements with the ^{241}Am and ^{133}Ba ratio method were used to calculate the FAV of the detectors. The mass weighted average of 29 working BEGe detectors is $f_{\mathrm{FAV}} = 0.919^{+0.007}_{-0.004}(\mathrm{corr.})^{+0.004}_{-0.004}(\mathrm{uncorr.})$. MC simulations of $0\nu\beta\beta$ decays were performed for each detector to determine the detection efficiency of this process. The mass weighted average detection efficiency is $f_{\mathrm{det}} = 0.897 \pm 0.002(\mathrm{corr.}) \pm 0.001(\mathrm{uncorr.})$. The uncertainty budgets for all numbers are separated into a correlated and uncorrelated component between the detectors. This information can be incorporated into GERDA PHASE II analyses: The uncorrelated component is reduced when considering multiple detectors in a dataset whereas the correlated component is intrinsic and is not reduced.

Finally, the energy resolution in the vacuum cryostats was determined for all BEGe detectors. The resolution of all 29 working BEGe detectors is better than $2\,\mathrm{keV}$ FWHM at $1332.5\,\mathrm{keV}$. An investigation of the correlation between energy resolution and detector mass found no significant effect.

Chapter 8

New Pulse Shape Model for Surface Events in BEGe Detectors

Surface events are mainly created by beta emitting radioactive isotopes that are on the detector surface or are present in its vicinity. Roughly $96 - 98\%$ of the surface of a PHASE II BEGe detector is covered by the n^+ electrode which has a thickness of $0.5 - 0.9\,\mathrm{mm}$. Thus, the focus in this chapter is on n^+ electrode surface events. Betas penetrating the n^+ electrode can deposit energy inside the active volume. Clearly visible radioactive isotopes in GERDA PHASE I are ^{39}Ar, ^{42}K and ^{214}Bi ([115] and Sec. 5.5.2). Especially the ^{42}K betas with up to $3.5\,\mathrm{MeV}$ endpoint in the ground state transition (82% probability) pose a background risk for $0\nu\beta\beta$ decay at $2039\,\mathrm{keV}$.

MC simulations of n^+ electrode surface events are difficult and have been largely ignored in the past. The non-existing electric field makes diffusion the dominating charge transport mechanism which results in significantly longer rise times (see also Sec. 4.2.1). Due to the long rise time these events are called slow pulses. The isotropic diffusion of the charge carriers in the field-free region leads to a reduced charge collection efficiency when charges diffuse away from the active volume. This energy loss is dependent on the interaction depth below the surface.

Surface events dominate the background for BEGe detectors in GERDA. ^{39}Ar is by far the largest overall background component and ^{42}K dominates the background around the ROI of $0\nu\beta\beta$ decay in PHASE I with around 60%. Yet, so far the energy spectra of these background components could not be adequately simulated. Furthermore, the slow pulse character of surface events allows strong suppression with pulse shape discrimination. A good understanding of this suppression is required to optimize PSD efficiencies. Additionally, the n^+ electrode accounts for roughly 10% of the total detector volume and, to a smaller degree, also affects internal decays. Especially decays with continuous energy deposition such as the $2\nu\beta\beta$ decay and the $0\nu\beta\beta$ decay with Majoron emission are subject to a larger active volume when the n^+ electrode is considered semi-active compared to simply ignoring it in the old approach. This effect becomes important when measuring the $2\nu\beta\beta$ decay with high precision.

The development of a new n^+ electrode model is presented in this chapter. The goal is a tool that can be used to post process existing GEANT4 simulations to correctly describe surface events on the pulse shape level.

The chapter is organized as follows: First, the pulse shape parameter A/E is investigated

for ^{228}Th, ^{90}Sr and ^{241}Am calibration sources in Sec. 8.1 that can be used to design and test the new model[1]. In an intermediate step, a simplified ad-hoc model is developed in Sec. 8.2 and used to extract and compare n$^+$ electrode properties of the PHASE II BEGe detectors with data from the HADES characterization. Then a more sophysticated n$^+$ electrode model is constructed from first principles in Sec. 8.3 and folded into GEANT4 simulations. Those simulations are compared with data from the upside-down mounting of GD91C at LNGS to test the validity of the model in Sec. 8.5. Finally, in Sec. 8.6 the new model is extrapolated to surface background and signal events in GERDA and predictions are made for PHASE II.

8.1 A/E Spectra of Calibration Sources

The pulse shapes in BEGe detectors can be effectively described by the A/E parameter (Sec. 4.2.3). Slow pulses result in a larger width of the current pulse, thus a smaller amplitude and thus a smaller A/E value compared to bulk events. A specific energy deposition in the n$^+$ electrode leads to a reduced E measurement due to charge loss in the detector and to an even more reduced A due to slowness. Hence the A/E is affected twofold compared to the same energy deposition in the bulk. Betas create charge carriers with ionization continuously along their trajectory. If betas pass through the n$^+$ electrode, they will always have a fraction of their pulse influenced by this slow pulse character.

The A/E is reduced for both slow pulses and multi-site events (MSE) compared to single-site events (SSE) in the bulk (Fig. 4.10). The SSE topology of the ^{208}Tl DEP is used as a reference for A/E. If a 2614.5keV γ-ray from ^{208}Tl is interacting via pair production, two 511.0 keV γ-rays from the positron annihilation can escape the detector. The detected 1592.5 keV energy of the electron is typically confined to a small volume[2]. The A/E versus E spectrum of a ^{228}Th calibration source is shown in Fig. 8.1. The markings are explained below:

(a) A/E scatter plot   (b) A/E slice
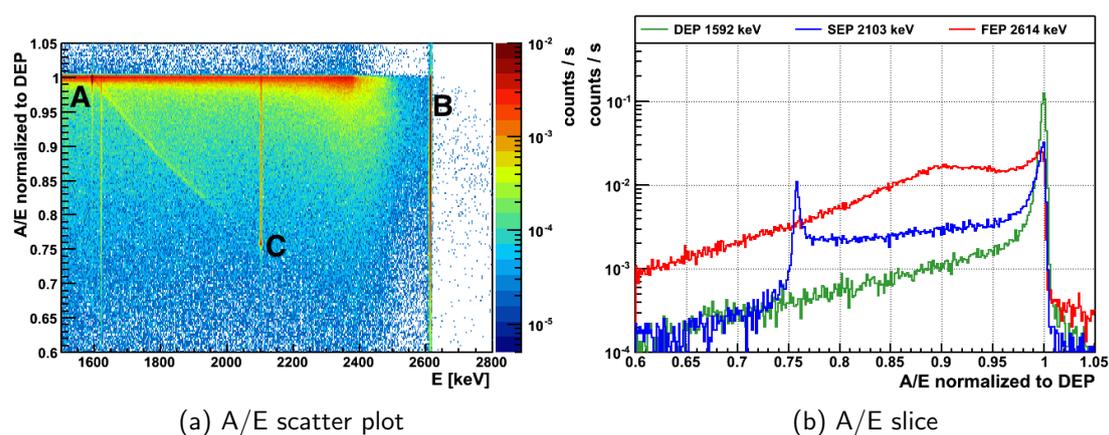
Figure 8.1 ^{228}Th calibration source measurement. Shown is the A/E versus E scatter plot (left) and A/E slices for given energy regions (right). Note that the spectra contain background. The spectral section is dominated by ^{208}Tl with the main features (A) DEP, (B) FEP and (C) SEP.

---

[1]In principle also other pulse shape properties such as the rise time can be compared; however this work focuses on A/E as used in the GERDA analyses.

[2]In some cases a wider spread of the energy deposition may occur if the electron or positron emit a Bremsstrahlung photon which can have a larger range in Ge. The average fraction of Bremsstrahlung energy loss at 1.5 MeV is around 3 % (see Fig. 4.4a). Another event topology creating MSE is caused by a Compton scattering followed by pair production.

A Double escape peak (DEP) at 1592.5 keV: Two annihilation γ-rays escape. Used as reference for SSE in the bulk.

B Full energy peak (FEP) at 2614.5 keV: Likely Compton scattering or pair production at higher energies. This results in MSE topologies and reduced A/E in most cases[3].

C Single escape peak (SEP) at 2103.5 keV: One annihilation γ-ray escapes and the other is detected. This often results in a very defined MSE: An energy deposition of 511.0 keV in one place and 1592.5 keV in another. If the energy depositions occur in sufficiently different locations in the detector such that the charges arrive separately and no Bremsstrahlung occurs, the A value is that of the larger energy deposition and A/E is constant. This can be seen in Fig. 8.1 at 2103.5 keV and A/E=0.76. The A/E value is the ratio of the two energy depositions $\frac{2103.5 \text{ keV} - 511.0 \text{ keV}}{2103.5 \text{ keV}}$.

The maximum range of a ^{42}K 3.5 MeV electron in germanium is 5 mm. The typical depth at which charges are fully collected is about $0.5 - 0.9$ mm for the PHASE II BEGe detectors. Hence, only a small fraction of the pulse shape is influenced by n$^+$ electrode effects which reduce the A/E with respect to ^{208}Tl DEP events in the bulk. This results in a band of events that collectively have a smaller A/E value than bulk events.

A ^{90}Sr calibration source (2.28 MeV beta endpoint of ^{90}Y) is used to investigate the effect of high energetic betas such as from ^{42}K. An A/E versus E spectrum of a ^{90}Sr calibration source is shown in Fig. 8.2. The A/E is calibrated such that the DEP of ^{208}Tl has the value 1. The following features are visible:

(a) A/E scatter plot   (b) A/E slice
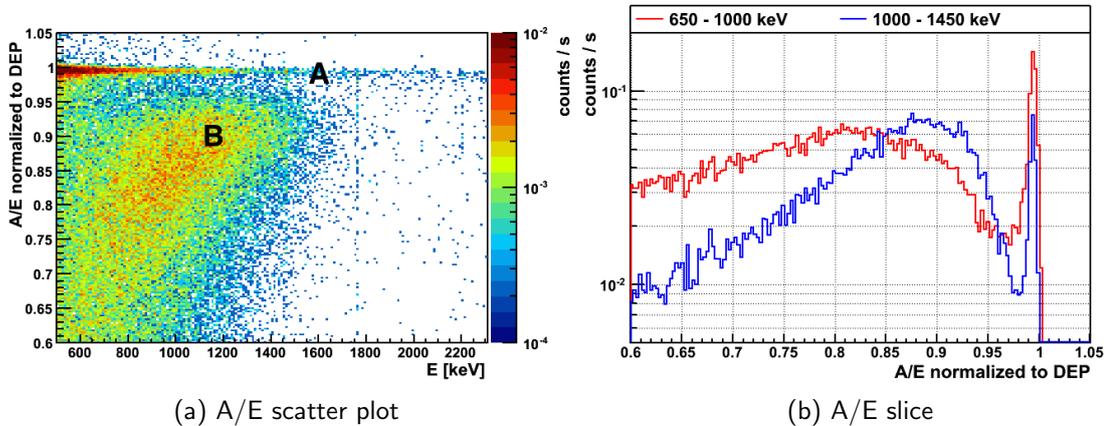
Figure 8.2 ^{90}Sr calibration source measurement. Shown is the A/E versus E scatter plot (left) and A/E slices for given energy regions (right). The spectral section is dominated by ^{90}Y betas with the main features (A) SSB and (B) SPB.

A Single site band (SSB): A band of events with the same A/E values as the DEP. These evens are created by background radiation as e.g. Compton scattered γ-rays from the outside. Another source is Bremsstrahlung induced by ^{90}Y betas in material between source and the active detector volume e.g. source material, cryostat wall, inactive germanium material on the outer side of the n$^+$ electrode.

B Slow pulse band SPB: A band of events with commonly shifted A/E values. This shift is similar for a specific initial beta energy in which a certain fraction of the

---

[3]Note that the A/E can still be equivalent to a SSE if two energy depositions are in locations with degenerated charge trajectories i.e. for same z and r but different ϕ.

energy is deposited in the n^+ electrode. For larger energies this fraction is smaller and the SPB is closer to the SSB. For smaller energies the argument reverses. In the continuous ^{90}Sr spectrum, this can be seen as a widening of the gap between SSB and SPB towards lower energies in Fig. 8.2a and 8.2b. However, the separation of SSB and SPB is always strong.

To avoid the complications with the continuous energy depositions from a beta source, the 59.5 keV γ-ray from ^{241}Am is used for investigations with point-like interactions. 59.5 keV γ-rays interact 10 times more likely via the photoelectric effect than via Compton scattering and have an attenuation length of 1 mm in germanium. The A/E versus E spectrum of an ^{241}Am calibration source is shown in Fig. 8.3. The A/E values are normalized to the 59.5 keV peak. The following features can be seen in the spectrum:

(a) A/E scatter plot
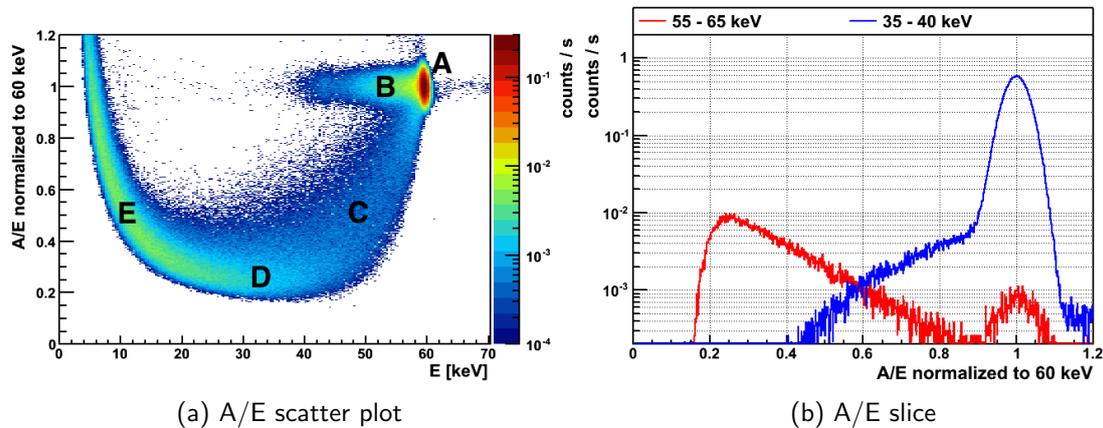
(b) A/E slice

Figure 8.3 ^{241}Am calibration source measurement. Shown is the A/E versus E scatter plot (left) and A/E slices for given energy regions (right). The main features are (A) FEP, (B) ^{241}Am SSE, (C) slow pulse degraded 59.5 keV events, (D) the minimum A/E value and (E) DAQ effects on the A/E reconstructions at low energies.

A **Full energy peak (FEP) at 59.5 keV:** Events interacting in the FAV below the FCCD. The resolution of A/E is significantly worse at low energies and the SSB is much wider.

B **Other events:** Events that are Compton scattered outside the detector. Low energy Compton backscattering results only in a small energy loss of the scattered γ-ray.

C **Energy degraded 59.5 keV events:** Events interacting in the n^+ electrode are measured with a reduced energy. The further above the FCCD, the stronger the energy loss, the slower the pulse and the smaller the A/E. This forms an arc below the peak which is an important feature that has to be reproduced by the model.

D **Minimal observed A/E value due to noise and the trigger threshold.**

E **DAQ effects:** The trigger becomes less effective for slow pulses at low energies. The A/E reconstruction results in large variations due to a stronger influence of the noise on the current pulse maximum. Typically the noise increases A rather than decreasing it such that A/E values > 1 can be reconstructed below 10 keV.

To understand and reproduce these A/E features with MC simulations is the main goal of this chapter. ^{90}Sr is used as a proxy for ^{42}K. However, the initial step of the model construction is performed with ^{241}Am which has a more defined point-like event signature.

8.2   Ad-hoc Empirical Model for n$^+$-Electrode

During the standard characterization in HADES, ^{241}Am measurements were obtained for all PHASE II detectors in the same conditions which were already used to determine the FCCD in Chap. 7. However, no pulse shape information was recorded for these measurements and the investigation is limited to the energy degradation of events ignoring the slow pulse character.

As an ad-hoc assumption, the n$^+$ electrode can be separated into three layers which are illustrated in Fig. 8.4. From the layer close to the surface no charges are collected and it is called dead layer (DL). The layer below the DL is semi-active with incomplete charge collection and is called transition layer (TL). In the volume below the TL all charges are collected and it is called fully active volume (FAV).
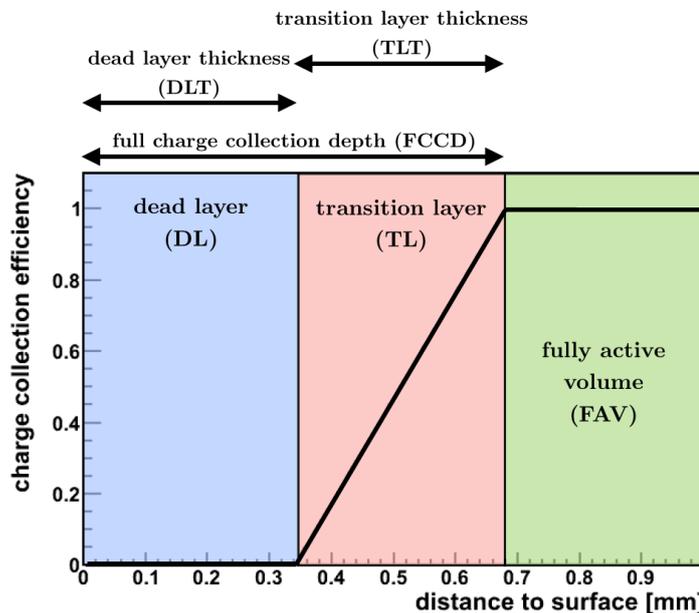
Figure 8.4 Definition of n$^+$ electrode layers on the BEGe surface: Dead layer (DL) shown in blue, transition layer (TL) shown in red and fully active volume (FAV) shown in green.

As another ad-hoc assumption the charge collection efficiency (CCE) profile in the TL is assumed linear starting from 0 at the boundary DL-TL increasing towards 1 at the FCCD (TL-FAV boundary). Different possible linear CCE profiles can be compared as illustrated in Fig. 8.5a. The different models are parameterized with the dead layer fraction (DLF) which is the ratio of the DL thickness and the FCCD. An extreme case is DLF=1 (gray curve) describing the old standard n$^+$ model without TL in which the CCE curve has a discrete step from 0 to 1 at the FCCD. Another extreme case is DLF=0 (orange curve) where there is no DL and the TL reaches up to the detector surface.

A given CCE curve can be folded into MC simulations of ^{241}Am similar to the DLPP approach (Sec. 7.1.2). The energy of a MC hit is weighted with the CCE value at the depth of the interaction and added to the event energy. The hits in the DL do not contribute to the event energy; hits in the TL contribute only partly to the event energy; hits in the FAV contribute fully to the event energy. The simulated ^{241}Am energy spectra for the CCE

models in Fig. 8.5a are shown in Fig. 8.5b. The simulated geometry is that of GD91C in the HADES setup. It can be seen that the region below the 59.5 keV peak is dominated by degraded events even for a large DLF with small TL effect. The DLF parameter and hence the dead layer thickness (DLT) and transition layer thickness (TLT) are encoded in the region below the peak and can be experimentally obtained by comparing MC simulations with data in this region.

(a) CCE Models with different DLF   (b) simulated ^{241}Am spectra for different DLF
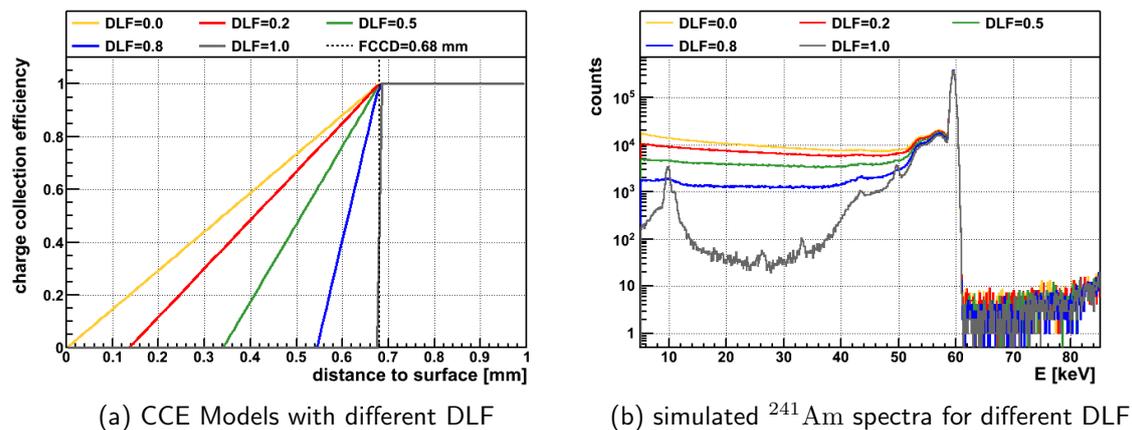
Figure 8.5 Linear charge collection efficiency model with different dead layer fractions (DLF) on the left and correspondingly simulated ^{241}Am energy spectra on the right. The DLF is scanned from 0 to 1 in the model. DLF=1 is equivalent of having no transition region and a discrete step of CCE reduction at the FCCD.

A single ^{241}Am measurement in the HADES setup was taken with pulse shapes for detector GD32D and is shown in Fig. 8.6. From the energy spectrum in Fig. 8.6a it can be clearly seen that the region below the peak cannot be explained with the old DLF=1 model. This is a strong indication for the presence of a TL just from the energy spectrum alone. The A/E versus E scatterplot is shown in Fig. 8.6b. An A/E cut of 0.9 is illustrated in red separating the energy spectrum in Fig. 8.6a into bulk events (green) and slow pulse events (brown). The residual spectrum of the bulk events shows the same features as the simulated DLF=1 model. The slow pulse spectrum is flat and dominant at low energies. These features are already well described by the simple ad-hoc assumption of a linear CCE in the TL.

8.2.1   Data Selection and Observable

The HADES ^{241}Am MCA data is used to determine the DLF for all 30 BEGe detectors. A slow pulse region is defined as $35 - 40$ keV containing energy degraded 59.5 keV γ-ray events. At the energy of $35 - 40$ keV the energy degradation is $59 - 67\%$ testing the linear TL at this value. The counts in the slow pulse region can be compared to the 59.5 keV FEP counts with full charge collection efficiency. The ratio between slow pulse region counts and peak counts is defined as observable and compared to MC simulations in a similar way as for determining the FCCD in Chap. 7. The slow pulse counts are corrected for background which is taken from a region above the peak at $80 - 85$ keV.

The information content of the slow pulse region is illustrated in Fig. 8.7 showing the ^{241}Am calibration spectra for all enriched BEGe detectors. The spectra are normalized to the peak counts in the 59.5 keV peak. With a fixed number of peak counts, a variation of

(a) energy spectra after A/E cuts

(b) A/E versus E
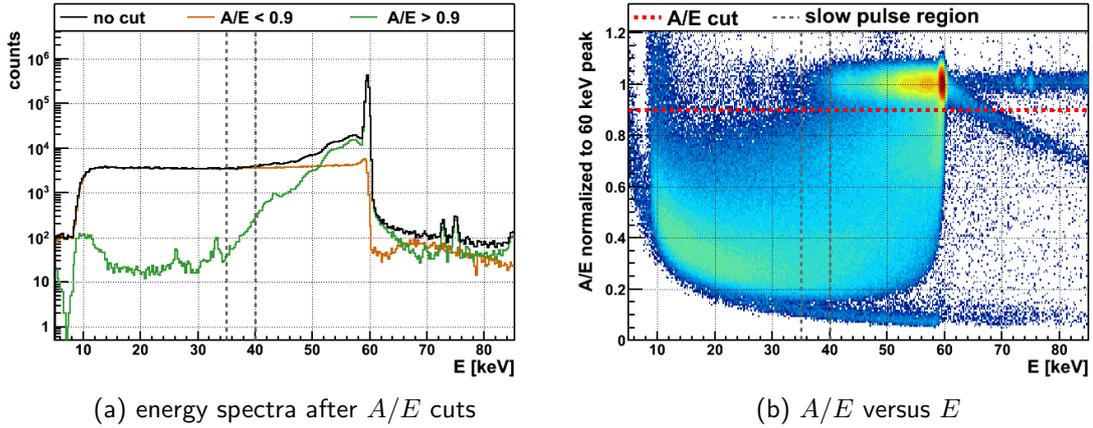
Figure 8.6 Energy spectra for a representative measurement with FADC and GD32D (left). The data is taken with an uncollimated source and pile up can be seen in the spectrum. Shown is the total spectrum (black), the spectrum after A/E cut (green) and the residual spectrum (brown). The corresponding A/E scatter plot along with the A/E cut value is also shown (right). The vertical dashed lines illustrate the slow pulse region.

up to a factor of 3 is visible in the slow pulse region between the detectors. This variation can be interpreted as a difference in DL and TL thickness between the detectors.

Slow pulse selection

The A/E cut in Fig. 8.6a illustrates that the slow pulse region contains roughly a factor 15 more slow pulse events than bulk events. The peak region is populated by two orders of magnitude more bulk events than slow pulse events. Hence, the selected regions contain a rather clean event sample even when limited to comparing the energy spectrum alone. More selection criteria for the slow pulse and background region and various experimental difficulties are presented in Sec. D.1 in the appendix.

8.2.2   Analysis

The observable is constructed with the counts in the slow pulse region C_{SP} and the peak counts $C_{59.5\,\mathrm{keV}}$:

$$O = \frac{C_{\mathrm{SP}}}{C_{59.5\,\mathrm{keV}}}. \tag{8.1}$$

$C_{59.5\,\mathrm{keV}}$ is determined with integrating events in the peak region and correcting for background with side bands as described in Sec. C.2 in the appendix for the counting method. The C_{SP} is taken as the integral in the slow pulse region corrected for non slow-pulse background as described above.

The observable is determined once for the experimental spectrum and for a set of post processed MC simulations. The post processing of the MC sample is done as described in Sec. 7.1.2 but this time for different DLF instead of a different FCCD. The FCCD is fixed to the determined value in Tab. 7.3. The DLF is scanned from 0 to 1 in 100 steps.

The observable is plotted in Fig. 8.8 for the experimental spectrum (green horizontal line) and the MC set (histogram). The MC values are interpolated with a spline function and the best match of the experimental value with one of the MC values is chosen as inferred

(a) wide region   (b) zoom
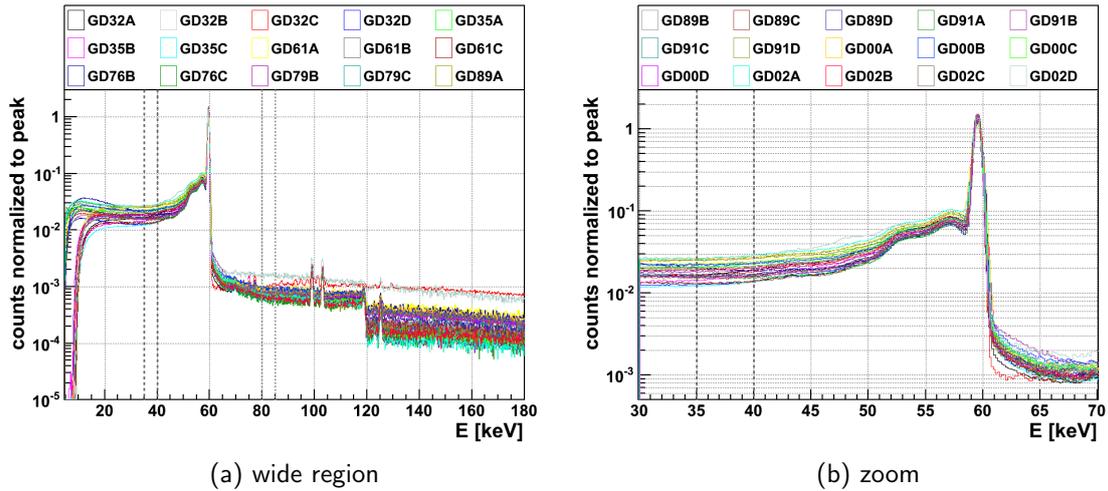
Figure 8.7   Illustration of the ^{241}Am spectra for all investigated BEGe detectors normalized to the 59.5 keV peak counts. The spectra are taken in the same conditions. Variations in the slow pulse region are visible and used for this investigation. Two detectors show differences in the above peak region (left) which is due to a low activity source measurement (GD32C) and a not fully depleted detector (GD02D).

DLF. The largest value for the observable is typically ≈ 0.13 given by the no DL / TL only scenario. The smallest value is almost 0 in the DL only / no TL scenario when no energy degraded events are present and the slow pulse region contains only scattered γ-rays in the MC.
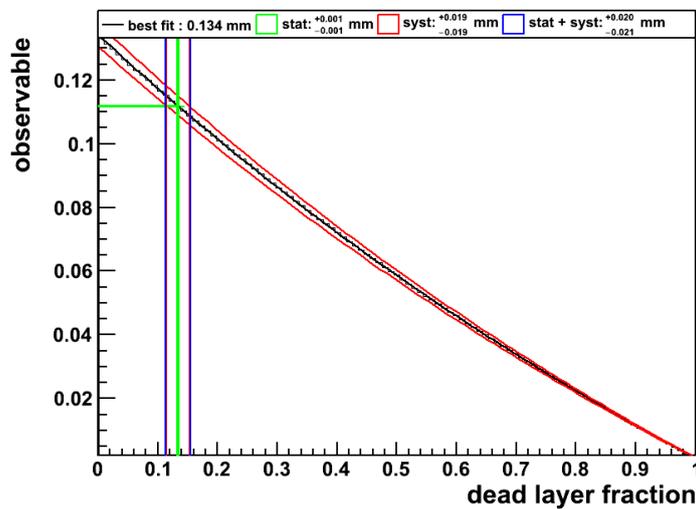
Figure 8.8 Fit of observables to determine DLF. The experimental observable (green horizontal line) is matched to the MC observables (black histogram).

The statistical uncertainty of the observable is propagated with Gaussian errors starting from the counting uncertainties. The first part of the uncertainty of the DLF is obtained as described in Sec. 7.1.3 and illustrated as blue vertical lines in Fig. 8.8. A second contribution originates from the fixed FCCD. To estimate this contribution, the post processing is performed three times, once with the mean value of the FCCD and once with the lower

and upper bounds as reported in Tab. 7.3. Both contributions are added in quadrature for a combined uncertainty on the DLF.

Eventually, the dead layer thickness (DLT) and transition layer thickness (TLT) can be determined with the experimentally inferred dead layer fraction (DLF) and full charge collection depth (FCCD):

$$DLT = FCCD \cdot DLF , \qquad (8.2)$$

$$TLT = FCCD \cdot (1 - DLF) . \qquad (8.3)$$

The results for all 30 BEGe detectors are shown in the next section. Here the analysis is exemplified for GD91C: The FCCD was determined with the ^{241}Am and ^{133}Ba peak ratio method to $0.68^{+0.04}_{-0.04}$ mm considering only the uncorrelated uncertainty. The best fit for the DLF using the peak to slow pulse ratio is $0.13^{+0.05}_{-0.05}$. The uncertainty is the summed quadrature of the statistical uncertainty of the DLF fit ($^{+0.02}_{-0.02}$) and the uncertainty propagated from the FCCD uncertainty ($^{+0.04}_{-0.04}$). The dead layer thickness is $DLT = FCCD \cdot DLF = 0.09^{+0.03}_{-0.03}$ mm. The transition layer thickness is $TLT = FCCD \cdot (1 - DLF) = 0.59^{+0.05}_{-0.05}$ mm.

8.2.3 Results and Interpretation

The results for DLF, DLT and TLT are shown in Tab. 8.1 together with the previously determined FCCD. The fitted values of the DLF are typically between 0 and 0.5 indicating that the dead layer has a smaller fraction than the transition layer. Note however that this conclusion is based on the assumption of a linear CCE curve.

Table 8.1 Results from fitting ad-hoc model to ^{241}Am data. The columns denote the BEGe name, the full charge collection depth (FCCD), the dead layer fraction (DLF), the dead layer thickness (DLT) and the transition layer thickness (TLT). The uncertainties of DLF, DLT and TLT are the combined from the fit and FCCD contribution.

det.	FCCD [mm]	DLF	DLT [mm]	TLT [mm]	det.	FCCD [mm]	DLF	DLT [mm]	TLT [mm]
GD32A	$0.57^{+0.02}_{-0.02}$	$0.17^{+0.03}_{-0.03}$	$0.09^{+0.02}_{-0.02}$	$0.48^{+0.02}_{-0.02}$	GD89B	$0.82^{+0.03}_{-0.02}$	$0.28^{+0.03}_{-0.02}$	$0.23^{+0.02}_{-0.02}$	$0.59^{+0.03}_{-0.02}$
GD32B	$0.80^{+0.02}_{-0.02}$	$0.21^{+0.03}_{-0.02}$	$0.17^{+0.02}_{-0.02}$	$0.63^{+0.03}_{-0.02}$	GD89C	$0.69^{+0.04}_{-0.03}$	$0.33^{+0.04}_{-0.03}$	$0.23^{+0.03}_{-0.02}$	$0.46^{+0.04}_{-0.03}$
GD32C	$0.70^{+0.02}_{-0.03}$	$0.28^{+0.02}_{-0.03}$	$0.19^{+0.02}_{-0.02}$	$0.51^{+0.02}_{-0.03}$	GD89D	$0.75^{+0.03}_{-0.03}$	$0.36^{+0.03}_{-0.03}$	$0.27^{+0.02}_{-0.02}$	$0.48^{+0.03}_{-0.03}$
GD32D	$0.52^{+0.03}_{-0.03}$	$0.31^{+0.04}_{-0.04}$	$0.16^{+0.02}_{-0.02}$	$0.36^{+0.03}_{-0.03}$	GD91A	$0.69^{+0.03}_{-0.04}$	$0.14^{+0.03}_{-0.04}$	$0.10^{+0.02}_{-0.03}$	$0.59^{+0.03}_{-0.04}$
GD35A	$0.61^{+0.02}_{-0.01}$	$0.13^{+0.03}_{-0.02}$	$0.08^{+0.02}_{-0.01}$	$0.53^{+0.03}_{-0.02}$	GD91B	$0.68^{+0.03}_{-0.03}$	$0.19^{+0.03}_{-0.03}$	$0.13^{+0.02}_{-0.02}$	$0.55^{+0.03}_{-0.03}$
GD35B	$0.55^{+0.06}_{-0.06}$	$0.16^{+0.09}_{-0.07}$	$0.09^{+0.05}_{-0.04}$	$0.46^{+0.07}_{-0.06}$	GD91C	$0.68^{+0.04}_{-0.05}$	$0.13^{+0.05}_{-0.05}$	$0.09^{+0.03}_{-0.03}$	$0.59^{+0.05}_{-0.05}$
GD35C	$0.55^{+0.01}_{-0.02}$	$0.34^{+0.02}_{-0.02}$	$0.19^{+0.01}_{-0.02}$	$0.36^{+0.01}_{-0.02}$	GD91D	$0.68^{+0.04}_{-0.04}$	$0.36^{+0.04}_{-0.03}$	$0.24^{+0.03}_{-0.03}$	$0.44^{+0.04}_{-0.03}$
GD61A	$0.72^{+0.04}_{-0.05}$	$0.15^{+0.04}_{-0.05}$	$0.11^{+0.03}_{-0.03}$	$0.61^{+0.04}_{-0.05}$	GD00A	$0.63^{+0.04}_{-0.04}$	$0.13^{+0.05}_{-0.04}$	$0.08^{+0.03}_{-0.02}$	$0.55^{+0.05}_{-0.03}$
GD61B	$0.72^{+0.03}_{-0.04}$	$0.37^{+0.03}_{-0.03}$	$0.27^{+0.02}_{-0.03}$	$0.45^{+0.03}_{-0.03}$	GD00B	$0.76^{+0.03}_{-0.04}$	$0.20^{+0.03}_{-0.04}$	$0.16^{+0.03}_{-0.03}$	$0.60^{+0.03}_{-0.04}$
GD61C	$0.68^{+0.04}_{-0.04}$	$0.44^{+0.03}_{-0.03}$	$0.30^{+0.03}_{-0.03}$	$0.38^{+0.03}_{-0.03}$	GD00C	$0.70^{+0.02}_{-0.02}$	$0.17^{+0.03}_{-0.03}$	$0.12^{+0.02}_{-0.02}$	$0.58^{+0.03}_{-0.03}$
GD76B	$0.86^{+0.03}_{-0.04}$	$0.32^{+0.03}_{-0.03}$	$0.28^{+0.03}_{-0.03}$	$0.58^{+0.03}_{-0.04}$	GD00D	$0.73^{+0.02}_{-0.02}$	$0.37^{+0.02}_{-0.02}$	$0.27^{+0.02}_{-0.02}$	$0.46^{+0.02}_{-0.02}$
GD76C	$0.85^{+0.03}_{-0.03}$	$0.45^{+0.02}_{-0.02}$	$0.39^{+0.02}_{-0.02}$	$0.46^{+0.02}_{-0.02}$	GD02A	$0.62^{+0.04}_{-0.03}$	$0.02^{+0.03}_{-0.04}$	$0.01^{+0.02}_{-0.02}$	$0.61^{+0.04}_{-0.04}$
GD79B	$0.73^{+0.03}_{-0.03}$	$0.25^{+0.03}_{-0.03}$	$0.18^{+0.02}_{-0.02}$	$0.55^{+0.03}_{-0.03}$	GD02B	$0.70^{+0.04}_{-0.04}$	$0.24^{+0.04}_{-0.04}$	$0.17^{+0.03}_{-0.03}$	$0.53^{+0.04}_{-0.04}$
GD79C	$0.85^{+0.03}_{-0.03}$	$0.45^{+0.02}_{-0.02}$	$0.38^{+0.02}_{-0.02}$	$0.47^{+0.02}_{-0.02}$	GD02C	$0.75^{+0.04}_{-0.04}$	$0.49^{+0.03}_{-0.03}$	$0.37^{+0.03}_{-0.03}$	$0.38^{+0.03}_{-0.03}$
GD89A	$0.67^{+0.03}_{-0.04}$	$0.19^{+0.03}_{-0.04}$	$0.12^{+0.02}_{-0.03}$	$0.55^{+0.03}_{-0.04}$	GD02D	$1.17^{+0.06}_{-0.06}$	$0.54^{+0.01}_{-0.00}$	$0.63^{+0.03}_{-0.03}$	$0.54^{+0.03}_{-0.03}$

Correlation plots between the n$^+$ layer properties are shown in Fig. 8.9 for DLF versus FCCD and DLT versus FCCD in Fig. 8.10 for TLT versus FCCD and DLT versus TLT for all 30 detectors. The color code distinguishes the position of the crystal slice in the ingot from seed to tail as AA, BB, CC and DD (see an illustration of the slice positions in

(a) DLF versus FCCD   (b) DLT versus FCCD
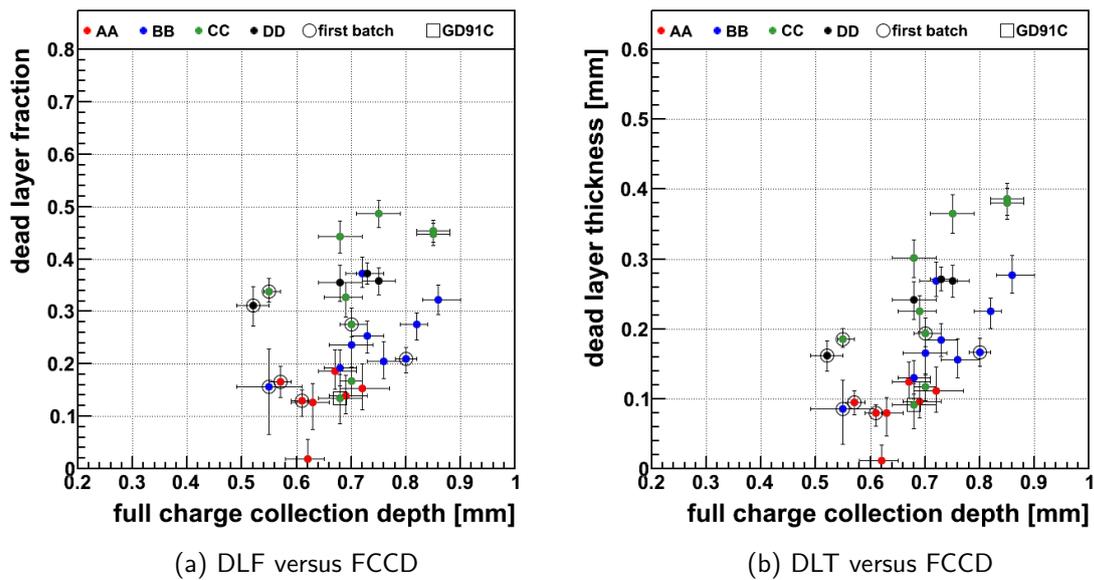
Figure 8.9 (I of II) Correlation of n$^+$ electrode layers as defined in the text. Note that only FCCD and DLF are independently obtained. DLT and TLT are intrinsically correlated between FCCD and DLF.

Fig. 6.1). The circles denote detectors from the first batch. The box indicates the reference detector GD91C.

In the plot showing DLF versus FCCD, a weak correlation between FCCD and DLF is visible. A larger FCCD seems to result in a larger fraction of the DL and hence a smaller fraction of the TL. The same effect is visible comparing the DLT versus FCCD and TLT versus FCCD plots: The TL thickness seems to be less dependent on the FCCD than the DL thickness. Hence, an increase in FCCD seems to increase the non-active volume more than the semi-active volume.

Another unexpected correlation can be seen comparing different crystal slice positions in the DLF versus FCCD plot: AA and BB detectors seem to show a significantly reduced DL fraction compared to CC and DD detectors. This effect can also be observed in the other correlations. In general the TL seems to have a larger absolute and relative size in AA and BB slices.

The production of the diodes from crystal slices was not ordered according to the slice position but selected randomly. Hence, only the intrinsic crystal properties such as e.g. crystal defects can create such an effect[4]. It should be noted that all AA slices have a conical geometry which potentially introduces an unknown bias in the analysis of FCCD or DLF; however, there is no such geometrical difference between BB and CC/DD slices which show nevertheless a different behavior. Finally it should be stressed that the quoted quantitative results are only valid in the assumption of a linear CCE profile. However, the qualitative difference in slice populations visible in the correlation plots show a strong indication for a dependence of the n$^+$ electrode properties on the crystal slice position.

The conclusions of this n$^+$ electrode study with an empirical model for GERDA PHASE II detectors are summarized below:

---

[4]A comparison with the measured electrical impurity concentration shows no correlation.

(a) TLT versus FCCD

(b) DLT versus TLT
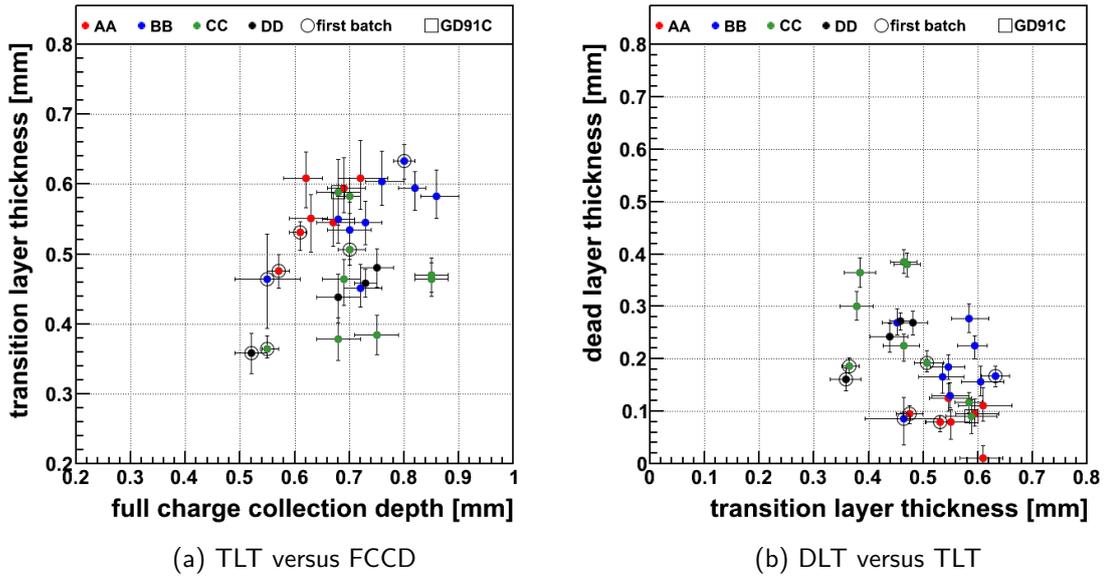
Figure 8.10 (II of II) Correlation of n^+ electrode layers as defined in the text. Note that only FCCD and DLF are independently obtained. DLT and TLT are intrinsically correlated between FCCD and DLF.

- The n^+ electrode has a larger semi-active region than dead region. In other words, the TL is larger than the DL.

- An increase in the general n^+ electrode thickness (or FCCD) contributes more to increasing the size of the DL than to increasing the size of the TL.

- The n^+ electrode properties are qualitatively and quantitatively different for AA, BB, CC and DD slice positions in the ingots: AA and BB slices show an absolute and relative larger TL than CC and DD slices.

8.3 First Principle Model of the n⁺-Electrode

In order to fully understand the slow pulses character and A/E features of events at the n^+ electrode, a more complex model is needed than the ad-hoc model in the previous section. The idea is to start from first principles and to construct the p-n junction, the depletion boundary and the recombination zone from the lithium impurity profile. In a next step the charges are propagated in the previously defined n^+ electrode layers by diffusion. The concept of this model is based on an idea by David Radford and also presented in chapter 6 in Ref. [148]. Here, the model is applied for GERDA PHASE II BEGe detectors.

8.3.1 Modeling the n⁺ Lithium Concentration

The n^+ electrode is produced with the diffusion of lithium into the detector surface. This is typically done in a furnace with one or multiple annealing cycles. The result is a lithium concentration profile being largest on the surface and decreasing towards the bulk. The lithium profile can be modeled assuming a simple diffusion equation:

$$\frac{\delta C(x,t)}{\delta t} = D \cdot \frac{\delta^2 C(x,t)}{\delta x^2}.$$

(8.4)

$C(x,t)$ is the concentration at depth x and time t. D is the diffusion coefficient. The analytic solution to this equation assuming a constant surface concentration $C(0,t) = C_s = \text{const}$ is given by a complementary error function

$$C(x,t) = C_s \cdot \text{erfc}\left(\frac{x}{2 \cdot \sqrt{D \cdot t}}\right) \tag{8.5}$$

with the diffusion length $2 \cdot \sqrt{D \cdot t}$. The constant surface concentration during the annealing process is the first of many assumptions made in this model. The diffusion coefficient was experimentally determined in Ref. [149]. The authors find the temperature dependence of D as

$$D = 9.1 \cdot 10^{-3} \cdot e^{\frac{-13100}{R \cdot T}} \tag{8.6}$$

in units of $\text{cm}^2 \cdot \text{s}^{-1}$ with the temperature T in Kelvin and $R = 1.98 \, \text{cal/K}$. The diffusion process in Ref. [148] for the Majorana MALBEK detector was assumed to be 5 min long in a furnace with 573 K and a constant flushing of a lithium gas mixture. In this case the surface lithium concentration is assumed constant at $4 \cdot 10^{16} \, \text{cm}^{-3}$ which is the saturation concentration of lithium in germanium at this temperature. For the GERDA BEGe detectors, the lithium is imposed onto the surface with an electrolytic process in a lithium solution. The annealing is then performed in a furnace at a temperature of 473 K. The annealing time is 2 h for the first batch of 7 detectors and 4 h for the second batch [146]. In this case the initial lithium concentration from the bath in the lithium solution is not well defined and large variations are possible for different detectors.

Typical surface impurity concentrations after annealing are $\mathcal{O}(10^{15} \, \text{cm}^{-3})$. In Ref. [150] the solubility of lithium in germanium was found as $2 \cdot 10^{15} \, \text{cm}^{-3}$ at $250 \, ^\circ\text{C}$ which is 50 K larger than the annealing temperature. In an older publication [151] the lithium solubility is quoted for temperatures as low as room temperature and a concentration of $3 \cdot 10^{15} \, \text{cm}^{-3}$ at $200 \, ^\circ\text{C}$ is stated. This value is not in agreement with Ref. [150] because it is larger for a lower temperature. Nevertheless, for solving the diffusion equation, the lithium surface concentration C_S during the annealing is taken from the older publication as $3 \cdot 10^{15} \, \text{cm}^{-3}$ to be later consistent with the solubility at a wider temperature range. For 473 K, D is equal to $7.66 \cdot 10^{-9} \, \text{cm}^2 \cdot \text{s}^{-1}$.
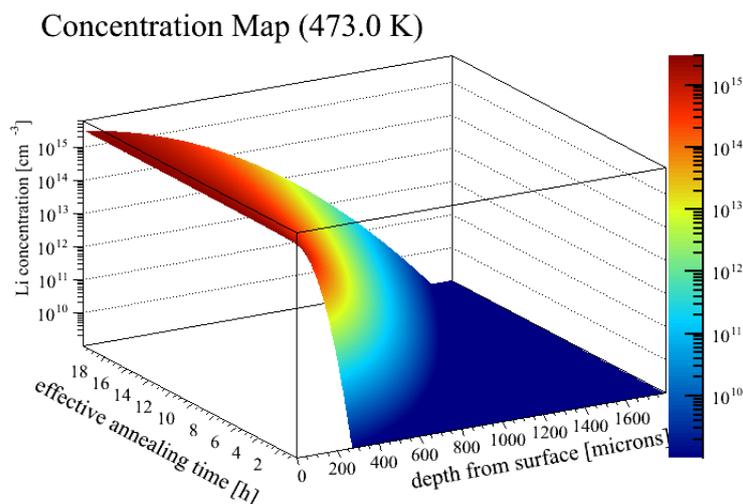
Figure 8.11 Lithium concentration profile for various effective annealing times at 473 K.

The solution of Eq. 8.5 for different annealing times is illustrated in Fig. 8.11. The variation of the annealing time is chosen to sample different possible lithium profiles for a given detector. In fact the annealing time is known much better than the initial surface concentration or the uncertainty of Eq. 8.6. All these uncertainties and assumptions are expressed in an effective annealing time which is more intuitively comparable to the real annealing time; however, effective and real annealing time may differ.

8.3.2 Modeling the n$^+$ Properties of a Specific Detector

For a given detector the effective annealing time and the corresponding specific lithium concentration profile is selected from the set of profiles (Fig. 8.11). The choice is based on the FCCD which can be reliably measured after detector production (Chap. 7). The determination of the n$^+$ electrode properties is done in three steps.

In a first step the depth of the p-n junction is determined where the lithium concentration (donors) is equal to the bulk impurity concentration (acceptors). The bulk impurity concentration is measured and unique for each detector between $0.5 - 3.0 \cdot 10^{10}\,\mathrm{cm}^{-3}$ for the Gerda Phase II detectors. In Fig. 8.12a the set of lithium concentrations together with the p-n junction depth for GD91C is illustrated as the dotted line.

(a) set of Li concentration profiles   (b) selected Li profile matching measured FCCD
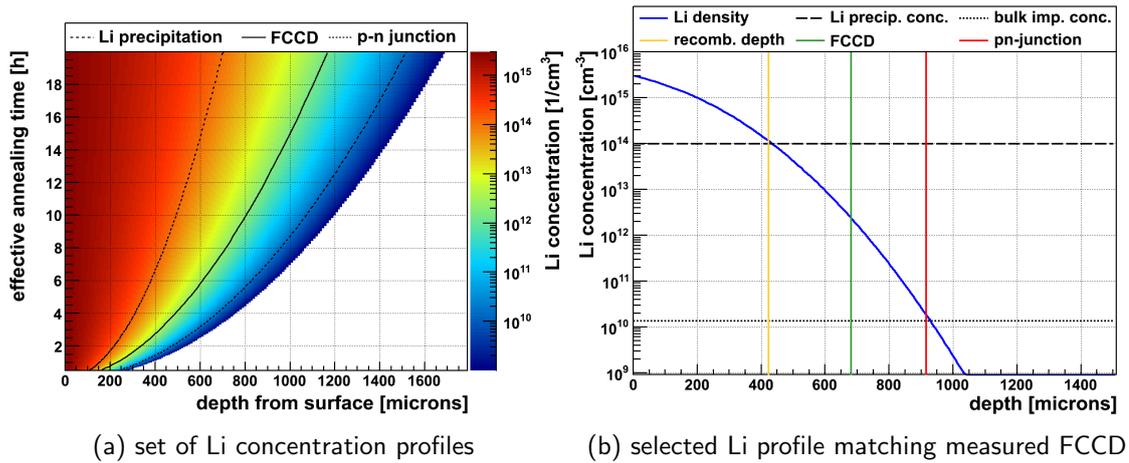
Figure 8.12 Lithium concentration profile for BEGe GD91C. Left: The p-n junction, the FCCD and the recombination depth is calculated for each effective annealing time. Right: The lithium concentration profile at the measured FCCD is selected at an effective annealing time of $7.3 \pm 0.8\,\mathrm{h}$. The FCCD depth is at 680 ± 40 micron, the p-n junction at 914 ± 38 micron and the depth of the recombination dominate region (RDR) at 420 ± 18 micron.

In a second step the FCCD is determined for all lithium profiles in the set. When the detector is biased with HV, the depletion starts at the p-n junction and proceeds into the p-type region and n-type region simultaneously such that equal amount of charges are on either side of the junction. Above the depletion voltage the full p-type region i.e. the bulk of the detector is depleted[5]. With a bulk concentration of e.g. $2 \cdot 10^{10}\,\mathrm{cm}^{-3}$ and an active volume of e.g. $100\,\mathrm{cm}^3$ this amounts to $2 \cdot 10^{12}$ charges. On the n-type side the depletion zone penetrates only a few $0.1\,\mathrm{mm}$ because of the exponentially increasing lithium concentration towards the surface. This creates a thin shell of depletion region above the p-n

---

[5]The depletion reaches until the p$^+$ electrode and is stopped there by the blocking contact of a larger implanted p-type concentration

junction. The electric field is present inside the depletion zone and separated charges can be collected; outside the depletion zone there is no electric field and charges only diffuse. The boundary of the depletion zone is also the end of the FAV of the detector and defined as the full charge collection depth. The FCCD versus effective annealing time is illustrated for GD91C in Fig. 8.12a as the solid line. Note that for other detectors with different volume size and impurity concentration the plot is different.

In a third step the recombination zone is determined. The solubility of lithium in germanium is around $3 \cdot 10^{15}\,\mathrm{cm}^{-3}$ at $200\,^\circ\mathrm{C}$ [151]. After cooling down to ambient temperature the solubility decreases significantly to around $1 \cdot 10^{14}\,\mathrm{cm}^{-3}$ [151]. This results in a supersaturated state in a certain surface layer of the germanium crystal. This situation is unstable and lithium starts to precipitate at point defects in the lattice. The surrounding lithium in this region diffuses towards these precipitation centers until the lithium concentration is below supersaturation. The lithium in the precipitation centers is electrically inactive and does not serve as donors. As a hypothesis in [148] it is assumed that the precipitation centers in the previously supersaturated region serve as recombination centers for separated charges. Therefore the region is referred to as recombination dominated region (RDR) defined between the surface and the depth where the calculated lithium concentration reaches supersaturation at room temperature[6] i.e. $1 \cdot 10^{14}\,\mathrm{cm}^{-3}$. Charges drifting into this region will be lost according to a certain probability model which is investigated later. The recombination boundary is illustrated in Fig. 8.12a as the dashed line.

Fig. 8.12b summarizes the n^+ electrode modeling of GD91C. The lithium profile is chosen to match the measured FCCD value of 680 ± 40 micron (Tab. 7.3) with considering only the uncorrelated uncertainty. This selects an effective annealing time of $7.3 \pm 0.8\,\mathrm{h}$. Note that the actual annealing time was around $4\,\mathrm{h}$ for this detector. The p-n junction is calculated to be at 914 ± 38 micron and the recombination depth at 420 ± 18 micron. The uncertainties are derived from the uncorrelated uncertainties of the FCCD performing the full calculation again with the upper and lower FCCD bound as new input parameter.

So far many assumptions are made and are summarized below:

1. Lithium surface concentration of $3 \cdot 10^{15}\,\mathrm{cm}^{-3}$ during annealing

2. Constant lithium surface concentration during annealing

3. Charge recombination on precipitation centers in the region with lithium concentration $> 1 \cdot 10^{14}\,\mathrm{cm}^{-3}$

4. Solubility static and similar between cryogenic temperature and room temperature

Under these assumption the effective annealing time is calculated for each of the 29 working BEGe detectors and shown Fig. 8.13. In blue the detectors of the first batch are shown with real annealing times of $2\,\mathrm{h}$. In red the detectors of the second batch are shown with real annealing times of $4\,\mathrm{h}$. The effective annealing time is roughly a factor two to three larger than the real annealing time in all cases. This suggest a problem in the assumption which is most likely due to the surface concentration. Note that the uncertainties for the input parameters, especially the surface concentration, are likely much larger than a factor of two or three. However, in general the first batch (with the exception of GD32B) shows a

---

[6]A potential difference in solubility between room temperature and cryogenic temperature or the time dependence of the process is ignored by this assumption.

smaller effective annealing time than the second batch which is connected with the smaller FCCD of the first batch. Hence, qualitatively the production of the n$^+$ electrode can be reproduced.
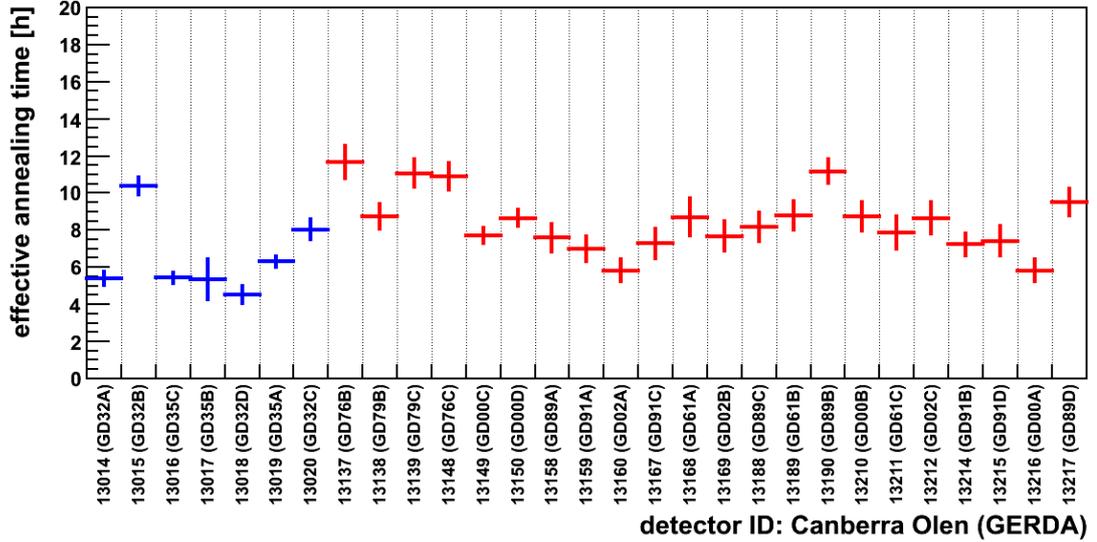
Figure 8.13 Effective annealing time for all GERDA PHASE II detectors ordered according to production sequence.

The detectors in the plot are shown according to the sequence of their production which is encoded in the Canberra Olen ID as a running number by the manufacturer (see Tab. B.2 in the appendix). The production of the second batch was done in typical sets of three to four detectors at a time. This can be seen in connected numbers as e.g. $13137 - 13139$ and $13148 - 13150$. Strong variations can be seen when comparing the effective annealing time over the evolution of the production. The values seems to be similar within the same set. This behavior suggests a dependence on the production process which is not included in the model, e.g. small changes in procedure, small changes in the electrolytic material, different time frames between production or characterization. However, note that these observations should be treated as conjectures only.

Finally, the main motivation for constructing the lithium profile was to determine the RDR from a first principle approach. The position of the p-n junction is not important for the simulation of charges and the FCCD was measured after the production of the n$^+$ electrode.

8.4   Charge Propagation via Diffusion

The electric field outside the depleted region, i.e. above the FCCD, is zero and the dominant charge transport is diffusion. A charge cloud created above the FCCD diffuses in all directions. If a part of the charge cloud is entering the FAV i.e. passing below the FCCD, it is collected.

The charge transport can be modeled with diffusion using equation Eq. 8.4. Initially, the approximation of a one-dimensional model is used. Later this is compared to a 3-D model. In the 1-D case the starting condition is a delta charge at a certain depth x_c from the

surface. This requires a numerical solution which can be done with the explicit Euler scheme described by the following algorithm:

$$C_{i+1,x} = C_{i,x+1} \cdot f + C_{i,x-1} \cdot f - C_{i,x} \cdot (1 - 2f) \tag{8.7}$$

$$f = D \cdot \frac{\Delta t}{\Delta x^2} \tag{8.8}$$

Here, i and x are the temporal and spatial bins respectively. The depth is sampled from 0 to the FCCD in bins of 10 micron. The time is sampled from 0 to 10000 ns in steps of 1 ns. D is the diffusion constant given by

$$D = \frac{\mu \cdot kT}{q}, \tag{8.9}$$

with the Boltzmann constant k, the temperature T and the elementary charge q. The mobility μ is taken as the hole mobility in germanium at 77 K as $4.2 \, \text{m}^2/(\text{V·s})$ [91]. Note that the holes give the dominant contribution to the signal and the electron contribution is negligible for n^+ electrode events. To achieve convergence of Eq. 8.7 the Neumann condition $f < 1/2$ must be fulfilled. This determines the binning of 10 micron and 1 ns in which $D = 28.9 \, \text{micron}^2/\text{ns}$ and $f = 0.29$.

Now a charge distribution is simulated according to the recipe above. Charges that drift through the FCCD into the FAV are collected and recorded in the simulation. Their time dependent arrival in the FAV creates a charge pulse. Charges that drift inside the RDR recombine with a certain probability and are killed in the simulation. The recombination of charges is investigated later; for now, the recombination rate is set to the constant probability of 0.002 per time bin within the RDR which will be determined as the rate which best matches the data.

(a) charge pulse   (b) current pulse
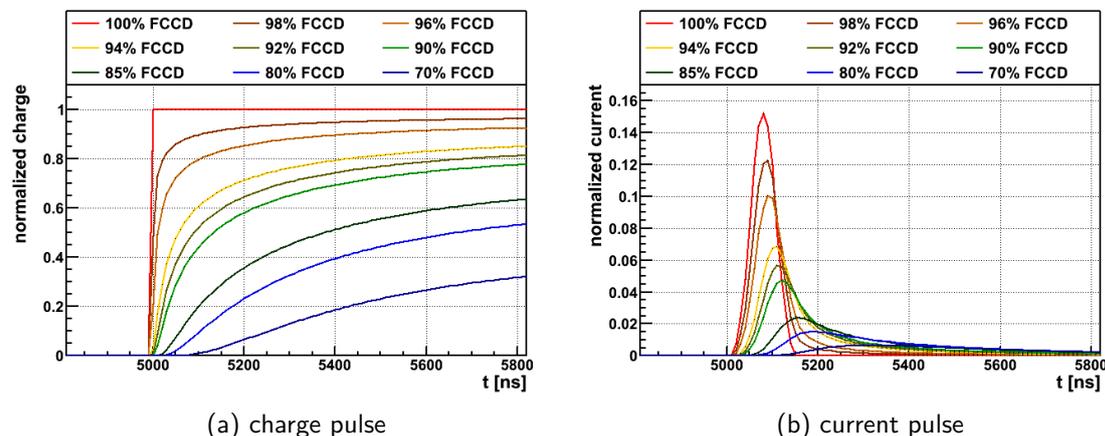
Figure 8.14 Left: Charge pulses for different interaction depth in percentage of FCCD for GD91C. Pulses from FAV interactions (100 % FCCD) are started as step-like. Right: Corresponding current pulses after differentiation and shaping with 3x 50 ns MWA.

A point-like[7] charge cloud is simulated starting at a certain distance below the surface. This is representative of e.g. an ^{241}Am 59.5 keV γ-ray interaction with the photoelectric effect at a certain depth inside a BEGe. Fig. 8.14a shows charge pulse shapes at different interaction depths in GD91C expressed in percentage of the FCCD of 680 micron. The time

---

[7]All charges start within one spatial bin of 10 micron.

binning is decreased from 1 ns in the simulation to match the 10 ns sampling of the GERDA FADC. The current pulses are created with a differentiation and shaped with a 3-fold 50 ns MWA as in the standard GERDA DAQ chain (see Sec. 4.2.3). They are shown in Fig. 8.14b.

Interactions in the FAV (at 100 % FCCD) are not described by the diffusion model. They are taken as a step-like charge pulse and processed as all other pulses to obtain a natural transition between simulated n^+ electrode events and bulk events. The solution in Eq. 8.7 does not converge for initial point-like charge clouds located 1 spatial bin above the FCCD. For this case, a linearly interpolated pulse is created with the step-like FAV pulse and the last simulated pulse 2 spatial bins above the FCCD.

Simulations are performed for point-like charge clouds at all possible distances below the surface. In case of GD91C with 680 micron FCCD these are 66 simulations, the calculation of the FAV pulse and the interpolation of the pulse from just above the FCCD. The energy E is taken as the integral of the current pulse. The A is taken as the amplitude of the current pulse. Fig. 8.15 shows the charge collection efficiency (CCE), the current pulse amplitude A and the A/E for point-like interactions at a certain depth. A and A/E in the logarithmic representation in Fig. 8.15a are natural as resulting from the shaping; an energy deposition of 1 results in a current pulse height of roughly 0.15. In the linear representation in Fig. 8.15b the A and A/E are normalized to 1 for the step-like FAV pulse for better visualization in the linear scale. The CCE and thus the energy measurement is reduced for interactions further above the FCCD. The reduction of CCE is roughly linear until a depth which corresponds to the RDR. The A/E is reduced much faster above the FCCD resulting in a different pulse shape compared to bulk events for practically all interactions in the n^+ electrode. The A/E approaches a constant value above a certain depth.

(a) logarithmic scale   (b) linear scale
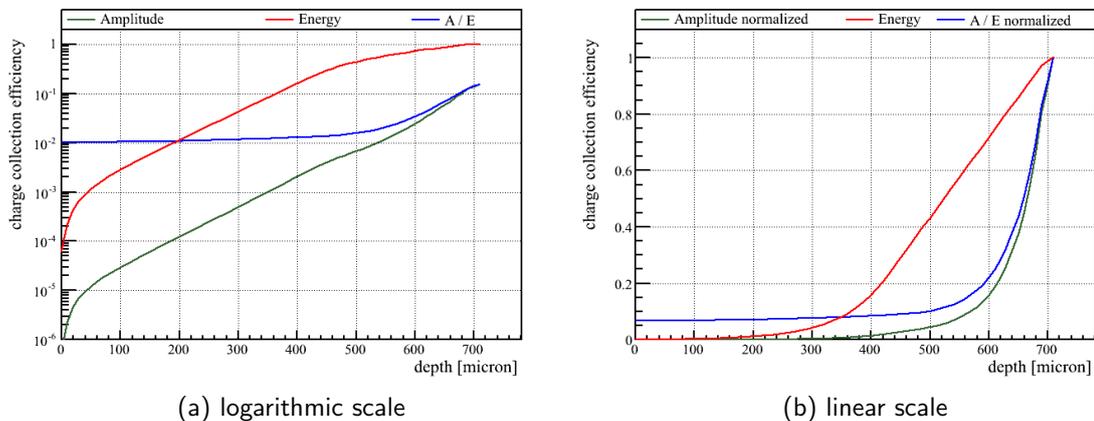
Figure 8.15 Charge collection efficiency for the energy, the amplitude and the A/E. Left: Natural values for A and A/E as resulting from the signal shaping. Right: Normalized A and A/E values to bulk pulse values. The energy is normalized in both cases.

Constructing the n^+ electrode model for all detectors shows that the linear dependence for the CCE is true for a larger range of FCCD values and hence an accidental feature of the n^+ electrode. It is also worth noting that the only information taken from the lithium profile is the RDR depth. Potential uncertainties in the initial lithium profile will only have effect on this quantity. The ad-hoc recombination model of 0.002 per time bin in the RDR is not motivated from first principles and investigated further in the following.

8.4.1 Recombination Models

The model of charge recombination in the RDR has a strong impact on interactions inside and close to the RDR, i.e. at shallow depth. Fig. 8.16a shows the CCE curves of various recombination rates starting from immediate full recombination in the RDR (red curve) to no recombination (blue curve):

(a) CCE   (b) CCE and A/E
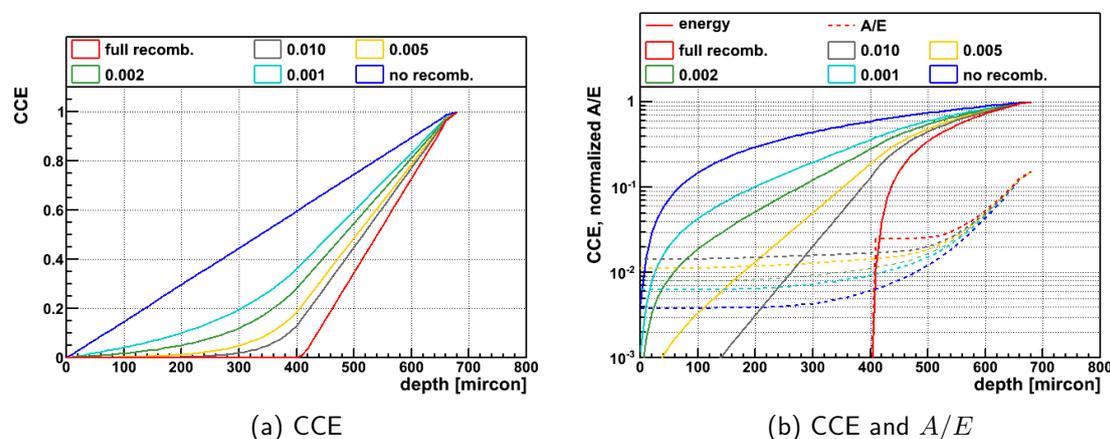
Figure 8.16 Charge collection efficiency curve for different charge recombination models in the RDR. The recombination rate is shown in the legend as probability of recombination per ns. Left: The CCE curves are shown in linear scale. Right: The same CCE curves are shown in logarithmic scale. Additionally also the A/E curves are shown.

The following list describes the models that are shown in Fig. 8.16:

1. Charges recombine instantly inside RDR (Scenario equivalent to ad-hoc model in Sec. 8.2 with empirically inferred RDR)

2. Charges recombine with a constant probability of 0.010 per ns in RDR

3. Charges recombine with a constant probability of 0.005 per ns in RDR

4. Charges recombine with a constant probability of 0.002 per ns in RDR (later determined as best choice)

5. Charges recombine with a constant probability of 0.001 per ns in RDR

6. Charges do not recombine in RDR. Charges are killed on the detector surface (Scenario equivalent to ad-hoc model in Sec. 8.2 without DL)

The CCE curve with instant recombination is practically linear decreasing from the FCCD to the precipitation boundary where the RDR starts. Charge collection is only possible in the drift dominated region (DDR) below the RDR. This model is the almost exact description of the ad-hoc model in Sec. 8.2. In this case the DDR is equivalent to the TL and the RDR is equivalent to the DL. The other extreme, assuming no recombination rate, is also equivalent to the ad-hoc model in the case of DLF = 0. The recombination models with finite recombination probability are smoothening the transition between RDR and DDR. For these models the TL and DDR are not equivalent. However, also these models show an almost linear decrease of energy from the FCCD towards the surface over a large depth[8].

---

[8]On first glance it may appear counter-intuitive that the CCE curve linearly increases from 0 to 1. One may expect that half of the charges are lost instantly if initially diffusing into the "wrong" direction e.g.

This investigation shows that the slope of the linear CCE changes significantly with the recombination model. Hence, the model of recombination in the outer detector layers has a significant influence on the charge collection in deeper layers just above the FCCD.

The A/E curve dependence on the recombination model is additionally shown in Fig. 8.16b. The strong decrease of A/E just above the FCCD is not strongly affected by the model. However, as noted before, the A/E value is approaching a constant value for shallower interaction depth. The constant A/E value now depends on the recombination model[9].

In conclusion, it was found that the recombination rate in the RDR affects the whole CCE curve. To the knowledge of the author, the recombination rate is unconstrained from first principles and is used as a free parameter in the following. For this investigation the recombination rate is assumed constant inside the full RDR for simplicity. It is however more likely that the recombination rate is increasing towards the surface due to more precipitation centers created by a larger supersaturated lithium concentration. Such an effect would depend on the creation of precipitation centers[10] and potentially subject to strong local variations throughout the surface.

8.4.2 1-D versus 3-D Diffusion

The diffusion of charges in the n^+ electrode is a 3-dimensional process which so far was approximated by 1-dimensional diffusion perpendicular to the surface. Now the influence of the dimensions parallel to the surface is investigated. The numerical solution of a 3-D diffusion with explicit Euler scheme is described below:

$$C_{i+1,x,y,z} = C_{i,x+1}f + C_{i,x-1}f - C_{i,x} \cdot (1-2f) \tag{8.10}$$
$$C_{i,y+1}f + C_{i,y-1}f - C_{i,y} \cdot (1-2f) \tag{8.11}$$
$$C_{i,z+1}f + C_{i,z-1}f - C_{i,z} \cdot (1-2f) \tag{8.12}$$
$$f = D \cdot \Delta t \cdot \left(\frac{1}{\Delta x^2} + \frac{1}{\Delta y^2} + \frac{1}{\Delta z^2} \right) \tag{8.13}$$

The spatial coordinates are described by x for the depth dimension perpendicular to the surface as in the 1-D case and by y and z for the dimensions parallel to the surface. The spatial binning is kept at 10 micron for each dimension. To fulfill the Neumann condition for the stability of the solution in the 3-D case, the time binning is reduced to 0.5 ns resulting in $f = 0.43$.

The solution is calculated with 4 loops over the temporal and three spatial dimensions. The temporal dimension is traversed from 0 to 10000 ns. The x dimension is traversed from 0 micron to the FCCD and the y and z dimensions are traversed from -750 to +750 micron.

The comparison of the CCE curves derived with the 1-D diffusion and the 3-D diffusion is shown in Fig. 8.17. The 1-D diffusion is shown in black whereas the 3-D diffusion is shown for three different sizes of the parallel dimensions (500 micron, 1000 micron and

---

closely above the FCCD. However, the diffusion simulation can be interpreted as a random-walk in which charges can change "direction" in any of the 10.000 1 ns time bins. This results in a smooth transition at boundaries.

[9]This behavior may be used as an additional handle to constrain the model parameters when comparing simulations with data. However, a very good understanding of the trigger and reconstruction chain will be necessary for pulses with small A and A/E.

[10]Many small accumulations versus fewer large accumulations.

(a) CCE   (b) CCE and A/E
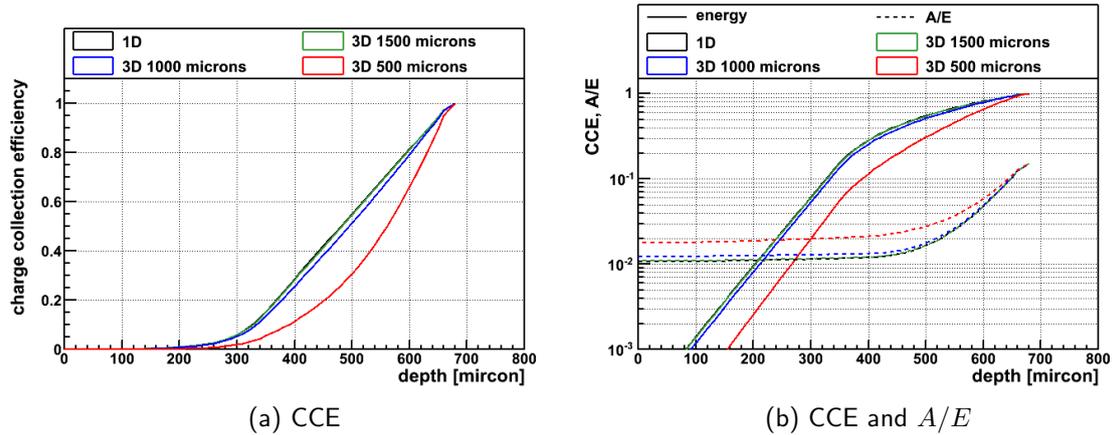
Figure 8.17 Comparison of 1D and 3D diffusion.

1500 micron). It can be seen that the CCE curve in the 3-D case is depending on the size of the two parallel dimensions. If their sizes are too small, charges are lost on the borders of the dimensions which would otherwise still have the chance to diffuse into the FAV.

At the size of 1500 micron the 1-D and 3-D diffusion are practically identical. However, the reduced time binning and additional two loops for the extra spatial dimensions in the 3-D case, require significantly more computing time. The 1-D approach is followed as a good approximation from here on. A possible use of the 3-D diffusion model is the application on curved surfaces as e.g. the lateral detector sides.

8.5   Comparison with Data

The comparison of the n^+ electrode model with data is based on the energy and A/E spectra. Low A/E values are created by slow pulses and by MSE events. Hence, for a quantitative comparison both processes have to be considered.

Two pulse shape libraries are created: (1) a slow pulse library based on the n^+ electrode model describing only interactions above the FCCD and (2) a bulk pulse library based on ADL (AGATA Detector Library) describing only interactions below the FCCD. This includes MSE features and high A/E events around the p^+ electrode.

The slow pulse library is 1-dimensional and contains pulses for interactions above the FCCD in steps of 10 micron. Pulses are created in 10 ns time bins for 20 μs and stored as arrays in a ROOT nTuple. The library size is a few 100 kB and requires less than 5 min to be created.

The bulk pulse library is created with ADL and contains pulses for 2-dimensional cylindrical coordinates with the BEGe radius and height as the two dimensions. In this work ADL is used as a black box and not further described. Refer to [152] or [153, 154, 155] for further information. For this work, ADL is first used to calculate the electric field based on the detector dimensions, the FCCD and the bias voltage. Then the pulses are simulated with a single site unit energy deposition in a grid of 100 micron. Pulses are created for every point in the grid below the FCCD and contain the pulse form and drift time information. This naturally includes high A/E pulses from around the p^+ electrode. The features of MSE are created in a later step when the simulated single site pulses are combined according

to the GEANT4 hit distribution. The pulses are stored as arrays in a ROOT nTuple with a time binning of 10 ns and a trace length of 20 μs. The file size is around 300 MB for an average BEGe detector and the library creation requires around 1 h.
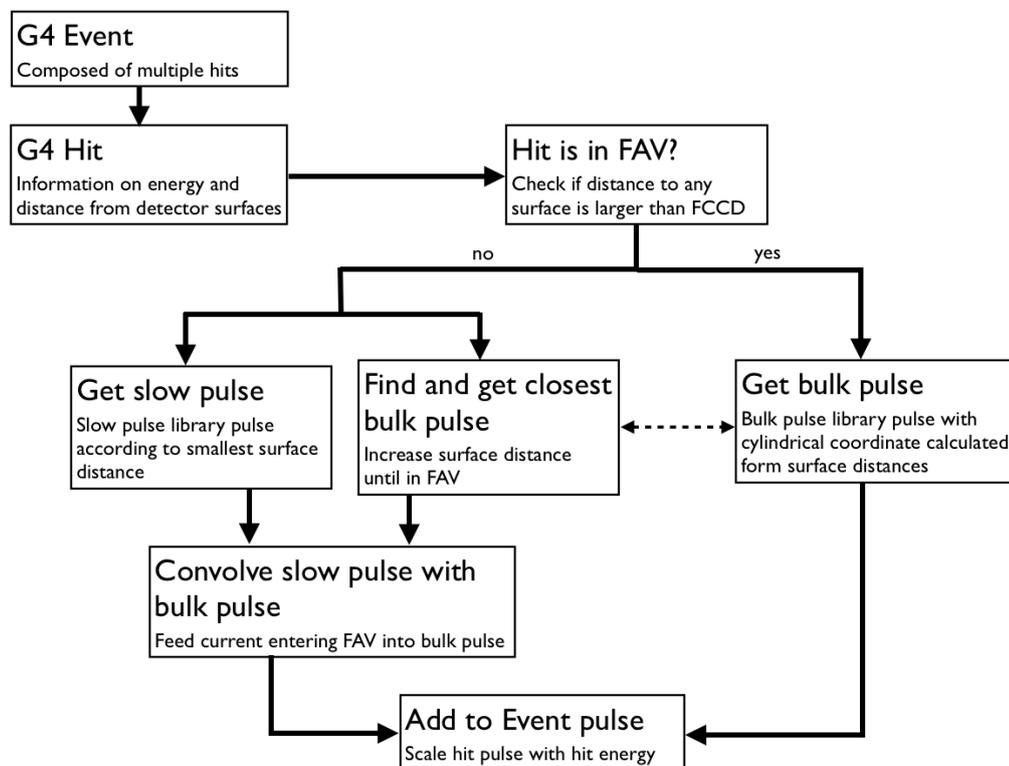
Figure 8.18   Scheme of pulse shape post processing.   The pulse of each hit in a GEANT4 event is processed independently, weighted according to its energy and summed to the pulse of the whole event.

Pulses from both libraries are then used in a post processing of GEANT4 simulations which is developed for this study and is illustrated in Fig. 8.18. A GEANT4 event is separated into several hits. The pulse for each hit is formed individually and then combined into a pulse for the full event. First, a decision is made if the hit occurred in the FAV (bulk pulse) or above the FCCD (slow pulse) by comparing the distance to each detector surface with the FCCD. In case of a bulk pulse, the pulse is taken from the bulk library according to its cylindrical coordinates. Then it is scaled according to the hit energy and summed to the event pulse. In case of a slow pulse, the current pulse is linearly interpolated from the slow pulse library[11]. In parallel, the closest grid point in the bulk is determined and its pulse is convolved with the slow pulse[12]. This matches the drift time of the slow pulse to that of the bulk pulses depending on the position on the detector surface. The convolved slow pulse automatically contains the correct energy degradation from the n$^+$ electrode. It is weighted with the original energy deposition of the hit and added to the event pulse.

The energy and A/E information is extracted from the current pulse of the constructed

---

[11]The 10 micron grid size requires a interpolation since otherwise artifacts in the energy spectrum occur. E.g. a detector with 0.6 mm FCCD has 60 different slow pulses in the library which, in case for ^{241}Am, have to cover a 60 keV wide slow pulse region below the γ-line. Artifacts with the size of $\mathcal{O}(1$ keV$)$ would occur.

[12]The goal is to add the correct drift time to the slow pulse depending on its location in the n$^+$ electrode. Technically this is done by creating a bulk pulse at each time bin (10 ns) with the charge fraction of the slow pulse that is entering the FAV in that time.

event after shaping with a 3x50 ns MWA. The energy is taken as the integral of the current pulse and the amplitude is taken as the value of the maximum bin. No further artificial noise or detector response is included.

(a) normalized A/E map

(b) energy difference

(c) map of current pulse maximum time
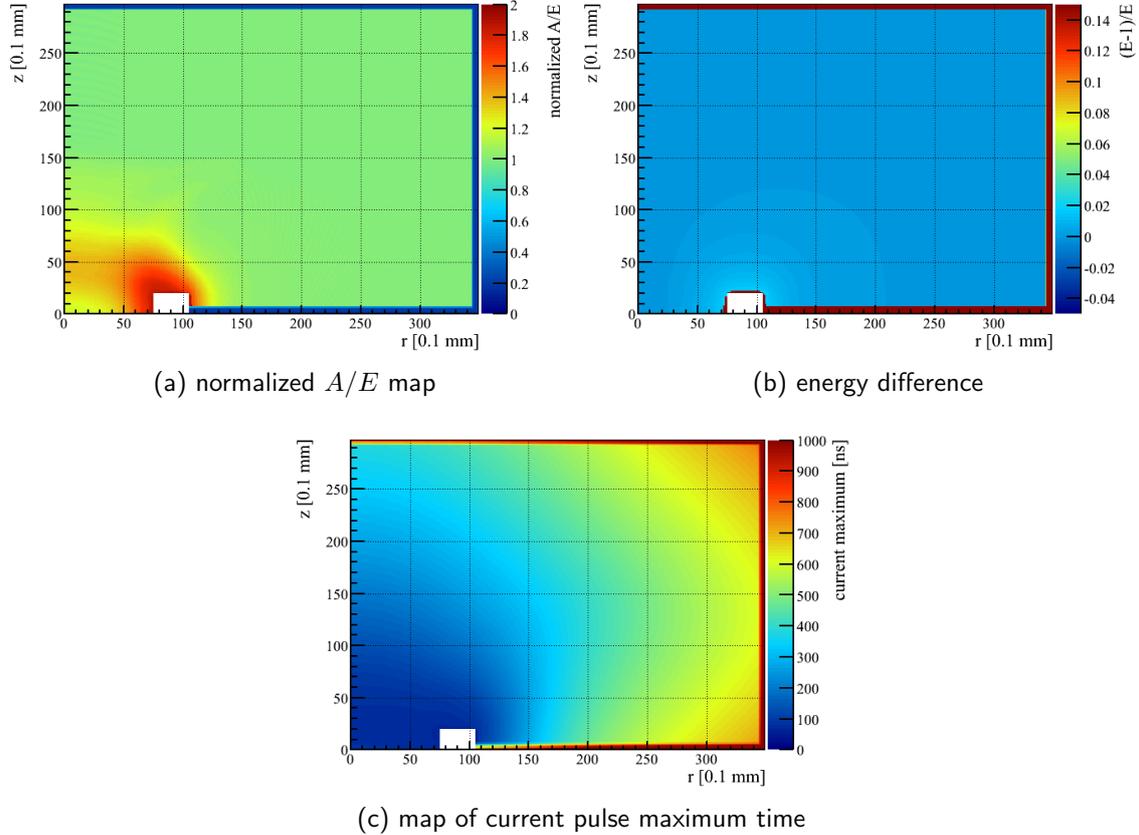
Figure 8.19 Pulse shape property map of GD91C. A unit energy is deposited at single-site locations in cylindrical coordinates. Top left: A/E normalized to a bulk pulse at position (200,200). Top right: Difference between deposited unit energy and reconstructed energy. Bottom: Time of current pulse amplitude with respect to the beginning of the pulse.

The reconstructed values of A/E, the energy and the time of the current pulse maximum are shown in cylindrical coordinates in Fig. 8.19 for GD91C with a bias voltage of 3800 V. The A/E values are normalized to a bulk pulse and show increased values around the groove and the p$^+$ electrode as expected. The A/E values in the n$^+$ electrode are reduced. Fig. 8.19b shows the difference of reconstructed energy to deposited (unit) energy. The energy reconstruction in the bulk is complete whereas it is reduced above the FCCD. A simulation artifact is present in a small volume around the groove with up to 15 % energy loss on the groove surface. However, for the present application of an ^{241}Am and ^{90}Sr source exposing the n$^+$ electrode this effect is negligible in first order[13]. Also shown is the time of the maximum of the current pulse with respect to the energy deposition in Fig. 8.19c. This illustrates the drift time of the charges starting at a certain location inside the detector which is used to create MSE features.

After the reconstruction of the energy and A/E value for an event, the values are convolved with a resolution. The energy and A/E resolution is taken from the calibration data of

---

[13]A bias might occur for scattered betas and low energy γ-rays that partially expose the groove.

the GD91C measurements at LNGS (Fig. 6.9) which is also used for comparison with the simulations.

8.5.1   Qualitative Comparison

First the slow pulses library is qualitatively compared with the low energy spectrum of ^{241}Am which is also used to constrain the recombination rate in the n$^+$ electrode model. The recombination rate is further tested with a ^{90}Sr source spectrum where, however, slow pulse and MSE features overlap. Then the bulk library and the corresponding MSE effects are tested with a ^{228}Th source spectrum. After qualitative validation of slow pulse and bulk library, the ^{90}Sr data is compared with the MC on a quantitative level. The application to ^{42}K, $2\nu\beta\beta$ decay and ^{39}Ar follows in the next section.

^{241}Am Source

The low energy spectrum of an ^{241}Am calibration source is dominated by SSE slow pulses and can be used to tune the n$^+$ electrode model at different depths independent of MSE effects. A given energy degradation of the 59.5 keV γ-ray and a given A/E value correspond to a certain distance of the interaction from the FCCD. Hence, the distribution of A/E versus E below the γ-line can be used to infer the most suitable recombination rate as defined in Sec. 8.4.1.

(a) data   (b) MC model 0.002
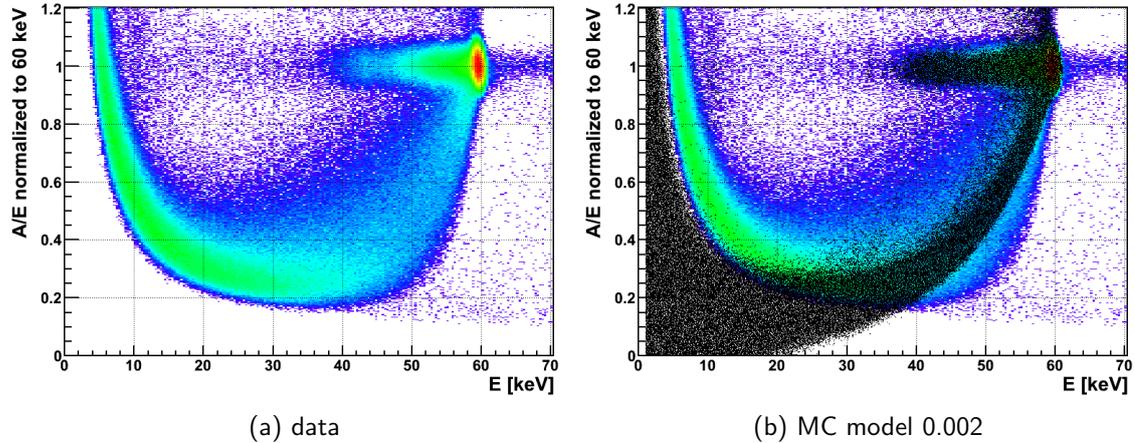
Figure 8.20   Comparison of ^{241}Am A/E values between measurement (left) and best recombination model in the MC (black scatter plot on the right).

The measurement was performed with GD91C at LNGS using the *Beta2000* collimator pointed at the 0 deg position on the n$^+$ electrode (Fig. 6.17a). Fig. 8.20 shows the A/E versus E plot for data (left) and for data overlaid with MC according to the best fitting recombination rate (right). The model which qualitatively best describes the data has a recombination probability of 0.002 per ns in the RDR. The same plots with the other recombination rates can be found in Fig. D.4 in the appendix for comparison. The choice of the best recombination rate is based on the form of the arc below the 59.5 keV peak which is created by events just above the FCCD where the n$^+$ electrode is the most sensitive. A beta going through the whole n$^+$ electrode is seeing the integral effect and will get the largest slow pulse contribution from this region; thus, here the model has to fit best. The region below 30 keV is affected by noise which is not included in the simulation and cannot

(a) ^{241}Am   (b) ^{90}Sr
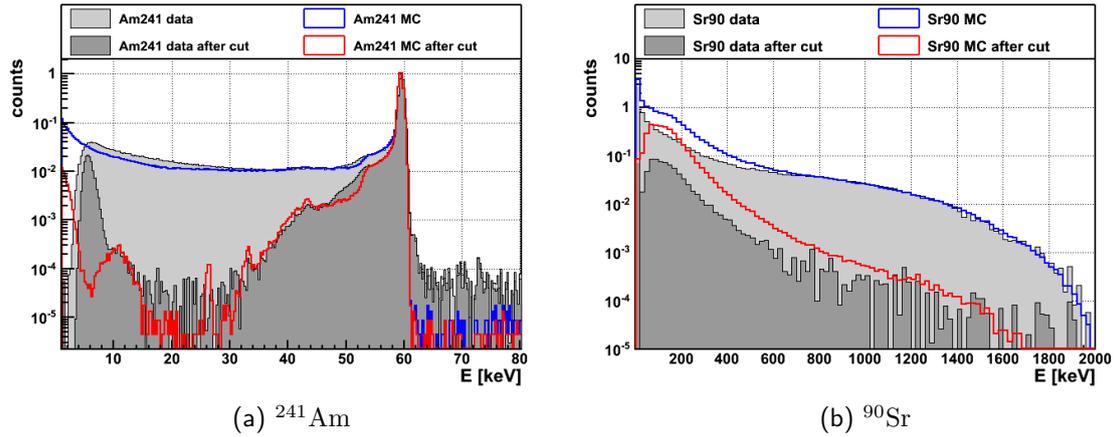
Figure 8.21 Comparison of energy spectra between MC and data before and after an A/E cut. The data histograms are subtracted with a background spectrum for illustration. For ^{241}Am (left) MC and data are normalized to the peak counts. The A/E cut is based on $0.9 < A/E < 1.1$. For ^{90}Sr (right) the spectra are normalized to the energy region $650 - 1450$ keV. The A/E cut is based on $0.98 < A/E < 1.07$.

be used for comparison.

In Fig. 8.21b it can be seen that for a given energy below the peak, the A/E distribution in the data is wider than in the MC. This is likely due to local variation of the n$^+$ electrode properties[14]. Such effects are not modeled in the MC and can create larger variations in the slow pulse behavior at a given depth than expected. This is a point of improvement for further studies.

The energy spectrum of ^{241}Am can be seen in Fig. 8.21a for data and MC, before and after an A/E cut of $0.9 < A/E < 1.1$. The data histograms are subtracted with a background spectrum[15]. The unsuppressed data and MC spectra are normalized to the 59.5 keV peak before cut. The general shape is well described by the MC with the n$^+$ electrode model. The strong suppression below the peak can be reproduced. Discrepancies arise below 30 keV due to noise. The slow pulse component is slightly underrepresented in the MC. However, the spectrum after cut which is less affected by noise is well reproduced until below 10 keV. A mismatch around 50 keV is likely due to Compton scattering on material that is not implemented in the MC (see Sec. D.1 in the appendix for a similar phenomenon). It should be stressed that it would not be possible to reproduce the low energy ^{241}Am spectrum without an n$^+$ model.

^{90}Sr Source

The A/E versus E spectrum of a ^{90}Sr source is shown in Fig. 8.22. The data was taken with the same collimator on the same n$^+$ electrode section as the ^{241}Am measurement. The MC spectrum on the right is based on the same best recombination model as found with ^{241}Am. Only ^{90}Y decays of the ^{90}Sr $- ^{90}$Y decay chain are simulated which is only valid for comparison above the ^{90}Sr beta endpoint of 545.9 keV. The decays were sampled

---

[14]These can be e.g. local impurities variations which influence the creation of recombination centers.

[15]Source and background histograms are scaled with the live-time and quality cut efficiency (pile-up and baseline spread) and subtracted which can results in negative bin contents and is only performed for illustration.

(a) data   (b) MC model 0.002
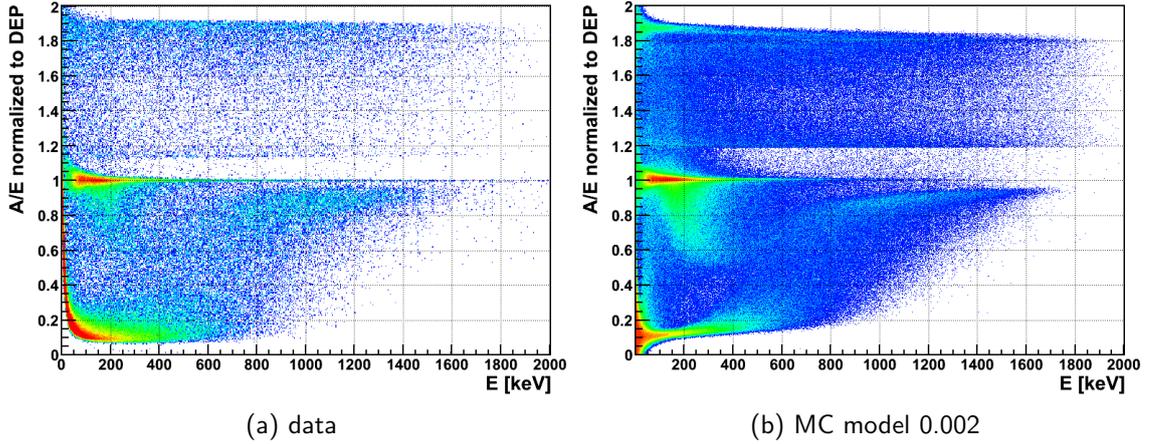
Figure 8.22 Comparison of ^{90}Sr A/E values between measurement (left) and best recombination model in the MC (right).

with Decay0[16]. The ^{90}Sr spectra for other recombination rates are shown in Fig. D.4 in the appendix. The qualitative comparison is based on the position of the slow pulse band below the SSE band and the lowest A/E values.

The same recombination probability is found to be optimal for the high energy region of ^{90}Sr as well as for the low energy region of ^{241}Am. This is remarkable given the fact that the features of ^{241}Am are created by single site interaction whereas the features of ^{90}Sr are created by the integral effect of the beta trajectory. This is a strong indication that the n^+ electrode model with the inferred recombination rate can qualitatively describe very different event topologies and can hence be extrapolated to event types which are not easily accessible for data i.e. ^{42}K and $2\nu\beta\beta$ decay.

The energy spectra of data and the MC with the best recombination model are shown in Fig. 8.21b. The background is subtracted from the data histograms. The unsuppressed data and MC spectra, are normalized to the energy region of $650 - 1450$ keV. The full spectrum and the spectrum after an A/E cut of $0.98 < A/E < 1.07$ is distinguished. The shape of the unsuppressed spectrum is well reproduced above 600 keV by the MC. At lower energies the data has additional contributions from ^{90}Sr decays. However, the MC strongly overestimates the events at those energies. This is likely due to noise and the trigger threshold in the data since a large fraction of events has A/E values below 0.2 (see Fig. 8.22). Some of those very slow events might not pass the hardware trigger or quality cuts in the data. This is likely to be improved by adding experimental noise to the simulated pulses and processing them in the same framework as the data pulses. The strong suppression after A/E cut can be reproduced at higher energies but seems to be slightly underestimated in the MC. This will be further discussed in the quantitative comparison below.

---

[16]The decay generation with Geant4 based on the `RadioactiveDecay3.3` database includes a 1760.7 keV γ-ray with 0.0115 % emission probability. However, the latest nuclear data [138] does not include a valid emission probability. The MC with Geant4 suggest that this γ-line would be a dominant feature at this energy before and after A/E cut; however, there is no evidence in the data. Hence, the ^{90}Y decays are sampled with Decay0 which does not include this γ-ray.

^{228}Th Source

The validation of the ADL code and the bulk library is performed with a ^{228}Th source measurement in the GD91C setup at LNGS. The A/E values of the 2614.5 keV γ-line, the DEP and the SEP are compared with simulated ^{208}Tl decays in Fig. 8.23. The spectra are normalized to all events in the ± 6 keV energy range of the A/E spectrum for data and MC individually. The ^{228}Th calibration source is dominant in the peak regions so that no background subtraction is needed.

(a) ^{208}Tl FEP

(b) ^{208}Tl SEP

(c) ^{208}Tl DEP

(d) ^{208}Tl DEP zoom
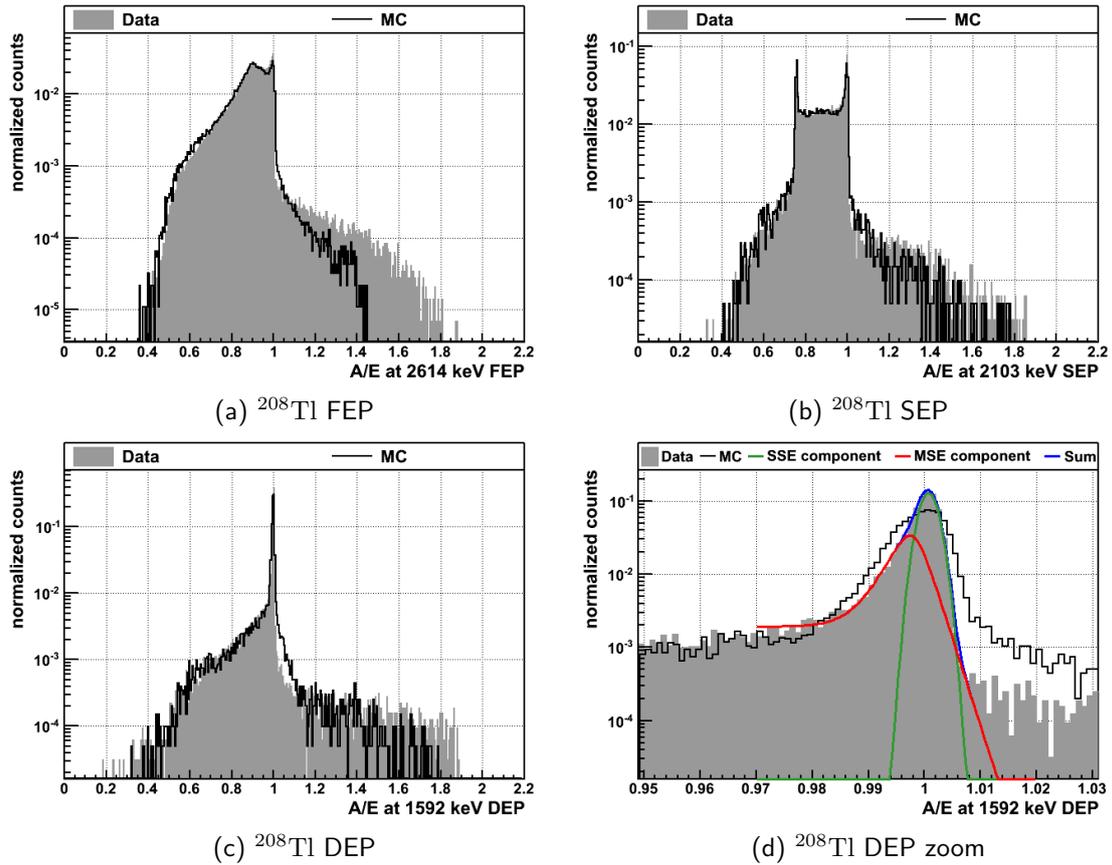
Figure 8.23 A/E values for data and simulation at the ^{208}Tl FEP, SEP and DEP. The bottom right shows a zoom of the SSE band of the DEP in which the SSE and MSE components are fitted to the data.

The general shape of the simulated A/E distributions fit well with the data for all spectra. Small discrepancies can be observed on the far end of the high A/E side which may be due to the ADL artifacts around the groove or strongly decreasing statistics in the histograms. Those artifacts are irrelevant for this work since those events can be clearly separated from other event types. However, for the DEP spectrum a slightly larger high A/E tail on the SSB is visible in the MC compared to the data which can potentially introduce a bias in the p$^+$ electrode event separation. At the low A/E side the agreement between MC and data is good which validates the bulk library to be used for estimation of the MSE components.

A zoom into the DEP region is shown in Fig. 8.23d. Here the A/E distribution of the data is fitted with a Gaussian for the SSE component (green) and an exponential tail for the

MSE component (red). The fit function is defined as in [97][17]:

$$f(x = A/E) = \frac{n}{\sigma_{A/E} \cdot \sqrt{2\pi}} \cdot e^{-\frac{\left(x - \mu_{A/E}\right)^2}{2\sigma^2_{A/E}}} + m \cdot \frac{e^{g \cdot (x-l)} + d}{e^{\frac{1}{t}(x-l)} + 1}, \qquad (8.14)$$

with n and m being the strength of the Gaussian and tail term respectively and g, l, d and t being empirical parameters of the tail. The width of the Gaussian $\sigma_{A/E}$ is directly used for the smearing of A/E values in the MC; however, the simulated distributions shows a broader width than the $\sigma_{A/E}$. The difference is due to a binning artifact arising from the A/E reconstruction in the bulk library creating an additional resolution of simulated A/E values. Certain positions inside the bulk have periodically slightly different A/E values in the order of 1 % as illustrated with a control plot in Fig. D.3 in the appendix. However, the MSE tail region is well described by the MC below A/E< 0.985 which can be taken as the tightest A/E cut value which is valid for this investigation.
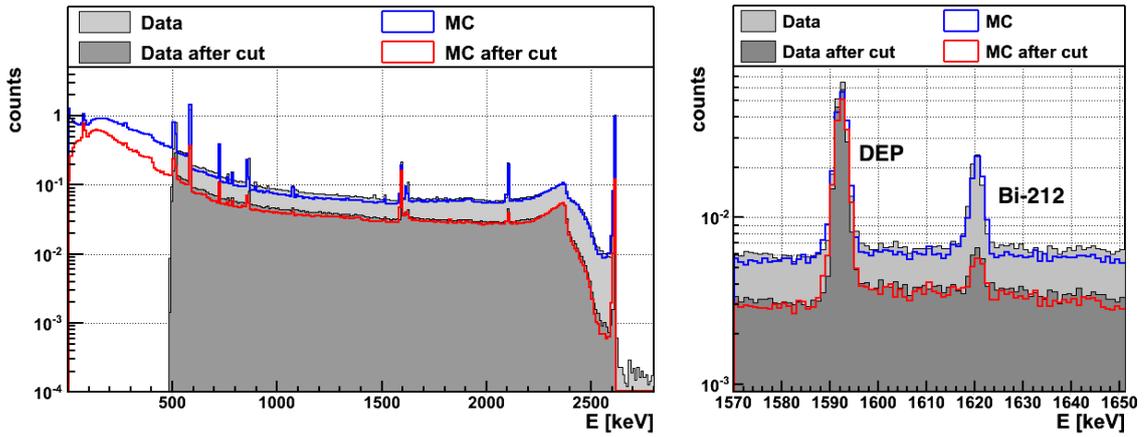
Figure 8.24 Comparison of ^{228}Th energy spectra between MC and data before and after an A/E cut of $0.98 < A/E < 1.07$. The data spectrum was taken with a trigger threshold of ≈ 500 keV and is subtracted with a background spectrum for illustration. The MC spectra consist only of ^{208}Tl and ^{212}Bi events. The full spectral range is shown on the left and a zoom on the 1620.5 keV ^{212}Bi γ-line and the ^{208}Tl DEP is shown on the right. The unsuppressed spectra are normalized to the 2614.5 keV peak counts.

The energy spectrum before and after A/E cut of $0.98 < A/E < 1.07$ is shown in Fig. 8.24 for background corrected data and MC. The unsuppressed spectra are normalized to the 2614.5 keV peak. The spectral shape can be well reproduced before and after cut. The energy range of the ^{208}Tl DEP and the 1620.5 keV ^{212}Bi γ-line is shown on the right. The small suppression of the DEP as well as the larger suppression of the γ-line can also be reproduced. This validates the bulk library for estimations of MSE.

8.5.2 Quantitative Comparison

Fig. 8.25 shows the A/E distributions for the ^{90}Sr measurement and MC simulation with different recombination rates. The two ROIs of $650 - 1000$ keV and $1000 - 1450$ keV are distinguished in the left and right plots. The interesting region around the SSB is enlarged in the bottom plots. Also shown is the spectrum of a 63.9 h background measurement

---

[17]Note that this reference contains a typo: The "+l" in the denominator of the last term in formula (1) should read "+1".

which was scaled to the ^{90}Sr measurement live-time of 1.3 h. It is used to subtract the
background influence in the quantitative analysis. Both spectra are then normalized to the
background corrected number of ^{90}Sr events in the respective energy region of the A/E
spectrum. The same normalization is done for each MC spectrum individually[18]. The
vertical dashed lines are the A/E cut values at 0.98 and 1.07, separating the spectrum into
three regions: low A/E, SSB and high A/E region. The cuts are chosen to separate the
three regions as best as possible in the data and MC alike.

(a) $650 - 1000$ keV

(b) $1000 - 1450$ keV

(c) $650 - 1000$ keV zoom

(d) $1000 - 1450$ keV zoom
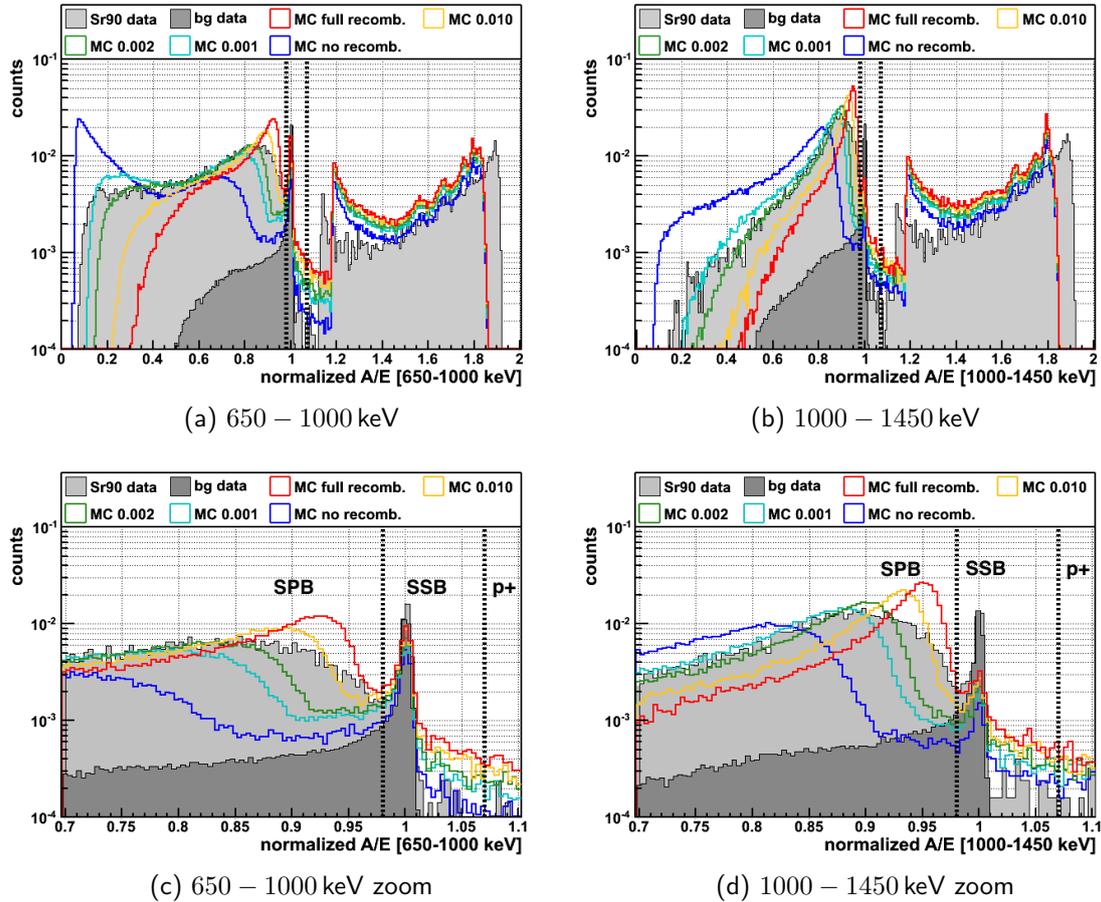
Figure 8.25 Comparison of ^{90}Sr A/E values between measurement (solid gray) and various recombi-
nation models (colored lines).

It can be seen that the overall shape of the A/E spectrum can be reproduced by the MC
with the recombination probability of 0.002 per ns (green histogram) which was identified
as the best model. The extreme cases of full recombination and the zero combination do
not reproduce the shape. This is a strong indication that a finite charge recombination rate
is realized in the outer layers of the n$^+$ electrode and that this kind of analysis is sensitive
to its value. Even a measurement of the recombination rate can be envisioned with more
investigations on the systematic influence of the other model parameters.

The high A/E region is the same for all MC spectra since the recombination models only
affect slow pulses. A larger high A/E tail can be seen in the MC compared to the data
similar to the observation with the DEP in ^{208}Tl. However, the generally strong reduction

---

[18]Note that the total number of events in the various MC spectra differ and that each MC spectrum has
its own normalization.

of events in the valley just above the SSB is reproduced and can be used to strongly separate p$^+$ electrode events from the rest. The minimum and maximum value of high A/E events in the data is larger and lower respectively, which, however, does not affect this analysis. The fraction of background corrected high A/E events compared to all events is shown in Tab. 8.2. In the ROI 1 spectrum it is $29.5 \pm 0.4\,\%$ in the data compared to $33.9 \pm 0.2\,\%$ in the best fit model. In ROI 2 the fractions are $40.1 \pm 0.7\,\%$ and $42.5 \pm 0.2\,\%$ respectively. It is not clear if the difference between data and MC is due to a mismatch in number of p$^+$ electrode events or a mismatch in the number of events in the other regions.

The SSB band itself is dominated by background in the data and only $32\,\%$ of SSB events can be attributed to ^{90}Sr in ROI 1 and only $23\,\%$ in ROI 2. The large subtraction of background creates a significant uncertainty on the quantitative comparison.

The maximum of the SPB is best reproduced by the 0.002 model. However, the gap between SPB and SSB is not qualitatively reproduced since the SPB is significantly wider in the data. Also the extension to the lowest A/E values is wider in the data. A possible explanation are local variation in the n$^+$ electrode which are not modeled in the MC and which would widen any slow pulse component of an A/E distribution. This goes along with the observation of a larger than expected variety of slow pulses in the A/E versus E spectrum of ^{241}Am (Fig. 8.20).

Table 8.2 A/E event fractions in % in the two ROIs of ^{90}Sr. The data is background corrected and the MC is based on the best recombination model.

region range	ROI 1 [650 − 1000 keV]		ROI 2 [1000 − 1450 keV]	
	data	MC	data	MC
A/E < 0.98	69.1 ± 0.6	62.8 ± 0.2	59.0 ± 0.8	55.8 ± 0.3
$0.98 < A/E < 1.07$	1.4 ± 0.2	3.3 ± 0.1	0.9 ± 0.2	1.7 ± 0.1
A/E > 1.07	29.5 ± 0.4	33.9 ± 0.2	40.1 ± 0.7	42.5 ± 0.2

Even with the qualitatively different shape of the SPB between data and MC, an A/E cut at 0.98 separates the SPB and the SSB maximally in both cases. The fraction of events in the low A/E region and the SSB region is also shown in Tab. 8.2 and compared between data and MC. The fractions are defined with respect to all events in the respective ROI and sum up to $100\,\%$. The fraction of SSB events can be interpreted as the survival fraction of ^{90}Sr events with an A/E cut of $0.98 < A/E < 1.07$ and is crucial for understanding surface events of BEGe detectors in GERDA. The survival fraction is measured with about $1\,\%$ in both energy ranges and shows the strong discrimination capability of surface events. The prediction by the MC is about a factor of 2 to 3 larger. The mismatch between data and MC might be explained by a few arguments concerning the experimental setup. (1) The beta beam of the ^{90}Sr source was focused on the n$^+$ electrode but a large population of scattered betas is interacting on the p$^+$ electrode and groove surface creating high A/E events. This scattering is highly dependent on the exact geometrical implementation of the setup such that small systematic uncertainties introduce a large bias in the high A/E population. Such an influence would be reduced in an alternative measurement on a different side of the detector where the p$^+$ electrode is not partially exposed. (2) Events in the SSB band are dominated by background and small systematic differences between the background and source measurement as e.g. introduced by correcting the efficiency of quality cuts, propagate strongly into the ^{90}Sr SSB population and thus into the survival

fraction via background subtraction. (3) The high A/E tail on the SSB might slightly change the event separation between data and MC which can have a strong effect on the few surviving events in the SSB. But in any case, the discrepancies result in a conservative overestimation of the survival fraction of surface events in the MC.

(a) ROI 1   (b) ROI 2
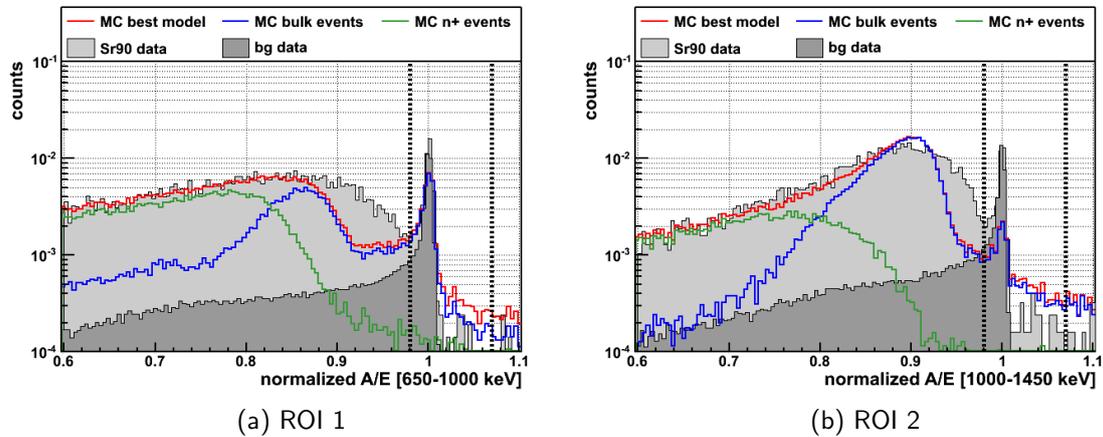
Figure 8.26 Separation of simulated ^{90}Sr events in majority bulk events and majority n$^+$ events. The event by event separation is based on the region in which the largest energy fraction is deposited. The simulation is based on the best fit recombination model.

Finally, the A/E distribution from the MC can be separated into majority bulk events and majority n$^+$ events depending on the location of the deposited energy. This is shown for the best recombination model in Fig. 8.26. If a larger fraction of energy is deposited in the n$^+$ electrode the event is counted as n$^+$ event and included in the green histogram; the mutually exclusive case of a larger energy fraction in the bulk or FAV of the detector is shown in the blue histogram[19]. It becomes clear that the events in the slow pulse band are events were the major part of the energy is deposited in the bulk. Those events define the gap between SPB and SSB. It can be also seen that this effect is increased for larger measured energies. Hence, the mismatch of the gap in the MC is created by event topologies where less energy is deposited in the n$^+$ electrode. This would e.g. occur if the charge recombination is locally larger[20]. The same effect would be expected if the FCCD were locally thinner which is however, not supported by the data from the ^{241}Am scans (Sec. 7.2). On the other hand, events with a larger energy deposition in the n$^+$ electrode have significantly lower A/E values and will be vetoed with any A/E cut.

8.5.3 Conclusion

The n$^+$ model developed in the previous section was compared with calibration data of GD91C. The model is based on the measured FCCD, the dimensions and the impurity concentration of an individual detector. The recombination rate of charges in the RDR is left as a free parameter and was tuned to data from ^{241}Am and ^{90}Sr. The two different event types are best described by the same recombination rate of 0.002 per ns. The

---

[19]Note that the separation is based on the original GEANT4 energy deposition of the event. Also energy in largely dead detector volume is counted.

[20]This may sound counter intuitive but can be observed in Fig. 8.25. A larger charge recombination would give less slow pulse character to an event with a given beta trajectory. The measured energy of this event would also be smaller; however, by definition such an event has sufficient energy to populate the energy region of the A/E spectrum. Hence, for a larger charge recombination rate, the SPB moves closer to the SSB for events in a certain energy range.

extreme cases of no recombination and full recombination are not supported by the data suggesting a finite recombination rate in the outer layers of the n$^+$ electrode which can be measured by such investigations. The result is valid for GD91C but may differ for other detectors. It is suggested to measure ^{90}Sr and ^{241}Am data with other PHASE II BEGe detectors in order to determine if the recombination rate is (1) an individual property of each BEGe detector, (2) has a similar value for all PHASE II BEGe detectors or (3) can be correlated and predicted with other detector properties such as the impurity concentration.

The quantitative comparison showed that the order of magnitude of the ^{90}Sr survival fraction can be reproduced by the n$^+$ model. An exact reproduction is not achieved which, however, might be due to systematics effects in the experimental setup which are independent of the n$^+$ model. Different ^{90}Sr measurements without exposure of the p$^+$ electrode contact are suggested to clarify this point. The quantitative comparison was based on a specific A/E cut manually set into the gap between the SSB and SPB at 0.98. However, the shape of the gap between those bands is different between data and MC such that the prediction of a survival probability for a non-optimized A/E cut e.g. below 0.95 is not valid. Further investigations on potential slow pulse variations are suggested.

This is the first time that a full simulation of surface and bulk events has been compared to a set of various calibration source spectra. The small discrepancies could be reduced with further tuning of the manifold n$^+$ model parameters. However, this should be accompanied with calibration measurements of other detectors in order to retain a generic model. At this stage, the agreement between data and MC is good enough to be applied to other background sources.

8.6 Application of the n$^+$ Model in Phase II

The n$^+$ electrode model developed in the previous sections is applied to predictions of ^{42}K and ^{39}Ar surface events, $2\nu\beta\beta$ decays and $0\nu\beta\beta$ decays with Majoron emission. In this section the n$^+$ electrode model developed from first principles is called "new model" and is compared to the simple dead layer model[21] called "old model". The comparison illustrates the quantitative impact of this work on PHASE II analyses and is mainly based on GD91C as a reference detector. A selection of other PHASE II BEGe detectors is investigated in some cases to illustrate difference between detectors. Furthermore, the performance of ^{42}K background rejection is explored for hypothetical BEGe detectors in a future LAr based ^{76}Ge $0\nu\beta\beta$ decay experiment with FCCD values reaching up to 1.5 mm.

8.6.1 Application to ^{42}K Background

The slow pulse influence on the spectral shape of ^{42}K and the survival probability of ^{42}K events after A/E cut in the ROI of $Q_{\beta\beta} \pm 200$ keV are determined with MC simulations. Preliminary results of this study have been already used in the construction of the BEGe background model in PHASE I [115]. The simulation of the ^{42}K A/E values and its strong potential for the rejection of surface events has been included in the pulse shape discrimination for the PHASE I $0\nu\beta\beta$ decay analysis [97].

---

[21]This model was used in Chap. 7 to determined the FCCD with peak rations. The charge collection efficiency changes step-like from 0 in the dead layer to 1 in the active volume. This model does not predict any A/E information for surface events.

In a first scenario ^{42}K decays are sampled with DECAY0 in a LAr volume 6 cm thick around the single detector GD91C. This sampling volume is sufficiently large so that no emitted beta from outside that volume can contribute to the spectrum. The n$^+$ electrode and p$^+$ electrode are equally exposed according to a homogeneous distribution of ^{42}K in the detector vicinity. Another scenario is simulated where ^{42}K events are sampled directly on the detector surface describing a situation in which charged ^{42}K ions are attracted towards and stick onto the electrical contacts. The results of the homogeneous scenario in the 6 cm thick volume are presented in the main text and the pure surface scenario is shown in the appendix for comparison (Sec. D.2).

The MC simulations are post processed with the new and the old model. Fig. 8.27b shows the energy spectra of the new n$^+$ electrode model in red, the old model in black as well as the new model after A/E cut in green. The energy and A/E values of the simulation are convolved with the resolution determined for the setup of GD91C at LNGS. Note that the A/E resolution in GERDA might be different which can affect the qualitative statements below[22].

(a) A/E versus E
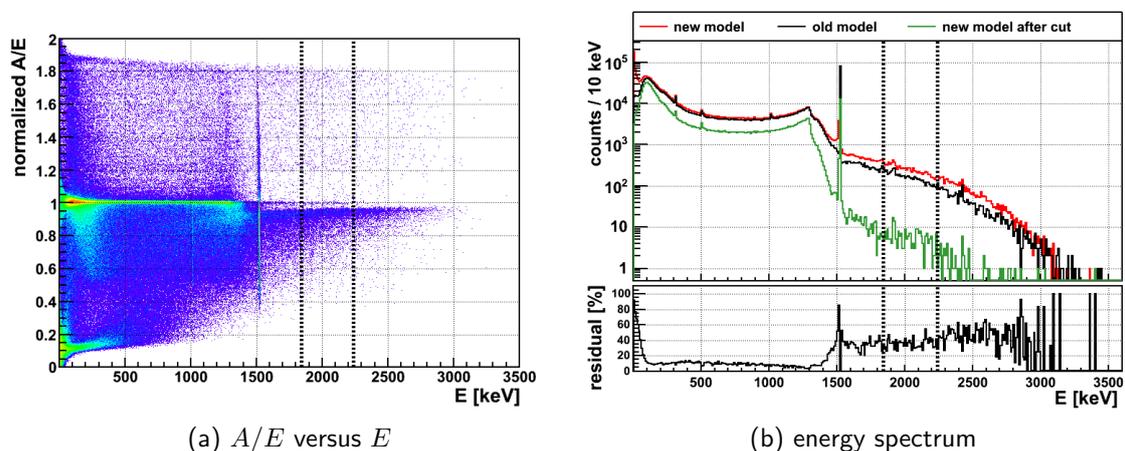
(b) energy spectrum

Figure 8.27 Comparison of n$^+$ models with simulated ^{42}K decays in a 6 cm wide LAr volume around the detector. Left: A/E versus E spectrum of simulated ^{42}K decays with the new model. Right: Energy spectrum with the new model (red), the old model (black) and the new model after A/E cut (green). The residual refers to the unsuppressed new and old model.

The new model shows a substantial increase of the event rate in the whole spectrum compared to the old model since the surface layers are now semi-active. More events are detected for the same activity of ^{42}K. This effect is especially significant above the 1524 keV peak where the energy spectrum is dominated by betas. In $Q_{\beta\beta}\pm200$ keV, the expected number of events increases by 35 %. The plot also illustrates the strong suppression after A/E cut which could previously not be understood in detail. The suppression will be quantified below.

The A/E versus E plot according to the new model is shown in 8.27a. Below the peak the spectrum is dominated by SSE populating the SSB being created by the Compton scattered γ-rays. Above the peak the spectrum is dominated by slow pulses which almost exclusively populate the SPB. The A/E spectrum in $Q_{\beta\beta}\pm200$ keV is shown in Fig. 8.28

---

[22]Typically a better energy and A/E resolution is achieved for BEGe detectors in a vacuum cryostat than for deployment in LAr in GERDA. This is due a longer cable length and larger noise pickup in GERDA.

separated into two plots showing the whole range and a zoom onto the SSB and SPB. The majority bulk and majority n$^+$ events are distinguished in red and green respectively. It becomes evident that almost all events in this energy range are majority bulk events which have been shifted towards lower A/E by a small slow pulse contribution while passing through the n$^+$ electrode. In fact the SPB is almost peak-like suggesting a single dominant event topology for those events. Note however, that the comparison with ^{90}Sr and ^{241}Am suggested that the MC code is underestimating the variety of slow pulses and that the peak-like structure is likely to be washed out in the data.

(a) wide   (b) zoom
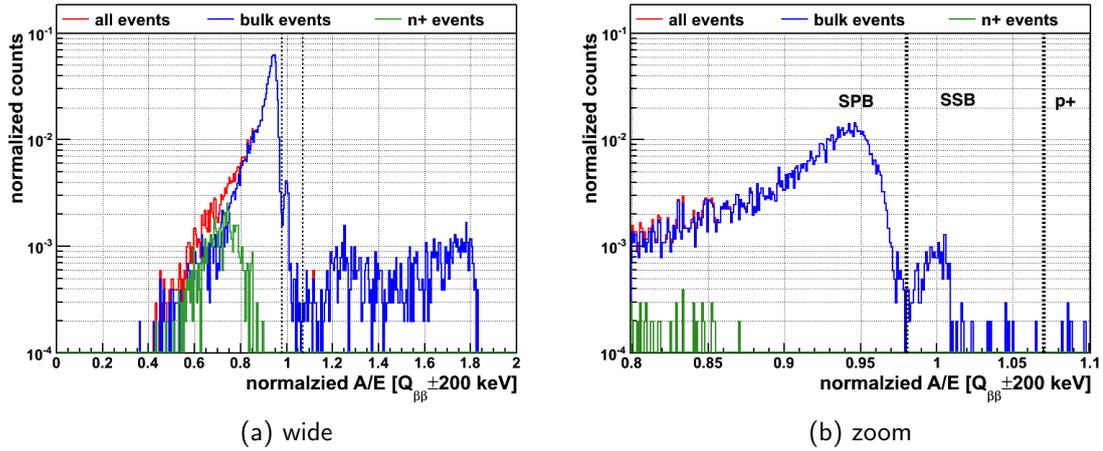
Figure 8.28 A/E spectra of ^{42}K decays in a 6 cm wide volume around the detector in the energy range of $Q_{\beta\beta}\pm200$ keV as predicted by the new model (red). The events are separated into majority bulk events (blue) and majority n$^+$ events (green).

The same plots for the scenario of ^{42}K events on the detector surface is shown in Fig. D.5 and D.6 in the appendix. The energy spectrum is more dominated by the beta components and a larger fraction of events extend to higher energies[23]. In the A/E spectra almost no events are present in the SSB. This can be explained by less dead volume between the origin of the decay and the sensitive detector volume in which Bremsstrahlung can be created that can jump the n$^+$ electrode.

A quantitative prediction is performed as for ^{90}Sr with a low and a high A/E cut of 0.98 and 1.07, respectively. These cut values clearly separate the SSB and SPB and are illustrated as vertical dashed lines in Fig. 8.28. The dominant event type are low A/E events with a fraction of 89.0 ± 0.9 %. The rest of the total fraction is shared by high A/E events with 8.8 ± 0.3 % and SSB events with 2.2 ± 0.2 %.

The SSB event fraction of 2.2 ± 0.2 % is the survival fraction of ^{42}K events close to the detector surface after A/E cut. For ^{42}K directly on the surface the survival fraction is even lower with 0.69 ± 0.02 %. This was the dominant background component for the BEGe detectors in PHASE I and will also be the dominant background in PHASE II. This background component can be suppressed by a factor of 45 in the homogeneous scenario

---

[23]A simulation artifact can be seen at the endpoint of the spectrum where less events are present in the new model compared to the old model. Events around the endpoint are created by betas entering the detector via the p$^+$ electrode or the groove. The artificial energy loss for interactions around the groove in the ADL simulations shifts those events towards lower energy. However, only very few events are affected and the effect is only visible at the endpoint.

and by a factor of 145 in the pure surface scenario for GD91C.

The n$^+$ electrode properties are influencing the suppression of ^{42}K of each detector indi-vidually. The full construction of the slow pulse and bulk library is repeated for a selection of PHASE II detectors based on the individual BEGe dimensions, impurity concentrations and FCCD values. The selection includes GD35B, GD02C and GD79C as detectors with a small, medium and large FCCD, respectively.

(a) energy   (b) A/E
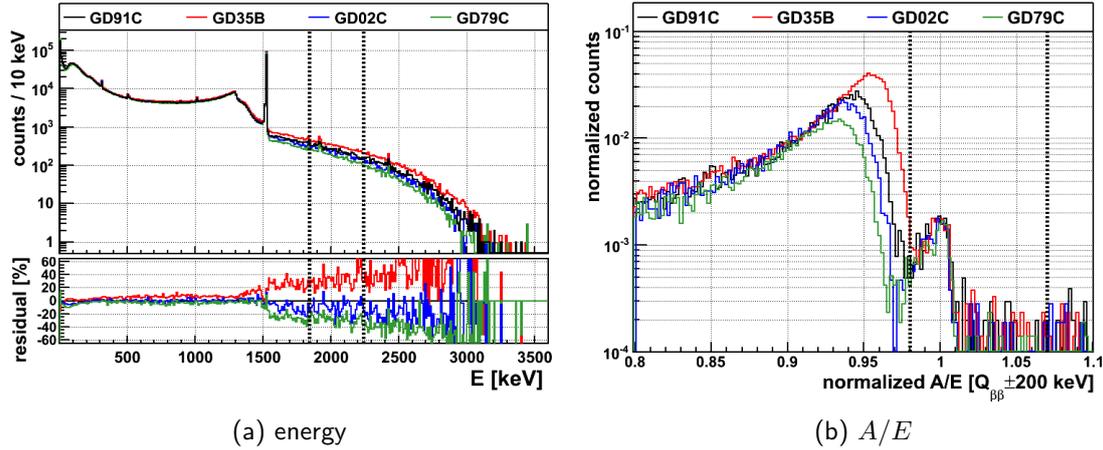
Figure 8.29 Comparison of ^{42}K decays in a 6 cm thick volume around selected PHASE II detectors. The energy spectrum is shown left and the A/E spectrum in $Q_{\beta\beta}\pm200$ keV is shown right. The residuals in the energy spectra are defined with respect to the energy spectrum of GD91C.

The energy spectra are shown in Fig. 8.29a. The same number of ^{42}K decays are simulated for each detector. The residual plots show the difference with respect to GD91C. The largest difference can seen above the peak. The count difference before cut in the energy range of $Q_{\beta\beta}\pm200$ keV is shown in the third row in Tab. 8.3 and is up to 60 % between the two extreme cases of GD35B and GD79C.

Table 8.3 Suppression of ^{42}K decays in a 6 cm wide volume around selected PHASE II BEGe detectors. The first two rows show the FCCD and the relative counts in $Q_{\beta\beta}\pm200$ keV compared to GD91C. The next three rows show the fraction of events after A/E cut separated in low A/E, SSB, and high A/E events. The last row shows the relative number of ^{42}K counts after A/E cut for the same number of simulated decays normalized to GD91C.

detector	GD35B	GD91C	GD02C	GD79C
FCCD [mm]	0.55	0.68	0.75	0.85
relative ^{42}K counts before cut [%]	131.1	100	90.0	71.2
$A/E > 1.1$ [%]	6.1 ± 0.2	8.8 ± 0.3	8.4 ± 0.3	10.2 ± 0.4
$0.98 < A/E < 1.07$ [%]	1.7 ± 0.1	2.2 ± 0.2	2.0 ± 0.2	2.4 ± 0.2
$A/E < 0.98$ [%]	92.2 ± 0.8	89.0 ± 0.9	89.6 ± 1.0	87.4 ± 1.1
relative ^{42}K counts after cut [%]	101.3	100	81.8	77.6

Fig. 8.29b shows the A/E spectra in the energy range of $Q_{\beta\beta}\pm200$ keV. The event fraction in each region is shown in Tab. 8.3 for the selected BEGe detectors. With increasing FCCD, the relative fraction of events in the SPB is decreasing whereas the fraction of p$^+$ electrode

events is increasing. This can be explained by the additional attenuation of betas with larger FCCD whereas the number of p$^+$ electrode events is not influenced. These fractions are, however, also dependent on the individual BEGe size and n$^+$ electrode surface area (see Tab. B.3 in the appendix).

The SSB fraction and hence the survival probability of ^{42}K events is slightly increasing with increasing FCCD. This is explained by a similar amount of SSB events but a fewer amount of slow pulse events: The SSB events are created by Bremsstrahlung photons and low probability γ-rays which are not as much attenuated with a larger FCCD as betas which create the slow pulses. The number of surviving ^{42}K counts after attenuation in the n$^+$ electrode and after the A/E cut is shown in the last row of Tab. 8.3 relatively compared to GD91C. The expected ^{42}K background is decreasing with larger FCCD and can vary up to 30 % between detectors

This large difference in ^{42}K background can be expected for the various PHASE II BEGe detectors and is a combination of beta attenuation and PSD suppression. In case of a worse A/E resolution in GERDA it might be necessary to loosen the A/E cut to retain a large survival fraction for $0\nu\beta\beta$ events in the SSB. This would significantly change the conclusion. A lower A/E cut would not as well separate the SSB and SPB especially for small FCCD detectors (see Fig. 8.29b). This would strongly affect the PSD suppression which, however, cannot be reliably described by the current n$^+$ model since the MC seems to overestimate the band gap. It might be worthwhile to consider different A/E cuts for each detector to optimize the ^{42}K background reduction against the $0\nu\beta\beta$ survival efficiency for each detector individually.

The scenario of ^{42}K decays directly on the detector surface is shown in Fig. D.7 and Tab. D.1 in the appendix. The survival fraction of ^{42}K events decreased by roughly a factor of 3 to 4 compared to the homogeneous scenario. The difference of ^{42}K counts after cuts can differ up to 50 %.

This investigation shows that ^{42}K events can be suppressed with PSD by a factor of 45 in the 6 cm wide homogeneous scenario and by a factor of 145 in the pure surface scenario. The PSD suppression is complementary to the LAr veto (Chap. 9). Betas which create Bremsstrahlung in the LAr that jumps the n$^+$ electrode in the homogeneous scenario will deposit energy in the LAr and can be vetoed to some degree. On the other hand, ^{42}K decays on the surface practically cannot be vetoed since the beta enters directly the detector. Hence the combined PSD and LAr veto suppression for pure surface events is the suppression of PSD alone. The combined suppression of close to surface events requires the combined simulation of PSD and LAr veto and is larger than the PSD suppression alone.

So far these conclusion are drawn from detailed measurements of GD91C and extrapolated to the other detectors. However, ^{90}Sr measurements of other PHASE II detectors would significantly strengthen the presented arguments and open the possibility for cut optimization based on direct measurements[24].

---

[24]The in-situ optimization for individual detectors is not feasible with the low count rate around $Q_{\beta\beta}$ in GERDA.

8.6.2   Detector Development for a 1 t ^{76}Ge Experiment

If a future 1 t scale ^{76}Ge $0\nu\beta\beta$ decay experiment is designed along the GERDA concept with detectors immersed in LAr, the mitigation of the ^{42}K surface background will be crucial. The first batch of BEGe detectors which were partially deployment in PHASE I had been produced with one annealing cycle showing FCCD values between $0.5 - 0.7$ mm. For them, ^{42}K on the surface is accounting for 60% of the total background before PSD. The second batch of BEGe detectors which will only be deployed in PHASE II was intentionally produced with two annealing cycles resulting in FCCD values between $0.6 - 0.9$ mm. For them, the influence of ^{42}K is expected to be reduced. With the n$^+$ electrode model from this work it is possible to optimize the detector design for a future LAr based experiment between ^{42}K suppression and the FAV reduction for $0\nu\beta\beta$.

The study of selected PHASE II detectors above showed that the expected ^{42}K background after PSD strongly depends on the individual detector including all the input parameters for the n$^+$ model. Now, all other detector properties are kept constant in the model and only the FCCD is changed as a property which can be roughly controlled and chosen by the annealing time during production.

(a) energy   (b) A/E
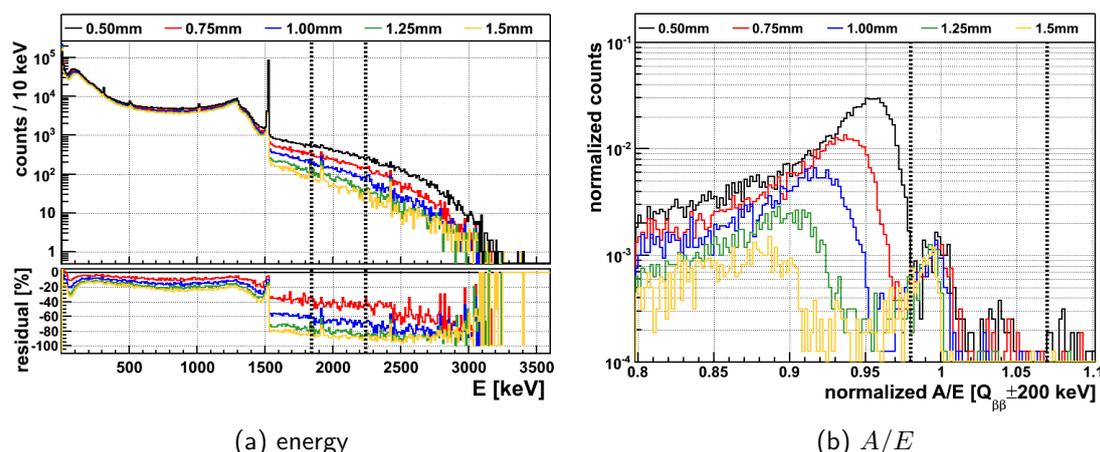
Figure 8.30 Comparison of ^{42}K decays in a 6 cm thick volume around hypothetical BEGe detectors with different FCCD based on the geometry of GD91C. Shown are the energy spectra (left) and the A/E spectra in $Q_{\beta\beta}\pm200$ keV (right) for different FCCD values indicated in the legend. The residuals in the energy spectra are defined with respect to the 0.5 mm FCCD case.

Fig. 8.30 shows the energy spectra and the A/E spectra for hypothetical BEGe detectors with FCCD between 0.5 mm and 1.5 mm. The GD91C geometry and a single simulation of ^{42}K decays was taken as starting point and only the post processing was changed with a different n$^+$ electrode and bulk library based on the different FCCD values. A clear reduction of the number of events in the ROI can be observed with increasing FCCD. The slow pulse band is moving towards lower A/E values making it easier to be separated from the SSB with a looser A/E cut. These are essentially the same observations as for the selected PHASE II detectors but this time based on the same detector with all other model parameters kept constant and for a wider range of FCCD values.

A simple sensitivity estimation is performed below based on the figure of merit $\epsilon/\sqrt{B}$. Here ϵ is the detection efficiency for $0\nu\beta\beta$ decay taken as the active volume fraction for a given FCCD and B is the background. Tab. 8.4 summarizes the ingredients and results for

Table 8.4 Suppression of ^{42}K decays in a 6 cm thick volume around hypothetical BEGe detectors with different FCCD. The first rows show the FCCD. The second row shows the number of ^{42}K events in the energy range of $Q_{\beta\beta}\pm 200$ keV when sampled in a LAr volume 6 cm around the detector. The third row shows the survival fraction of those events with an A/E cut of $0.98 < A/E < 1.07$. The forth row shows the fully active volume fraction equivalent to the detection efficiency of $0\nu\beta\beta$ in this case. The last rows show 4 sensitivity scenarios taken as the ratio of FAV and background reduction as a figure of merit.

FCCD	0.50 mm	0.75 mm	1.00 mm	1.25 mm	1.50 mm
^{42}K events in ROI	8215	4667	2806	1672	1125
A/E cut survival [%]	2.1 ± 0.1	2.6 ± 0.2	3.7 ± 0.3	5.3 ± 0.4	7.4 ± 0.6
FAV [%]	94.0	91.1	88.3	85.5	82.8
1. Sensitivity: ^{42}K only	0.87	1	1.05	1.10	1.10
2. Sensitivity PHASE I like	1.02	1	0.97	0.95	0.92
3. Sensitivity PHASE II like	0.97	1	1.00	0.99	0.96
4. Sensitivity Ge 1 t like	0.89	1	1.04	1.07	1.06

the hypothetical BEGe detectors with different FCCD. The first row shows the detected ^{42}K events in $Q_{\beta\beta}\pm 200$ keV for 10^6 simulated events in a LAr volume 6 cm wide around the detector surfaces. The second row shows the survival fraction of those events with an A/E cut of $0.98 < A/E < 1.07$. The third row shows the FAV fraction.

The last rows show four sensitivity scenarios normalized to the 0.75 mm FCCD detector. The first scenario is based on ^{42}K as the only background where B is taken as the surviving ^{42}K events (e.g. $B = 4667 \cdot 0.026$ for the 0.75 mm case). In this scenario the sensitivity increases up to 20 % between the 0.5 mm case and the 1.25 mm case. The largest improvement can be seen below 1.00 mm.

The second scenario follows the PHASE I findings where half of the background is created by ^{42}K before PSD. Here, B is taken as the suppressed ^{42}K background plus a constant for the other background components. The constant is based on the ^{42}K background of the 0.75 mm BEGe suppressed by a factor of two (e.g. $B = 4667 \cdot 0.026 + 4667/2$ for the 0.75 mm case). The constant is set to the same value for all detectors and represents the other half of the total background budget after PSD. In this case the surviving ^{42}K is negligible compared the other background components such that the sensitivity is decreasing with larger FCCD due to the smaller FAV for $0\nu\beta\beta$.

The third scenario is based on the PHASE II goal to reduce the overall background by one order of magnitude whereas the unsuppressed ^{42}K background will remain the same. B is calculated as in the second scenario but this time the constant is divided by 10 to account for the overall background reduction (e.g. $B = 4667 \cdot 0.026 + 466.7/2$ for the 0.75 mm case). In this case the unsuppressed background is even stronger dominated by ^{42}K. All the detectors perform similar in sensitivity with an optimum between 0.75 mm and 1.00 mm. Most of the BEGe detectors for PHASE II are in this range.

In a fourth scenario a BI goal of 10^{-4} cts/(kg $\cdot$ yr $\cdot$ keV) is assumed and the constant term is further reduced by one order of magnitude (e.g. $B = 4667 \cdot 0.026 + 46.67/2$ for the 0.75 mm case). Now the ^{42}K background would account for 99 % of the total unsuppressed

background. In this scenario an optimum sensitivity is achieved with a 1.25 mm BEGe.

The results for the pure surface scenario of ^{42}K is shown in Fig. D.8b and Tab. D.2 in the appendix. The difference in sensitivity between the hypothetical detectors is larger in this case but the conclusions remain the same.

This sensitivity estimation is strongly simplified assuming that ^{42}K background is constant and not reduced by other techniques such as the LAr veto. More importantly, the aspect of A/E resolution is not considered. In case of poor A/E resolution the gap between SSB and SPB narrows which predominantly effects small FCCD detectors. In this case detectors ≥ 0.75 mm will be strongly preferred as can be seen in Fig. 8.30b.

Nevertheless, the study shows that a thoughtful design of the n$^+$ electrode thickness can help to optimize the sensitivity of a future experiment. Improvements of such a study are expected from including slow pulse variations in the n$^+$ model. This will result in a better description of the gap between SSB and SPB and potentially enable a quantitative description for non-optimal A/E cuts. Measurements of ^{241}Am and ^{90}Sr surface events with other BEGe detectors as well as experience from A/E resolution in GERDA PHASE II will help to better constrain the parameters of such a study.

8.6.3   Application to $2\nu\beta\beta$ Decay and $0\nu\beta\beta$ Decay Majoron Modes

The active volume of the $2\nu\beta\beta$ decay is increased if the n$^+$ electrode is considered semi-active. This will result in an underestimation of the active volume and hence an underestimation of the half-life measurement when using the old model as often done in past analyses. To quantify this effect, $2\nu\beta\beta$ decays are created with DECAY0 and sampled in the total volume of GD91C. The energy spectrum with the old and the new model is shown in Fig. 8.31a.

(a) $2\nu\beta\beta$ decay

(b) $0\nu\beta\beta$ decay with Majoron emission
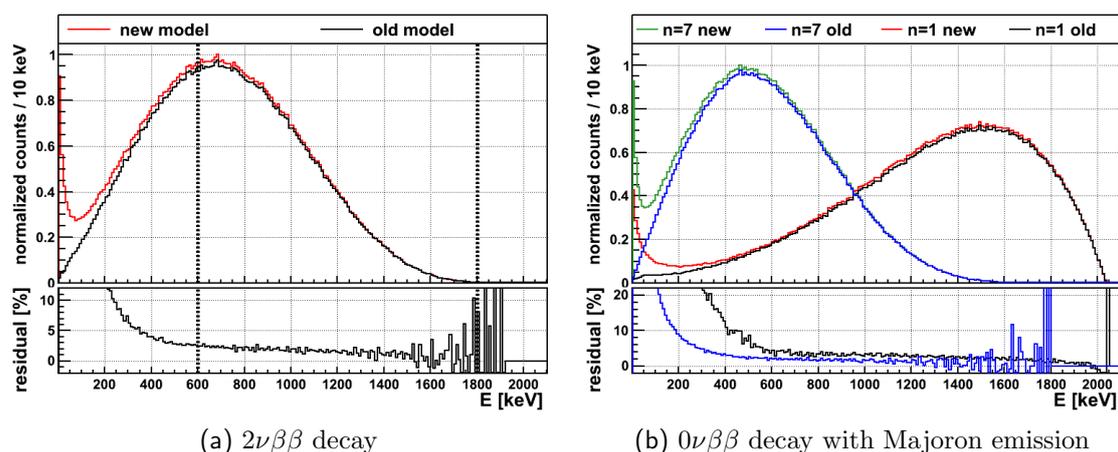
Figure 8.31   Left: Energy spectrum of simulated $2\nu\beta\beta$ decays. Right: Energy spectrum of simulated $0\nu\beta\beta$ with Majoron emission for the two spectral indices of $n = 1$ and $n = 7$. Each decay mode is shown for the new and the old model.

The major increase of events in the new model is below 600 keV. In GERDA this energy range is dominated by ^{39}Ar and hence irrelevant for a $2\nu\beta\beta$ analysis. For germanium detectors not immersed in LAr as e.g. in case of the Majorana experiment, the effect would become more visible. In GERDA PHASE I the spectrum above 600 keV was used to

construct a background model and to fit the $2\nu\beta\beta$ contribution. In the energy range of $600-1800$ keV, the new model predicts $1.9\,\%$ more events than the old one. This difference directly translates into the half-life estimation. It can also be seen that the spectral shape is slightly different with a relatively larger mismatch at lower energies. This might affect the spectral fit in a non-linear way.
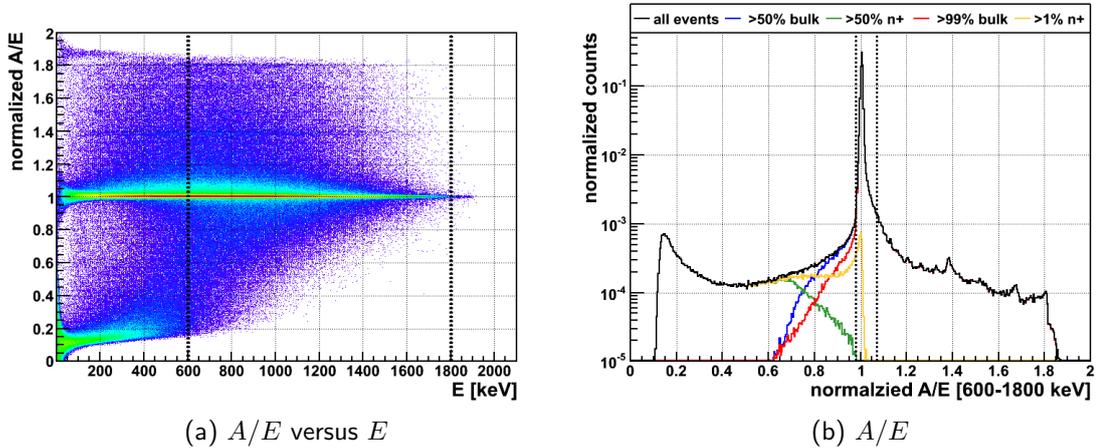
(a) A/E versus E (b) A/E

Figure 8.32 Left: A/E versus E spectrum of simulated $2\nu\beta\beta$ decays with the new n$^+$ electrode model. Right: A/E spectrum in the energy range of $600-1800$ keV separated into majority bulk and majority n$^+$ events. Another separation into $>99\,\%$ bulk events and $>1\,\%$ n$^+$ events is shown.

The $2\nu\beta\beta$ analysis in GERDA PHASE I was performed without pulse shape discrimination. In case that a full background model will be constructed after PSD, the $2\nu\beta\beta$ decay detection efficiency will be reduced. Fig. 8.32 shows the A/E versus E spectrum and the A/E spectrum in the energy range of $600-1800$ keV with illustrated A/E cuts of $0.98 < A/E < 1.07$ as dashed lines. The majority of $2\nu\beta\beta$ events are SSE resulting in a strong SSB. Lower A/E events are created if part of the beta trajectory is in the n$^+$ electrode and by Bremsstrahlung. The fraction of $2\nu\beta\beta$ events below $A/E = 0.98$ is $5.7\,\%$. Fig. 8.32b also shows a separation of event which have $>99\,\%$ of their energy deposited in the bulk and the mutual exclusive case in which $>1\,\%$ of the energy is deposited in the n$^+$ electrode. This illustrates that events directly below the SSB are dominate by Bremsstrahlung ($>99\,\%$ case) until $A/E{=}0.87$.

High A/E events are created by decays in the volume around the p$^+$ electrode. The fraction of events above $A/E = 1.07$ is $4.4\,\%$[25]. The fraction of events in the SSB and hence the survival fraction of $2\nu\beta\beta$ events after the A/E cuts is $90.0\,\%$. Note that the A/E resolution in GERDA may differ which affects the survival fraction; however, the applied A/E cut is rather loose and not strongly affected by the A/E resolution. In any case, for a precise determination of the increased active volume due to the semi-active n$^+$ electrode, this analysis should be repeated for all PHASE II detectors including the final A/E resolution and A/E cut.

A similar investigation has been performed for $0\nu\beta\beta$ decays with Majoron emission which results in a continuous electron energy spectrum as well. The energy spectra of two scenarios with spectral indices $n = 1$ and $n = 7$ are shown in Fig. 8.31b. In general, the

---

[25]This fraction is potentially overestimated due a simulation artifact similar to the high A/E tail observed in the DEP of ^{208}Tl in the MC compared to the data.

impact of the n$^+$ electrode layer is similar as for $2\nu\beta\beta$ decays. In the energy range of $600 - 1800$ keV the number of events in the new model are increased by 2.6% for the $n = 1$ mode and by 1.7% for the $n = 7$. The spectral shapes are affected differently for the different decay modes. The $n = 1$ spectrum peaks at larger energies and shows a stronger variation compared to the old model.

8.6.4   Application to ^{39}Ar Background

^{39}Ar by far dominates the background spectrum in GERDA but is limited to the low energy range (Fig. 5.4). The comparably large rate of the pure beta emitter with 565 keV endpoint energy can be used for in-situ stability monitoring and further investigations of the n$^+$ electrode during PHASE II. ^{39}Ar decays are generated with DECAY0 and sampled in a cylindrical volume 6 cm around GD91C. The energy spectra for the new and the old model are shown in Fig. 8.33b. Additionally the separation between majority bulk and n$^+$ events is shown in blue and red, respectively. Fig. 8.33a shows the corresponding A/E versus E plot for the new model. The major difference between the old and the new model can be seen for energies below 100 keV. The tail above this energy is dominantly produced by p$^+$ electrode events and by events with Bremsstrahlung γ-rays passing through the n$^+$ electrode as can be seen by the dominant contribution of majority bulk events. Hence the tail is not affected by the n$^+$ electrode model.

(a) A/E versus E (b) energy spectrum
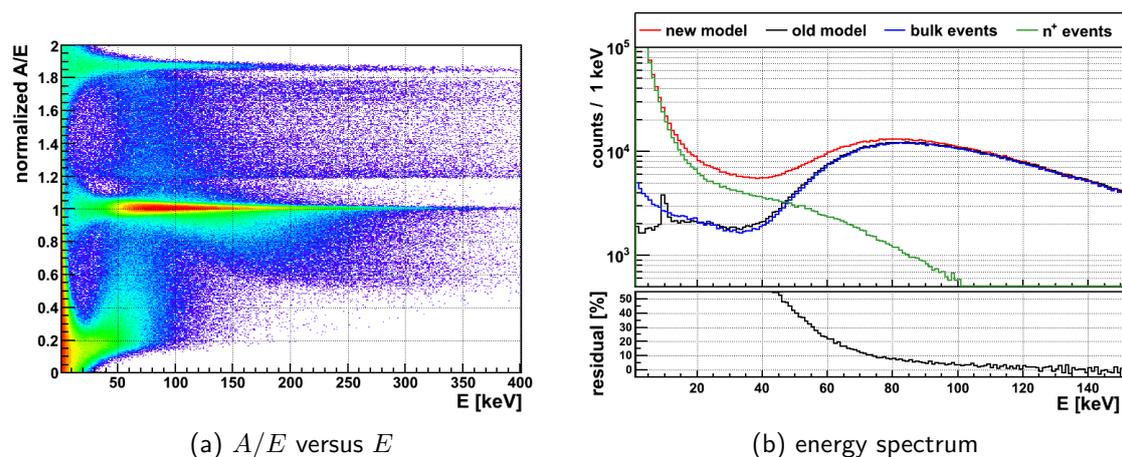
Figure 8.33 Left: A/E versus E spectrum of simulated ^{39}Ar decays with the new model. Right: Energy spectrum for the new model (red) and the old model (black). The new model spectrum is distinguished into majority bulk events (blue) and majority n$^+$ events (green).

The potential for precise in-situ measurements with the large rate of ^{39}Ar is tricky because of three unknowns: (1) The energy spectrum of the emitted electron in the first unique forbidden ^{39}Ar decay is not well known and can introduce a bias. (2) The n$^+$ electrode thickness has an uncertainty. (3) The efficiency of the trigger threshold and the quality cuts has to be well known at low energies[26]. All these uncertainties will influence the measured ^{39}Ar spectrum. However, if two of these uncertainties are controlled, the third can be constrained. The most prominent feature of the ^{39}Ar spectrum is its maximum. In the energy range of $60 - 120$ keV the new model predicts 7.2% more detected events in GD91C for the same ^{39}Ar activity as with the old model. The maximum position of the beta spectrum is determined with a simple Gaussian fit which shows a shift from 84 keV

---

[26]E.g. the trigger efficiency for slow pulses is difficult to determine.

in the old model to $81\,\mathrm{keV}$ in the new model[27]. This shift is due to the larger amount of low energy events.
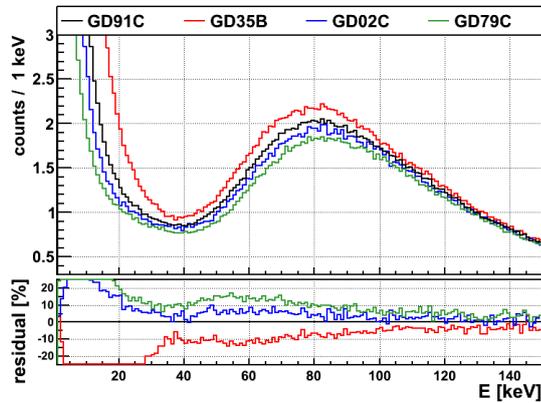
Figure 8.34 $^{39}\mathrm{Ar}$ MC spectrum processed with the new model for selected BEGe detectors in Phase II.

Fig. 8.34 shows the expected $^{39}\mathrm{Ar}$ energy spectra for selected Phase II detectors. The relative difference to GD91C is shown in the residual plot. A count difference of up to $\approx 20\,\%$ can be seen around the maximum between the extreme cases of GD35B and GD79C. This difference encodes the sensitivity of the $^{39}\mathrm{Ar}$ spectrum to the n^+ electrode properties which could be further investigated in-situ in Gerda. The difference between the BEGe detectors is around the same order of magnitude as the difference between the old and the new model making the correct description of n^+ electrode imperative for this type of investigation.

8.7   Conclusion and Outlook

Surface events in BEGe detectors have been investigated with two new n^+ electrode models. First, a simple ad-hoc model based on a linearly increasing charge collection efficiency dividing the n^+ electrode into a non-active dead layer and a semi-active transition layer was used. A single model parameter (the dead layer fraction) was fitted to $^{241}\mathrm{Am}$ energy spectra of all Phase II detectors. It was found that the semi-active part of the n^+ electrode is generally larger than the non-active part for all detectors. Additionally, differences of the n^+ electrode were observed between the detectors. Detectors with large FCCD show a larger non-active region compared to detectors with small FCCD. Furthermore, evidence was observed for a dependence on the original position in the germanium ingot during production: Detector slices cut out closer to the seed end of the ingot show a smaller dead layer fraction compared to slices cut out closer to the tail end.

A more complex n^+ electrode model was developed from first principles based on charge carrier diffusion in order to describe the pulse shape features of surface events. A framework was created to combine traditional pulse shape simulations of bulk events and the new pulse shape simulations of surface events in a post processing of Geant4 simulations. Data of various calibration sources were compared with the new simulations which resulted in an

---

[27]A Gaussian function was used to interpolate the maximum of the spectrum. This is an approximation since the beta spectrum is described by a polynomial which in this case is convoluted with detector effects and additionally influenced by a Bremsstrahlung component. The stated numbers should not be taken at face value and only illustrate the qualitative shift of the maximum.

overall good description of surface events. The strong suppression of surface events with A/E pulse shape cuts could be reproduced. Smaller discrepancies are observed which should be studied. Additional investigations which are believed to result in improvements of the model are:

- Investigation of slow pulse variations. Randomization of n^+ electrode model parameters which would naturally smear A/E distributions as seen in the data.

- Investigation of other non constant recombination models and their effect on the A/E distributions.

- Including of noise and electronic response functions in the pulse creation.

- Processing data pulses and simulated pulses in the same framework with the same quality cuts e.g. with the MGDO and GELATIO framework (Sec. 5.3.1).

- Improvement of the bulk pulse shape simulations with ADL which was treated as a black box in this work. Especially the artifact of energy loss around the groove and the excessive high A/E tail should be corrected.

- Measurement of pulse shape properties on different detector sides of the same detector[28].

- Measurements of ^{90}Sr for other BEGe detectors under the same conditions to determine if model parameters are generic or detector individual.

After development verification and tuning, the new n^+ electrode model was used to predict surface events in GERDA PHASE II. In general, the rate and shape of energy spectra of all surface events are influenced due to the semi-active layer in the n^+ electrode. This will significantly improve the construction of a background model in the future since the major background components are surface events. The strong pulse shape discrimination of ^{42}K surface events seen in PHASE I could be explained with the new model. An A/E cut of $0.98 < A/E$ can effectively separate the majority of bulk events from the majority of surface events. With the optimized A/E cut of $0.98 < A/E < 1.07$ for GD91C, a maximal suppression factor of 45 is predicted for ^{42}K decays close to detector surface and a suppression factor of 145 for decays directly on the detector surface. The suppression efficiency with this cut is dependent on the individual detector, especially the FCCD, and can be as different as 30 % between two extremes of PHASE II detectors. The possibility to choose and optimize the n^+ electrode thickness for ^{42}K suppression in future BEGe detectors was investigated. With an optimal A/E cut, FCCD values ≥ 0.75 mm are favored. In case of a poor A/E resolution, the optimal cut value will shift and becomes very dependent on the individual detector. Detectors with larger FCCD can clearer separate bulk from surface events and are strongly preferred in this case.

The n^+ electrode model also predicts an increase of active volume for internal events such as $2\nu\beta\beta$ decays with up to 2 %. This will improve the precision of further $2\nu\beta\beta$ decay measurements. Finally, the use of ^{39}Ar as an in-situ calibration source was discussed which can be used to further investigate detectors during run-time when surface events are well understood.

---

[28]Some ^{241}Am measurements were taken on the lateral side which could, however, not be analyzed in the frame of this work. They showed a different A/E distribution which could be attributed to a different source collimation, the curved detector surface or different n^+ electrode properties on the lateral side.

Chapter 9

Background Study for a LAr Scintillation Veto in Phase II

The liquid argon (LAr) in GERDA is instrumented as a scintillation veto within the upgrade for PHASE II. Background events that deposit energy inside the germanium detectors and the LAr simultaneously can be vetoed. The veto efficiency is dependent on the optical properties of the LAr, the arrangement of the HPGe array as well as on the detailed geometry and position of the material that contains the radioactive background. Thus, the veto efficiency cannot be determined with calibration sources alone and MC simulations are needed to predict and understand the suppression factors for key background sources in GERDA PHASE II.

This chapter is organized as follows: The general concept of the LAr veto and the background sources that can be suppressed are presented in Sec. 9.1. The final design of instrumentation based on PMTs and light guiding fibers with SiPMs is described in Sec. 9.2. New MC simulations are developed for the LAr veto including the full tracking of optical photons which are presented Sec. 9.3. The simulations are first validated and tuned with a simple geometry in the LArGe setup and later followed by a more complex geometry in a GERDA commissioning string. Finally, the MC simulations are applied to quantitatively predict the background suppression factors in PHASE II and the topology of such event in Sec. 9.4.

9.1 Concept of a LAr Veto for GERDA

The instrumentation of the LAr in GERDA was initially planned in the design for PHASE II of the experiment [123]. The goal is to reduce certain background contributions such that an overall BI of 10^{-3} cts/(kg $\cdot$ yr $\cdot$ keV) can be reached. The background event topologies that can be vetoed are very specific and complementary to other background reduction methods, especially to pulse shape discrimination (PSD) and detector anti-coincidence (AC) cuts.

To veto an event in a single germanium detector with an energy deposition around $Q_{\beta\beta}=$ 2039 keV, the background event must have sufficient remaining energy of $E-Q_{\beta\beta}$ which can be deposited inside the LAr. Five different classes of event topologies are distinguished which can be effectively discriminated. They are illustrated in Fig. 9.1.

1. A high energy γ-ray from outside the LAr veto volume scatters inside a germanium detector and deposits the remaining energy inside the LAr veto volume. E.g. for
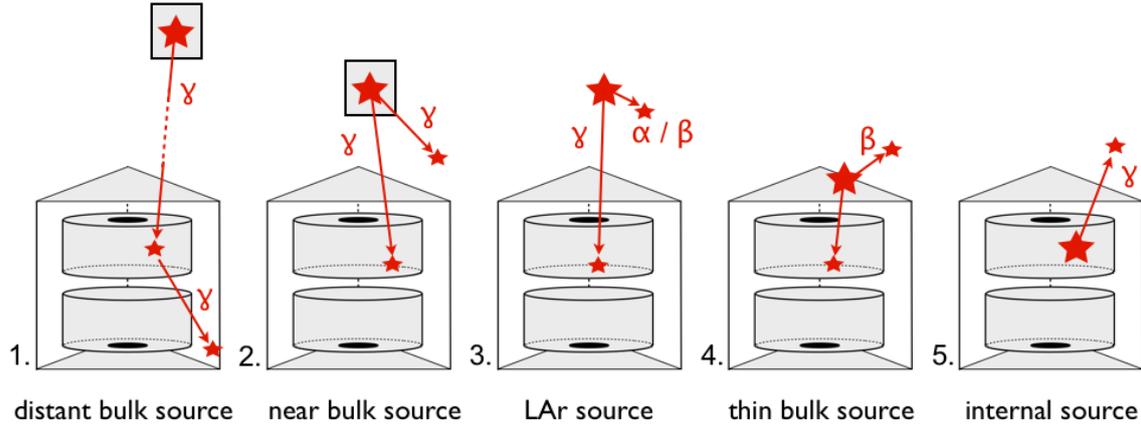
Figure 9.1 Five classes of event topologies which can be discriminated by the LAr veto. Shown are a BEGe pair with holders and the decay and the interacting particles of a likely prominent background source in red. See detailed description in the text.

a 2614.5 keV ^{208}Tl γ-ray creating an event at $Q_{\beta\beta}$, around 575 keV remain to be deposited in the LAr. The reverse sequence is also possible in which the γ-ray first scatters inside the LAr and then goes into the detector.

2. A close decay is emitting multiple γ-rays of which some γ-rays are interacting inside the germanium and others inside the LAr. This topology is likely for ^{214}Bi and ^{208}Tl e.g. inside the detector holders (see Fig. A.2 and A.3 in the appendix for the decay schemes of these isotopes with large γ-ray multiplicity).

3. An alpha or beta decay occurs inside the LAr. A γ-ray deposits energy inside the germanium and the alpha or beta particle depots energy inside the LAr. This event topology is realized by ^{42}K and ^{214}Bi homogeneously distributed inside the LAr. For ^{42}K which is not on or close by the detector surface, only the 2424.1 keV γ-ray with 0.02 % emission probability can trigger an event around $Q_{\beta\beta}$ (see decay scheme in Fig. A.4 in the appendix). For ^{42}K on the surface it is much more likely that an event around $Q_{\beta\beta}$ is triggered by a beta penetrating the n$^+$ electrode (see Chap. 8). In this case however, there is little or no energy deposition inside the LAr and the LAr veto is not effective.

4. A beta decay that occurs inside thin bulk material e.g. the detector holders. In this case the beta can escape the bulk material and deposit energy inside the LAr. The amount of this energy is strongly dependent on the detailed geometry of the material. This event topology is also very likely for the GERDA ^{228}Th calibration sources.

5. An internal decay is emitting a γ-ray which escapes the detector and deposits energy inside the LAr e.g. ^{60}Co or ^{68}Ga as cosmogenically activated isotopes. The same topology occurs for $2\nu\beta\beta$ decays into excited states for which the LAr veto can be used as a selection tag in PHASE II (see Sec. 10.6 for an outlook of such an analysis.).

The presented event topologies are simplified and not unique for a given background component. E.g. a ^{208}Tl decay in a close bulk source is likely to have a type (1) and (2) topology. Another example is a ^{214}Bi decay in the thin silicon holders which is likely to deposit energy in the LAr via the beta (4) and via additional γ-rays (2).

The main background in GERDA PHASE I for semi-coaxial detectors around $Q_{\beta\beta}$ are ^{214}Bi and ^{228}Th in the detector assembly, ^{42}K homogeneously distributed in the LAr and α-emitters on the p$^+$ electrode. For BEGe detectors with a smaller FCCD, ^{42}K on the n$^+$ electrode becomes the dominant contribution around $Q_{\beta\beta}$ (see Sec. 5.5.2 or Ref. [115]). This is also the dominant background expected in PHASE II.

This background study for the LAr veto focuses on background contributions where the veto has a good performance. The following background components are considered:

- ^{208}Tl in the detector holders

- ^{214}Bi in the detector holders

- ^{214}Bi homogeneously distributed in the LAr

- ^{42}K homogeneously distributed in the LAr

- ^{60}Co inside the detectors

- ^{68}Ga inside the detectors

Fig. 9.2 illustrates the simulated event topologies of four distinct background components: ^{214}Bi decays placed in the detector holders, ^{42}K decays homogeneously placed inside the LAr, ^{60}Co decays placed inside the germanium detectors and ^{42}K on the detector surface illustrating a source that cannot be effectively discriminated by the LAr veto. There are 4 plots for each background component shown in a 2x2 matrix. The first column shows the vertex position of decays which deposit an energy in the background index (BI) window of $Q_{\beta\beta}\pm200\,$keV inside a single germanium detector. For these events the position of the energy deposition in the LAr is shown in the second column[1]. The first row shows the projection of the array from the top and the second row shows the projection from the side. The vertex positions illustrate the hot-spot locations in which background decays dominantly contribute to the BI. The energy depositions in the LAr illustrate the location and quantity of scintillation light which is produced and where the LAr veto needs to be most sensitive. The amount of energy deposited in the LAr serves as a first estimate for the qualitative veto efficiency. Later these energy depositions are the source of scintillation light which is fully propagated in the simulation and used to quantitatively predict the veto efficiency.

For ^{214}Bi inside the detector holders, γ-rays deposit energy in the LAr (type 2). This can be seen in the widespread energy distribution around the germanium array. Also electrons escaping the holders can deposit energy inside the LAr as can be seen by the increased and very localized energy depositions around the holder positions (type 4). The energy deposition around the holders is large but those events are more difficult to veto since their scintillation light is significantly shadowed by the holder surface. Events with a widespread energy deposition created by γ-rays are expected easier to veto.

For ^{42}K homogeneously inside the LAr (type 3), the majority of events contributing to the BI are close to the detectors surface. In this simulation, those decays occur with a small distance to the detector surface such that a beta can trigger a germanium event as well as deposits energy inside the LAr. This can be seen especially close to the thin p$^+$ electrodes of the BEGe detectors and semi-coaxial detectors. Due to the vicinity of the detector

---

[1]Plotted is the MC hit coordinate weighted with the hit energy.

(a) ^{214}Bi in the detector holders   (b) ^{42}K in LAr

(c) ^{60}Co inside the detectors   (d) ^{42}K on detector surface
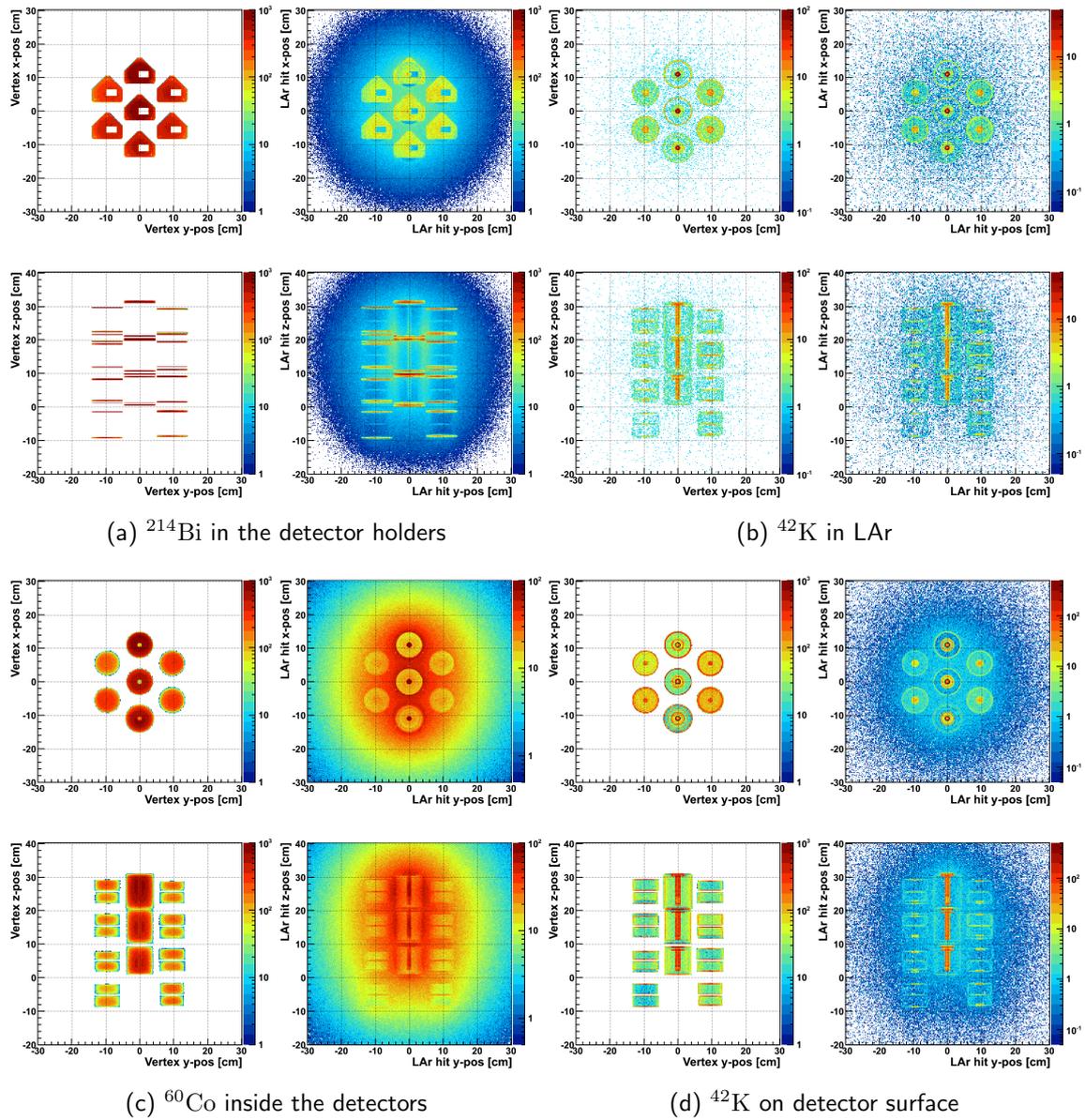
Figure 9.2 MC simulation of four background components. For each component, the left column of plots shows the vertex position of simulated events that deposit an energy in $Q_{\beta\beta}\pm200$ keV inside one germanium detector. This illustrates hot-spots in which decays have an increased chance to generate background. The right columns show the energy deposition inside the LAr of these events. This illustrates the position where scintillation light is created. For each component, the upper row of plots shows the top-down projection of the detector array and lower row shows the projection from the side. The color scale is in arbitrary numbers.

surface, the scintillation light of those events will be largely shadowed. In the bore-hole of the semi-coaxial detectors the light will be completely blocked. Some decay vertices can be seen at a larger distance around the array. Those decays trigger the germanium event with the low probability 2424.1 keV γ-ray. However, the majority of events in this background component is close to the detector and the LAr veto has only a small discrimination power.

The homogeneously sampled and surface sampled ^{42}K events are separated in the background models due to an observed attraction of charged ^{42}K ions towards the detector

surface in the electric field of the detectors. For the surface simulation of ^{42}K, the germanium event is practically always triggered by a beta. The wider spread of the energy deposition around the array is created by γ-rays in some of the final states. However, the major decay mode is the ground state transition with 82 % probability, which has the highest beta energy and no γ-ray. Hence, for this background contribution the LAr veto has almost no sensitivity[2]. Surface and close to surface ^{42}K events in BEGe detectors can be effectively discriminated by PSD as shown in Sec. 8.6.1 with suppression factors of around 150 and 50 respectively. The combination of PSD and LAr veto will not improve the suppression for pure ^{42}K surface decays but increase the suppression of homogeneously distributed ^{42}K decays which predominantly occur close to the surface when detected around $Q_{\beta\beta}$.

A ^{60}Co event inside the detectors will require the two γ-rays (1173.2 keV and 1332.5 keV) and the beta (endpoint 318 keV) to be at least partially interacting in the germanium to trigger an event in the BI region. Such topologies can be efficiently discriminated by PSD. The excess energy in form of a scattered γ-ray deposits energy in a small area around the germanium array (type 5).

It becomes clear that the majority of events around $Q_{\beta\beta}$ deposit energy in-between the detector array. This creates significant shadow effects for a light detector outside of the array. Additionally, the XUV photons have an attenuation length around the same size as typical photon trajectories in the GERDA array. The shadowing as well as the distance from creation to detection or from creation to a wavelength shifting surface has to be considered with the propagation of optical photons.

9.2   Veto Design

The 128 nm LAr scintillation light needs to be shifted to larger wavelength before detection for detection of single photons). The attenuation length of scintillation photons in the GERDA LAr is estimated to be ≈ 60 cm and requires a surface with wavelength shifter (WLS) properties relatively close to the production site, i.e. in-between or around the detectors. The necessary proximity to the germanium array has to be optimized against the radioactive background induced by the instrumentation components.

Two different independent veto design concepts were suggested for GERDA: (1) A **PMT array** on top and bottom of the germanium detector array and (2) a curtain of wavelength shifting light guiding **Fibers** cylindrically surrounding it. The two design concepts were initially competing and a MC simulation campaign was initiated to assess the veto efficiencies for key background components. The Fiber design had a small advantage over the PMT array collecting more light on a larger surface closer to the germanium array. This especially improved the rejection of events with small excess energy in the LAr and a consequently small scintillation photon production. However, the concept of the PMT array was successfully operated and had proven its performance during longterm operations in the LArGe facility [156]. Eventually, both designs were merged into the so called **Hybrid** design forming a largely redundant scintillation veto for GERDA PHASE II.

The final Hybrid design is shown in Fig. 9.3. The instrumented LAr volume has a cylin-

---

[2]Previous investigations showed a LAr veto suppression of around 10 % for this background. Due to this small value detailed simulations for this background are not repeated here.
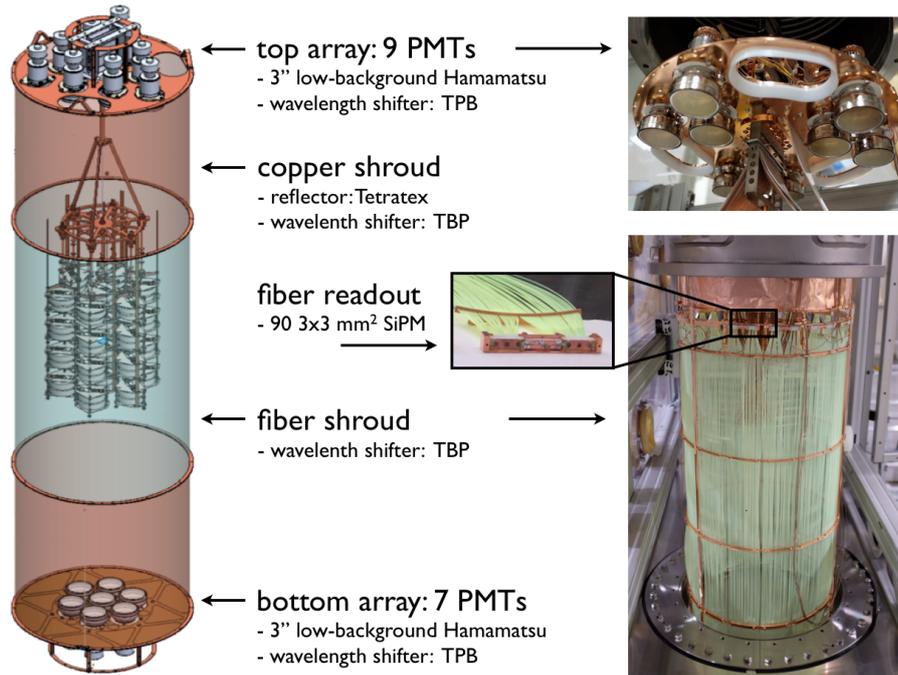
Figure 9.3 Design of the LAr veto.

drical shape of 49 cm diameter and 220 cm height. It is confined by the PMT array on the top and the bottom and by two copper shrouds and the Fiber shroud on the lateral sides. The Fiber shroud forms the center of the cylinder around the height of the germanium array.

The PMT array consists of 3" low-background Hamamatsu PMTs (R11065-10/20 MOD) with less than 2 mBq per PMT. 9 PMTs are in the top array looking downwards and 7 PMTs are in the bottom array looking upwards. The entrance windows of the PMTs are coated with tetraphenyl butadiene (TPB, $C_{28}H_{22}$) as a WLS. Each PMT has an individual read out channel.

The Fiber shroud has a height of 100 cm and is formed by 810 1x1 mm^2 thick light guiding fibers which are also coated with TPB as a WLS. The individual fibers are bend on the bottom of the shroud and both ends are optically coupled to SiPMs on the top. A total of 90 3x3 mm^2 SiPMs are combined into 15 readout channels. The total fiber surface of 3.2 m^2 is collecting XUV photons from inside and outside the shroud, thus extending the sensitive LAr volume beyond the 49 cm diameter cylinder. Simulations have shown that the extended volume is aiding the background rejection for type (1) event topologies (Fig. 9.1) where either the decay or the scattered γ-ray interaction occurs outside the cylinder. After wavelength shifting on a fiber surface the TPB has an isotropic photon emission which results in some light being trapped inside the fiber, some emitted back and some passing through avoiding total reflection inside. The latter effect serves as a WLS entrance window for photons from outside the cylinder which also increases the veto efficiency for the PMT array. In a similar way, the backward emission reflects some of the inside light back into the cylinder which can then be detected by a PMT or a different fiber.

The cylindrical copper shroud segments above and below the fiber shroud are coated with a Tetratex textile treated with TPB. Together this surface acts as a wavelength shifting, non-specular reflector.

9.2.1 ^{42}K Mitigation With a Mini-Shroud

From the Phase I commissioning data and the Phase I background model it is clear that special measures are needed to strongly mitigate the ^{42}K background. The solution in Phase I was the copper Mini-Shroud (MS) which was surrounding each detector string individually. However, this solution is not suitable for Phase II since it blinds the crucial volume around the strings from the LAr veto. A MS solution for Phase II ideally needs to fulfill the following criteria:

1. Hermetically closed to prevent convection of neutral ^{42}K and ^{222}Rn.

2. Electrically conductive to apply a potential that prevents the drift of charged ^{42}K ions close to the detectors or onto their surfaces.

3. Transparent for XUV or optical photons in order to maximize the LAr veto efficiency.

Various options were suggested to meet these requirement: (1) A hermetically closed conductive Phase I-type copper MS with large area SiPMs inside the shrouds to additionally instrument this LAr volume. This design option was coined **Super-Hybrid**. (2) A nylon MS coated with WLS such that XUV photons are shifted on the MS surface and then propagate to the outside as visible photons. This design was named **Nylon-Hybrid**. (3) A copper mesh MS which is put on electric potential. This option was refereed to as **MMS-Hybrid**. These options were compared with the default possibilities to either use the standard Phase I MS (**SMS-Hybrid**) or to use no MS (**Hybrid**). A summary of the MS options is shown in Tab. 9.1.

Table 9.1 Features of different Mini-Shroud options.

Mini-Shroud option	hermetic	conductive	transparent
Super-Hybrid	yes	yes	(yes)
Nylon-Hybrid	yes	no	yes
MMS-Hybrid	no	yes	yes
SMS-Hybrid	yes	yes	no
Hybrid	no	no	yes

The comparison of the MS solutions was performed with a MC campaign testing the effect on the LAr veto. The efficiency to mitigate ^{42}K as well as the hardware feasibility was tested with dedicated measurements in LArGe. For this purpose the LAr was enriched with artificially produced ^{42}K.

The Nylon-Hybrid was found to be the best option and will be used in Phase II. A nylon MS is shown in Fig. 9.4 (a). MC simulations show that the veto efficiency is not reduced by the nylon MS compared to no MS in the array. For some background components an even increased efficiency is observed which is due to the close wavelength shifting of the photons inside the germanium array. Additionally, the light can be trapped by total reflection inside the shroud and guided to both ends as can be seen in the picture. This is also observed in the MC simulations and is illustrated in Fig. 9.4 (b) and (c) with simulated photon trajectories. This effect can guide some photons towards the top and bottom PMT arrays and increase the veto efficiency for these instrumentation parts.
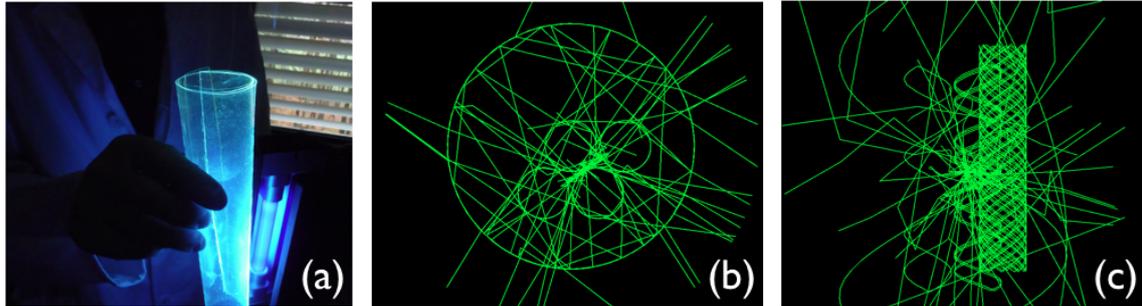
Figure 9.4 Illustration of nylon MS light guiding. (a) Illumination of a WLS coated nylon MS with black light. (b) Top view: Optical photon trajectories created by a 3 keV energy deposition in the LAr. Light guiding is visible in the nylon MS as well as in the large instrumentation shroud. (c) Side view: Optical photon trajectories of a different 3 keV event. Photons can escape on the top and bottom of the MS towards the PMT array.

9.3 Monte Carlo Simulations with Optical Photons

9.3.1 Optical Photon Tracking

MC simulations of the LAr veto are performed with MaGe (Sec. 5.3.2). The full tracking of optical photons is implemented for this purpose. The tracking of many thousands optical photons per event is significantly increasing the CPU requirements. Thus, to save CPU power and storage, the optical tracking can be restricted to events that fulfill certain requirements which is illustrated in Fig. 9.5. The optical photons are created by the `G4Scintillation` process along a particle track. Additionally, also Cherenkov photons are created along the track which, however, have a negligible contribution. First the high energy particles are propagated while the optical photons are stored in a waiting queue. Upon processing all other particles, a decision is made whether the optical photons are propagated. A typical requirement is the deposition of $Q_{\beta\beta}\pm200$ keV inside the germanium array or a detector anti-coincidence. If the optical photons are processed the event is stored with additional information for the photons: the sensitive surface which is hit, the incident angle and the wavelength.
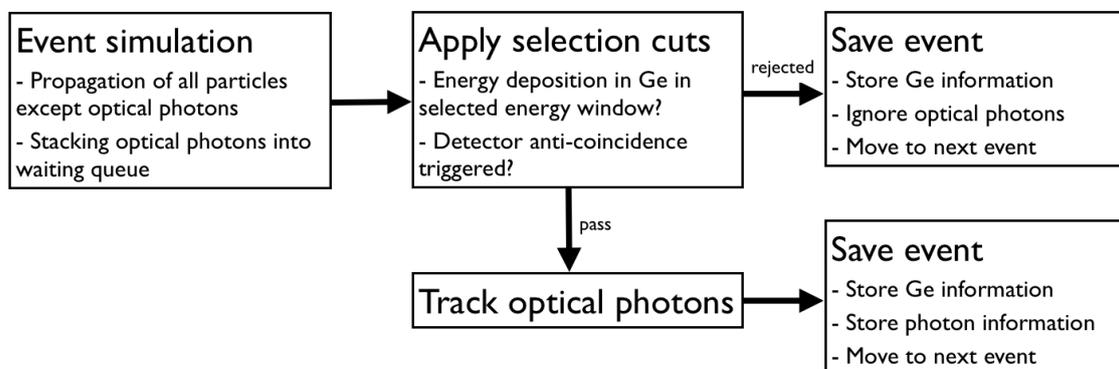
Figure 9.5 Flow chart of online event processing for MC simulations with optical photon tracking.

The main output of the MC simulation is the number of photon electrons (p.e.) per event inside a PMT or SiPM[3]. The p.e. yield in the MC is defined after all detection efficiencies and can be directly compared to the single photo electron signal in the data. The veto is sensitive to singe photon detection and thus, a MC event is vetoed when a single p.e. is registered in a PMT or SiPM.

The CPU time needed to simulate an event with photon tracking is strongly depending on the specific event topology. On average, a ^{208}Tl event in the detector holders requires 20 s to be simulated. The same event without photon tracking requires on average 4 ms on the same system. For background components with smaller Q-value the simulation time decreases.

9.3.2   Optical Properties

GEANT4 requires the implementation of optical properties for materials and surfaces in the setup in order to faithfully track the optical photons. Some of these properties have been measured, some are known from literature and others are based on assumptions and approximations. The key properties which are expected to be most influential on the simulation are the light yield and the attenuation length of the LAr (see also Sec. 4.3.1 for general LAr properties).

Table 9.2 Implemented properties of LAr. The LAr spectrum is defined as a Gaussian with 2.9 σ at 128 nm. Values determined from literature and measurements (see text).

property	GERDA LAr
emission spectrum	128 nm (2.9 σ)
triplet lifetime	922 ns
singlet lifetime	5.95 ns
yield ratio (singlet/triplet)	0.23
light yield	28.120 γ/MeV
attenuation length XUV (< 200 nm)	60 cm
attenuation length optical (> 200 nm)	1000 m

The implemented properties of the LAr are summarized in Tab. 9.2. The triplet lifetime was determined with a dedicated measurement in the GERDA cryostat. The light yield is scaled to the triplet lifetime and is roughly a fraction of 0.7 compared to pure LAr [156]. The attenuation length is set to 60 cm as an educated guess but remains largely unknown. A dedicated in-situ measurement in the GERDA cryostat was performed [157, 158] but remains inconclusive at the time of this analysis. The refractive index is implemented as $\eta = \sqrt{\epsilon(\lambda)}$ with $\epsilon(\lambda)$ calculated with the Bideau-Sellmeier formula [159]. The wavelength dependence of the refractive index is shown in Fig. 9.6a. The Rayleigh scattering is strongly dependent on the wavelength ($\propto \lambda^{-4}$) and the scattering length is shown in Fig. 9.6b for LAr. At 128 nm the scattering length is ≈ 70 cm but changes rapidly within the width of the emission peak.

---

[3]At the time of this work the Fiber shroud was implemented as a single entity and only the detected number of p.e. in the full shroud was available.

(a) refractive index

(b) Rayleigh scattering length
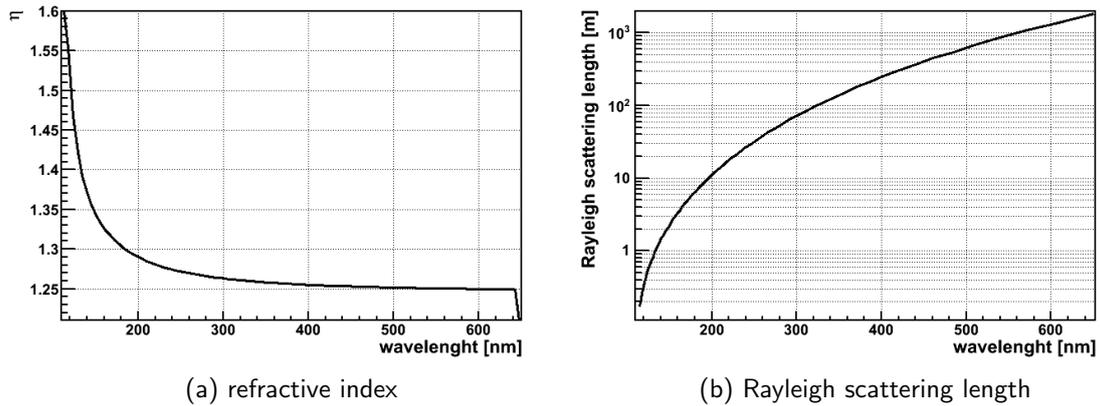
Figure 9.6 Refractive index (left) and Rayleigh scattering in LAr for different wavelengths. Shown are values that are implemented in MaGe and used for the MC in this work.

The WLS tetraphenyl butadiene is used to transform 128 nm scintillation photons into detectable optical photons. The TPB emission spectrum is rather wide and peaks around 425 nm. A measured spectrum is shown in Fig. 9.7a (red curve) [160, 161]. Also shown in this figure is the implemented LAr scintillation spectrum for comparison (black curve). The TPB is applied to different surfaces such as Tetratex, PMT glass, the fibers and nylon. Different admixture of TPB with polystyrene is optimal for different surfaces to assure adhesion and long-term stability. The different admixtures show a similar spectral shape but a different wavelength shifting yield due to different TPB concentrations. The XUV yield is set to 0.84 for nylon and 1.2 for all other materials. The time-constant for TPB is set small ($\tau = 0.01$ ns) and the refractive index is set to 1.15.

(a) emission spectra
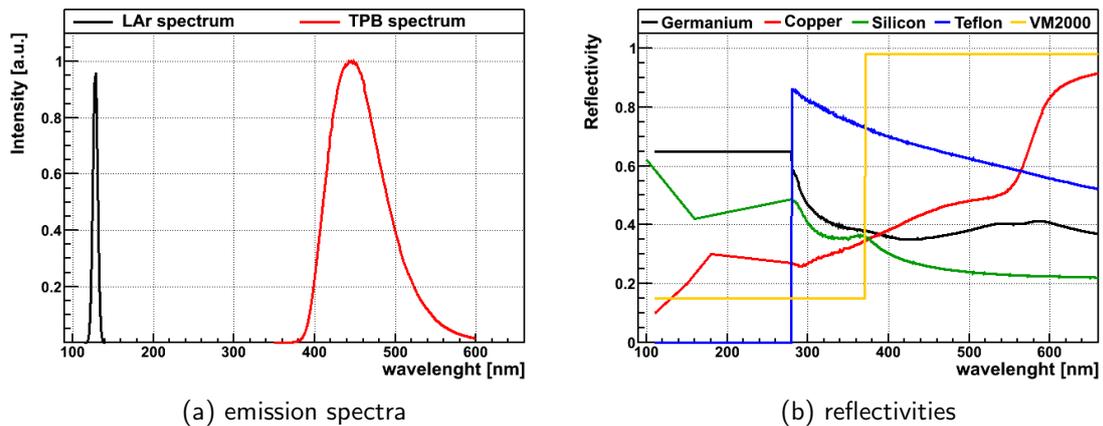
(b) reflectivities

Figure 9.7 Left: Emission spectrum of scintillation light in LAr (black) and of wavelength shifter TPB (red) as implemented in MaGe. The TBP spectrum is measured. Right: Reflectivities for different materials in GERDA as implemented in the MC.

The reflectivity of optical photons on metals is dependent on surface properties. The polishing is set to 50 %. The wavelength dependent reflectivity from XUV to optical photons is crudely estimated from various literature values, measurements and tuned to data from the LArGe setup below. The implemented reflectivities for germanium, copper, silicon, teflon and VM2000 are shown in Fig. 9.7b.

9.3.3 Tuning and Validation of MC Simulation

The simulation with optical photons can be compared with data to test its validity. In addition it is possible to tune some of the lesser known optical properties to the experimental measurements. A first validation is performed with the LArGe setup containing a single BEGe detector. ^{228}Th, ^{226}Ra and ^{60}Co calibration sources were immersed into the LAr as internal sources and placed outside the cryostat as external sources [156]. The setup is shown in Fig. 9.8a.

(a) source positions in LArGe

(b) energy spectra for data and MC
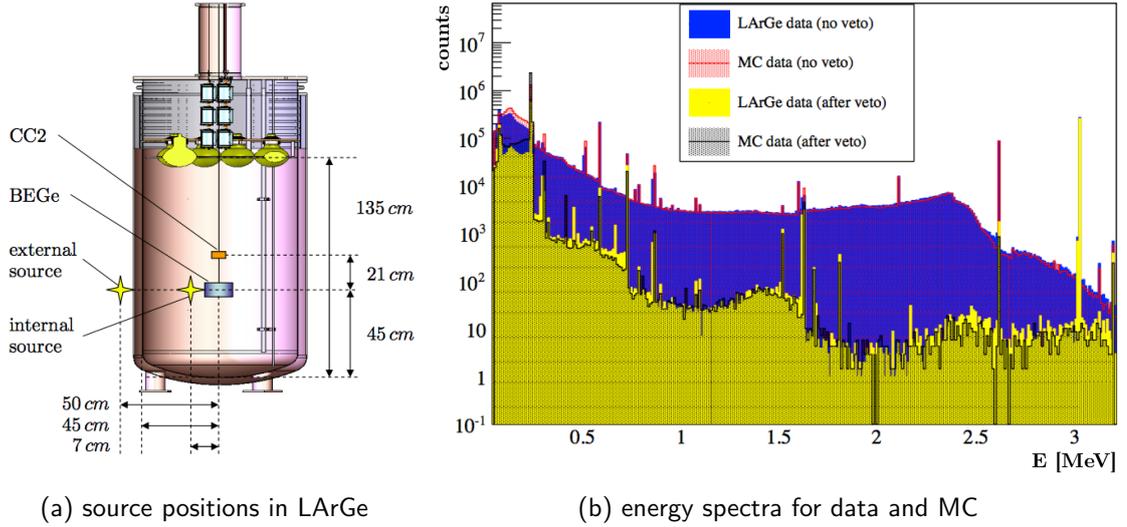
Figure 9.8 Left: Illustration of measurement in LArGe with internal and external sources [156]. Right: Comparison of data and MC with and without LAr veto. Data is taken with an internal ^{228}Th source [156]. MC is performed with light propagation and optimized optical properties [162].

This simple geometry can be used to test the general performance of the simulation. The comparison between data and MC is based on suppression factors (SF) defined for events that deposit an energy in $Q_{\beta\beta}\pm200$ keV inside a single HPGe detector:

$$\text{SF} = \frac{\text{events before cut}}{\text{events after cut}}. \tag{9.1}$$

The simulation of the calibration sources are based on the dominant isotopes ^{208}Tl, ^{214}Bi and ^{60}Co which can trigger an event in $Q_{\beta\beta}\pm200$ keV. Optical photons are only tracked for events in this energy range. The WLS thickness, WLS efficiency, material reflectivities and LAr light yield is tuned in the simulation to achieve the best match of the SFs. The LAr light yield is set to 20565 scintillation photons per MeV. However, the LAr in LArGe and its properties can be different to the one in the GERDA cryostat. This value cannot be transferred to the GERDA case. Another validation is later performed with a PHASE II commissioning run in the GERDA cryostat with a more complex geometry. The other tuned optical parameters are those presented in the section above.

The measured SFs and simulated SFs based on the tuned parameters are shown in Tab. 9.3. ^{228}Th and ^{228}Rn source measurements exist for internal and external sources. Internal sources show significant larger SFs if the betas penetrate the source encapsulation and if additional γ-rays deposit energy in the LAr. The fundamental difference is illustrated in Fig. 9.1 between case (1) for the external sources and case (2,3) for the internal sources.

Table 9.3 Comparison of suppression factors from measurements and simulations in LArGe.

source	SF data [156]	SF MC
^{208}Tl internal	1180 ± 250	909 ± 235
^{214}Bi internal	4.6 ± 0.2	3.8 ± 0.1
^{60}Co internal	27 ± 1.7	16.1 ± 1.3
^{208}Tl external	25 ± 1.2	17.2 ± 1.6
^{214}Bi external	3.2 ± 0.2	3.2 ± 0.4

The simulation can well reproduce the order of magnitude of the effect. Some discrepancies in the MC can be seen for the ^{60}Co internal and ^{208}Tl external source. For ^{60}Co the difference is attributed to a poorly known source geometry. A dedicated investigation showed that a systematic change of the encapsulation thickness has a strong effect on the SF. For the ^{208}Tl external measurement the differences are attributed to uncertainties of the distance between detector and wire source. A larger distance reduces the chance of other initial γ-rays hitting the LAr.

A full scale simulation is performed for the internal ^{228}Th calibration source, tracking the optical photons for all events. With this simulation it is possible to compare the LAr veto performance over the full energy range. All successive decay chain isotopes are included in the simulation. The energy spectra of the data and MC before and after LAr veto is shown in Fig. 9.8b. The MC spectra are scaled to the 2614.5 keV peak in the data before the veto is applied. The comparison shows a remarkable agreement between MC and data over multiple orders of magnitude and a wide energy range. Small discrepancies are visible at low energies and for some γ-lines. This is attributed to a potential out-of secular equilibrium state of the source and imperfect implementation of the BEGe size and n$^+$ electrode thickness.

9.4   Background Suppression in the GERDA Phase II Array

First, another validation of the MC simulations is performed with preliminary data from a PHASE II commissioning string. This measurement has a more complex geometry than the LArGe measurement and is performed in the same LAr that will be used in GERDA PHASE II. After tuning and validation, the MC is applied to the full tentative PHASE II array and predictions are made for SFs of important background components in PHASE II.

9.4.1   Tuning and Validation with Phase II Commissioning Data

The setup of the PHASE II commissioning string in April 2015 with 8 BEGe detectors in 4 pairs is illustrated in Fig. 9.9. The data was taken with a ^{228}Th calibration source around the height of the second BEGe pair. A nylons MS was deployed around the detector string. During the data taking 5 out of 8 detectors were operational and fully depleted which are highlighted in green. Only those detectors are used for the comparison with the MC[4]. In the LAr veto, 8 out of 9 PMTs were fully operational in the top PMT array and 5 out of 7 PMTs in the bottom array. The non working PMTs are excluded in a post processing

---

[4]Detectors that were operational but not fully depleted are excluded from the analysis since their behavior cannot be properly described with MC which would result in a biased comparison.
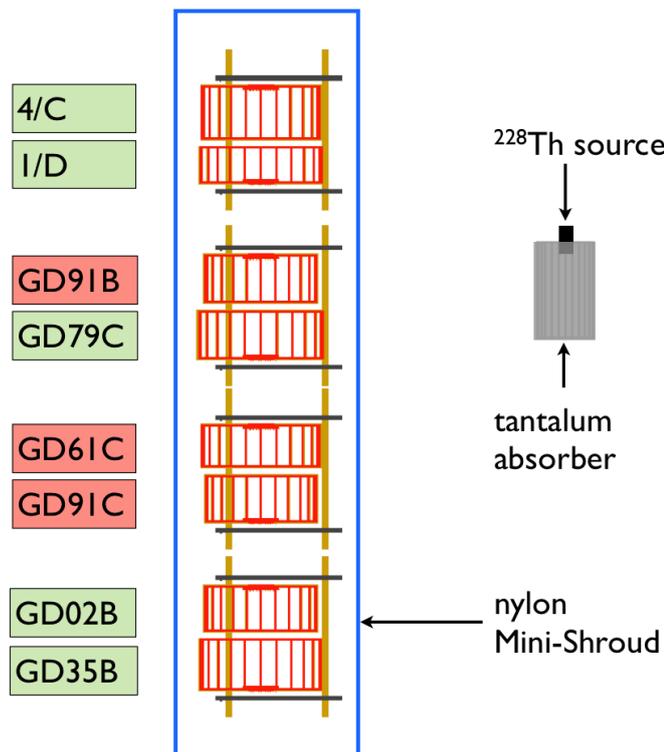
Figure 9.9 Illustration of the PHASE II commissioning string in April 2015. Shown are 8 detectors in 4 pairs surrounded by the nylon MS. The calibration source is around the height of the second pair. The color coding of the detector name tag shows fully working detectors used for analysis (green) and omitted detectors (red).

of the MC simulations. All SiPM channels were working.

At the time of this analysis the implemented MC setup still includes two main approximations. Of the material around the detectors only the holders are implemented. Electronic components and cabling are not present. Any additional material will result in dead volume in which energy can be deposited instead of the LAr. This will reduce the veto performance. Another effect is the shadowing of additional material e.g. by the cables. The other approximation is the Fiber shroud which is implemented as a single cylindrical volume and not as individual fibers. The cylindrical surface in the MC is overestimating the solid angle which is covered by the Fiber shroud. The individual fibers can overlap and reduce the coverage by up to a factor of 2. Additionally, the single light guiding volume will allow some additional light trajectories in the MC which would otherwise not be possible.

The simulation of the calibration source and the commissioning string is first performed with the nominal optical parameters as described above. The simulated photo electrons (p.e.) per event can be compared to the measured photo electrons in the data. The simulated p.e. spectrum for the individual veto components is shown along with the measured p.e. spectrum in Fig. 9.10a. The maxima of the distributions are about an order of magnitude larger in the MC than observed in the data. This indicates a strong mismatch of the LAr light yield or a mismatch in the propagation - detection chain, i.e. a WLS efficiency or p.e. yield. In addition, the discrepancy seems to be different between the individual veto components.

Two representative parameters are chosen to tune the MC to the data: (1) The LAr light yield which directly effects the number of p.e. per event in a near linear scale for all LAr components. With this parameter the maxima of the p.e. distributions can be matched. (2) The area coverage of the Fiber shroud which is in any case overestimated in the MC. This parameter is implemented as an additional efficiency for the detection of a single photon with the Fibers[5] and can be used to match the difference between the PMT and Fiber distribution.

(a) nominal optical properties   (b) tuned optical properties
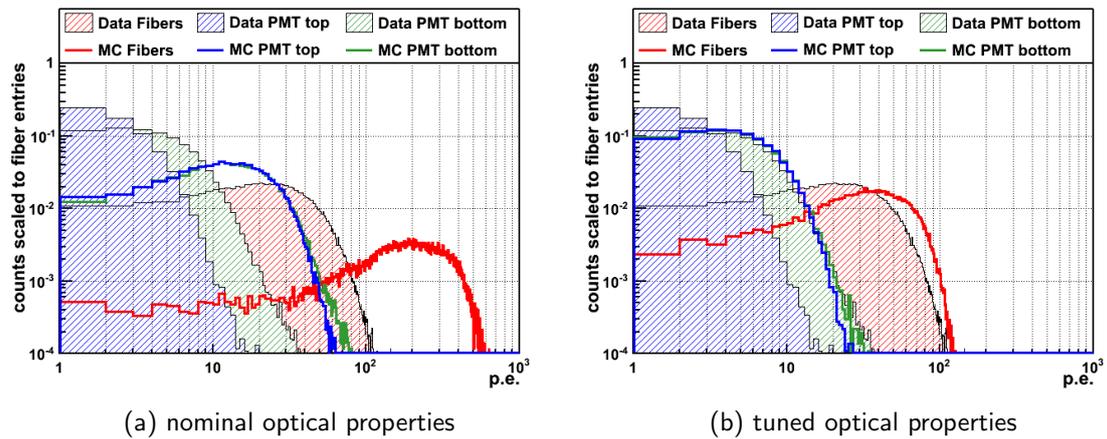
Figure 9.10 Photo electron spectra for events of the ^{208}Tl calibration source and tuned MC simulation in the ROI.

The same simulation was iterated about 10 times with manually changing the two parameters. The p.e. distribution of the top and bottom PMT array are very similar in the MC but different in the data. The difference could be explained by the detector cables, mainly going upwards and blocking the light for the top PMT array in the data. Hence the matching was performed on the bottom PMT array (green). A light yield of 30 % compared to the nominal value and a Fiber coverage of 60 % is found as best describing the data of both veto components. The optimized p.e. distribution can be seen in Fig. 9.10b.

The tuned LAr light yield of 8436 photons per MeV is very low and does not match the measured triplet lifetime of 922 ns in the GERDA cryostat. However, the effect of the light yield on the p.e. distribution and the SFs is strongly correlated with other optical parameters common to both veto components as e.g. the WLS efficiency. The tuned light yield can be interpreted as an effective parameter empirically matching the p.e. distributions to the data[6]. The tuned Fiber coverage can be interpreted as an effective parameter scaling between the PMT and Fiber p.e. distributions; however, the derived value of 60 % is realistic.

In addition, the SFs were compared which are defined in the regions $1840 - 2090$ keV and $2110 - 2140$ keV for this purpose[7]. The experimental SFs as well as the simulated nominal and tuned SFs are summarized in Tab. 9.4. The top part of the table shows the suppression

---

[5]Note that applying an additional efficiency to the Fiber read out is only a crude approximation to fix the p.e. distribution and SFs for the Fiber component. The secondary effect where the Fiber shroud is acting as a WLS surface or entrance window from the outside for the PMTs as well as for the Fibers themselves is not addressed.

[6]An advantage of scaling the LAr light yield instead of a detection efficiency of the photons is the reduction of photons that need to be simulated which reduces the computing requirements.

[7]The energy range was chosen to exclude known γ-lines considering the resolution in the data.

of the individual veto components. The bottom part of the table shows the suppression for each detector if the full veto is applied. The SF in the data are provided by [163] and are corrected for randomly vetoed events using a pulser acceptance which is written in parentheses in the second column of Tab. 9.4.

Table 9.4 Comparison of suppression factors (SF) for a ^{228}Th calibration source with the commissioning string in April 2015. The SF is defined in the energy regions $1840 - 2090$ keV and $2110 - 2140$ keV. The columns show the SF in the data corrected for pulser acceptance (written in parentheses), the SF of the nominal MC, the SF of the tuned MC and the SF of the tuned MC in case all detectors were operational. The first row shows the combined LAr veto SF followed by each component. The last rows show the SFs with the combined LAr veto for each detector individually.

Component	data (pulser) [163]	nominal MC	tuned MC	tuned MC all det.
LAr veto	67.7 ± 1.8 (86.7 %)	77.1 ± 4.8	66.9 ± 2.6	88.1 ± 3.4
Fiber	54.1 ± 1.2 (88.9 %)	76.8 ± 4.7	64.7 ± 2.5	85.5 ± 3.2
PMT all	25.6 ± 0.4 (95.4 %)	57.0 ± 3.1	30.0 ± 0.8	35.7 ± 0.9
PMT top	5.06 ± 0.1 (97.8 %)	39.2 ± 1.8	13.8 ± 0.3	15.0 ± 0.3
PMT bottom	14.5 ± 0.2 (96.6 %)	40.7 ± 1.9	14.3 ± 0.3	16.7 ± 0.3
4/C	115.7 ± 7.6 (86.8 %)	150.7 ± 21.5	157.2 ± 15.1	160.3 ± 15.6
1/D	83.7 ± 4.9 (86.8 %)	149.8 ± 23.8	101.9 ± 9.0	136.6 ± 14.3
GD91B	-	-	-	99.8 ± 8.9
GD79C	49.0 ± 1.7 (86.7 %)	48.2 ± 3.7	40.6 ± 2.0	71.7 ± 5.1
GD61C	-	-	-	44.3 ± 4.4
GD91C	-	-	-	41.5 ± 5.0
GD02B	50.2 ± 6.2 (86.7 %)	28.2 ± 6.5	35.7 ± 6.1	38.6 ± 7.1
GD35B	64.1 ± 10.9 (86.7 %)	38.4 ± 11.8	33.9 ± 6.7	34.6 ± 6.9

The nominal MC is strongly overestimating the suppression of the individual veto components. However, the full veto suppression is not as strongly affected indicating a larger redundancy in the MC than in the data. With the tuned simulation, the full veto suppression perfectly matches the data. The SFs of the individual components are now better reproduced but still slightly overestimated. The strong discrepancy between top and bottom PMT array can also be seen in the SFs. However, the overestimated top PMT array as well as the PMTs in general do not have a strong contribution to the overall SF of the LAr veto. The dominant veto component is the Fiber shroud as can be seen in the data as well as in the MC.

The last column of Tab. 9.4 shows the tuned MC case in which all detectors are set active. In this scenario the overall veto performance is increased. This effect is especially strong for individual detectors next to a previously inactive detector. The reason is the additional dead volume where the energy of scattered γ-rays can be lost from the veto. In case the neighboring detectors are active, those events are removed by the anti-coincidence veto and do not enter into the SF calculation of the LAr veto. In case of inactive detectors in the GERDA PHASE II array the LAr veto performance will be significantly reduced compared to the predictions in this work.

A full scale simulation of the same setup is performed with the tuned parameters and the optical photon tracking for every germanium event. This allows to see the suppression
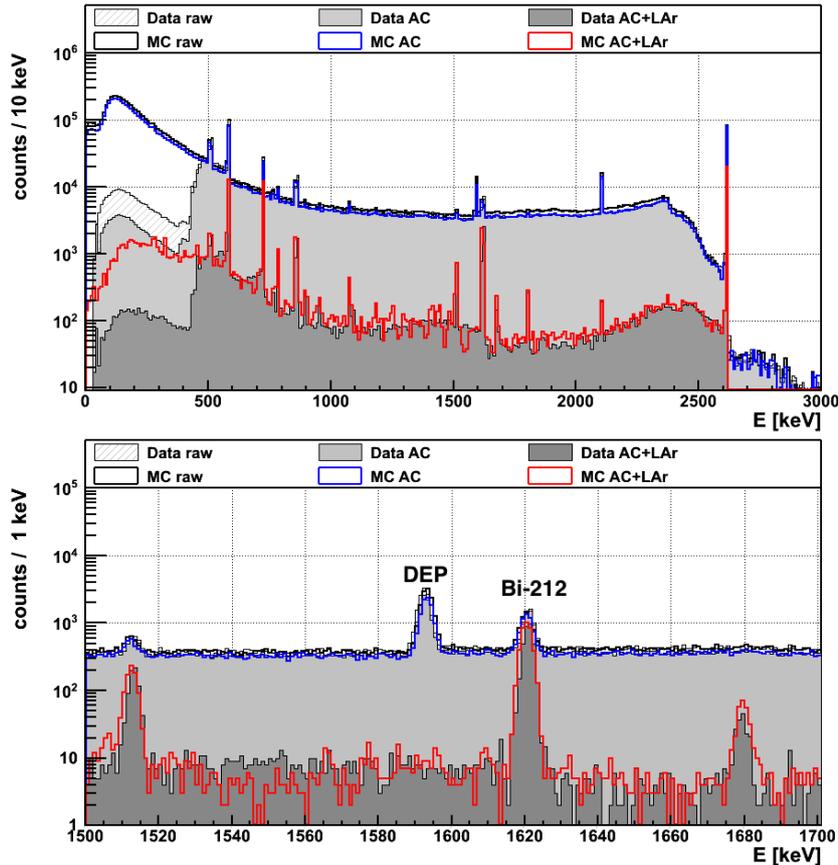
Figure 9.11 Energy spectrum of the ^{208}Tl calibration source and the tuned MC simulation. The unsuppressed MC spectrum is scaled to the data in $1700 - 2500$ keV.

of the LAr veto over the full energy range. The vetoed and non-vetoed energy spectrum from this simulation as well as from the data is shown in Fig. 9.11. The non-vetoed MC spectrum is scaled to the data in an energy range $1700 - 2500$ keV. The trigger threshold in the data was around 500 keV. The simulation includes the dominant isotopes ^{208}Tl and ^{212}Bi but small discrepancies may arise due to other contributions at lower energies. The suppression of the full LAr veto is well in agreement over a wide energy range.

The tuning of the light yield and the Fiber coverage could significantly improve the agreement between data and MC for the p.e. spectra as well as the SFs. The suppression of the energy spectra is reproduced over a wider energy range which gives confidence that the MC simulations with optical photons can be used to extrapolate the veto efficiency for a variety of background components in the full PHASE II array.

9.4.2   Prediction for the Phase II Array

The MC simulations of key background sources are performed with the tentative GERDA PHASE II array (Fig. 5.7). The simulations are the same as shown in Fig. 9.2 but this time including the optical photon tracking. The photon tracking is only activated for events with an energy of $1800 - 2300$ keV in the HPGe detectors to save CPU time. The LAr veto is triggered if a single p.e. is registered in one of the instrumentation parts.

The germanium energy spectra of the simulated background contributions are shown in

Fig. 9.12. The raw spectra include events with all detector multiplicities and are show in black. The spectra after AC cut are shown in blue and after AC and LAr veto cut in red. Also highlighted is the ROI used to determine the SF, taken as $Q_{\beta\beta}\pm200\,\text{keV}$ with known γ-lines excluded from the region. Those are the SEP at 2103.5 keV for ^{208}Tl and the 1935.5 keV, 1994.6 keV, 2010.8 keV, 2016.7 keV, 2021.6 keV, 2052.9 keV, 2085.1 keV, 2089.7 keV, 2109.9 keV, 2118.6 keV and 2120.0 keV γ-lines for ^{214}Bi[8].

(a) ^{208}Tl holders

(b) ^{214}Bi holders

(c) ^{214}Bi homoegeneous

(d) ^{42}K homoegeneous

(e) ^{60}Co internal

(f) ^{68}Ga internal
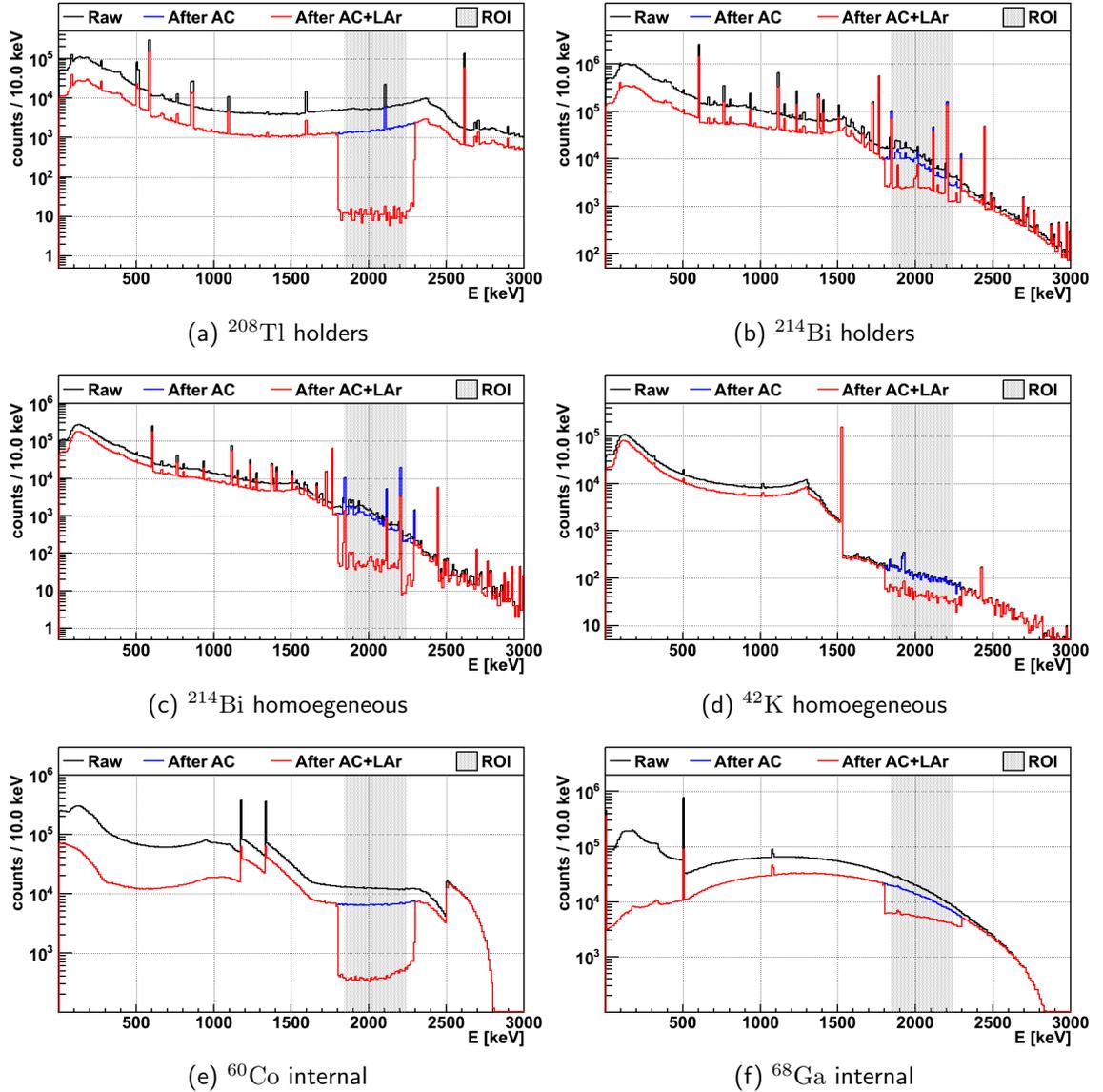
Figure 9.12 Energy spectra of raw events, events after anti-coincidence cut and after additional LAr veto cut for various background components. The photon tracking and thus the LAr veto suppression is only activated in the region around $Q_{\beta\beta}$.

The SFs for each background component separated into each instrumentation part are listed in Tab. 9.5. Furthermore, the p.e. distributions are shown in Fig. 9.13 for the Fiber and PMT readout.

---

[8]The peak position $\pm2\,\text{keV}$ are excluded which is sufficient for the MC spectra without energy resolution folded in. For comparison with data, once available, the regions should be redefined based on visible γ-lines and the peaks widened accounting for the energy resolution in the data.

Table 9.5 Suppression factors of various background components in the tentative PHASE II array. The SF are defined in $Q_{\beta\beta}\pm 200$ keV with known γ-lines excluded. Values with asterisk denote an energy range of $Q_{\beta\beta}\pm 35$ keV.

background	LAr veto	Fibers	PMT all	PMT top	PMT bot.
^{208}Tl holders	133.8 ± 8.8	119.3 ± 5.7	40.4 ± 1.2	8.7 ± 0.1	14.9 ± 0.3
^{214}Bi holders(*)	2.91 ± 0.02	2.71 ± 0.02	2.16 ± 0.01	1.44 ± 0.01	1.86 ± 0.01
^{214}Bi holders	1.74 ± 0.01	1.69 ± 0.01	1.55 ± 0.01	1.26 ± 0.01	1.45 ± 0.01
^{214}Bi homog.(*)	16.3 ± 1.3	14.2 ± 1.1	6.1 ± 0.3	2.69 ± 0.11	3.6 ± 0.2
^{214}Bi homog.	9.2 ± 0.2	8.3 ± 0.1	4.4 ± 0.6	2.41 ± 0.03	2.96 ± 0.03
^{42}K homog.	2.63 ± 0.10	2.35 ± 0.09	1.81 ± 0.06	1.37 ± 0.04	1.58 ± 0.05
^{60}Co internal	16.5 ± 0.2	15.0 ± 0.1	7.0 ± 0.1	3.0 ± 0.1	3.7 ± 0.1
^{68}Ga internal	2.45 ± 0.01	2.40 ± 0.01	2.07 ± 0.01	1.60 ± 0.01	1.75 ± 0.01

(a) Fibers   (b) PMTs
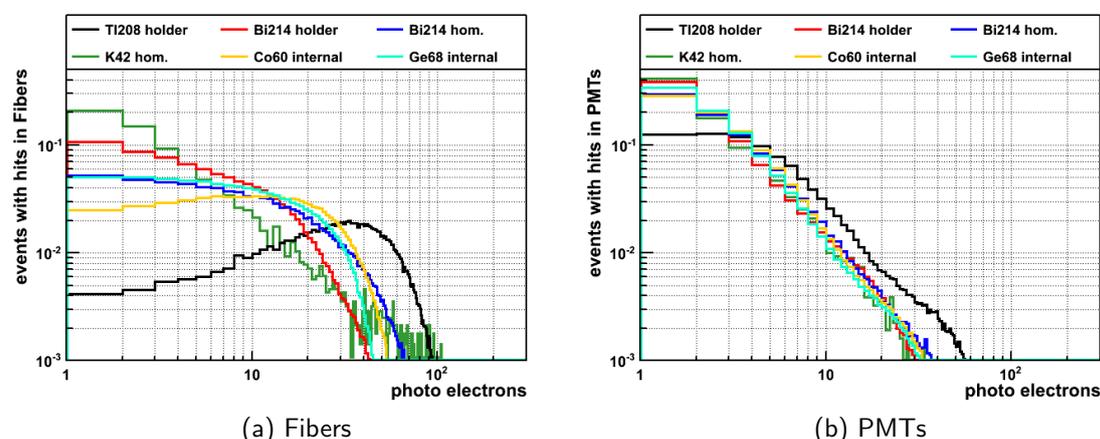
Figure 9.13 Photo electron distributions of events in $Q_{\beta\beta}\pm 200$ keV from various background components for the Fiber shroud (left) and both PMT arrays (right). Each distribution is normalized to the number of events.

^{208}Tl in the holders can be suppressed by a factor 134 and is the most efficiently vetoed background component. The p.e. distribution of the Fibers peaks at around 30 p.e. per event. Hence, the strong SF is stable even for a larger p.e. veto threshold. The main veto component is the Fiber shroud individually reaching a SF of 120 compared to 40 of the PMT array. This can be understood in the p.e. distributions where significantly less light is seen by the PMTs.

^{214}Bi in the holders shows a SF of 1.7 in $Q_{\beta\beta}\pm 200$ keV and 2.9 in $Q_{\beta\beta}\pm 35$ keV[9]. The difference between the energy ranges can be explained with the energy spectrum where the upper end of the ROI shows a lower suppression. The reason is that for larger germanium energy depositions smaller LAr energy depositions are available. This prevents a veto trigger for more and more decay branches at higher germanium energies in the complex decay

---

[9]Previous simulations predicted a larger suppression for this background up to SF 8. The reason for the reduction can be a combination of various improvements in the MC. The tuning of optical properties significantly reduced the light yield compared to old simulations. The simulations are now performed for all detector holders and not only for the BEGe holders as previously. The tentative PHASE II germanium array is now constructed with the proper BEGe detectors and not with a single sized template BEGe.

scheme of ^{214}Bi. The p.e. distribution peaks at 1 making this background component very sensitive to the p.e. threshold. ^{214}Bi homogeneously in the LAr shows a larger suppression due to the additional beta component directly inside the LAr. This background can be suppressed by a factor 16.

^{42}K homogeneously inside the LAr can be suppressed by a factor 2.6 ± 0.1. The small fraction of events in the ROI makes the simulation of this background component subject to low statistics. As discussed before, most of the events in the ROI originate from decays close to the detector surface and trigger the germanium detectors via the beta. This results in the poor LAr veto suppression even with the decay occurring inside the LAr itself. However, for BEGe detectors such events can be effectively vetoed by PSD with SFs up to 45 (Sec. 8.6.1). The larger p$^+$ electrode in the bore hole of the semi-coaxial detectors reduces the LAr veto performance for homogeneous ^{42}K events for this detector class. A separation of the array into BEGe detectors and semi-coaxial detectors yields a SF of 3.8 ± 0.2 for BEGe detectors and 2.0 ± 0.1 for semi-coaxial detectors[10]. The combination of PSD and LAr veto for BEGe detectors is expected to be complementary because they favor different event topologies[11] such that a simple multiplication of these values is conservative. The linear combination yields a combined SF of ≈ 170 for BEGe detectors. This is similar to the SF of 145 for ^{42}K directly on the surface and the PSD discrimination alone.

Cosmogenic ^{60}Co inside the germanium detectors can be suppressed by a factor of 17. ^{60}Co practically always decays with the emission of two γ-rays which partly need to escape the detector for the event to occur in the ROI. The comparably small beta component with 318 keV endpoint does not allow for different event topologies and merely results in peak tails in the internal decays. The Fiber p.e. distribution of ^{60}Co shows a maximum at around 10 p.e., illustrating the large amount of light per event.

^{68}Ga is the daughter of the cosmogenically produced ^{68}Ge inside the germanium detectors and decays via EC / β^+ practically without de-excitation γ-rays. The more likely β^+ decay branch with 1899 keV endpoint produces additionally two 511 keV γ-rays which can escape the detector and deposit energy in the LAr. The 511 keV and 1022 keV summation peak can be seen in the germanium energy spectrum before the AC cut or afterwards in case the decay occurs in the dead volume of a detector. For an event in the ROI, the positron and some of the annihilation γ-ray energy has to be deposited inside the detector. This decreases the chance of the LAr veto at higher germanium energies. A suppression factor of 2.5 can be achieved. However, the event topology suggests a much better suppression with PSD.

9.4.3 Energy Scale and Resolution of the Veto

The LAr veto was constructed as a pure veto and not as an energy detector. However, its is instructive to know the expected number of photo electrons for a given energy deposition in the LAr. The amount of energy deposited in the LAr cannot be determined experimentally in GERDA but is contained in the MC. Fig. 9.14 shows the number of photo electrons per

---

[10]For the SF calculation of a subset of detectors in the array, the remaining detectors are used for the AC cut.

[11]Events surviving the PSD (A/E) cut create Bremsstrahlung in the LAr which can jump the n$^+$ electrode or p$^+$ region but deposit some energy in the LAr. Events surviving the LAr veto occur almost directly on the surface or in a confined volume e.g. the semi-coax detector borehole or in the narrow space between detector and holder.

deposited energy in the LAr for events that deposit $Q_{\beta\beta}\pm200\,\mathrm{keV}$ in the germanium.

(a) ^{208}Tl holders

(b) ^{214}Bi holders

(c) ^{214}Bi homogeneously

(d) ^{42}K homogeneously

(e) ^{60}Co internal

(f) ^{68}Ga internal
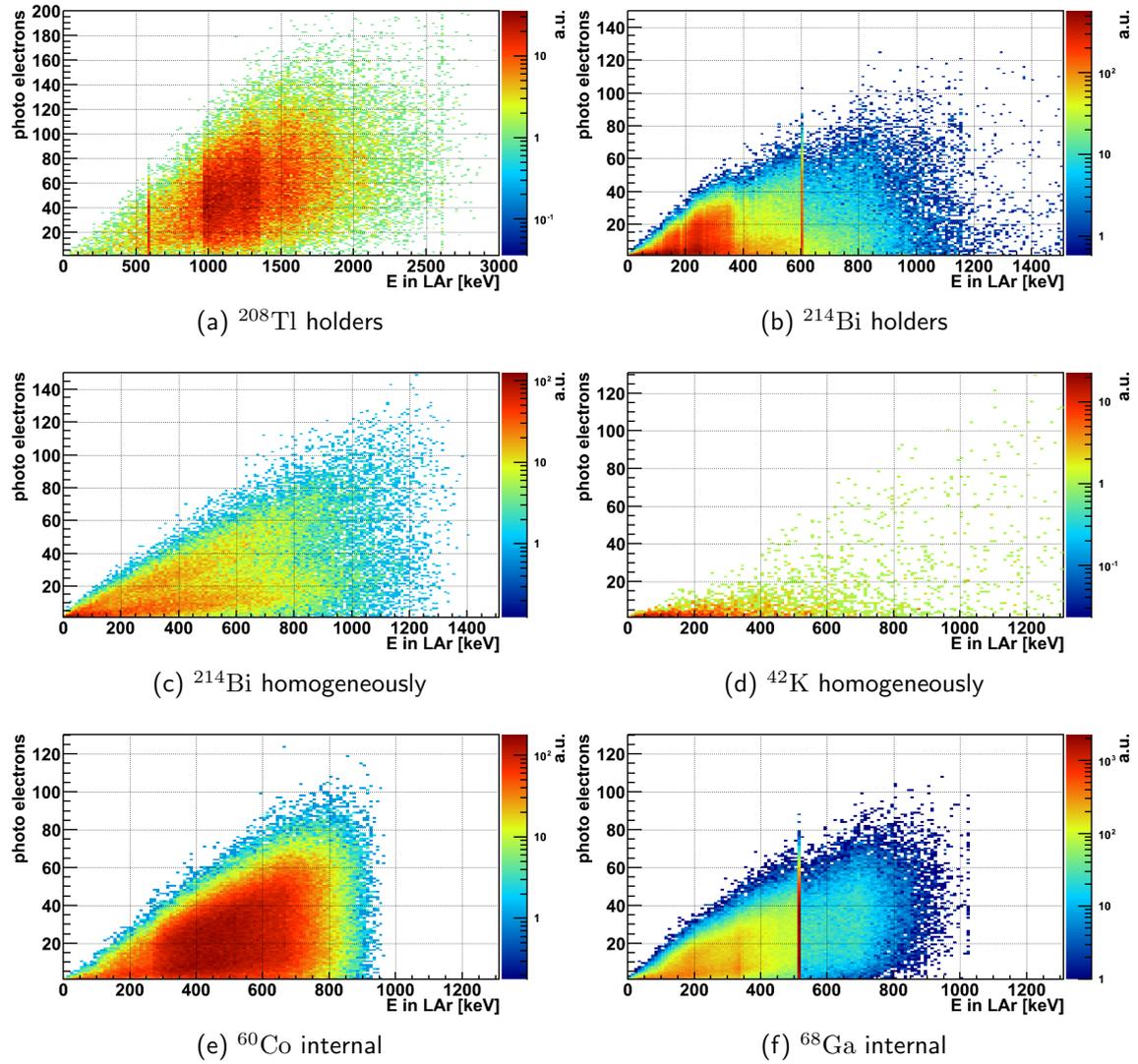
Figure 9.14 Detected photo electrons in all instrumentation parts versus energy deposited in the LAr for events which deposit an energy of $Q_{\beta\beta}\pm200\,\mathrm{keV}$ in a single germanium detector.

A correlation can be seen for all background components: In general, a larger energy deposition in the LAr results in a larger number of photo electrons. γ-ray structures can be seen at $583.2\,\mathrm{keV}$ for ^{208}Tl which occurs always in coincidence with the $2614.5\,\mathrm{keV}$ γ-ray. For ^{214}Bi in the holders the $609.3\,\mathrm{keV}$ γ-ray can be identified always occurring in coincidence with another γ-ray. For ^{214}Bi in the LAr, the structure is washed out. In ^{68}Ga the single escape γ-ray is clearly visible.

The upper end of the p.e. distribution is well defined and translates roughly into 100 detected photons per $1\,\mathrm{MeV}$ deposited in the LAr. However, the lower end of the p.e. distribution is consistent with zero detected photons in almost all cases. Only for a ^{208}Tl decay with above $1.5\,\mathrm{MeV}$ energy deposition in the LAr, almost always a p.e. is detected. Note that around $2\,\mathrm{MeV}$ is additionally needed to trigger the event in the germanium making this large energy excess only possible for ^{208}Tl. On the other hand, a large fraction

of ^{214}Bi decays in the holders with significant energy deposition in the LAr results in few or no detected photon electrons. Those event might be betas escaping the holders and creating scintillation light in the LAr which is then largely shadowed by the holder surface.

These plots can be interpreted as a detector response matrix which enables to constrain the deposited energy with the number of detected photo electrons. If, for instance, 60 p.e. were detected in the whole light instrumentation, it can be assumed that more than 600 keV are deposited in the LAr. Note however, that this conversion is only a rough estimate for the considered background components and events in $Q_{\beta\beta}\pm200$ keV.

More information may be learned when separating the instrumentation parts. The same plots split into Fiber and PMT distributions are shown in Fig. E.1 and E.2 in the appendix. The main structures in the plots are created by the Fiber shroud. The PMT distributions by itself do not yield further conclusions. However, as an outlook for further studies the correlation between top and bottom PMT array could be investigated as well as the correlation between individual Fiber segments when implemented in the MC simulation. This may allow to roughly constrain the position of an event and hence improve the response matrix.

9.5 Conclusion

The background rejection capabilities of the LAr scintillation light veto has been investigated for GERDA PHASE II. The GERDA MC simulations were extended to include the full tracking of optical photons after energy depositions in the LAr. Many optical parameters were implemented which are, however, subject to large uncertainties. Chief among these are the LAr light yield, the attenuation length and the efficiency of the wave length shifter. A validation of these parameters was performed with the LArGe setup tuning many optical properties to data in the process. Some optical properties which are inherent to the GERDA setup were further investigated with a PHASE II commissioning string. Strong discrepancies were observed in the p.e. distributions between data and MC with the nominal optical properties. The LAr light yield and the Fiber shroud geometrical coverage were used as two effective parameters to tune the MC to the data. With these tuned effective parameters a good agreement was achieved for the p.e. distribution, the SF as well as for the suppressed energy spectrum over the full range.

The MC simulation were used to predict quantitative suppression factors for key background components in the PHASE II array. They are 134 ± 9 for ^{208}Tl and 2.91 ± 0.02 for ^{214}Bi in the detector holders, 16.3 ± 1.3 for ^{214}Bi and 2.6 ± 0.1 for ^{42}K homogeneously distributed inside the LAr and 16.5 ± 0.2 for ^{60}Co and 2.45 ± 0.01 for ^{68}Ga cosmogenically produced inside the germanium detectors. The veto is largely ineffective for ^{42}K decays on the detector surface. The values describe the average suppression of semi-coaxial and BEGe detectors combined and are valid for the tentative PHASE II array with all detectors operational. Only the statistical uncertainties are given. In general, all of these background components can also be vetoed by PSD. LAr veto and PSD each prefers different event topologies and are largely complementary. This is likely improving the overall veto performance compared to the expectation by the individual techniques. The combined suppression is also strongly influenced by the detector anti-coincidence in the full germanium array. A complete background study using the PSD method presented in Chap. 8 in the full PHASE II array together with the LAr veto presented in this chapter is highly

suggested but was beyond the scope of this work[12]. For ^{42}K on the detector surface the suppression is dominated by the PSD and reaches up to a factor 145 for BEGe detectors. For ^{42}K distributed homogeneously in the LAr, mainly decays close to the detector surface contribute and the LAr veto performs differently for semi-coaxial (SF = 2.0 ± 0.1) and BEGe (SF = 3.8 ± 0.2) detectors. The linear combined SF of PSD and LAr veto is estimated as 170 for BEGe detectors.

Various improvements are possible for the LAr veto simulations. Better knowledge of the LAr attenuation length as well as the LAr light yield is foreseeable with an in-situ measurement in the GERDA cryostat which was already performed but not conclusively analyzed at the time of the writing. The geometrical implementation of the PHASE II setup lacks the detector cables and electronics creating additional dead volume and shadowing. The Fiber shroud is implemented as a single volume but can be segmented into individual fibers to better match the real setup.

Finally, a correlation of individual veto components as far as individual read out channels might enable to reconstruct more information of the event topology in the data. However, additional constrains on the event selection will require a much larger set of simulated events and hence a significant effort in computing power.

---

[12]Pulse shape libraries need to be constructed for all detectors and a post processing needs to be implemented for the output scheme of the full array.

Chapter 10

Search for $2\nu\beta\beta$ Excited State Transition in ^{76}Ge

This chapter presents an analysis of $2\nu\beta\beta$ decays of ^{76}Ge into excited states of ^{76}Se with GERDA PHASE I data. The analysis is based on coincidence events between two detectors where a de-excitation γ-ray is detected in one detector and the two electrons in another.

No signal has been observed and a profile likelihood analysis has been used to determine Frequentist 90 % C.L. bounds for three transitions: $0^+_{\text{g.s.}} - 2^+_1$: $T_{1/2}$> $1.6 \cdot 10^{23}$ yr, $0^+_{\text{g.s.}} - 0^+_1$: $T_{1/2}$> $3.7 \cdot 10^{23}$ yr and $0^+_{\text{g.s.}} - 2^+_2$: $T_{1/2}$> $2.3 \cdot 10^{23}$ yr. These bounds are more than two orders of magnitude larger than those reported previously. Bayesian 90 % credibility bounds are then extracted and used to exclude several models for the $0^+_{\text{g.s.}} - 0^+_1$ transition. The study has been published in [164].

This chapter is organized as follows: First the event signatures and theoretical predictions are presented in Sec. 10.1 followed by the data selection and MC simulations in Sec. 10.2. The analysis is based on a cut and count approach and developed and tuned in Sec. 10.3. The statistical extraction of the half-life limits is presented in Sec. 10.4. Finally, the PHASE I results are summarized in Sec. 10.5 and a sensitivity study for an excited state analysis in PHASE II is given in Sec. 10.6.

10.1 Introduction

The double beta decay of ^{76}Ge into ^{76}Se has a Q-value of 2039.061 ± 0.007 keV [165] and can potentially occupy any 0^+ or 2^+ excited state in ^{76}Se up to this energy (see Fig. 10.1). Transitions into higher excited states are suppressed by a reduced phase space factor (PSF) scaling with the total energy by E^{11} and E^5 for the $2\nu\beta\beta$ and $0\nu\beta\beta$ mode respectively. 2^+ states are further suppressed by spin-constrains on the final state particles. The search in this work focuses on the $2\nu\beta\beta$ $0^+_{\text{g.s.}} - 2^+_1$, $0^+_{\text{g.s.}} - 0^+_1$ and $0^+_{\text{g.s.}} - 2^+_2$ transitions which have one or two γ-rays associated with the decay in addition to the beta energy deposition in the source detector. The decay scheme is illustrated in Fig. 10.1.

The $0^+_{\text{g.s.}} - 2^+_1$(559.1 keV) transition has one de-excitation γ-ray of 559.1 keV and a $\beta\beta$ spectrum with 1480.2 keV endpoint.

The $0^+_{\text{g.s.}} - 0^+_1$(1122.3 keV) transition has a final state de-excitation via the 2^+_1 state and in addition to the 559.1 keV γ-ray a 563.2 keV γ-ray that occurs practically simultane-
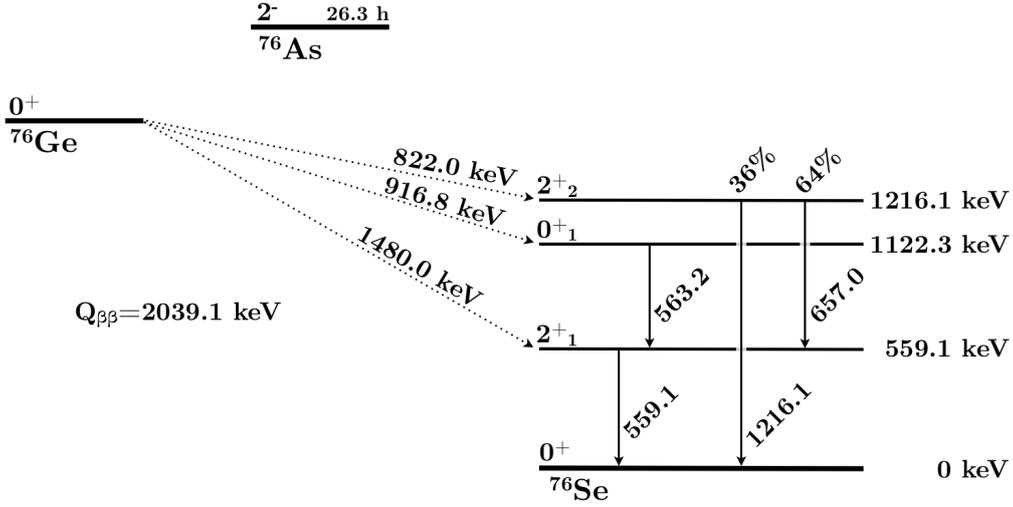
Figure 10.1 Possible decay modes of ^{76}Ge to excited states of ^{76}Se which are investigated in this work.

ously. The angular distribution of the two γ-rays in the $0_1^+ - 2_1^+ - 0_{\text{g.s.}}^+$ cascade is $W(\theta) \propto 1 - 3\cos^2\theta + 4\cos^4\theta$ [166]. The angular correlation and angular distribution are illustrated in Fig. F.2 in the appendix and are considered in the MC. The $\beta\beta$-endpoint is reduced to 917 keV.

The $0_{\text{g.s.}}^+ - 2_2^+ (1216.1\,\text{keV})$ transition has two decay branches: Branch 1 with two de-excitation γ-rays via the 2_1^+ state with a 657.0 keV and the 559.1 keV γ-ray and branch 2 with a single de-excitation γ-ray of 1216.1 keV directly into the ground state. The branching ratio is 64 % for branch 1 and 36 % for branch 2. The angular distribution of the two γ-rays in the $2_2^+ - 2_1^+ - 0_{\text{g.s.}}^+$ cascade of branch 1 is $W(\theta) \propto 1 - \frac{15}{13}\cos^2\theta + \frac{16}{13}\cos^4\theta$ [166] and is considered in the MC. The angular correlation and distribution are shown in Fig. F.2 in the appendix. The $\beta\beta$ endpoint is reduced to 823.2 keV.

For these transitions there is a variety of experimental upper limits with the latest dating back to 2000. In addition there are many theoretical calculations based on the various nuclear models. Most of theses calculations are older than 15 years; however, this work has recently triggered three new calculations for the 0_1^+ mode. One is based on the renormalized proton-neutron QRPA using wave functions from [167]. This calculation is predicting a half-life for the $2\nu\beta\beta$ $0_{\text{g.s.}}^+ - 0_1^+$ transition of $(1.15 - 5.77) \cdot 10^{23}$ yr [168] for an axial vector coupling between $g_A = 1.00 - 1.26$. For this calculation the particle strength parameter g_{pp} was adjusted to reproduce the ground state half-life. Another recent calculation is based on the IBM-2 model. The half-life ratio between the $0_{\text{g.s.}}^+ - 0_1^+$ and the ground state transition is calculated with NMEs and PSFs from [49, 34]. The predicted half-life ratio is 3300 for ^{76}Ge. Scaling this ratio with the recently measured ground state half-life of $(1.926 \pm 0.095) \cdot 10^{21}$ yr [52] results in a $2\nu\beta\beta$ $0_{\text{g.s.}}^+ - 0_1^+$ half-life prediction of $6.4 \cdot 10^{24}$ yr [169] independently of g_A. A calculation using the shell model (ShM) predicts $(2.3 - 2.6) \cdot 10^{24}$ yr [170] assuming $g_A = 1.26$ and quenching factor q=0.6 [171]. The range includes the use of two different effective interactions as e.g. also used in [77] and [171]. The shell model prediction of the $2\nu\beta\beta$ ground state half-life is in good agreement with the experimental data. These last two predictions are significantly larger than other calculations. The current status for the experimental and theoretical situation is condensed in Tab. 10.1.

Table 10.1 Experimental half-life limits and theoretical half-life predictions for $2\nu\beta\beta$ excited state decay modes in ^{76}Ge discussed in this work. Abbreviations denote: HFB: Hartree-Fock-Bogoliubov, QRPA: Quasi Random Phase Approximation, MCM-QRPA: Multiple Commutator Model QRPA, RQRPA: Renormalized proton-neutron QRPA, IBM: Interactive Boson Model, ShM: Shell Model.

$2\nu\beta\beta$ decay	$T_{1/2}$ [yr]	model	ref.	year
$0^+_{\text{g.s.}} - 2^+_1$ (559.1 keV)	$> 6.3 \cdot 10^{20}$ (68 % C.L.)	exp.	[172]	1992
	$> 1.1 \cdot 10^{21}$ (90 % C.L.)	exp.	[173]	1995
	$1.2 \cdot 10^{30}$	ShM	[174]	1984
	$5.8 \cdot 10^{23}$	HFB	[175]	1994
	$5.0 \cdot 10^{26}$	QRPA	[176]	1994
	$2.4 \cdot 10^{24}$	QRPA	[56]	1996
	$7.8 \cdot 10^{25}$	MCM-QRPA	[54]	1996
	$1.0 \cdot 10^{26}$	RQRPA	[55]	1997
	$(2.4 - 4.3) \cdot 10^{26}$	RQRPA	[177]	1998
	$2.0 \cdot 10^{27}$	RQRPA	[178]	2014
$0^+_{\text{g.s.}} - 0^+_1$ (1122.3 keV)	$> 6.3 \cdot 10^{20}$ (68 % C.L.)	exp.	[172]	1992
	$> 1.7 \cdot 10^{21}$ (90 % C.L.)	exp.	[173]	1995
	$> 6.2 \cdot 10^{21}$ (90 % C.L.)	exp.	[53]	2000
	$1.32 \cdot 10^{21}$	HFB	[175]	1994
	$4.0 \cdot 10^{22}$	QRPA	[176]	1994
	$4.5 \cdot 10^{22}$	QRPA	[56]	1996
	$7.5 \cdot 10^{21}$	MCM-QRPA	[54]	1996
	$(1.0 - 3.1) \cdot 10^{23}$	RQRPA	[55]	1997
	$(1.2 - 5.8) \cdot 10^{23}$	RQRPA	[168]	2014
	$6.4 \cdot 10^{24}$	IBM-2	[169]	2014
	$(2.3 - 2.6) \cdot 10^{24}$	ShM	[170]	2014
$0^+_{\text{g.s.}} - 2^+_2$ (1216.1 keV)	$> 1.4 \cdot 10^{21}$ (90 % C.L.)	exp.	[173]	1995
	$1.0 \cdot 10^{29}$	QRPA	[176]	1994
	$1.3 \cdot 10^{29}$	MCM-QRPA	[54]	1996
	$(0.7 - 2.2) \cdot 10^{28}$	RQRPA	[55]	1997

10.2 Dataset and Corresponding Monte Carlo Simulations

10.2.1 Data Set

The data for this analysis is equivalent to the "golden" dataset of the PHASE I $0\nu\beta\beta$ decay analysis [27] summing up the runs 25-32 in subset PHASE Ia and runs 36-46b in subset PHASE Ic. Additionally, all available $^{\text{nat}}$Ge semi-coaxial detectors and $^{\text{enr}}$Ge BEGe detectors are considered during these runs. The detector deployment scheme is described in Sec. 5.2 (Tab. 5.1) and illustrated in Fig. 5.3.

The granular installation of the GERDA setup is used to measure coincidences between two detectors. A two-detector event is defined as an event in which two detectors have an energy deposition above a certain threshold. This threshold, called single detector threshold (SDT), is an enforced posterior energy cut on each detector in a coincidence event. The DAQ threshold is a fuzzy region between 40 and 100 keV in which the anti-noise cuts have $< 100\,\%$ efficiency for physical events; the MC simulations do not have an inherent energy threshold. To quantitatively compare data and MC events, a minimum of 100 keV threshold is enforced. The effect of the SDT is studied later in the analysis. The definition is also used for different detector multiplicities e.g. a one-detector event has only one detector

above the SDT and a three-detector event has three detectors above threshold[1].

In case of two-detector events the energy spectra can be represented in two ways: (1) The single detector spectrum in which each of the two detector energies has a separate entry in the histogram and (2) the sum detector spectrum in which the sum of the two detector energies has one entry in the histogram. Furthermore, the two detectors are distinguished between (1) the "source" detector where the $2\nu\beta\beta$ decay occurs and the two electrons are detected and (2) the "gamma" detector where the de-excitation γ-ray is detected[2].

The number of events in the dataset with a certain detector multiplicity for a SDT of 100 keV after quality cuts and the μ-veto is shown in Tab. 10.2.

Table 10.2   Distribution of multiplicities in the PHASE I dataset for a SDT of 100 keV after muon veto and quality cuts.

multiplicity	1	2	3	4	> 4	total
events	726935	2710	82	2	1	729730

One-detector events, as used for the $0\nu\beta\beta$ decay search into the ground state, are dominated by background in the region of the low energy γ-lines of the excited state process, especially by the $2\nu\beta\beta$ decay into the ground state. Events with multiplicities larger than two occur too rarely to be used in the analysis in combination with additional cuts. Furthermore, those events require scatterings that reduce the signal efficiency significantly. These are the base arguments for the search with two-detector events.

The energy reconstruction of coincidence events requires a cross-talk correction between the detectors. The energy resolution after this correction is determined with two representative ^{228}Th calibrations during Run29 and Run36 for the two different array configurations. The calibration is performed on two-detector single energy spectra separated in semi-coaxial detectors and BEGe detectors. The peaks at 2614.5 keV, 2103.5 keV, 1592.5 keV, 860.6 keV and 583.2 keV are used to fit the function $\sigma_E = \sqrt{a \cdot E + b}$. The fit parameters for Run36 are $a_{\mathrm{coax}} = 0.00058$ and $b_{\mathrm{coax}} = 3.09$ for semi-coaxial detectors and $a_{\mathrm{bege}} = 0.00035$ and $b_{\mathrm{bege}} = 0.82$ for BEGe detectors. The resolution is 4.35 keV and 2.37 keV FWHM at ≈ 560 keV for semi-coaxial and BEGe detectors respectively. In the combined semi-coaxial and BEGe dataset, the energy resolution for multi-trigger events at the 583 keV ^{208}Tl γ-line is 4.2 keV FWHM compared to 3.8 keV FWHM in the single-trigger case where no cross-talk correction is used. The uncertainty on the resolution is estimated to be 10 %.

10.2.2   MC Simulations

For this analysis each germanium detector is the target material for every other detector in the array with the exception of cross-arm events. The relative height between the arms is not precisely known and events with detectors in both arms are excluded from the dataset. The source-detector unity requires the stable and unchanged operation of the

---

[1]For coincidence events the SDT may also affect higher energy events where the multiplicity is downgraded. This happens e.g. in a cases where three detectors have an energy deposition but only two are above the SDT.

[2]Note, that the distinction is made on the analysis level and may not correctly describe the physical process in some cases. Also, for energy depositions with the same energy, the distinction cannot be made.

whole GERDA array during a certain time which is realized in the run number definition[3]. For some runs, individual detectors are excluded from the analysis due to temporary instabilities; thus, the number of detecting detectors can vary per run whereas the number of source detectors is constant within the two subsets of PHASE I. In the analysis the target mass is kept constant within an array configuration; changes due to inactive detectors are condensed into the signal detection efficiency.

The status of the different detectors is summarized in Tab. F.5 in the appendix with the live-time written in black for detecting detectors and in red for only passive detectors, i.e. detectors that are excluded from the analysis.

The effect of the array configuration on the efficiency can be seen in Fig. F.1 in the appendix; efficiency values for various coincidence cuts (explained in the next section) are plotted against the run number. Exclusion of detectors from the analysis result in a drop of the coincidence detection efficiency depending on the detector characteristics and position in the array (compare also detector status in Tab. F.5 with detector position in Fig. 5.3).

The live-time for PHASE Ia and PHASE Ic is 174.1 days and 285.6 days respectively, summing up to an exposure of $31.04\,\mathrm{kg}\cdot\mathrm{yr}$ for the whole dataset. The isotopic exposure of $^{76}\mathrm{Ge}$ is $22.3\,\mathrm{kg}\cdot\mathrm{yr}$.

The MC simulations for the efficiency calculation and the construction of the background model are performed with MaGe and the event generator DECAY0 (Sec. 5.3.2). The simulations are precisely matched to the dataset. Each PHASE I subset has individual MC simulations for the signal processes and the background contributions. Within each subset the MC data is processed according to the individual run configurations, i.e. disregarded detectors in a GERDA data run are also disregarded in the post processing of the MC. The conjunction between data and MC is performed on the run level. The MC data is then combined according to the run live-times. The signal process is additionally scaled to the target mass in each array configuration. The convolution of the MC events with the energy resolution is done for each PHASE I subset individually. Also the semi-coaxial detector and BEGe detector energies are convolved with their respective resolution. In the end, this work considers the combined semi-coaxial and BEGe data. All plots are shown for the combined data of all runs, configurations and detectors.

In detail, the efficiency ϵ for a coincidence cut is calculated as follows: $N_{i_c}^{\mathrm{gen}}$ $2\nu\beta\beta$ decays are generated inside a single detector i_c in the array. The simulations are done for each array configuration c individually and the i_c denote the set of detectors in this configuration. After the coincidence cut, $N_{i_c,r}^{\mathrm{obs}}$ events are observed in the full germanium array for a given run r. These observed events depend on the map of active detectors in run r. The efficiency $\epsilon_{i_c,r}$ to detect a $2\nu\beta\beta$ decay from a given detector i_c in run r in configuration c is

$$\epsilon_{i_c,r} = \frac{N_{i_c,r}^{\mathrm{obs}}}{N_{i_c}^{\mathrm{gen}}}.$$

Now the efficiency for each detector is combined into an efficiency for the run ϵ_r. The $\epsilon_{i_c,r}$ are scaled with the mass of the source material m_{Ge76,i_c} in detector i_c:

$$\epsilon_r = \frac{\sum_{i_c} m_{\mathrm{Ge76},i_c} \cdot \epsilon_{i_c,r}}{\sum_{i_c} m_{\mathrm{Ge76},i_c}}.$$

---

[3]A posteriori decision lead to run number separations into 39a and 39b; 44 and 44a and 46a and 46b.

The combination into a single efficiency ϵ for the whole dataset is performed with the scaling of the live-time of the runs t_r and the target mass:

$$\epsilon = \frac{\sum_r \epsilon_r \cdot t_r \cdot \sum_{i_c} m_{\text{Ge76},i_c}}{\sum_r t_r \cdot \sum_{i_c} m_{\text{Ge76},i_c}}.$$

10.2.3 Background Model

The background model is separated into semi-coaxial detectors and BEGe detectors. It follows along the line of the GERDA PHASE I background model for the $0\nu\beta\beta$ decay ground state analysis [115] but is specifically constructed for coincidence events. It is composed of contributions from ^{214}Bi, ^{212}Bi, ^{208}Tl, ^{228}Ac, ^{40}K, ^{60}Co and ^{108m}Ag on the holders, ^{42}K and ^{39}Ar homogeneously in the LAr, ^{42}K on the n$^+$ contact and ^{214}Bi on the p$^+$ contact. The individual components are listed in Tab. 10.3 along with their activities.

Table 10.3 Components of background model and their activity. The activity is given in μBq per detector component and background component in the dataset, separated into semi-coaxial and BEGe parts. E.g. the first entry in the first line quotes the average activity of each semi-coaxial holders for ^{214}Bi in the full dataset. The average is performed over 11 semi-coaxial holders in PHASE Ia and 9 semi-coaxial holders in PHASE Ic. The p$^+$ and n$^+$ components are quoted as the averaged surface activity of one detector in one class. ^{39}Ar and ^{42}K homogeneously in LAr is shown as the activity per kg LAr.

nuclide	location	activity in semi-coaxial [μBq / component]	activity in BEGe [μBq / component]
^{214}Bi	holders	34.9	14
^{214}Bi	p$^+$ contacts	3	1
^{212}Bi	holders	24.6	1.6
^{208}Tl	holders	8.5	0.6
^{60}Co	holders	2.2	-
^{40}K	holders	258	82
^{228}Ac	holders	27.1	-
^{42}K	n$^+$ contacts	136	80
^{108m}Ag	vertical bars	4.3	-
^{42}K	LAr homogeneous	85 μBq/kg	
^{39}Ar	LAr homogeneous	1.01 Bq/kg	

The model uses various input parameters for each component. For the semi-coaxial detectors the components are first fitted to the two-detector sum detector spectrum. The results are used to fix the activities of the ^{42}K and ^{40}K components. In a second step a fit to the two-detector single detector spectrum fixes the remaining free parameters. ^{208}Tl and ^{212}Bi are fixed in secular equilibrium. The activity for ^{214}Bi on the p$^+$ contact is taken from the GERDA α model [115]. For the BEGe detectors the number of two-detector events in the dataset is too small to perform a reasonable fit. The activities are scaled from the one-detector background model presented in [115]. The activity for the homogeneous ^{42}K component inside the LAr is also taken from [115] and fixed for the whole array in order to have a consistent scenario including the ^{42}K contribution on the n$^+$ contact.

A large number of primary events is simulated for the signal and background components in order to have a sufficiently large sample of coincidence events. For each background

component at least 10^8 events were produced per individual detector or holder. The homogeneous ^{42}K component was simulated with $5 \cdot 10^9$ events in a volume of 6800 l. That also generates a large enough event sample for individual detector - detector pair topologies.

The energy spectra for the two-detector background model is shown in Fig. 10.2 for a SDT of 100 keV with the single detector energies on the left and the sum detector energies on the right. The shaded histograms show events in the dataset which can be directly compared to the background model shown in black. The individual background components for the semi-coaxial detectors are shown in color. Components for the BEGe detectors are not shown to increase visibility. There is a small excess in the data over the background model for low energies. This excess is limited to < 250 keV in the single detector spectrum and to < 500 keV in the sum detector spectrum. At this energy events from the ^{39}Ar beta decay with an endpoint of 565 keV dominate. The spectral shape is highly sensitive to the exact knowledge of the FCCD of the detectors which is not available for the semi-coaxial ones. Furthermore, the probability of a two-detector coincidence event due to ^{39}Ar is very small and hence difficult to describe by MC. However, this effect is not relevant for the energy regions investigated in this analysis. Another excess is visible around 1.8 MeV in the single detector spectrum. However, it cannot be explained by a missing γ-line or beta spectrum in the background model and furthermore the excess is not very significant. The agreement between the model and the data is sufficient for this analysis since the former is only used for cut optimization.
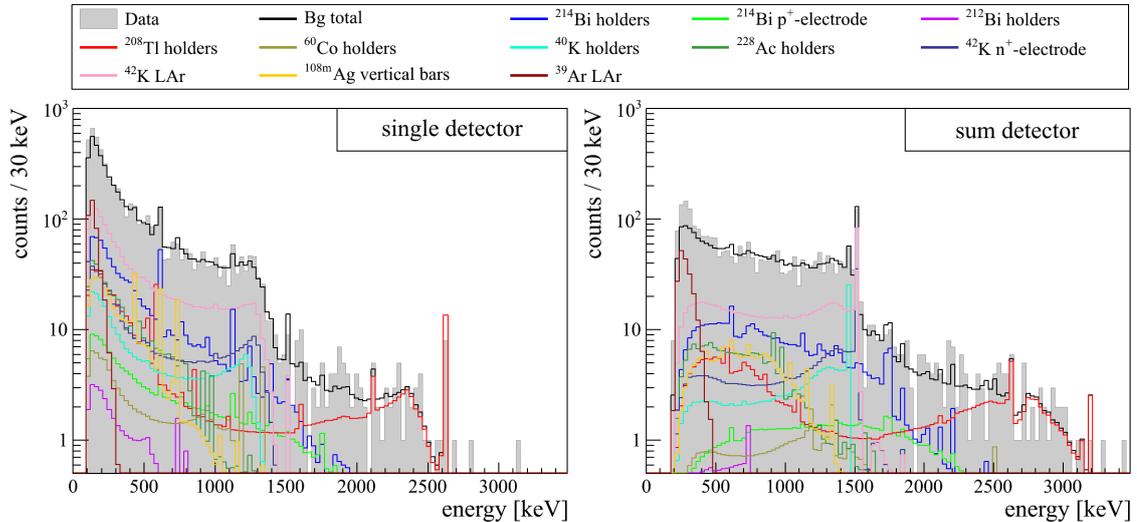
Figure 10.2 Data and background model for two-detector events and a single detector threshold of 100 keV. In the single detector spectra (left) each detector has a separate entry per event in the histogram whereas in the sum detector spectra (right) the sum of the two detector energies is shown. Data events are shown in solid gray and background components in colored lines.

The detector distribution of two-detector events in the background model and in the dataset is shown in Fig. F.3 in the appendix for a SDT of 100 keV. Also shown is the expected distribution of $2\nu\beta\beta$ events for the excited state decay modes assuming a half-life of 10^{23} yr. The distribution of two-detector events is mainly determined by the position of the detector in the array relative to the other detectors, the detector size and the life-time of the detector in the dataset. The differences in coincidence counts between the detectors is well described by the MC background model and thus strengthens its validity in terms

of geometry implementation and life-time calculation. There is an excess of data over background model for BEGe detectors. This is potentially due to the extrapolation of the one-detector data background model to two-detector events instead of directly fitting two-detector data as for the semi-coaxial detectors.

10.2.4 Signal Efficiencies

The signal processes scaled to 10^{23} yr along with the PHASE I dataset and the background model are shown for two-detector events in Fig. 10.3. The single detector spectra and the sum detector spectra are distinguished. The signal processes have a continuous shape in the sum detector spectra due to the continuous electron component of $2\nu\beta\beta$ that is almost always detected in the source detector[4]. The single detector spectra show the distinguished de-excitation γ-lines being detected outside the source detector which enables strong background discrimination.
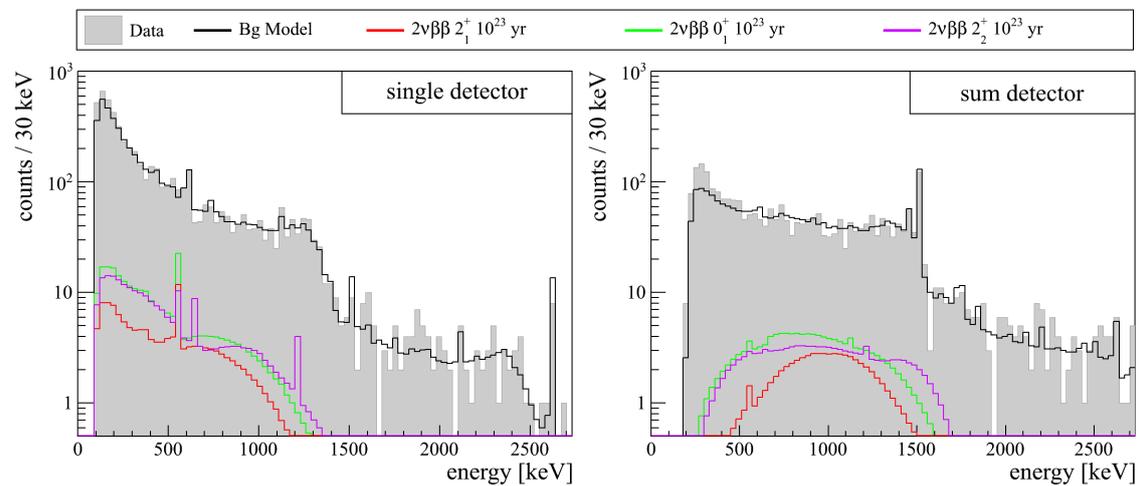
Figure 10.3 Illustration of the $2\nu\beta\beta$ decays for two-detector events scaled to a half-life of 10^{23} yr for each decay mode. Shown are the single detector spectra (left) and the sum detector spectra (right). Also shown are the background model (black line) and data (gray histogram)

Two-detector events can be illustrated in a scatter plot showing the energy-energy distribution (Fig. 10.4). Shown are the signal processes and the background model. The color scale denotes the expected numbers of events for an excited state half-life of 10^{23} yr and for the expected number of background events in the dataset. The black points are the data events. In this representation, horizontal and vertical lines are features in the single detector spectra whereas diagonal lines are features in the sum detector spectra. The de-excitation γ-lines from the signal process are mainly detected in one detector and show as horizontal and vertical lines. Many background γ-lines originate outside the detectors and scatter into two detectors creating diagonal lines. This can be suppresses with a cut on the sum energy. In Fig. 10.4 the diagonal γ-line from ^{42}K is clearly visible in the data. Additional γ-lines from ^{208}Tl, ^{40}K and ^{214}Bi are only visible in Fig. 10.2.

---

[4]Note that in principle it is possible that the decay occurs inside a detector that is switched off or not considered for analysis or inside the dead layer of a detector. Then, only the de-excitation γ-rays can produce a two-detector event. Such a topology is very rare but inherently considered in the efficiency in this work. See for example the peak structures in the signal p.d.f. of the sum detector spectra in Fig. 10.5.

(a) $2\nu\beta\beta$ $0^+_{g.s.} - 2^+_1$ transition.

(b) $2\nu\beta\beta$ $0^+_{g.s.} - 0^+_1$ transition.

(c) $2\nu\beta\beta$ $0^+_{g.s.} - 2^+_2$ branch 1 transition.

(d) Background model for PHASE I dataset
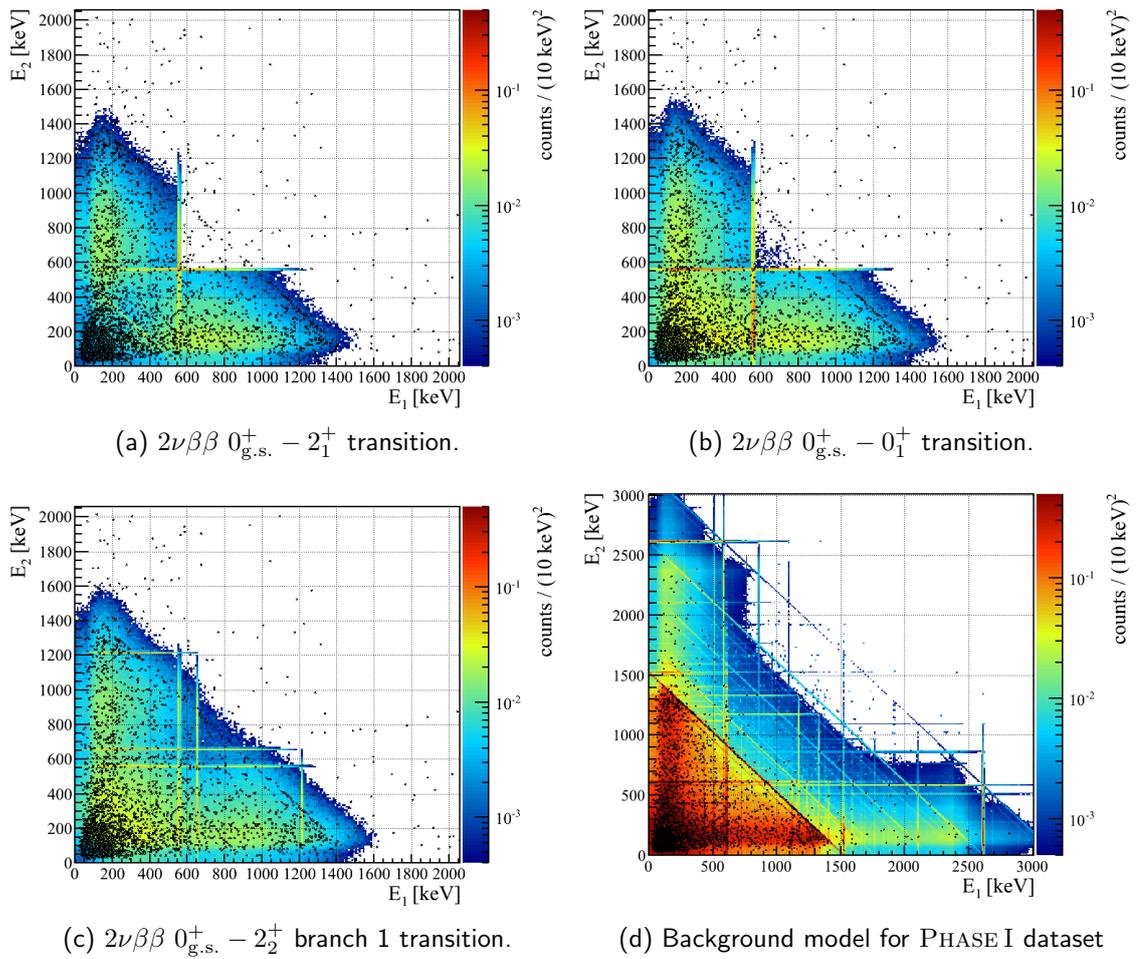
Figure 10.4 Two-detector event energy-energy correlations showing the simulated $2\nu\beta\beta$ decay for the 2^+_1, 0^+_1, 2^+_2 decay modes in (a), (b) and (c) respectively. Also the simulated background model is shown (d). Simulated events are shown in color and the GERDA PHASE I data events in black. The number of simulated events is scaled to the PHASE I dataset and a half-life of 10^{23} yr.

The same plot is shown for the $0\nu\beta\beta$ excited state transitions in Fig. F.4 in the appendix. Here the discrete energy depositions of the betas create diagonal features where the whole Q-value is detected. The horizontal and vertical lines are now mainly created by the betas when γ-rays are only partly detected in another detector. These plots are only shown for completeness since this analysis focuses on the $2\nu\beta\beta$ decays.

10.3   Analysis

The analysis is based on event counting in a region of interest (ROI) after a sequence of cuts. This analysis is not a blind analysis but special care is taken to avoid biases. The construction of the sequence of cuts starts with initial choices that are then optimized to maximize sensitivity. This prevents ad hoc choices of analysis parameters. The MC background model and efficiency are used for the cut optimization. Systematic uncertainties and potential deficiencies in the background model only affect the choice of analysis parameters and do not have a direct effect on the derived half-life results since the background in the ROI is estimated from side bands (SB).

10.3.1   Basic Cut Flow

The cut flow is separated into four layers:

1. **Standard cuts**: Quality cuts and muon veto

2. **Coincidence cuts**: Specific two-detector cuts optimized for each decay mode

3. **Background cuts**: Exclusion of background γ-lines

4. **Detector pair cuts**: Cuts to select detector pairs that exhibit a high efficiency

The challenge is to find a cut combination that optimizes the sensitivity S, i.e. highest signal efficiency and larges background suppression which is expressed by the figure of merit

$$S = \frac{\epsilon}{\sqrt{B}} \tag{10.1}$$

with the signal survival efficiency ϵ and the surviving background counts B. This figure of merit is proportional to the half-life assuming no signal and a $1\,\sigma$ Gaussian upward fluctuation being interpreted as a signal[5]. The efficiency is extracted from MC simulations of the $2\nu\beta\beta$ excited state process. The background in the ROI is determined from the MC background model. Hence, this sensitivity study is entirely based on MC simulations.

The **standard cuts** include quality cuts and the muon veto cut and are initially applied to the dataset. They are identical to the cuts in the GERDA $0\nu\beta\beta$ decay analysis in [27] and references therein.

The **coincidence cuts** are specific for each decay mode. They require a two-detector event with either of the two detectors having the full energy of any de-excitation γ-ray within the peak window size (PWS) of $\pm 2\,\sigma_\mathrm{E}$. This corresponds to $\pm 3.6\,\mathrm{keV}$ at $560\,\mathrm{keV}$. The SDT of $100\,\mathrm{keV}$ is applied at this level. In addition, also a sum energy limit (SEL) of $2039\,\mathrm{keV}$ is applied to exclude events with a total energy deposition larger than the possible energy release for $2\nu\beta\beta$ decay in ^{76}Ge. These baseline cut parameters are later optimized for maximum sensitivity.

The energy resolution for two-detector events at $560\,\mathrm{keV}$ is $4.2\,\mathrm{keV}$ FWHM and does not allow to separate these two γ-lines of the 0^+_1 transition; hence the peak region is combined into one. The two branches of the 0^+_2 transitions are treated separately and later combined in the statistical analysis.

The detector energy requirement of a de-excitation γ-line is shifted to lower and higher energies for the side bands. The size of a single SB is the same size as the ROI and together optimized with the PWS[6]. In total 4 SBs are defined for each decay mode; two at lower energies and two at higher energies. The number of 4 SBs is chosen to decrease the statistical uncertainty in the background estimation and to keep the signal efficiency high at the same time. The signal efficiency is reduced due to the side bands because a

---

[5]Gaussian uncertainties do not adequately describe background fluctuation for low count rates. Here they are used only to compare qualitatively different cuts and not to infer an expected half-life for the background only scenario.

[6]The equal size of SB and ROI is required because of the special construction of the pair cut (explained later). The detector with an energy inside the ROI is tagged as the "gamma" detector. If the SB size would be different to the ROI size, this tagging efficiency would be altered for background event.

two-detector event can be tagged for the ROI and a SB at the same time. Those events are rejected which reduces the signal efficiency by $\approx 4\%$ relatively[7]. Consequently, also background events are rejected if they are present in two SB regions or in a SB and the ROI. This reduces the background by $\approx 2\%$ relatively. One event in the ROI of the 0_2^+ transition is removed by this requirement.

The SB regions are chosen for each decay mode individually even though similar γ-ray energies are involved. The choice is based on the MC background model only. They are as close as possible to the ROI without overlap and avoid background γ-lines in the single and sum detector spectra. An illustration of the ROI and SB regions along with the decomposed MC background model is shown in Fig. F.6 in the appendix. The SB regions are considered in the following cut flow optimization since their size influences the signal and background survival of events and hence the sensitivity.

The **background cuts** are motivated by background γ-lines that interfere with the ROI. Fig. 10.5 shows the sum detector spectrum of the background model after the baseline coincidence cut for the different excited state transitions (black). Also shown are the signal processes (colored). The low energy cutoff is the γ-ray energy in one detector plus 100 keV SDT in the other. The high energy cutoff is the SEL. The dips in the spectra are created by rejecting events that are tagged in the ROI and a SB or two SBs simultaneously. The peaks in the signal spectrum at 1122.3 keV for the 0_1^+ transition and at 1216.1 keV for branch 1 of the 2_2^+ transition are created by decays that occur in the dead volume of a detector or inside an excluded detector. In this case the beta energy is not detected and the two γ-rays trigger a two-detector event which often results in a discrete sum energy. Therefore, such a peak is not present in the sum spectra of the 2_1^+ transition and branch 2 of the 2_2^+ transition which only emit a single γ-ray.

The strongest peaks in the background spectra are at 1524.7 keV and 1460.8 keV belonging to ^{42}K and ^{40}K respectively. They represent the region in the scatter plot (Fig. 10.4d) where the diagonal sum energy γ-lines cross the straight single detector lines of the signal process. In other words, a single background γ-ray scatters, leaves an energy deposition around the ROI in one detector and the remaining energy in the other. This background can be suppressed with a cut on the sum energy. On the other hand, the next strongest feature is the peak around 1170 keV which is a combined structure: First, a 609.3 keV ^{214}Bi γ-ray coincides with another ^{214}Bi γ-ray that scatters and deposits an energy around the ROI of 559.1 keV[8] in one detector; the 609.3 keV γ-ray is fully detected in the other detector creating a sum energy around 1170 keV. Second, a similar coincidence with a 614.3 keV ^{108m}Ag γ-ray and another ^{108m}Ag γ-ray happens. A contribution from the ^{60}Co 1173.2 keV γ-line is negligible since no prominent 1332.5 keV γ-line is visible. The other smaller peaks originate mainly from ^{214}Bi, ^{228}Ac or ^{60}Co. They are either created by (1) a single γ-ray scattering into two detectors or by (2) two γ-rays with one γ-ray fully detected in one detector. In both cases a specific energy has to be deposited in one detector for the event to survive the coincidence cut. The scenarios can be illustrated with the scatter plots in Fig. 10.4. The horizontal / vertical cut window crosses the diagonal background lines in scenario (1) or the horizontal / vertical background lines in scenario (2).

---

[7]Double counting events as signal and background creates inconstancy in the statistical treatment. Roughly 1% of signal events in the ROI are also tagged in one SB.

[8]For the 0_1^+ transition, the peak window is extended to 563.2 keV which effectively widens the 1170 keV structure.

(a) $0^+_{g.s.} - 2^+_1$

(b) $0^+_{g.s.} - 0^+_1$

(c) $0^+_{g.s.} - 2^+_2$ branch 1

(d) $0^+_{g.s.} - 2^+_2$ branch 2
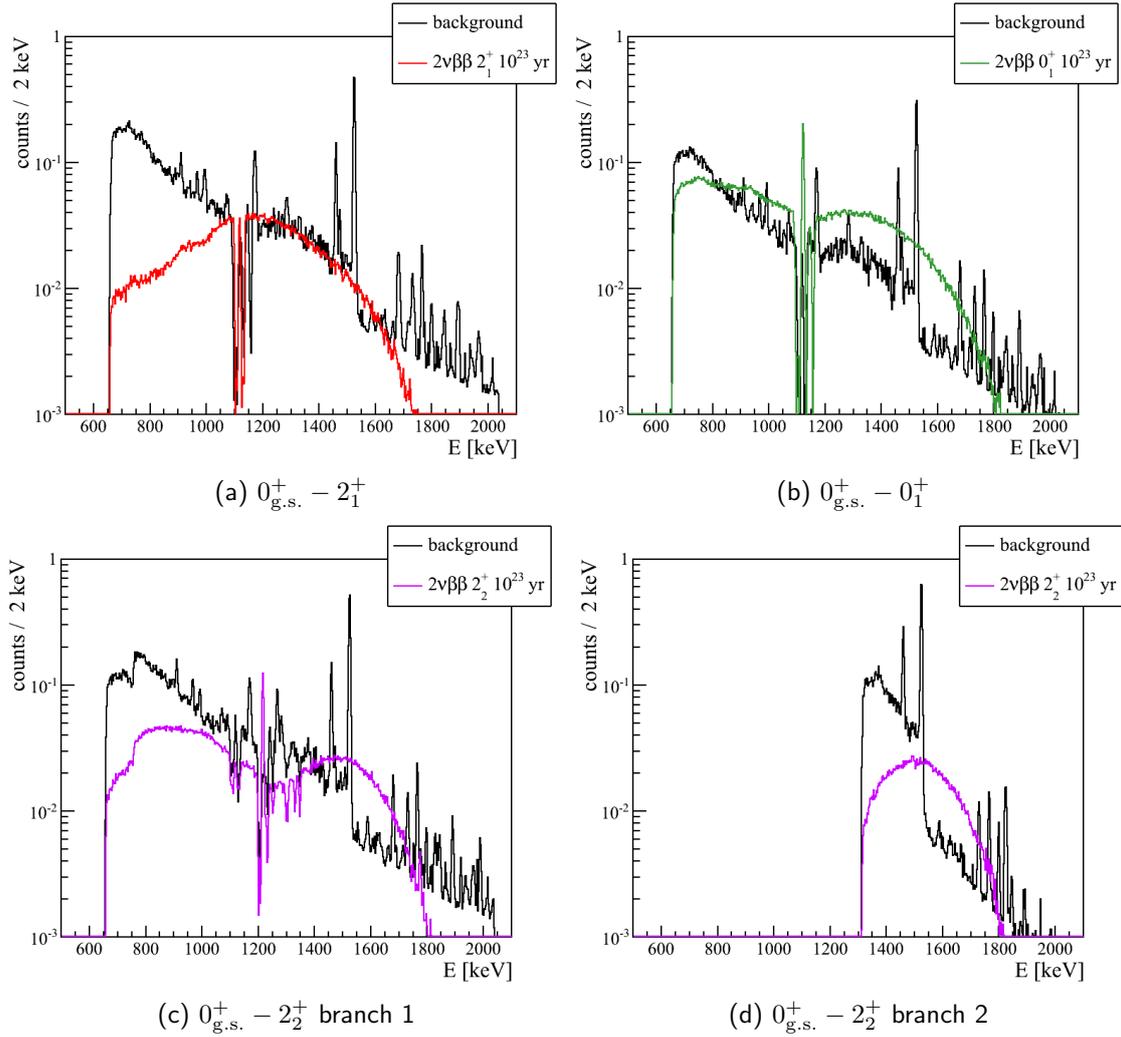
Figure 10.5 Sum detector spectra after coincidence cuts for background (black) and signal process scaled to 10^{23} yr half-life (colored). The lower cutoff is created by the smallest γ-ray energy in one detector and the SDT in the other. The dips in the spectra are created by rejecting events that are tagged in the ROI and a SB or in two SBs simultaneously.

The background cuts are applied for all decay modes in the same way. ^{42}K and ^{40}K are excluded by requiring the detector sum energy not to be in $1524.7 \pm 5.5\,\text{keV}$ nor in $1460.8 \pm 5.4\,\text{keV}$ with the energy windows corresponding to the region of $2\sigma_E$. Additionally the single detector energy is required to be not in $611.0 \pm 5.7\,\text{keV}$ to exclude the ^{214}Bi and ^{108m}Ag background[9].

At this stage, the combination of coincidence cuts and background cuts can be optimized in various ways. The SDT of $100\,\text{keV}$, the SEL of $Q_{\beta\beta}=2039\,\text{keV}$ and the PWS of $\pm 2\,\sigma_E$ are baseline values and different values are potentially more favorable for the individual decay modes. These parameters are scanned for maximizing the sensitivity (Eq. 10.1).

---

[9]This cuts out a peak window that is wider than $2\sigma_E$ to accommodate the two γ-lines.

The **single detector threshold** is varied from $100\,\text{keV}$ to $500\,\text{keV}$ in steps of $50\,\text{keV}$. The increasing threshold reduces the signal efficiency with cutting away the low energy side of the $\beta\beta$-spectrum in the source detector. The $\beta\beta$-distribution peaks at roughly $\frac{1}{3}$ of the endpoint being $\approx 490\,\text{keV}$, $\approx 300\,\text{keV}$ and $\approx 270\,\text{keV}$ for the 2^+_1, 0^+_1 and 2^+_2 transition respectively. On the other hand, the background for two-detector events increases towards low energies (see Fig. 10.2). The normalized sensitivity is plotted against the SDT and shown in Fig. 10.6a and 10.6b with and without the background cut respectively. The normalization is based on the $100\,\text{keV}$ SDT without the background cut to also illustrate its improvement.

(a) without background cuts (b) with background cuts
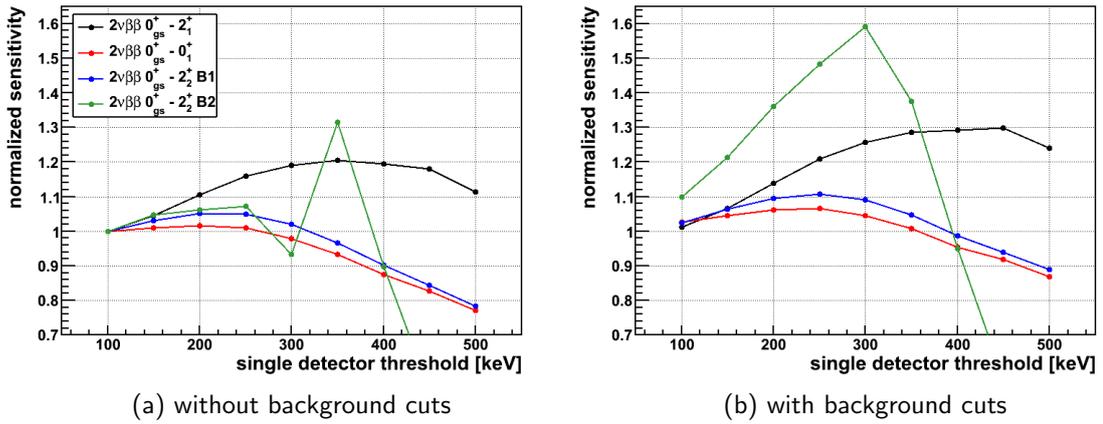
Figure 10.6 Sensitivity for different values of the SDT. The sensitivity is normalized to the $100\,\text{keV}$ SDT after the coincidence cuts.

The effect of the SDT on the sensitivity can be understood with Fig. 10.5. The background in the sum detector spectra after coincidence cuts is significantly larger at lower energies than the signal process. Those regions are removed with a larger SDT increasing the sensitivity. The peak-like structure in the sensitivity plot for branch 2 of the 2^+_2 mode (green curve) arises from passing the ^{42}K γ-line at $1525\,\text{keV}$ which occurs when the coincidence requirement of $1216.1\,\text{keV}$ in a single detector is applied together with an SDT of $300\,\text{keV}$ / $350\,\text{keV}$. Before background cuts the sensitivity is strongly influenced by the γ-line wheres this is not the case after background cuts in which the γ-line region is removed. The best sensitivity is reached with the background cut and a SDT of $450\,\text{keV}$, $250\,\text{keV}$, $250\,\text{keV}$ and $300\,\text{keV}$ for the 2^+_1, 0^+_1, 2^+_2 branch 1 and 2^+_2 branch 2 transitions respectively.

The **sum energy limit** is varied from $1000\,\text{keV}$ to $Q_{\beta\beta}$ in steps of $50\,\text{keV}$. The effect on the efficiency is also due to the $\beta\beta$-spectrum which strongly decreases towards the endpoint. The sensitivity dependence on the SEL is shown in Fig. 10.7. There is a kink in the sensitivity curve at $\approx 1500\,\text{keV}$ before the background cuts but not after the background cuts. The reason is again the prominent ^{42}K γ-line which is passed by the SEL cut at this energy. This can also be seen in the sum detector spectra of Fig. 10.5 where the decreasing SEL is equivalent of cutting away the end of the spectra. Kinks appear if a large background γ-line is passed by the SEL and not anymore affected by the background cut. In fact the sensitivity dependence on the SEL is almost identical with and without background cuts for smaller SEL. In conclusion, the maximal sensitivity is found after the background cuts for an SEL of $1750\,\text{keV}$, $1750\,\text{keV}$, $1800\,\text{keV}$ and $1850\,\text{keV}$ for the 2^+_1, 0^+_1, 2^+_2 branch 1 and 2^+_2 branch 2 transitions, respectively.

(a) without background cuts   (b) with background cuts
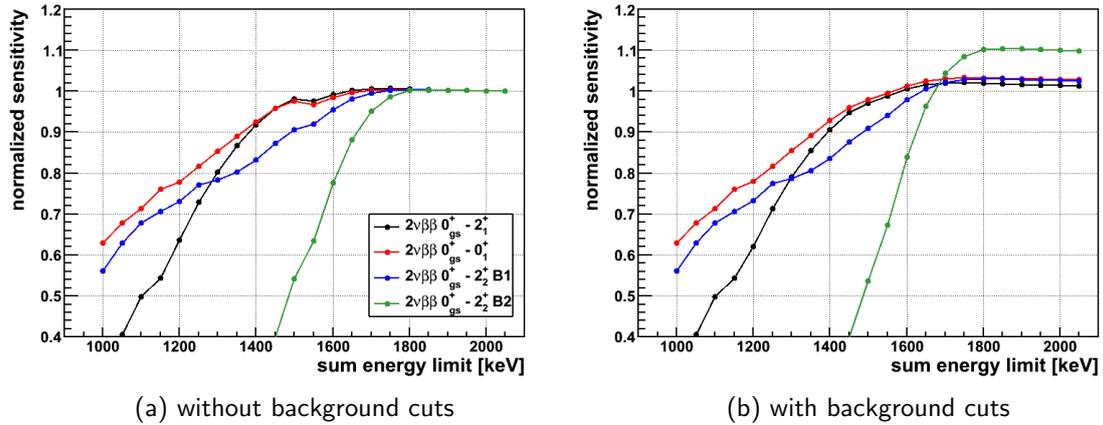
Figure 10.7 Sensitivity for different values of the SEL. The sensitivity is normalized to the 2050 keV SEL after the coincidence cuts.

The **peak window size** for the de-excitation γ-rays is varied between roughly $1\,\sigma_E$ and $2\,\sigma_E$ of the energy resolution. This corresponds to a width in energy between 1.8 keV to 3.6 keV for the peaks around 560 keV and 2.0 keV to 4.0 keV for the peak around 1216 keV. The window size is increased in 21 steps of 0.2 keV. The 657 keV peak window of the 2_2^+ transition is fixed at 3 keV due to constrains by background γ-lines in the vicinity. The sensitivity dependence on the PWS is shown in Fig. 10.8. The sensitivity is only slightly changing with the PWS and the optimal values are found at 2.6 keV and 2.2 keV for the 2_1^+ and 0_1^+ transitions respectively. For the 2_2^+ transition the optimal values are 2.4 keV for branch 1 and 2.8 keV for branch 2.

(a) without background cuts   (b) with background cuts
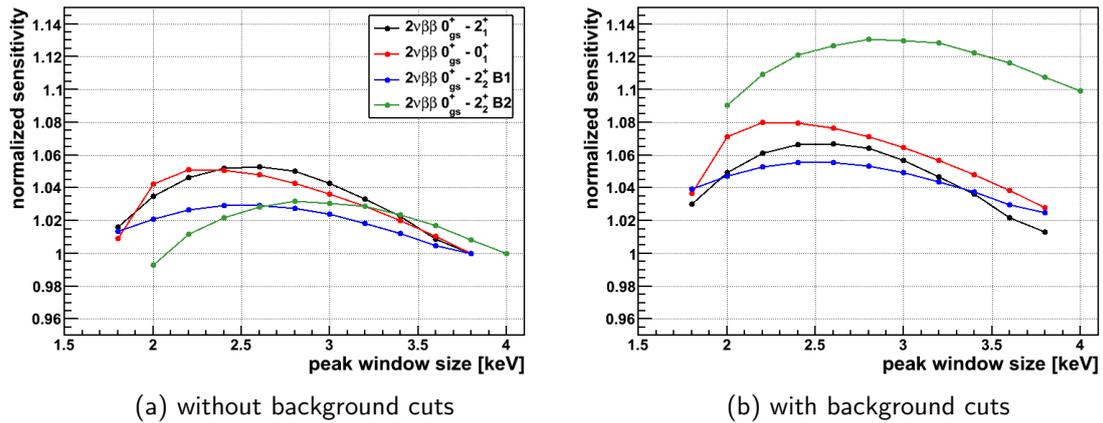
Figure 10.8 Sensitivity for different values of the PWS. The sensitivity is normalized to the 3.8 keV PWS after the coincidence cuts.

The summary of the cut optimization is shown in Tab. 10.4. In all cases a better sensitivity is reached with the background cuts.

The actual **detector pairs** of coincidence events that are considered for the analysis can also be tuned to favor the signal over background. The idea of this cut is to select only

Table 10.4 Base values (first row) and optimized values (other rows) for single detector threshold (SDT), sum energy limit (SEL) and the peak window size (PWS). The sensitivity gain is related to the base values before background cuts.

mode	SDT [keV]	SEL [keV]	PWS [keV]	size ROI [keV]	sensitivity gain [%]
base values	100	2039	$2\sigma_E$		
$0_{\text{g.s.}}^+ - 2_1^+$	450	1750	± 2.6	$[556.5 - 561.7]$	41.3
$0_{\text{g.s.}}^+ - 0_1^+$	250	1750	± 2.2	$[556.9 - 565.4]$	18.9
$0_{\text{g.s.}}^+ - 2_2^+$ B1	250	1800	± 2.4	$[556.7 - 561.5]$	20.4
				$\vee[654.0 - 660.0]$	
$0_{\text{g.s.}}^+ - 2_2^+$ B2	300	1850	± 2.8	$[1213.3 - 1218.9]$	98.5

detectors pairs that enhance the overall sensitivity. Additionally, each detector pair is further split into the "gamma" detector and the "source" detector identified by containing an energy deposition in the ROI or an arbitrary energy deposition respectively. This splitting shows a non symmetrical effect on the sensitivity due to differences for enriched and non-enriched pairs, pairs with different sizes or pairs in specific geometrical constellation in the array.

The study is performed on signal and background MC events after the optimized background cut level. For every possible detector pair the surviving signal and background events are recorded. Then the sensitivity is calculated with Eq. 10.1 for each pair and normalized to the sensitivity of all pairs. The resulting normalized pair sensitivity is equivalent to a sensitivity contribution of each detector pair to the total sensitivity. This sensitivity contribution for all detector pairs is shown in Fig. 10.9a for the 0_1^+ transition and in Fig. F.5a to F.5e in the appendix for the other transitions. A cut is applied on the sensitivity contribution, selecting only detector pairs above a certain contribution threshold. The signal and background events of the surviving detector pairs are used to calculated a new sensitivity for the analysis. Now, the cut value for the pair contribution threshold is scanned from 0 to 6 %. With increasing contribution threshold, the number of selected detector pairs is reduced which results in a step by step reduction of signal efficiency and background counts; however, the sensitivity as defined with the figure of merit in Eq. 10.1 reaches a maximum for a certain pair selection. The effect of increasing cut threshold is shown in Fig. 10.9b. Plotted is the sensitivity, the signal efficiency and the background counts against the sensitivity contribution threshold. All curves are normalized to the values in the case that all detector pairs are considered, i.e. a cut threshold of 0 %.

The scan of the pair contribution threshold shows a maximum in sensitivity between 0.5 to 1.0 % pair contribution. In other words, it is favorable to ignore detector pairs that contribute less than 0.5 or 1.0 % to the total sensitivity. The selected detector pairs for the optimized selection are shown in bold frames in Fig. 10.9a. The optimized selections reduce the expected background counts to 80 % while keeping the signal efficiency at 95 to 98 % compared to the full selections. This yields a sensitivity gain of 7 to 9 % which is summarize in Tab. 10.5.

The sensitivity map in Fig. 10.9a also shows the effect of the array configuration on the analysis. There are various detector pairs with no sensitivity which illustrates detectors which were not operated at the same time or removed from analysis at a given time. The

(a) sensitivity map for detector pairs

(b) scan of the pair contribution cut
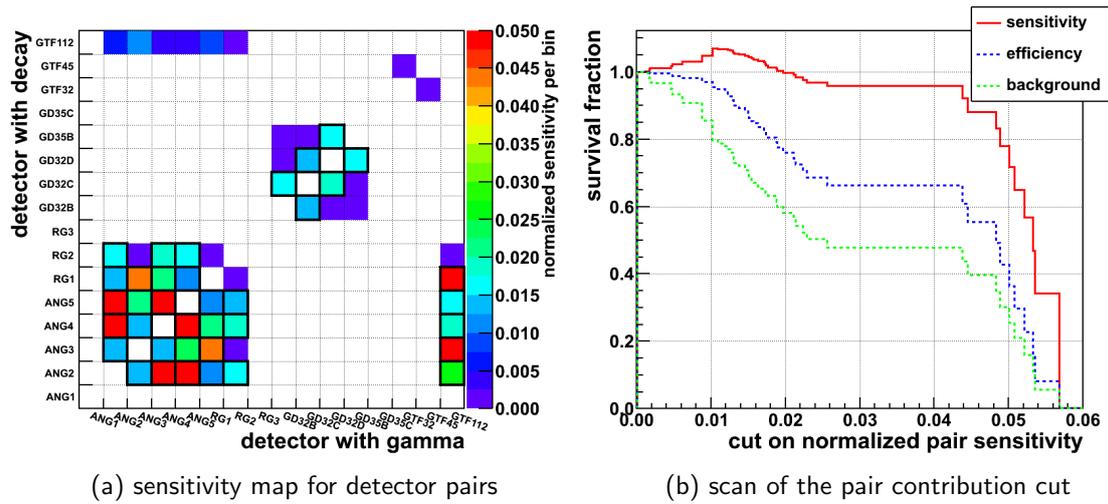
Figure 10.9 $2\nu\beta\beta$ 0_1^+ transition: Map of sensitivities for individual detector pairs with distinguished "gamma" and "source" detector (left). The detector pair contribution cut results in different detector pair selections; the sensitivity, signal efficiency and background for such selections is plotted against the contribution cut with a relative threshold between 0 % and 6 % (right). These values are normalized to the selection of all pairs (i.e. no cut). The surviving pairs for the optimized cut threshold are shown with bold frames.

Table 10.5 Summary of detector pair cut. Listed from left to right is the cut level on the pair contribution to the normalized sensitivity, the number of surviving detector pairs, the efficiency and background as the fraction before / after cut and the sensitivity gain.

decay mode	cut level [%]	# pairs	efficiency [%]	background [%]	sensitivity gain [%]
$0_{\text{g.s.}}^+ - 2_1^+$	0.57	37	97.5	79.4	9.4
$0_{\text{g.s.}}^+ - 0_1^+$	1.02	37	95.5	79.8	6.9
$0_{\text{g.s.}}^+ - 2_2^+$ branch 1	1.01	37	95.3	79.6	6.8
$0_{\text{g.s.}}^+ - 2_2^+$ branch 2	0.69	37	96.9	79.2	8.8

GTF32 and GTF45 detectors were substituted with the BEGe detectors (GD*) and have hence not been operated simultaneously. RG3, ANG1 and GD35C were never operational. Comparing the sensitivity maps with the array geometry (Fig. 5.3) illustrates that neighboring detectors show the largest contribution. Pairs containing ANG2, ANG4 and ANG5 yield the largest benefits to the analysis being in the center of the 3-string arm and facing each other with the lateral sides. In general, lateral facing detectors show the largest contributions followed by top-bottom facing detectors. Diagonal detector pairs show only little contribution but are inside the optimized pair selection for large detectors. The BEGe detectors in the separated string only significantly contribute to themselves in the top-bottom facing pairs. Another interesting feature includes the $^{\text{nat}}$Ge (GTF*) detectors which show a significant contribution only as "gamma" detectors. In fact GTF112, in the 3-string arm, gives a major contribution to the sensitivity, detecting the de-excitation γ-rays but not the $\beta\beta$ component as a source detector of $2\nu\beta\beta$ decay. The exclusion of $^{\text{nat}}$Ge detectors as source detectors reduces a large fraction of background while not reducing the signal efficiency in a significant way.

The rather extensive cut flow optimization is performed with clearly defined selection crite-

ria chosen as the optimization of the sensitivity. This strategy is pursued to be as ignorant as possible without being blinded and to avoid seemingly arbitrary choices of analysis parameters such as energy thresholds, window width and pair selections which could otherwise introduce a human bias. This is especially important since the half-life sensitivity of the GERDA PHASE I dataset is closely overlapping with many theoretical predictions of the $2\nu\beta\beta$ 0_1^+ transition. Furthermore, the cut flow optimization is entirely based on MC simulations of the dataset. Up to this point the GERDA PHASE I data is not used apart from constructing the background model.

The final results are based on background estimation from the SB which were selected with the help of background model and illustrated in Fig. F.6 in the appendix. After applying the full sequence of cuts, the validity of the SB regions is tested. For these regions a flat background is required. In case the SBs are symmetrically placed around the ROI, also a linear background is sufficient. Tab. 10.6 shows the background model prediction for each SB. Also shown are the observed number of events in the SBs for comparison. The individual SBs of the 2_1^+ decay mode show similar numbers of expected background events. This validates the flat background assumption. For the 0_1^+ and 2_2^+ decay modes, the individual SBs show small variations; SBs shifted to higher energies have a smaller expected background than SBs shifted to lower energies. However, the average background expectation from the MC model in all four SBs and the background expectation in the ROI are in good agreement indicating a linear background. This validates the SBs to be used as background estimators for the ROI.

Table 10.6 Summary of SBs for each decay mode after the complete sequence of cuts. Listed are the relative position ΔE of the four SBs compared to the ROI, the number of events in the MC background model N_{MC} and the number of events in the dataset N_{data}. Additionally the background expectations in the ROI and the observed events are shown after application of all cuts. The uncertainty of the MC expectations denote statistical uncertainties only.

region	ΔE	N_{MC}	N_{data}	region	ΔE	N_{MC}	N_{data}
$0_{g.s.}^+ - 2_1^+$ 559.1 keV				$0_{g.s.}^+ - 0_1^+$ 559.1 & 563.2 keV			
SB 1	$-7.5\,\mathrm{keV}$	2.5 ± 0.1	2	SB 1	$-12\,\mathrm{keV}$	8.0 ± 0.1	7
SB 2	$+7.5\,\mathrm{keV}$	2.4 ± 0.1	0	SB 2	$+12\,\mathrm{keV}$	7.5 ± 0.1	11
SB 3	$-15\,\mathrm{keV}$	2.6 ± 0.1	3	SB 3	$-24\,\mathrm{keV}$	8.3 ± 0.1	7
SB 4	$+15\,\mathrm{keV}$	2.4 ± 0.1	5	SB 4	$+35\,\mathrm{keV}$	6.8 ± 0.1	9
average SB		2.5 ± 0.1	2.5	average SB		7.7 ± 0.1	8.5
ROI		2.5 ± 0.1	2	ROI		7.9 ± 0.1	5
$0_{g.s.}^+ - 2_2^+$ branch 1: 559.1 & 657.0 keV				$0_{g.s.}^+ - 2_2^+$ branch 2: 1216.1 keV			
SB 1	$-8\,\mathrm{keV}$	8.5 ± 0.1	6	SB 1	$-19\,\mathrm{keV}$	0.52 ± 0.02	1
SB 2	$+18\,\mathrm{keV}$	8.1 ± 0.1	5	SB 2	$+10\,\mathrm{keV}$	0.39 ± 0.02	0
SB 3	$-16\,\mathrm{keV}$	8.7 ± 0.1	6	SB 3	$-27\,\mathrm{keV}$	0.58 ± 0.02	0
SB 4	$+35\,\mathrm{keV}$	7.9 ± 0.1	12	SB 4	$+47\,\mathrm{keV}$	0.32 ± 0.02	1
average SB		8.3 ± 0.1	7.25	average SB		0.45 ± 0.01	0.5
ROI		8.3 ± 0.1	6	ROI		0.40 ± 0.02	0

10.4   Results and Limit Setting

The single detector spectra around the ROI are shown in Fig. 10.10 for all decay modes. All two-detector coincident events with decay mode optimized SDT and SEL are shown in light gray; no background cut and pair cut are applied. The corresponding background p.d.f. is shown in black for illustration. Events surviving the sequence of cuts are only defined inside 5 intervals corresponding to the five tags of ROI and SB[1-4]. The two detector energies of these events are shown in red for the ROI tag and blue for the SB[1-4] tag. Note that there are two entries per event in the histograms.
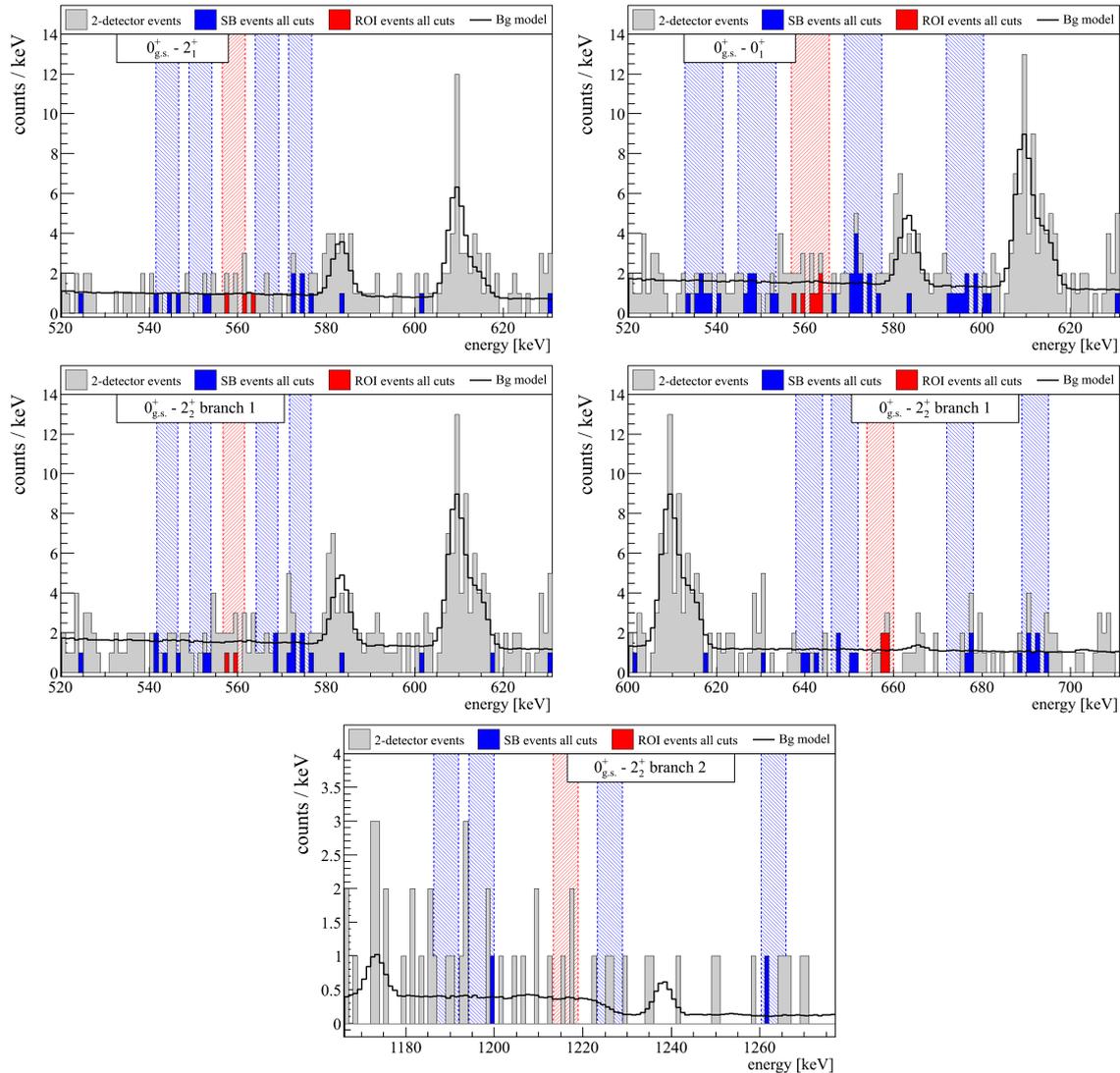
Figure 10.10   Single energy spectra around the ROI for all decay modes. Shown are all two-detector events for the optimized SDT and SEL (light gray) and the corresponding background curves (black). The optimized cuts result in different two-detector spectra for each decay mode. Also shown are the ROI (shaded red) and SB region (shaded blue). Highlighted are events that are tagged as ROI (red) and SB (blue) after all cuts which are used for the limit setting. Note that the histograms contain two entries per event and that one entry may lie outside the tagging region.

Frequentist 90 % confidence level and Bayesian 90 % credibility lower values are calculated for $T_{1/2}$. In both approaches the same likelihood is used which is constructed for the inverse

half-life $T_{1/2}^{-1}$. In case of the two decay branches of the $0_{\text{g.s.}}^+ - 2_2^+$ transition, the likelihood is treated as two individual datasets with a common $T_{1/2}^{-1}$. The expectation for the signal counts for a given decay branch (k) is:

$$s_k = \ln 2 \cdot \eta_k \cdot \mathcal{E} \cdot T_{1/2}^{-1}, \tag{10.2}$$

with the decay branch specific efficiency η_k [10]. The efficiency is the live-time weighted averaged detection efficiency of a $2\nu\beta\beta$ decay excited state event over all runs in the two GERDA array configurations of PHASE I. The exposure $\mathcal{E} = N_{\text{Ge76}} \cdot T$ is defined as the combined total isotopic exposure for ^{76}Ge in the dataset for all detectors. The expected number of events in the ROI is:

$$\mu_k = \frac{b_k}{4} + s_k \tag{10.3}$$

using the total background from all 4 SBs b_k. The full expression of the likelihood is constructed with three terms: (1) a Poisson term describing the probability of signal and background in the ROI, (2) a Poisson penalty term accounting for the uncertainty of the background level in the ROI and (3) a Gaussian penalty term accounting for all systematic uncertainties condensed into the efficiency. The likelihood depends on $T_{1/2}^{-1}$, the number of counts in the ROI (n_k), the number of counts in all SBs (m_k) and the efficiency expectation (ϵ_k):

$$\mathcal{L}\left(n_k, m_k, \epsilon_k | T_{1/2}^{-1}, b_k, \eta_k\right) = \prod_k \left[\frac{(\mu_k)^{(n_k)}}{(n_k)!} \cdot e^{-\mu_k} \right]$$
$$\cdot \left[\frac{(b_k)^{(m_k)}}{(m_k)!} \cdot e^{-b_k} \right] \tag{10.4}$$
$$\cdot \left[\frac{1}{\sigma_{\epsilon_k}\sqrt{2\pi}} \cdot e^{-\frac{1}{2}\left(\frac{\epsilon_k - \eta_k}{\sigma_{\epsilon_k}}\right)^2} \right].$$

The likelihood is numerically treated as $-2\log\mathcal{L}$. The Frequentist values are based on a bounded profile likelihood test statistic [179] increased by 2.7 compared to the minimum. It was verified that this method has always sufficient coverage. In the extraction of the posterior probability [180] for the Bayesian case, flat priors for all fit parameters $T_{1/2}^{-1}$, b_k and η_k are used since the prior information on the background and efficiency is included in the likelihood with penalty terms.

Systematic uncertainties on the signal efficiency are estimated with MC simulations and combined into a single value σ_{ϵ_k} assuming no correlations. The sources of these uncertainties are the fully active volume (FAV) and the full charge collection depth (FCCD) of the detectors, the energy resolution after cross talk correction, the uncertainty introduced by the statistics and physics processes of MC simulations and the uncertainty on the isotopic abundance. A summary is shown in Tab. 10.7.

The effect on FAV and FCCD uncertainty is investigated with dedicated MC simulations. In one case, the FCCD of all detectors is set once to their maximum and once to their minimum value. The effect on the efficiency is $\pm 8\%$. This is a strong overestimation since it is

---

[10]Note that ϵ_k is the detection efficiency determined with MC simulations and η_k is the corresponding floating parameter in the fit.

Table 10.7 Summary of systematic uncertainties.

systematic	uncertainty	effect on ϵ
FAV / FCCD	average	5 %
energy resolution	10 %	3 %
isotopic abundance	2.5 %	2.5 %
MC statistics	0.5 %	0.5 %
MC physics processes	4 %	4 %
sum		7.5 %

unlikely that the FCCD of all detectors is fluctuating in the same direction. If the FCCD of ANG5[11] is set to the maximum and minimum FCCD value, the effect on the efficiency is $\pm 2\,\%$. To mediate between these two extreme cases, an FAV / FCCD uncertainty of $\pm 5\,\%$ on the efficiency is chosen.

The energy resolution is investigated with the post smearing of the MC simulations. A variation of $10\,\%$ on the FWHM of the Gaussian smearing results in a $3\,\%$ effect for the efficiency. The other systematic uncertainties enter directly on the efficiency level.

A sensitivity study is performed using a toy MC under the assumption of no signal. The inverse half-life limit is calculated 10^4 times with randomly changing input parameters; n_k^{rand} and m_k^{rand} are each randomized according to a Poisson distribution. The expectation values of this distribution are taken from the background model prediction N_{MC} and $4\,N_{\mathrm{MC}}$ respectively (Tab. 10.6). $\epsilon_k^{\mathrm{rand}}$ is randomized with a Gaussian distribution with a mean of ϵ_k and a width of σ_{ϵ_k}. The median of the $90\,\%$ quantile inverse half-life limit distribution is taken as the sensitivity for the Frequentist and Bayesian case, respectively.

10.4.1 ^{76}Ge Decay Mode $2\nu\beta\beta$ $0_{\mathrm{g.s.}}^+ - 2_1^+$

The transition to the excited 2_1^+ has one $559.1\,\mathrm{keV}$ de-excitation γ-ray and hence a small coincidence efficiency compared to the other excited state decay modes. The optimization of the sequence of cuts shows a maximal sensitivity for a SDT of $450\,\mathrm{keV}$, a SEL of $1750\,\mathrm{keV}$ and a ROI size of $559.1 \pm 2.6\,\mathrm{keV}$. The pair optimization selects 37 detector pairs with significant contribution. The results after the different steps in the sequence of cuts are shown in Tab. 10.8. After all cuts 2 events are observed in the ROI and 2.5 events are expected from the side bands. No signal is found and a Frequentist lower half-life limit of $1.6 \cdot 10^{23}\,\mathrm{yr}$ ($90\,\%$ C.L.) with a sensitivity of $1.3 \cdot 10^{23}\,\mathrm{yr}$ is determined. The Bayesian analysis yields a lower bound of $1.3 \cdot 10^{23}\,\mathrm{yr}$ ($90\,\%$ C.I.) with a sensitivity of $1.2 \cdot 10^{23}\,\mathrm{yr}$.

A list showing the properties of all events in the ROI including the last survived cut level is shown in Tab. F.1 in the appendix. The time distribution of events in the ROI is shown in Fig. F.8a. The determination of the inverse half-life limit for the Frequentist and Bayesian analysis is illustrated in Fig. 10.11. The distribution of the randomized inverse half-life limits in the zero signal hypothesis for the sensitivity estimation is shown in Fig. F.7 in the appendix.

The lower half-life limit could be improved by two orders of magnitude compared to the

---

[11]Chosen as a representative detector in the array with a high sensitivity contribution to the analysis

Table 10.8 Input parameters for the likelihood of $2\nu\beta\beta$ $0^+_{\text{g.s.}} - 2^+_1$ after different cut flow steps. Shown from left to right are: n_k - number of events with ROI tag, m_k - number of events with a SB[1-4] tag, ϵ_k - detection efficiency.

cut level	n_k	m_k	ϵ_k [%]
after 2. (coincidence cuts)	6	18	0.413
after 3. (background cuts)	3	15	0.393
after 4. (detector pair cuts)	2	10	0.389

previously best limit. However, the current theoretical prediction are beyond the experimental reach. The lowest half-life prediction by the Hartree-Fock-Bogoliubov approach are a factor of 6 above the current sensitivity. The largest half-life prediction by shell model calculations are even 7 orders of magnitude above the current limit.

10.4.2 ^{76}Ge Decay Mode $2\nu\beta\beta$ $0^+_{\text{g.s.}} - 0^+_1$

The transition to the excited 0^+_1 state has two de-excitation γ-rays of 559.1 keV and 563.2 keV in the final state and the largest detection efficiency of the considered decay modes. It has also the lowest theoretically predicted half-life and is thus of special interest. The cut optimization yields a maximum sensitivity with a SDT of 250 keV, a SEL of 1750 keV and a combined peak window of $556.9 - 565.4$ keV. The pair optimization selects 37 detector pairs. The results after each step in the sequence of cuts are shown in Tab. 10.9. The list of events is shown in Tab. F.2. After all cuts, 8.5 events are expected in the ROI and 5 events are observed. No signal is found; a lower half-life limit of $3.7 \cdot 10^{23}$ yr (90 % C.L.) is set for the Frequentist analysis and $2.7 \cdot 10^{23}$ yr (90 % C.I.) for the Bayesian analysis. The sensitivities are $1.9 \cdot 10^{23}$ yr and $1.8 \cdot 10^{23}$ yr, respectively.

Table 10.9 Input parameters for the likelihood of $2\nu\beta\beta$ $0^+_{\text{g.s.}} - 0^+_1$ after different cut flow steps. Shown from left to right are: n_k - number of events with ROI tag, m_k - number of events with a SB[1-4] tag, ϵ_k - detection efficiency.

cut level	n_k	m_k	ϵ_k [%]
after 2. (coincidence cuts)	13	47	0.973
after 3. (background cuts)	10	42	0.945
after 4. (detector pair cuts)	5	34	0.919

This lower half-life limit is 2.5 orders of magnitude better than previous results. The new limit is well within the region of theoretical predictions. Bayes factors are calculated for testing the hypothesis of each NME model in Tab. 10.1 by taking the ratio $B = p(H_1)/p(H_0)$ in which H_1 is the NME model hypothesis with $T^{\text{Model}}_{1/2}$ and H_0 the hypothesis of only background. The models in Refs. [175, 176, 56, 54] have $B < 10^{-6}$ and are ruled out. The QRPA model [55] has $B = 0.001 - 0.19$ for $T_{1/2} = (1.0 - 3.1) \cdot 10^{23}$ yr, respectively. Recent calculations with RQRPA [168], IBM-2 [169] and ShM [170] predict significantly longer half-lives. For RQRPA a range can be constrained: $B = 0.005$ for $g_A = 1.26$ ($T_{1/2} = 1.2 \cdot 10^{23}$ yr) compared to $B = 0.45$ for $g_A = 1.00$ ($T_{1/2} = 5.8 \cdot 10^{23}$ yr). The IBM-2 and ShM prediction are still above the current experimental reach.

The counts in the ROI show less events than expected from the SB. The expected events in the MC background model are 7.9 in the ROI and 7.7 as average from SB[1-4] Tab. 10.6. This indicates a downward fluctuation in the ROI and an upward fluctuation in the SB. As a result the limit is higher than the sensitivity.

10.4.3 ^{76}Ge Decay Mode $2\nu\beta\beta$ $0^+_{\mathrm{g.s.}} - 2^+_2$

The transition into the excited 2^+_2 state has two de-excitation branches: Branch 1 with two γ-ray emissions of 559.1 keV and 657.0 keV and branch 2 with a single γ-ray emission of 1216.1 keV. The branching ratio is 64 % to 36 % respectively. The cuts are optimized for both branches individually. The optimal cut values are a SDT of 250 keV and 300 keV and a SEL of 1800 keV and 1850 keV for branch 1 and 2 respectively. The peak window is optimal in 559.1 ± 2.4 keV and 657.0 ± 3.0 keV for branch 1 and 1216.1 ± 2.8 keV for branch 2. The pair optimization selects 37 detector pairs for both branches.

Table 10.10 Input parameters for the likelihood of $2\nu\beta\beta$ $0^+_{\mathrm{g.s.}} - 2^+_2$ after different cut flow steps. Shown from left to right are: n_k - number of events with ROI tag, m_k - number of events with a SB[1-4] tag, ϵ_k - detection efficiency.

cut level	decay branch $k = 1$			decay branch $k = 2$		
	n_k	m_k	ϵ_k [%]	n_k	m_k	ϵ_k [%]
after 2. (coincidence cuts)	13	46	0.633	3	9	0.102
after 3. (background cuts)	10	42	0.612	0	2	0.094
after 4. (detector pair cuts)	6	29	0.594	0	2	0.092

The results for each step in the sequence of cuts and both branches are listed in Tab. 10.10. Limits are calculated for both branches separately and combined according to Eq. 10.4 with $k = 1, 2$. Branch 1 shows a significantly larger efficiency due to the favored branching ratio; on the other hand, the ROI for branch 2 is at higher energy resulting in a lower background level. 7.25 events are expected for branch 1 and 6 are observed. The half-life limit for this branch is $1.7 \cdot 10^{23}$ yr and $1.4 \cdot 10^{23}$ yr in the Frequentist and Bayesian interpretation, respectively. In branch 2, 0.5 events are expected and no event is observed. The half-life limit for this branch is $7.4 \cdot 10^{22}$ yr and $4.9 \cdot 10^{22}$ yr, respectively. A list of all events is shown in Tab. F.3 and Tab. F.4 and the time distribution in Fig. F.8c and Fig. F.8d in the appendix.

The combined lower half-life limit is $2.3 \cdot 10^{23}$ yr (90 % C.L.) and $1.8 \cdot 10^{23}$ yr (90 % C.I.) for the Frequentist and Bayesian analysis, respectively. The corresponding combined half-life sensitivities are $1.4 \cdot 10^{23}$ yr and $1.3 \cdot 10^{23}$ yr, respectively. This limit is an improvement by 2 orders of magnitude compared to previous limits. However, the theoretical predictions for this transition are $>10^{28}$ yr and cannot be tested with the current sensitivity.

An illustration of the limit extraction is shown in Fig. 10.11. On the left is shown the profile likelihood for each decay mode. The horizontal line is the target value of 2.7 for the one-sided 90 % quantile. The vertical lines are the corresponding 90 % C.L. upper inverse half-life limits. On the right is shown the marginalized posterior probability distribution for the inverse half-lives in the Bayesian case. The vertical lines denote the adopted 90 % C.I. limit. Fig. F.7 shows the limit distributions for the 10.000 toy MC experiments with

(a) Frequentist profiled likelihood

(b) Bayesian marginalized posterior propbability.
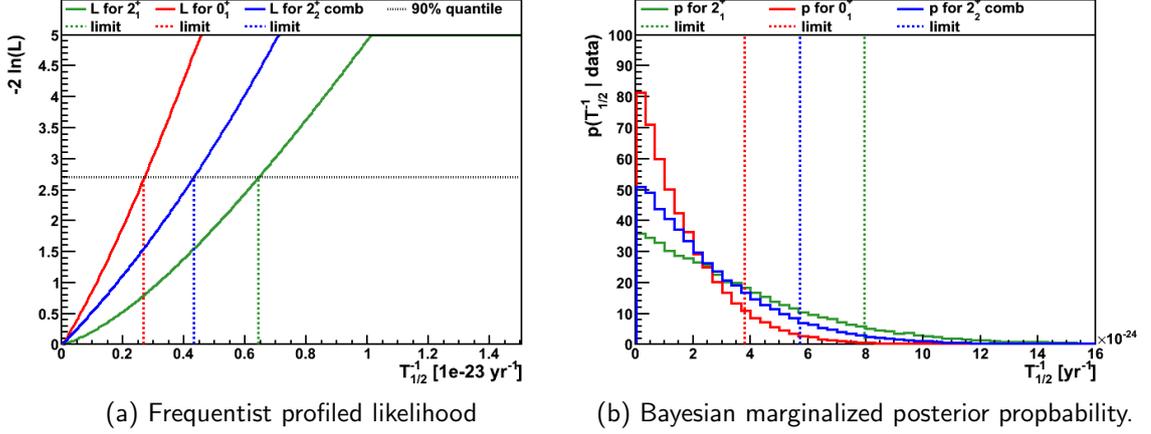
Figure 10.11   Illustration of obtained inverse half-lives for Frequentist and Bayesian analysis for all decay modes after the full sequence of cuts. Left: Plotted is the likelihood after profiling all nuisance parameter. The horizontal dashed lines are the 90 % C.L. quantile for a one-sided limit. The vertical lines are the obtained inverse half-life limits. Right: Plotted is the marginalized posterior probability of the inverse half-life. The vertical lines show the obtained half-life limit for a 90 % C.I.

randomized input parameters in the background only scenario for all decay modes. The vertical red line is the median of the distribution and the adopted value for the sensitivity. The vertical green line is the adopted half-limit.

10.5   Conclusions

An analysis for $2\nu\beta\beta$ excited state transitions in ^{76}Ge with the GERDA PHASE I data set has been performed for the decay modes $0^+_{g.s.} - 2^+_1$, $0^+_{g.s.} - 0^+_1$ and $0^+_{g.s.} - 2^+_2$. The analysis is performed unblinded but a strict policy of selecting the analysis cuts has been adopted: All cut parameters are chosen such that the sensitivity calculated from MC simulations is maximized. No signal has been found and new lower half-life limits are set for all decay modes which are summarized in Tab. 10.11. These limits are at least two orders of magnitude larger than previous limits. Bayes factors are calculated for the predictions of the $0^+_{g.s.} - 0^+_1$ half-life with various nuclear models. Many old NME calculations could be ruled out.

Table 10.11 Summary of results for all decay modes from the Frequentist and the Bayesian analysis.

decay mode	Frequentist 90 % C.L.		Bayesian 90 % C.I.	
	$T_{1/2}$ [10^{23} yr]	$T_{1/2}^{\text{sensitivity}}$ [10^{23} yr]	$T_{1/2}$ [10^{23} yr]	$T_{1/2}^{\text{sensitivity}}$ [10^{23} yr]
$0^+_{g.s.} - 2^+_1$	> 1.6	> 1.3	> 1.3	> 1.2
$0^+_{g.s.} - 0^+_1$	> 3.7	> 1.9	> 2.7	> 1.8
$0^+_{g.s.} - 2^+_2$	> 2.3	> 1.4	> 1.8	> 1.3

The analysis is based on the assumption that only one decay mode is realized at a time. This is valid in the present case for the non-observation of a signal. Hence, the analysis is performed on each decay mode completely independently. However, it should be noted that the results of the different decay modes are not independent since they have a similar event signature i.e. they share the same ROIs in the data. Especially the 559.1 keV γ-line of the $0^+_{g.s.} - 2^+_1$ transition is part of all decay modes. The Frequentist lower half-life limits

are larger than the sensitivity in all cases. The observed statistical downward fluctuation of the background in the 559.1 keV region has a similar influences on all limits.

10.6   Outlook and Sensitivity for Gerda Phase II

The tentative GERDA PHASE II array is used to estimate the sensitivity of the 2_1^+ and 0_1^+ excited states transitions with $100 \, \text{kg} \cdot \text{yr}$ exposure in PHASE II. The array consists of 30 enriched BEGe detectors, 8 enriched semi-coaxial detectors and GTF112 as a natural semi-coaxial detector. The array is separated into 4 BEGe strings and 3 semi-coaxial strings (see Fig. 5.7). Improvements are expected due to larger exposure, a larger segmentation of the array increasing the detection efficiency and an overall lower background level. Furthermore, the LAr instrumentation can be used to tag events with energy depositions in the LAr which provides an additional handle for the analysis.

Exposure   The detectors sum up to a total mass of $39.7 \, \text{kg}$ requiring $920 \, \text{d}$ of continuous operation to reach an exposure of $100 \, \text{kg} \cdot \text{yr}$. The equivalent isotopic exposure of ^{76}Ge is $82.7 \, \text{kg} \cdot \text{yr}$. The exposure for this study is increased by roughly a factory of 4 compared to the PHASE I analysis[12].

Detection Efficiency   The sensitivity study is performed with the baseline cuts of $100 \, \text{keV}$ SDT, $2039 \, \text{keV}$ SEL and $2 \, \sigma_E$ PWS which are not optimized. Also the background cuts are applied. The simulated efficiency is $4.6 \, \%$ for the 0_1^+ transition and $2.9 \, \%$ for the 2_1^+ transition for the case that all detector are operational. This is a factor of 5 and 7 more than for the average efficiency in PHASE I[13]. The significant increase in efficiency is due to the larger amount of detectors in the array making it more likely for the γ-rays to be captured. The effect is further increased by the smaller BEGe detectors which lead to more segmentation of the array.

Systematic Uncertainties   The largest systematic uncertainty in the PHASE I analysis is the limited knowledge of the FAV / FCCD values for the semi-coaxial detectors which dominated the exposure. In PHASE II an equivalent exposure of BEGe detectors will be added for which the FAV and FCCD have been precisely characterized in Chap. 7 of this work. This will help to reduce this systematic uncertainty to a subdominant level for a large part of the detectors.

Background   The background estimation for PHASE II is based on a simplified model with only few components. In the PHASE I analysis the background expectation for the 0_1^+ transition in the full dataset is 7.9 events after all cuts. The major background components are ^{42}K in the LAr (2.5 events), ^{214}Bi on the holders (1.5 events) and ^{208}Tl on the holders (0.4 events)[14]. Those components are used for the PHASE II estimation.

The MC simulation of ^{42}K homogeneously in the LAr around the PHASE II array yields an expected number of 89 events after baseline and background cuts for the 0_1^+ transition in

---

[12]Note that the comparison is based on the isotopic exposure and that the nominal exposure for the excited state analysis is larger than for the $0\nu\beta\beta$ decay analysis since all detectors in the array are included.

[13]Note that the PHASE I detection efficiency is based on sensitivity optimized cuts including pair selection. An optimization of the PHASE II cuts might reduce the detection efficiency slightly. Also the PHASE I efficiency is averaged over all runs where some detectors were not operational. In the case of non-operational detectors in the PHASE II array the detection efficiency will be reduced.

[14]Note that ^{42}K and ^{214}Bi are already strongly reduced after the background cuts.

$100 \, \text{kg} \cdot \text{yr}$. The activity of ^{42}K was set to the fit value in the Phase I background model. ^{214}Bi and ^{208}Tl were simulated in the Phase II silicon holders. The specific activity of the components was taken from the copper holders in the Phase I background model. This is a conservative assumption since the mono-crystalline silicon is expected to have a strongly reduced activity and is one of the major improvements in Gerda Phase II. The expected number of events after baseline and background cuts for the 0_1^+ transition in $100 \, \text{kg} \cdot \text{yr}$ exposure are 54 events for ^{214}Bi and 13.0 events for ^{208}Tl. For the 2_1^+ transition 58 events from ^{42}K, 35 events from ^{214}Bi and 8.4 events from ^{208}Tl are expected.

The ^{42}K coincidence background in the Phase II array is much stronger increased than just expected by the larger exposure. This is an effect created by the larger segmentation which leads to more coincidence events in general. All background events which are removed by the anti-coincidence veto for a $0\nu\beta\beta$ analysis will enter into the coincidence analysis and consequently increase the background there. The expected multiplicities of signal and background events are shown in Tab. 10.12 with an SDT of $100 \, \text{keV}$ applied. The generally larger multiplicity of events might justify the investigation of three-detector events for this analysis to better discriminate the signal from background. This is especially true for ^{42}K for which only $0.9\,\%$ of all detected events are three-detector events whereas $7.9\,\%$ of $2\nu\beta\beta$ 0_1^+ events are three-detector events[15].

Table 10.12 Distribution of multiplicities for simulated signal and background events in the Phase II array. An SDT of $100 \, \text{keV}$ is applied.

multiplicity [%]	1	2	3	4
$2\nu\beta\beta$ 0_1^+ all detectors	55.7	35.6	7.9	0.8
$2\nu\beta\beta$ 2_1^+ all detectors	73.9	24.2	1.8	< 0.1
^{42}K homogeneously LAr	86.9	12.1	0.9	< 0.1
^{214}Bi Phase II holders	67.0	26.8	5.5	0.7
^{208}Tl Phase II holders	56.3	31.7	9.8	1.9

Sensitivity   The number of background events from the three major background components is around 150 for the 0_1^+ and 100 for the 2_1^+ transition. Note that additional components will increase this number and a lower overall background environment will reduce this number. However, the specific activity of ^{42}K, as the largest background component, will not be strongly reduced in Phase II. The Gaussian sensitivity with $90\,\%$ C.L. given 150 background events is $1.64 \cdot \sqrt{N_{\text{bg}}} = 20$ counts. This translates into a half-life sensitivity of $1.0 \cdot 10^{24} \, \text{yr}$ ($90\,\%$ C.L.) for the 0_1^+ transition. The estimated sensitivity for the 2_1^+ transition is $8.2 \cdot 10^{23} \, \text{yr}$.

With the predicted sensitivity in Phase II the QRPA calculations for the 0_1^+ transition can be fully tested. The ShM predicts a half-life still a factor of 2 above the sensitivity. However, the strong influence of the array segmentation on the signal efficiency and background level suggest a large potential for improvement with optimization of cuts as done for the Phase I analysis where an improvement of $30 - 100\,\%$ was achieved depending on the decay mode. The IBM-2 calculated half-life is still a factor of 6 above the Gerda Phase II sensitivity and is unlike to be tested without a significantly improved exposure or analysis technique.

---

[15]Note, that the application of a different SDT will change the multiplicity of some events. The enforced SDT of at least $100 \, \text{keV}$ for Phase I might be relaxed with the improved Phase II electronics and energy reconstruction.

10.6.1   Including the Liquid Argon Light Read Out

The LAr instrumentation can be used to gain additional information in the analysis. This is investigated with the MC simulations developed in Chap. 9. The specific application strongly depends on the event topology and hence on the decay mode.

In the case of the 2_1^+ transition, a two-detector event with the de-excitation γ-ray fully contained in one detector will not deposit energy in the LAr. In this case the LAr instrumentation can be used as a veto, further reducing the background for this decay mode.

In the case of the 0_1^+ transition and a two-detector analysis, the second γ-ray is deposited outside of a germanium detector which is most likely in the LAr. The coincidence between germanium single detector energy and LAr energy deposition for $2\nu\beta\beta$ 0_1^+ decays is shown in Fig. 10.12a. Strong correlations can be seen between full γ-ray energies either deposited in the LAr (horizontal lines) or the germanium (vertical lines) or scatterings between the two media (diagonal lines). In this case the LAr instrumentation is not applicable as a veto without significantly reducing the detection efficiency.

(a) LAr energy versus germanium energy   (b) LAr p.e. versus germanium energy
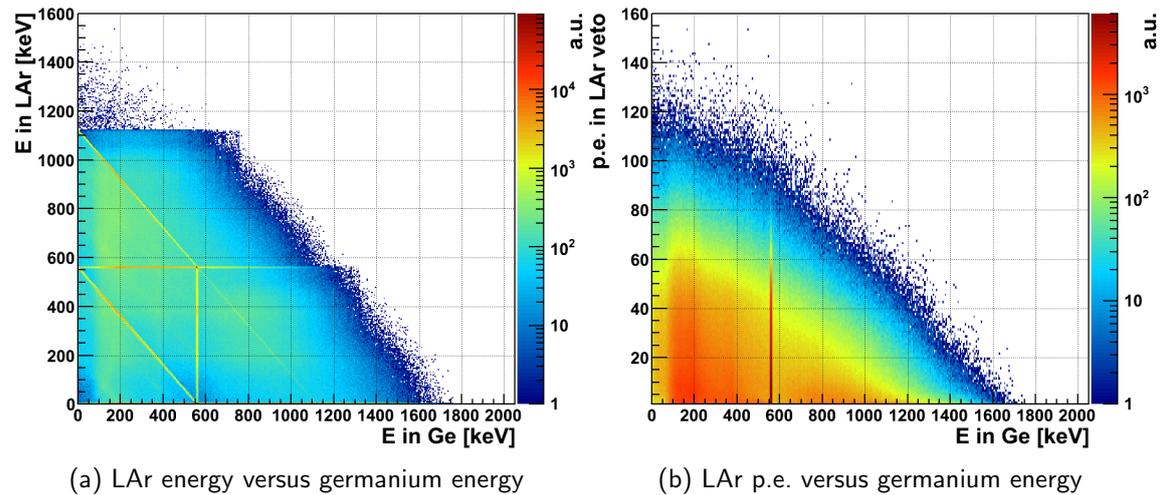
Figure 10.12 $2\nu\beta\beta$ decay simulation of ^{76}Ge into the 0_1^+ excited state with LAr veto in the Phase II array. Only two-detector events are selected. Shown is the single detector germanium energy versus energy deposited in LAr on the left and versus the detected number of photo electrons on the right.

In addition, the LAr instrumentation cannot be included in the analysis in a quantitative way due to the poor energy resolution given its design as a simple veto. Using the MC simulations with the full tracking of optical photons, the expected number of detected p.e. for a given germanium energy is shown in Fig. 10.12b. This plot can be understood as Fig. 10.12a with the applied resolution of the LAr instrumentation. The γ-line features are completely washed out.

However, an important application of the LAr instrumentation is the possibly to distinguish between the 2_1^+ and 0_1^+ decay mode in case of a signal observation. In the present Phase I analysis the experimental signature is degenerated between the two modes due to the similar energies of the de-excitation γ-rays. With the LAr instrumentation, a population of $2\nu\beta\beta$ excited state candidate events can be distinguished into (1) two-detector events with LAr veto trigger excluding 2_1^+ decays and indicating 0_1^+ decays and (2) two-detector events

without LAr veto trigger indicating 2_1^+ decays. Whereas almost no 2_1^+ decay will survive the two-detector coincidence cut and trigger the LAr veto, the situation is ambivalent for 0_1^+ decays.

Fig. 10.13a shows the simulation of 0_1^+ decays after coincidence cut which is essentially the same plot as Fig. 10.5b now extended with the dimension of the LAr energy[16]. For events in this plot, one HPGe detector is required to have an energy in 560 ± 10 keV. The horizontal line is created by the second γ-ray which is fully absorbed in the LAr. The diagonal line is created by decays in the dead volume of detectors in which one γ-ray is absorbed in one HPGe detector and the other γ-ray is scattered between a different HPGe detector and the LAr. After tracking of optical photons, the same plot with the expected number of p.e. is shown in Fig. 10.13b in which the features are smeared. However, 69 % of all 0_1^+ events after the coincidence cut trigger the LAr instrumentation with at least one p.e., whereas 31 % of the events do not produce a photo electron. If a signal excess is found in a PHASE I type analysis where it is not clear whether the excess is due to the 2_1^+ or the 0_1^+ transition, the number of events triggering the LAr instrumentation can be used to separate the two decay modes. Such a technique will be crucial to claim the observation of a specific excited stated decay mode in ^{76}Ge with GERDA PHASE II.

(a) LAr energy versus germanium energy   (b) LAr p.e. versus germanium energy
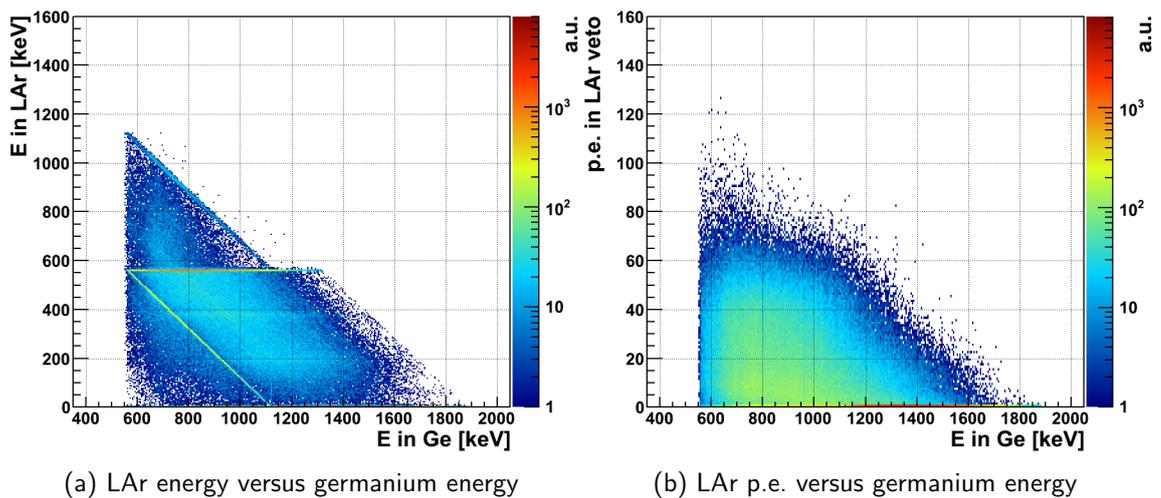
Figure 10.13 $2\nu\beta\beta$ decay simulation of ^{76}Ge into the 0_1^+ excited state with LAr veto in the PHASE II array. Only two-detector events are selected. Shown is the sum detector germanium energy after coincidence cut (one detector energy in 560 ± 10 keV) versus energy deposited in LAr on the left and versus the detected number of photo electrons on the right.

---

[16]No SDT is applied.

Chapter 11

Search for $0/2\nu\beta\beta$ Excited State Transition in ^{110}Pd and ^{102}Pd

This chapter presents a search for $2\nu\beta\beta$ and $0\nu\beta\beta$ decays of ^{110}Pd and ^{102}Pd into the excited 2_1^+, 0_1^+ and 2_2^+ states of the daughter isotopes. A new measurement is performed at LNGS and combined with two previous measurements of the same 802.4 g palladium sample at the Felsenkeller and HADES laboratories. The analysis is based on detecting the de-excitation γ-rays with gamma spectroscopy setups. No signal is observed in either isotopes and a Bayesian maximum posterior spectral fit is used to extract 90 % credibility bounds for the three transitions. The results are: $0_{g.s.}^+ - 2_1^+$: $T_{1/2} > 2.9 \cdot 10^{20}$ yr, $0_{g.s.}^+ - 0_1^+$: $T_{1/2} > 3.9 \cdot 10^{20}$ yr and $0_{g.s.}^+ - 2_2^+$: $T_{1/2} > 2.9 \cdot 10^{20}$ yr for ^{110}Pd and $T_{1/2} > 7.9 \cdot 10^{18}$ yr, $0_{g.s.}^+ - 0_1^+$: $T_{1/2} > 9.2 \cdot 10^{18}$ yr and $0_{g.s.}^+ - 2_2^+$: $T_{1/2} > 1.5 \cdot 10^{19}$ yr for ^{102}Pd. These new bounds are a factor of 1.3 to 3 larger than those reported previously.

This chapter is organized as follows: The DBD isotopes ^{110}Pd and ^{102}Pd including their experimental signature and theoretical predictions are presented in Sec. 11.1. The palladium sample used in all three measurements is described in Sec. 11.2. The three measurements with a focus of the new measurement at LNGS are presented in Sec. 11.3. The combined Bayesian analysis of all three dataset is shown in Sec. 11.4 followed by a detailed discussion of the results in Sec. 11.5 and the conclusions is Sec. 11.6.

11.1 Introduction

The element under study is palladium with the isotopes of interest ^{110}Pd and ^{102}Pd. Among the 35 isotopes expected to undergo $\beta^-\beta^-$ decay (Tab. A.1 in the appendix), ^{110}Pd has the second highest natural abundance with 11.72 %. Recently, the Q-value was remeasured to 2017.85(64) keV [181] and places ^{110}Pd among the 11 $\beta^-\beta^-$ isotopes with a Q-value larger than 2 MeV. The second isotope ^{102}Pd has a Q-value of 1172 keV, a natural abundance of 1.02 % and is able to decay via $0/2\nu$ECEC and $0/2\nu$ECβ^+.

Three measurements of ^{110}Pd have been performed in the past, one in 1954 [60] and two more recently in 2011 in the Felsenkeller [182] (see pages G-10 to G-14 in the appendix for this paper) and in 2013 in HADES [61] (see pages G-15 to G-22 in the appendix for this paper). The latter two measurements were the first to investigate excited states in palladium. This search is based on a new measurement at LNGS (Sec. 4.5.1) with the same palladium sample used for the previous two measurements. The analysis of excited state transitions uses the combined data of all three measurements.

1^+ 24.6 s
^{110}Ag

0^+
^{110}Pd

542.1 keV
544.8 keV
1360.1 keV

2^+_2 35.5%   64.5%   1475.8 keV
0^+_1 1473.1 keV

$Q_{\beta\beta}$=2017.9 keV

815.3   818.0

2^+_1 657.8 keV

657.8   1475.8

0^+ 0 keV
^{110}Cd
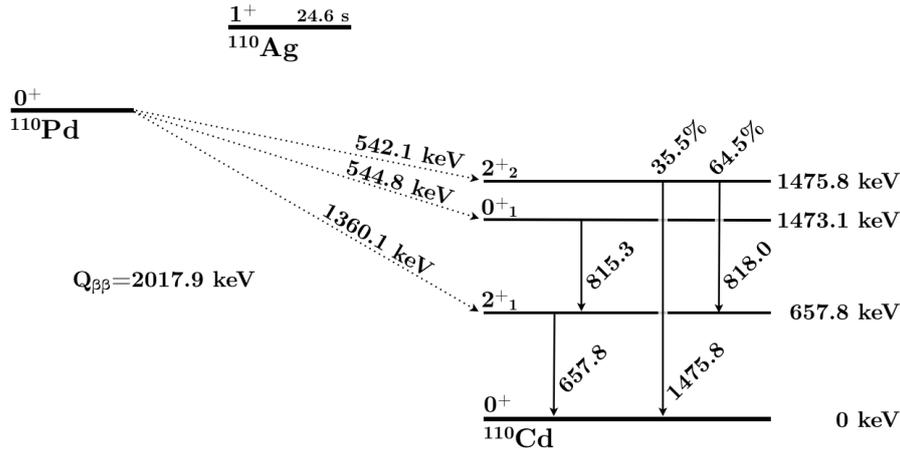
Figure 11.1 ^{110}Pd level scheme of investigated decay modes.

$1^-,2^-$ 207.3 d
^{102}Rh

0^+
^{102}Pd

1103.1 keV 2^+_2 37.1%   62.9%   68.9 keV
943.7 keV 0^+_1 228.3 keV

468.6   627.9   696.9 keV

$Q_{\beta\beta}$=1172 keV

475.1 keV 2^+_1

475.1   1103.1

0 keV 0^+
^{102}Ru
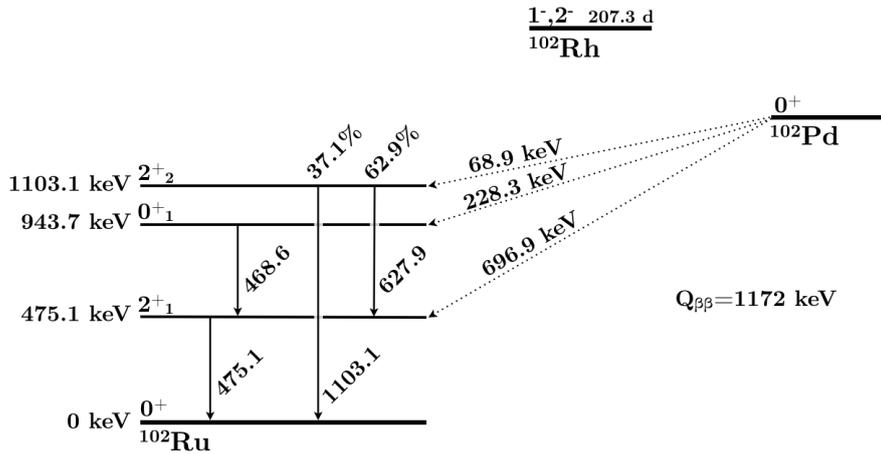
Figure 11.2 ^{102}Pd level scheme of investigated decay modes.

The search is based on gamma spectroscopy, hence only γ-rays are considered in the event topology. This makes the obtained half-life limits valid for the $2\nu\beta\beta$ and the $0\nu\beta\beta$ regime. Each excited state transition is followed by an unique set of decay branches and γ-ray cascades which are illustrated in Fig. 11.1 and 11.2. This work investigates transitions into the final states of 2^+_1, 0^+_1 and 2^+_2 in both isotopes.

For ^{110}Pd $2\nu\beta\beta$ decay exist many theoretical calculations for the ground state transition and transitions into excited states to which the experimental limits can be compared. For ^{102}Pd only experimental half-life limits are known and no theoretical calculation have been published up to date. The existing experimental and theoretical half-life limits ares summarized in Tab. 11.1.

Table 11.1 Experimental and theoretical half-life limits for various DBD modes in ^{110}Pd and ^{102}Pd. The columns show from left to right the quoted half-life, the theoretical model, the reference and the year of publication. Abbreviations denote: PHFM - Projected Hartree-Fock-Bogoliubov, SSDH - Single-State-Dominance Hypothesis, SRPA - Second quasi Random Phase Approximation, OEM - Operator Expansion Method, QRPA - Quasi Random Phase Approximation, SSD - Single State Dominance and pnQRPA - proton-neutron quasiparticle random-phase approximation.

$2\nu\beta\beta$ decay	$T_{1/2}$ [yr]	model	ref.	year
^{110}Pd $0^+_{g.s.} - 0^+_{g.s.}$	$1 \cdot 10^{17}$ (68 % CL)	exp.	[60]	1952
	$1.16 \cdot 10^{19}$	QRPA	[183]	1990
	$1.6 \cdot 10^{20}$	SRPA	[184]	1994
	$1.24 \cdot 10^{21}$	OEM	[185]	1994
	$1.2 - 1.8 \cdot 10^{20}$ [a]	SSDH	[186]	1998
	$1.75 \cdot 10^{20}$	SSDH	[187]	2000
	$1.2 \cdot 10^{20}$	SSD	[188]	2005
	$1.41 \cdot 10^{20}$ and $3.44 \cdot 10^{20}$ [b]	PHFM	[189]	2005
	$1.1 \cdot 10^{20}$ and $0.91 \cdot 10^{20}$ [c]	pnQRPA	[62]	2011
	$1.5 \cdot 10^{20}$ [d]	IBM-2	[44]	2015
^{110}Pd $0^+_{g.s.} - 2^+_1$ (657.76 keV)	$4.40 \cdot 10^{19}$ (95 % CL)	exp.	[182]	2011
	$1.72 \cdot 10^{20}$ (95 % CL)	exp.	[61]	2013
	$8.37 \cdot 10^{25}$	SRPA	[184]	1994
	$4.4 \cdot 10^{25}$	SSD	[188]	2005
	$1.48 \cdot 10^{25}$	pnQRPA	[190]	2007
	$0.62 \cdot 10^{25}$ and $1.3 \cdot 10^{25}$ [c]	pnQRPA	[62]	2011
^{110}Pd $0^+_{g.s.} - 0^+_1$ (1473.12 keV)	$5.89 \cdot 10^{19}$ (95 % CL)	exp.	[182]	2011
	$1.98 \cdot 10^{20}$ (95 % CL)	exp.	[61]	2013
	$2.4 \cdot 10^{26}$	SSD	[188]	2005
	$4.2 \cdot 10^{23}$ and $9.1 \cdot 10^{23}$ [c]	pnQRPA	[62]	2011
	$2.9 \cdot 10^{26}$ [d]	IBM-2	[44]	2015
^{110}Pd $0^+_{g.s.} - 2^+_2$ (1475.80 keV)	$9.26 \cdot 10^{19}$ (95 % CL)	exp.	[61]	2013
	$3.8 \cdot 10^{31}$	SSD	[188]	2005
	$11 \cdot 10^{30}$ and $7.4 \cdot 10^{30}$ [c]	pnQRPA	[62]	2011
^{110}Pd $0^+_{g.s.} - 0^+_2$ (1731.33 keV)	$1.38 \cdot 10^{20}$ (95 % CL)	exp.	[61]	2013
	$5.3 \cdot 10^{29}$	SSD	[188]	2005
^{110}Pd $0^+_{g.s.} - 2^+_3$ (1783.48 keV)	$1.09 \cdot 10^{20}$ (95 % CL)	exp.	[61]	2013
	$1.3 \cdot 10^{35}$	SSD	[188]	2005
^{102}Pd $0^+_{g.s.} - 2^+_1$ (475.10 keV)	$2.68 \cdot 10^{18}$ (95 % CL)	exp.	[182]	2011
	$5.95 \cdot 10^{18}$ (95 % CL)	exp.	[61]	2013
^{102}Pd $0^+_{g.s.} - 0^+_1$ (943.69 keV)	$7.64 \cdot 10^{18}$ (95 % CL)	exp.	[182]	2011
	$5.81 \cdot 10^{18}$ (95 % CL)	exp.	[61]	2013
^{102}Pd $0^+_{g.s.} - 2^+_2$ (1103.05 keV)	$8.55 \cdot 10^{18}$ (95 % CL)	exp.	[61]	2013

[a] Different experimental input for calculations
[b] $g_A = 1.25$ and 1.0 respectively
[c] For Woods-Saxon Potential and adjusted base respectively (see [62] for details)
[d] See appendix Sec. G.1 for this calculation.

11.2   Palladium Sample

The sample consists of 802.4 g of irregular shaped 1 mm x 1 cm^2 palladium plates. For this measurement the plates are placed inside two measuring containers of 55 mm diameter and 30 mm height (Fig. 11.3 measurement at LNGS). They are piled inside the container as dense as possible and an effective density of 7.59 g/cm^3 is obtained. The second container is not completely filled and placed on top of the first container such that the sample is connected as a single volume apart from the 1 mm thick container walls. The effective sample density can be compared to the density of solid palladium at room temperature with 12.02 g/cm^3. The palladium is approximated with a homogeneous distribution and the effective density is used in MC simulations to determine the detection efficiency.

For the past measurements [182, 61] the palladium was placed in a single container with 70 mm diameter and 21 mm height. Here the effective density is larger due to more efficient packing in a single container and is estimated as 10.2 g/cm^3.

Prior to any of the measurements, the sample was purified by C. HAFNER GmbH + Co. KG in 2010 to a certified purity of > 99.95 % which lowered the continuous background in the peak regions by approximately 20 % [182]. In order to avoid radioisotopes produced by cosmic ray spallation, the palladium was kept underground and exposed only $\approx$ 3 weeks during purification in 2010, $\approx$ 3 week for surface transport in fall 2011, and $\approx$ 2 d transport in spring 2012 of which 3 h were done by air. A picture of the palladium sample is shown in Fig. 11.3 before purification (left) as used for the measurements [182, 61] (center) and as used for this measurement (right).

prior purification   **measurements in Felsenkeller and HADES**   **measurement at LNGS**
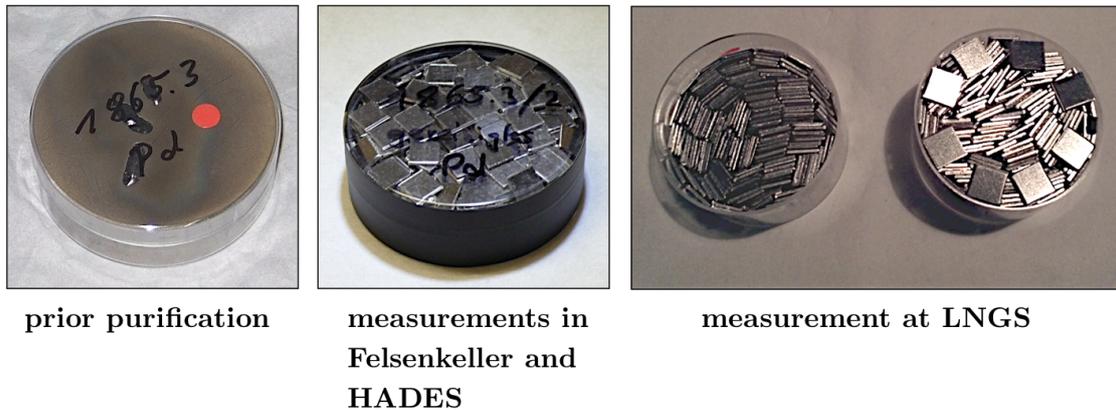
Figure 11.3 Palladium sample before purification in solid block (left). The sample after purification in form of small plates in the container used in the Felsenkeller and HADES measurements (center) and in the two measuring containers used in the LNGS measurement (right).

11.3   Measurements

The three measurements of the palladium sample are summarized in Tab. 11.2 with the overburden of the underground laboratory, the measuring time and the background level in a selected ROI. In addition the complete sample spectra of the measurements are compared in Fig. 11.4 scaled to counts per keV, kg HPGe detector mass and day.

Table 11.2 Overview of excited state palladium measurements

location	overburden [m] / [m.w.e.]	time [d]	Bg at 657.8 keV [cts/keV/d]	gamma spectroscopy setup
Felsenkeller	47 / 110	16.2	1.81	single HPGe
HADES	223 / 500	44.8	0.28	two HPGe sandwich
LNGS	1400 / 3200	87.2	0.30	four HPGe setup
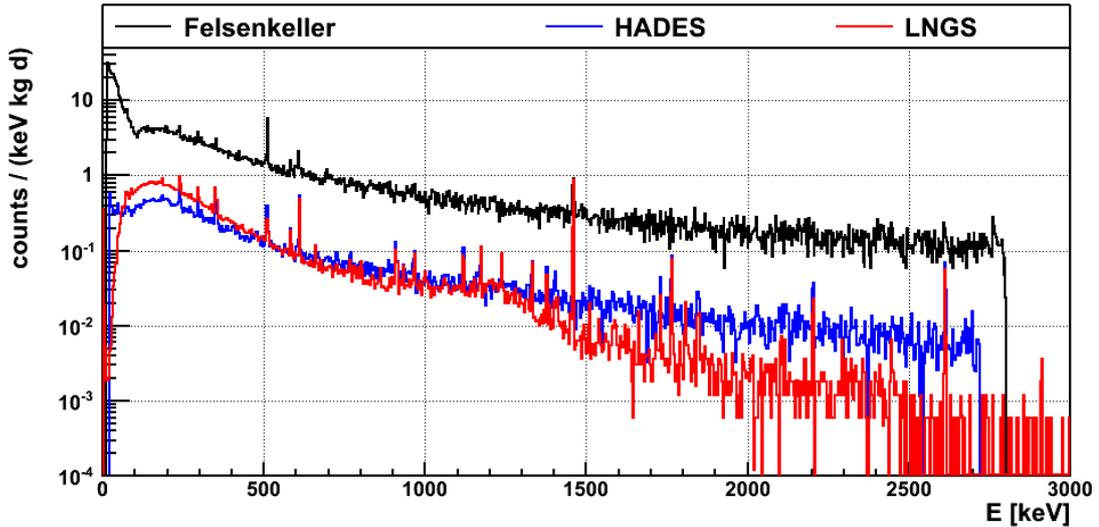
Figure 11.4 Energy spectra of all three measurements normalized to counts per keV, kg HPGe detector mass and day.

For comparison it should be noted that the number and geometrical setup of detectors is different between the measurements. The first measurement in the Felsenkeller was performed with a large single germanium detector (90 % relative efficiency) where the sample was placed on top of the endcap. The second measurement in HADES was performed with a two-detector setup (80 % and 90 % relative efficiency) where the sample was sandwiched between the endcaps of the two detectors. The last measurement was performed with a four-detector setup. Hence the spectra seen in Fig. 11.4 do not include the inherently different detection efficiencies and are not representative for the actual background in the analysis. The absolute background in the analysis is indicated in Tab. 11.2 for the 657.8 keV ROI. This is e.g. smaller in the HADES setup compared to the deeper LNGS setup because of using only two instead of four HPGe detectors.

The first two measurements are reported in [182] and [61]. A detailed description of the experimental setups can be found in these references and will not be repeated here. The new measurement at LNGS is presented below.

11.3.1   Measurement at LNGS

The setup of four HPGe detectors is shown in Fig. 11.5. The detectors are installed inside a single cryostat with the endcap facing upwards. The palladium sample is arranged in the central well facing the lateral sides of the detectors. This configuration is less ideal for low energy γ-rays since the sample is not facing the entrance window of the endcap

and the γ-rays have to pass through additional material to be detected, e.g. the detector holders. The whole setup is enclosed in a passive shielding made of lead and copper and is ventilated with nitrogen to remove radon.
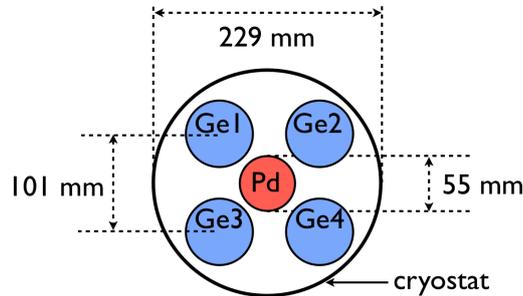
Figure 11.5 Setup of four HPGe detectors for the LNGS measurement.

The four semi-coaxial detectors are very similar in size having a volume of $225.2\,\mathrm{cm}^3$, $225.0\,\mathrm{cm}^3$, $225.0\,\mathrm{cm}^3$ and $220.7\,\mathrm{cm}^3$. The energy resolution, determined with standard calibration sources, has similar values for each detector and is averaged in the analysis.

The data acquisition consists of four ADCs recoding the energy of each detector and the time of the event if a trigger is give by any detector. The data can be used for an *a posteriori* coincidence analysis investigating multi-detector events in case of a γ-ray cascade. It can also be used for an anti-coincidence analysis investigating single detector events with reduced overall background. The palladium sample was measured in two runs of 38.41 d and 48.83 d respectively summing up to a palladium exposure of $70\,\mathrm{kg} \cdot \mathrm{d}$.

The full energy γ-ray detection efficiency of the system is determined with MC simulations based on MaGe Sec. 5.3.2. A validation of the simulation has been performed e.g. in [191] and references therein. A systematic uncertainty of 10 % was estimated. A dedicated study shows that the analysis of coincidence events results in a significantly lower sensitivity compared to the analysis of single detector events taking each detector individually. For the ^{110}Pd 0_1^+ decay mode, the efficiency to fully detect the 657.8 keV or the 815.3 keV γ-ray in one detector and triggering one other detector as well is 0.42 %. This can be compared to the efficiency of 2.64 % and 2.30 % to detect these γ-rays in any single detector without triggering another one. The reason is the large self absorption in the sample reducing the detection efficiency of γ-ray cascades in multiple detectors. Thus, for the analysis only an anti-coincidence cut was applied between the detectors which reduces the environmental background more than it reduces the detection efficiency.

11.3.2 Background Investigation

The radioactive impurity of the palladium sample was assessed during the gamma spectroscopy measurement in HADES [61]. The sample spectrum is compared to the background spectrum measured without sample. The count rates of prominent background peaks in the background spectrum are subtracted from those in the sample spectrum. The result, if positive, is then used for the evaluation of the activity for impurities in the sample. Positive evidence for ^{214}Pb and ^{214}Bi with around $2\,\mathrm{mBq/kg}$ activity was found. For γ-lines with a negative results, a decision threshold was calculated according to [192]. The results can be found in Tab. III in Ref. [61] which is also in the appendix at pages G-15 ff.

Additionally, a potential contamination of the following radionuclides was investigated: ^{102}Rh ($T_{1/2}=$ 207.3 d), ^{102m}Rh ($T_{1/2}=$ 3.742 yr) and ^{110m}Ag ($T_{1/2}=$ 249.76 d). The reason is the possible interference with the search for ^{110}Pd and ^{102}Pd isotopes, because of the emission of γ-rays from the same excited daughter states. The investigation was performed with additional γ-lines of these decays which are not part of the experimental signal of the DBD transitions due to the larger Q-value of the beta decay and the additional EC. No presence of these radionuclides was found.

A detailed comparison of the sample spectrum with the background spectrum is shown in the appendix in Fig. G.2 and G.3 for the Felsenkeller measurement, in Fig. G.4 and G.5 for the HADES measurement and in Fig. G.6 and G.7 for the LNGS measurement.

11.4 Combined Analysis

The analysis is performed on the three datasets d (Felsenkeller, HADES and LNGS). Each de-excitation γ-line k in a given decay mode has its own fit region r. An exception is the ^{102}Pd 0_1^+ mode in which the two de-excitation γ-lines of 468.6 keV and 475.1 keV are combined into a single fit region. Thus the ^{110}Pd transitions have $r = 1$, $r = 2$ and $r = 3$ fit regions in each dataset for the 2_1^+, 0_1^+ and 2_2^+ transitions, respectively. The ^{102}Pd transitions have $r = 1$, $r = 1$ and $r = 3$ fit regions for the 2_1^+, 0_1^+ and 2_2^+ modes, respectively.

The signal counts $s_{d,k}$ of each γ-line in each dataset translate into the half-live $T_{1/2}$ of the decay mode as

$$s_{d,k} = \ln 2 \cdot \frac{1}{T_{1/2}} \cdot \epsilon_{d,k} \cdot N_A \cdot t_d \cdot M \cdot f_{\text{Pd}} \cdot \frac{1}{m_{\text{Pd}}} \ , \tag{11.1}$$

where $\epsilon_{d,k}$ is the full energy detection efficiency of γ-line k in dataset d, N_A is the Avogadro's constant, t_d is the live-time of the dataset, M is the mass of the palladium sample, f_{Pd} is the isotopic natural abundance and m_{Pd} the molar mass of ^{102}Pd and ^{110}Pd, respectively. The data is binned with 0.68 keV, 0.5 keV, 1.0 keV wide bins for the Felsenkeller, HADES and LNGS datasets respectively[1].

The Bayesian Analysis Toolkit (BAT) [180] is used to perform a maximum posterior fit combining all three datasets and γ-lines for a given decay mode. The likelihood $\mathcal{L}$ is defined as the product of the Poisson probabilities of each bin i in fit region r in every dataset d

$$\mathcal{L}(\mathbf{p}|\mathbf{n}) = \prod_d \prod_r \prod_i \frac{\lambda_{d,r,i}(\mathbf{p})^{n_{d,r,i}}}{n_{d,r,i}!} e^{-\lambda_{d,r,i}(\mathbf{p})} \ , \tag{11.2}$$

where $\mathbf{n}$ denotes the data and $\mathbf{p}$ the set of floating parameters. $n_{d,r,i}$ is the measured number of counts and $\lambda_{d,r,i}$ is the expected number of counts in bin i. $\lambda_{d,r,i}$ is taken as the integral of the p.d.f. $P_{d,r}$ in this bin as

$$\lambda_{d,r,i}(\mathbf{p}) = \int_{\Delta E_{d,r,i}} P_{d,r}(E|\mathbf{p})dE \ , \tag{11.3}$$

where $\Delta E_{d,r,i}$ is the bin width. The counts in the fit region are expected from three different types of contributions which are used to construct $P_{d,r}$: (1) A linear background, (2) the

---

[1]The different binning arises either directly from the MCA or from a rebinning to combine different detectors.

Gaussian signal peak and (3) a number of Gaussian background peaks. The number and type of background peaks depend on the fit region and will be described later. The full expression of $P_{d,r}$ is written as:

$$P_{d,r}(E|\mathbf{p}) \quad = B_{d,r} + C_{d,r}(E - E_0) \qquad (11.4)$$

$$+ \frac{s_{d,k}}{\sqrt{2\pi}\sigma_{d,k}} \cdot \exp\left(-\frac{(E - E_k)^2}{2\sigma_{d,k}^2}\right)$$

$$+ \sum_{l_r}\left[\frac{b_{d,l_r}}{\sqrt{2\pi}\sigma_{d,k}} \cdot \exp\left(-\frac{(E - E_{l_r})^2}{2\sigma_{d,k}^2}\right)\right].$$

The first line is describing the linear background with the two parameters $B_{d,r}$ and $C_{d,r}$. The second line is describing the signal peak with the energy resolution $\sigma_{d,k}$ and the γ-line energy E_k. The third line is describing the l_r background peaks in fit region r with the strength of the peak b_{d,l_r} and the peak position E_{l_r}[2]. The same p.d.f. with different parameter values is used for all three datasets. Hence, the same number of background peaks is used in the fit even if a given dataset does not show such a background.

The free parameters $\mathbf{p}$ in the fit are:

- 1 inverse half-life $(T_{1/2})^{-1}$ with flat prior

- 2 x 3 x r linear background parameters $B_{d,r}$ and $C_{d,r}$ with flat priors

- 3 x k energy resolutions $\sigma_{d,k}$ with Gaussian priors

- 3 x k detection efficiencies $\epsilon_{d,k}$ with Gaussian priors

- k signal peak positions E_k with Gaussian priors

- 3 x l_r x r background peak strength b_{d,l_r} with flat priors

- l_r x r background peak positions E_{l_r} with Gaussian priors

In total this amounts to 30 fit parameters for the 2_1^+ mode, 59 parameters for the 0_1^+ mode and 76 parameters for the 2_2^+ mode of ^{110}Pd and 18 parameters for the 2_1^+ mode, 25 parameters for the 0_1^+ mode and 52 parameters for the 2_2^+ mode of ^{102}Pd.

The energy resolutions are determined with calibration spectra for each dataset independently. The mean of the Gaussian priors is taken from these calibrations and reported in Tab. 11.3. The width of these priors is taken as the uncertainty of the resolution calibration curve and approximated with 5 % for all datasets and γ-lines.

The detection efficiencies were determined with MC simulations for each dataset independently, partly based on different codes. The mean value of the Gaussian prior is reported in Tab. 11.4. For the HADES dataset the efficiencies are taken from [61]. For the Felsenkeller dataset the efficiencies are reevaluated to include the 2^+2 transitions. The uncertainty of the detection efficiencies is approximated with 10 % for each dataset and γ-line and used for the width of the prior. The mean values and uncertainties of the signal and background peak positions are taken from nuclear data sheets.

Table 11.3 Energy resolution in σ_E for all peaks and datasets. For the HADES and LNGS measurements the quoted values are the average of all detectors. The uncertainty is approximated with 5 %.

γ-line energy	Felsenkeller	HADES	LNGS
657.8 keV	0.642 keV	0.828 keV	0.768 keV
815.3 keV	0.683 keV	0.868 keV	0.794 keV
818.0 keV	0.684 keV	0.868 keV	0.794 keV
1475.8 keV	0.837 keV	1.003 keV	0.912 keV
468.6 keV	0.590 keV	0.773 keV	0.739 keV
475.1 keV	0.592 keV	0.775 keV	0.740 keV
627.9 keV	0.634 keV	0.819 keV	0.764 keV
1103.1 keV	0.754 keV	0.932 keV	0.844 keV

The posterior is calculated from the likelihood and priors with BAT. The marginalized posterior distribution of $(T_{1/2})^{-1}$ is extracted and the 90 % quantile of this distribution is used for setting a 90 % credibility limit on the half-life.

11.5 Results

The analysis of each decay mode is discussed separately starting with ^{110}Pd as the more interesting isotope. No signal is observed and single half-life limits are extracted for every decay mode individually.

11.5.1 ^{110}Pd Decay Mode $2/0\nu\beta\beta$ $0^+_{\text{g.s.}} - 2^+_1$

The fit region of ± 30 keV is centered around the single γ-line of 657.8 keV and illustrated in Fig. 11.6 for all three datasets. Three known background peaks from decay chain isotopes are included in the fit coming from ^{210}Bi at 649.6 keV (3.4 %), ^{214}Bi at 665.5 keV (1.5 %) and from ^{228}Ac at 674.8 keV (2.1 %), where the value in parentheses is the emission probability of this γ-ray. A general list of natural decay chain γ-lines with an emission probability larger than 1 % is shown in Tab. A.5 in the appendix.
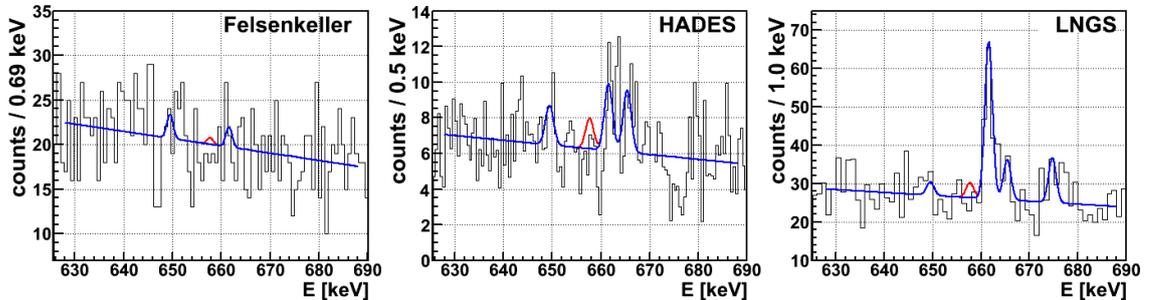
Figure 11.6 Fit regions for the ^{110}Pd 2^+_1 decay mode for all datasets. Shown is the best fit in blue and the best fit with the signal strength set to the 90 % C.I. half-life limit in red.

---

[2]Note that the energy resolution of a background peak in the region is taken as the value of the signal peak energy resolution sharing the same parameter $\sigma_{d,k}$. This reduces the number of parameters and is valid because the resolutions are sufficiently close within a typical region size of ± 30 keV.

Table 11.4 Detection efficiencies for all γ-lines in all decay modes for all datasets. Values for the HADES setup are taken from [61]. The uncertainty is approximated with 10 %. Note that branching rations and summation effects change the full energy detection efficiency of a γ-line in different decay modes.

γ-line energy [keV]	Felsenkeller	HADES	LNGS
^{110}Pd 2_1^+ 657.8 keV decay mode:			
657.7 keV (100.0 %)	3.06 %	4.70 %	2.57 %
^{110}Pd 0_1^+ 1473.1 keV decay mode:			
657.8 keV (100.0 %)	2.56 %	3.94 %	2.08 %
815.3 keV (100.0 %)	2.30 %	3.68 %[a]	1.97 %
^{110}Pd 2_2^+ 1475.80 keV decay mode:			
657.8 keV (64.5 %)	1.68 %	2.53 %	1.38 %
818.0 keV (64.5 %)	1.53 %	2.40 %	1.28 %
1475.8 keV (35.5 %)	0.87 %	1.32 %	0.69 %
^{102}Pd 2_1^+ 475.1 keV decay mode:			
475.1 keV (100.0 %)	3.32 %	5.09 %	2.75 %
^{102}Pd 0_1^+ 943.7 keV decay mode:			
475.1 keV (100.0 %)	2.72 %	4.31 %	2.26 %
468.6 keV (100.0 %)	2.75 %	4.32 %	2.30 %
^{102}Pd 2_2^+ 1103.05 keV decay mode:			
475.1 keV (62.9 %)	1.76 %	2.67 %	1.48 %
627.9 keV (62.9 %)	1.63 %	2.54 %	1.39 %
1103.1 keV (37.1 %)	1.04 %	1.60 %	0.83 %

[a] typo in Ref. [61]

Additionally, ^{137}Cs at 661.7 keV (85.1 %) is included in the fit as an anthropogenic background. This contamination can be clearly seen in the HADES and LNGS datasets. In comparison, the background peaks in the Felsekeller dataset are not significant. Here, the background is dominated by atmospheric muons due to the smaller overburden. This increases the overall background by about one order of magnitude compared to the other datasets and washes out background peaks (see also Fig. 11.4 for the full energy spectra.)

The best fit value is shown as the blue p.d.f. in Fig. 11.6. The signal peak according to the 90 % C.I. is shown as the red p.d.f. The best fit yields an inverse half-life[3] equivalent to $0\,\mathrm{yr}^{-1}$. The obtained 90 % quantile of the posterior translates into a half-life limit for the ^{110}Pd 2_1^+ decay mode of

$$T_{1/2} > 2.9 \cdot 10^{20} \text{ yr } (90\,\% \text{ C.I.}) \ . \tag{11.5}$$

The size of the signal peak at 90 % C.I. illustrates the sensitivity of the dataset. The Felsenkeller measurement with a larger background, less measuring time and a single detector setup with smaller full energy detection efficiency has a smaller sensitivity. The HADES and LNGS datasets show roughly the same sensitivity.

---

[3]The inverse half-life is directly proportional to the number of counts (Eq. 11.1). Since the number of counts for a given inverse half-life is different for each dataset, the best fit result is given in inverse half-life units of yr^{-1}. For numerical reasons the range of the inverse half-life parameter is finite and a best fit value consistent with the lower bound is equivalent to $0\,\mathrm{yr}^{-1}$.
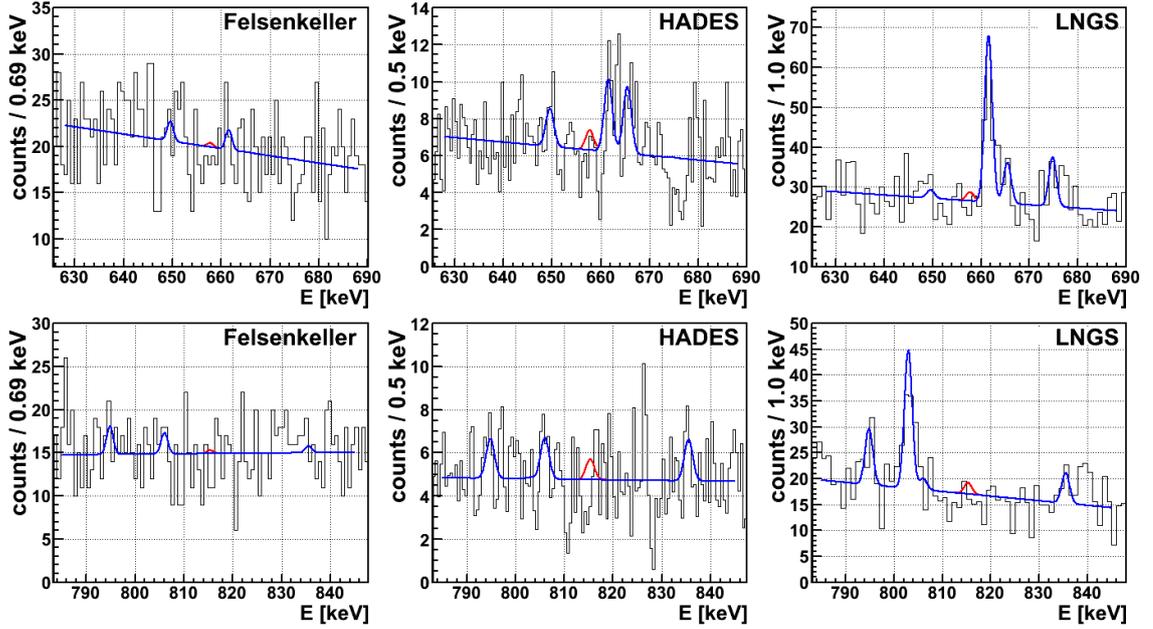
Figure 11.7 Fit regions for the ^{110}Pd 0_1^+ decay mode for all datasets. Shown is the best fit in blue and the best fit with the signal strength set to the 90 % C.I. half-life limit in red.

11.5.2 ^{110}Pd Decay Mode $2/0\nu\beta\beta$ $0_{\text{g.s.}}^+ - 0_1^+$

For this decay mode two fit regions are selected. The first is the same as for the 2_1^+ transition and the second has a range of ± 30 keV centered around the de-excitation γ-line of 815.3 keV. Both γ-rays occur in coincidence with an angular correlation ($W(\theta) \propto 1 - 3\cos^2\theta + 4\cos^4\theta$ [166]) which is considered in the MC simulations using Decay0. The fit regions are shown in Fig. 11.7.

Three known background γ-lines are included in the second fit region coming from ^{228}Ac at 795.0 keV (4.3 %) and at 835.7 keV (1.6 %) and from ^{214}Bi at 806.1 keV (1.3 %).

Another prominent γ-line is visible in the LNGS dataset at 803.1 keV which is potentially[4] coming from the first exited state in ^{206}Pb after excitation with elastic neutron scattering (n,n'). It is included in the fit as a background γ-line.

Yet another potential γ-line can be seen at 826.5 keV in the HADES dataset. This γ-line could not be identified and is therefore not included as a background[5]. However, including this γ-line in a test fit yields a $1.5\,\sigma$ significance in the HADES dataset and changes the combined half-life limit by only 2.2 % compared to not including it in the fit.

The final half-life limit for the ^{110}Pd 0_1^+ decay mode is

$$T_{1/2} > 3.9 \cdot 10^{20}\, \text{yr} \ (90\,\% \ \text{C.I.}) \ . \tag{11.6}$$

---

[4]An investigation could not attribute the γ-line to any other background.

[5]Including non identified γ-lines might lead to the interpretation of statistical fluctuation as background γ-lines which then reduces the linear background level. This can lead to a biased result based on the personal choice of including non-identified background features.
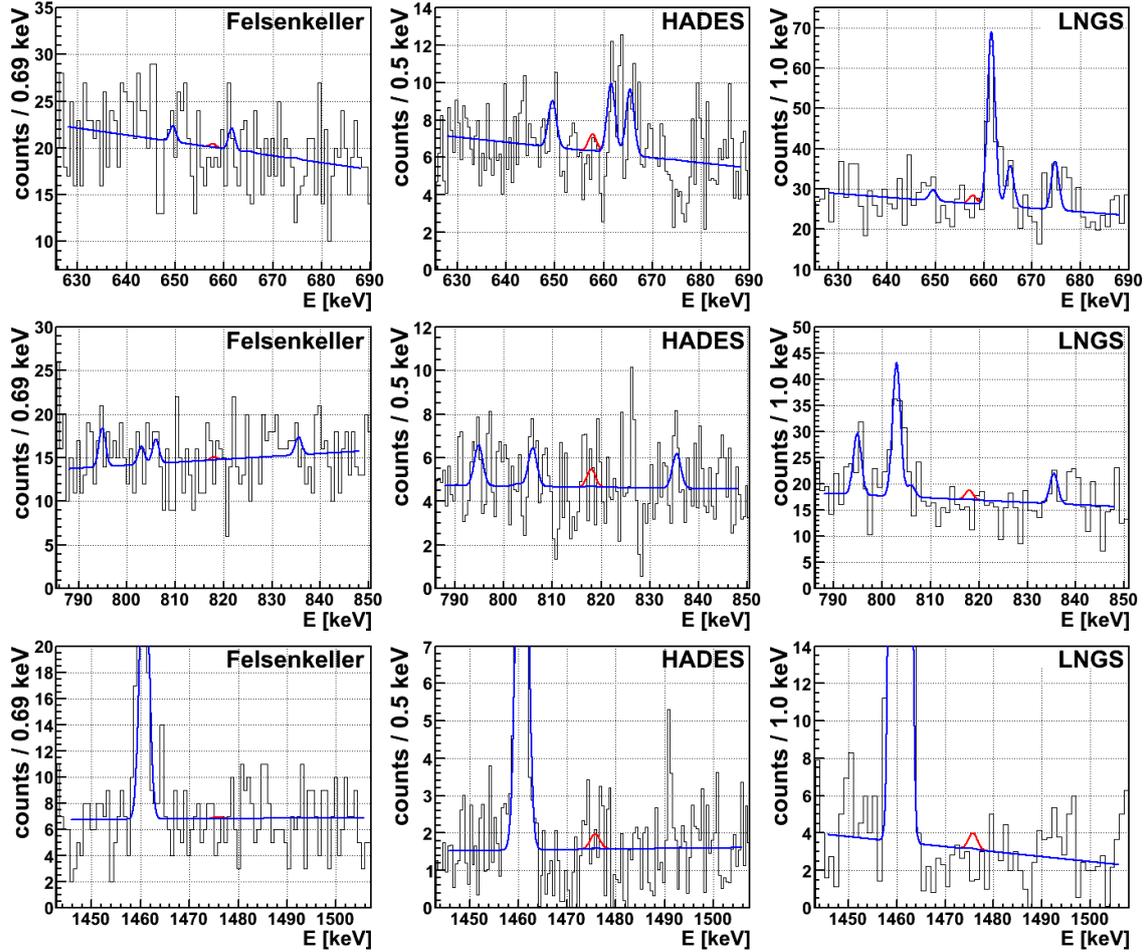
Figure 11.8 Fit regions for the ^{110}Pd 2_2^+ decay mode for all datasets. Shown is the best fit in blue and the best fit with the signal strength set to the 90 % C.I. half-life limit in red.

11.5.3 ^{110}Pd Decay Mode $2/0\nu\beta\beta$ $0_{\text{g.s.}}^+ - 2_2^+$

This decay mode has two decay branches, one with a single γ-ray emission (35.5 %) and one with two coincident γ-rays (64.5 %). The two γ-rays are emitted with an angular correlation ($W(\theta) \propto 1 - \frac{15}{13}\cos^2\theta + \frac{16}{13}\cos^4\theta$ [166]) which is included in the MC via DECAY0. In total three fit regions are selected. The first is the same as for the 2_1^+ transition. The second is centered ± 30 keV around the 818.0 keV γ-line and thus nearly identical to the second peak region in the 0_1^+ transition. The third region is centered ± 30 keV around the 1475.8 keV de-excitation γ-ray energy. All fit regions are shown in Fig. 11.8.

In the first and second fit region the background γ-lines are included as described in the other transitions above. In the third fit region the ^{40}K γ-line at 1460.83 keV (10.7 %) is the most prominent feature in all datasets and is included in the fit. Another potential γ-line at 1490.7 keV can be seen in the HADES dataset with $1.8\,\sigma$ significance. Some indication can also be seen in the LNGS dataset with $1.3\,\sigma$. This potential γ-line, however, could not be identified and is therefore not included in the fit. The difference in the half-life limit between including and not including the potential γ-lines at 826.5 keV and 1490.7 keV is 3 % and thus not very strong.

The final half-life for the ^{110}Pd 2_2^+ decay mode is

$$T_{1/2} > 2.9 \cdot 10^{20} \text{ yr } (90\% \text{ C.I.}) \ . \tag{11.7}$$

11.5.4 ^{102}Pd Decay Mode $2/0\nu\beta\beta$ $0_{\text{g.s.}}^+ - 2_1^+$

The single fit region of the ^{102}Pd 2_1^+ transition is centered ± 30 keV around the 475.1 keV de-excitation γ-ray energy and is shown in Fig. 11.9.
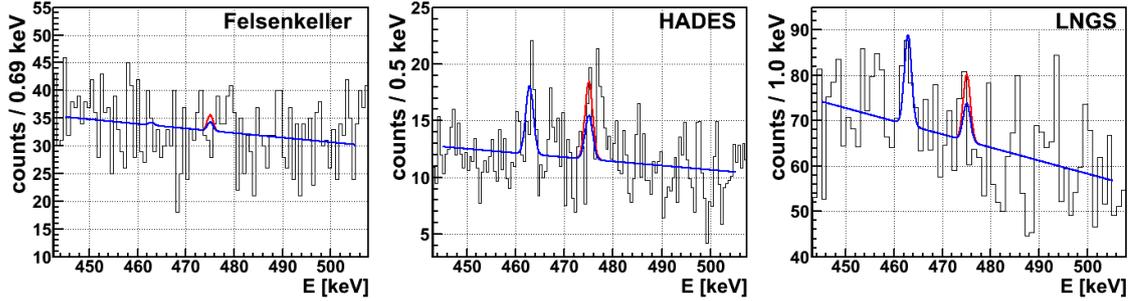
Figure 11.9 Fit regions for the ^{102}Pd 2_1^+ decay mode for all datasets. Shown is the best fit in blue and the best fit with the signal strength set to the 90 % C.I. half-life limit in red.

The known ^{228}Ac background γ-line at 463.0 keV (4.4 %) is included in the fit. Some potential peak structures can be seen in the HADES spectrum close to or directly underneath the signal peak. They cannot be clearly identified and appear to be at ≈ 475 keV and ≈ 477 keV. A search for radioactive isotopes with γ-ray emission at those energies as well as a search for potential γ-ray summation or escape effects remained inconclusive. Another investigation was performed looking at the two detectors in the HADES measurements individually. Their spectra is shown in their original binning in Fig. G.1 in the appendix. Also shown is a live-time scaled background spectrum of both detectors in gray. The peak structures are only visible in the bottom detector of the two detectors which is Ge6 shown in red (Cu endcap and 0.9 mm dead layer). The top detector, Ge7 shown in blue (Al endcap and 0.3 micron dead layer), does not show these features[6]. They are also not visible in the background spectrum of the setup. Hence, those γ-line features are either a background fluctuation in one of the HADES detectors or an unknown irreducible background contribution. In both cases they cannot be included in the fit.

Performing the fit on all three datasets results in a best fit and limit as shown in Fig. 11.9. The best fit finds a half-life of $1.3 \cdot 10^{19}$ yr which includes the no signal case in the smallest connected 98.4 % or 2.41 σ interval. The significance of the signal peak is almost entirely due to the background features in the HADES dataset. Performing the same fit only on the Felsenkeller and LNGS datasets results in a best fit consistent with zero at the 0.77 σ level. The inverse half-life distributions for both cases are shown in Fig. G.8 in the appendix for comparison. The 90 % C.I. lower limit with the HADES dataset is $7.9 \cdot 10^{18}$ yr compared to $7.5 \cdot 10^{18}$ yr without the HADES dataset. With the HADES dataset the limit is reduced due to the upwards fluctuations of background in the peak region whereas without the HADES dataset the sensitivity is smaller.

[6]See Ref. [61] at pages G-15 to G-22 in the appendix for more information on the setup.
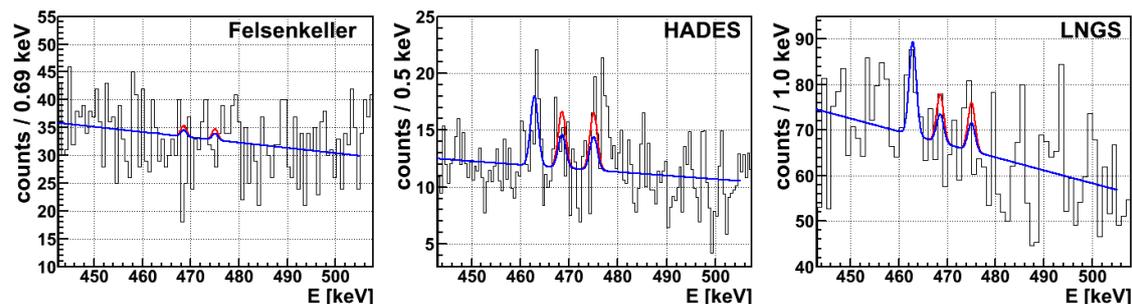
Figure 11.10 Fit regions for the ^{102}Pd 0_1^+ decay mode for all datasets. Shown is the best fit in blue and the best fit with the signal strength set to the 90 % C.I. half-life limit in red. Note that two signal peaks are included in the same fit region.

For the final limit of the ^{102}Pd 2_1^+ transition the HADES dataset is included due to the larger sensitivity. The limit is set to

$$T_{1/2} > 7.9 \cdot 10^{18} \, \text{yr} \, (90 \, \% \, \text{C.I.}) \, . \tag{11.8}$$

11.5.5 ^{102}Pd Decay Mode $2/0\nu\beta\beta$ $0_{\text{g.s.}}^+ - 0_1^+$

This decay mode has two coincident γ-ray emissions at 475.1 keV and 468.6 keV which are analyzed in a single fit region identical to the one for the 2_1^+ transition above. This is the only decay mode with two signal peaks in the same fit region with adds another signal term to the p.d.f. in Eq. 11.4. The fit is shown in Fig. 11.10 using the same background γ-line from ^{228}Ac at 463.0 keV as before.

Also in this case the unidentified peak features are present and are treated in the same way as above. In addition there is a small upwards fluctuation underneath the 468.6 keV signal peak in the HADES dataset as well. Also this fluctuation is only visible in one of the HADES detectors (Fig. G.1 in the appendix) and is thus treated as a background fluctuation. The marginalized posterior inverse half-life distribution of the fit with and without the HADES dataset is shown in Fig. G.9 in the appendix. With the HADES dataset the smallest interval containing the no signal case is 98.7 % or 2.49 σ. Excluding the HADES dataset results in a 0.1 σ difference to the no signal case. The difference in half-life limit is $9.2 \cdot 10^{18}$ yr including HADES and $1.1 \cdot 10^{19}$ yr excluding HADES.

The final limit for the ^{102}Pd 0_1^+ transition is taken as the one with the HADES dataset and set to

$$T_{1/2} > 9.2 \cdot 10^{18} \, \text{yr} \, (90 \, \% \, \text{C.I.}) \, . \tag{11.9}$$

11.5.6 ^{102}Pd Decay Mode $2/0\nu\beta\beta$ $0_{\text{g.s.}}^+ - 2_2^+$

This decay mode has two decay branches with a coincident double γ-ray emission of 475.1 keV and 627.9 keV (62.9 %) and a single γ-ray emission of 1103.1 keV (37.1 %). The first fit region is identical to the one in the 2_1^+ transition. The second fit region is centered ±30 keV around the 627.9 keV γ-line and includes the ^{214}Bi background γ-line at 609.3 keV (45.5 %). The third fit region is centered ±30 keV around the 1103.1 keV γ-line and includes the ^{214}Bi background γ-line at 1120.3 keV (14.9 %). All three regions including the fit are shown in Fig. 11.11.
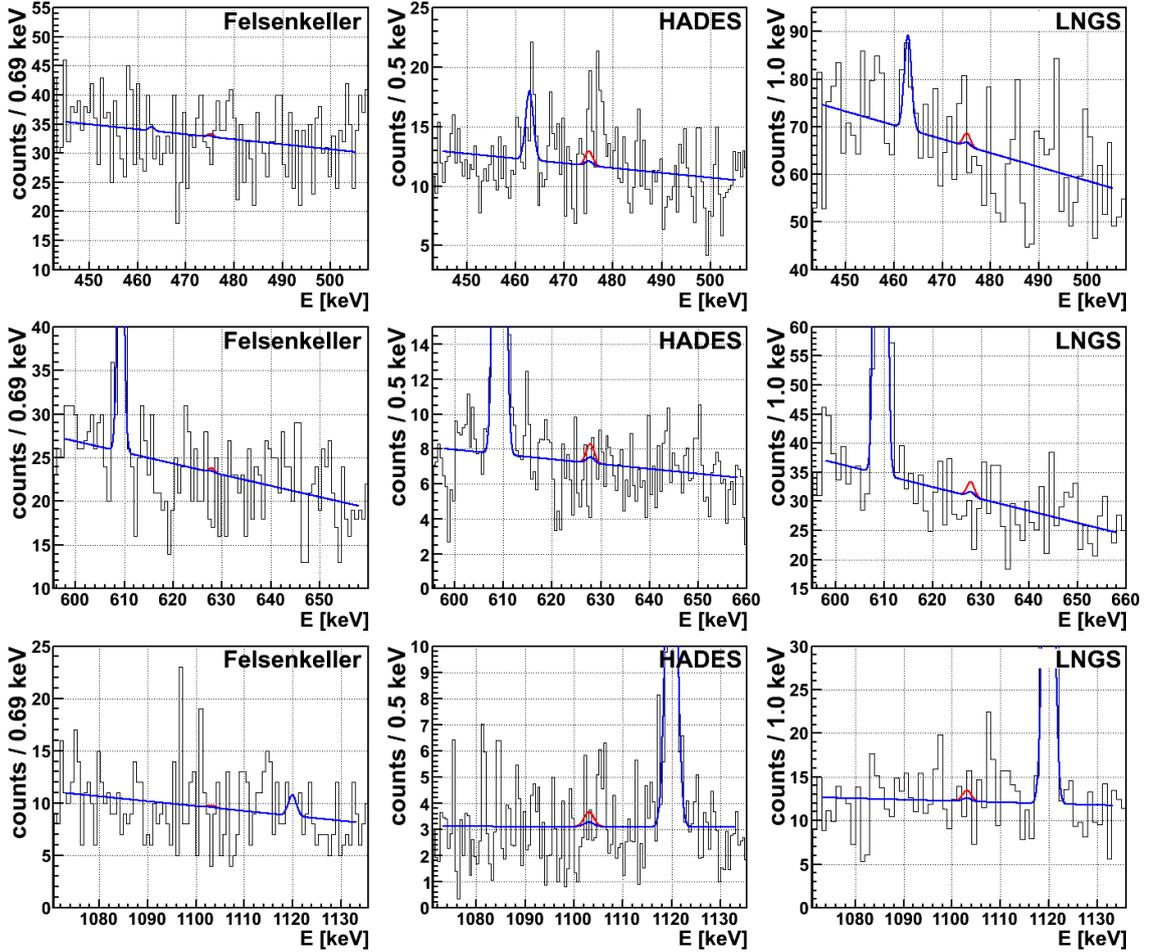
Figure 11.11 Fit regions for the ^{102}Pd 2_2^+ decay mode for all datasets. Shown is the best fit in blue and the best fit with the signal strength set to the 90 % C.I. half-life limit in red.

In this case, the background fluctuations in the first fit region of the HADES dataset do not have a strong influence since the fit is dominated by the other fit regions in which no fluctuations occur. The final limit for the ^{102}Pd 2_2^+ transition is found as

$$T_{1/2} > 1.5 \cdot 10^{19} \, \text{yr} \; (90\% \; \text{C.I.}) \; . \tag{11.10}$$

11.6   Conclusion

An analysis of excited state transitions was performed for the DBD candidate isotopes of ^{110}Pd and ^{102}Pd. A new measurement was performed at LNGS and its data was combined with two previous measurements at the Felsenkeller and HADES underground laboratories. The analysis is performed for each decay mode independently and based on spectral fits of all three datasets and all possible de-excitation γ-lines together.

No signal was found for any decay mode and 90 % credibility lower half-life bounds are obtained which are summarized in Tab. 11.5. The limits include systematic uncertainties on the efficiency, energy resolution and peak position which are, however, effecting the limit only by $< 2\%$ [7]. The limits for the ^{102}Pd decay modes are roughly one order

[7]This number was obtained by fixing the otherwise floating nuisance parameters of efficiency, resolution

Table 11.5 Summary of measured half-life limits for investigated ^{110}Pd and ^{102}Pd double beta decay excited state transitions.

decay mode	$T_{1/2}$ [yr] 90 % C.I.	decay mode	$T_{1/2}$ [yr] 90 % C.I.
^{110}Pd 2_1^+	$2.9 \cdot 10^{20}$	^{102}Pd 2_1^+	$7.9 \cdot 10^{18}$
^{110}Pd 0_1^+	$3.9 \cdot 10^{20}$	^{102}Pd 0_1^+	$9.2 \cdot 10^{18}$
^{110}Pd 2_2^+	$2.9 \cdot 10^{20}$	^{102}Pd 2_2^+	$1.5 \cdot 10^{19}$

of magnitude weaker than for the ^{110}Pd decay modes due to the smaller isotopic abundance.

The previous best limits could be improved by factors of 1.3 to 3 depending on the decay mode[8]. The improvements are mainly due to the combination of three datasets including the new LNGS dataset. The spectral fit and the combination of different fit regions in a single fit especially improves the limits for the higher excited states with multiple γ-ray emission and multiple branching ratios. The current experimental sensitivity is still three orders of magnitude smaller than the lowest half-life prediction for the 0_1^+ transition by the QRPA model [62].

The measurement at LNGS alone could not improve the previously achieved limits due to unfavorable geometrical constrains in the detector setup in combination with the sample: A true coincidence analysis was not feasible since the solid packing of the dense palladium sample is lowering the detection efficiency with detector coincidences.

Potential future improvements can be achieved with lowering the background level which is dominated by ambient background sources and not by intrinsic impurities in the palladium. The background level would be reduced with additional shielding and purer materials in general reducing the natural decay chain contributions and ^{40}K. The muonic contribution of the background is already subdominant for the LNGS setup. If the detection setup allows, the shape of the sample could be optimized reducing its thickness and thus lowering the intrinsic self-absorption as well as enabling a true coincidence analysis in a multi-detector system. E.g. the large granularity of the small palladium plate would allow them to be glued on a thin foil which is wrapped around multiple detectors.

The results obtained in this work are already the third generation of excited states half-life limits in palladium with subsequently more advanced gamma-spectroscopy setups. It is advised that a thorough investigation of the sensitivity and sample optimization is performed prior to any new measurement.

---

and peak positions to their nominal values and repeating the fit.

[8]Note that previous limits were obtained with the Frequentist Feldman Cousins Method and are quoted for 95 % confidence level.

Chapter 12

Conclusions

This dissertation has been developed within the GERDA experiment focusing on double beta decay transitions into excited states and improvements for PHASE II. All new BEGe detectors for GERDA PHASE II were characterized for their surface and active volume properties which are a necessary ingredient for all physics analyses in GERDA PHASE II. A new framework was developed in order to characterize a large number of detectors with high precision. The results have lowered the systematic uncertainty of the active volume for $0\nu\beta\beta$ decay to a subdominant level. Following these standard measurements, a new model was developed describing the pulse shapes properties of n^+ electrode surface events in BEGe detectors. This new model is essential to understand and simulate surface events which are by far the largest background component for the new BEGe detectors in PHASE II. The new model will additionally increase the precision of $2\nu\beta\beta$ decay measurements in the future. Furthermore, MC simulations were developed for the new LAr scintillation veto and predictions were made for its background suppression capabilities in PHASE II. In addition to the detector characterization and development of simulation tools, this thesis presents new results for $2\nu\beta\beta$ decay transitions into excited states in ^{76}Ge, ^{110}Pd and ^{102}Pd. New world best lower half-life limits were obtained and published for all of these isotopes. The new results for ^{76}Ge are two orders of magnitude more stringent than the previous ones and exclude many older theoretical predictions. They are valuable experimental input for the calculation of nuclear matrix elements.

All 30 new BEGe detectors for GERDA PHASE II were characterized in vacuum cryostats in the HADES underground facility. The full charge collection depth (FCCD) and the fully active volume (FAV) were determined with two different approaches measuring the FCCD with low energy peak count ratios and the FAV with high energy γ-rays of various calibration sources. The FCCD and the FAV are connected by the assumption of a homogeneous thick n^+ electrode in a given detector. The results between the two approaches are systematically different, however, they agree within their uncertainties. In the following, the underlying assumption of a homogeneous FCCD was extensively investigated with top and lateral scans of the detector surface as well as with a dedicated upside-down mounting of a single detector to exemplarily investigate the bottom side. No indication of an inhomogeneously thick n^+ surface was found apart from two detectors. Thus, the final results are based on the FCCD measurements due to their smaller systematic uncertainty budget. The FCCD values vary between $0.52 - 0.86$ mm for the individual detectors and translate into FAV fractions of $88.4 - 94.2\,\%$. The corresponding detection efficiency of $0\nu\beta\beta$ decay in the FAV was determined with MC simulations for each detector and is between $79.1 - 84.7\,\%$.

For n$^+$ surface events and internal decays with continuous energy spectrum, a more sophisticated model was developed to account for the semi-active volume of the n$^+$ electrode. This is especially important for ^{42}K decays on the detector surface which account for $\approx 60\%$ of the total background in the search of $0\nu\beta\beta$ decay with BEGe detectors in GERDA. Energy depositions in the n$^+$ electrode result in a reduced charge collection efficiency and pulses with longer rise time. This behavior can be used to effectively veto such events with PSD. At first, a simple empirical ad-hoc model was developed and used to investigate the n$^+$ electrode of BEGe detectors solely based on the energy spectrum of 59.5 keV ^{241}Am γ-rays. Within this model the composition of the n$^+$ electrode is separated into an inactive dead layer and a semi-active transition layer. The data suggests that the transition layer is accounting for $50 - 100\%$ of the FCCD depending on the detector and is thus generally larger than the dead layer. The division between dead and transition layer seems to be correlated with the crystal slice position in the original germanium ingot: Detector slices cut out closer to the seed end of the ingot show a smaller dead layer fraction compared to slices cut out closer to the tail end.

In a second step, a more sophisticated n$^+$ electrode model was developed from first principles based on diffusion of the charge carriers. This model was folded into GEANT4 MC simulations and tuned and compared to calibration source measurements resulting in a good description of the data. The new model was applied to simulations of the ^{42}K surface background predicting a suppression factor of up to 145. This is the first time that the large suppression of surface backgrounds is understood in detail. The pulse shape discrimination is depending on the individual BEGe detector. This allows the optimization of the n$^+$ electrode thickness in the production of new BEGe detectors for a future LAr based 1-ton ^{76}Ge $0\nu\beta\beta$ experiment, which was briefly explored in this thesis. Detectors with FCCD values of ≥ 0.75 mm yield the best ^{42}K suppression with an optimized A/E cut. Precise quantitative predictions for non-optimal A/E cuts require more development of the model. However, larger FCCD values lead to a better separation of surface and bulk events and are strongly preferred in this case. Additionally, the active volume and the spectral shape of $2\nu\beta\beta$ decays is affected by the n$^+$ electrode. A 2% increase of the $2\nu\beta\beta$ event rate above 600 keV is expected if the semi-active layer is added to the active volume. The new n$^+$ electrode model will help to increase the precision of future ^{76}Ge $2\nu\beta\beta$ decay half-life measurements which have a current precision of 5% [52].

Apart from the superior PSD performance of BEGe detectors, the LAr scintillation veto is a major component to reduce the background in GERDA PHASE II to the level of 10^{-3} cts/(kg $\cdot$ yr $\cdot$ keV). The performance of the LAr veto is very sensitive to different detector and source geometries and the amount of dead material around the detector array. The veto performance cannot be determined with calibration sources alone. Therefore, MC simulations are needed to understand the background suppression and guide the LAr veto design. Within this thesis, MC simulations were developed for the LAr veto, including the full tracking of optical photons. The simulations were tuned to a calibration measurement with a GERDA commissioning string until a good agreement with the data was achieved. The tuned simulations were then used to predict key background components in the full PHASE II array. LAr veto suppression factors achieved by the LAr veto are 134 ± 9 for ^{208}Tl and 2.91 ± 0.02 for ^{214}Bi in the detector holders, 16.3 ± 1.3 for ^{214}Bi and 2.6 ± 0.1 for ^{42}K homogeneously distributed inside the LAr and 16.5 ± 0.2 for ^{60}Co and 2.45 ± 0.01 for ^{68}Ga cosmogenically produced inside the germanium detectors. These values include only the statistical uncertainty in the simulation and are valid for the case that all detectors in the array are operational. The combined suppression of PSD and LAr veto for ^{42}K decays

in the LAr close to the detector can be conservatively taken as the product of suppression factors. This results in a suppression of ≈ 170 (45 PSD, 3.8 LAr veto) for BEGe detectors. ^{42}K decays on the detector surface cannot be discriminated by the LAr veto and in this case the maximal suppression is given by PSD alone with a factor of 145 for BEGe detectors.

The most important achievement of this dissertation is the search for $2\nu\beta\beta$ excited state transitions in ^{76}Ge with GERDA PHASE I data [164]. The Frequentist profile likelihood analysis based on two-detector coincidence events did not find a positive signal and established 90 % C.L. lower half-life limits for transitions into the 2_1^+, 0_1^+ and 2_2^+ excited state of ^{76}Se:

	$0_{\text{g.s.}}^+ - 2_1^+$	$0_{\text{g.s.}}^+ - 0_1^+$	$0_{\text{g.s.}}^+ - 2_2^+$
^{76}Ge:	$1.6 \cdot 10^{23}$ yr	$3.7 \cdot 10^{23}$ yr	$2.3 \cdot 10^{23}$ yr

These limits are more than 2 orders of magnitude larger than previous ones and could exclude a number of older nuclear matrix element calculations. New calculations based on the QRPA, ShM and IBM-2 nuclear models were triggered by this search and predict larger half-lives. A half-life range predicted by the QRPA model based on different values of g_A could be constrained favoring $g_A < 1.26$ for this calculation. The ShM and IBM-2 predictions could not be tested with the current sensitivity. Using the results from the BEGe characterization and the new simulation of the LAr veto, a sensitivity study was performed for PHASE II. The expected sensitivity for the 0_1^+ transition is $\approx 1 \cdot 10^{24}$ yr with large potential for improvement by tuning the analysis parameters. The larger and more segmented PHASE II array will increase the detection efficiency by a factor of 5. PHASE II will allow to completely test the QRPA calculations. In case of a positive signal, the LAr veto can be used to separate the 2_1^+ from the 0_1^+ transition which would not have been possible in the PHASE I analysis due to their similar experimental signature.

Finally, a search for excited state transitions was performed with the double beta decay isotope ^{110}Pd and the double electron capture isotope ^{102}Pd. A 802.4 g palladium sample was measured with successively improved gamma spectroscopy setups at the Felsenkeller laboratory in Dresden (Germany), at the HADES laboratory in Mol (Belgium) and at LNGS in L'Aquila (Italy). A combined Bayesian maximum posterior spectral fit of the three measurements was performed in this thesis. No signal was observed and 90 % C.I. lower half-limits were obtained for the 2_1^+, 0_1^+ and 2_2^+ excited state transitions in both isotopes. The search was entirely based on the detection of de-excitation γ-rays and the results are valid for the $0\nu\beta\beta$ and the $2\nu\beta\beta$ regime:

	$0_{\text{g.s.}}^+ - 2_1^+$	$0_{\text{g.s.}}^+ - 0_1^+$	$0_{\text{g.s.}}^+ - 2_2^+$
^{110}Pd:	$2.9 \cdot 10^{20}$ yr	$3.9 \cdot 10^{20}$ yr	$2.9 \cdot 10^{20}$ yr
^{102}Pd:	$7.9 \cdot 10^{18}$ yr	$9.2 \cdot 10^{18}$ yr	$1.5 \cdot 10^{19}$ yr

The previous published best limits could be improved by a factor 1.3 to 3 depending on the decay mode. The lowest predicted half-life for the 0_1^+ transition is still three orders of magnitude above the experimental limits and therefore the theoretical predictions could not be tested with the current sensitivity.

Appendix A

Nuclear Data

Table A.1 Nuclides that can decay via $\beta^-\beta^-$. Columns denote the nuclide, the decay mode, the isotopic abundance and the Q-value of the decay. Values are taken from [35] and [193] unless otherwise noted.

nuc.	mode	abun. [%]	Q-value [keV]	nuc.	mode	abun. [%]	Q-value [keV]
^{46}Ca	$\beta^-\beta^-$	0.004	988.35	^{130}Te	$\beta^-\beta^-$	34.08	2527.518 [194]
^{48}Ca	$\beta^-\beta^-$	0.187	4262.96 [195]	^{134}Xe	$\beta^-\beta^-$	10.436	825.38
^{70}Zn	$\beta^-\beta^-$	0.631	998.46	^{136}Xe	$\beta^-\beta^-$	8.8573	2457.83 [196][197]
^{76}Ge	$\beta^-\beta^-$	7.83	2039.006 [198]	^{142}Ce	$\beta^-\beta^-$	11.114	1416.72
^{80}Se	$\beta^-\beta^-$	49.61	132.56	^{146}Nd	$\beta^-\beta^-$	17.2	70.83
^{82}Se	$\beta^-\beta^-$	8.73	2997.9 [199]	^{148}Nd	$\beta^-\beta^-$	5.7	1928.77
^{86}Kr	$\beta^-\beta^-$	17.279	1258.01	^{150}Nd	$\beta^-\beta^-$	5.6	3371.38 [200]
^{94}Zr	$\beta^-\beta^-$	17.38	1142.87	^{154}Sm	$\beta^-\beta^-$	22.75	1251.62
^{96}Zr	$\beta^-\beta^-$	2.8	3347.7 [201]	^{160}Gd	$\beta^-\beta^-$	21.86	1729.44
^{98}Mo	$\beta^-\beta^-$	24.19	112.75	^{170}Er	$\beta^-\beta^-$	14.91	654.35
^{100}Mo	$\beta^-\beta^-$	9.67	3034.40 [202]	^{176}Yb	$\beta^-\beta^-$	12.76	1083.38
^{104}Ru	$\beta^-\beta^-$	18.62	1301.17	^{186}W	$\beta^-\beta^-$	28.43	489.94
^{110}Pd	$\beta^-\beta^-$	11.72	2017.85 [181]	^{192}Os	$\beta^-\beta^-$	40.78	412.36
^{114}Cd	$\beta^-\beta^-$	28.73	539.96	^{198}Pt	$\beta^-\beta^-$	7.163	1046.77
^{116}Cd	$\beta^-\beta^-$	7.49	2808.7	^{204}Hg	$\beta^-\beta^-$	6.87	419.49
^{122}Sn	$\beta^-\beta^-$	4.63	368.08	^{232}Th	$\beta^-\beta^-$	100	837.57
^{124}Sn	$\beta^-\beta^-$	5.79	2292.64 [203]	^{238}U	$\beta^-\beta^-$	99.274	1144.2
^{128}Te	$\beta^-\beta^-$	31.74	867.95				

Table A.3 Nuclides that can decay via ECEC, ECβ^+ and $\beta^+\beta^+$. Columns denote the nuclide, the possible decay modes, the isotopic abundance and the Q-value of the decay. Values are taken from [35] and [193].

nuc.	mode	abun. [%]	Q-value [keV]	nuc.	mode	abun. [%]	Q-value [keV]
^{36}Ar	$\epsilon\epsilon$	0.3365	433.5	^{126}Xe	$\epsilon\epsilon$	0.09	897
^{40}Ca	$\epsilon\epsilon$	96.94	193.78	^{130}Ba	$\epsilon\epsilon, \epsilon\beta^+, \beta^+\beta^+$	0.106	2611
^{50}Cr	$\epsilon\epsilon, \epsilon\beta^+$	4.345	1171.4	^{132}Ba	$\epsilon\epsilon$	0.101	839.9
^{54}Fe	$\epsilon\epsilon$	5.845	679.9	^{136}Ce	$\epsilon\epsilon, \epsilon\beta^+, \beta^+\beta^+$	0.185	2400
^{58}Ni	$\epsilon\epsilon, \epsilon\beta^+$	68.077	1925.8	^{138}Ce	$\epsilon\epsilon$	0.251	693
^{64}Zn	$\epsilon\epsilon, \epsilon\beta^+$	48.63	1096.4	^{144}Sm	$\epsilon\epsilon, \epsilon\beta^+$	3.07	1781.1
^{74}Se	$\epsilon\epsilon, \epsilon\beta^+$	0.89	1209.4	^{152}Gd	$\epsilon\epsilon$	0.20	55.6
^{78}Kr	$\epsilon\epsilon, \epsilon\beta^+, \beta^+\beta^+$	0.35	2866	^{156}Dy	$\epsilon\epsilon, \epsilon\beta^+$	0.06	2011
^{84}Sr	$\epsilon\epsilon, \epsilon\beta^+$	0.56	1786.8	^{158}Dy	$\epsilon\epsilon$	0.10	283.3
^{92}Mo	$\epsilon\epsilon, \epsilon\beta^+$	14.84	1649.1	^{162}Er	$\epsilon\epsilon, \epsilon\beta^+$	0.14	1844.5
^{96}Ru	$\epsilon\epsilon, \epsilon\beta^+, \beta^+\beta^+$	5.54	2719	^{164}Er	$\epsilon\epsilon$	1.61	24.1
^{102}Pd	$\epsilon\epsilon, \epsilon\beta^+$	1.02	1172.0	^{168}Yb	$\epsilon\epsilon, \epsilon\beta^+$	0.13	1422.1
^{106}Cd	$\epsilon\epsilon, \epsilon\beta^+, \beta^+\beta^+$	1.25	2771	^{174}Hf	$\epsilon\epsilon, \epsilon\beta^+$	0.16	1101.1
^{108}Cd	$\epsilon\epsilon$	0.89	269	^{180}W	$\epsilon\epsilon$	0.12	146
^{112}Sn	$\epsilon\epsilon, \epsilon\beta^+$	0.97	1922	^{184}Os	$\epsilon\epsilon, \epsilon\beta^+$	0.02	1451.5
^{120}Te	$\epsilon\epsilon, \epsilon\beta^+$	0.09	1698	^{190}Pt	$\epsilon\epsilon, \epsilon\beta^+$	0.014	1383
^{124}Xe	$\epsilon\epsilon, \epsilon\beta^+, \beta^+\beta^+$	0.09	2865.6	^{196}Hg	$\epsilon\epsilon$	0.15	819.7

Table A.4 Excited state structure in important DBD isotopes. The columns denote: nuclide and transition, Q-value of the decay into the ground state, Q-value of the decay into the excited state, energy level of first excited 2_1^+ and 0_1^+ state and lowest excited states until 0_1^+. All information from [138] if not otherwise noted.

transition	Q-value $0_{g.s.}^+$ [keV]	Q-value 0_1^+ [keV]	2_1^+ state [keV]	0_1^+ state [keV]	first excited states
$^{48}_{20}$Ca $\rightarrow$ $^{48}_{20}$Ti	4262.96 ± 0.84[195]	1264.78 ± 0.84	983.54	2997.22	$0_{g.s.}^+, 2_1^+, 4_1^+, 2_2^+, 0_1^+$
$^{76}_{32}$Ge $\rightarrow$ $^{76}_{34}$Se	2039.006 ± 0.050[198]	916.73 ± 0.05	559.10	1122.28	$0_{g.s.}^+, 2_1^+, 0_1^+$
$^{82}_{34}$Se $\rightarrow$ $^{82}_{36}$Kr	2997.9 ± 0.3 [199]	1510.30 ± 0.3	776.52	1487.60	$0_{g.s.}^+, 2_1^+, 2_2^+, 0_1^+$
$^{96}_{40}$Zr $\rightarrow$ $^{96}_{42}$Mo	3347.7 ± 2.2 [201]	2199.6 ± 2.2	778.24	1148.13	$0_{g.s.}^+, 2_1^+, 0_1^+$
$^{100}_{42}$Mo $\rightarrow$ $^{100}_{44}$Ru	3034.40 ± 0.17[202]	1904.08 ± 0.17	539.51	1130.32	$0_{g.s.}^+, 2_1^+, 0_1^+$
$^{110}_{46}$Pd $\rightarrow$ $^{110}_{48}$Cd	2017.85 ± 0.64[181]	544.78 ± 0.64	657.76	1473.07	$0_{g.s.}^+, 2_1^+, 0_1^+$
$^{116}_{48}$Cd $\rightarrow$ $^{116}_{50}$Sn	2813.50 ± 0.13[204]	1056.64 ± 0.13	1293.56	1756.86	$0_{g.s.}^+, 2_1^+, 0_1^+$
$^{124}_{50}$Sn $\rightarrow$ $^{124}_{52}$Te	2292.64 ± 0.39 [203]	635.36 ± 0.39	602.73	1657.28	$0_{g.s.}^+, 2_1^+, 4_1^+, 2_2^+, 0_1^+$
$^{130}_{52}$Te $\rightarrow$ $^{130}_{54}$Xe	2527.518 ± 0.013[194]	734.00 ± 0.01	536.07	1793.52	$0_{g.s.}^+, 2_1^+, 2_2^+, 4_1^+, 3_1^+, 0_1^+$
$^{136}_{54}$Xe $\rightarrow$ $^{136}_{56}$Ba	2457.83 ± 0.37[196][197]	878.84 ± 0.37	818.50	1578.99	$0_{g.s.}^+, 2_1^+, 2_2^+, 0_1^+$
$^{150}_{60}$Nd $\rightarrow$ $^{150}_{62}$Sm	3371.38 ± 0.20[200]	2630.92 ± 0.20	333.96	740.46	$0_{g.s.}^+, 2_1^+, 0_1^+$

(a) ^{238}U decay chain

(b) ^{232}Th decay chain

(c) ^{235}U decay chain
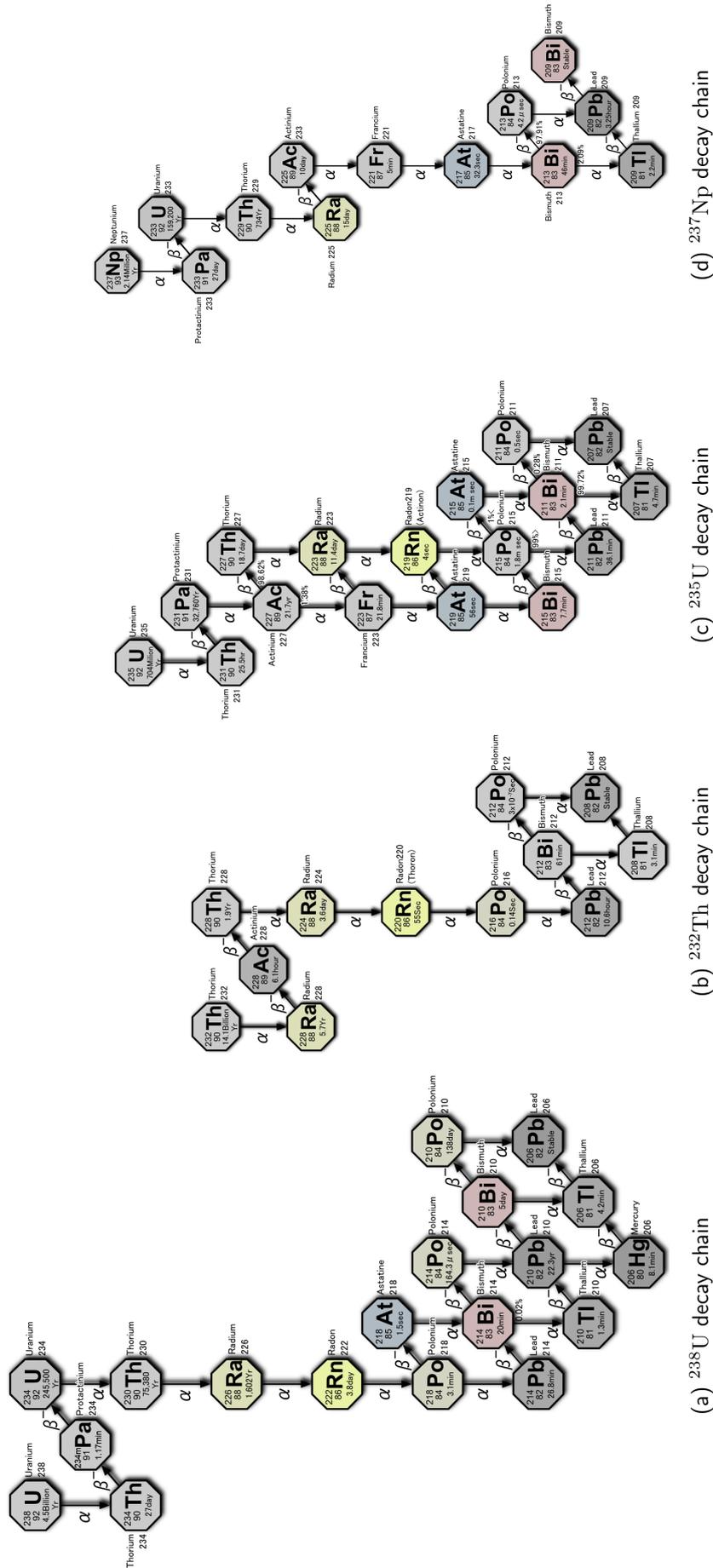
(d) ^{237}Np decay chain

Figure A.1 Primordial decay chains from left to right: The ^{238}U chain containing nuclides with A=4n+2, the ^{232}Th chain containing nuclides with A=4n, the ^{235}U chain containing nuclides with A=4n+3 and the ^{237}Np chain containing nuclides with A=4n+1. Source: creative commons.

Table A.5 ^{238}U and ^{232}Th decay chain γ-rays ordered by energy E$_\gamma$. Also given is the emitting nuclide, the emission probability for the nuclide η_{nuclide} and the emission probability for the decay chain η_{chain}. Only γ-ray with $\eta_{\mathrm{nuclide}} > 1\,\%$ are shown. Data from [138].

^{238}U chain				^{232}Th chain			
E$_\gamma$ [keV]	nuc.	η_{nuc} [%]	η_{chain} [%]	E$_\gamma$ [keV]	nuc.	η_{nuc} [%]	η_{chain} [%]
13.30	^{234}Th	7.10	7.10	13.52	^{228}Ra	1.60	1.60
46.54	^{210}Pb	4.25	4.25	84.37	^{228}Th	1.22	1.22
53.23	^{214}Pb	1.08	1.08	99.51	^{228}Ac	1.26	1.26
63.29	^{234}Th	3.70	3.70	129.07	^{228}Ac	2.42	2.42
92.38	^{234}Th	2.13	2.13	209.25	^{228}Ac	3.89	3.89
92.80	^{234}Th	2.10	2.10	238.63	^{212}Pb	43.60	43.60
186.21	^{226}Ra	3.64	3.64	240.99	^{224}Ra	4.10	4.10
242.00	^{214}Pb	7.25	7.25	270.25	^{228}Ac	3.46	3.46
265.60	^{210}Bi	51.00	51.00	277.37	^{208}Tl	6.60	2.37
295.22	^{214}Pb	18.42	18.42	300.09	^{212}Pb	3.30	3.30
304.60	^{210}Bi	28.00	28.00	328.00	^{228}Ac	2.95	2.95
351.93	^{214}Pb	35.60	35.60	338.32	^{228}Ac	11.27	11.27
609.32	^{214}Bi	45.49	45.49	409.46	^{228}Ac	1.92	1.92
649.60	^{210}Bi	3.40	3.40	463.00	^{228}Ac	4.40	4.40
665.45	^{214}Bi	1.53	1.53	510.77	^{208}Tl	22.60	8.12
768.36	^{214}Bi	4.89	4.89	583.19	^{208}Tl	85.00	30.55
785.96	^{214}Pb	1.06	1.06	674.75	^{228}Ac	2.10	2.10
806.18	^{214}Bi	1.26	1.26	727.33	^{212}Bi	6.67	6.67
934.06	^{214}Bi	3.11	3.11	755.32	^{228}Ac	1.00	1.00
1120.29	^{214}Bi	14.92	14.92	772.29	^{228}Ac	1.49	1.49
1155.21	^{214}Bi	1.63	1.63	785.37	^{212}Bi	1.10	1.10
1238.12	^{214}Bi	5.83	5.83	794.95	^{228}Ac	4.25	4.25
1280.98	^{214}Bi	1.43	1.43	835.71	^{228}Ac	1.61	1.61
1377.67	^{214}Bi	3.99	3.99	860.56	^{208}Tl	12.50	4.49
1401.52	^{214}Bi	1.33	1.33	911.20	^{228}Ac	25.80	25.80
1407.99	^{214}Bi	2.39	2.39	964.77	^{228}Ac	4.99	4.99
1509.21	^{214}Bi	2.13	2.13	968.97	^{228}Ac	15.80	15.80
1661.27	^{214}Bi	1.05	1.05	1588.20	^{228}Ac	3.22	3.22
1729.60	^{214}Bi	2.88	2.88	1620.50	^{212}Bi	1.47	1.47
1764.49	^{214}Bi	15.30	15.30	1630.63	^{228}Ac	1.51	1.51
1847.43	^{214}Bi	2.03	2.03	2614.51	^{208}Tl	99.75	35.85
2118.51	^{214}Bi	1.16	1.16				
2204.06	^{214}Bi	4.92	4.92				
2447.70	^{214}Bi	1.55	1.55				

Table A.6 ^{238}U and ^{232}Th decay chain steps. Given are the nuclide, the decay mode ordered in occurrence inside the chain, the half-life and the Q-value. Only components $> 0.1\,\%$ are listed. Data from [138].

	^{238}U chain				^{232}Th chain		
nuc.	mode	$T_{1/2}$	Q-value [keV]	nuc.	mode	$T_{1/2}$	Q-value [keV]
^{238}U	α	$4.46 \cdot 10^9$ yr	4269.7	^{232}Th	α	$1.40 \cdot 10^{10}$ yr	4081.6
^{234}Th	β	24.10 d	273	^{228}Ra	β	5.75 yr	45.8
^{234m}Pa	β	1.159 min	2195	^{228}Ac	β	6.15 h	2134
^{234}U	α	$2.455 \cdot 10^5$ yr	4859.8	^{228}Th	α	1.91 yr	5520.1
^{230}Th	α	$7.538 \cdot 10^4$ yr	4770	^{224}Ra	α	3.66 d	5788.9
^{226}Ra	α	1600 yr	4870.6	^{220}Rn	α	55.6 s	6404.7
^{222}Rn	α	3.8235 d	5590.3	^{216}Po	α	0.14 s	6906.3
^{218}Po	α	3.098 min	6114.7	^{212}Pb	β	10.6 h	569.9
^{214}Pb	β	26.8 min	1019	^{212}Bi	$35.94\,\%$ α	60.5 min	6207.3
^{214}Bi	β	19.9 min	3270	^{212}Bi	$64.06\,\%$ β	60.5 min	2252.1
^{214}Po	α	164.3 μs	7833.5	^{212}Po	$64.06\,\%$ α	0.29 μs	8954.1
^{210}Pb	β	22.20 yr	63.5	^{208}Tl	$35.94\,\%$ β	3.05 min	4999
^{210}Bi	β	5.012 d	1162.1	^{208}Pb	stable		
^{210}Po	α	138.376 d	5407.5	^{206}Pb	stable		
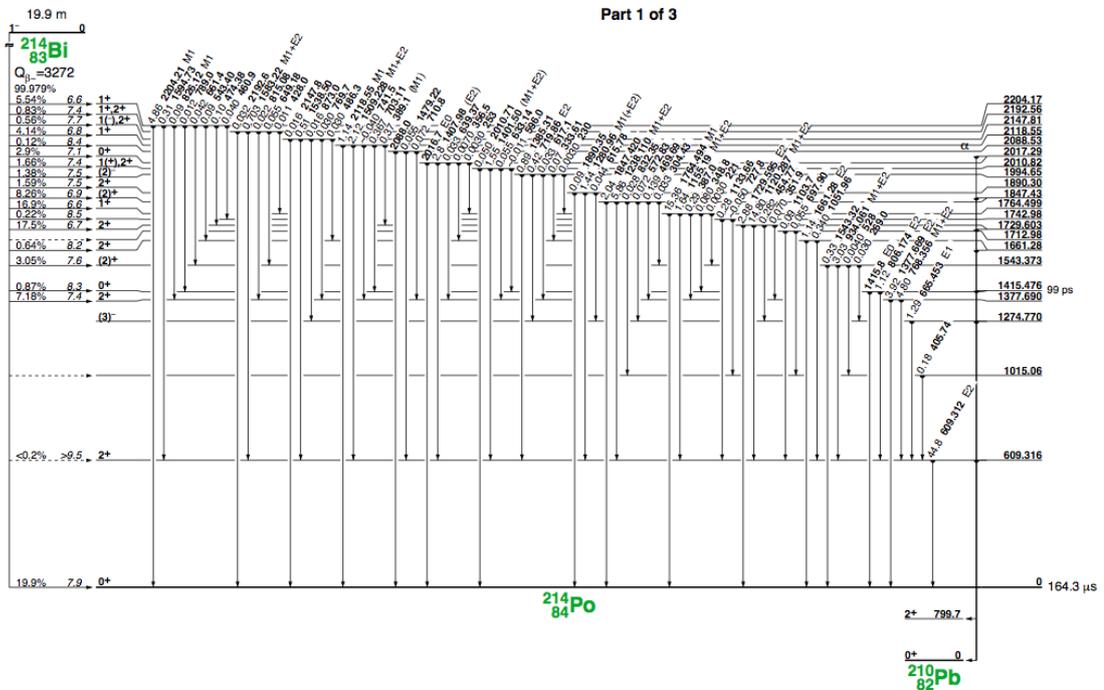
Figure A.2 Decay scheme of ^{214}Bi. Only decay branches of the lowest excited states are shown. From [30].
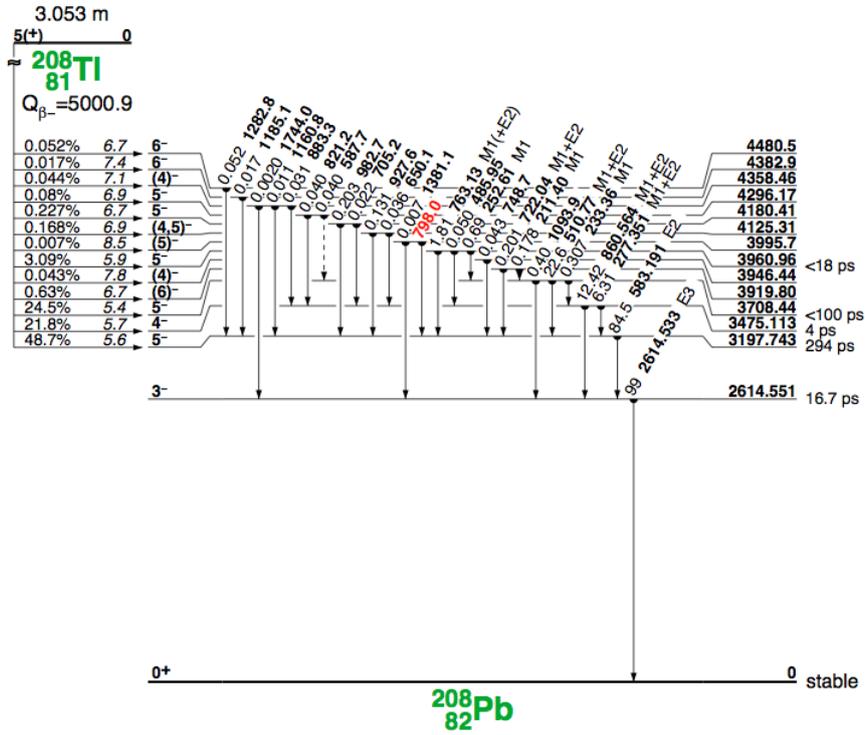
Figure A.3 Decay scheme of ^{208}Tl. From [30].
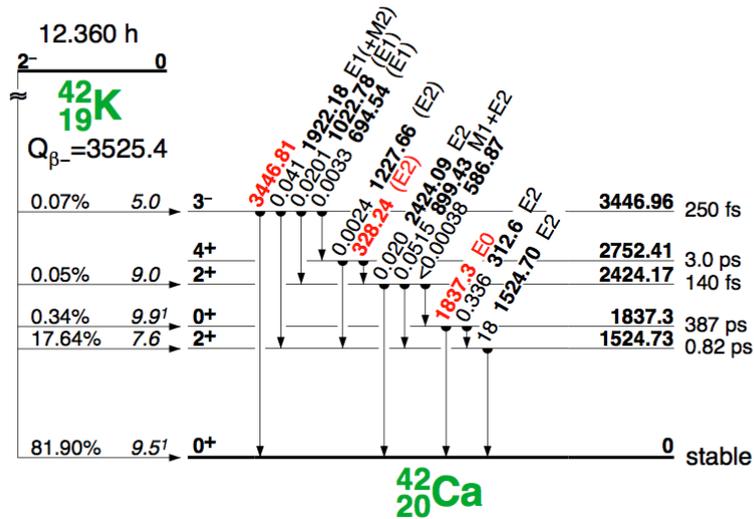
Figure A.4 Decay scheme of ^{42}K. From [30].
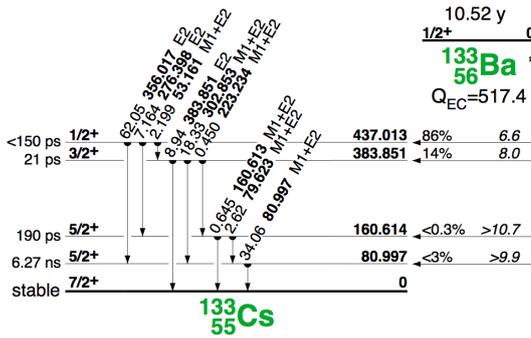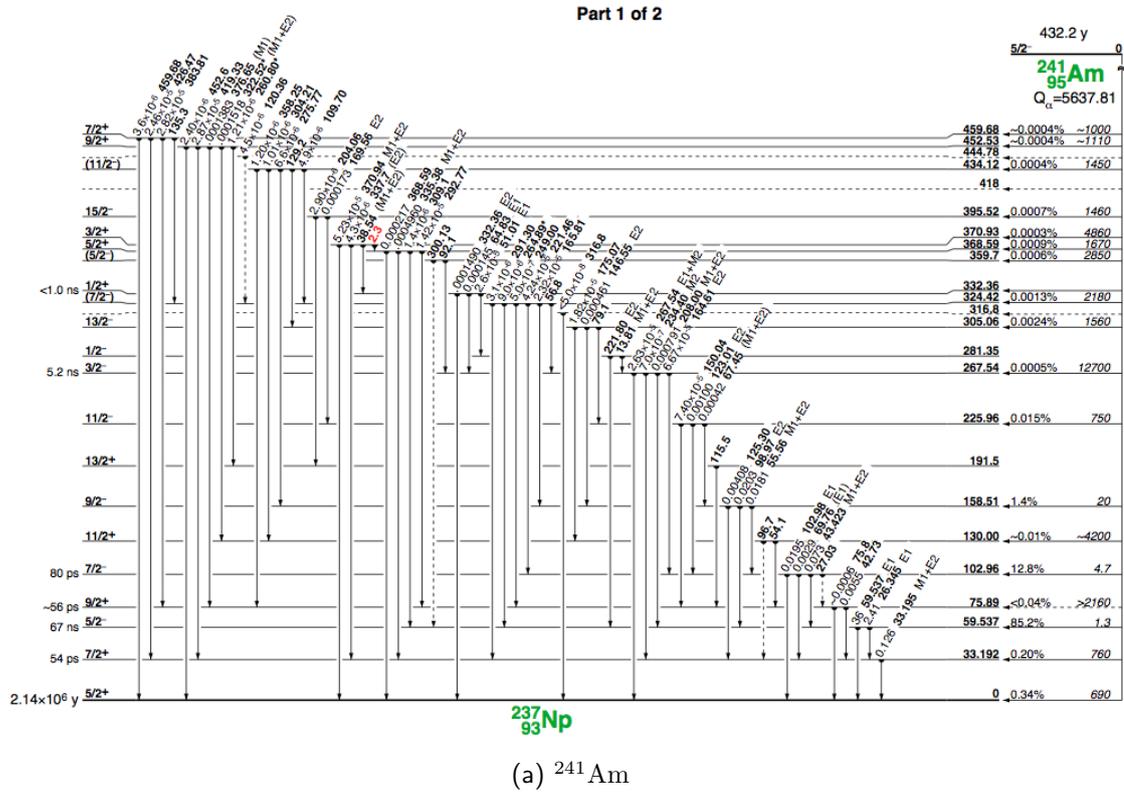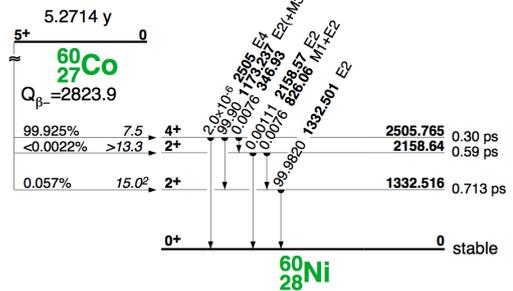
(a) ^{241}Am

(b) ^{133}Ba

(c) ^{60}Co

Figure A.5 Decay schemes of ^{133}Ba, ^{60}Co and ^{241}Am calibration sources. From [30].

Appendix B

Phase II BEGe Production and Characterization Setups

Table B.1 Original information on the Canberra data sheets for all 30 BEGe detectors. The resolution (FWHM - Full Width at Half Maximum and FWTM - Full Width at Tenth Maximum) is measured with a 4 μs time constant at two energies: At 122 keV with a ^{57}Co source and at 1333 keV with a ^{60}Co source.

detector	active diameter [mm]	active area [mm^2]	height [mm]	depl. voltage [V]	bias voltage [V]	FWHM 122 keV [eV]	FWHM 1333 keV [eV]	FWTM 122 keV [eV]	FWTM 1333 keV [eV]
GD32A	66.2	3318	25.0	2500	3000	632	1695	1162	3124
GD32B	71.8	3857	32.2	3500	4000	654	1747	1206	3266
GD32C	72.0	3914	33.2	3500	4000	596	1658	1097	3117
GD32D	72.2	3935	32.0	3500	3500	629	1757	1157	3213
GD35A	73.6	4094	35.3	3000	4000	607	1785	1131	3279
GD35B	76.6	4441	32.0	3500	4000	642	1748	1181	3260
GD35C	74.8	4254	26.4	3000	3500	618	1643	1137	3031
GD61A	74.0	4298	33.6	4000	4500	650	1820	1196	3348
GD61B	76.0	4532	30.4	3500	4000	644	1734	1188	3225
GD61C	74.4	4347	26.8	3000	4000	634	1708	1168	3194
GD76B	58.2	2660	26.3	3000	3500	678	1694	1250	3134
GD76C	75.8	4510	33.0	3000	3500	625	1710	1143	3129
GD79B	68.0	4632	29.0	3000	3500	648	1820	1201	3458
GD79C	79.0	4900	30.5	3000	3500	624	1812	1148	3352
GD89A	68.3	3660	28.5	3500	4000	654	1720	1206	3164
GD89B	76.1	4548	25.0	3000	3500	609	1684	1120	3098
GD89C	75.0	4415	25.0	3500	4000	633	1686	1176	3116
GD89D	73.1	4197	22.9	3500	4000	604	1721	1111	3201
GD91A	70.5	3900	31.0	3000	3500	650	1746	1204	3265
GD91B	70.5	3900	30.4	3000	3500	619	1708	1138	3159
GD91C	70.0	3850	30.0	3500	4000	659	1708	1214	3159
GD91D	71.5	4015	31.5	4000	4500	639	1742	1174	3191
GD00A	71.1	3860	26.4	1500	2500	714	1724	1319	3186
GD00B	74.0	4300	30.0	2500	3500	668	1745	1229	3263
GD00C	75.5	4474	33.0	3000	3500	670	1762	1232	3260
GD00D	76.0	4534	32.0	3000	3500	610	1782	1122	3261
GD02A	70.4	3895	28.0	2000	2500	684	1749	1258	3269
GD02B	71.2	3981	28.9	2500	3000	650	1720	1204	3164
GD02C	75.0	4418	33.0	2500	3500	672	1748	1236	3268
GD02D	74.5	4359	28.0	3000	4000	621	1846	1143	3585

Table B.2 Dictionary of different detector names. From left to right: Final detector name in GERDA, the working name during the acceptance tests, the diode name at Canberra Olen, the crystal name at Canberra Oak Ridge. The GERDA and Oak Ridge names encode the ingot number and the slice position. The Olen name encodes the sequence of diode construction with increasing production numbers in time. The HEROICA names do not follow a consistent encoding.

GERDA	HEROICA	Canberra Olen	Canberra Oak Ridge	GERDA	HEROICA	Canberra Olen	Canberra Oak Ridge
GD32A	Archimedes	13014	2432AA	GD89B	Cleopatra	13190	40189BB
GD32B	Agamennone	13015	2432BB	GD89C	Catequil	13188	40189CC
GD32C	Andromeda	13020	2432CC	GD89D	Durius	13217	40189DD
GD32D	Anubis	13018	2432DD	GD91A	Buri	13159	2491AA
GD35A	Argo	13019	2435AA	GD91B	Calypso	13214	2491BB
GD35B	Achilles	13017	2435BB	GD91C	Bhima	13167	2491CC
GD35C	Aristoteles	13016	2435CC	GD91D	Caesar	13215	2491DD
GD61A	Chaos	13168	2461AA	GD00A	Cheops	13216	2500AA
GD61B	ChiYou	13189	2461BB	GD00B	Chronos	13210	2500BB
GD61C	Cassiopeia	13211	2461CC	GD00C	Bellerophons	13149	2500CC
GD76B	Enkidu	13137	2476BB	GD00D	Brahma	13150	2500DD
GD76C	Briseis	13148	2476CC	GD02A	Bes	13160	2502AA
GD79B	Babel	13138	2479BB	GD02B	Bacchus	13169	2502BB
GD79C	Bastet	13139	2479CC	GD02C	Centaur	13212	2502CC
GD89A	Brian	13158	40189AA	GD02D	Diana	13213	2502DD

Table B.3 Surface geometry of BEGe detectors. Shown is the n^+ electrode surface, the n^+ electrode surface fraction and the surface to volume ratio. The p^+ electrode surface and groove dimensions are the same for all BEGe detectors. The last three rows show the minimum, maximum and average value of the dimensions.

detector	n^+ surface [cm^2]	n^+ fraction [%]	A/V [cm^{-1}]	detector	surface [cm^2]	n^+ fraction [%]	A/V [cm^{-1}]
GD32A	117.31	97.13	1.45	GD89B	146.68	97.69	1.33
GD32B	150.07	97.75	1.18	GD89C	142.20	97.62	1.35
GD32C	152.99	97.79	1.16	GD89D	133.53	97.47	1.43
GD32D	150.93	97.76	1.18	GD91A	143.69	97.65	1.30
GD35A	163.16	97.92	1.24	GD91B	141.81	97.62	1.23
GD35B	165.63	97.95	1.15	GD91C	138.66	97.56	1.25
GD35C	146.39	97.69	1.30	GD91D	147.69	97.71	1.19
GD61A	158.76	97.87	1.22	GD00A	132.52	97.45	1.59
GD61B	159.15	97.87	1.19	GD00B	150.83	97.76	1.22
GD61C	145.74	97.68	1.30	GD00C	165.85	97.96	1.13
GD76B	97.95	96.59	1.45	GD00D	165.58	97.95	1.15
GD76C	165.85	97.96	1.13	GD02A	135.44	97.51	1.41
GD79B	159.30	97.87	1.21	GD02B	139.61	97.58	1.26
GD79C	169.31	98.00	1.17	GD02C	161.19	97.90	1.15
GD89A	131.56	97.44	1.44	GD02D	149.26	97.73	1.28
minimum	97.95	96.59	1.13				
maximum	169.31	98.00	1.17				
average	147.62	97.68	1.59				

(a) GD91C crystal   (b) GD91A crystal   (c) GD02D crystal

(d) GD00A crystal   (e) GD00A diode

(f) GD61A crystal   (g) GD89D diode

Figure B.1 Examples of a regular (GD91C) and irregular shaped BEGe detectors before and after diode conversion.
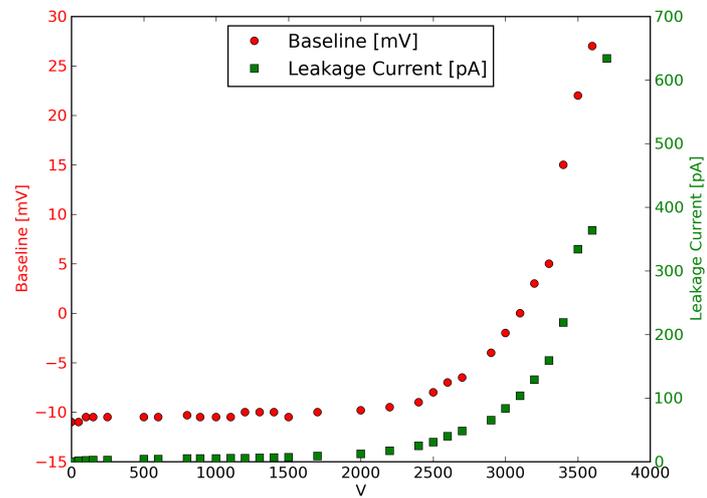
Figure B.2 Baseline voltage and leakage current during HV ramp up. The baseline voltage is measured with an oscilloscope and the leakage current with the cryostat test point.

(a) 14 mm n$^+$ electrode

(b) 13 mm n$^+$ electrode

(c) 12 mm p$^+$ electrode and groove

(d) 11 mm groove and n$^+$ electrode

(e) 10 mm groove

(f) 9 mm p$^+$ electrode and groove

(g) 8 mm p$^+$ electrode and groove
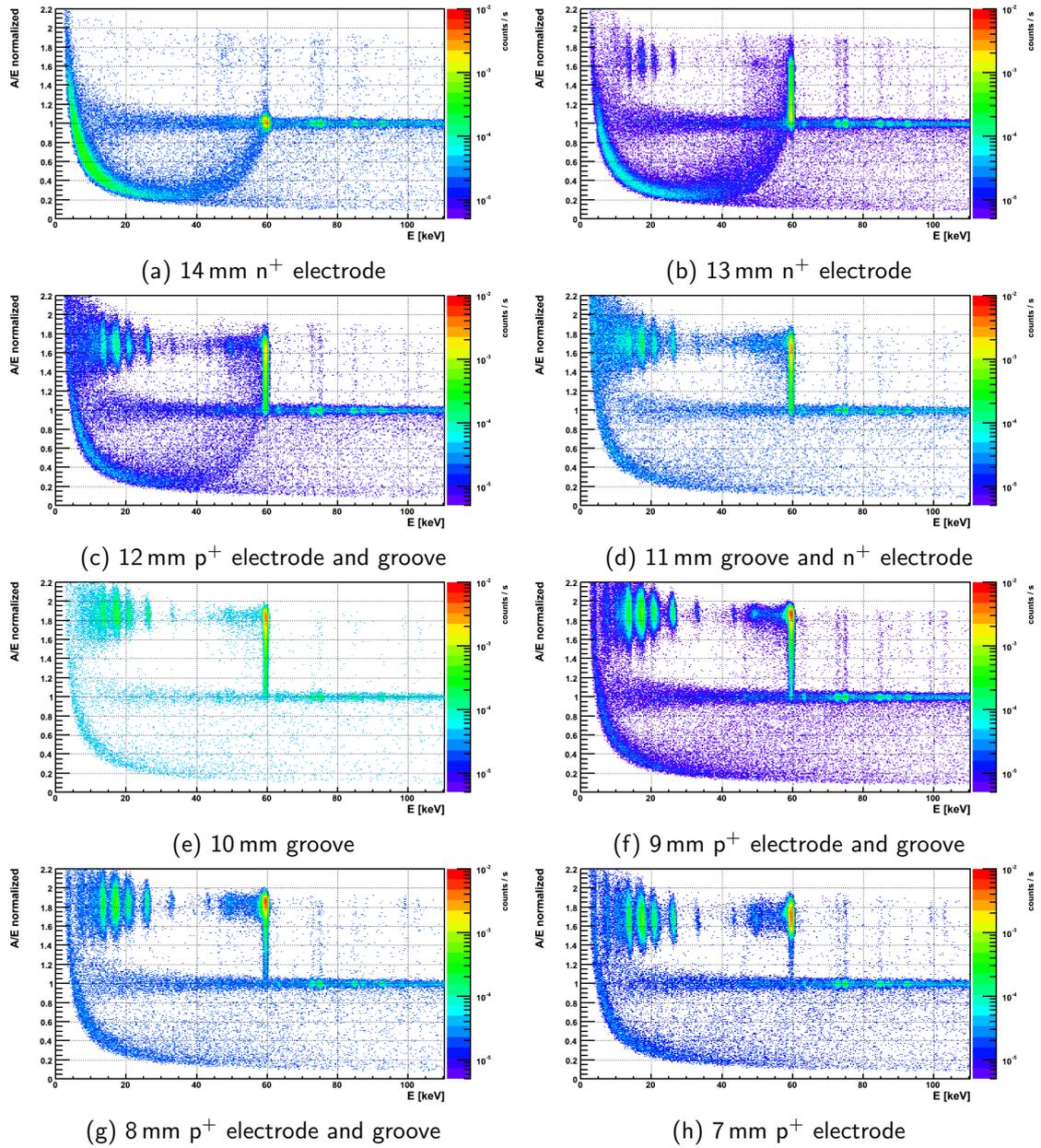
(h) 7 mm p$^+$ electrode

Figure B.3 Radial scan with *1mm Brass* collimator and ^{241}Am source from n$^+$ electrode over the groove onto the p$^+$ electrode in 1 mm steps. (Part I/II)

(a) 6 mm p$^+$ electrode

(b) 5 mm p$^+$ electrode

(c) 4 mm p$^+$ electrode

(d) 3 mm p$^+$ electrode

(e) 2 mm p$^+$ electrode

(f) 1 mm p$^+$ electrode
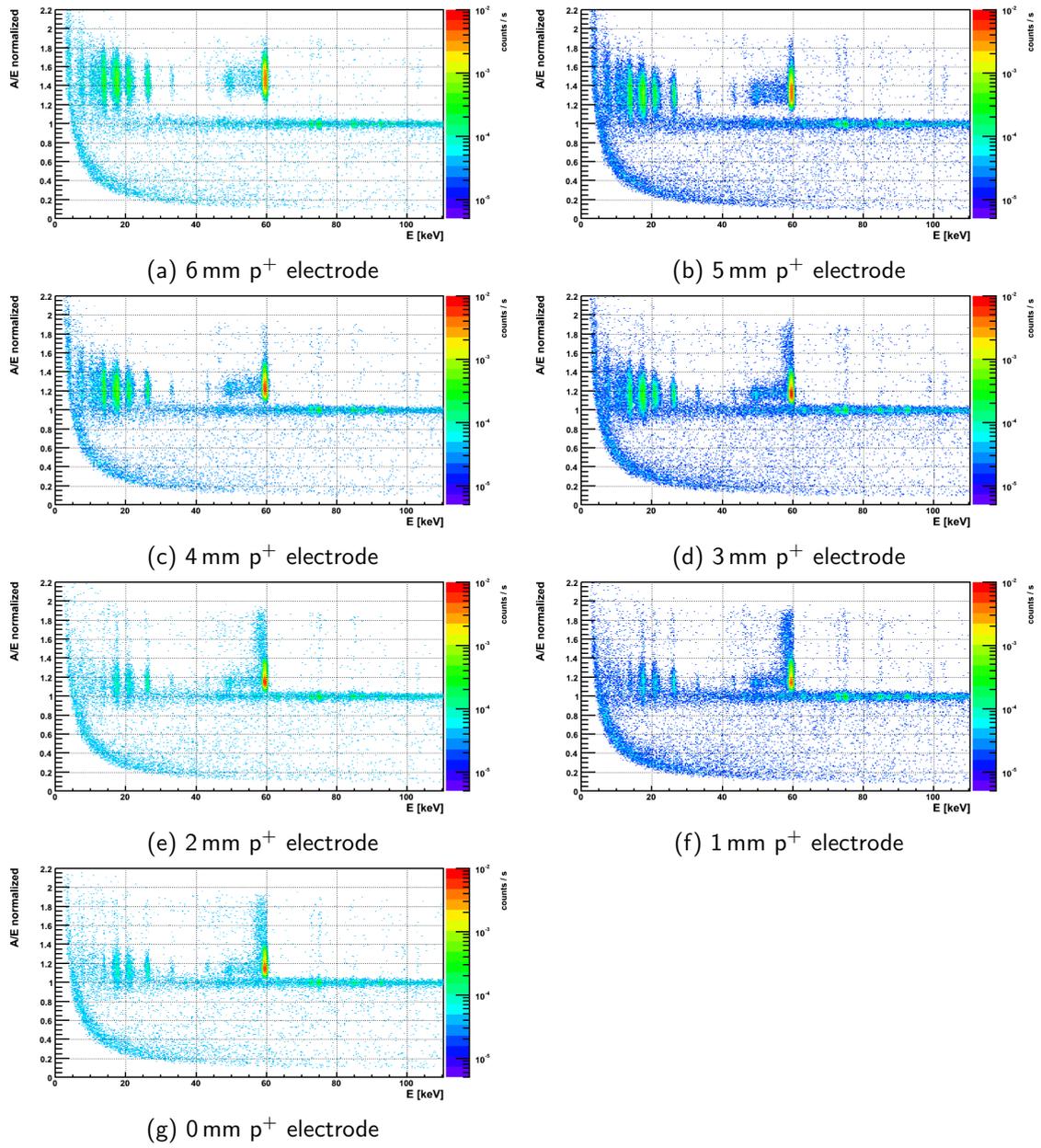
(g) 0 mm p$^+$ electrode

Figure B.4 Radial scan with *1mm Brass* collimator and ^{241}Am source from n$^+$ electrode over the groove onto the p$^+$ electrode in 1 mm steps. (Part II/II)

Appendix C

Dead Layer and Active Volume Characterization of BEGe Detectors

C.1 Active Volume Calculation

The calculation of the fully active volume (FAV) of a BEGe detector is based on the total volume (TV) of the diode with the subtraction of the n^+ electrode layer described by the full charge collection depth (FCCD). A cylindrical and conical idealized BEGe geometry is distinguished as shown in Fig. 6.2. The parameter values for each BEGe are reported in Tab. 6.1. A more detailed view introducing the geometry parameters for the calculation below is shown in Fig. C.1.
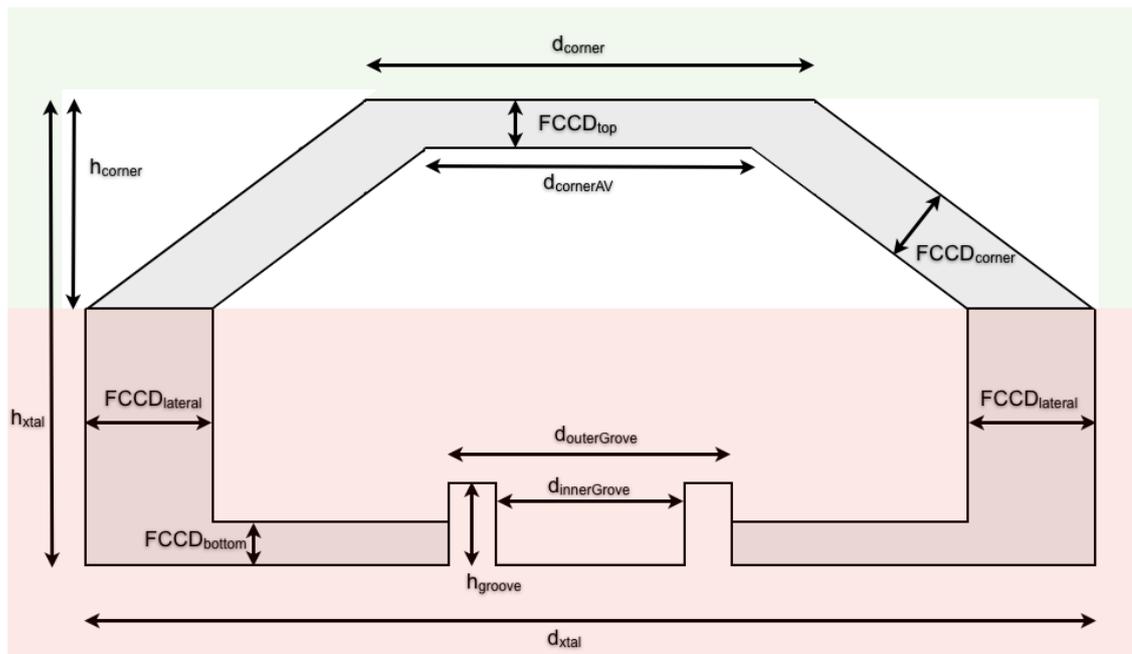
Figure C.1 BEGe geometry illustration for FAV calculation.
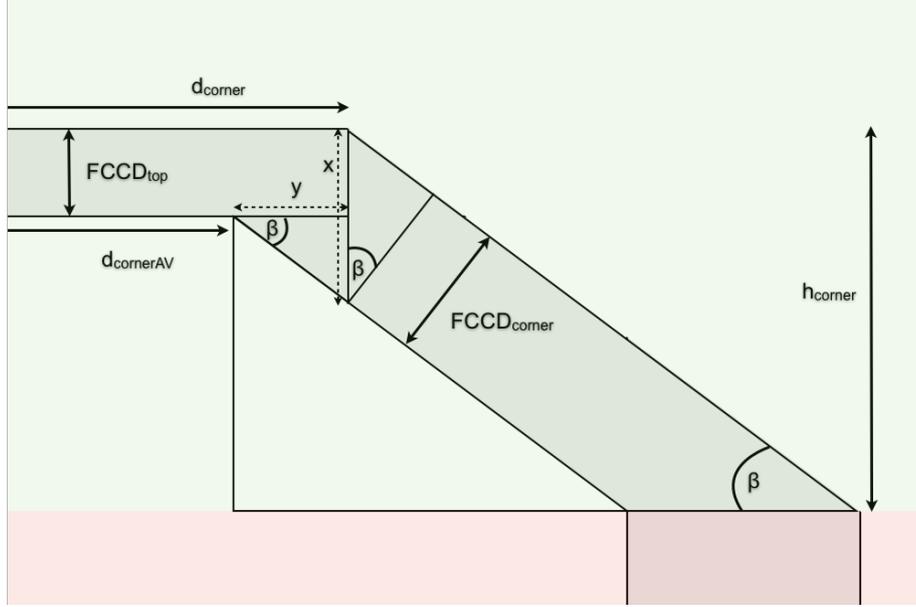
Figure C.2 BEGe geometry of conical part for FAV calculation.

The TV of a **cylindrical BEGe** is calculated as a full cylinder V_{cylinder} from which the groove volume V_{groove} is subtracted:

$$V_{\text{cylinder}} = \frac{\pi}{4} \cdot d_{\text{xtal}}^2 \cdot h_{\text{xtal}}$$

$$V_{\text{groove}} = \frac{\pi}{4} \cdot \left(d_{\text{outerGroove}}^2 - d_{\text{innerGroove}}^2\right) \cdot h_{\text{groove}}$$

$$TV = V_{\text{cylinder}} - V_{\text{groove}} \tag{C.1}$$

In principle the FCCD can be different on each side and is described as $FCCD_{\text{top}}$, $FCCD_{\text{lateral}}$ and $FCCD_{\text{bottom}}$. The FAV of a cylindrical BEGe is calculated similar to the TV above but is based on a cylinder reduced by the FCCD values on each side. An additional term describing the residual p$^+$ electrode volume above the FCCD is necessary ($V_{\text{p+}}$). The FAV of a cylindrical BEGe is:

$$V_{\text{cylinder}} = \frac{\pi}{4} \cdot \left(d_{\text{xtal}} - 2 \cdot FCCD_{\text{lateral}}\right)^2 \cdot \left(h_{\text{xtal}} - FCCD_{\text{top}} - FCCD_{\text{bottom}}\right)$$

$$V_{\text{groove}} = \frac{\pi}{4} \cdot \left(d_{\text{outerGroove}}^2 - d_{\text{innerGroove}}^2\right) \cdot \left(h_{\text{groove}} - FCCD_{\text{bottom}}\right)$$

$$V_{\text{p+}} = \frac{\pi}{4} \cdot d_{\text{innerGroove}}^2 \cdot FCCD_{\text{bottom}}$$

$$FAV = V_{\text{cylinder}} - V_{\text{groove}} + V_{\text{p+}} \tag{C.2}$$

The calculation of the TV of a **conical BEGe** is separated into a cylindrical part (similar to above) and an additional frustum[1] part (V_{frustum}). The TV of a conical BEGe is:

---

[1] truncated cone

$$V_{\text{cylinder}} = \frac{\pi}{4} \cdot d_{\text{xtal}}^2 \cdot (h_{\text{xtal}} - h_{\text{corner}})$$

$$V_{\text{groove}} = \frac{\pi}{4} \cdot \left(d_{\text{outerGroove}}^2 - d_{\text{innerGroove}}^2\right) \cdot h_{\text{groove}}$$

$$V_{\text{frustum}} = \frac{\pi}{3} \cdot h_{\text{corner}} \cdot \frac{1}{4} \left[d_{\text{xtal}}^2 + d_{\text{corner}}^2 + d_{\text{xtal}} \cdot d_{\text{corner}}\right]$$

$$TV = V_{\text{cylinder}} + V_{\text{frustum}} - V_{\text{groove}} \tag{C.3}$$

In the case of a conical diode also the corner side may have an individual FCCD ($FCCD_{\text{corner}}$). The calculation of V_{frustum} is more complex in this case and done with parameters β, x, y and $d_{\text{cornerFAV}}$ as illustrated in Fig. C.2:

$$\beta = \arctan\left(\frac{2 \cdot h_{\text{corner}}}{d_{\text{xtal}} - d_{\text{corner}}}\right)$$

$$x = \frac{FCCD_{\text{corner}}}{\cos\beta}$$

$$y = \frac{x - FCCD_{\text{top}}}{\tan\beta}$$

$$d_{\text{cornerFAV}} = d_{\text{corner}} - 2 \cdot y$$

$$V_{\text{frustum}} = \frac{\pi}{3} \cdot (h_{\text{corner}} - FCCD_{\text{top}}) \tag{C.4}$$

$$\cdot \frac{1}{4} \left[(d_{\text{xtal}} - 2 \cdot FCCD_{\text{lateral}})^2 + d_{\text{cornerFAV}}^2 + (d_{\text{xtal}} - 2 \cdot FCCD_{\text{lateral}}) \cdot d_{\text{corner}}\right]$$

Together with V_{frustum} from above, the FAV of a conical BEGe is calculated as:

$$V_{\text{cylinder}} = \frac{\pi}{4} \cdot (d_{\text{xtal}} - 2 \cdot FCCD_{\text{lateral}})^2 \cdot (h_{\text{xtal}} - h_{\text{corner}} - FCCD_{\text{bottom}})$$

$$V_{\text{groove}} = \frac{\pi}{4} \cdot \left(d_{\text{outerGroove}}^2 - d_{\text{innerGroove}}^2\right) \cdot (h_{\text{groove}} - FCCD_{\text{bottom}})$$

$$V_{\text{p+}} = \frac{\pi}{4} \cdot d_{\text{innerGroove}}^2 \cdot FCCD_{\text{bottom}}$$

$$FAV = V_{\text{frustum}} + V_{\text{cylinder}} - V_{\text{groove}} + V_{\text{p+}} \tag{C.5}$$

(a) ^{241}Am 59.5 keV events   (b) ^{133}Ba 80.5 ± 1.0 keV events   (c) ^{60}Co 1173.2 keV events

(d) ^{241}Am 101 ± 4 keV events   (e) ^{133}Ba 356.2 keV events   (f) ^{60}Co 1332.5 keV events.
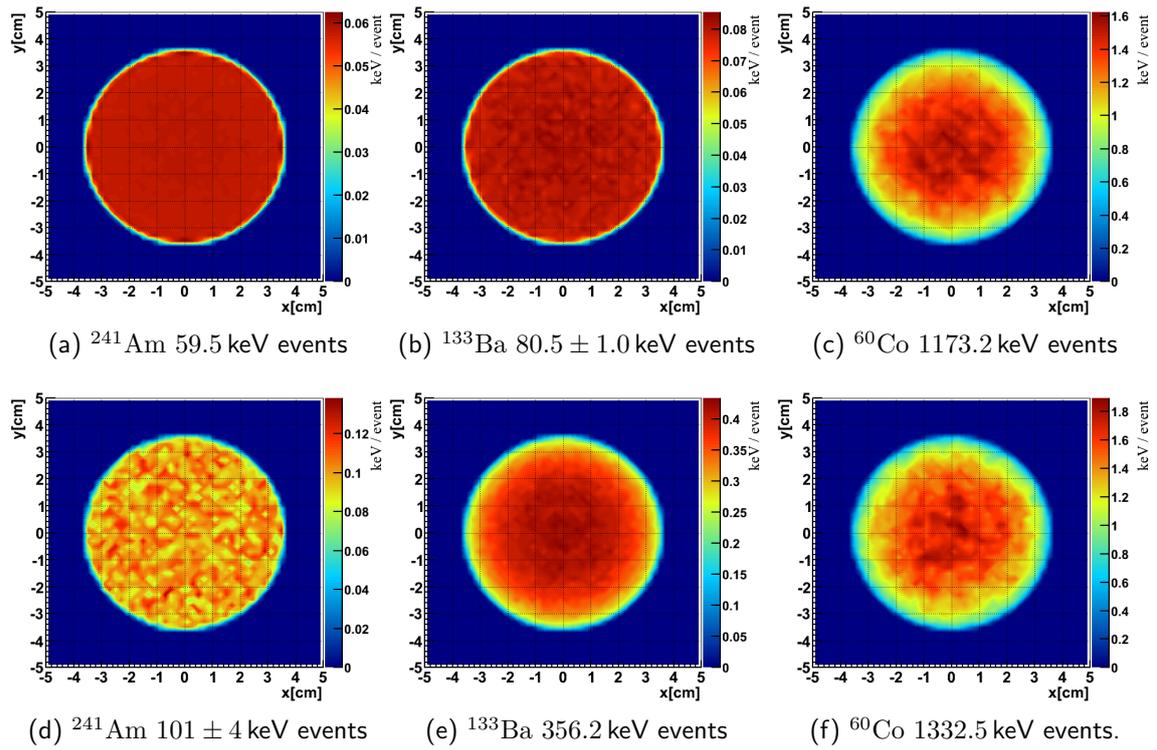
Figure C.3   Localization of energy position in a typical BEGe detector for γ-ray energies in the FCCD measurements. Shown are the MC hit positions weighted with the energy deposition in the projected $x - y$-plane.
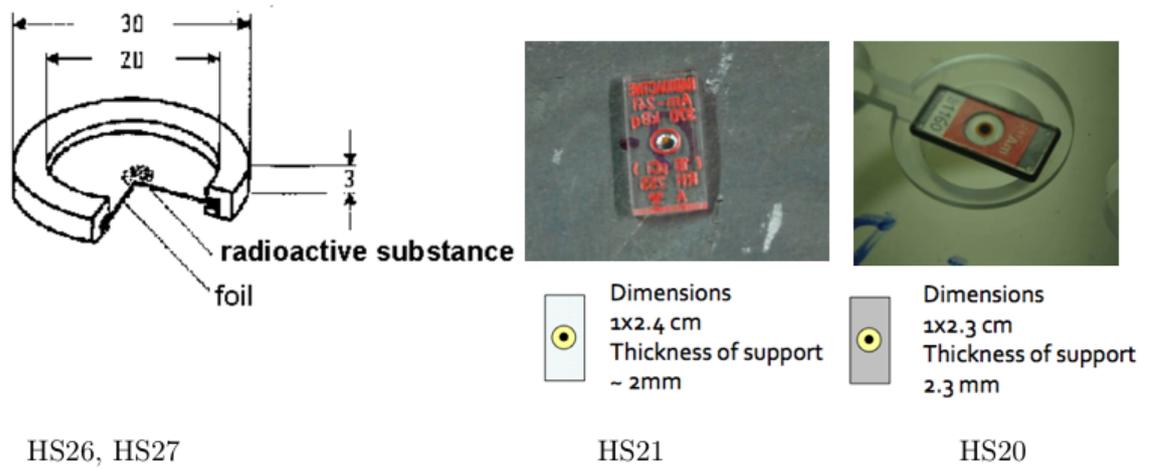
Figure C.4 Geometry of calibration sources used for the FCCD/FAV determination.
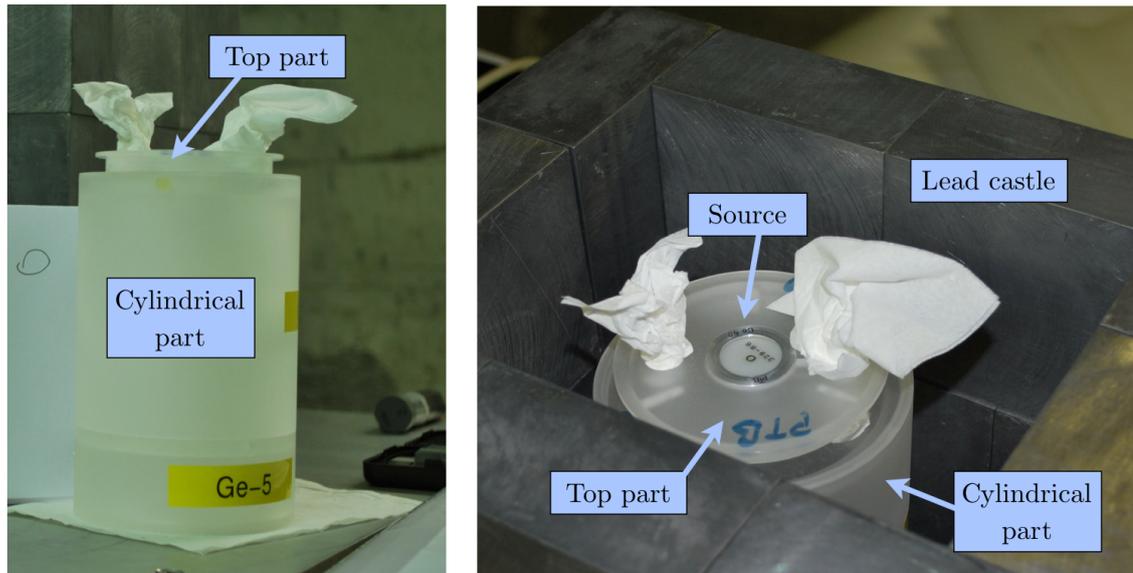
Figure C.5 Plexiglass source holder. Cylindrical part and top part are separated by paper towels for illustration.

Table C.1 Cryostat dimensions and materials for 7500SL Dipstick Cryostat. The interior components are equal for all cryostats. The outer dimensions for the Tuebingen Cryostat are provided in parentheses.

cryostat diameter	$101.6 \pm 0.1\,\text{mm}$ $(95.2 \pm 0.1\,\text{mm})$
cryostat height	$122.2 \pm 0.1\,\text{mm}$ $(146.2 \pm 0.1\,\text{mm})$
cryostat endcap thickness	$1.5 \pm 0.1\,\text{mm}$ $(1.6 \pm 0.1\,\text{mm})$
cryostat wall thickness	$1.5 \pm 0.1\,\text{mm}$ $(1.6 \pm 0.1\,\text{mm})$
cryostat material	Al alloy: AL 6061 T6
detector holder thickness	$1.5 \pm 0.1\,\text{mm}$
detector holder ring thickness	$3.0 \pm 0.1\,\text{mm}$
detector holder material	Al alloy: EN AW-2011 Al Cu6BiPb
detector cup top thickness	$1.0 \pm 0.1\,\text{mm}$
detector cup lateral thickness	$0.5 \pm 0.1\,\text{mm}$
detector cup material	polyethylene
detector base material	copper

Table C.2 Activity of calibration sources used for the FCCD/FAV analysis.

source name	nuclide	activity [kBq]	date [dd/mm/yyyy]	geometry
HS1	^{60}Co	$397 \cdot (1 \pm 0.01)$	01/01/1981	PTB
HS2	^{60}Co	$415 \cdot (1 \pm 0.01)$	01/01/1981	PTB
HS3	^{60}Co	$399 \cdot (1 \pm 0.01)$	01/01/1987	PTB
HS4	^{60}Co	$413 \cdot (1 \pm 0.01)$	01/01/1984	PTB
HS20	^{241}Am	$450 \cdot (1 \pm 0.05)$	01/01/1984	HS20
HS21	^{241}Am	$396 \cdot (1 \pm 0.03)$	01/01/1984	HS21
HS17	^{241}Am	$4220 \cdot (1 \pm 0.08)$	01/04/2012	EuZ
HS18	^{241}Am	$4335 \cdot (1 \pm 0.08)$	01/04/2012	EuZ
HS19	^{241}Am	$4330 \cdot (1 \pm 0.08)$	01/04/2012	EuZ
HS26	^{133}Ba	$56.2 \cdot (1 \pm 0.02)$	01/12/2008	PTB
HS27	^{133}Ba	$40.7 \cdot (1 \pm 0.02)$	01/12/2008	PTB
HS28	^{133}Ba	$56 \cdot (1 \pm 0.02)$	01/12/2008	PTB
HS29	^{133}Ba	$390 \cdot (1 \pm 0.02)$	01/04/1974	PTB

(a) flexible control of geometry parameters   (b) new output scheme for easy DLPP
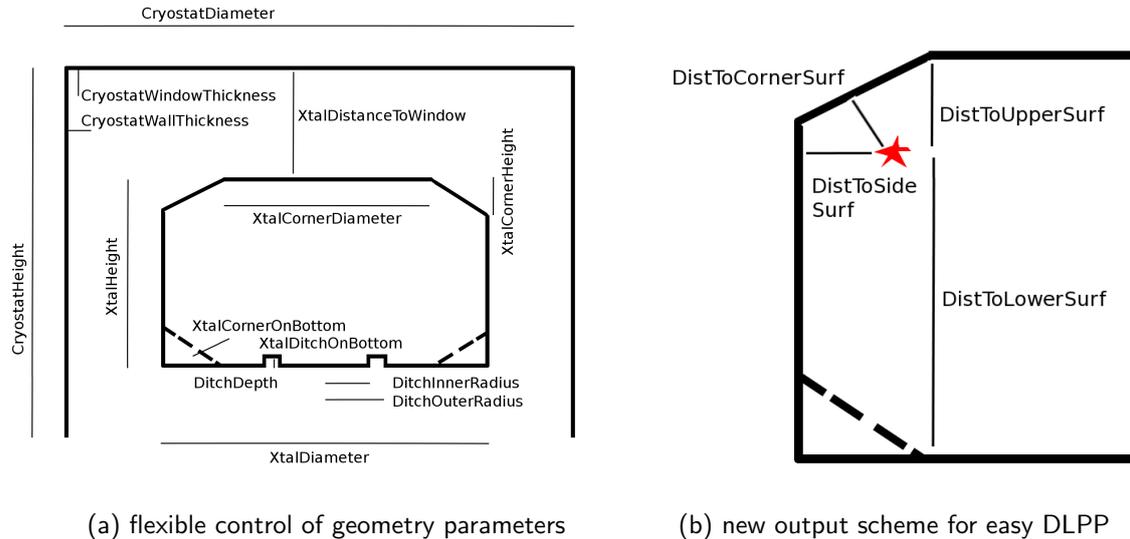
Figure C.6 Features of GEANT4 class developed for the BEGe acceptance tests. Left: Macro commands to control the cryostat and BEGe geometry at run time. Right: New output variables for easy DLPP posterior cuts. A cut can be simply applied to the value of the hit distance to surface. No geometry information has to be transported outside the simulation code in order to convert absolute hit positions to distances.

C.2 Methods for Peak Count Determination

In all cases, the counting and fitting is performed within the ROOT package on the binned data in histograms. For the fitting methods the fit result is returned and checked for convergence and consistency of the covariance matrix. In case of inconsistencies the fit is repeated up to 20 times with the newly found input parameters until convergence is achieved. In rare cases it was accepted that the covariance matrix for a MC spectrum fit is not complete and the error correlation imprecise. A few imprecisions within 150 fits have no influence on the result.

Counting Method ^{241}**Am** A number of bins is integrated for the peak window and side band windows. For the first peak region the peak window range is $59.5 \pm 3.5\sigma_E$ keV. The side band windows range from $56.5 - 57.5$ keV and $61.5 - 62.5$ keV. In the second peak region the range is $99.0 \pm 3\sigma_E$ keV for the left signal peak, $103.0 \pm 3\sigma_E$ keV for the right signal peak. The two side band regions range from $94.0 - 96.0$ keV and $105.0 - 107.0$ keV. The actual energy ranges are adjusted to the selected bins, i.e. from the low edge of the first bin to the high edge of the last bin. Thus the ranges become slightly larger individually for each measurement. The number of counts in the peak window is reduced by the expected number of background counts in that window. The background is determined from the side band counts by scaling the window sizes accordingly. The peak regions are illustrated with the counting windows in Fig. C.7 for GD91C.

(a) ^{241}Am measured   (b) ^{241}Am simulated
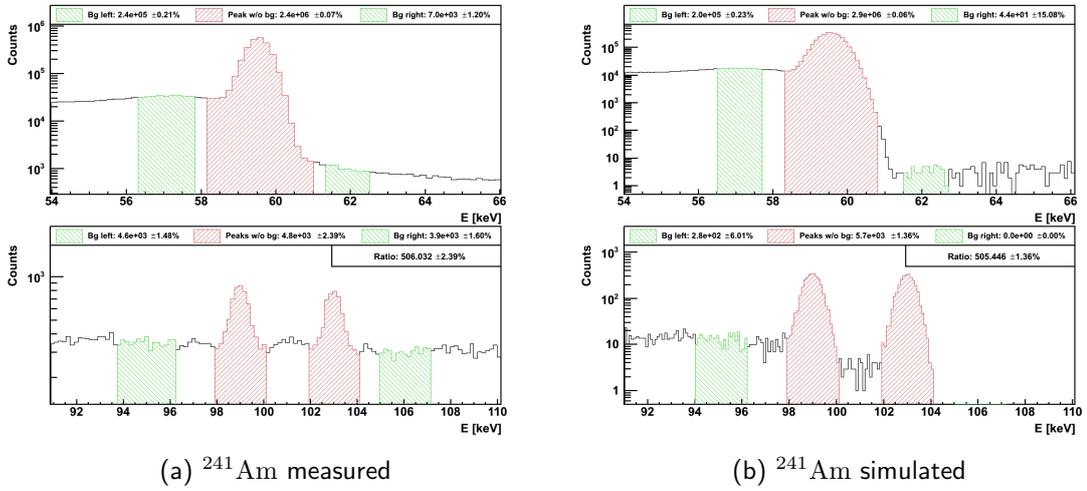
Figure C.7 Determination of peak counts of ^{241}Am with counting event in the peak and in side band regions. Experimental spectrum of GD91C.

Fitting Method ^{241}**Am** Two functions are defined for fitting the ^{241}Am peak regions. The function for the first peak window (Eq. C.6) is defined from $58 - 62$ keV. The background component is segmented into two constant parts (p_0 and p_1) below and above the peak which are connected by a Gaussian cumulative distribution function (CDF). The low energy boundary of the function is close to the peak such that the non-linear Compton features below the peak have small influence. The width and mean of the CDF is the same as for the peak.

For the second peak region the fit function (Eq. C.7) is segmented in three constant backgrounds (p_6, p_7 and p_8) with two CDFs as junctions. The function is constructed such that the three Gaussian peaks (two signal peaks and one background peak) can be scaled by relative strength between them (p_3 and p_9). This enables to set and constrain the branching rations in the fit. The peak regions including the fit functions are illustrated for GD91C in Fig. 7.8. The regions for the other detectors are shown in Fig. C.10 to C.10. The parameter descriptions for Eq. C.6 and Eq. C.7 including the stating values and boundaries are reported in Tab. C.3 and C.4.

$$
\begin{aligned}
f_{\text{Region1}}(E) = {} & p_0 \\
& - p_1 \cdot \text{gaussian\_cdf}(E, p_4, p_3) \\
& + p_2 \cdot \text{Gaus}(E, p_3, p_4)
\end{aligned} \tag{C.6}
$$

$$
\begin{aligned}
f_{\text{Region2}}(E) = {} & p_6 \\
& - p_7 \cdot \text{gaussian\_cdf}(E, p_2, p_1) \\
& - p_8 \cdot \text{gaussian\_cdf}(E, p_5, p_4) \\
& + p_0 \cdot \text{Gaus}(E, p_1, p_2) \\
& + p_0 \cdot p_3 \cdot \text{Gaus}(E, p_4, p_5) \\
& + p_0 \cdot p_9 \cdot \text{Gaus}(E, p_{10}, p_{11})
\end{aligned} \tag{C.7}
$$

Counting Method ^{133}Ba   The counting method for ^{133}Ba is similar as for ^{241}Am. For the first peak region the peak window ranges from $79.6 - 3\sigma_E$ keV to $81.0 + 3\sigma_E$ keV. The side band windows are defined from $75.0 - 77.5$ keV and from $83.5 - 86.0$ keV. The second peak window ranges from $97.8 - 100.0$ keV and the corresponding side band windows from $345.0 - 353.5$ keV and $356.0 \pm 3.5\sigma_E$ keV. The two regions for the ^{133}Ba method along with the illustrated peaks and side band regions are illustrated in Fig. C.8 for GD91C. Lead X-rays can interfere with the side band regions which is the case for measurements of GD32B, GD32D and GD35B.

(a) ^{133}Ba measured   (b) ^{133}Ba simulated
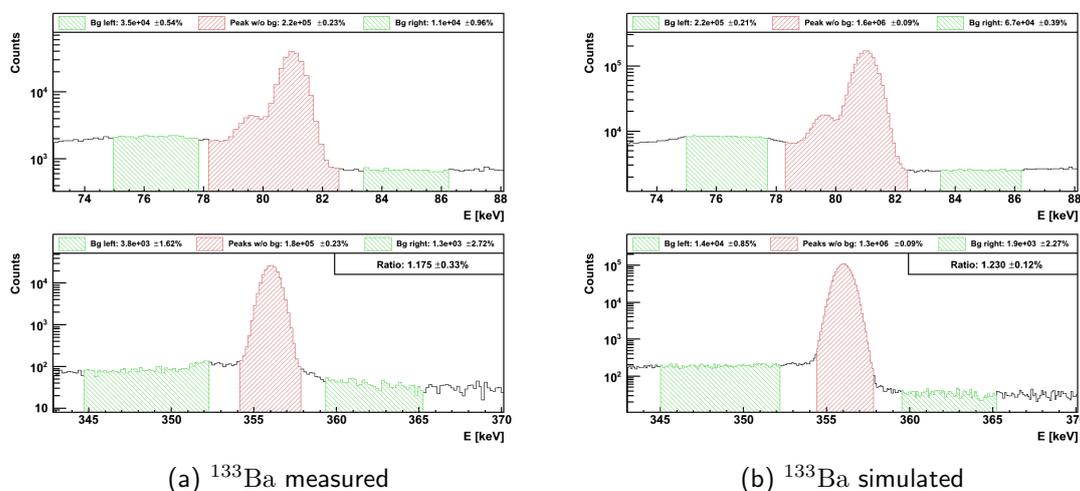
Figure C.8   Determination of peak counts of ^{133}Ba with counting event in the peak and in side band regions. Experimental spectrum of GD91C.

Fitting Method ^{133}Ba   Two fit functions are defined for the two ^{133}Ba peak regions. The function describing the double peak in the first region (Eq. C.8) ranges from $78.5 - 83.0$ keV. It is complicated to fit since subtle changes in the energy resolution affect the separation of the two peaks. This requires strong constraints on the parameters. The background is constructed with two constant terms (p_0 and p_1) below and above the peak respectively. Two CDFs describe the junction below the first smaller peak (P1) and the second larger peak (P2). The strength of the two CDF background steps is coupled to fixed branching ratio (A and B) of P1 and P2. The strength of P1 is coupled to the strength of

P2 by the branching ratio (p_2) which is left floating within strong bounds.

The fit function for the second peak window is defined in Eq. C.9 in the range of $353.5 - 361.0\,\text{keV}$. The parameter descriptions for the two functions are reported in Tab. C.5 and C.6 respectively. The fit of the ^{133}Ba peak windows for GD91C is shown in Fig. 7.9 and for all other detectors in Fig. C.14 to C.17.

$$
\begin{aligned}
f_{\text{Region1}}(E) = p_0 \\
&- p_1 \cdot A \cdot \text{gaussian\_cdf}(E, p_4, p_3) \\
&- p_1 \cdot (A + B) \cdot \text{gaussian\_cdf}(E, p_7, p_6) \\
&+ p_5 \cdot p_2 \cdot \text{Gaus}(E, p_3, p_4, 1) \\
&+ p_5 \cdot \text{Gaus}(E, p_6, p_7, 1)
\end{aligned}
\tag{C.8}
$$

$$
\begin{aligned}
f_{\text{Region2}}(E) = p_0 \\
&- p_1 \cdot \text{gaussian\_cdf}(E, p_7, p_6) \\
&+ p_2 \cdot \text{Gaus}(E, p_3, p_4, 1)
\end{aligned}
\tag{C.9}
$$

Fitting Method ^{60}Co The ^{60}Co peaks are fitted with a Gaussian peak on a step-like background. The background is composed of two constant functions (p_0 and p_1) which are connected at the peak energy with a Gaussian CDF. The peaks in the experimental spectra are fitted with an additional exponential tail on the low energy side whereas the peak in the MC spectra are fitted with a pure Gaussian. The fit function is described in Eq. C.10 for the experimental case and separated into a Gaussian part above the junction point and Gaussian with a tail below the junction point. The junction point p_5 is a single additional parameter to describe the tail [205]. The fit range is set from the peak energy $\pm 9\,\sigma$ and the description of the fit parameters along with their boundaries are shown in Tab. C.7.

$$
\begin{aligned}
f_{\text{Tail}}(E) = p_0 \\
&- p_1 \cdot \frac{1}{2} \cdot \text{Erfc}\left(\frac{p_3 - E}{\sqrt{2} \cdot p_4}\right) \\
\text{if } x \geq p_4 - p_5: \quad &+ p_2 \cdot \exp\left(-\frac{1}{2} \cdot \frac{(E - p_3)^2)}{(p_4)^2}\right) \\
\text{if } x < p_4 - p_5: \quad &+ p_2 \cdot \exp\left(-\frac{1}{2} \cdot \frac{p_5^2 + 2 \cdot (E - p_3)^2) \cdot p_5}{(p_4)^2}\right)
\end{aligned}
\tag{C.10}
$$

The peak counts are obtained by integrating the fit function with the background parameters p_0 and p_1 set to zero. The ROI for the ^{60}Co peaks along with the fit function is shown in Fig. 7.10. Additionally, a counting method with side band subtraction has been implemented for ^{60}Co. The background is smooth and constant on either side of both peaks and the counting windows were chosen large enough to account for a possible low energy tail. Thus the two methods practically yield the same result for the peak counts. However, the fitting method was chosen for the final analysis to obtain the additional information on the peak asymmetry.

Table C.3 Parameter description and values for the first peak window in the ^{241}Am ratio method.

parameter	description	starting value (range)
p_0	bg left	unconstrained
p_1	bg right	unconstrained
p_2	peak counts	unconstrained
p_3	peak mean	59.54 (± 0.5)
p_4	peak width	$\sigma(E)$ (± 0.2)

Table C.4 Parameter description and values for the second peak window in the ^{241}Am ratio method.

parameter	description	starting value (range)
p_0	left signal peak counts	unconstrained
p_1	left signal peak mean	98.97 (± 0.3)
p_2	left signal peak width	$\sigma(E)$ $\binom{+0.3}{-0.1}$
p_3	ratio between left and right signal peak counts	0.96 (0.8;1.2)
p_4	right signal peak mean	102.98 (± 0.2)
p_5	right signal peak width	$\sigma(E)$ $\binom{+0.3}{-0.05}$
p_6	bg left	unconstrained
p_7	bg difference left-center	unconstrained
p_8	bg difference left-right	unconstrained
p_9	ratio between bg peak and left signal peak	0.089 (0.03;0.20)
p_{10}	bg peak mean	101.2 (± 0.1)
p_{11}	bg peak width	$\sigma(E)$ (fixed)
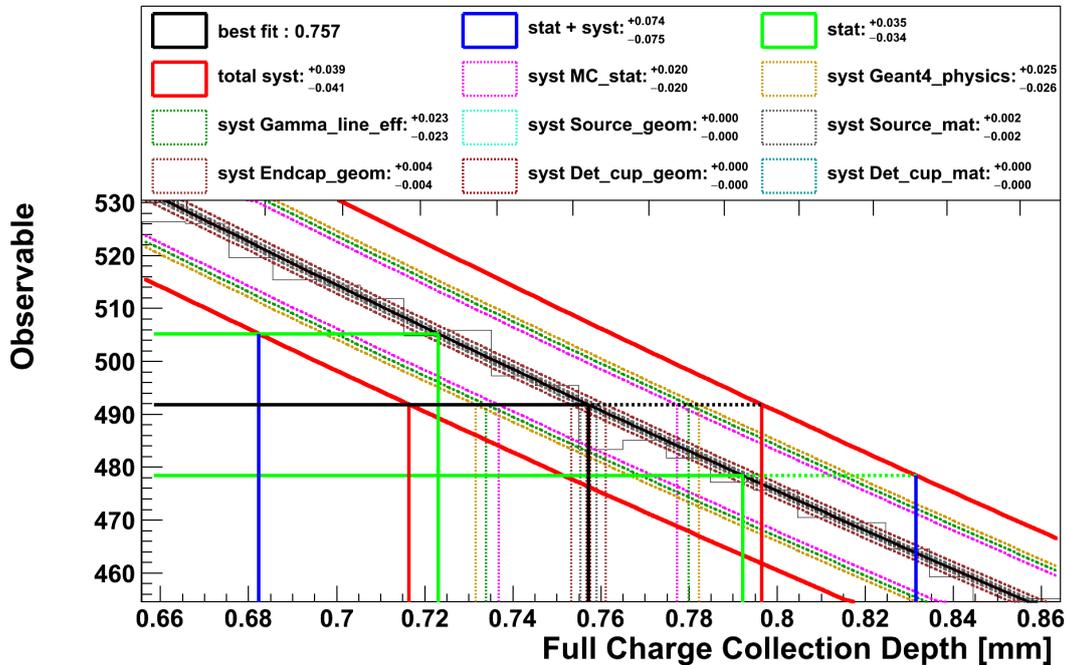
Figure C.9 Illustration of systematic uncertainty propagation in the FCCD fitting for an ^{241}Am measurement of GD91C. The figure is essentially a zoomed version of Fig. 7.11a in which additionally all systematic uncertainties are shown unfolded.

Table C.5 Parameter description and values for the first peak window in the ^{133}Ba ratio method.

parameter	description	starting value (range)
A	branching ratio left signal peak	2.65 (fixed)
B	branching ratio right signal peak	32.9 (fixed)
p_0	bg left	unconstrained
p_1	bg difference left-right	unconstrained
p_2	ratio between left and right signal peak counts	0.0427 (fixed)
p_3	left signal peak mean	79.61 $\left(^{+0.2}_{-0.5}\right)$
p_4	left signal peak width	$\sigma(E)$ ($\pm$0.5)
p_5	right signal peak counts	unconstrained
p_6	right signal peak mean	81.00 ($\pm$0.5)
p_7	right signal peak width	$\sigma(E)$ ($\pm$0.5)

Table C.6 Parameter description and values for the second peak window in the ^{133}Ba ratio method.

parameter	description	starting value (range)
p_0	bg left	unconstrained
p_1	difference bg left and right	unconstrained
p_2	signal peak counts	unconstrained
p_3	signal peak mean	356.02 ($\pm$1.0)
p_4	signal peak width	$\sigma(E)$ ($\pm$0.2)

Table C.7 Parameter description and values for the peak fitting with tail for the ^{60}Co method.

parameter	description	starting value (range)
p_0	bg left	unconstrained
p_1	difference bg left and right	unconstrained
p_2	signal peak counts	unconstrained
p_3	signal peak mean	1173.2 / 1332.5 ($\pm$2.0 σ)
p_4	signal peak width	$0.5 - 5.0\,\sigma$
p_5	junction point	$0.1 - 5.0\,\sigma$

Table C.8 FCCD results for the counting method of ^{241}Am, ^{133}Ba. Also the FCCD value reported by the manufacturer is given. The uncertainties are separated in correlated and uncorrelated components.

det.	^{241}Am [mm]	^{133}Ba [mm]	manuf. [mm]	BEGe	^{241}Am [mm]	^{133}Ba [mm]	manuf. [mm]
GD32A	$0.58^{+0.03+0.01}_{-0.03-0.01}$	$0.51^{+0.06+0.01}_{-0.06-0.01}$	0.60	GD89B	$0.85^{+0.03+0.03}_{-0.04-0.03}$	$0.72^{+0.07+0.01}_{-0.07-0.01}$	0.80
GD32B	$0.83^{+0.03+0.01}_{-0.03-0.01}$	$0.66^{+0.07+0.01}_{-0.07-0.01}$	0.90	GD89C	$0.71^{+0.03+0.03}_{-0.03-0.03}$	$0.65^{+0.07+0.01}_{-0.07-0.01}$	0.85
GD32C	$0.82^{+0.04+0.03}_{-0.04-0.03}$	$0.55^{+0.06+0.01}_{-0.06-0.01}$	0.70	GD89D	$0.81^{+0.03+0.03}_{-0.04-0.03}$	$0.59^{+0.07+0.01}_{-0.07-0.01}$	0.76
GD32D	$0.59^{+0.03+0.03}_{-0.04-0.03}$	$0.30^{+0.07+0.01}_{-0.07-0.01}$	0.70	GD91A	$0.71^{+0.03+0.03}_{-0.03-0.03}$	$0.63^{+0.05+0.01}_{-0.05-0.01}$	0.80
GD35A	$0.60^{+0.03+0.01}_{-0.03-0.01}$	$0.57^{+0.05+0.01}_{-0.05-0.01}$	0.70	GD91B	$0.70^{+0.04+0.04}_{-0.03-0.03}$	$0.61^{+0.06+0.01}_{-0.06-0.01}$	0.80
GD35B	$0.55^{+0.03+0.04}_{-0.04-0.04}$	$0.42^{+0.07+0.01}_{-0.07-0.01}$	0.70	GD91C	$0.72^{+0.03+0.04}_{-0.04-0.03}$	$0.59^{+0.06+0.01}_{-0.06-0.01}$	0.76
GD35C	$0.59^{+0.04+0.01}_{-0.04-0.01}$	$0.51^{+0.06+0.01}_{-0.07-0.01}$	0.60	GD91D	$0.66^{+0.03+0.03}_{-0.04-0.03}$	$0.64^{+0.06+0.01}_{-0.06-0.01}$	0.80
GD61A	$0.82^{+0.04+0.04}_{-0.04-0.04}$	$0.64^{+0.05+0.01}_{-0.06-0.01}$	0.76	GD00A	$0.64^{+0.03+0.03}_{-0.03-0.03}$	$0.62^{+0.05+0.01}_{-0.05-0.01}$	0.75
GD61B	$0.73^{+0.03+0.03}_{-0.04-0.03}$	$0.69^{+0.06+0.01}_{-0.06-0.01}$	0.80	GD00B	$0.82^{+0.03+0.03}_{-0.03-0.03}$	$0.69^{+0.06+0.01}_{-0.06-0.01}$	0.76
GD61C	$0.69^{+0.03+0.03}_{-0.04-0.03}$	$0.66^{+0.06+0.01}_{-0.07-0.01}$	0.76	GD00C	$0.76^{+0.03+0.01}_{-0.04-0.01}$	$0.60^{+0.06+0.01}_{-0.06-0.01}$	0.76
GD76B	$1.02^{+0.03+0.04}_{-0.03-0.04}$	$0.75^{+0.07+0.01}_{-0.07-0.01}$	1.00	GD00D	$0.77^{+0.03+0.02}_{-0.03-0.02}$	$0.68^{+0.06+0.01}_{-0.06-0.01}$	0.80
GD76C	$0.88^{+0.03+0.02}_{-0.04-0.02}$	$0.81^{+0.06+0.01}_{-0.06-0.01}$	0.92	GD02A	$0.73^{+0.03+0.03}_{-0.03-0.03}$	$0.51^{+0.05+0.01}_{-0.05-0.01}$	0.75
GD79B	$0.75^{+0.04+0.02}_{-0.04-0.02}$	$0.67^{+0.06+0.01}_{-0.06-0.01}$	0.85	GD02B	$0.76^{+0.03+0.03}_{-0.04-0.03}$	$0.60^{+0.06+0.01}_{-0.06-0.01}$	0.80
GD79C	$0.90^{+0.03+0.02}_{-0.04-0.02}$	$0.77^{+0.06+0.01}_{-0.06-0.01}$	0.90	GD02C	$0.77^{+0.03+0.03}_{-0.04-0.03}$	$0.70^{+0.06+0.01}_{-0.06-0.01}$	0.76
GD89A	$0.71^{+0.03+0.03}_{-0.03-0.03}$	$0.62^{+0.05+0.01}_{-0.05-0.01}$	0.80	GD02D	$1.20^{+0.03+0.05}_{-0.03-0.04}$	$0.00^{+0.03+0.01}_{-0.00-0.00}$	N/A

(a) GD32A

(b) GD32B

(c) GD32C

(d) GD32D

(e) GD35A

(f) GD35B

(g) GD35C
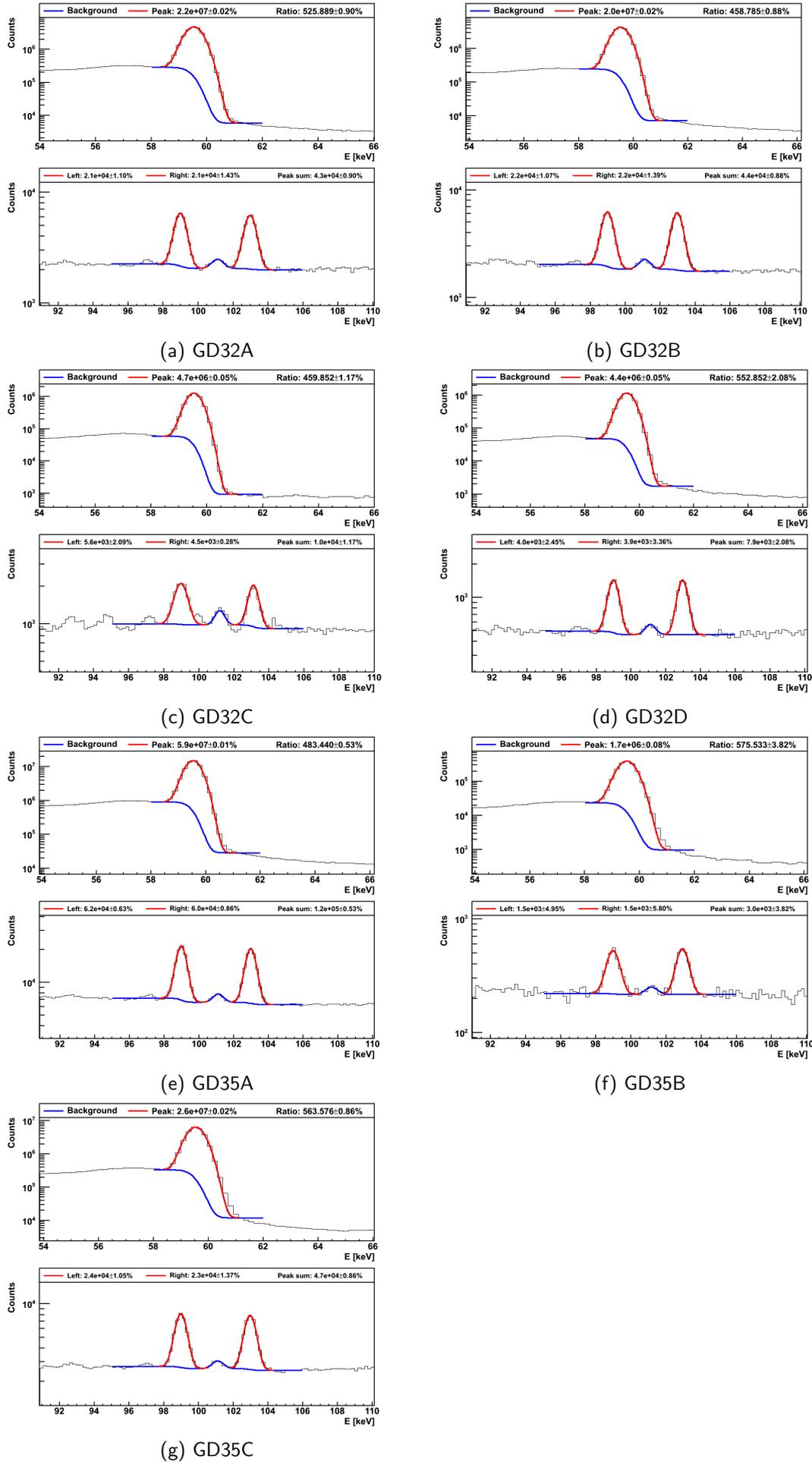
Figure C.10 Experimental spectra of fitting method for ^{241}Am. Part I/IV

(a) GD61A

(b) GD61B

(c) GD61C

(d) GD76B

(e) GD76C

(f) GD79B

(g) GD79C
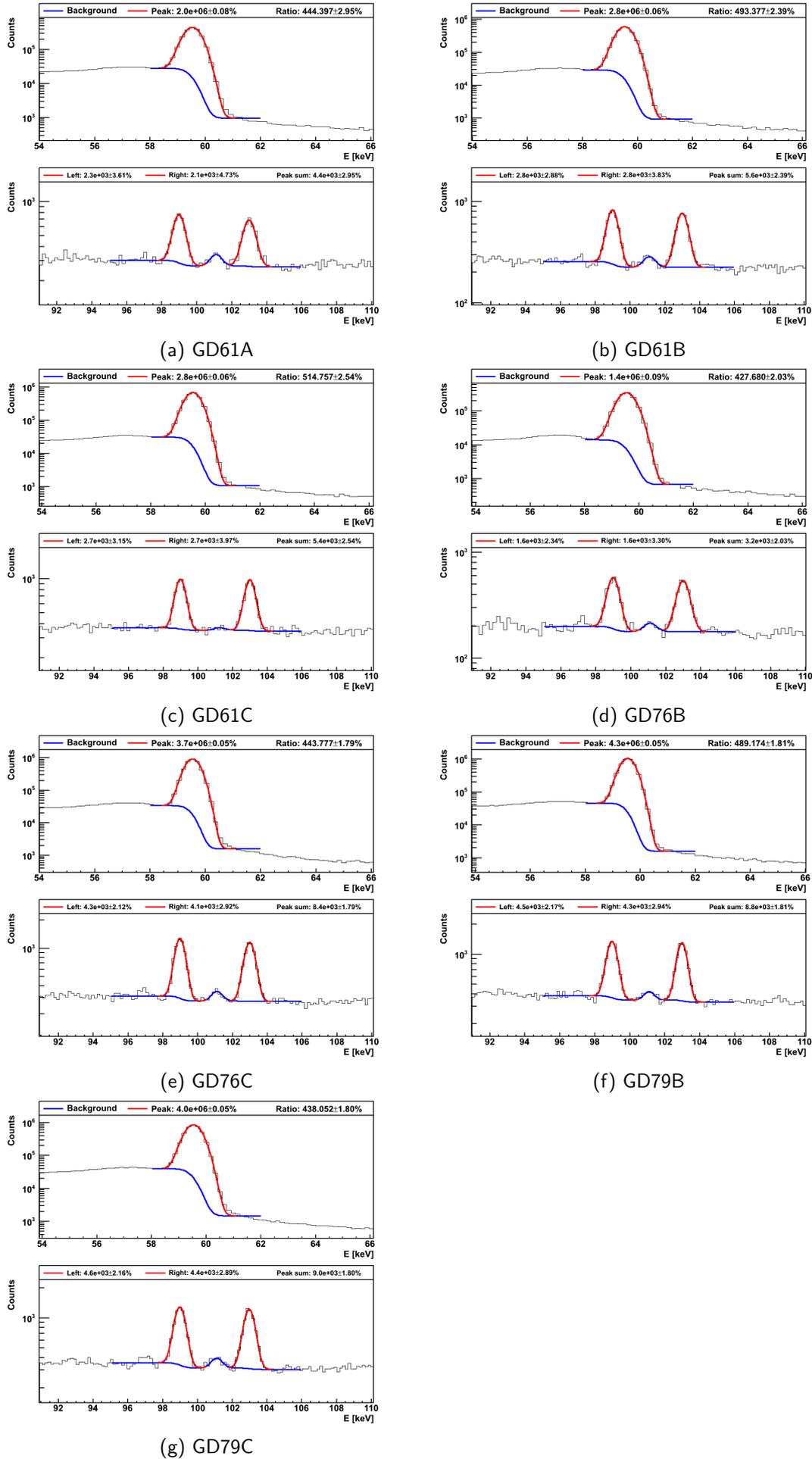
Figure C.11 Experimental spectra of fitting method for ^{241}Am. Part II/IV
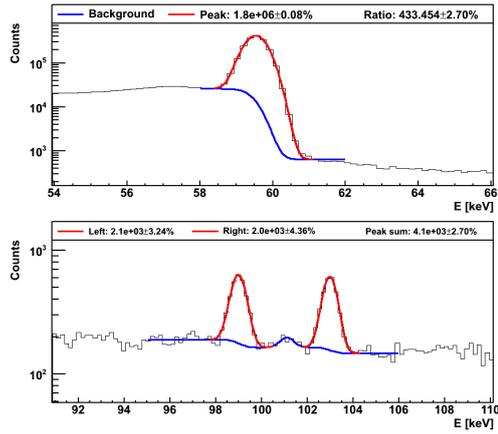
(a) GD89A
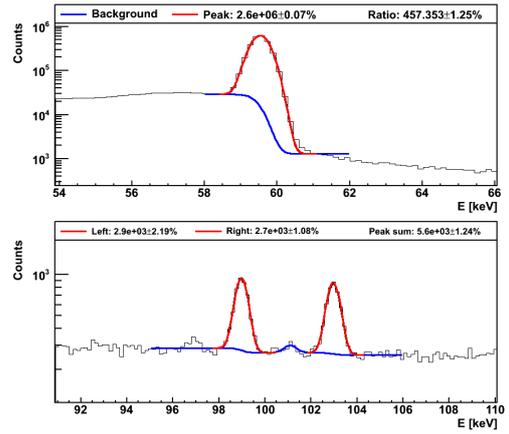
(b) GD89B
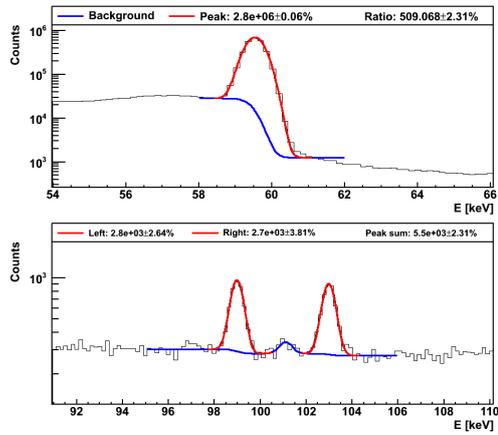
(c) GD89C
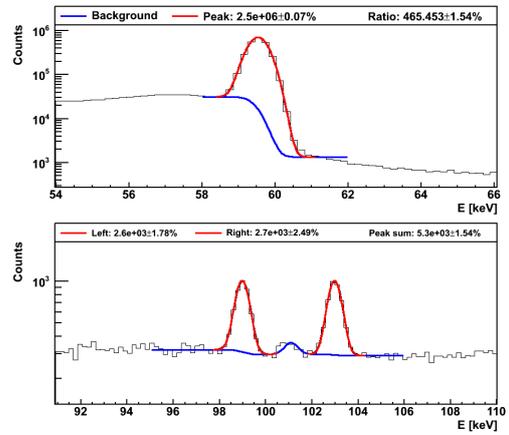
(d) GD89D
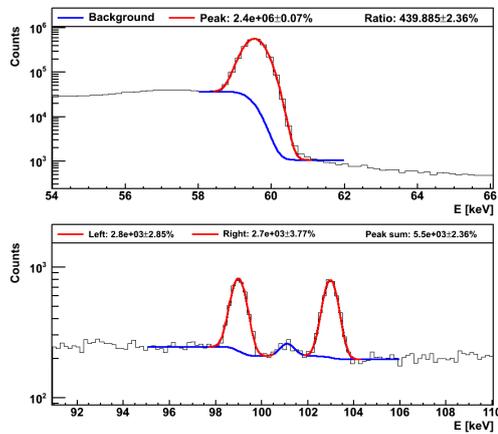
(e) GD91A
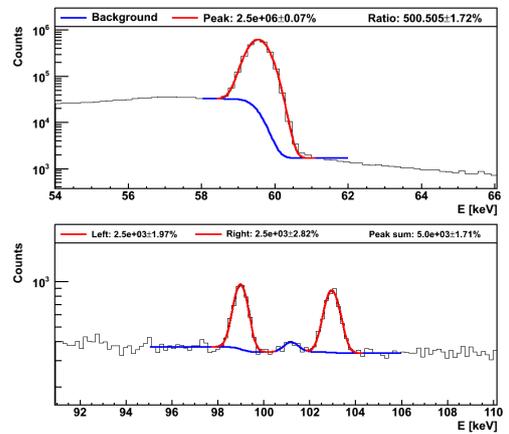
(f) GD91B
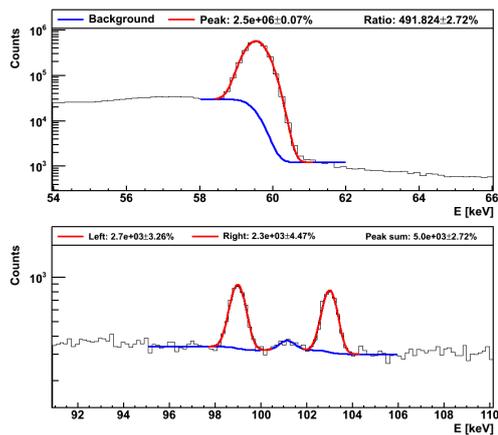
(g) GD91C
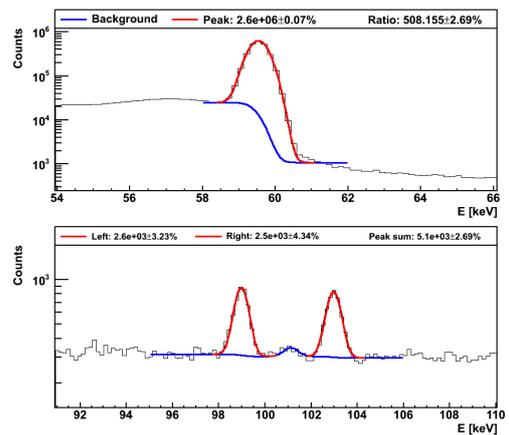
(h) GD91D

Figure C.12 Experimental spectra of fitting method for ^{241}Am. Part III/IV

(a) GD00A

(b) GD00B

(c) GD00C

(d) GD00D

(e) GD02A

(f) GD02B

(g) GD02C

(h) GD02D
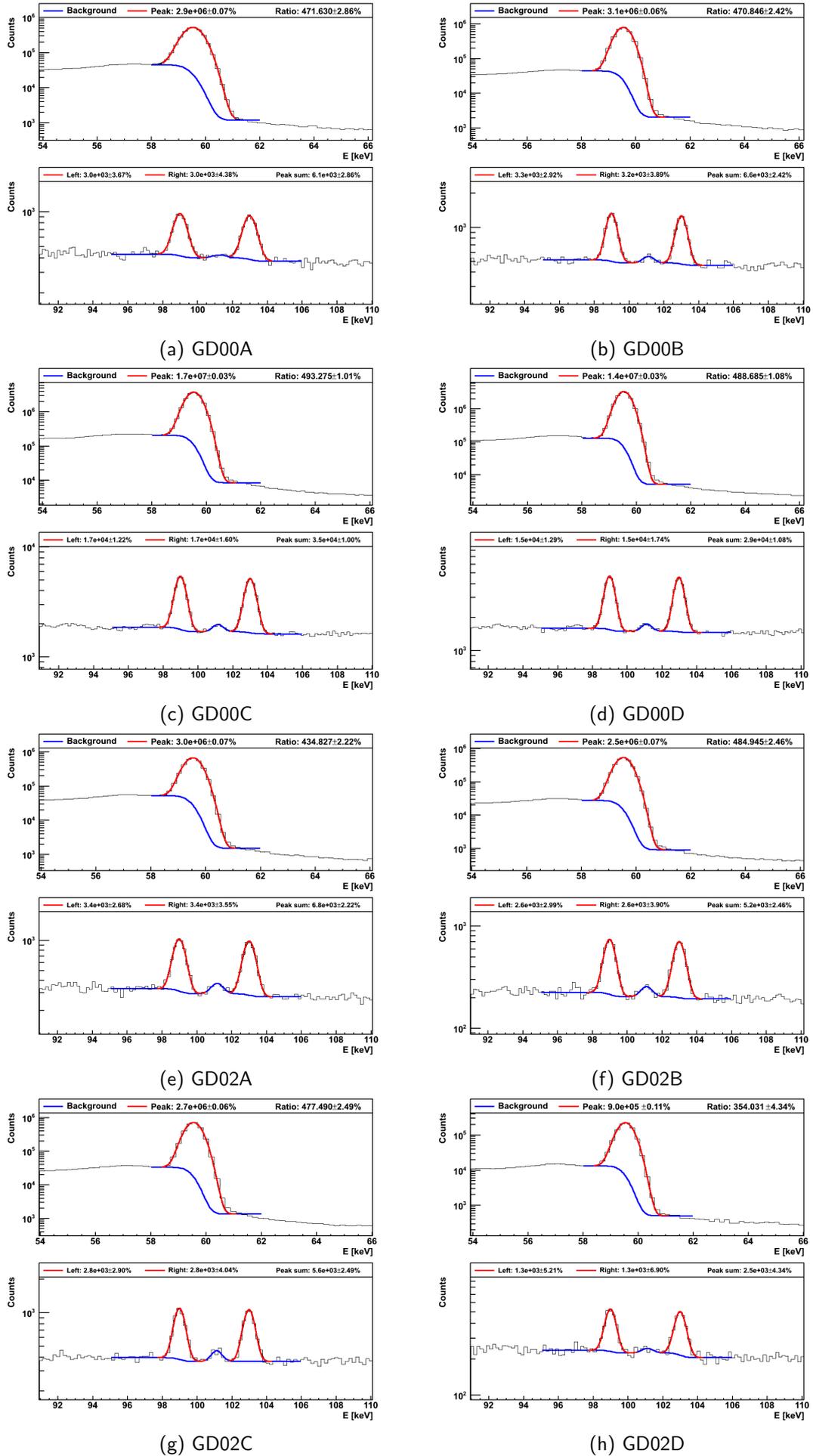
Figure C.13 Experimental spectra of fitting method for ^{241}Am. Part IV/IV

(a) GD32A

(b) GD32B

(c) GD32C

(d) GD32D

(e) GD35A

(f) GD35B

(g) GD35C
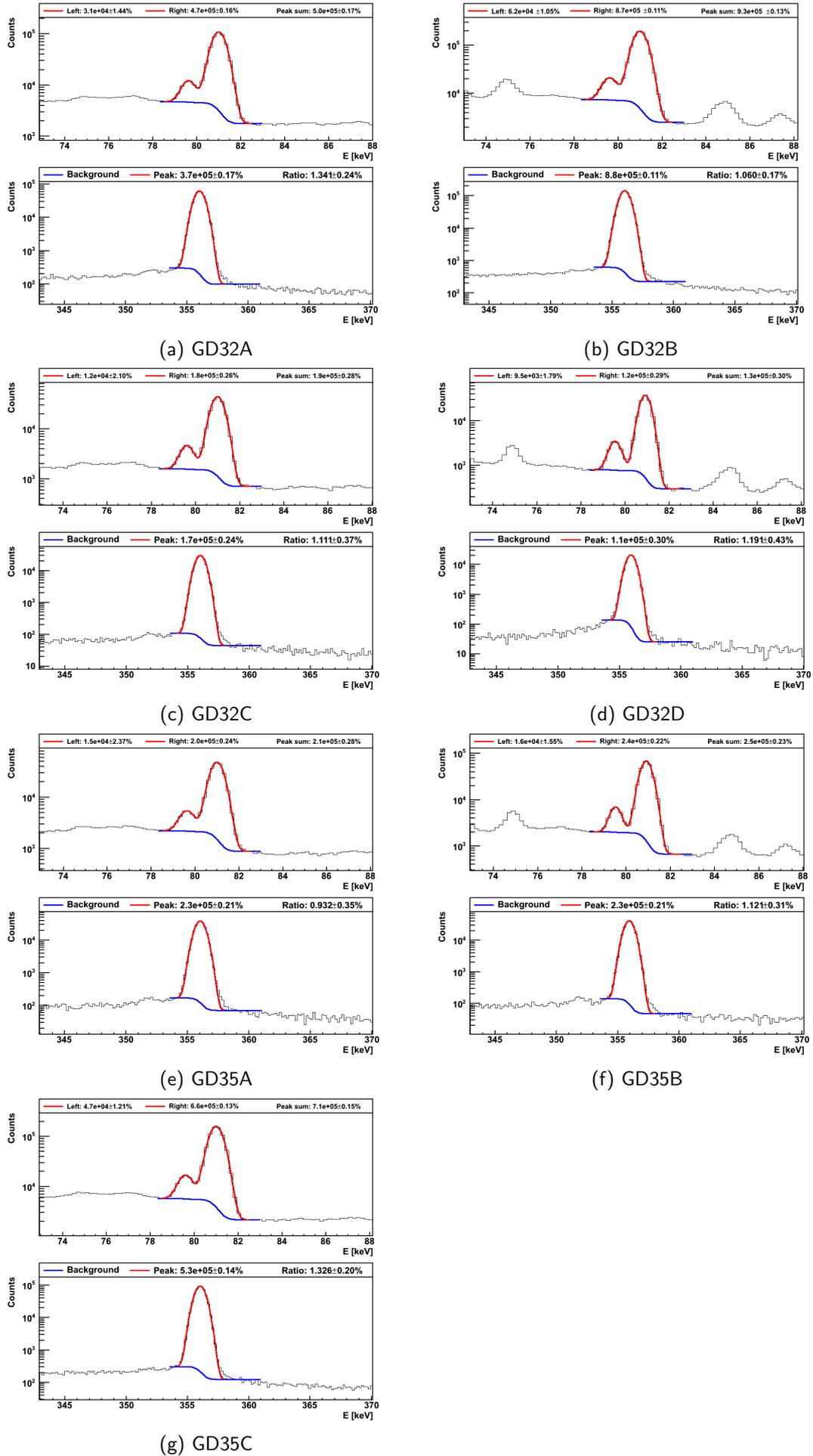
Figure C.14 Experimental spectra of fitting method for ^{133}Ba. Part I/IV

(a) GD61A

(b) GD61B

(c) GD61C

(d) GD76B

(e) GD76C

(f) GD79B

(g) GD79C
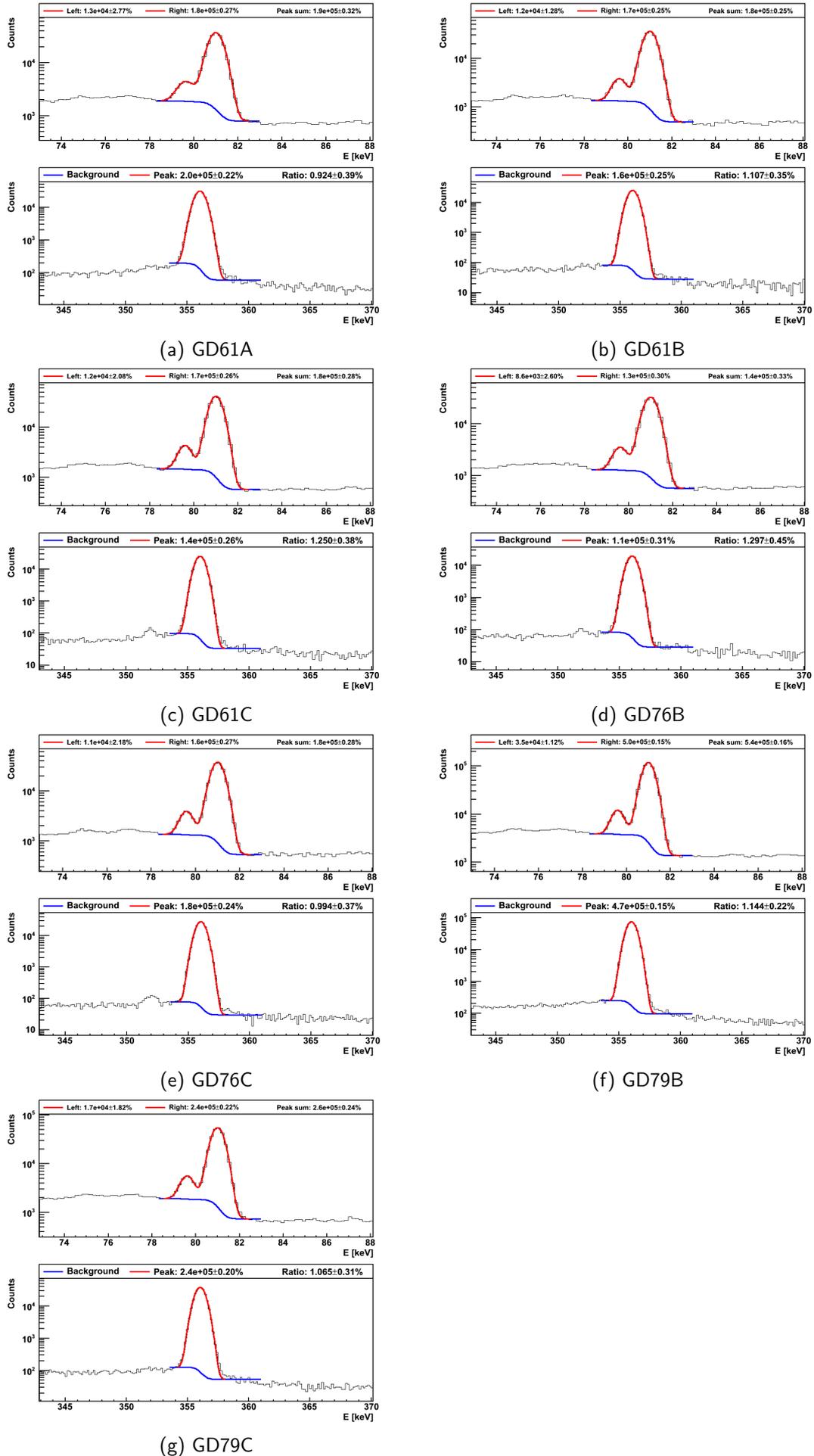
Figure C.15 Experimental spectra of fitting method for ^{133}Ba. Part II/IV

(a) GD89A

(b) GD89B

(c) GD89C

(d) GD89D

(e) GD91A

(f) GD91B

(g) GD91C

(h) GD91D
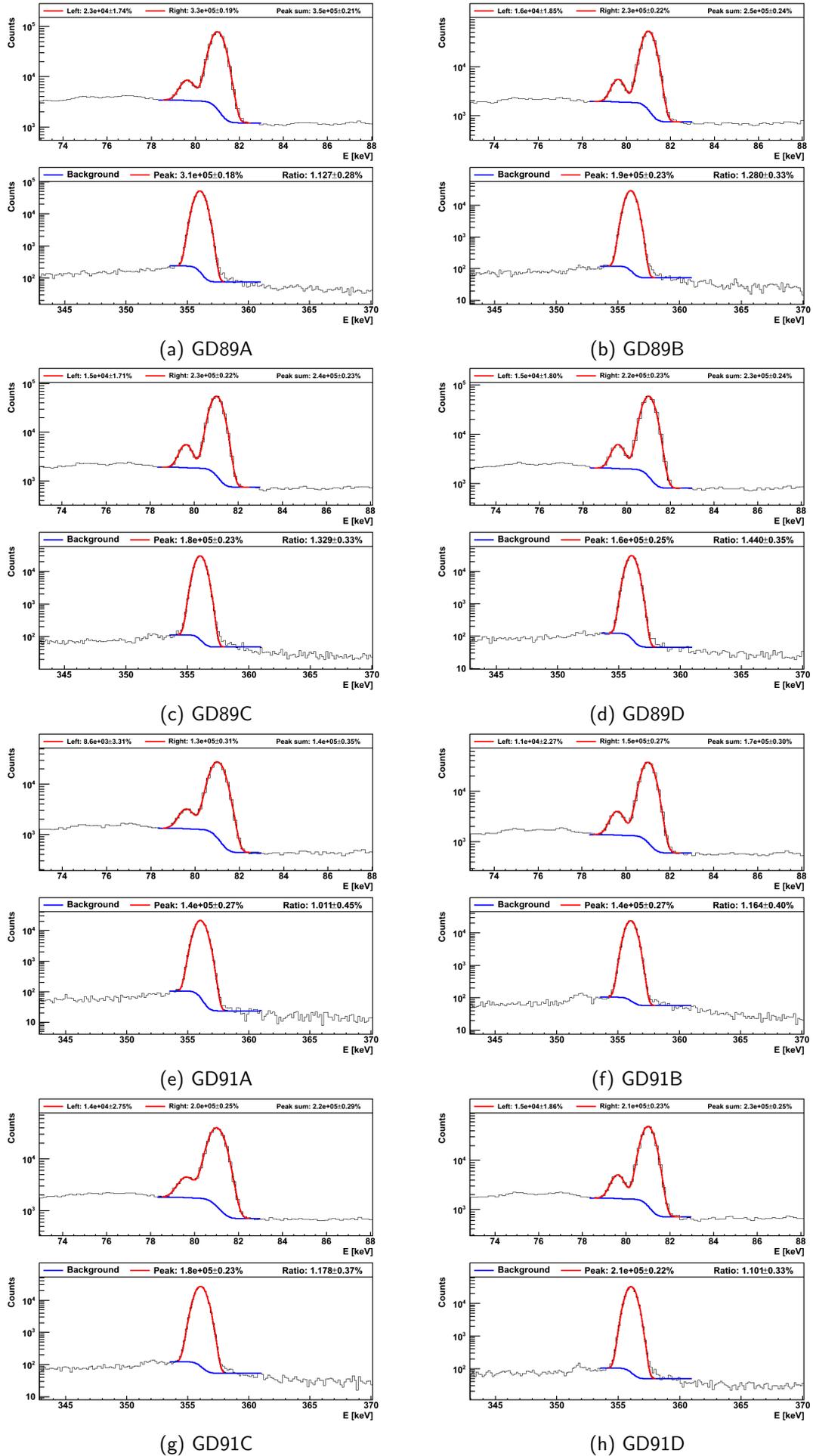
Figure C.16 Experimental spectra of fitting method for ^{133}Ba. Part III/IV

(a) GD00A

(b) GD00B

(c) GD00C

(d) GD00D

(e) GD02A

(f) GD02B

(g) GD02C

(h) GD02D
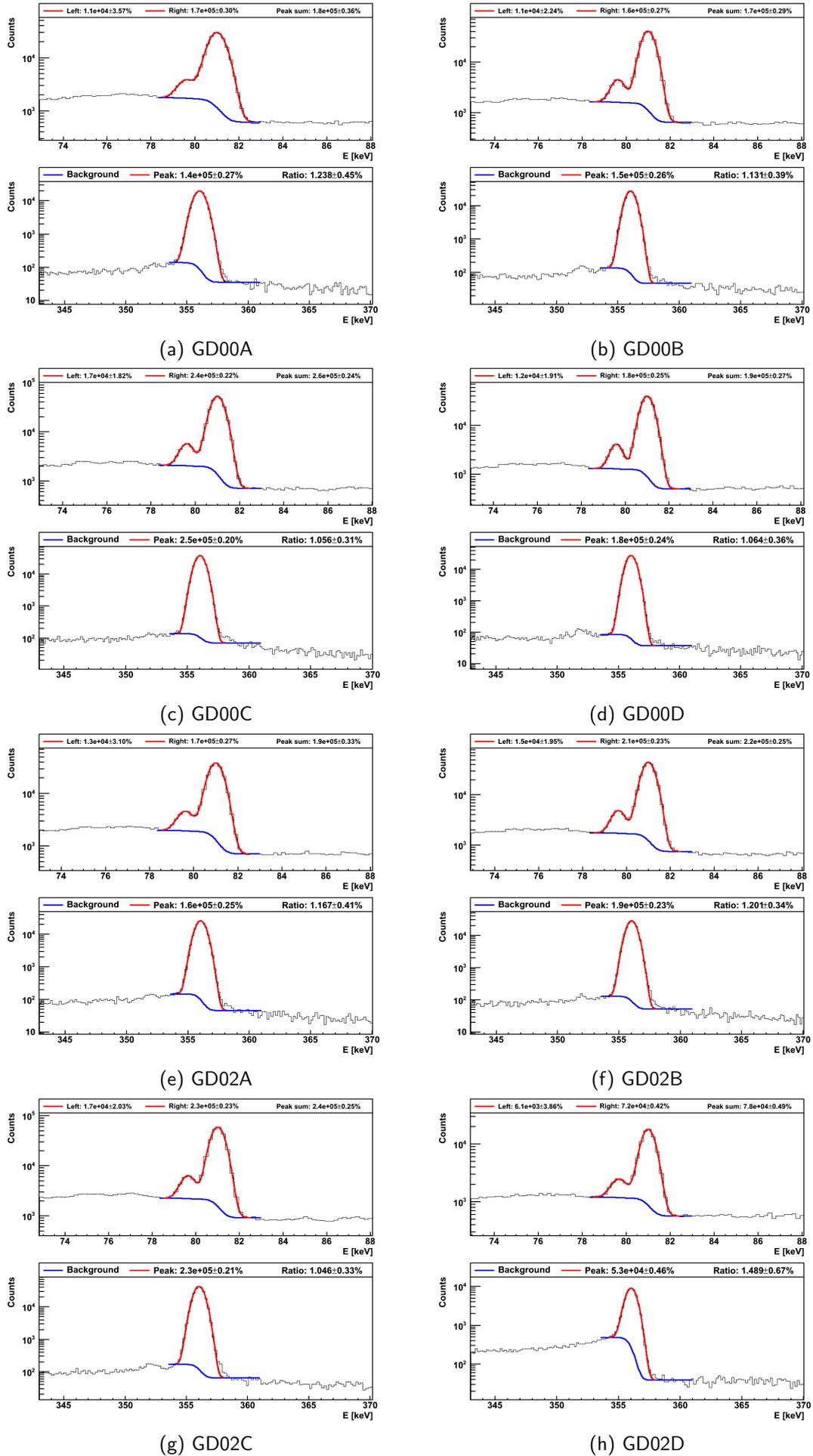
Figure C.17 Experimental spectra of fitting method for ^{133}Ba. Part IV/IV

(a) GD02D 1173.2 keV

(b) GD02D 1332.5 keV

(c) GD35B 1173.2 keV

(d) GD35B 1332.5 keV

(e) GD02C 1173.2 keV

(f) GD02C 1332.5 keV
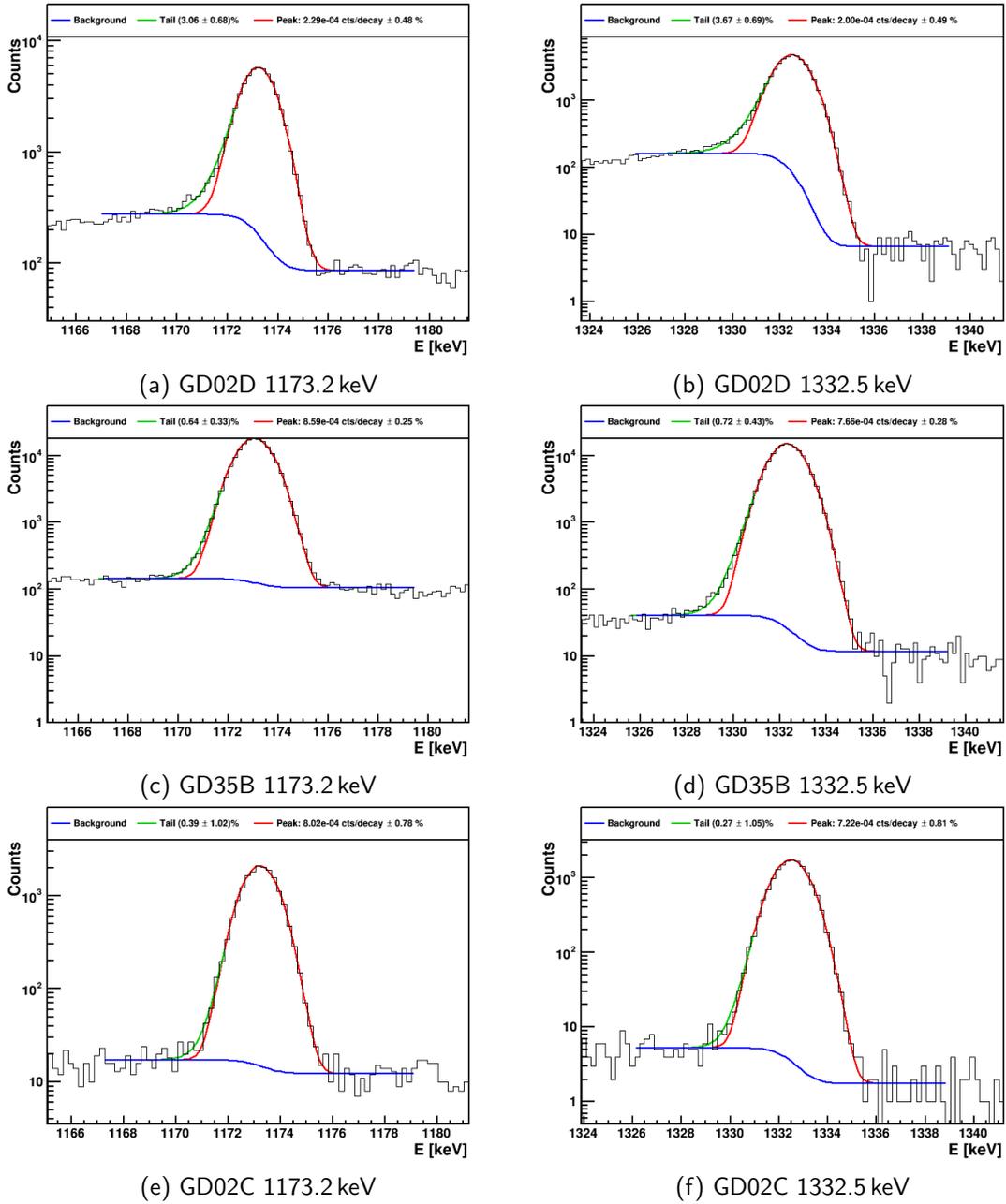
Figure C.18 ^{60}Co peak regions of selected detectors.

Table C.9 ^{60}Co FCCD results for the fitting method with the 1173.2 keV and 1332.5 keV peaks. The uncertainties are separated in correlated and uncorrelated components. Also shown is the fraction of tail events compared to all peak events. The number of individual ^{60}Co measurements for a given detector which is used for the combination is shown in the second column. Particularities of some detectors are listed in the footnotes.

detector	# measurements	1173.2 keV FCCD [mm]	tail fraction %	1332.5 keV FCCD [mm]	tail fraction %
GD32A	50	$0.81^{+0.23+0.07}_{-0.24-0.08}$	0.10	$0.82^{+0.23+0.08}_{-0.25-0.09}$	0.09
GD32B	2	$1.01^{+0.27+0.06}_{-0.29-0.07}$	0.06	$1.00^{+0.27+0.06}_{-0.29-0.07}$	0.08
GD32C	1	$0.85^{+0.28+0.09}_{-0.30-0.09}$	0.15	$0.82^{+0.28+0.08}_{-0.29-0.09}$	0.07
GD32D	1	$0.78^{+0.27+0.09}_{-0.29-0.09}$	0.00	$0.80^{+0.27+0.09}_{-0.29-0.10}$	0.01
GD35A	46	$0.71^{+0.29+0.09}_{-0.31-0.10}$	0.08	$0.72^{+0.29+0.09}_{-0.31-0.10}$	0.07
GD35B^{c}	4	$0.70^{+0.29+0.07}_{-0.33-0.10}$	0.67	$0.70^{+0.28+0.08}_{-0.30-0.09}$	0.73
GD35C	1	$0.81^{+0.24+0.07}_{-0.26-0.08}$	0.09	$0.78^{+0.24+0.07}_{-0.26-0.08}$	0.00
GD61A	1	$1.02^{+0.28+0.09}_{-0.30-0.09}$	0.98	$1.11^{+0.28+0.09}_{-0.30-0.10}$	0.00
GD61B^{b}	1	$1.09^{+0.26+0.08}_{-0.28-0.10}$	0.31	$1.09^{+0.26+0.08}_{-0.28-0.10}$	0.17
GD61C	1	$0.83^{+0.24+0.07}_{-0.26-0.08}$	0.07	$0.87^{+0.24+0.08}_{-0.26-0.08}$	0.13
GD76B	1	$1.19^{+0.22+0.07}_{-0.24-0.08}$	0.03	$1.19^{+0.22+0.08}_{-0.24-0.08}$	0.06
GD76C^{b}	2	$1.02^{+0.27+0.07}_{-0.31-0.09}$	0.27	$1.04^{+0.28+0.08}_{-0.30-0.09}$	0.23
GD79B	1	$0.88^{+0.26+0.07}_{-0.28-0.08}$	0.00	$0.88^{+0.26+0.07}_{-0.28-0.08}$	0.10
GD79C	2	$1.17^{+0.26+0.06}_{-0.28-0.08}$	0.13	$1.21^{+0.26+0.03}_{-0.28-0.08}$	0.18
GD89A	3	$0.85^{+0.25+0.08}_{-0.26-0.08}$	0.00	$0.86^{+0.24+0.08}_{-0.26-0.09}$	0.00
GD89B	1	$0.99^{+0.23+0.07}_{-0.24-0.08}$	0.03	$1.02^{+0.22+0.07}_{-0.24-0.08}$	0.05
GD89C	1	$0.93^{+0.23+0.06}_{-0.24-0.06}$	0.00	$0.93^{+0.22+0.06}_{-0.24-0.07}$	0.09
GD89D	1	$1.16^{+0.20+0.05}_{-0.22-0.06}$	0.08	$1.16^{+0.21+0.06}_{-0.22-0.06}$	0.12
GD91A	2	$0.86^{+0.27+0.07}_{-0.28-0.08}$	0.01	$0.88^{+0.26+0.07}_{-0.28-0.08}$	0.01
GD91B^{b}	1	$1.01^{+0.26+0.09}_{-0.27-0.09}$	0.11	$0.92^{+0.26+0.09}_{-0.27-0.10}$	0.27
GD91C	3	$1.01^{+0.25+0.07}_{-0.27-0.08}$	0.16	$1.00^{+0.25+0.08}_{-0.27-0.08}$	0.16
GD91D	1	$0.99^{+0.27+0.08}_{-0.29-0.09}$	0.00	$0.99^{+0.27+0.08}_{-0.29-0.09}$	0.12
GD00A^{b}	2	$0.83^{+0.23+0.09}_{-0.24-0.10}$	0.21	$0.84^{+0.23+0.10}_{-0.24-0.10}$	0.28
GD00B	1	$1.00^{+0.26+0.09}_{-0.28-0.10}$	0.05	$1.06^{+0.25+0.09}_{-0.27-0.10}$	0.00
GD00C	1	$1.10^{+0.26+0.07}_{-0.31-0.09}$	0.00	$1.06^{+0.28+0.08}_{-0.30-0.09}$	0.17
GD00D	2	$1.00^{+0.27+0.08}_{-0.30-0.09}$	0.04	$0.95^{+0.28+0.08}_{-0.29-0.09}$	0.11
GD02A	3	$1.05^{+0.24+0.07}_{-0.26-0.08}$	0.12	$1.02^{+0.24+0.07}_{-0.26-0.08}$	0.06
GD02B	2	$1.00^{+0.25+0.07}_{-0.27-0.08}$	0.00	$0.98^{+0.25+0.07}_{-0.27-0.08}$	0.06
GD02C^{b}	1	$0.92^{+0.28+0.10}_{-0.30-0.11}$	0.39	$0.86^{+0.28+0.10}_{-0.30-0.11}$	0.27
GD02D^{ad}	2	$7.29^{+0.21+0.08}_{-0.22-0.08}$	3.21	$7.36^{+0.21+0.08}_{-0.22-0.08}$	3.72

^{a} Strong peak tails on both peaks.

^{b} Small peak tails on both peaks.

^{c} Only FADC data available.

^{d} Not fully depleted. Homogeneous FCCD assumption does not hold. Results not reliable
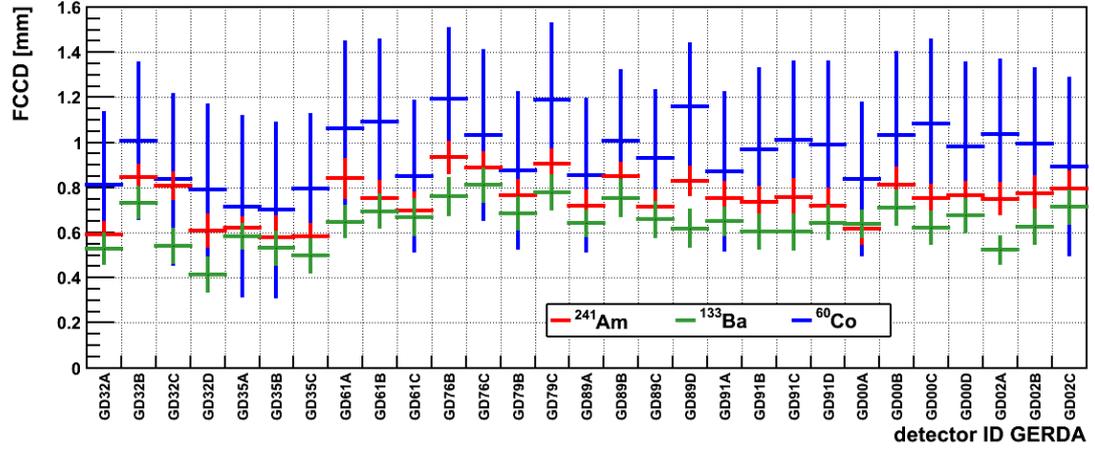
Figure C.19 FCCD values for all three methods ^{241}Am, ^{133}Ba and ^{60}Co. Ordered according to detector name.

Table C.10 ^{241}Am source activities as measured in [206]. Absolute uncertainties are $\pm 8\,\%$ (2σ CL). The relative uncertainty between the sources is $0.2\,\%$.

table name	Brady	Garfield	Morla
source name	HS17	HS18	HS19
activity [kBq]	4218	4335	4327

Table C.11 Properties and attenuation factors of materials in the beam paths.

support structure part	material	d [mm]	μ [cm^2/g]	ρ [g/cm^3]	$f_{\mathrm{att}} \pm \sigma_{f_{\mathrm{att}}}$
TOP det. cup (A)	HDPE	1.0 ± 0.1	0.198	0.96 ± 0.03	0.981 ± 0.002
LAT det. cup (B,C)	HDPE	0.5 ± 0.1	0.198	0.96 ± 0.03	0.991 ± 0.002
TOP cryo. endcap (A)	AL 6061 T6	1.5	0.284	2.7	0.891
LAT cryo. endcap (B,C)	AL 6061 T6	1.5	0.284	2.7	0.891
LAT thin det. holder (B)	AW-2011 AL	1.5 ± 0.1	$0.374 - 0.430$	2.84	0.843 ± 0.02
LAT thick det. holder (C)	AW-2011 AL	3.0 ± 0.1	$0.374 - 0.430$	2.84	0.710 ± 0.02

Table C.12 Surface scan measurements. Shown are all surface scan measurements that pass the selection described in the text. Four types of scans are distinguished. TOP = top linear scan, TC = top circular scan, LAT = lateral linear scan and LC = lateral circular scan. The diode, type of measurement, position and the data are encoded in the first column string. r??? and x???? denote the fixed position of the source in radius and arm length respectively (a question mark denotes one digit). The second column denotes the segment type for the lateral scan: above the thick holder part (0), on the thick holder part (1) and below the thick holder part (2). For other scan types the segment ID is 0. The third column shows the number of counts (C_i) as fitted with a constant of the segment. The forth and the fifth columns show the degree of freedom (DOF) and the fit quality as χ^2/DOF of the fit. The next two columns show the measuring time and the ^{241}Am source code. The last column shows the count rate (R_i) normalized to the top surface attenuation and to $1\,$MBq. This count rate can be directly compared between different scans and different detectors and its variation only depends on the FCCD on the surface section.

measurement	seg.	C_i	DOF	χ^2/DOF	T [s]	source	R_i [cts/s/MBq]
GD32B_TOP_r000_20120417	0	3739.5 ± 7.8	67	3.2	100	HS17	8.87 ± 0.02
GD32B_TOP_r090_20120417	0	3713.1 ± 8.3	60	3.5	100	HS17	8.80 ± 0.02
GD32B_TOP_r090_20120418	0	4313.5 ± 8.9	60	2.8	120	HS17	8.52 ± 0.02
GD32B_TOP_r120_20120508	0	4155.4 ± 8.7	62	2.5	120	HS17	8.21 ± 0.02
GD32B_TOP_r260_20120508	0	4095.4 ± 8.4	65	2.9	120	HS17	8.09 ± 0.02
GD32B_LC_x2400_20120509	0	3337.9 ± 17.7	11	0.8	120	HS17	7.75 ± 0.10
GD32B_LC_x2440_20120509	0	3361.8 ± 17.9	11	0.9	120	HS17	7.81 ± 0.10
GD32B_LC_x2480_20120509	1	2940.6 ± 16.8	11	1.1	120	HS17	8.10 ± 0.20
GD32B_LC_x2600_20120509	0	3292.1 ± 17.4	11	1.7	120	HS17	7.64 ± 0.10
GD32B_TC_x0280_20120509	0	3907.7 ± 19.2	11	2.7	120	HS17	7.72 ± 0.04
GD32B_TC_x0330_20120509	0	4083.8 ± 19.7	11	1.8	120	HS17	8.07 ± 0.04
GD32B_TC_x0380_20120509	0	4263.6 ± 20.6	11	3.1	120	HS17	8.42 ± 0.04
GD32B_TC_x0530_20120509	0	4128.5 ± 19.8	11	3.4	120	HS17	8.16 ± 0.04
GD32B_TC_x0570_20120509	0	4149.6 ± 19.8	11	1.1	120	HS17	8.20 ± 0.04
GD32C_TOP_r120_20120430	0	5146.9 ± 9.4	63	3.1	120	HS17	10.17 ± 0.02
GD32C_LC_x2520_20120531	0	4134.0 ± 11.4	40	1.4	120	HS17	9.60 ± 0.12
GD32C_LC_x2700_20120531	0	4186.1 ± 11.5	41	2.0	120	HS17	9.72 ± 0.12
GD32C_TC_x0250_20120507	0	4681.3 ± 20.5	11	1.6	120	HS17	9.25 ± 0.04
GD32C_TC_x0300_20120507	0	4865.4 ± 21.0	11	2.3	120	HS17	9.61 ± 0.04
GD32C_TC_x0220_20120602	0	4934.1 ± 16.0	23	1.9	120	HS17	9.75 ± 0.03
GD32C_TC_x0240_20120602	0	4997.6 ± 16.1	23	1.5	120	HS17	9.87 ± 0.03
GD32C_TC_x0260_20120602	0	5026.7 ± 16.1	23	1.9	120	HS17	9.93 ± 0.03
GD32C_TC_x0440_20120602	0	5042.5 ± 16.1	23	1.4	120	HS17	9.96 ± 0.03
GD32C_TC_x0460_20120602	0	5018.8 ± 16.0	23	1.5	120	HS17	9.92 ± 0.03
GD32C_TC_x0480_20120602	0	5000.4 ± 16.0	23	1.1	120	HS17	9.88 ± 0.03
GD32D_LC_x2430_20120422	0	4295.0 ± 8.0	71	1.1	120	HS17	9.97 ± 0.12
GD32D_LC_x2460_20120422	0	4331.1 ± 8.1	71	1.0	120	HS17	10.06 ± 0.12
GD32D_LC_x2620_20120422	0	4300.4 ± 8.0	71	1.1	120	HS17	9.99 ± 0.12
GD32D_LC_x2650_20120422	0	4199.6 ± 7.9	71	1.2	120	HS17	9.75 ± 0.12
GD32D_LC_x2380_20120430	0	4329.9 ± 8.0	71	1.2	120	HS17	10.05 ± 0.12
GD32D_LC_x2420_20120430	0	4361.1 ± 8.1	71	1.1	120	HS17	10.13 ± 0.13
GD32D_LC_x2580_20120430	0	4318.3 ± 8.0	71	1.0	120	HS17	10.03 ± 0.12
GD32D_TOP_r120_20120427	0	5205.1 ± 9.4	63	2.3	120	HS17	10.28 ± 0.02
GD32D_TOP_r240_20120427	0	5241.7 ± 9.4	63	3.4	120	HS17	10.36 ± 0.02
GD32D_TC_x0250_20120421	0	4910.0 ± 8.5	71	1.5	120	HS17	9.70 ± 0.02
GD32D_TC_x0300_20120421	0	5163.1 ± 8.9	71	1.7	120	HS17	10.20 ± 0.02
GD32D_TC_x0350_20120421	0	5409.3 ± 9.2	71	2.6	120	HS17	10.69 ± 0.02
GD32D_TC_x0400_20120421	0	5276.8 ± 9.0	71	2.3	120	HS17	10.43 ± 0.02
GD32D_TC_x0300_20120428	0	5052.2 ± 8.7	71	1.5	120	HS17	9.98 ± 0.02
GD32D_TC_x0300_20120429	0	5055.6 ± 8.7	71	1.9	120	HS17	9.99 ± 0.02
GD32D_TC_x0350_20120428	0	5216.5 ± 8.9	71	1.7	120	HS17	10.31 ± 0.02
GD32D_TC_x0350_20120429	0	5219.6 ± 8.9	71	2.0	120	HS17	10.31 ± 0.02
GD32D_TC_x0400_20120428	0	5393.9 ± 9.1	71	2.0	120	HS17	10.66 ± 0.02
GD32D_TC_x0400_20120429	0	5415.2 ± 9.1	71	2.7	120	HS17	10.70 ± 0.02
GD32D_TC_x0450_20120428	0	5248.8 ± 8.9	71	1.2	120	HS17	10.37 ± 0.02
GD32D_TC_x0450_20120429	0	5285.6 ± 8.9	71	1.4	120	HS17	10.44 ± 0.02
GD35B_TOP_r120_20120423	0	5292.9 ± 9.4	66	2.0	120	HS17	10.46 ± 0.02
GD35B_TOP_r240_20120423	0	5288.9 ± 9.4	65	1.5	120	HS17	10.45 ± 0.02
GD35B_TOP_r120_20120424	0	5270.5 ± 9.4	66	1.6	120	HS17	10.41 ± 0.02
GD35B_LC_x2400_20120425	0	4367.7 ± 8.1	71	1.2	120	HS17	10.14 ± 0.13
GD35B_LC_x2430_20120425	0	4374.1 ± 8.1	71	1.6	120	HS17	10.16 ± 0.13

Continued on next page

Table C.12 – continued from previous page

measurement	seg	C_i	DOF	χ^2/DOF	T [s]	source	R_i [cts/s/MBq]
GD35B_LC_x2580_20120425	0	4361.2 ± 8.1	71	1.0	120	HS17	10.13 ± 0.13
GD35B_LC_x2610_20120425	0	4314.5 ± 8.1	71	1.5	120	HS17	10.02 ± 0.12
GD35B_TC_x0300_20120424	0	5301.3 ± 9.1	71	3.0	120	HS17	10.47 ± 0.02
GD35B_TC_x0350_20120424	0	5333.9 ± 9.0	71	2.2	120	HS17	10.54 ± 0.02
GD35B_TC_x0400_20120424	0	5316.1 ± 9.1	71	1.8	120	HS17	10.50 ± 0.02
GD35B_TC_x0450_20120424	0	5273.7 ± 9.0	71	1.6	120	HS17	10.42 ± 0.02
GD35B_TC_x0500_20120426	0	5220.7 ± 8.9	71	2.3	120	HS17	10.31 ± 0.02
GD35B_TC_x0530_20120426	0	5175.9 ± 9.4	63	1.2	120	HS17	10.23 ± 0.02
GD35C_TOP_r000_20120504	0	5088.3 ± 9.2	64	2.0	120	HS17	10.05 ± 0.02
GD35C_TOP_r120_20120504	0	5139.3 ± 9.3	64	1.6	120	HS17	10.15 ± 0.02
GD35C_TOP_r240_20120504	0	5136.8 ± 9.3	64	2.0	120	HS17	10.15 ± 0.02
GD35C_LC_x2400_20120506	0	8518.1 ± 27.7	11	0.5	240	HS17	9.89 ± 0.13
GD35C_LC_x2440_20120506	0	8704.9 ± 28.0	11	0.9	240	HS17	10.11 ± 0.13
GD35C_LC_x2480_20120506	0	8692.4 ± 28.0	11	0.7	240	HS17	10.09 ± 0.13
GD35C_LC_x2600_20120506	0	8310.3 ± 27.5	11	2.7	240	HS17	9.65 ± 0.12
GD35C_TC_x0220_20120505	0	9833.0 ± 21.1	23	3.6	240	HS17	9.71 ± 0.02
GD35C_TC_x0220_20120506	0	9840.3 ± 21.1	23	3.5	240	HS17	9.72 ± 0.02
GD35C_TC_x0270_20120505	0	10201.8 ± 21.5	23	1.7	240	HS17	10.08 ± 0.02
GD35C_TC_x0270_20120506	0	10196.1 ± 21.5	23	1.5	240	HS17	10.07 ± 0.02
GD35C_TC_x0320_20120505	0	10410.2 ± 21.7	23	1.5	240	HS17	10.28 ± 0.02
GD35C_TC_x0320_20120506	0	10414.5 ± 21.7	23	1.9	240	HS17	10.29 ± 0.02
GD35C_TC_x0480_20120506	0	10270.9 ± 30.4	11	1.2	240	HS17	10.15 ± 0.03
GD35C_TC_x0520_20120506	0	10252.3 ± 30.3	11	0.3	240	HS17	10.13 ± 0.03
GD61B_LAT_r000_20121114	0	5622.3 ± 18.8	16	1.8	180	HS18	8.47 ± 0.11
GD61B_LAT_r000_20121114	1	4736.6 ± 19.1	13	2.1	180	HS18	8.46 ± 0.21
GD61B_LAT_r090_20121114	0	5385.7 ± 18.4	16	1.9	180	HS18	8.11 ± 0.10
GD61B_LAT_r090_20121114	1	4651.6 ± 18.9	13	0.4	180	HS18	8.31 ± 0.20
GD61B_TOP_r000_20121113	0	6760.8 ± 7.6	127	1.6	180	HS18	8.66 ± 0.01
GD61B_TOP_r090_20121113	0	6739.9 ± 7.5	127	1.3	180	HS18	8.64 ± 0.01
GD61B_TOP_r000_20130116	0	4957.4 ± 13.7	28	1.0	120	HS19	9.54 ± 0.03
GD61B_TOP_r090_20130116	0	4944.8 ± 13.6	28	1.7	120	HS19	9.52 ± 0.03
GD61B_TOP_r000_20130207	0	4555.6 ± 12.8	29	1.6	120	HS18	8.76 ± 0.02
GD61B_TOP_r090_20130207	0	4601.4 ± 12.9	29	1.7	120	HS18	8.85 ± 0.03
GD61B_LC_x2530_20130209	0	5944.9 ± 13.5	34	1.7	200	HS18	8.06 ± 0.10
GD61B_LC_x2550_20121115	0	3578.1 ± 7.3	70	0.9	120	HS19	8.09 ± 0.10
GD61B_LC_x2560_20130209	0	6034.4 ± 13.4	35	1.6	200	HS18	8.18 ± 0.10
GD61B_LC_x2600_20130119	0	6155.8 ± 13.8	34	1.0	180	HS19	9.28 ± 0.12
GD61B_LC_x2620_20130119	0	6209.3 ± 13.6	35	1.2	180	HS19	9.36 ± 0.12
GD61B_LC_x2640_20130119	0	6228.2 ± 13.7	35	1.1	180	HS19	9.39 ± 0.12
GD61B_LC_x2650_20130209	1	5233.9 ± 12.5	35	2.1	200	HS18	8.42 ± 0.20
GD61B_LC_x2680_20130209	1	5222.8 ± 12.5	35	1.6	200	HS18	8.40 ± 0.20
GD61B_LC_x2700_20130119	1	5382.9 ± 12.8	35	1.7	180	HS19	9.63 ± 0.23
GD61B_LC_x2740_20130209	0	5940.1 ± 13.4	35	1.5	200	HS18	8.05 ± 0.10
GD61B_TC_x0430_20130208	0	7459.9 ± 14.2	39	1.7	200	HS18	8.60 ± 0.02
GD61B_TC_x0440_20130118	0	7250.3 ± 14.1	39	2.0	180	HS19	9.30 ± 0.02
GD61B_TC_x0460_20130208	0	7526.4 ± 15.1	35	2.0	200	HS18	8.68 ± 0.02
GD61B_TC_x0470_20130118	0	7367.6 ± 15.0	35	1.9	180	HS19	9.45 ± 0.02
GD61B_TC_x0490_20130208	0	7593.2 ± 15.8	32	1.6	200	HS18	8.76 ± 0.02
GD61B_TC_x0495_20121114	0	4582.1 ± 8.4	70	1.9	120	HS19	8.82 ± 0.02
GD61B_TC_x0500_20130118	0	7470.7 ± 15.8	32	1.6	180	HS19	9.59 ± 0.02
GD61B_TC_x0520_20130208	0	7511.6 ± 17.1	27	1.3	200	HS18	8.66 ± 0.02
GD61B_TC_x0530_20130118	0	7494.8 ± 17.2	27	1.1	180	HS19	9.62 ± 0.02
GD61B_TC_x0545_20121114	0	4597.7 ± 8.4	71	1.3	120	HS19	8.85 ± 0.02
GD61B_TC_x0550_20130208	0	7358.6 ± 18.2	23	1.5	200	HS18	8.49 ± 0.02
GD61B_TC_x0560_20130118	0	7446.5 ± 18.5	23	1.0	180	HS19	9.55 ± 0.02
GD61B_TC_x0580_20130208	0	7336.6 ± 20.4	18	1.1	200	HS18	8.46 ± 0.02
GD61B_TC_x0590_20130118	0	7443.9 ± 20.7	18	1.3	180	HS19	9.55 ± 0.03
GD61B_TC_x0610_20130208	0	7300.9 ± 22.2	15	0.8	200	HS18	8.42 ± 0.03
GD61B_TC_x0620_20130118	0	7376.9 ± 22.4	15	1.5	180	HS19	9.46 ± 0.03
GD61B_TC_x0635_20121114	0	4552.1 ± 11.7	35	0.7	120	HS19	8.76 ± 0.02
GD61B_TC_x0640_20130208	0	7292.8 ± 25.6	11	1.4	200	HS18	8.41 ± 0.03
GD61B_TC_x0650_20130118	0	7381.1 ± 25.8	11	0.6	180	HS19	9.47 ± 0.03
GD61B_TC_x0685_20121114	0	4503.2 ± 11.6	35	1.2	120	HS19	8.67 ± 0.02
GD61C_LAT_r000_20121207	0	5760.4 ± 17.6	19	1.9	180	HS18	8.68 ± 0.11
GD61C_LAT_r090_20121207	0	5863.6 ± 18.2	18	1.0	180	HS18	8.83 ± 0.11
GD61C_LAT_r090_20121207	1	5232.2 ± 21.7	11	0.6	180	HS18	9.35 ± 0.23
GD61C_TOP_r000_20121213	0	3466.1 ± 7.7	61	1.6	90	HS18	8.88 ± 0.02
GD61C_TOP_r090_20121213	0	3468.0 ± 7.7	61	2.4	90	HS18	8.89 ± 0.02

Table C.12 – continued from previous page

measurement	seg	C_i	DOF	χ^2/DOF	T [s]	source	R_i [cts/s/MBq]
GD61C_TOP_r000_20121208	0	6927.2 ± 7.5	130	4.2	180	HS18	8.88 ± 0.01
GD61C_TOP_r090_20121208	0	6907.5 ± 7.5	130	3.9	180	HS18	8.85 ± 0.01
GD61C_TOP_r000_20130111	0	3532.4 ± 11.1	30	1.8	90	HS18	9.05 ± 0.03
GD61C_TOP_r090_20130111	0	3474.6 ± 11.0	30	2.1	90	HS18	8.91 ± 0.03
GD61C_LC_x2380_20130113	0	5729.5 ± 13.0	35	0.8	180	HS18	8.63 ± 0.11
GD61C_LC_x2400_20130113	0	5793.4 ± 13.1	35	1.2	180	HS18	8.73 ± 0.11
GD61C_LC_x2420_20130113	0	5796.8 ± 13.1	35	1.2	180	HS18	8.73 ± 0.11
GD61C_LC_x2430_20121214	0	3862.8 ± 7.6	11	6.5	120	HS18	8.73 ± 0.11
GD61C_LC_x2440_20130113	0	5786.7 ± 13.1	35	1.2	180	HS18	8.72 ± 0.11
GD61C_LC_x2460_20130113	0	5154.5 ± 12.4	35	0.8	180	HS18	7.76 ± 0.10
GD61C_LC_x2520_20130113	1	5071.4 ± 12.3	35	1.2	180	HS18	9.06 ± 0.22
GD61C_LC_x2540_20130113	1	5578.2 ± 17.7	18	1.2	180	HS18	9.97 ± 0.24
GD61C_LC_x2508_20121209	0	3924.1 ± 7.7	70	0.8	120	HS18	8.87 ± 0.11
GD61C_TC_x0463_20121208	0	4400.2 ± 12.9	27	1.5	120	HS18	8.46 ± 0.03
GD61C_TC_x0513_20121208	0	4494.9 ± 12.3	31	1.2	120	HS18	8.64 ± 0.02
GD61C_TC_x0563_20121208	0	4682.2 ± 13.4	27	2.6	120	HS18	9.00 ± 0.03
GD61C_TC_x0575_20130103	0	6634.8 ± 13.3	39	1.3	180	HS18	8.50 ± 0.02
GD61C_TC_x0600_20130111	0	6740.7 ± 13.4	39	1.6	180	HS18	8.64 ± 0.02
GD61C_TC_x0605_20130103	0	6789.8 ± 14.2	35	1.2	180	HS18	8.70 ± 0.02
GD61C_TC_x0630_20130111	0	6852.7 ± 14.3	35	2.0	180	HS18	8.78 ± 0.02
GD61C_TC_x0635_20130103	0	6948.9 ± 15.0	32	1.6	180	HS18	8.91 ± 0.02
GD61C_TC_x0643_20121208	0	4637.9 ± 18.9	13	1.4	120	HS18	8.92 ± 0.04
GD61C_TC_x0660_20130111	0	6992.4 ± 15.1	32	1.6	180	HS18	8.96 ± 0.02
GD61C_TC_x0665_20130103	0	7058.7 ± 16.4	27	1.8	180	HS18	9.05 ± 0.02
GD61C_TC_x0675_20121214	0	4732.2 ± 14.2	24	1.1	120	HS18	9.10 ± 0.03
GD61C_TC_x0690_20130111	0	7104.0 ± 16.6	27	3.0	180	HS18	9.10 ± 0.02
GD61C_TC_x0695_20130103	0	7061.1 ± 17.7	23	1.9	180	HS18	9.05 ± 0.02
GD61C_TC_x0720_20130111	0	7108.5 ± 17.9	23	1.1	180	HS18	9.11 ± 0.02
GD61C_TC_x0725_20130103	0	7032.3 ± 19.9	18	2.5	180	HS18	9.01 ± 0.03
GD61C_TC_x0750_20130111	0	7027.1 ± 19.9	18	1.2	180	HS18	9.01 ± 0.03
GD61C_TC_x0755_20130103	0	7009.1 ± 21.7	15	1.0	180	HS18	8.98 ± 0.03
GD61C_TC_x0775_20121214	0	4654.9 ± 20.4	11	0.9	120	HS18	8.95 ± 0.04
GD61C_TC_x0780_20130111	0	6993.6 ± 21.7	15	0.8	180	HS18	8.96 ± 0.03
GD61C_TC_x0785_20130103	0	6981.4 ± 25.0	11	1.7	180	HS18	8.95 ± 0.03
GD61C_TC_x0810_20130111	0	6955.3 ± 25.0	11	0.2	180	HS18	8.91 ± 0.03
GD76B_TOP_r000_20130130	0	3997.4 ± 13.1	24	2.6	120	HS19	7.69 ± 0.03
GD76B_LC_x2630_20130206	0	6476.0 ± 14.1	34	1.9	180	HS19	9.77 ± 0.12
GD76B_LC_x2660_20130206	0	6641.7 ± 14.1	35	1.2	180	HS19	10.02 ± 0.12
GD76B_LC_x2690_20130206	0	6711.3 ± 14.2	35	2.4	180	HS19	10.12 ± 0.13
GD76B_TC_x0500_20130201	0	10532.3 ± 18.5	32	1.7	300	HS19	8.11 ± 0.01
GD76B_TC_x0530_20130201	0	10427.6 ± 20.1	27	2.1	300	HS19	8.03 ± 0.02
GD76B_TC_x0560_20130201	0	10163.9 ± 21.4	23	3.0	300	HS19	7.82 ± 0.02
GD76B_TC_x0590_20130201	0	9972.7 ± 23.8	18	1.6	300	HS19	7.68 ± 0.02
GD76B_TC_x0610_20130201	0	9866.1 ± 25.0	16	1.8	300	HS19	7.60 ± 0.02
GD76B_TC_x0630_20130201	0	9819.0 ± 27.5	13	0.9	300	HS19	7.56 ± 0.02
GD76B_TC_x0650_20130201	0	9740.5 ± 29.5	11	1.2	300	HS19	7.50 ± 0.02
GD76C_LAT_r000_20120918	0	2648.9 ± 10.6	24	2.0	90	HS17	8.20 ± 0.11
GD76C_LAT_r000_20120918	1	2304.0 ± 11.8	17	0.7	90	HS17	8.46 ± 0.21
GD76C_LAT_r000_20120918	2	2653.0 ± 13.3	15	0.7	90	HS17	8.21 ± 0.11
GD76C_TOP_r000_20120916	0	3139.6 ± 5.1	128	1.4	90	HS17	8.27 ± 0.01
GD76C_TOP_r090_20120916	0	3161.8 ± 5.1	132	1.8	90	HS17	8.33 ± 0.01
GD76C_TOP_r000_20120918	0	3128.2 ± 5.0	136	1.8	90	HS17	8.24 ± 0.01
GD76C_TOP_r090_20120918	0	3148.7 ± 5.0	136	2.4	90	HS17	8.29 ± 0.01
GD76C_LC_x2620_20120919	0	3521.9 ± 7.2	71	1.0	120	HS17	8.18 ± 0.10
GD76C_TC_x0080_20120918	0	4013.1 ± 7.7	71	3.5	120	HS17	7.93 ± 0.02
GD76C_TC_x0130_20120918	0	4140.8 ± 7.9	71	1.5	120	HS17	8.18 ± 0.02
GD76C_TC_x0230_20120918	0	4213.6 ± 11.3	35	0.9	120	HS17	8.32 ± 0.02
GD76C_TC_x0280_20120918	0	4181.4 ± 11.2	35	0.7	120	HS17	8.26 ± 0.02
GD79B_LAT_r000_20120929	0	5976.7 ± 17.9	19	1.9	180	HS19	9.01 ± 0.11
GD79B_LAT_r000_20120929	1	5157.1 ± 19.3	14	0.8	180	HS19	9.23 ± 0.22
GD79B_LAT_r090_20120929	0	5918.0 ± 17.8	19	3.5	180	HS19	8.92 ± 0.11
GD79B_LAT_r090_20120929	1	5171.9 ± 19.4	14	1.0	180	HS19	9.25 ± 0.22
GD79B_TOP_r000_20120927	0	7225.3 ± 7.7	133	3.6	180	HS19	9.27 ± 0.01
GD79B_TOP_r000_20120928	0	7223.2 ± 7.7	133	3.9	180	HS19	9.27 ± 0.01
GD79B_TOP_r090_20120928	0	7232.3 ± 7.7	133	3.9	180	HS19	9.28 ± 0.01
GD79B_LC_x2550_20121001	0	3992.8 ± 7.7	71	1.1	120	HS19	9.03 ± 0.11
GD79B_TC_x0460_20120930	0	4706.4 ± 8.5	71	2.2	120	HS19	9.06 ± 0.02
GD79B_TC_x0510_20120930	0	4815.8 ± 8.6	71	2.3	120	HS19	9.27 ± 0.02

Table C.12 – continued from previous page

measurement	seg	C_i	DOF	χ^2/DOF	T [s]	source	R_i [cts/s/MBq]
GD79B_TC_x0610_20120930	0	4959.0 ± 12.4	35	3.6	120	HS19	9.54 ± 0.02
GD79B_TC_x0660_20120930	0	4943.4 ± 12.3	35	2.1	120	HS19	9.51 ± 0.02
GD79C_LAT_r000_20121019	0	5048.5 ± 16.6	19	2.1	180	HS17	7.82 ± 0.10
GD79C_LAT_r000_20121019	1	4413.9 ± 19.3	12	1.8	180	HS17	8.11 ± 0.20
GD79C_LAT_r090_20121020	0	2559.4 ± 11.8	19	1.6	90	HS17	7.92 ± 0.10
GD79C_LAT_r090_20121020	1	2232.4 ± 13.7	12	0.8	90	HS17	8.20 ± 0.20
GD79C_TOP_r000_20121017	0	6043.2 ± 7.0	135	1.9	180	HS17	7.96 ± 0.01
GD79C_TOP_r090_20121017	0	6066.4 ± 7.0	135	1.7	180	HS17	7.99 ± 0.01
GD79C_LC_x2350_20121024	0	3387.3 ± 7.1	71	1.2	120	HS17	7.87 ± 0.10
GD79C_LC_x2550_20121024	0	3356.5 ± 7.2	70	0.9	120	HS17	7.79 ± 0.10
GD79C_TC_x0300_20121023	0	3948.2 ± 10.9	35	1.8	120	HS17	7.80 ± 0.02
GD79C_TC_x0350_20121023	0	4047.8 ± 11.2	35	1.6	120	HS17	8.00 ± 0.02
GD79C_TC_x0585_20121023	0	4047.5 ± 7.8	71	1.2	120	HS17	8.00 ± 0.02
GD79C_TC_x0635_20121023	0	4052.9 ± 7.8	71	1.0	120	HS17	8.01 ± 0.02
GD89B_LAT_r000_20121114	0	5401.2 ± 17.2	19	1.0	180	HS17	8.36 ± 0.11
GD89B_LAT_r000_20121114	1	4620.6 ± 19.1	13	1.1	180	HS17	8.49 ± 0.21
GD89B_LAT_r090_20121114	0	5325.4 ± 17.0	19	1.9	180	HS17	8.24 ± 0.10
GD89B_LAT_r090_20121114	1	4523.3 ± 18.9	13	2.3	180	HS17	8.31 ± 0.20
GD89B_TOP_r000_20121113	0	6371.9 ± 7.3	130	2.2	180	HS17	8.39 ± 0.01
GD89B_TOP_r090_20121113	0	6418.6 ± 7.4	130	2.4	180	HS17	8.45 ± 0.01
GD89B_TOP_r000_20130124	0	4492.0 ± 12.4	31	1.3	120	HS19	8.65 ± 0.02
GD89B_TOP_r090_20130124	0	4489.1 ± 12.4	31	1.0	120	HS19	8.64 ± 0.02
GD89B_TOP_r045_20130223	0	6112.3 ± 10.0	65	2.6	180	HS18	7.83 ± 0.01
GD89B_TOP_r067_20130223	0	6106.1 ± 10.1	65	2.5	180	HS18	7.83 ± 0.01
GD89B_TOP_r090_20130223	0	6135.0 ± 10.4	62	2.4	180	HS18	7.86 ± 0.01
GD89B_TOP_r112_20130223	0	6133.6 ± 10.1	65	1.8	180	HS18	7.86 ± 0.01
GD89B_TOP_r135_20130223	0	6136.1 ± 10.1	65	3.3	180	HS18	7.86 ± 0.01
GD89B_TOP_r157_20130223	0	6126.3 ± 10.1	65	1.8	180	HS18	7.85 ± 0.01
GD89B_LC_x2350_20121115	0	3549.0 ± 7.4	70	1.1	120	HS17	8.24 ± 0.10
GD89B_LC_x2520_20130309	0	4967.5 ± 12.3	35	1.0	180	HS18	7.48 ± 0.09
GD89B_LC_x2550_20130309	0	5038.6 ± 12.3	35	0.9	180	HS18	7.59 ± 0.09
GD89B_LC_x2580_20130309	0	5033.9 ± 12.3	35	1.9	180	HS18	7.58 ± 0.09
GD89B_LC_x2670_20130309	1	4215.4 ± 11.3	35	0.8	180	HS18	7.53 ± 0.18
GD89B_TC_x0355_20121114	0	4311.5 ± 8.3	70	1.4	120	HS17	8.52 ± 0.02
GD89B_TC_x0405_20121114	0	4338.5 ± 8.3	71	1.7	120	HS17	8.57 ± 0.02
GD89B_TC_x0495_20121114	0	4246.2 ± 11.4	35	1.6	120	HS17	8.39 ± 0.02
GD89B_TC_x0545_20121114	0	4219.5 ± 11.3	35	1.6	120	HS17	8.34 ± 0.02
GD89B_TC_x0440_20130125	0	6661.7 ± 13.5	39	1.5	180	HS19	8.55 ± 0.02
GD89B_TC_x0470_20130125	0	6812.3 ± 14.5	35	1.7	180	HS19	8.74 ± 0.02
GD89B_TC_x0500_20130125	0	6803.5 ± 15.1	32	1.8	180	HS19	8.73 ± 0.02
GD89B_TC_x0530_20130125	0	6905.6 ± 16.6	27	2.9	180	HS19	8.86 ± 0.02
GD89B_TC_x0560_20130125	0	6871.8 ± 17.9	23	1.9	180	HS19	8.82 ± 0.02
GD89B_TC_x0590_20130125	0	6790.4 ± 19.9	18	0.9	180	HS19	8.71 ± 0.03
GD89B_TC_x0620_20130125	0	6755.3 ± 21.5	15	0.9	180	HS19	8.67 ± 0.03
GD89B_TC_x0650_20130125	0	6714.9 ± 24.6	11	1.1	180	HS19	8.62 ± 0.03
GD89C_LAT_r000_20121106	0	5831.5 ± 17.4	20	2.2	180	HS17	9.03 ± 0.11
GD89C_LAT_r000_20121106	1	4999.3 ± 19.8	13	1.3	180	HS17	9.18 ± 0.22
GD89C_LAT_r090_20121106	0	5878.7 ± 17.4	20	2.2	180	HS17	9.10 ± 0.11
GD89C_LAT_r090_20121106	1	5056.9 ± 19.9	13	1.7	180	HS17	9.29 ± 0.23
GD89C_TOP_r000_20121105	0	7007.5 ± 7.6	131	1.5	180	HS17	9.23 ± 0.01
GD89C_TOP_r090_20121105	0	6992.8 ± 7.6	131	1.2	180	HS17	9.21 ± 0.01
GD89C_TOP_r000_20130116	0	4525.3 ± 12.7	30	1.3	120	HS17	8.94 ± 0.03
GD89C_TOP_r090_20130116	0	4537.2 ± 12.7	30	1.6	120	HS17	8.96 ± 0.03
GD89C_LC_x2300_20121108	0	3819.2 ± 7.6	70	2.1	120	HS17	8.87 ± 0.11
GD89C_LC_x2350_20121108	0	3928.0 ± 7.8	70	1.3	120	HS17	9.12 ± 0.11
GD89C_LC_x2330_20130119	0	5714.5 ± 13.2	35	1.7	180	HS17	8.85 ± 0.11
GD89C_LC_x2350_20130119	0	5762.7 ± 13.3	35	1.2	180	HS17	8.92 ± 0.11
GD89C_LC_x2370_20130119	0	5788.1 ± 13.3	35	1.8	180	HS17	8.96 ± 0.11
GD89C_LC_x2390_20130119	0	5806.2 ± 13.3	35	2.0	180	HS17	8.99 ± 0.11
GD89C_LC_x2490_20130119	1	4804.0 ± 12.2	35	1.5	180	HS17	8.82 ± 0.21
GD89C_TC_x0340_20121106	0	4565.0 ± 11.8	35	1.8	120	HS17	9.02 ± 0.02
GD89C_TC_x0340_20121107	0	4559.5 ± 11.7	35	1.8	120	HS17	9.01 ± 0.02
GD89C_TC_x0360_20130118	0	6842.7 ± 13.8	39	1.5	180	HS17	9.01 ± 0.02
GD89C_TC_x0390_20121106	0	4682.0 ± 12.0	35	2.0	120	HS17	9.25 ± 0.02
GD89C_TC_x0390_20121107	0	4695.7 ± 12.0	35	1.9	120	HS17	9.28 ± 0.02
GD89C_TC_x0390_20130118	0	6836.5 ± 14.5	35	2.0	180	HS17	9.00 ± 0.02
GD89C_TC_x0420_20130118	0	6867.8 ± 15.2	32	0.8	180	HS17	9.05 ± 0.02
GD89C_TC_x0450_20130118	0	6817.5 ± 16.4	27	1.1	180	HS17	8.98 ± 0.02

Continued on next page

Table C.12 – continued from previous page

measurement	seg	C_i	DOF	χ^2/DOF	T [s]	source	R_i [cts/s/MBq]
GD89C_TC_x0480_20130118	0	6820.7 ± 17.7	23	0.5	180	HS17	8.98 ± 0.02
GD89C_TC_x0510_20121107	0	4670.4 ± 8.5	70	0.8	120	HS17	9.23 ± 0.02
GD89C_TC_x0510_20130118	0	6814.4 ± 19.9	18	1.0	180	HS17	8.98 ± 0.03
GD89C_TC_x0540_20130118	0	6777.7 ± 21.5	15	0.8	180	HS17	8.93 ± 0.03
GD89C_TC_x0560_20121107	0	4651.9 ± 8.4	71	0.8	120	HS17	9.19 ± 0.02
GD89C_TC_x0570_20130118	0	6782.7 ± 24.9	11	1.2	180	HS17	8.93 ± 0.03
GD89C_TC_x0610_20121106	0	4660.4 ± 8.4	70	1.3	120	HS17	9.21 ± 0.02
GD89C_TC_x0660_20121106	0	4641.9 ± 8.3	71	0.8	120	HS17	9.17 ± 0.02
GD89D_TOP_r000_20130130	0	4155.6 ± 12.2	30	2.2	120	HS17	8.21 ± 0.02
GD89D_TOP_r090_20130130	0	4175.3 ± 12.2	30	1.3	120	HS17	8.25 ± 0.02
GD89D_LC_x2460_20130206	0	5844.4 ± 13.3	35	1.1	180	HS17	9.05 ± 0.11
GD89D_LC_x2490_20130206	0	5890.7 ± 13.4	35	1.2	180	HS17	9.12 ± 0.11
GD89D_TC_x0250_20130201	0	10639.4 ± 18.9	32	2.5	300	HS17	8.41 ± 0.01
GD89D_TC_x0280_20130201	0	10701.6 ± 20.6	27	2.5	300	HS17	8.46 ± 0.02
GD89D_TC_x0310_20130201	0	10602.1 ± 22.2	23	3.0	300	HS17	8.38 ± 0.02
GD89D_TC_x0340_20130201	0	10602.2 ± 25.0	18	2.4	300	HS17	8.38 ± 0.02
GD89D_TC_x0370_20130201	0	10664.5 ± 26.5	16	2.2	300	HS17	8.43 ± 0.02
GD89D_TC_x0400_20130201	0	10502.6 ± 29.0	13	2.3	300	HS17	8.30 ± 0.02
GD89D_TC_x0430_20130201	0	10410.1 ± 31.1	11	2.8	300	HS17	8.23 ± 0.02
GD91B_LAT_r000_20121130	0	6077.7 ± 17.8	20	1.5	180	HS17	9.41 ± 0.12
GD91B_LAT_r000_20121130	1	5335.6 ± 20.6	13	2.2	180	HS17	9.80 ± 0.24
GD91B_LAT_r090_20121130	0	5999.0 ± 17.8	20	3.2	180	HS17	9.29 ± 0.12
GD91B_LAT_r090_20121130	1	5309.2 ± 20.6	13	2.2	180	HS17	9.75 ± 0.24
GD91B_TOP_r000_20121130	0	7222.6 ± 8.2	120	2.1	180	HS17	9.51 ± 0.01
GD91B_TOP_r090_20121130	0	7281.4 ± 8.2	120	1.7	180	HS17	9.59 ± 0.01
GD91B_TOP_r000_20130116	0	4800.5 ± 13.2	29	3.0	120	HS18	9.23 ± 0.03
GD91B_TOP_r090_20130116	0	4801.1 ± 13.2	29	3.1	120	HS18	9.23 ± 0.03
GD91B_LC_x2500_20130119	0	5861.9 ± 13.3	35	2.0	180	HS18	8.83 ± 0.11
GD91B_LC_x2520_20130119	0	5934.1 ± 13.4	35	1.8	180	HS18	8.94 ± 0.11
GD91B_LC_x2540_20130119	0	5924.7 ± 13.4	35	2.3	180	HS18	8.92 ± 0.11
GD91B_LC_x2580_20130119	1	5131.7 ± 12.5	35	3.7	180	HS18	9.17 ± 0.22
GD91B_LC_x2660_20130119	0	5958.7 ± 13.4	35	2.0	180	HS18	8.98 ± 0.11
GD91B_TC_x0480_20130118	0	6945.3 ± 13.7	39	4.0	180	HS18	8.90 ± 0.02
GD91B_TC_x0510_20130118	0	7113.4 ± 14.7	35	2.1	180	HS18	9.12 ± 0.02
GD91B_TC_x0540_20130118	0	7176.4 ± 15.5	32	2.5	180	HS18	9.20 ± 0.02
GD91B_TC_x0570_20130118	0	7246.0 ± 16.9	27	1.6	180	HS18	9.29 ± 0.02
GD91B_TC_x0600_20130118	0	7273.8 ± 18.3	23	2.7	180	HS18	9.32 ± 0.02
GD91B_TC_x0630_20130118	0	7243.9 ± 20.4	18	2.3	180	HS18	9.28 ± 0.03
GD91B_TC_x0660_20130118	0	7143.9 ± 22.1	15	1.8	180	HS18	9.16 ± 0.03
GD91B_TC_x0690_20130118	0	7172.6 ± 25.5	11	1.1	180	HS18	9.19 ± 0.03
GD91C_LAT_r000_20121013	0	5956.6 ± 18.0	19	2.7	180	HS17	9.22 ± 0.12
GD91C_LAT_r000_20121013	1	5292.0 ± 21.2	12	0.5	180	HS17	9.72 ± 0.24
GD91C_LAT_r090_20121013	0	6011.4 ± 18.1	19	2.1	180	HS17	9.31 ± 0.12
GD91C_LAT_r090_20121013	1	5235.2 ± 21.1	12	0.7	180	HS17	9.62 ± 0.23
GD91C_TOP_r000_20121012	0	7369.8 ± 8.3	118	2.5	180	HS17	9.71 ± 0.01
GD91C_TOP_r090_20121012	0	7377.7 ± 8.4	118	3.1	180	HS17	9.72 ± 0.01
GD91D_LAT_r000_20121127	0	5961.4 ± 19.4	16	2.3	180	HS17	9.23 ± 0.12
GD91D_LAT_r000_20121127	1	5261.9 ± 19.6	14	1.7	180	HS17	9.66 ± 0.23
GD91D_LAT_r000_20121127	2	5981.1 ± 22.3	12	2.1	180	HS17	9.26 ± 0.12
GD91D_LAT_r090_20121127	0	6030.4 ± 19.6	16	2.1	180	HS17	9.34 ± 0.12
GD91D_LAT_r090_20121127	1	5287.9 ± 19.7	14	0.5	180	HS17	9.71 ± 0.24
GD91D_LAT_r090_20121127	2	6050.3 ± 22.4	12	1.3	180	HS17	9.37 ± 0.12
GD91D_TOP_r000_20121123	0	7289.0 ± 8.1	120	2.6	180	HS17	9.60 ± 0.01
GD91D_TOP_r090_20121123	0	7293.9 ± 8.1	120	2.4	180	HS17	9.61 ± 0.01
GD91D_LC_x2400_20121128	0	4006.8 ± 7.8	70	1.8	120	HS17	9.30 ± 0.12
GD91D_TC_x0300_20121126	0	4672.9 ± 8.2	74	1.4	120	HS17	9.23 ± 0.02
GD91D_TC_x0350_20121126	0	4806.9 ± 8.6	71	1.1	120	HS17	9.50 ± 0.02
GD91D_TC_x0500_20121126	0	4850.4 ± 12.2	35	0.8	120	HS17	9.58 ± 0.02
GD91D_TC_x0550_20121126	0	4792.1 ± 12.0	35	1.1	120	HS17	9.47 ± 0.02
GD00B_LAT_r000_20121207	0	5894.6 ± 20.1	15	2.0	180	HS19	8.89 ± 0.11
GD00B_LAT_r000_20121207	1	5238.4 ± 21.2	12	0.8	180	HS19	9.37 ± 0.23
GD00B_LAT_r090_20121207	0	5947.3 ± 20.3	15	0.6	180	HS19	8.97 ± 0.11
GD00B_LAT_r090_20121207	1	5270.3 ± 21.2	12	1.8	180	HS19	9.43 ± 0.23
GD00B_TOP_r000_20121208	0	6978.6 ± 8.1	118	3.0	180	HS19	8.95 ± 0.01
GD00B_TOP_r090_20121208	0	6995.5 ± 8.1	118	2.3	180	HS19	8.98 ± 0.01
GD00B_TOP_r000_20121213	0	3477.0 ± 7.8	63	2.1	90	HS19	8.92 ± 0.02
GD00B_TOP_r090_20121213	0	3538.8 ± 8.1	59	2.4	90	HS19	9.08 ± 0.02
GD00B_TOP_r000_20130124	0	4342.1 ± 12.7	29	3.2	120	HS18	8.35 ± 0.02

<div align="right">Continued on next page</div>

Table C.12 – continued from previous page

measurement	seg	C_i	DOF	χ^2/DOF	T [s]	source	R_i [cts/s/MBq]
GD00B_TOP_r090_20130124	0	4312.3 ± 12.5	30	1.9	120	HS18	8.29 ± 0.02
GD00B_LC_x2530_20130113	0	5654.3 ± 13.4	34	3.8	180	HS19	8.53 ± 0.11
GD00B_LC_x2550_20130113	0	5866.2 ± 13.4	35	1.3	180	HS19	8.85 ± 0.11
GD00B_LC_x2570_20130113	0	5948.4 ± 13.5	35	1.1	180	HS19	8.97 ± 0.11
GD00B_LC_x2590_20130113	0	5924.2 ± 13.5	35	1.1	180	HS19	8.93 ± 0.11
GD00B_LC_x2610_20130113	0	5941.3 ± 13.5	35	1.3	180	HS19	8.96 ± 0.11
GD00B_LC_x2690_20130113	1	5230.6 ± 12.7	35	1.1	180	HS19	9.36 ± 0.23
GD00B_LC_x2730_20130113	0	5794.3 ± 18.3	18	1.2	180	HS19	8.74 ± 0.11
GD00B_LC_x2630_20130126	0	5418.1 ± 12.9	35	1.6	180	HS18	8.16 ± 0.10
GD00B_LC_x2660_20130126	0	5502.6 ± 13.0	35	1.7	180	HS18	8.29 ± 0.10
GD00B_LC_x2690_20130126	0	5525.0 ± 13.0	35	1.9	180	HS18	8.32 ± 0.10
GD00B_LC_x2720_20130126	1	4907.9 ± 12.3	35	1.0	180	HS18	8.77 ± 0.21
GD00B_LC_x2810_20130126	0	5364.7 ± 12.8	35	1.5	180	HS18	8.08 ± 0.10
GD00B_LC_x2840_20130126	0	5149.8 ± 12.6	35	1.5	180	HS18	7.76 ± 0.10
GD00B_TC_x0350_20130125	0	6318.0 ± 13.2	39	2.2	180	HS18	8.10 ± 0.02
GD00B_TC_x0380_20130125	0	6407.0 ± 14.1	35	1.5	180	HS18	8.21 ± 0.02
GD00B_TC_x0410_20130125	0	6482.3 ± 14.8	32	2.6	180	HS18	8.31 ± 0.02
GD00B_TC_x0440_20130125	0	6570.9 ± 16.3	27	3.0	180	HS18	8.42 ± 0.02
GD00B_TC_x0470_20130125	0	6593.0 ± 17.6	23	2.3	180	HS18	8.45 ± 0.02
GD00B_TC_x0500_20130125	0	6553.2 ± 19.7	18	2.2	180	HS18	8.40 ± 0.03
GD00B_TC_x0530_20130125	0	6516.1 ± 21.3	15	2.9	180	HS18	8.35 ± 0.03
GD00B_TC_x0560_20130125	0	6439.2 ± 24.4	11	4.0	180	HS18	8.25 ± 0.03
GD00B_TC_x0480_20130111	0	6898.1 ± 13.9	39	2.9	180	HS19	8.85 ± 0.02
GD00B_TC_x0510_20130111	0	6989.1 ± 14.7	35	1.4	180	HS19	8.97 ± 0.02
GD00B_TC_x0540_20130111	0	7060.6 ± 15.5	32	2.6	180	HS19	9.06 ± 0.02
GD00B_TC_x0570_20130111	0	7039.7 ± 16.8	27	1.9	180	HS19	9.03 ± 0.02
GD00B_TC_x0630_20130111	0	7049.1 ± 20.4	18	1.7	180	HS19	9.04 ± 0.03
GD00B_TC_x0660_20130111	0	7006.9 ± 22.1	15	4.0	180	HS19	8.99 ± 0.03
GD00B_TC_x0690_20130111	0	6917.3 ± 25.3	11	1.4	180	HS19	8.88 ± 0.03
GD00C_LAT_r000_20121013	0	6169.6 ± 18.8	18	1.8	180	HS19	9.30 ± 0.12
GD00C_LAT_r000_20121013	1	5348.7 ± 19.7	14	0.5	180	HS19	9.57 ± 0.23
GD00C_LAT_r000_20121013	2	6154.3 ± 21.8	13	0.9	180	HS19	9.28 ± 0.12
GD00C_LAT_r090_20121013	0	6165.3 ± 18.8	18	1.5	180	HS19	9.30 ± 0.12
GD00C_LAT_r090_20121013	1	5374.7 ± 19.8	14	0.9	180	HS19	9.62 ± 0.23
GD00C_LAT_r090_20121013	2	6170.2 ± 21.8	13	1.0	180	HS19	9.30 ± 0.12
GD00C_LAT_r000_20121019	0	6185.1 ± 18.8	18	2.0	180	HS19	9.33 ± 0.12
GD00C_LAT_r000_20121019	1	5371.7 ± 19.8	14	0.7	180	HS19	9.61 ± 0.23
GD00C_LAT_r000_20121019	2	6155.9 ± 21.8	13	1.5	180	HS19	9.28 ± 0.12
GD00C_LAT_r090_20121020	0	3134.0 ± 13.4	18	1.6	90	HS19	9.45 ± 0.12
GD00C_LAT_r090_20121020	1	2709.0 ± 14.1	14	0.6	90	HS19	9.69 ± 0.24
GD00C_LAT_r090_20121020	2	3080.5 ± 15.5	13	1.4	90	HS19	9.29 ± 0.12
GD00C_LAT_r000_20121106	0	5539.6 ± 17.7	18	1.7	180	HS18	8.34 ± 0.11
GD00C_LAT_r000_20121106	1	4803.7 ± 18.6	14	1.2	180	HS18	8.58 ± 0.21
GD00C_LAT_r000_20121106	2	5558.1 ± 20.6	13	1.0	180	HS18	8.37 ± 0.11
GD00C_LAT_r090_20121106	0	5463.0 ± 17.6	18	1.9	180	HS18	8.23 ± 0.10
GD00C_LAT_r090_20121106	1	4705.2 ± 18.5	14	0.9	180	HS18	8.41 ± 0.20
GD00C_LAT_r090_20121106	2	5479.4 ± 20.5	13	0.6	180	HS18	8.25 ± 0.11
GD00C_TOP_r000_20121017	0	7616.4 ± 8.0	132	3.3	180	HS19	9.77 ± 0.01
GD00C_TOP_r090_20121017	0	7618.4 ± 8.0	132	2.9	180	HS19	9.77 ± 0.01
GD00C_TOP_r090_20121018	0	7645.5 ± 8.0	132	4.8	180	HS19	9.81 ± 0.01
GD00C_TOP_r000_20121105	0	6986.4 ± 7.6	132	4.7	180	HS18	8.95 ± 0.01
GD00C_TOP_r090_20121105	0	7000.6 ± 7.6	132	4.4	180	HS18	8.97 ± 0.01
GD00C_LC_x2550_20121108	0	3857.7 ± 7.7	70	1.6	120	HS18	8.72 ± 0.11
GD00C_LC_x2720_20121108	0	3841.0 ± 7.6	70	1.3	120	HS18	8.68 ± 0.11
GD00C_LC_x2550_20121120	0	4648.5 ± 8.5	70	0.9	120	HS18	10.50 ± 0.13
GD00C_LC_x2770_20121120	0	4651.0 ± 8.5	70	1.2	120	HS18	10.51 ± 0.13
GD00C_LC_x2600_20121024	0	4167.6 ± 8.0	71	1.1	120	HS19	9.43 ± 0.12
GD00C_LC_x2800_20121024	0	4197.7 ± 8.0	70	1.3	120	HS19	9.50 ± 0.12
GD00C_TC_x0440_20121106	0	4545.5 ± 11.7	35	2.5	120	HS18	8.74 ± 0.02
GD00C_TC_x0455_20121107	0	4662.8 ± 11.9	35	2.2	120	HS18	8.96 ± 0.02
GD00C_TC_x0490_20121106	0	4693.8 ± 12.0	35	1.8	120	HS18	9.02 ± 0.02
GD00C_TC_x0505_20121107	0	4751.9 ± 12.0	35	4.5	120	HS18	9.13 ± 0.02
GD00C_TC_x0625_20121107	0	4823.4 ± 8.7	70	2.7	120	HS18	9.27 ± 0.02
GD00C_TC_x0675_20121107	0	4826.1 ± 8.6	71	1.9	120	HS18	9.28 ± 0.02
GD00C_TC_x0725_20121106	0	4811.6 ± 8.7	70	2.2	120	HS18	9.25 ± 0.02
GD00C_TC_x0775_20121106	0	4833.2 ± 8.6	71	1.8	120	HS18	9.29 ± 0.02
GD00C_TC_x0415_20121119	0	4533.1 ± 8.4	70	2.0	120	HS18	8.71 ± 0.02
GD00C_TC_x0465_20121119	0	4568.3 ± 8.4	71	2.6	120	HS18	8.78 ± 0.02

<div align="right">Continued on next page</div>

Table C.12 – continued from previous page

measurement	seg	C_i	DOF	χ^2/DOF	T [s]	source	R_i [cts/s/MBq]
GD00C_TC_x0545_20121119	0	4643.1 ± 11.9	35	1.0	120	HS18	8.93 ± 0.02
GD00C_TC_x0595_20121119	0	4669.7 ± 12.0	35	0.9	120	HS18	8.98 ± 0.02
GD00C_TC_x0480_20121023	0	5082.1 ± 12.6	35	1.7	120	HS19	9.78 ± 0.02
GD00C_TC_x0530_20121023	0	5130.9 ± 12.7	35	1.1	120	HS19	9.87 ± 0.02
GD00C_TC_x0690_20121023	0	5163.7 ± 9.0	71	2.5	120	HS19	9.94 ± 0.02
GD00C_TC_x0740_20121023	0	5199.9 ± 9.0	71	0.8	120	HS19	10.01 ± 0.02
GD00D_LAT_r000_20120926	0	6109.6 ± 18.2	19	1.9	180	HS18	9.20 ± 0.12
GD00D_LAT_r000_20120926	1	5336.2 ± 19.7	14	0.6	180	HS18	9.54 ± 0.23
GD00D_LAT_r000_20120926	2	6068.2 ± 20.9	14	1.7	180	HS18	9.14 ± 0.12
GD00D_LAT_r090_20120926	0	6141.4 ± 18.3	19	1.6	180	HS18	9.25 ± 0.12
GD00D_LAT_r090_20120926	1	5372.5 ± 19.8	14	1.1	180	HS18	9.60 ± 0.23
GD00D_LAT_r000_20121008	0	5751.2 ± 17.6	19	1.3	180	HS17	8.90 ± 0.11
GD00D_LAT_r000_20121008	1	5006.8 ± 19.1	14	2.6	180	HS17	9.20 ± 0.22
GD00D_LAT_r000_20121008	2	5649.9 ± 20.2	14	3.1	180	HS17	8.75 ± 0.11
GD00D_LAT_r090_20121008	0	5785.2 ± 17.7	19	0.9	180	HS17	8.96 ± 0.11
GD00D_LAT_r090_20121008	1	4987.1 ± 19.1	14	0.7	180	HS17	9.16 ± 0.22
GD00D_LAT_r090_20121008	2	5688.3 ± 20.3	14	4.6	180	HS17	8.81 ± 0.11
GD00D_TOP_r000_20120925	0	3649.5 ± 5.4	134	1.5	90	HS18	9.35 ± 0.01
GD00D_TOP_r090_20120925	0	3670.9 ± 5.5	134	1.6	90	HS18	9.41 ± 0.01
GD00D_TOP_r000_20120924	0	3310.0 ± 5.2	134	1.9	90	HS18	8.48 ± 0.01
GD00D_TOP_r090_20120924	0	3571.0 ± 5.4	134	1.6	90	HS18	9.15 ± 0.01
GD00D_LC_x2550_20121009	0	3830.3 ± 7.6	71	1.0	120	HS17	8.89 ± 0.11
GD00D_TC_x0350_20121009	0	4523.0 ± 11.7	35	1.8	120	HS17	8.94 ± 0.02
GD00D_TC_x0550_20121009	0	4557.0 ± 8.3	71	1.2	120	HS17	9.00 ± 0.02
GD00D_TC_x0600_20121009	0	4573.0 ± 8.3	71	1.1	120	HS17	9.03 ± 0.02
GD00D_TC_x0503_20120925	0	4741.7 ± 8.5	71	1.3	120	HS18	9.12 ± 0.02
GD00D_TC_x0553_20120925	0	4920.3 ± 8.7	71	1.6	120	HS18	9.46 ± 0.02
GD00D_TC_x0653_20120925	0	4850.5 ± 13.8	27	1.0	120	HS18	9.32 ± 0.03
GD02B_LAT_r000_20121031	0	5821.9 ± 18.4	18	4.0	180	HS17	9.01 ± 0.11
GD02B_LAT_r000_20121031	1	5032.4 ± 20.8	12	1.6	180	HS17	9.24 ± 0.22
GD02B_LAT_r090_20121031	0	5835.0 ± 18.4	18	3.0	180	HS17	9.03 ± 0.11
GD02B_LAT_r090_20121031	1	5044.0 ± 20.8	12	1.2	180	HS17	9.26 ± 0.23
GD02B_LAT_r000_20121127	0	5723.7 ± 18.1	18	1.5	180	HS18	8.62 ± 0.11
GD02B_LAT_r000_20121127	1	4890.4 ± 20.3	12	0.8	180	HS18	8.74 ± 0.21
GD02B_LAT_r090_20121127	0	5648.8 ± 17.9	18	1.8	180	HS18	8.51 ± 0.11
GD02B_LAT_r090_20121127	1	4831.7 ± 20.2	12	0.6	180	HS18	8.63 ± 0.21
GD02B_TOP_r000_20121128	0	6871.6 ± 7.9	120	2.3	180	HS18	8.81 ± 0.01
GD02B_TOP_r090_20121128	0	6797.6 ± 7.8	120	1.8	180	HS18	8.71 ± 0.01
GD02B_TOP_r000_20121030	0	7076.1 ± 8.0	122	1.6	180	HS17	9.32 ± 0.01
GD02B_LC_x2510_20121128	0	3788.6 ± 7.6	70	0.9	120	HS18	8.56 ± 0.11
GD02B_TC_x0475_20121129	0	4425.0 ± 8.2	70	3.3	120	HS18	8.51 ± 0.02
GD02B_TC_x0525_20121129	0	4591.4 ± 8.4	71	3.1	120	HS18	8.83 ± 0.02
GD02B_TC_x0675_20121129	0	4565.2 ± 11.7	35	1.2	120	HS18	8.78 ± 0.02
GD02B_TC_x0725_20121129	0	4534.1 ± 11.7	35	1.2	120	HS18	8.72 ± 0.02
GD02B_TC_x0360_20121103	0	7053.1 ± 14.8	35	2.2	180	HS17	9.29 ± 0.02
GD02B_TC_x0410_20121103	0	7105.5 ± 10.5	71	1.3	180	HS17	9.36 ± 0.01
GD02B_TC_x0460_20121102	0	7074.8 ± 14.8	35	1.3	180	HS17	9.32 ± 0.02
GD02B_TC_x0460_20121103	0	7102.1 ± 10.5	71	1.2	180	HS17	9.35 ± 0.01
GD02B_TC_x0510_20121102	0	7041.2 ± 10.4	71	1.5	180	HS17	9.27 ± 0.01
GD02B_TC_x0560_20121102	0	7085.2 ± 10.4	71	0.7	180	HS17	9.33 ± 0.01
GD02C_LAT_r000_20121207	0	5801.3 ± 18.7	17	1.9	180	HS17	8.98 ± 0.11
GD02C_LAT_r000_20121207	1	5271.1 ± 22.0	11	1.1	180	HS17	9.68 ± 0.24
GD02C_LAT_r000_20121207	2	5892.3 ± 23.1	11	1.4	180	HS17	9.12 ± 0.12
GD02C_LAT_r090_20121207	0	5948.6 ± 19.0	17	1.1	180	HS17	9.21 ± 0.12
GD02C_LAT_r090_20121207	1	5395.1 ± 22.3	11	1.7	180	HS17	9.91 ± 0.24
GD02C_LAT_r090_20121207	2	5988.8 ± 23.4	11	2.0	180	HS17	9.27 ± 0.12
GD02C_TOP_r000_20121208	0	6886.3 ± 7.9	120	1.8	180	HS17	9.07 ± 0.01
GD02C_TOP_r090_20121208	0	6891.7 ± 7.9	120	2.4	180	HS17	9.08 ± 0.01
GD02C_TOP_r000_20130111	0	3467.1 ± 11.6	27	1.7	90	HS17	9.13 ± 0.03
GD02C_TOP_r090_20130111	0	3507.1 ± 11.7	27	1.1	90	HS17	9.24 ± 0.03
GD02C_LC_x2280_20130113	0	5613.0 ± 13.3	34	2.8	180	HS17	8.69 ± 0.11
GD02C_LC_x2300_20130113	0	5753.7 ± 13.2	35	2.0	180	HS17	8.91 ± 0.11
GD02C_LC_x2320_20130113	0	5868.2 ± 13.3	35	2.0	180	HS17	9.08 ± 0.11
GD02C_LC_x2340_20130113	0	5934.2 ± 13.4	35	1.4	180	HS17	9.19 ± 0.11
GD02C_LC_x2400_20130113	1	5312.4 ± 12.7	35	1.4	180	HS17	9.76 ± 0.24
GD02C_LC_x2355_20121209	0	3846.9 ± 7.7	70	1.7	120	HS17	8.93 ± 0.11
GD02C_LC_x2410_20121209	0	3932.7 ± 7.8	70	1.6	120	HS17	9.13 ± 0.11
GD02C_TC_x0370_20130111	0	6642.1 ± 13.5	39	3.8	180	HS17	8.75 ± 0.02

Continued on next page

Table C.12 – continued from previous page

measurement	seg	C_i	DOF	χ^2/DOF	T [s]	source	R_i [cts/s/MBq]
GD02C_TC_x0400_20130111	0	6819.6 ± 14.4	35	2.4	180	HS17	8.98 ± 0.02
GD02C_TC_x0430_20130111	0	6973.5 ± 15.2	32	1.5	180	HS17	9.18 ± 0.02
GD02C_TC_x0460_20130111	0	7043.4 ± 16.6	27	1.9	180	HS17	9.28 ± 0.02
GD02C_TC_x0490_20130111	0	7067.7 ± 18.0	23	1.7	180	HS17	9.31 ± 0.02
GD02C_TC_x0520_20130111	0	7032.3 ± 20.2	18	1.9	180	HS17	9.26 ± 0.03
GD02C_TC_x0550_20130111	0	6936.8 ± 21.8	15	2.2	180	HS17	9.14 ± 0.03
GD02C_TC_x0580_20130111	0	6873.7 ± 25.1	11	1.7	180	HS17	9.05 ± 0.03
GD02C_TC_x0323_20121208	0	4523.0 ± 9.1	59	1.7	120	HS17	8.94 ± 0.02
GD02C_TC_x0373_20121208	0	4604.4 ± 13.5	27	2.3	120	HS17	9.10 ± 0.03
GD02C_TC_x0473_20121208	0	4609.4 ± 18.9	13	1.4	120	HS17	9.11 ± 0.04
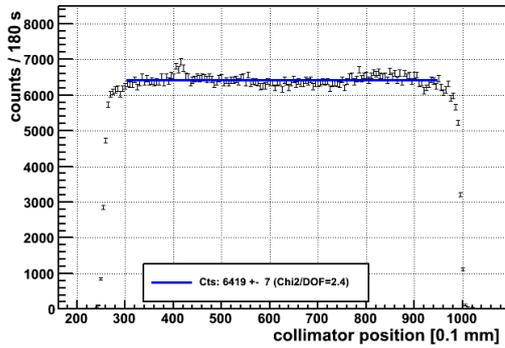
(a) GD89B top linear
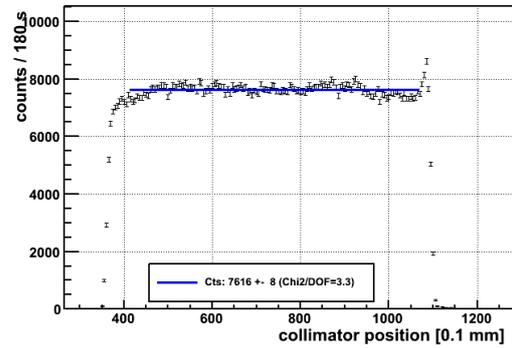
(b) GD00C top linear
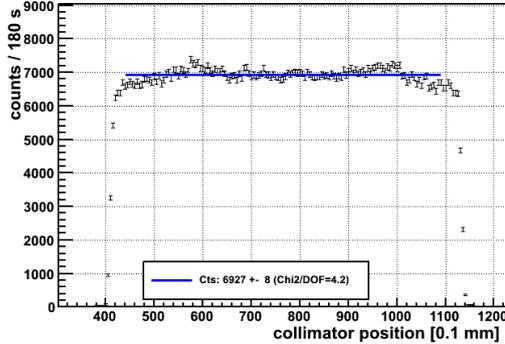
(c) GD61C top linear
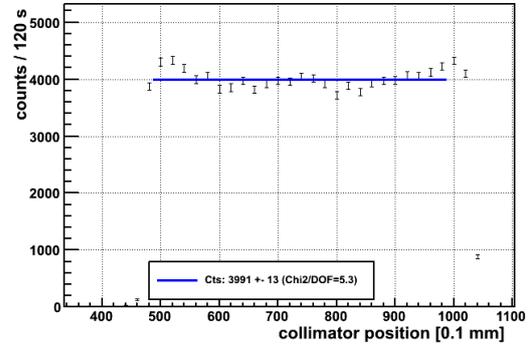
(d) GD76B top linear

Figure C.20 Examples of surface scans (I of II) with peculiar features. Note that these examples ares selected as worse cases.
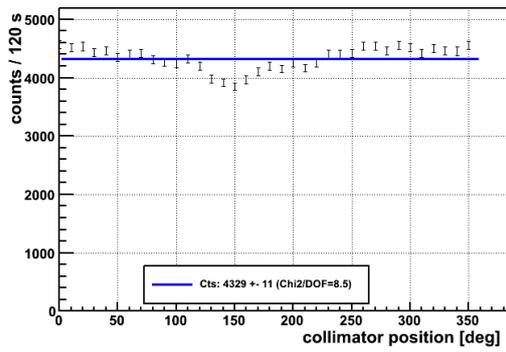
(a) GD00D top circular
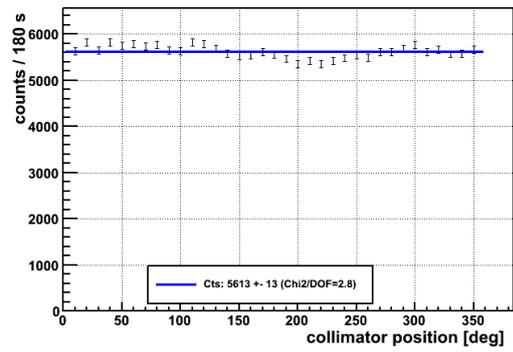
(b) GD02C lateral circular
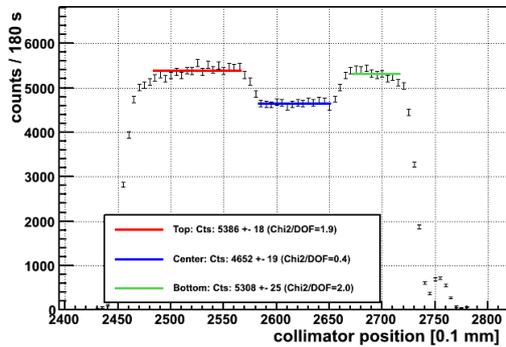
(c) GD61B lateral linear
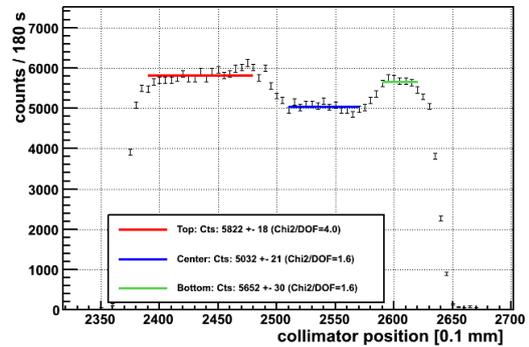
(d) GD02B lateral linear

Figure C.21   Examples of surface scans (II of II) with peculiar features. Note that these examples ares selected as worse cases.

Appendix D

New Pulse Shape Model for Surface Events on BEGe Detectors

D.1 Ad-hoc Empirical Model for n$^+$-Electrode

Background Region and Pile-up

The background spectrum of GD61B is illustrated together with an ^{241}Am spectrum in Fig. D.1a. It is visible that the background region is within a plateau of 59.5 keV random pile-up events. The pure background counts (red curve) illustrate a decrease in background towards lower energies. The ratio of slow pulse region counts to background region counts is 0.63 in the background spectrum and will be used to correct the background estimation from the ^{241}Am spectra. The ratio is assumed to be sufficiently equal for all detectors.

(a) background   (b) pile-up
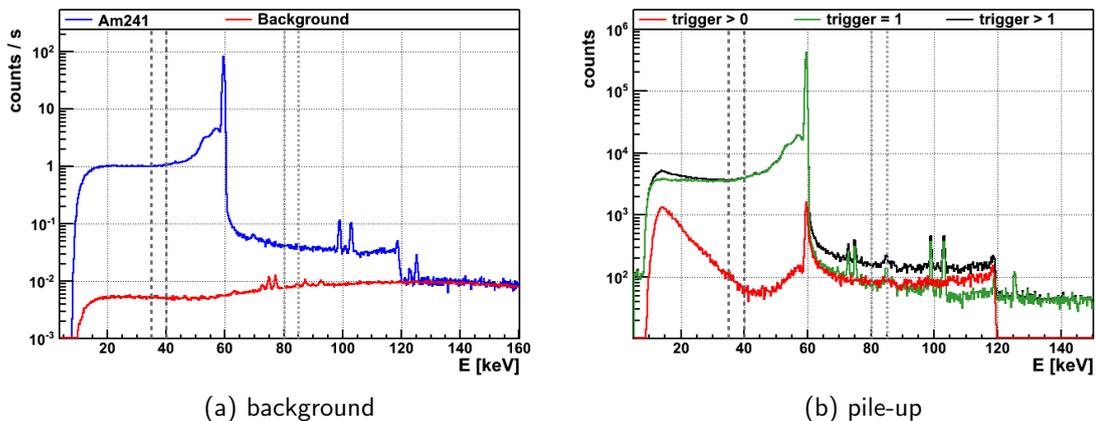
Figure D.1 Left: Determination of the background in the slow pulse region (dark gray dashed lines). A background region is defined from 80 to 85 keV (light gray dashed lines). Right: Investigation of pile-up with FADC data. Shown are the spectra for all triggered events, events with exactly one trigger and events with more than one trigger.

The pile-up effect is shown in Fig. D.1b for an FADC spectrum of GD32D. The spectrum is separated according to the FFTTrigger[1] and shown for (1) all triggered events, (2) events with exactly one trigger in the trace and (3) events with multiple triggers. The pile-up fraction of the spectrum (red curve with multiple triggers) contains roughly 0.3 % of the

---

[1]Fast fourier transformation trigger implemented in GELATIO [128]

events in the slow pulse region. A similar pile-up rate is seen in the background window. Hence, assuming a similar pile-up effect for energy spectra taken with the MCA DAQ, the pile-up effect is included in the background correction with good approximation.

DAQ Effects

The two MCA systems were set up with a different low energy threshold. This can be seen for all measurements in Fig. 8.7a. The effect is highlighted in Fig. D.2a for two selected detectors (GD79C and GD91A) that have been measured on both systems respectively. Also shown are spectra for the standard high activity source (HS21) and for the low activity source (HS24) for comparison. The spectra are normalized to the 59.5 keV peak counts. It can be seen that effects due to the different low energy thresholds disappear above ≈ 30 keV. It can also be seen that the pile-up in the background window of the HS21 source spectra is roughly compensated by the larger relative background contribution of the HS24 source spectra.

(a) DAQ effects   (b) MC tuning
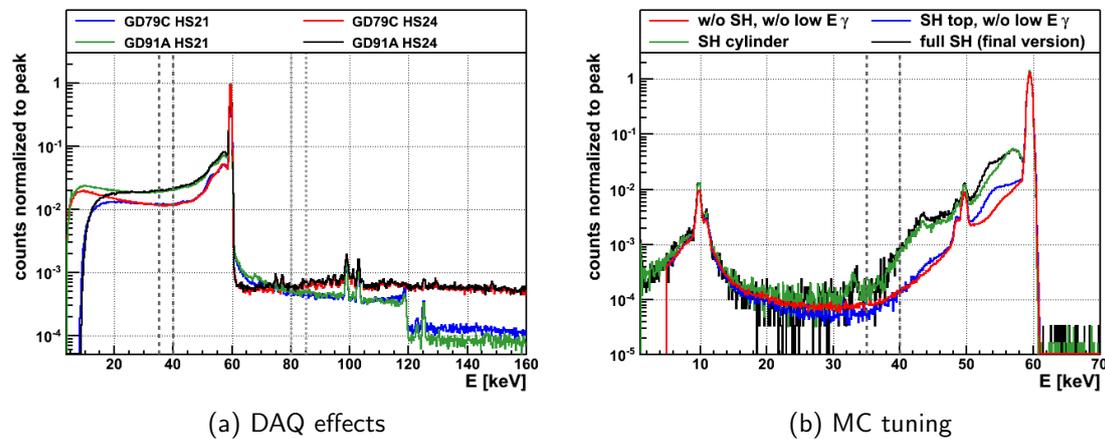
Figure D.2 Left: Comparison the two different MCA DAQ systems with two different detectors (GD79C and GD91A) and two different ^{241}Am calibration sources (HS21 and HS24). Visible is the different low energy threshold of the two systems. Also visible are pile-up effects with the stronger HS21 source. Right: Fine tuning of the MC simulations. Simulations performed without TL. Four different spectra show the impact of various MC components (SH - source holder,). All spectra are normalized to the 59.5 keV peak counts. See text for details.

Tuning of MC Simulations

A precise implementation of the MC geometry is imperative when comparing the peak to slow pulse ratio between MC simulations and data. The low energy part of the ^{241}Am spectra is being influenced by additional ^{241}Am γ-lines, X-ray peaks and Compton features. Fig. D.2b shows the evolution of tuning the MC simulation to match the experimental spectra. The MC spectra are normalized to the 59.5 keV peak counts and describe a standard BEGe with 0.7 mm FCCD. No TL is implemented so that these MC spectra are best compared to the experimental spectrum in Fig. 8.6a after removing the slow pulse events with the A/E cut.

In a first attempt (red curve) the setup was simulated without plexiglas source holder (Fig. C.5 in appendix), with a source encapsulation of PVC and no additional low energy

γ-rays. Clearly visible are the germanium X-ray lines around $10\,\mathrm{keV}$ and germanium X-ray escape lines around $50\,\mathrm{keV}$. The prominent X-ray (escape) lines are only visible in the MC without assuming a TL. The lines occur when X-rays enter into (escape) the active volume. In the data those lines are not visible even in the slow pulse removed spectra in Fig. 8.6a because they escape into the TL and their energy is degraded and smeared.

In a next attempt (blue curve) the source encapsulation was changed from PVC to acrylic and the top part of the source holder was implemented. This results in a strong Compton feature below the peak which is created by a $90\,\mathrm{deg}$ Compton scattering of a $59.5\,\mathrm{keV}$ γ-ray in the source holder. The energy of such a scattered γ-ray is $53.7\,\mathrm{keV}$ clearly visible in the spectrum.

In a parallel step (green curve) the low energy γ-rays are included in the MC and the cylindrical part of the source holder was implemented (Fig. C.5 in the appendix). The low energy γ-rays have a small emission probability and are heavily attenuated. Nevertheless they are visible. Especially the $43.4\,\mathrm{keV}$ γ-line is affecting the slow pulse region. The cylindrical source holder part is creating another Compton feature at $\approx 57\,\mathrm{keV}$ just below the peak. This feature can be explained by $50\,\mathrm{deg}$ Compton scattering along the $20\,\mathrm{cm}$ long acrylic source holder cylinder.

The black spectrum is obtained with the finalized version of MC simulations containing all features and is in good agreement with the experimental data when slow pulses are removed (compare with Fig. 8.6a).
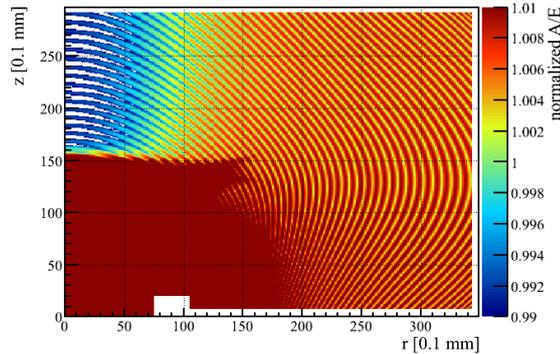
Comparison of Data with MC

Figure D.3   Control plot of normalized A/E values in the ADL bulk library. Binning effects in the A/E reconstruction create artifacts in the order of $1\,\%$ which introduce an additional width of the A/E distribution.

(a) ^{241}Am full recombination

(b) ^{90}Sr full recombination

(c) ^{241}Am model 0.010

(d) ^{90}Sr model 0.010

(e) ^{241}Am model 0.002

(f) ^{90}Sr model 0.002

(g) ^{241}Am model 0.001

(h) ^{90}Sr model 0.001

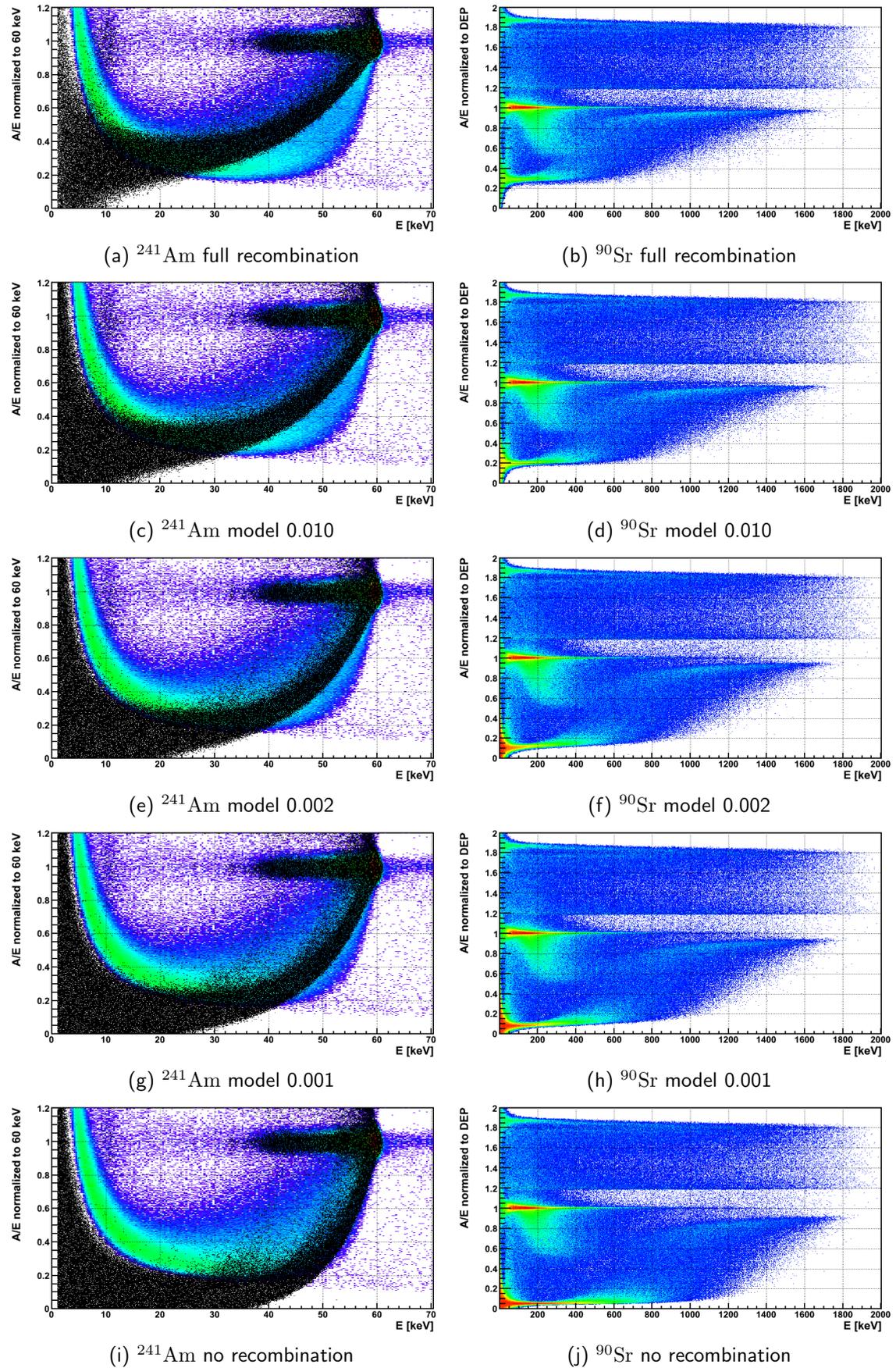(i) ^{241}Am no recombination

(j) ^{90}Sr no recombination

Figure D.4 Plot I/II: Comparison of recombination models with ^{241}Am (left row) and ^{90}Sr (right row). For ^{241}Am the colored plot shows the data and the black scatter plot the MC overlaid. For ^{90}Sr only the MC is shown.

D.2 ^{42}K Suppression

(a) A/E versus E
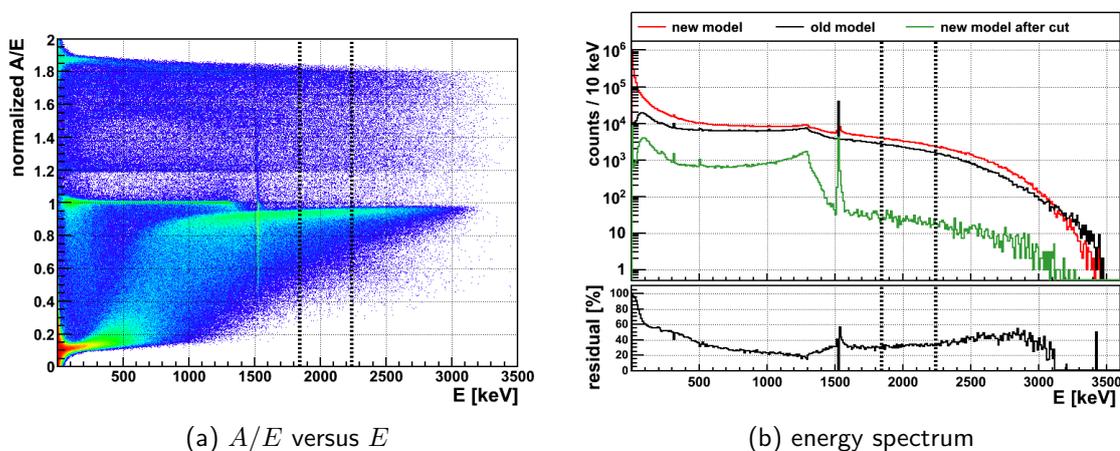
(b) energy spectrum

Figure D.5   Comparison of $^+$ models with simulated ^{42}K decays on the detector surface. Left: A/E versus E spectrum of simulated ^{42}K decays with the new model. Right: Energy spectrum with the new model (red), the old model (black) and the new model after A/E cut (green). The residual refers to the unsuppressed new and old model.

(a) wide

(b) zoom
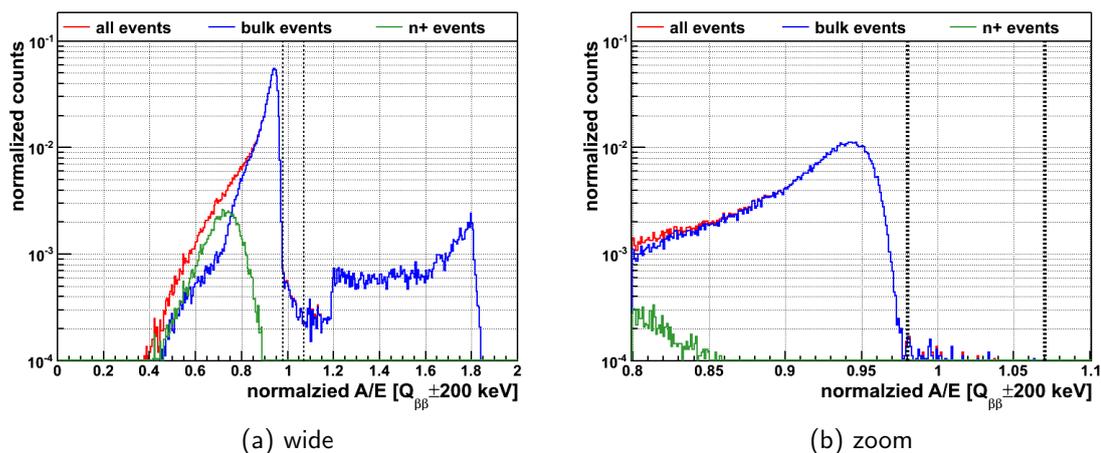
Figure D.6 A/E spectra of ^{42}K decays on the detector surface in the energy range of $Q_{\beta\beta}\pm200$ keV as predicted by the new model (red). The events are separated into majority bulk events (blue) and majority n$^+$ events (green).

Table D.1 Suppression of ^{42}K decays on the surface of selected PHASE II BEGe detectors. The first two rows show the FCCD and the relative counts in $Q_{\beta\beta}\pm200$ keV compared to GD91C. The next three rows show the fraction of events after A/E cut separated in low A/E, SSB, and high A/E events. The last row shows the relative number of ^{42}K counts after A/E cut for the same number of simulated decays normalized to GD91C.

detector	GD35B	GD91C	GD02C	GD79C
FCCD [mm]	0.55	0.68	0.75	0.85
relative ^{42}K counts before cut [%]	125.6	100	88.9	73.3
$A/E > 1.1$ [%]	7.7 ± 0.1	10.8 ± 0.1	10.0 ± 0.1	11.3 ± 0.1
$0.98 < A/E < 1.07$ [%]	0.60 ± 0.02	0.69 ± 0.02	0.48 ± 0.02	0.56 ± 0.02
$A/E < 0.98$ [%]	91.7 ± 0.2	88.5 ± 0.3	89.5 ± 0.3	88.1 ± 0.3
relative ^{42}K counts after cut [%]	109.2	100	61.8	59.5

Table D.2 Suppression of ^{42}K decays on the surface of hypothetical BEGe detectors with different FCCD. The first rows show the FCCD. The second row shows the number of ^{42}K events in the energy range of $Q_{\beta\beta}\pm200$ keV when sampled in a LAr volume 6 cm around the detector. The third row shows the survival fraction of those events with an A/E cut of $0.98 < A/E < 1.07$. The forth row shows the fully active volume fraction equivalent to the detection efficiency of $0\nu\beta\beta$ in this case. The last rows show 4 sensitivity scenarios taken as the ratio of FAV and background reduction as a figure of merit.

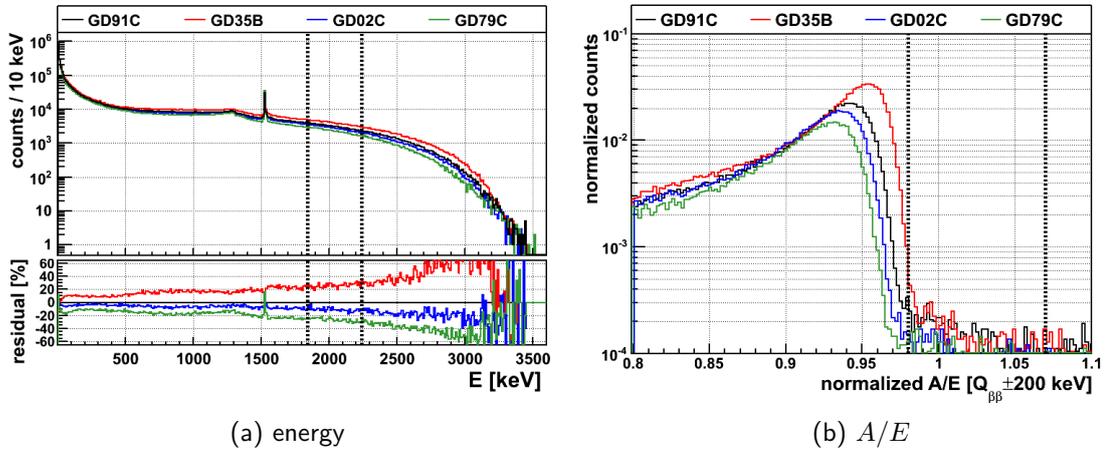| FCCD	0.50 mm	0.75 mm	1.00 mm	1.25 mm	1.50 mm
^{42}K events in ROI	71479	44924	28885	17799	11627
A/E cut survival [%]	0.93 ± 0.04	0.78 ± 0.04	0.72 ± 0.05	0.89 ± 0.07	1.15 ± 0.10
FAV [%]	94.0	91.1	88.3	85.5	82.8
1. Sensitivity: ^{42}K only	0.75	1	1.26	1.40	1.47
2. Sensitivity PHASE I like	1.03	1	0.97	0.94	0.91
3. Sensitivity PHASE II like	0.98	1	0.99	0.98	0.95
4. Sensitivity Ge 1 t like	0.83	1	1.12	1.15	1.15

(a) energy

(b) A/E

Figure D.7 Comparison of ^{42}K decays on the surface of selected PHASE II detectors. The energy spectrum is shown left and the A/E spectrum in $Q_{\beta\beta}\pm200$ keV is shown right. The residuals in the energy spectra are defined with respect to the energy spectrum of GD91C.
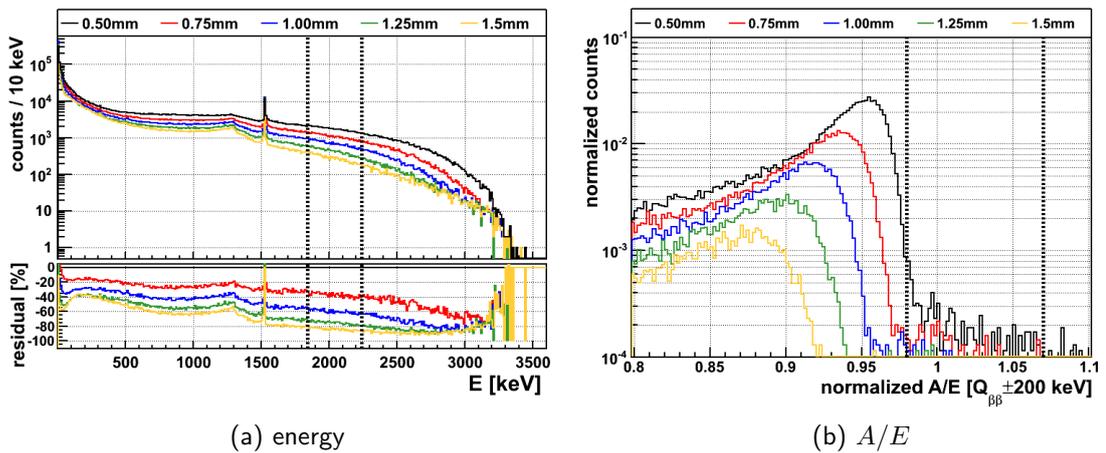

(a) energy

(b) A/E

Figure D.8 Comparison of ^{42}K decays on the surface of hypothetical BEGe detectors with different FCCD based on the geometry of GD91C. Shown are the energy spectra (left) and the A/E spectra in $Q_{\beta\beta}\pm200$ keV (right) for different FCCD values indicated in the legend. The residuals in the energy spectra are defined with respect to the 0.5 mm FCCD case.

Appendix E

Background Study for a LAr Scintillation Veto in Phase II

(a) Fiber shroud: ^{208}Tl holders

(b) PMT array: ^{208}Tl holders

(c) Fiber shroud: ^{214}Bi holders

(d) PMT array: ^{214}Bi holders

(e) Fiber shroud: ^{214}Bi homogeneously

(f) PMT array: ^{214}Bi homogeneously
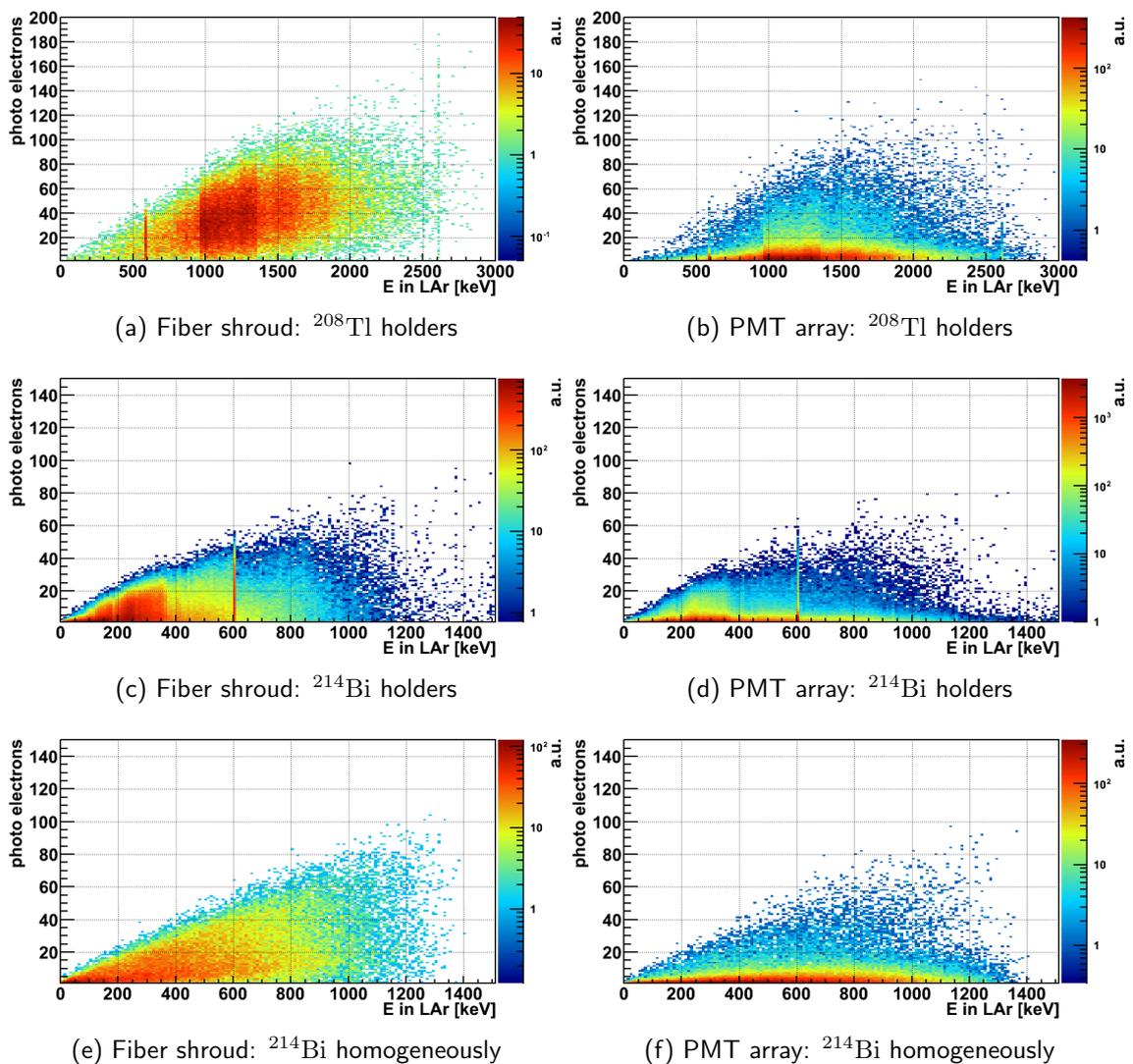
Figure E.1 (I/II) Photo electrons versus energy deposited in the LAr for events in $Q_{\beta\beta} \pm 200$ keV for the Fiber shroud (left row) and the PMT array (right row).

(a) Fiber shroud: ^{42}K homogeneously

(b) PMT array: ^{42}K homogeneously

(c) Fiber shroud: ^{60}Co internal

(d) PMT array: ^{60}Co internal

(e) Fiber shroud: ^{68}Ga internal

(f) PMT array: ^{68}Ga internal
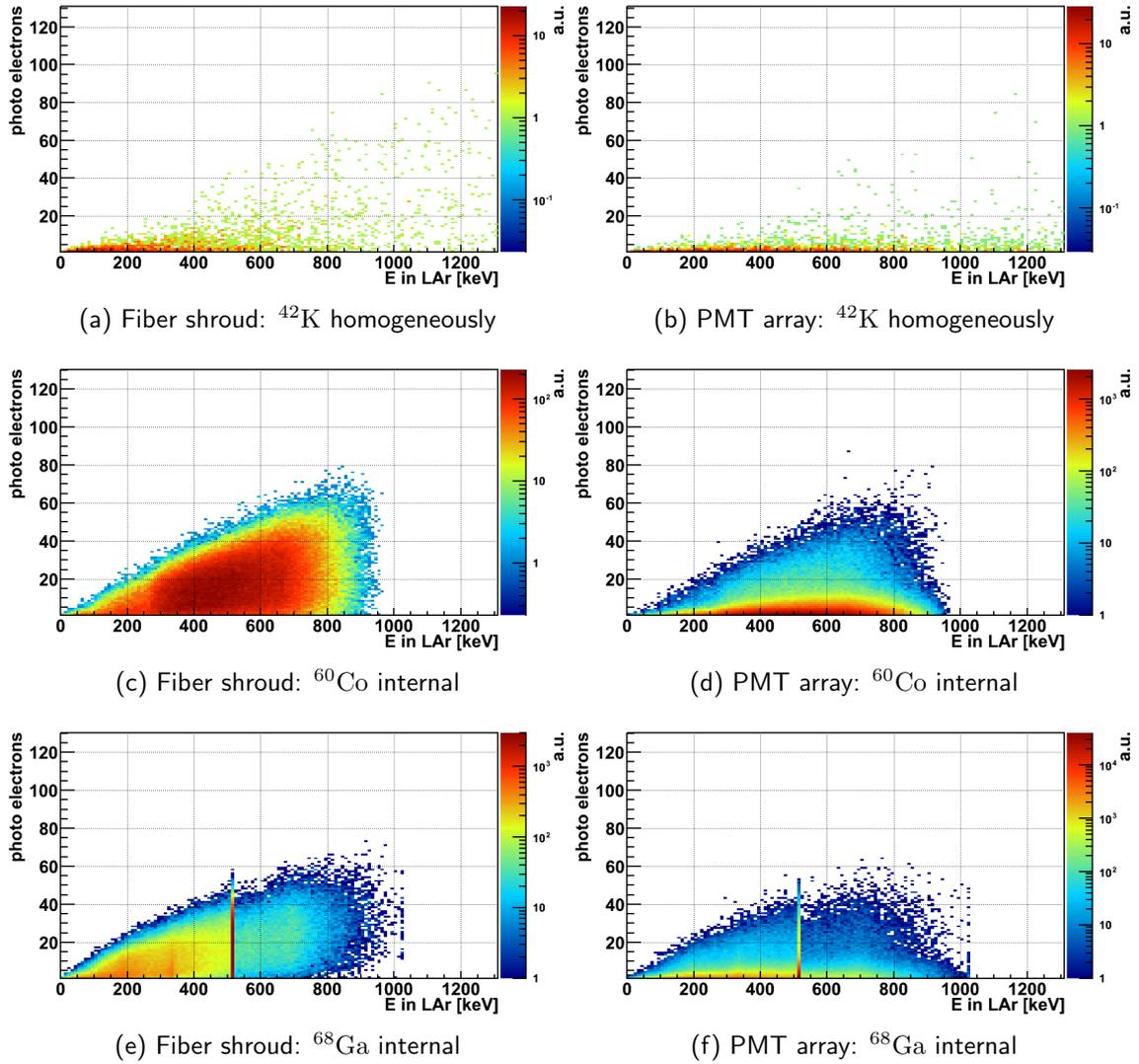
Figure E.2 (II/II) Photo electrons versus energy deposited in the LAr for events in $Q_{\beta\beta}\pm200$ keV for the Fiber shroud (left row) and the PMT array (right row).

Appendix F

Search for $2\nu\beta\beta$ Excited State Transition in ^{76}Ge

(a) $2\nu\beta\beta$ $0^+_{\text{g.s.}} - 2^+_1$

(b) $2\nu\beta\beta$ $0^+_{\text{g.s.}} - 0^+_1$

(c) $2\nu\beta\beta$ $0^+_{\text{g.s.}} - 2^+_2$ branch 1

(d) $2\nu\beta\beta$ $0^+_{\text{g.s.}} - 2^+_2$ branch 2
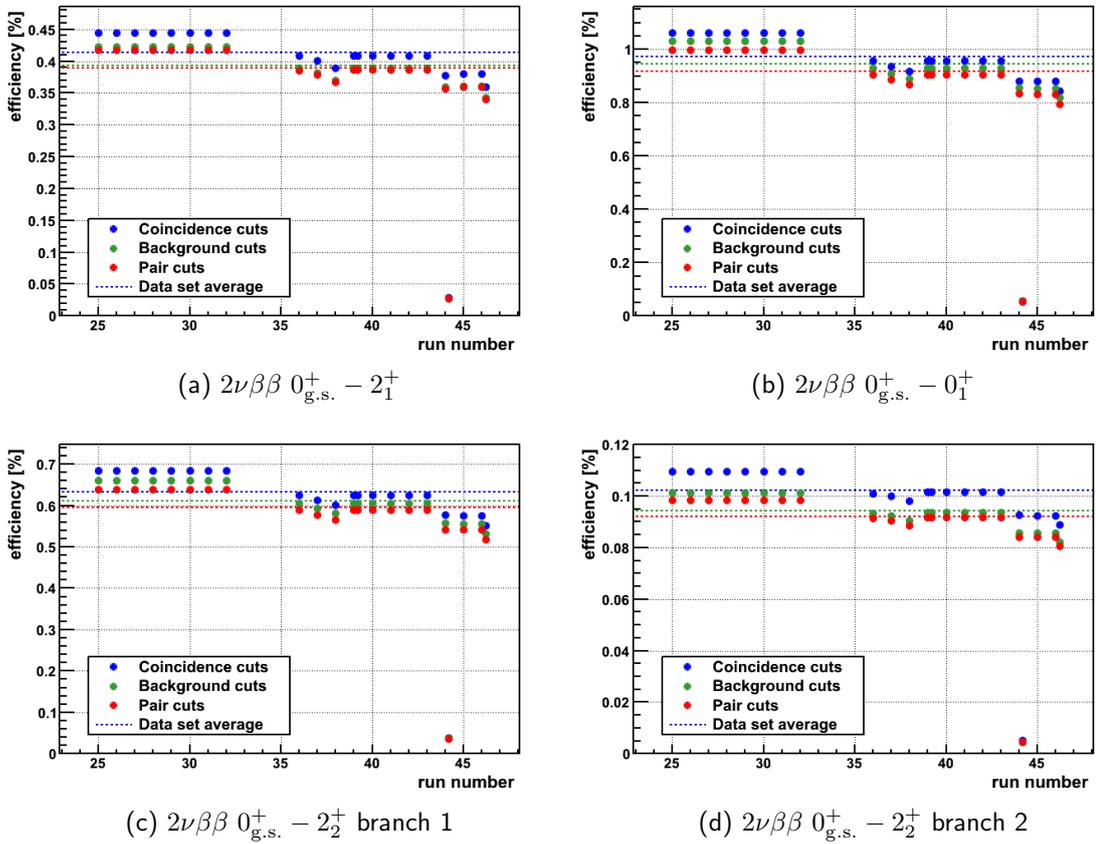
Figure F.1 Efficiency evolution during PHASE I of the GERDA array for decay modes and brances. The efficiency is plotted against the run number for the coincidence cuts (blue), with additional background cuts (green) and with additional pair cuts (red). The dashed lines are the live-time weighted averages for the considered dataset.

(a) angular correlation.   (b) angular distribution.
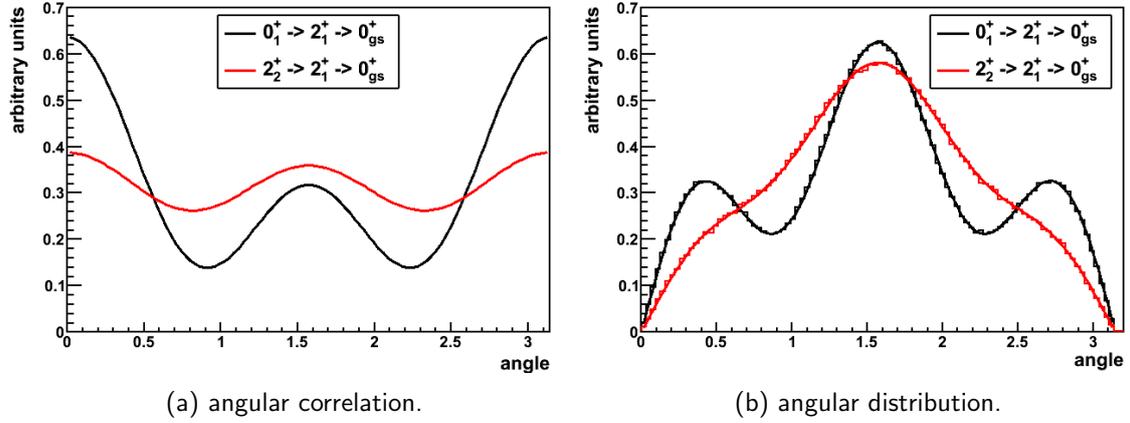
Figure F.2 Angular dependencies for two-gammas cascade in $0^+_{g.s.} - 0^+_1$ (black) and $0^+_{g.s.} - 2^+_2$ branch 1 (red). Left: Angular correlation between two gammas. Right: Distribution of gamma emissions with a given angle. The solid lines are the angular correlation convolved with the solid angle. The histograms show the sampling of 10^6 events with a modified version of the MC event generator DECAY0.
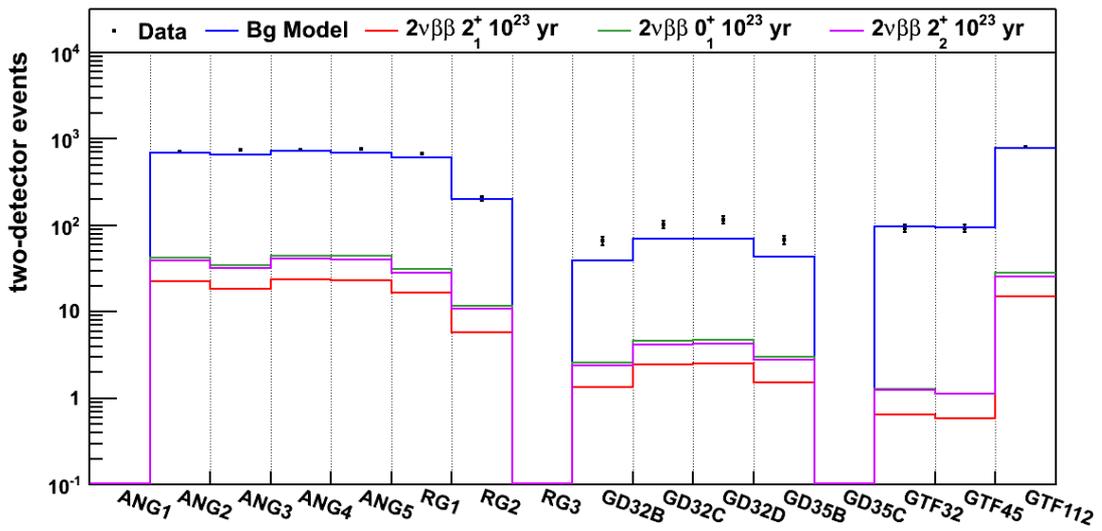
Figure F.3 Detector distribution of two-detector events with 100 keV SDT in data, background model and expected signal processes with 10^{23} yr half-life. The histograms contains two entries per event.

(a) $0\nu\beta\beta$ $0^+_{\mathrm{g.s.}} - 2^+_1$ transition.

(b) $0\nu\beta\beta$ $0^+_{\mathrm{g.s.}} - 0^+_1$ transition.

(c) $0\nu\beta\beta$ $0^+_{\mathrm{g.s.}} - 2^+_2$ branch 1 transition.
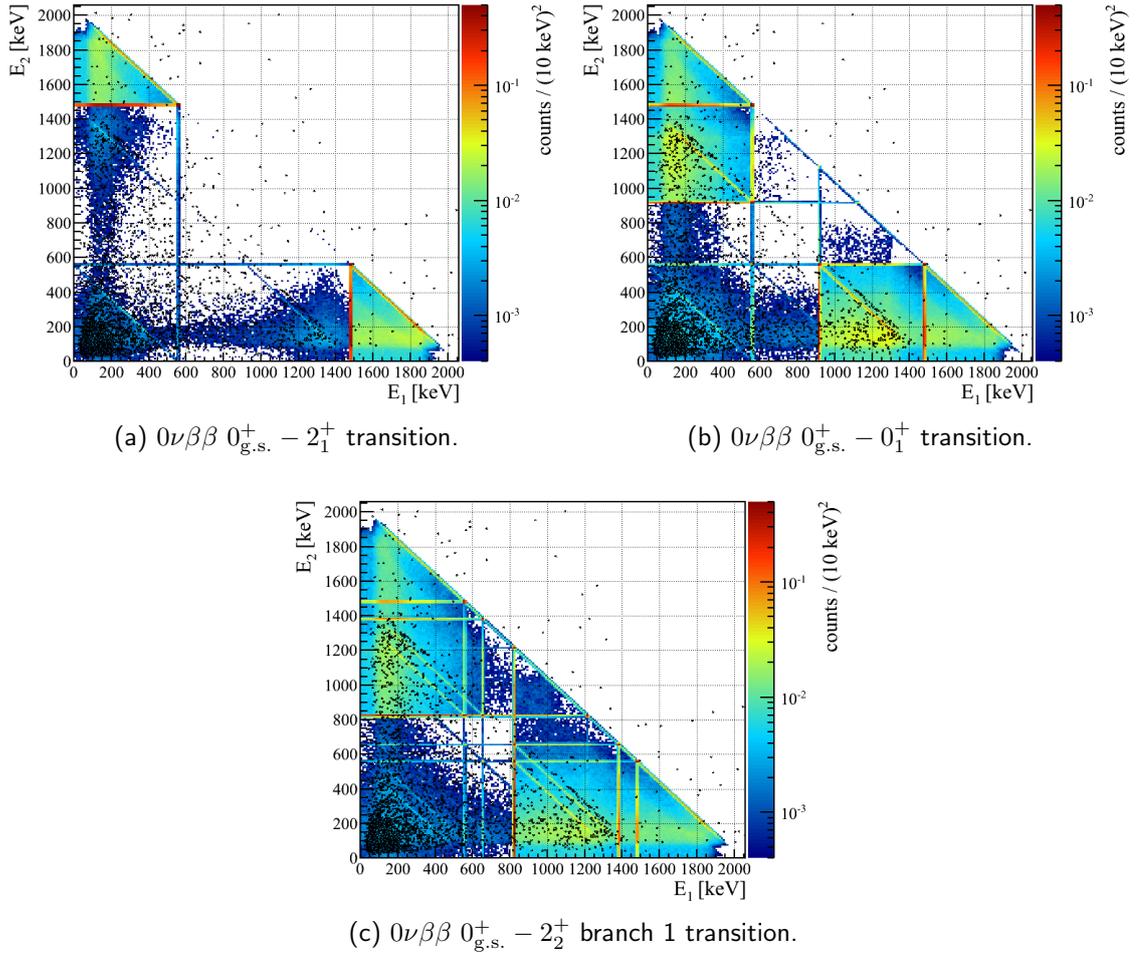
Figure F.4 Two-detector event energy-energy correlations showing the simulated $0\nu\beta\beta$ decay for the 2^+_1, 0^+_1, 2^+_2 decay modes in (a), (b) and (c) respectively. Also the simulated background model is shown (d). Simulated events are shown in color and the GERDA PHASE I data events in black. The number of simulated events is scaled to the PHASE I dataset and scaled to a half-life of 10^{23} yr.

(a) pbb2 2^+_1 sensitivity map

(b) pbb2 2^+_1 scan of cut

(c) 2^+_2 branch 1 sensitivity map

(d) 2^+_2 branch 1 scan of cut

(e) 2^+_2 branch 2 sensitivity map

(f) 2^+_2 branch 2 scan of cut
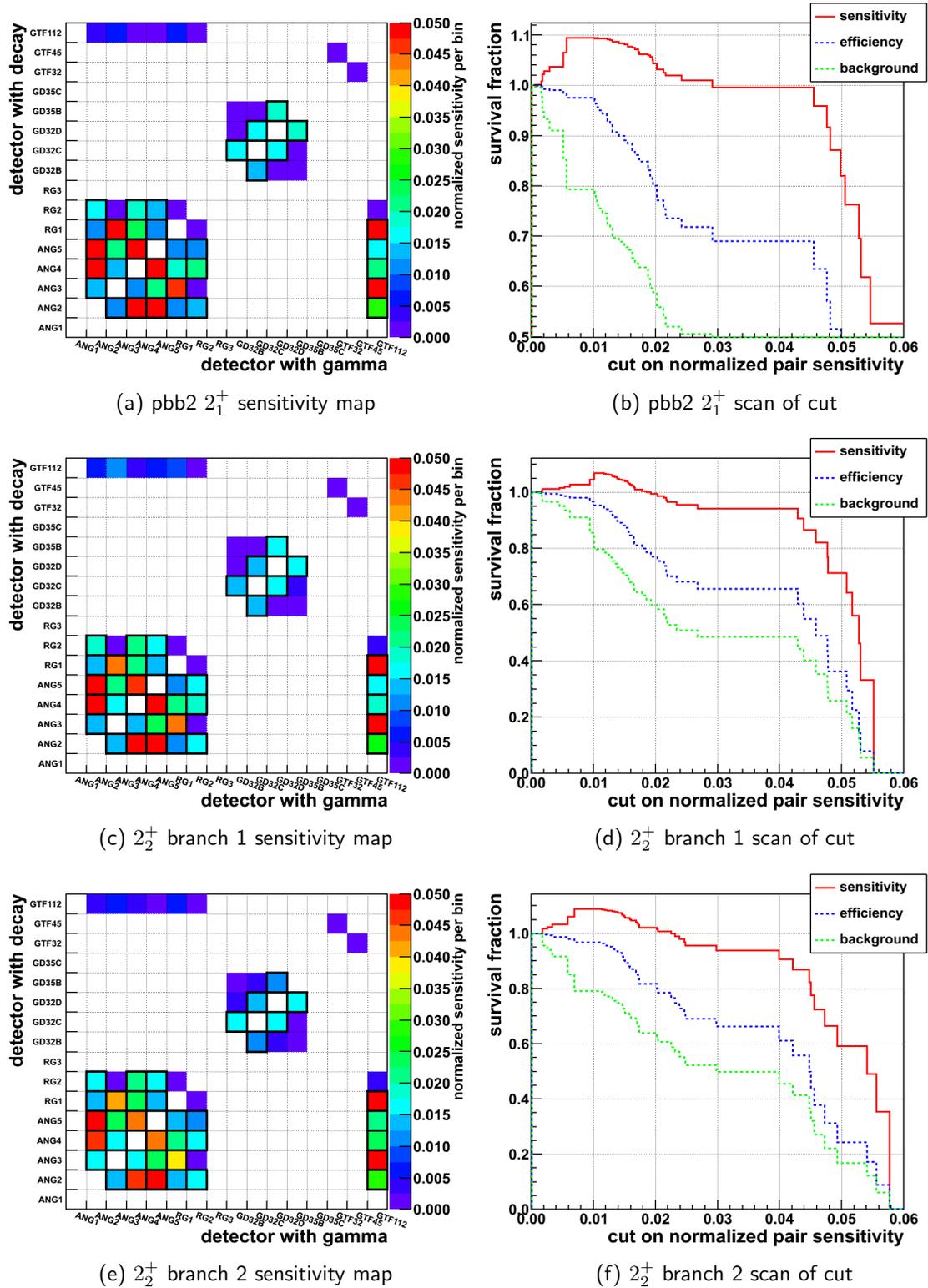
Figure F.5   Map of sensitivities for individual detector pairs with distinguished "gamma" and "source" detector (left). The detector pair contribution cut results in different detector pair selections; the sensitivity, signal efficiency and background for such selections is plotted against the contribution cut with a relative threshold between 0 % and 6 % (right). These values are normalized to the selection of all pairs (i.e. no cut). The surviving pairs for the optimized cut threshold are framed in the sensitivity map.

(a) $2\nu\beta\beta$ $0^+_{\text{g.s.}} - 2^+_1$ transition.

(b) $2\nu\beta\beta$ $0^+_{\text{g.s.}} - 0^+_1$ transition.

(c) $2\nu\beta\beta$ $0^+_{\text{g.s.}} - 2^+_2$ transition ROI 1.

(d) $2\nu\beta\beta$ $0^+_{\text{g.s.}} - 2^+_2$ transition ROI 2.

(e) $2\nu\beta\beta$ $0^+_{\text{g.s.}} - 2^+_2$ transition ROI 3.
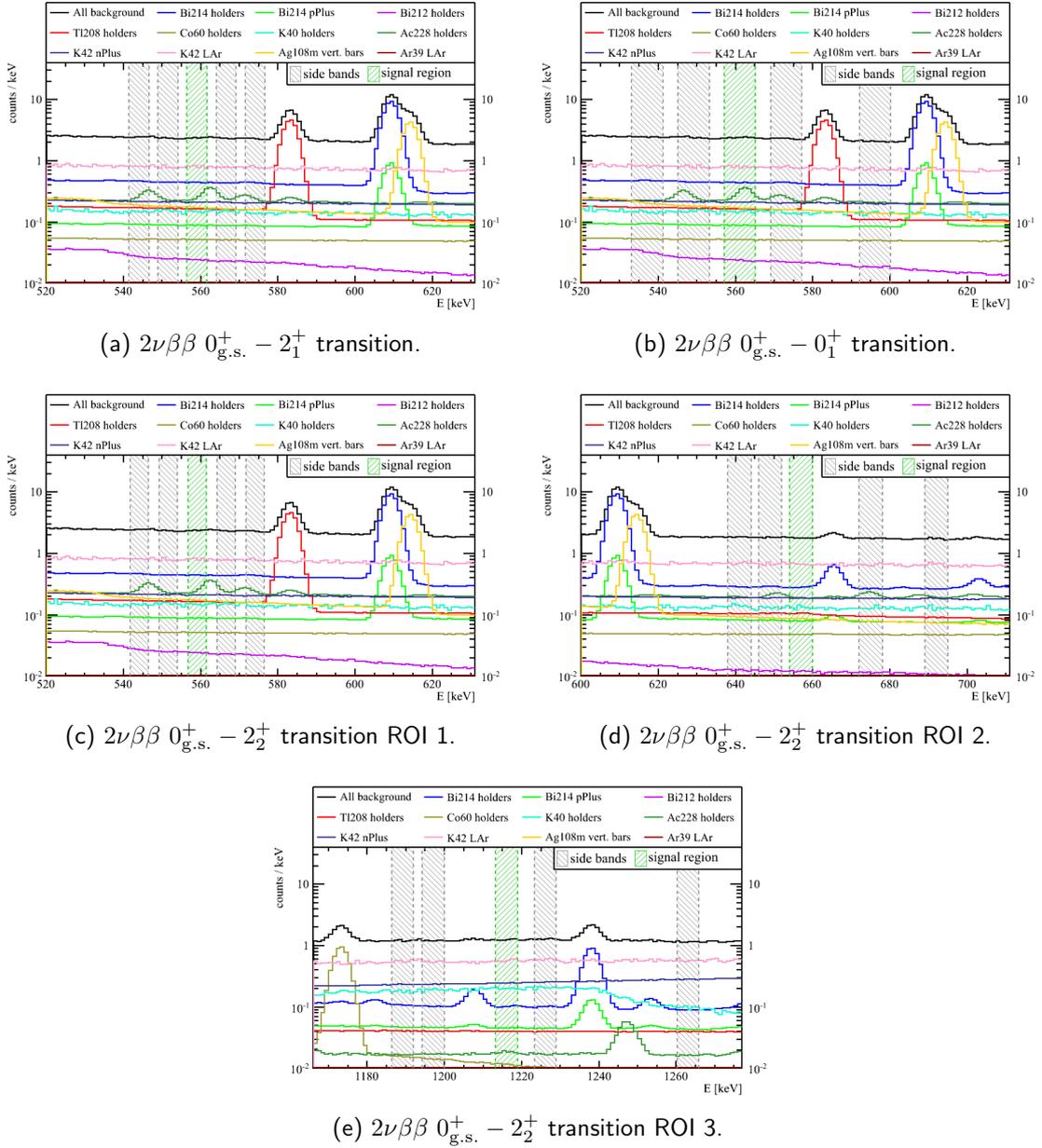
Figure F.6 Decomposition of MC background model around region of interests. These plots are used to select the side bands and verify the absence of prominent background γ-lines and the flatness of the background. Shown are the single detector energies of two detector events with a single detector threshold of 100 keV and a sum energy limit of 2039 keV for each decay mode. Only the contribution of the semi-coaxial detectors are shown for simplicity. The selected side bands are shown in gray whereas ROI is shown in green.

Table F.1 List of surviving events for $2\nu\beta\beta$ $2^+_{\text{g.s.}} - 2^+_1$. The last column denotes the cut level that is survived: (1) coincidence cuts, (2) additional background cuts and (3) additional pair cuts.

run	timestamp	E_1 [keV]	ID_1	E_2 [keV]	ID_2	E_{sum} [keV]	cut level
Run26	1325647732	615.0	RG1	557.0	GTF112	1172.0	1
Run32	1335943060	558.8	ANG3	966.1	GTF112	1524.9	1
Run36	1345032530	561.5	ANG3	563.8	RG1	1125.3	3
Run37	1346955931	559.8	ANG2	554.2	GTF112	1114.0	2
Run38	1348944227	769.4	ANG5	557.8	RG1	1327.2	3
Run41	1355708304	612.2	ANG3	561.4	ANG5	1173.6	1

Table F.2 List of surviving events for $2\nu\beta\beta$ $0^+_{\text{g.s.}} - 0^+_1$. The last column denotes the cut level that is survived: (1) coincidence cuts, (2) additional background cuts and (3) additional pair cuts.

run	timestamp	E_1 [keV]	ID_1	E_2 [keV]	ID_2	E_{sum} [keV]	cut level
Run26	1325647732	615.0	RG1	557.0	GTF112	1172.0	1
Run30	1331090308	558.2	ANG5	309.8	GTF112	868.0	2
Run32	1335943060	558.8	ANG3	966.1	GTF112	1524.9	1
Run36	1345032530	561.5	ANG3	563.8	RG1	1125.3	3
Run36	1346336163	559.7	ANG2	323.1	ANG5	882.8	3
Run37	1346955931	559.8	ANG2	554.2	GTF112	1114.0	2
Run37	1347127032	563.0	ANG3	373.1	ANG5	936.2	3
Run38	1348944227	769.4	ANG5	557.8	RG1	1327.2	3
Run40	1354579657	565.1	ANG3	577.8	GTF112	1142.9	2
Run41	1355708304	612.2	ANG3	561.4	ANG5	1173.6	1
Run41	1356810423	801.9	ANG2	562.4	ANG4	1364.4	3
Run42	1358873777	564.2	ANG3	513.0	GTF112	1077.2	2
Run44	1363394756	563.3	ANG3	438.3	GTF112	1001.6	2

Table F.3 List of surviving events for $2\nu\beta\beta$ $2^+_{\text{g.s.}} - 2^+_2$ branch 1. The last column denotes the cut level that is survived: (1) coincidence cuts, (2) additional background cuts and (3) additional pair cuts.

run	timestamp	E_1 [keV]	ID_1	E_2 [keV]	ID_2	E_{sum} [keV]	cut level
Run25	1322045910	295.1	ANG3	657.9	GTF112	952.9	3
Run26	1325647732	615.0	RG1	557.0	GTF112	1172.0	1
Run30	1331090308	558.2	ANG5	309.8	GTF112	868.0	2
Run31	1334314022	658.5	ANG4	431.7	RG2	1090.2	3
Run32	1335943060	558.8	ANG3	966.1	GTF112	1524.9	1
Run36	1345624897	658.6	GD32B	298.7	GD32C	957.3	3
Run36	1345713741	299.7	ANG2	657.3	ANG5	957.0	3
Run36	1346336163	559.7	ANG2	323.1	ANG5	882.8	3
Run37	1346955931	559.8	ANG2	554.2	GTF112	1114.0	2
Run38	1348944227	769.4	ANG5	557.8	RG1	1327.2	3
Run39a	1349996619	658.4	ANG5	510.2	GTF112	1168.6	2
Run40	1355200496	655.1	RG1	898.4	GTF112	1553.4	2
Run41	1355708304	612.2	ANG3	561.4	ANG5	1173.6	1

Table F.4 List of surviving events for $2\nu\beta\beta$ $2^+_{\text{g.s.}} - 2^+_2$ branch 2. The last column denotes the cut level that is survived: (1) coincidence cuts, (2) additional background cuts and (3) additional pair cuts.

run	timestamp	E_1 [keV]	ID_1	E_2 [keV]	ID_2	E_{sum} [keV]	cut level
Run36	1344008817	1215.9	RG1	307.6	GTF112	1523.5	1
Run36	1346352917	1217.6	ANG4	308.8	RG1	1526.4	1
Run44	1364133802	1217.6	ANG3	302.9	GTF112	1520.5	1

(a) PL: $2\nu\beta\beta$ $0^+_{\text{g.s.}} - 2^+_1$.

(b) PL: $2\nu\beta\beta$ $0^+_{\text{g.s.}} - 0^+_1$.

(c) PL: $2\nu\beta\beta$ $0^+_{\text{g.s.}} - 2^+_2$.

(d) B: $2\nu\beta\beta$ $0^+_{\text{g.s.}} - 2^+_1$.

(e) B: $2\nu\beta\beta$ $0^+_{\text{g.s.}} - 0^+_1$.

(f) B: $2\nu\beta\beta$ $0^+_{\text{g.s.}} - 2^+_2$.
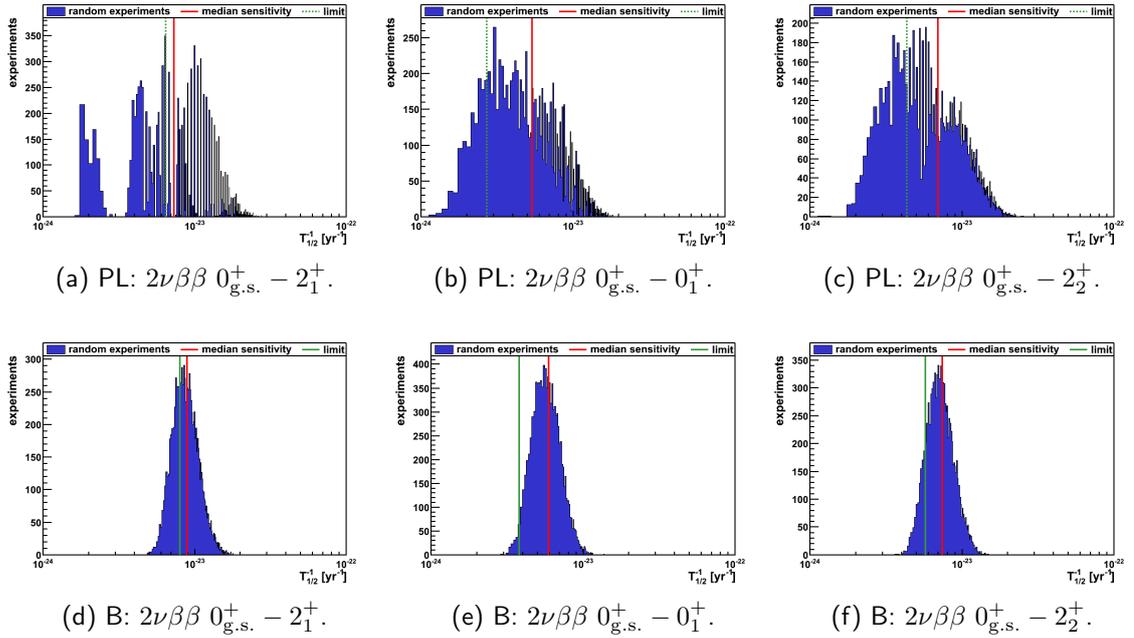
Figure F.7 Sensitivity estimation for all decay modes with the profile likelihood (PL) and Bayesian (B) analysis. The histograms show the distribution of 10.000 lower half-life limits under the zero signal hypothesis with randomly varied input parameters n_k, m_k, ϵ_k. The red vertical line shows the median of the distribution which is defined as the sensitivity. The green vertical line shows the half-life limit for comparison. Note that the x-axis is in log scale which results in smaller bin sizes for higher inverse half-lives.
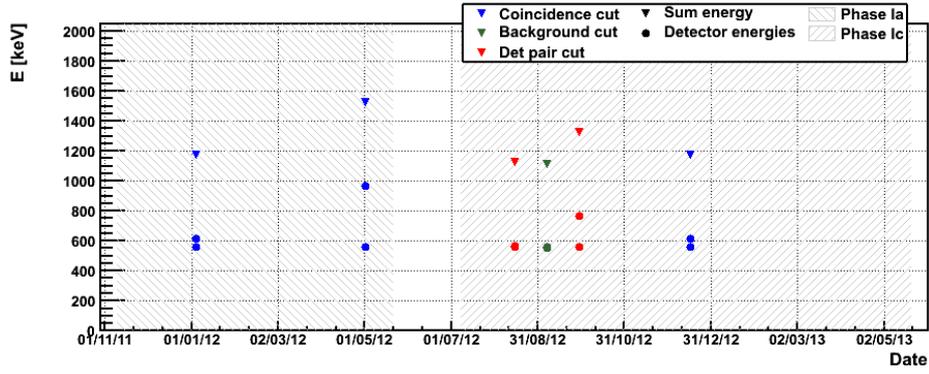
(a) $2\nu\beta\beta$ $0^+_{\text{g.s.}} - 2^+_1$
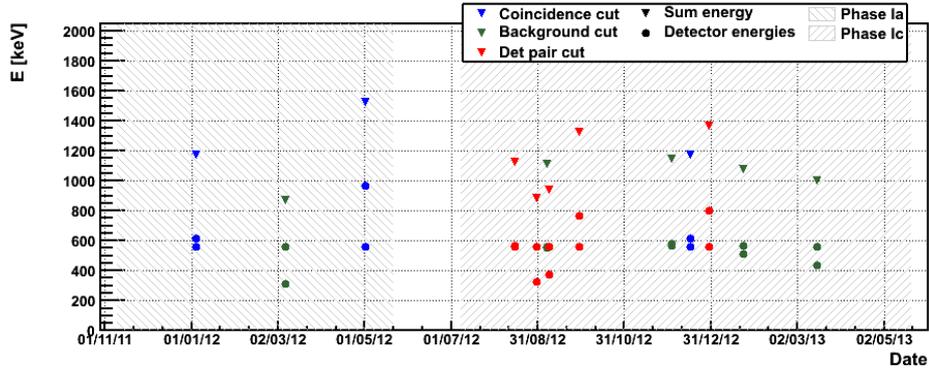
(b) $2\nu\beta\beta$ $0^+_{\text{g.s.}} - 0^+_1$
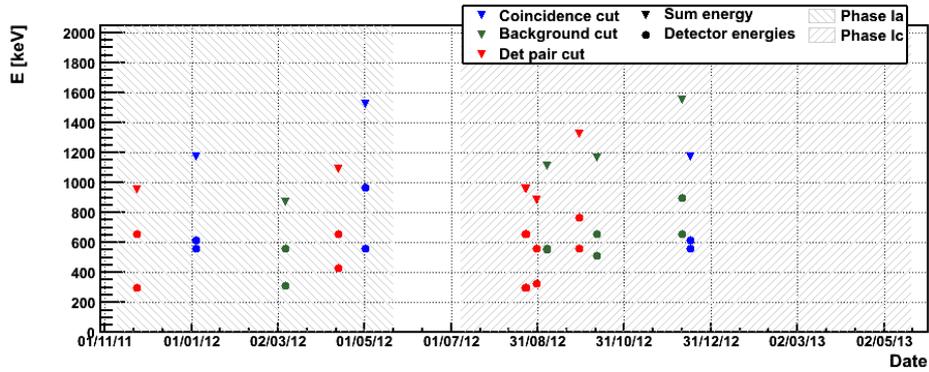
(c) $2\nu\beta\beta$ $0^+_{\text{g.s.}} - 2^+_2$
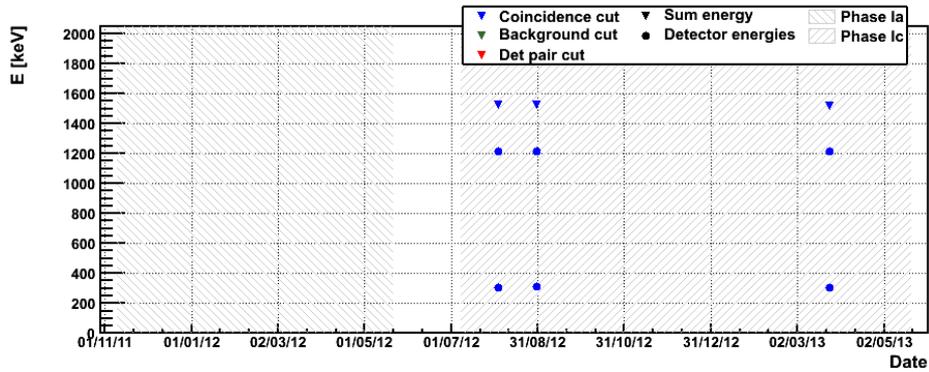
(d) $2\nu\beta\beta$ $0^+_{\text{g.s.}} - 2^+_2$

Figure F.8 Time distribution for $2\nu\beta\beta$ excited state candidate events separated for all decay modes. For each event the two detector energies are shown as circles and their sum energy as a triangle. The survived cut level is color coded for the coincidence cuts (blue), with additional background cuts (green) and with additional pair cuts (red).
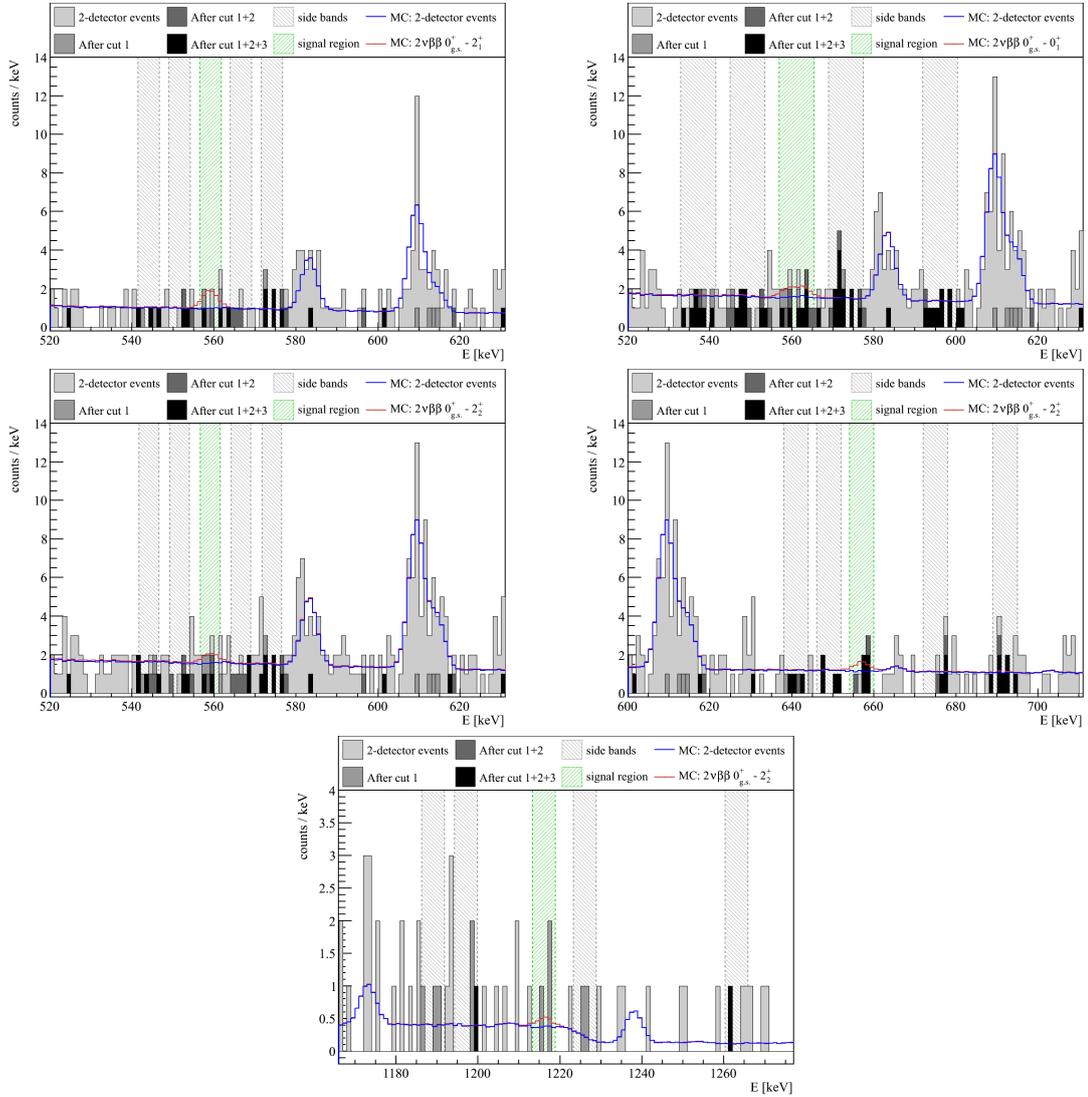
Figure F.9 Single energy spectra around the ROI for all decay modes. Shown are all two-detector events for the optimized single detector threshold and sum energy limit (light gray) and the corresponding background curves (black). The optimized cuts result in different two-detector spectra for each decay mode. Also shown are the ROI (shaded red) and SB region (shaded blue). Highlighted are events that are tagged as ROI (red) and SB (blue) after all cuts and are used for the limit setting. Note that the histograms contain two entries per event and that one entry may lie outside the tagging region.

Table F.5 Run and detector summary for considered dataset. Black numbers denote: detector and source; red numbers: source only; no number: detector not

exposure time [d]		ANG1	ANG2	ANG3	ANG4	ANG5	RG1	RG2	RG3	GD32B	GD32C	GD32D	GD35B	GD35C	GTF32	GTF45	GTF112
Run25	20.5	20.5	20.5	20.5	20.5	20.5	20.5	20.5	20.5	-	-	-	-	-	20.5	20.5	20.5
Run26	39.3	39.3	39.3	39.3	39.3	39.3	39.3	39.3	39.3	-	-	-	-	-	39.3	39.3	39.3
Run27	5.2	5.2	5.2	5.2	5.2	5.2	5.2	5.2	5.2	-	-	-	-	-	5.2	5.2	5.2
Run28	9.6	9.6	9.6	9.6	9.6	9.6	9.6	9.6	9.6	-	-	-	-	-	9.6	9.6	9.6
Run29	20.4	20.4	20.4	20.4	20.4	20.4	20.4	20.4	20.4	-	-	-	-	-	20.4	20.4	20.4
Run30	30.9	30.9	30.9	30.9	30.9	30.9	30.9	30.9	30.9	-	-	-	-	-	30.9	30.9	30.9
Run31	21.6	21.6	21.6	21.6	21.6	21.6	21.6	21.6	21.6	-	-	-	-	-	21.6	21.6	21.6
Run32	26.6	26.6	26.6	26.6	26.6	26.6	26.6	26.6	26.6	-	-	-	-	-	26.6	26.6	26.6
Run36	37.7	37.7	37.7	37.7	37.7	37.7	37.7	37.7	37.7	37.7	37.7	37.7	37.7	-	-	-	37.7
Run37	23.5	23.5	23.5	23.5	23.5	23.5	23.5	23.5	23.5	23.5	23.5	23.5	23.5	-	-	-	23.5
Run38	13.9	13.9	13.9	13.9	13.9	13.9	13.9	13.9	13.9	13.9	13.9	13.9	13.9	-	-	-	13.9
Run39a	15.3	15.3	15.3	15.3	15.3	15.3	15.3	15.3	15.3	15.3	15.3	15.3	15.3	-	-	-	15.3
Run39b	9.5	9.5	9.5	9.5	9.5	9.5	9.5	9.5	9.5	9.5	9.5	9.5	9.5	-	-	-	9.5
Run40	34.5	34.5	34.5	34.5	34.5	34.5	34.5	34.5	34.5	34.5	34.5	34.5	34.5	-	-	-	34.5
Run41	21.5	21.5	21.5	21.5	21.5	21.5	21.5	21.5	21.5	21.5	21.5	21.5	21.5	-	-	-	21.5
Run42	32.0	32.0	32.0	32.0	32.0	32.0	32.0	32.0	32.0	32.0	32.0	32.0	32.0	-	-	-	32.0
Run43	22.8	22.8	22.8	22.8	22.8	22.8	22.8	22.8	22.8	22.8	22.8	22.8	22.8	-	-	-	22.8
Run44a	1.4	1.4	1.4	1.4	1.4	1.4	1.4	1.4	1.4	1.4	1.4	1.4	1.4	-	-	-	1.4
Run44	22.8	22.8	22.8	22.8	22.8	22.8	22.8	22.8	22.8	22.8	22.8	22.8	22.8	-	-	-	22.8
Run45	33.1	33.1	33.1	33.1	33.1	33.1	33.1	33.1	33.1	33.1	33.1	33.1	33.1	-	-	-	33.1
Run46a	12.1	12.1	12.1	12.1	12.1	12.1	12.1	12.1	12.1	12.1	12.1	12.1	12.1	-	-	-	12.1
Run46b	5.6	5.6	5.6	5.6	5.6	5.6	5.6	5.6	5.6	5.6	5.6	5.6	5.6	-	-	-	5.6
$\sum$ exposure time [d]		459.9	459.9	459.9	459.9	459.9	459.9	459.9	459.9	285.8	285.8	285.8	285.8	285.8	174.1	174.1	459.9
Mass [kg]		0.958	2.833	2.391	2.375	2.746	2.113	2.168	2.087	0.717	0.743	0.723	0.812	0.635	2.321	2.312	2.957
Exposure [kg d]		440.58	1302.89	1099.62	1092.26	1262.88	971.77	997.06	959.81	204.92	212.35	206.64	232.08	181.49	404.07	402.50	1359.92
Abundance		0.859	0.864	0.881	0.863	0.856	0.874	0.874	0.874	0.877	0.877	0.877	0.877	0.877	0.078	0.078	0.078
^{76}Ge mass [kg]		0.823	2.449	2.108	2.050	2.351	1.847	1.895	1.825	0.629	0.652	0.634	0.712	0.557	0.182	0.181	0.232
^{76}Ge exposure [kg d]		378.55	1126.22	969.31	942.62	1081.03	849.62	871.73	839.16	179.72	186.23	181.22	203.53	159.16	31.64	31.52	106.48

Appendix G

Search for $0/2\nu\beta\beta$ Excited State Transition in ^{110}Pd and ^{102}Pd

G.1   Calculation of IBM-2 Half-Life Prediction for ^{110}Pd

The $2\nu\beta\beta$ decay half-life for the ^{110}Pd 0_1^+ transition is calculated as

$$\left[T_{1/2}^{2\nu}\right]^{-1} = G^{2\nu} \cdot \left|\mathcal{M}^{2\nu}\right|^2 \qquad \text{with} \qquad \mathcal{M}^{2\nu} = -g_A^2 \cdot m_e c^2 \cdot \left[\frac{\mathcal{M}_{GT}}{\widetilde{A}_{GT}}\right] \qquad \text{(G.1)}$$

with the PSF, $G^{2\nu}$, taken as $0.004842 \cdot 10^{-21}\,\mathrm{yr}^{-1}$ [34]. The Gamov-Teller component of the NME, $\mathcal{M}_{GT}$, is taken from the new IBM-2 calculation with isospin restoration as 0.38 [44] which naturally eliminates the Fermi component for $2\nu\beta\beta$ decay. $\widetilde{A}_{GT}$ is the closure energy and taken from TABLE XVI in Ref. [49] as 11.8 for ^{110}Pd. g_A is the axial-vector coupling and taken as $g_A = 1.269$ and $m_e c^2$ is a normalization defined as $0.511\,\mathrm{MeV}$. The half-life prediction for the $2\nu\beta\beta$ decay of ^{110}Pd into the excited 0_1^+ states is $T_{1/2}^{2\nu} = 2.9 \cdot 10^{26}$ yr. Note that there are indications from measured $2\nu\beta\beta$ decays into the ground state of other isotopes that the g_A value might be quenched which can significantly reduce the half-life predictions [44]. With $g_A = 0.7$ the half-life prediction changes to $T_{1/2}^{2\nu} = 3.2 \cdot 10^{27}$ yr.

For the ground state transition of ^{110}Pd, $G^{2\nu}$ is $137.7 \cdot 10^{-21}\,\mathrm{yr}^{-1}$ [34], $\mathcal{M}_{GT}$ is 3.08 [44] and the predicted half-life for $g_A = 1.269$ is $T_{1/2}^{2\nu} = 1.5 \cdot 10^{20}$ yr. With $g_A = 0.7$ the half-life prediction changes to $T_{1/2}^{2\nu} = 1.7 \cdot 10^{21}$ yr.
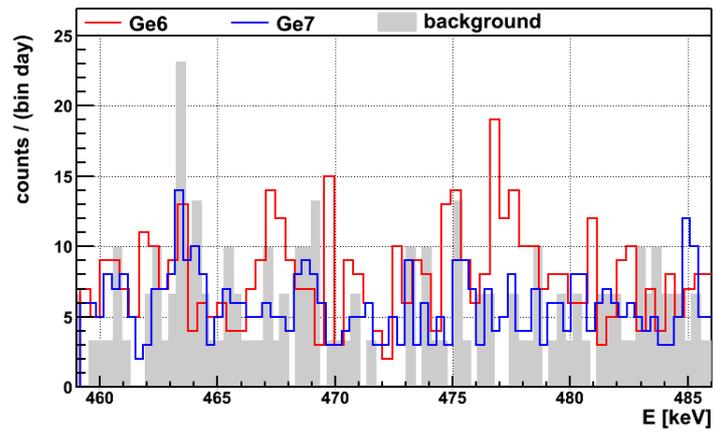
Figure G.1   Zoom into the ROI of ^{102}Pd 2_1^+, 0_1^+ and 2_2^+ transitions in the HADES dataset with problematic background. Shown are the individual spectra of both germanium detectors in original binning of the MCA DAQ. Also shown is a live-time scaled background measurement in shaded gray.
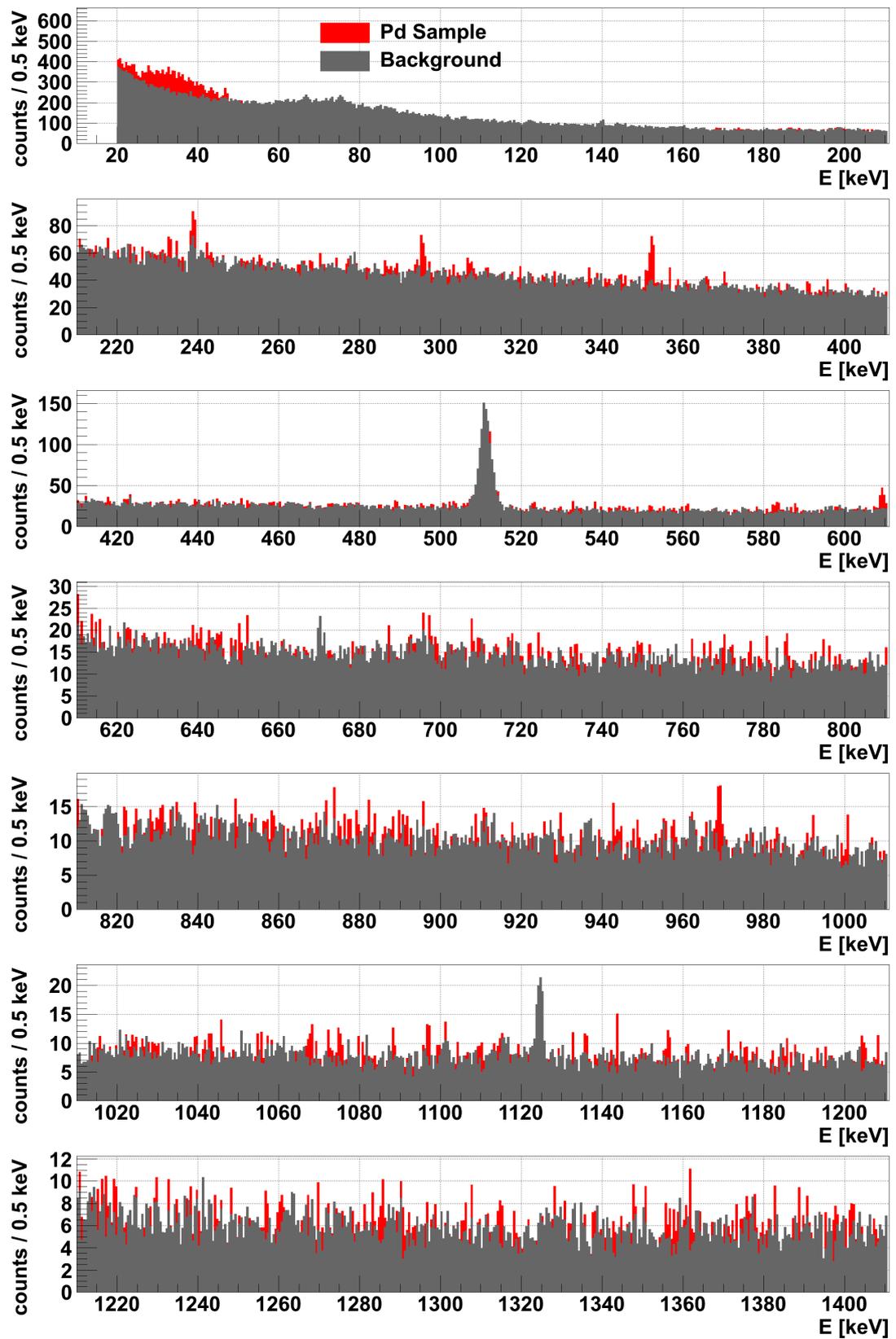
Figure G.2 Felsenkeller dataset 1 of 2. Comparison of palladium sample and background spectrum. The background spectrum is scaled to the live-time of the of the sample spectrum.
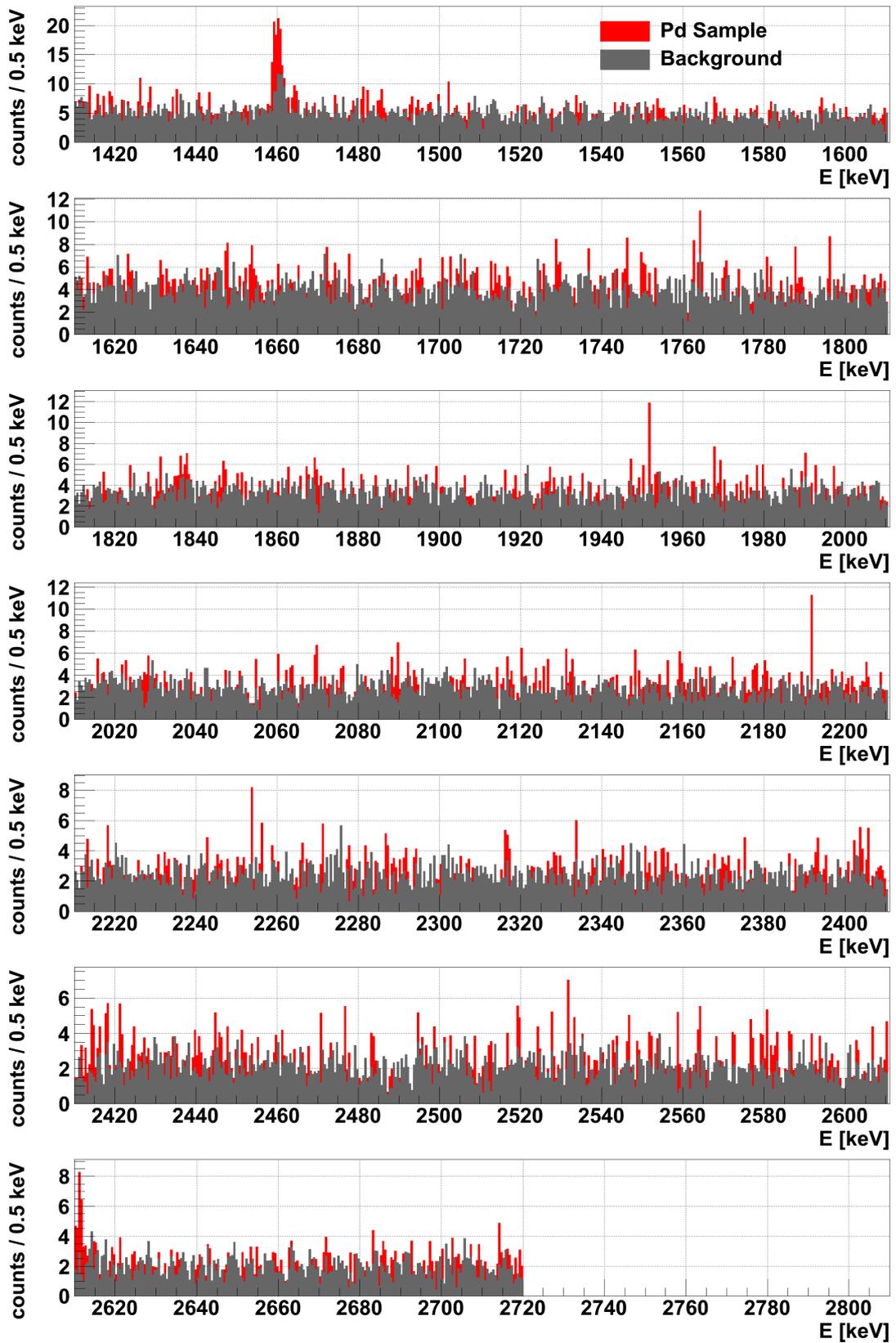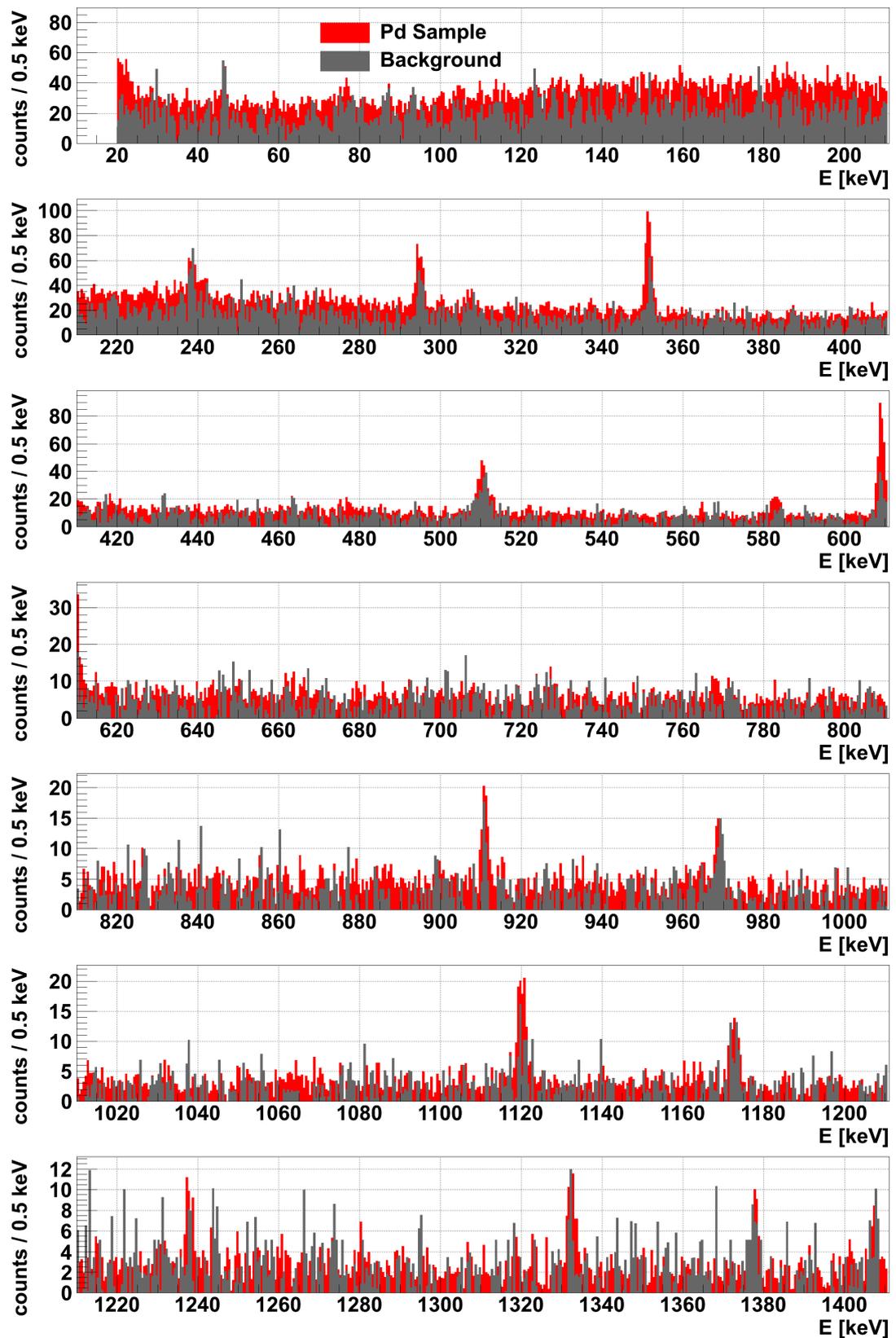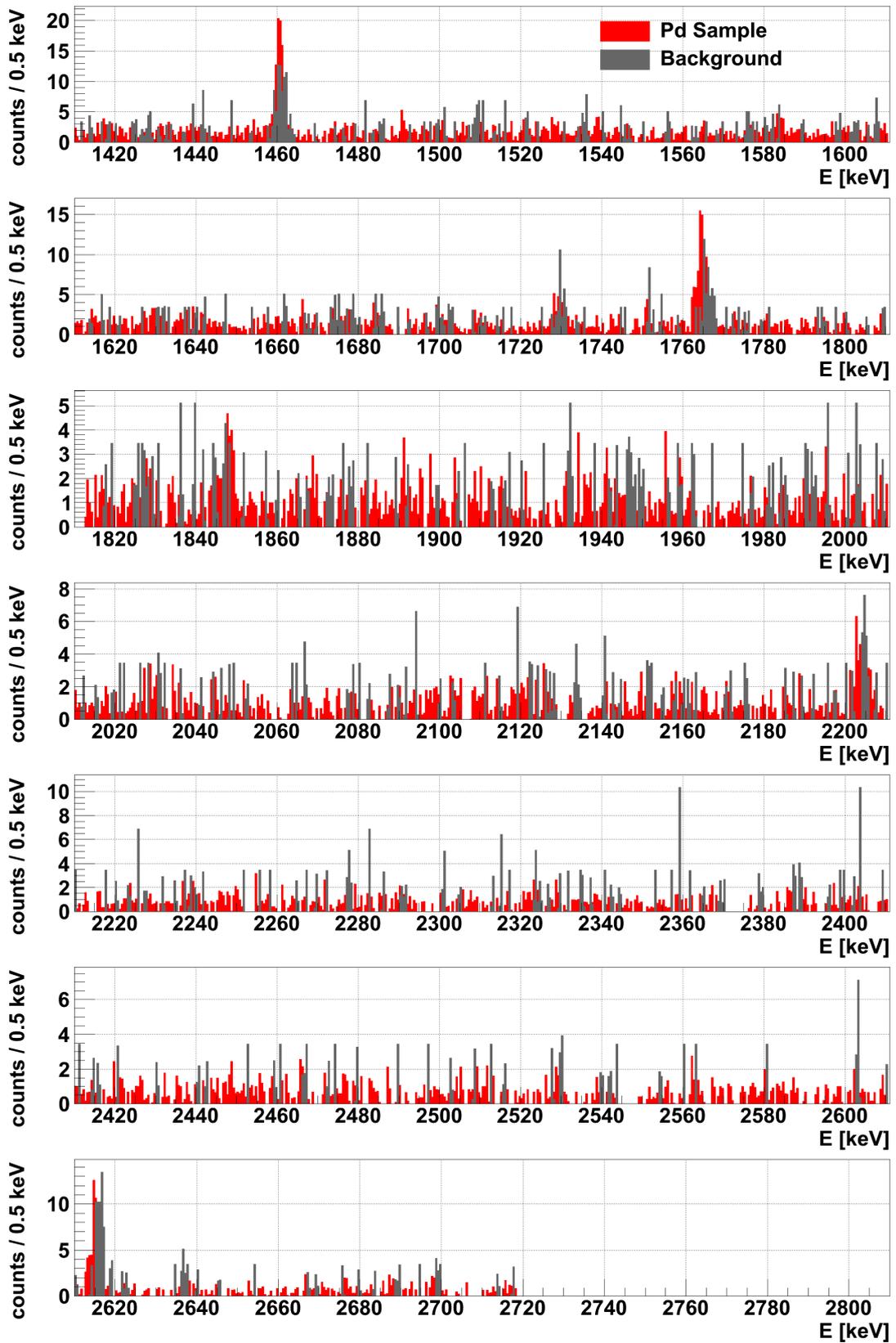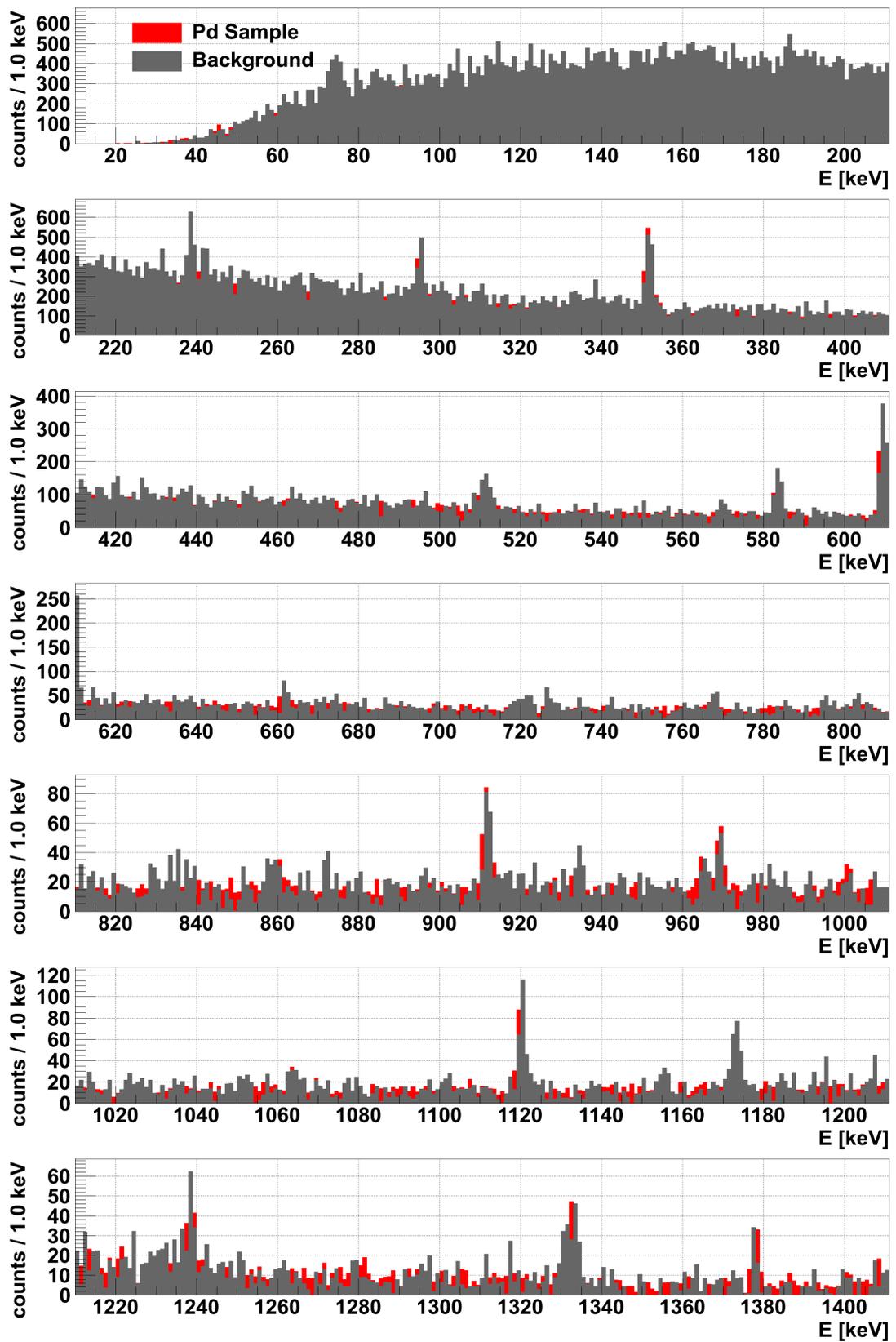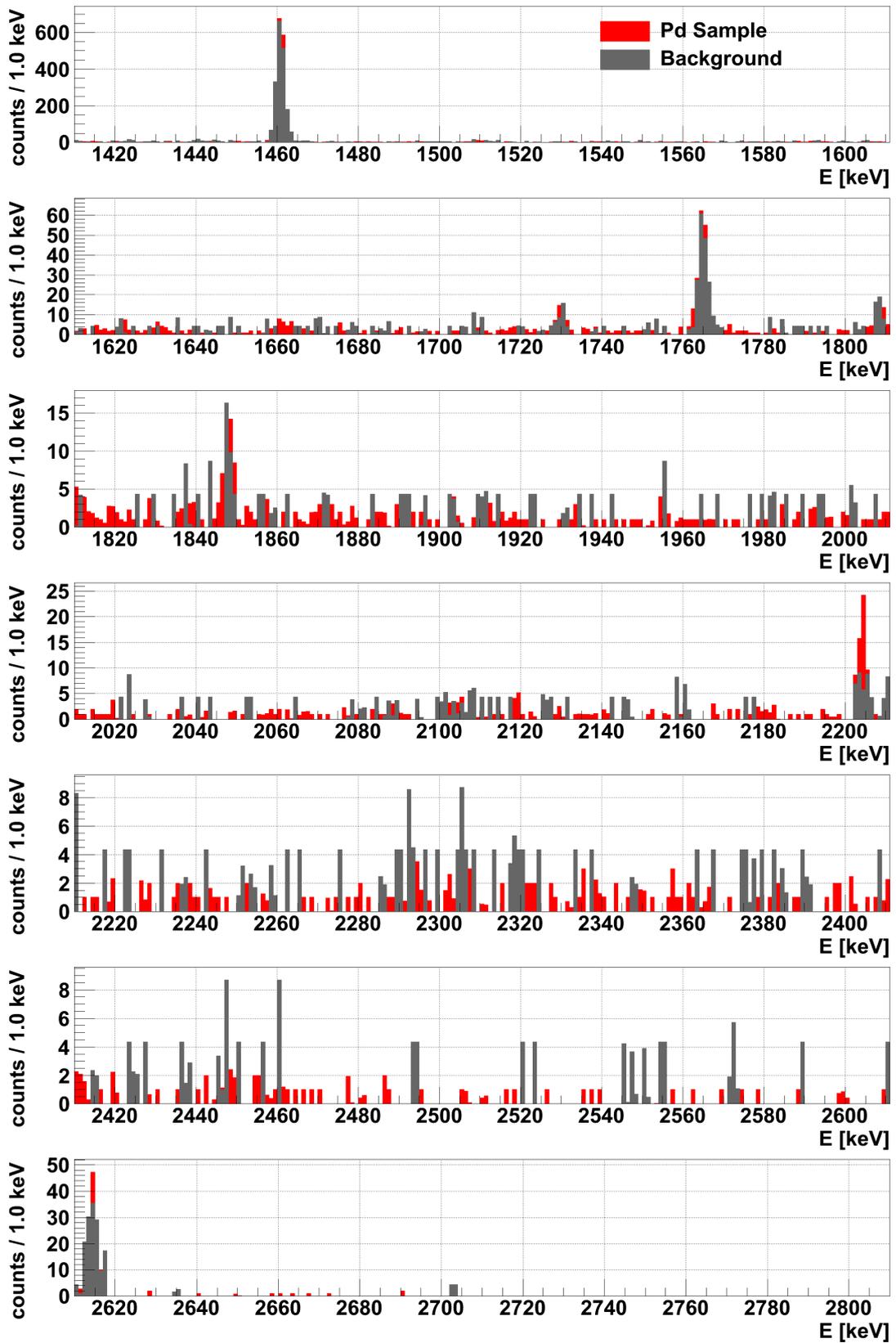
Figure G.3 Felsenkeller dataset 2 of 2. Comparison of palladium sample and background spectrum. The background spectrum is scaled to the live-time of the of the sample spectrum.

Figure G.4 HADES dataset 1 of 2. Comparison of palladium sample and background spectrum. The background spectrum is scaled to the live-time of the of the sample spectrum.

Figure G.5 HADES dataset 2 of 2. Comparison of palladium sample and background spectrum. The background spectrum is scaled to the live-time of the of the sample spectrum.

Figure G.6 LNGS dataset 1 of 2. Comparison of palladium sample and background spectrum. The background spectrum is scaled to the live-time of the of the sample spectrum.

Figure G.7 LNGS dataset 2 of 2. Comparison of palladium sample and background spectrum. The background spectrum is scaled to the live-time of the of the sample spectrum.

(a) with HADES   (b) without HADES
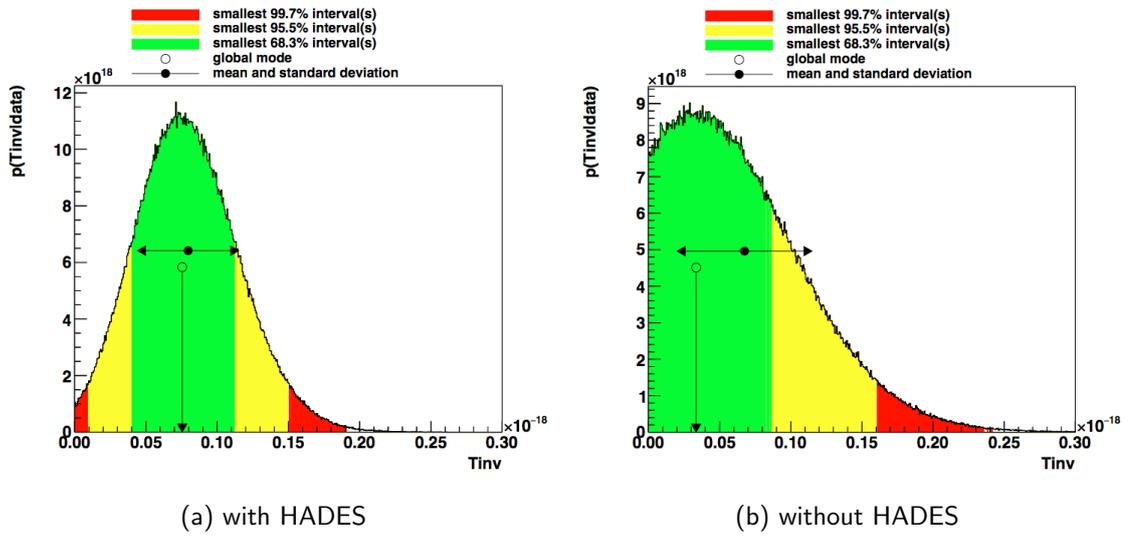
Figure G.8 Marginalized inverse half-life posterior distribution for the ^{102}Pd 2^+_1 transition including the
HADES dataset (left) and without the HADES dataset (right).

(a) with HADES   (b) without HADES
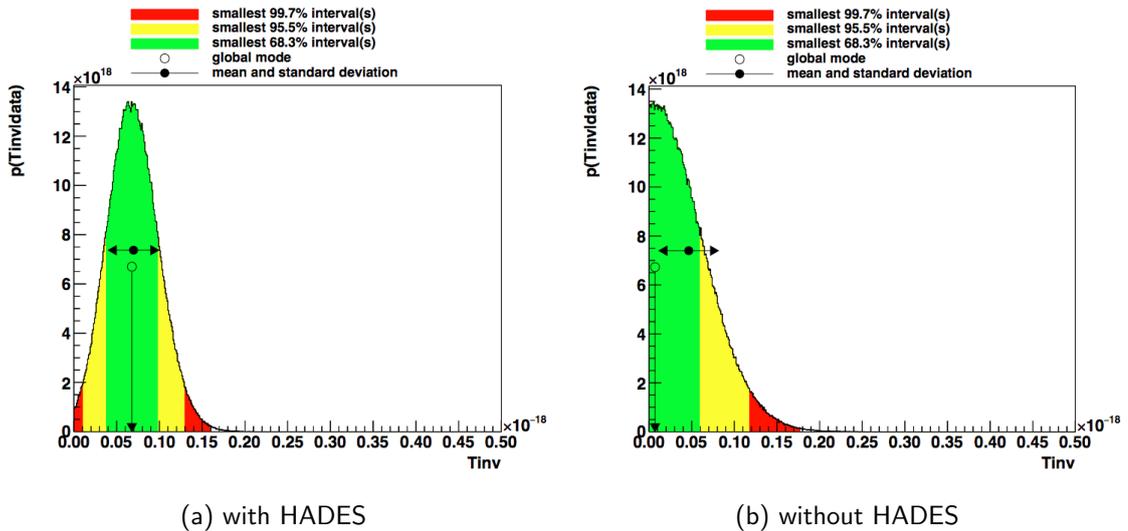
Figure G.9 Marginalized inverse half-life posterior distribution for the ^{102}Pd 0^+_1 transition including the
HADES dataset (left) and without the HADES dataset (right).

A first search of excited states double beta and double electron capture decays of ^{110}Pd and ^{102}Pd

B. Lehnert *, K. Zuber

Inst. für Kern- und Teilchenphysik, Technische Universität Dresden, 01069 Dresden, Germany

A B S T R A C T

A search for double beta decays of the palladium isotopes ^{110}Pd and ^{102}Pd into excited states of their daughters was performed and first half-life limits for the $2\nu\beta\beta$ and $0\nu\beta\beta$ decays into first excited 0^+ and 2^+ states of 5.89×10^{19} yr and 4.40×10^{19} yr (95% CL) for the ^{110}Pd decay were obtained. The half-life limits for the corresponding double electron capture transition of ^{102}Pd are 7.64×10^{18} yr and 2.68×10^{18} yr (95% CL) respectively. These are the first measurements for ^{102}Pd.

1. Introduction

During the past 20 years vast progress has been made in unveiling the properties of neutrinos. For decades neutrinos were thought to be massless, which no longer holds true: flavour oscillations found in the leptonic sector, studying neutrinos coming from the sun [1,2], the atmosphere [3], high energy accelerators beams [4,5] and nuclear power plants [6], are explained by neutrino oscillations requiring a non-zero neutrino mass. However, no absolute mass scale can be fixed with experiments studying the oscillatory behaviour. To achieve this, one has to investigate weak decays, such as beta decays or neutrinoless double beta decays

$$(Z, A) \rightarrow (Z + 2, A) + 2e^- \quad (0\nu\beta\beta\text{-decay}). \tag{1}$$

The latter violates total lepton number by two units and thus is not allowed in the Standard Model. The $0\nu\beta\beta$-decay is the gold plated process to distinguish whether neutrinos are Majorana or Dirac particles. Furthermore, a match of helicities of the intermediate neutrino states is necessary which is done in the easiest way by introducing a neutrino mass. This mass is linked with the experimentally observable half-life via

$$\left(T_{1/2}^{0\nu}\right)^{-1} = G^{0\nu}(Q, Z) \left|M_{GT}^{0\nu} - M_F^{0\nu}\right|^2 \left(\frac{\langle m_{\nu_e}\rangle}{m_e}\right)^2, \tag{2}$$

where $\langle m_{\nu_e}\rangle$ is the effective Majorana neutrino mass, given by $\langle m_{\nu_e}\rangle = |\sum_i U_{ei}^2 m_i|$ and U_{ei} is the corresponding element in the

leptonic PMNS mixing matrix, $G^{0\nu}(Q, Z)$ is a phase space factor and $M_{GT}^{0\nu} - M_F^{0\nu}$ describes the nuclear transition matrix element. The experimental signature is the emission of two electrons with a sum energy corresponding to the Q-value of the nuclear transition. A potential evidence has been claimed in the $0\nu\beta\beta$-decay of ^{76}Ge with $T_{1/2}^{0\nu} = 2.23^{+0.44}_{-0.31} \times 10^{25}$ yr at 90% CL [7]. In addition, the SM process of neutrino accompanied double beta decay,

$$(Z, A) \rightarrow (Z + 2, A) + 2e^- + 2\nu_e \quad (2\nu\beta\beta\text{-decay}) \tag{3}$$

can be investigated, which is expected with half-lives around 10^{20} yr. For recent reviews see [8].

Additional information is provided by the alternative process of positron decay in combination with electron capture (EC). Three different decay modes can be considered:

$$(Z, A) \rightarrow (Z - 2, A) + 2e^+ + (2\nu_e) \quad (\beta^+\beta^+), \tag{4}$$

$$e^- + (Z, A) \rightarrow (Z - 2, A) + e^+ + (2\nu_e) \quad (\beta^+/\text{EC}), \tag{5}$$

$$2e^- + (Z, A) \rightarrow (Z - 2, A) + (2\nu_e) \quad (\text{EC/EC}). \tag{6}$$

Decay modes containing a positron have a reduced Q-value as each generated positron accounts for a reduction of $2\,m_e c^2$. Thus, the full energy is only available in the EC/EC mode and makes it the most probable one. However, it is also the most difficult to detect, only producing X-rays instead of 511 keV gammas. Furthermore, it has been shown that β^+/EC transitions have an enhanced sensitivity to right-handed weak currents (V + A interactions) [9] and thus would help to disentangle the physics mechanism of $0\nu\beta\beta$-decay. In the last years, also neutrinoless EC/EC modes have been discussed with renewed interest, because of a potential resonance enhancement up to a factor of 10^6 in the decay if the initial

* Corresponding author.
 E-mail addresses: Bjoern.Lehnert@mailbox.tu-dresden.de (B. Lehnert), Zuber@physik.tu-dresden.de (K. Zuber).
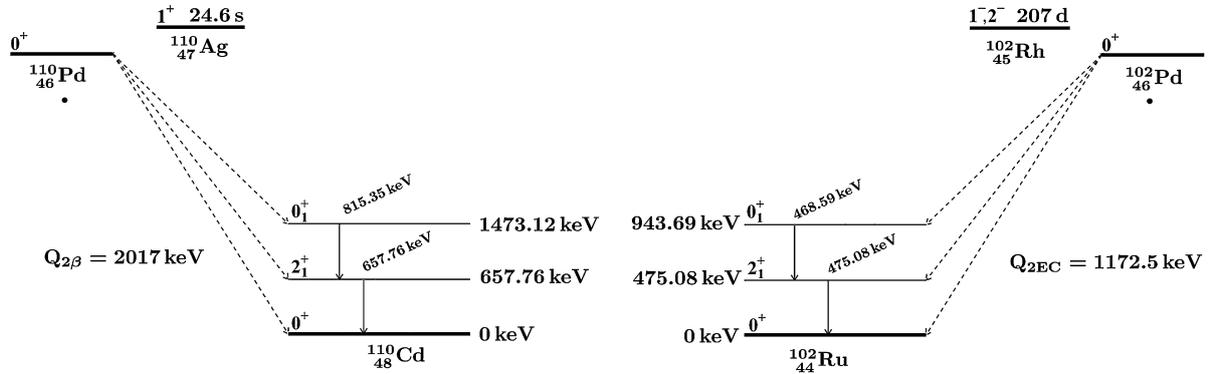
Fig. 1. Level schemes of ^{110}Pd (left) and ^{102}Pd (right) decays.
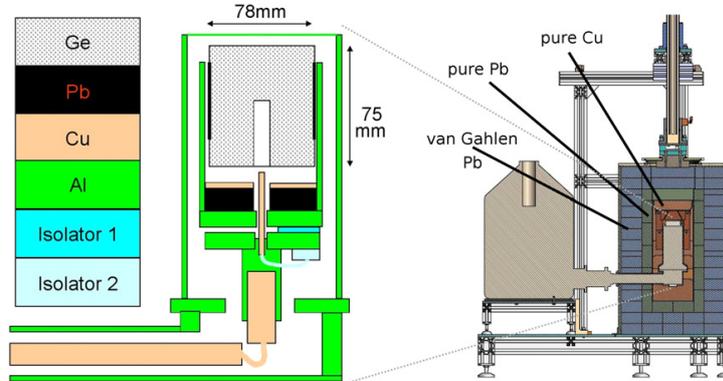

Fig. 2. Schematic drawing of the used setup. Composed from pictures in [23].

and final excited state are degenerate [10]. Recently, a series of isotopes with extreme low Q-value was explored for enhancement in the ECEC mode and with ^{152}Gd a very promising candidate was found [11].

Another branch of search is linked to excited state transitions. The signal in this case is extended by looking at the corresponding de-excitation gammas. However, in the approach of a passive sample on a Ge-detector it will not allow to distinguish between the $2\nu\beta\beta$-decay and $0\nu\beta\beta$-decay mode. Thus, the deduced half-live limits are valid for both. The investigation of $2\nu\beta\beta$-decay modes into excited states will add information on nuclear structure, valuable for matrix element calculations. Furthermore, a potential observation of $0\nu\beta\beta$-decay into an excited 2^+-state would likely point to other contributions besides neutrino masses. The searches described in this Letter are based on the search for excited state transitions.

An element getting little attention in the past is palladium with the isotopes of interest ^{110}Pd and ^{102}Pd. Among the eleven $0\nu\beta\beta$-decay candidates with a Q-value larger than 2 MeV, ^{110}Pd has several advantages: it has the second-highest natural abundance (11.72%) and, in addition, it is an excellent candidate to probe the single-state dominance hypothesis for $2\nu\beta\beta$-decay, i.e. that only the lowest lying intermediate 1^+-state will contribute to the nuclear transition matrix element describing its $2\nu\beta\beta$-decay. Only one rather weak experimental limit in the order of 10^{17} yr exists for $0\nu\beta\beta$-decay ground state transitions in ^{110}Pd [12]. Theoretical predictions for the $2\nu\beta\beta$-decay ground state mode are in the range of 0.12–29.96×10^{20} yr [13–19,21]. Theoretical predictions for the

excited state transitions are 4.4×10^{25} yr [19], 8.37×10^{25} yr [16], 1.5×10^{25} yr [20] and 0.62–1.3×10^{25} yr [21] for the 2_1^+ state and 2.4×10^{26} yr [19] and 4.2–9.1×10^{23} yr [21] for the 0_1^+ state.

The second isotope ^{102}Pd has a Q-value of 1172 keV, a natural abundance of 1.02% and is able to decay via EC/EC and β^+/EC. These decay modes have never been studied for ^{102}Pd experimentally and no theoretical predictions exist. The level schemes of both isotopes are shown in Fig. 1.

2. Experimental setup

The measurement was performed in the Felsenkeller Underground Laboratory in Dresden with a shielding depth of 120 mwe. A sample of 802.35 g of Pd was used, which was purified before by C. HAFNER GmbH + Co. KG. It was placed in a standard Marinelli baker (D6) of 70 cm diameter and 21 cm height. The sample was positioned on a HPGe detector with an efficiency of 90% routinely used for γ-spectroscopic measurements. The detector has an 1 mm thick Al-window towards the sample. It is surrounded by a 5 cm copper shielding embedded in another shielding of 15 cm of clean lead. The inner 5 cm of the lead shielding have a low contamination of ^{210}Pb of only 2.7 ± 0.6 Bq/kg while the outer 10 cm have an activity of 33 ± 0.4 Bq/kg.

The detector is placed inside a special building which acts as a Faraday cage and a Rn shield; additionally, the setup is flushed with nitrogen in order to reduce Rn contamination. More details can be found in [22,23] and a schematic drawing is shown in Fig. 2. The Pd was stored underground for more than one year prior to

the measurement except for 18 d of purification. The data were collected with a 8192 channel MCA from Ortec and were converted into the ROOT format for analysis.

An extensive calibration was performed using 17 γ-lines from 8 different nuclides resulting in a linear energy calibration curve of

$$E\ \mathrm{keV} = 0.342746\ \frac{\mathrm{keV}}{\mathrm{channel}} \times \mathrm{channel} - 4.337734\ \mathrm{keV}. \qquad (7)$$

The measurement range of the spectrum goes up to 2.8 MeV. The resolution was calibrated using the calibration lines and fitted with a second order polynomial. The actual values at the energies of the lines of interest will be discussed in the corresponding analysis section.

Despite purification, the measured spectrum is dominated by intrinsic contaminations of the Pd. Clear γ-lines from the ^{238}U and ^{232}Th decay chains as well as ^{40}K are visible. However, former Americium contributions have been removed completely by the purification. The actual background spectrum of the detector system itself without any sample is at least an order of magnitude smaller in the regions of interest and can be neglected, hence the spectrum is completely dominated by the Pd sample contaminations.

3. Analysis and results

A total of 16.2 d of data were accumulated resulting in 13.00 kg d of exposure. In the following the two isotopes of interest are discussed separately. For the analysis, the natural abundances of the latest IUPAC evaluation have been used which are 11.27% (^{110}Pd) and 1.02% (^{102}Pd) respectively [24]. As the searches are purely based on gamma detection, the obtained results apply for both, $0\nu\beta\beta$-decay and $2\nu\beta\beta$-decay modes. The decays into the first excited 0_1^+-state de-excite via an intermediate 2_1^+-state. Thus, there will be an angular correlation among the gammas, with an observational probability $W(\theta)$ that the second gamma is emitted with an angle θ with respect to the first one given by

$$W(\theta) = \frac{5}{4}\left(1 - 3\cos^2\theta + 4\cos^4\theta\right). \qquad (8)$$

It can be seen that the probability of both gammas being emitted in the same direction is larger than an uncorrelated emission. However, the detection efficiency for a single gamma is small which results in a low probability to observe a summation peak and thus the searches are based on the individual gamma energies only.

The efficiency for full energy detection was determined and cross checked in several ways. The most important one was replacing the actual used volume by a SiO$_2$ sample of exactly the same geometry. The intrinsic contaminations of the natural decay chains of ^{238}U and ^{232}Th as well as ^{40}K produced various γ-lines and acted as an extended calibration source. The 17 γ-lines used for the energy calibration were also used for the efficiency determination in the region from 238.6 keV (from ^{212}Pb decay) up to 2614.3 keV (from ^{208}Tl decay). The efficiency in the region above 200 keV can be well fitted by two exponential functions. It varies between 5.77% at 468 keV and 3.89% at 815 keV, being the lowest and highest energy lines of interest for the search described in this Letter. To account for the difference in self-absorption of Pd and SiO$_2$, extensive Monte Carlo simulations were performed using the AMOS code [25]. The amount of Monte Carlo was chosen in a way that the statistical error for the full energy peak for both, Pd and SiO$_2$, was less than 0.1%. The simulations agree within an error of less than 15% with the measurements and tend to be slightly higher. This can easily be explained by small geometric
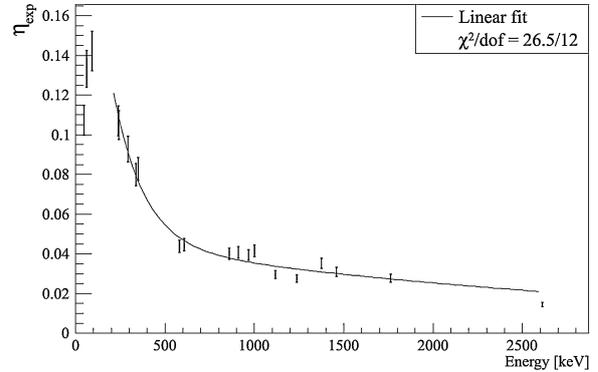

Fig. 3. Measured efficiencies and the fitting function.
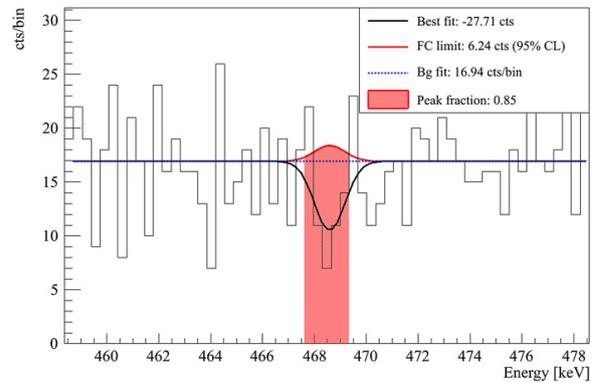

Fig. 4. Peak region of ^{102}Pd for the $0^+ \rightarrow 2^+$ transition with the illustration of the background model, the best fit and the peak with the upper count limit at 95% CL.

differences in the simulation and the experiment. However, independent from that is the ratio of both self-absorption simulations for Pd and SiO$_2$. Hence, the ratio was used to scale the experimentally well determined efficiency curve of SiO$_2$ to the one of Pd (Fig. 3). A validation of the procedure was performed within the vicinity of the lines of interest by using prominent background lines apparent in the spectrum, namely 295.21 keV and 351.92 keV (from ^{214}Pb), 233.63 keV (from ^{212}Pb), 583.19 keV (from ^{208}Tl) and 609.32 keV (from ^{214}Bi), which results in good agreement.

The analysis is based on the extraction of upper count limits with the Feldman Cousins method described in [26]. A simple constant was chosen as a background model after concluding that the area around the ROI is sufficiently flat. The background was determined with a likelihood fit in a selected region around the peak position taken to be ±30 keV excluding the peak range which is considered to be ±5 keV.

Likelihood fits with the Gaussian peak shapes and the background constants resulted in statistical downward fluctuations for all four peaks. This is a clear sign that no significant signal is observed (see Figs. 4 and 5). In this case, an upper limit for the count rate can be calculated using the background only hypothesis and the maximal statistical fluctuation of a Gaussian distributed background for a certain confidence level. This is commonly referred to as sensitivity. However, the Feldman Cousins approach also considers the observed downward fluctuations and results in more appropriate results for low count rates.
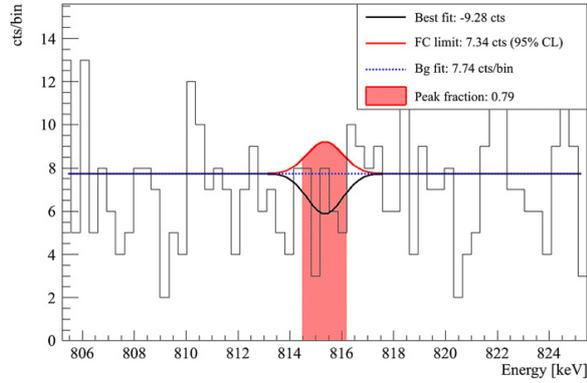
Fig. 5. Peak region of ^{110}Pd for the $0^+ \rightarrow 2^+$ transition with the illustration of the background model, the best fit and the peak with the upper count limit at 95% CL.

In order to obtain a numerical value for the upper limit, all bins within the FWHM of an expected peak are combined into a single analysis bin. The resulting fraction of the peak that is covered by the analysis bin is dependent on the binning of the data but always larger than 76%. The background expectation and the measured count rate are used to evaluate an upper count limit for this bin with the ROOT implementation of the Feldman and Cousins method. The result is then scaled to the full peak area.

From the background point of view, exactly the same γ-lines in the performed search could be produced from the beta decays of the intermediate nuclide of the investigated double beta system, which will be discussed in more detail in the next section. However, their contribution can be rejected by the non-observation of other, more prominent γ-lines at different locations in the spectrum. The only prominent background line to be expected within ± 5 keV of any of the four lines under investigation is from ^{137}Cs at 661.66 keV potentially influencing the 2_1^+-limit in the ^{110}Pd system. However, no indication of this line is observed.

3.1. The ^{110}Pd system

Two lines were investigated for ^{110}Pd at energies 657.76 keV (corresponding to the 2_1^+ transition) and 815.35 keV (additionally emitted in the 0_1^+ decay) respectively. The corresponding energy resolutions at these energies are 1.51 and 1.61 keV (FWHM). Potential γ-lines mimicking the signal would come from ^{110}Ag and ^{110m}Ag decays. ^{110}Ag has a half-life of 24.6 s only and thus has to be produced in-situ. With the given shielding this can be excluded. Potentially more dangerous is the long-living ^{110m}Ag (half-live of 249.79 d). This isotope has two prominent lines at 1384.3 keV and 1505.04 keV. They are not visible in the spectrum and thus this contribution can be excluded for this search. No lines were visible at both peak positions of interest and thus an upper limit (95% CL) of signal events of 10.53 and 7.34 could be extracted for 657.76 keV and 815.35 keV respectively.

Using the known Pd mass and efficiencies, this can be converted into lower half-live limits of

$$T_{1/2}^{(0\nu+2\nu)110}\text{Pd}$$
$$\rightarrow {}^{110}\text{Cd}(0_1^+, 815.3 \text{ keV}) > 5.89 \times 10^{19} \text{ yr} \quad (95\% \text{ CL}), \quad (9)$$

$$T_{1/2}^{(0\nu+2\nu)110}\text{Pd}$$
$$\rightarrow {}^{110}\text{Cd}(2_1^+, 657.8 \text{ keV}) > 4.40 \times 10^{19} \text{ yr} \quad (95\% \text{ CL}). \quad (10)$$

These are the first experimental limits for excited state transitions in the ^{110}Pd system.

3.2. The ^{102}Pd system

Two lines were investigated for ^{102}Pd at energies 468.59 keV (only emitted in the 0_1^+ decay) and 475.05 keV (corresponding to the 2_1^+ transition) respectively. The energy resolution at these energies is 1.39 keV (FWHM) for both lines. Potential γ-lines mimicking the signal would come from ^{102}Rh and ^{102m}Rh decays. ^{102}Rh with a half-life of 207 d has no reasonable line to check. The strongest one is the 475.05 keV line. As there is no signal in this region it can be concluded that it does not contribute to the 468.59 keV region. On the other hand ^{102m}Rh (half-live of 2.9 yr) has multiple lines to explore, the most restricting ones are a line at 631.28 keV with 56% emission probability and at 697.49 keV with 44%. Both of them are not observed in the spectrum and thus can exclude such a contribution. No lines were visible at both peak positions of interest and thus an upper limit (95% CL) of signal events of 17.64 and 6.24 could be extracted for 475.05 keV and 468.59 keV respectively. The obtained half-live limits are

$$T_{1/2}^{(0\nu+2\nu)102}\text{Pd}$$
$$\rightarrow {}^{102}\text{Ru}(0_1^+, 468.6 \text{ keV}) > 7.64 \times 10^{18} \text{ yr} \quad (95\% \text{ CL}), \quad (11)$$

$$T_{1/2}^{(0\nu+2\nu), 102}\text{Pd}$$
$$\rightarrow {}^{102}\text{Ru}(2_1^+, 475.1 \text{ keV}) > 2.68 \times 10^{18} \text{ yr} \quad (95\% \text{ CL}). \quad (12)$$

These are the first experimental limits on ^{102}Pd double beta decays.

4. Summary

Double beta decay transitions into excited states for the two Pd-isotopes ^{102}Pd and ^{110}Pd have been investigated for the first time. These transitions contain valuable informations about the physics mechanism of double beta decay and the involved nuclear physics. However, no signal into the first excited 0^+ and 2^+ states have been observed.

Acknowledgements

References

[1] B. Aharmim, et al., SNO Collaboration, Phys. Rev. Lett. 101 (2008) 111301.
[2] J.P. Cravens, et al., Super-Kamiokande Collaboration, Phys. Rev. D 78 (2008) 032002.
[3] R. Wendell, et al., Super-Kamiokande Collaboration, Phys. Rev. D 81 (2010) 092004.
[4] A. Habig, Mod. Phys. Lett. A 25 (2010) 1219.
[5] N. Agafonova, et al., OPERA Collaboration, Phys. Lett. B 691 (2010) 138.
[6] K. Eguchi, et al., KamLAND Collaboration, Phys. Rev. Lett. 90 (2003) 021802.
[7] H.V. Klapdor-Kleingrothaus, et al., Phys. Lett. B 586 (2004) 198;
    H.V. Klapdor-Kleingrothaus, et al., Mod. Phys. Lett. A 21 (2006) 1547.
[8] F.T. Avignone III, et al., Rev. Mod. Phys. 80 (2008) 481.
[9] M. Hirsch, et al., Z. Phys. A 347 (1994) 151.
[10] Z. Sujkowski, S. Wycech, Phys. Rev. C 70 (2004) 052501.
[11] S. Eliseev, et al., Phys. Rev. Lett. 106 (2011) 052504.
[12] R.G. Winter, Phys. Rev. 85 (1952) 687.
[13] R. Chandra, et al., Eur. Phys. J. A 23 (2005) 223.
[14] S.V. Semenov, et al., Phys. Atom. Nucl. 63 (2000) 1196.
[15] O. Civitarese, J. Suhonen, Phys. Rev. C 58 (1998) 1535.
[16] S. Stoica, Phys. Rev. C 49 (1994) 2240.

[17] M. Hirsch, et al., Phys. Rep. 242 (1994) 403.
[18] A. Staudt, et al., Europhys. Lett. 13 (1990) 31.
[19] P. Domin, et al., Nucl. Phys. A 753 (2005) 337.
[20] A.A. Raduta, C.M. Raduta, Phys. Lett. B 647 (2007) 265.
[21] J. Suhonen, Nucl. Phys. A 864 (2011) 63.

[22] M. Köhler, et al., Appl. Rad. and Isotopes 67 (2009) 736.
[23] D. Degering, M. Köhler, IEEE Nucl. Sci. Sym. Dresden (2008).
[24] P. De Bievre, P.D.P. Taylor, Int. J. Mass Spectrom. Ion. Phys. 123 (1993) 149.
[25] U. Reichelt, J. Henniger, Radiat. Protect. Dosim. 119 (2006) 479.
[26] G.J. Feldman, R.D. Cousins, Phys. Rev. D 57 (1998) 3873.

New half-life limits on double-β decays of ¹¹⁰Pd and ¹⁰²Pd into excited states

Björn Lehnert[*] and Kai Zuber[†]

Institut für Kern- und Teilchenphysik, Technische Universität Dresden, Dresden, Germany

Erica Andreotti[‡] and Mikael Hult[§]

Institute for Reference Materials and Measurements, Retieseweg 111, B-2440 Geel, Belgium
(Received 10 December 2012; published 8 March 2013)

Background: Excited-state transitions in double-β decays are a powerful tool to validate and tune calculations of nuclear matrix elements.

Purpose: The experimental lower half-life limits for double-β decays of ¹¹⁰Pd and ¹⁰²Pd into the excited 2_1^+ and 0_1^+ states are improved. Furthermore, the first limits of transitions into the 2_2^+, 0_2^+, and 2_3^+ states are published for ¹¹⁰Pd as well as a first limit for the 2_2^+ state transition in ¹⁰²Pd.

Methods: The Pd sample was measured with two HPGe detectors in sandwich configuration in the HADES underground laboratory during 44.77 d of lifetime. The analysis was performed with the frequentist Feldman-Cousins method.

Results: Lower half-life limits of 1.98×10^{20} and 1.72×10^{20} yr (95% CL) were found for the first 0^+ and 2^+ excited states in ¹¹⁰Pd, respectively. This is an improvement by more than a factor of 3 with respect to previous measurements. In ¹⁰²Pd, the lower half-life limit could be improved to 5.95×10^{18} yr (95% CL) for the first 0^+ excited state. Furthermore, first experimental lower half-life limits were found for all possible excited states in the ¹¹⁰Pd and ¹⁰²Pd systems.

Conclusions: Previous half-life limits were improved and experimental results were obtained for all theoretical calculations of palladium double-β decays into excited states.

I. INTRODUCTION

Groundbreaking progress has been made in the field of neutrino physics in recent years. Oscillation experiments studying neutrinos coming from the sun [1–3], the atmosphere [4], nuclear reactors [5–8], and accelerator beams [9–11] have found compelling evidence for flavor oscillation in the lepton sector. This changes the long-believed assumption that neutrinos are massless particles. The implication from neutrino oscillation that at least two neutrino mass eigenstates have a nonzero rest mass does not allow the fixing of an absolute mass scale and leaves two mass hierarchy scenarios open. Advanced oscillation experiments try to identify the hierarchy scenario by using oscillation effects in the earth or in dense stellar matter [12] but are not able to determine the absolute mass scale. This has to be done via β decay [13,14], cosmology [15], or neutrinoless double-β decay:

$$(Z, A) \rightarrow (Z + 2, A) + 2e^- \quad (0\nu\beta\beta), \qquad (1)$$

which would have a high sensitivity to determine the mass scale of neutrinos. This process violates total lepton number by two units and thus is not allowed in the standard model. Furthermore, it is the gold-plated process that distinguishes whether neutrinos are Majorana or Dirac particles.

For the $0\nu\beta\beta$ process to exist, it is necessary to match the helicities of the intermediate neutrino states, which is most

___

[*]bjoern.lehnert@tu-dresden.de

[†]zuber@physik.tu-dresden.de

[‡]erica.andreotti@ec.europa.eu

[§]mikael.hult@ec.europa.eu

easily done by introducing a neutrino mass. This mass is connected to the experimentally observable half-life via

$$\left(T_{1/2}^{0\nu}\right)^{-1} = G^{0\nu}(Q, Z) \left| M_{GT}^{0\nu} - M_F^{0\nu} \right|^2 \left(\frac{\langle m_{\nu_e} \rangle}{m_e} \right)^2, \qquad (2)$$

where $\langle m_{\nu_e} \rangle$ is the effective Majorana neutrino mass given by the coherent sum over the virtual electron neutrino mass eigenstates $\langle m_{\nu_e} \rangle = |\sum_i U_{ei}^2 m_i|$, with U_{ei} as the lepton flavor mixing matrix; $G^{0\nu}(Q, Z)$ is a phase space factor; and $M_{GT}^{0\nu} - M_F^{0\nu}$ describes the nuclear transition matrix element. The experimental signature is the emission of two electrons with a sum energy corresponding to the Q value of the nuclear transition. A potential evidence has been claimed for the $0\nu\beta\beta$ mode of ⁷⁶Ge with $T_{1/2}^{0\nu} = 2.23^{+0.44}_{-0.31} \times 10^{25}$ yr at 90% CL [16,17].

Experimentally observed in 11 nuclides [18,19] is the standard model process of neutrino-accompanied double-β decay:

$$(Z, A) \rightarrow (Z + 2, A) + 2e^- + 2\nu_e \quad (2\nu\beta\beta), \qquad (3)$$

which is expected with half-lives around 10^{20} yr depending on the Q value. For recent reviews, see Ref. [20]. An alternative process is the double-positron decay in combination with electron capture (EC). Three different decay modes can be considered:

$$(Z, A) \rightarrow (Z - 2, A) + 2e^+ + (2\nu_e) \quad (\beta^+\beta^+), \qquad (4)$$

$$e^- + (Z, A) \rightarrow (Z - 2, A) + e^+ + (2\nu_e) \quad (\beta^+/\text{EC}), \qquad (5)$$

$$2e^- + (Z, A) \rightarrow (Z - 2, A) + (2\nu_e) \quad (\text{EC}/\text{EC}). \qquad (6)$$

Decay modes containing a positron have a reduced Q value because each generated positron accounts for a reduction of $2\,m_e c^2$ and thus can only occur in nuclides with sufficient

energy difference from the daughter nuclide. The full energy is only available in the EC/EC mode, which makes it the most probable one; however, it is also the most difficult to detect, only producing x rays instead of 511-keV γ's.

Another set of searches focuses on excited-state transitions in double-β decays. This is experimentally interesting because the event topology is enhanced by deexcitation γ's, which are accessible with γ-ray spectroscopy. However, without information about the other final state particles, this technique cannot distinguish between the $0\nu\beta\beta$ mode and the $2\nu\beta\beta$ mode; hence, the deduced half-lives are valid for both. The investigation of $2\nu\beta\beta$ modes into excited states provides information on nuclear structure that is valuable for matrix element calculations. The understanding and tuning of parameters in matrix elements for $2\nu\beta\beta$ modes is imperative for translating the measured half-life of $0\nu\beta\beta$ experiments into a Majorana neutrino mass [Eq. (2)]. So far only transitions to the first-excited 0^+ state have been observed in ^{100}Mo [21] and ^{150}Nd [22]. The searches described in this paper are searches for excited-state transitions in palladium with γ-ray spectroscopy.

II. DOUBLE-β DECAYS IN PALLADIUM

The element under study is palladium with the isotopes of interest being ^{110}Pd and ^{102}Pd. Among the 35 isotopes expected to undergo $\beta^-\beta^-$ decay, ^{110}Pd has the second-highest natural abundance with 11.72%. Recently, the Q value was remeasured to 2017.85(64) keV [23] and this places ^{110}Pd among the 11 $\beta^-\beta^-$ isotopes with a Q value larger than 2000 keV. Two measurements of ^{110}Pd have been performed in the past in 1952 [24] and more recently in 2011 [25]. The latter measurement was the first to investigate excited states in palladium and is the direct predecessor of this search. There exist many theoretical calculations for transitions into the ground state and into the 2_1^+, 0_1^+, 2_2^+, 0_2^+, and 2_3^+ excited states to which the experimental limits can be compared. The existing experimental and theoretical half-life limits ares summarized in Table I. This paper aims to provide experimental information about every decay mode into excited states in ^{110}Pd and ^{102}Pd that has been investigated theoretically. Furthermore, ^{110}Pd is an excellent candidate to probe the single-state dominance hypothesis for $2\nu\beta\beta$ decay, i.e., that only the lowest-lying intermediate 1^+ state will contribute to the nuclear transition matrix element describing its $2\nu\beta\beta$ decay.

The second isotope ^{102}Pd has a Q value of 1172 keV, a natural abundance of 1.02%, and is able to decay via EC/EC and β^+/EC. The only experimental half-life limit is quoted in Ref. [25] and no theoretical calculation is published up to date. A summary can be found in Table II.

The search is based on γ spectroscopy; hence only γ lines are considered in the event topology. Each excited-state transition is followed by a unique set of decay branches and γ cascades, which are illustrated in Figs. 1 and 2.

III. EXPERIMENT

A. Measuring setup

The measurements were performed at the High Activity Disposal Experimental Site (HADES) underground laboratory

TABLE I. Experimental and theoretical half-life limits for various $\beta\beta$-decay modes in ^{110}Pd. The columns show from left to right the theoretical model, the quoted half-life, the reference, and the year of publication. Abbreviations are denote as follows: PHFM, projected Hartree-Fock-Bogoliubov; SSDH, single-state-dominance hypothesis; SRPA, second quasi-random-phase approximation; OEM, operator expansion method; QRPA, quasi-random- phase approximation; SSD, single-state dominance; and *pn*QRPA, proton-neutron quasiparticle random-phase approximation.

Expt./Th. model	Lower limit $T_{1/2}$ (yr)	Reference	Year of publication
^{110}Pd ground-state transition			
Expt.	1×10^{17} (68% CL)	[24]	1952
PHFM	1.41×10^{20} and 3.44×10^{20}[a]	[26]	2005
SSDH	1.75×10^{20}	[27]	2000
SSDH	1.2–1.8×10^{20}[b]	[28]	1998
SRPA	1.6×10^{20}	[29]	1994
OEM	1.24×10^{21}	[30]	1994
QRPA	1.16×10^{19}	[31]	1990
SSD	1.2×10^{20}	[32]	2005
*pn*QRPA	1.1×10^{20} and 0.91×10^{20}[c]	[33]	2011
^{110}Pd 2_1^+ excited-state transition @ 657.76 keV			
Expt.	4.40×10^{19}(95% CL)	[25]	2011
SSD	4.4×10^{25}	[32]	2005
SRPA	8.37×10^{25}	[29]	1994
*pn*QRPA	1.48×10^{25}	[34]	2007
*pn*QRPA	0.62×10^{25} and 1.3×10^{25}[c]	[33]	2011
^{110}Pd 0_1^+ excitedstate transition @ 1473.12 keV			
Expt.	5.89×10^{19} (95% CL)	[25]	2011
SSD	2.4×10^{26}	[32]	2005
*pn*QRPA	4.2×10^{23} and 9.1×10^{23}[c]	[33]	2011
^{110}Pd 2_2^+ excited-State transition @ 1475.80 keV			
SSD	3.8×10^{31}	[32]	2005
*pn*QRPA	11×10^{30} and 7.4×10^{30}[c]	[33]	2011
^{110}Pd 0_2^+ excited-State transition @ 1731.33 keV			
SSD	5.3×10^{29}	[32]	2005
^{110}Pd 2_3^+ excited-State transition @ 1783.48 keV			
SSD	1.3×10^{35}	[32]	2005

[a]$g_A = 1.25$ and 1.0, respectively.
[b]Different experimental input for calculations.
[c]For Woods-Saxon potential and adjusted base, respectively (see Ref. [33] for details).

on the premises of the Belgian Nuclear Research Centre SCK·CEN in Mol, Belgium. The underground laboratory is

TABLE II. Experimental half-life limits for various EC/EC and β^+/EC decay modes in ^{102}Pd.

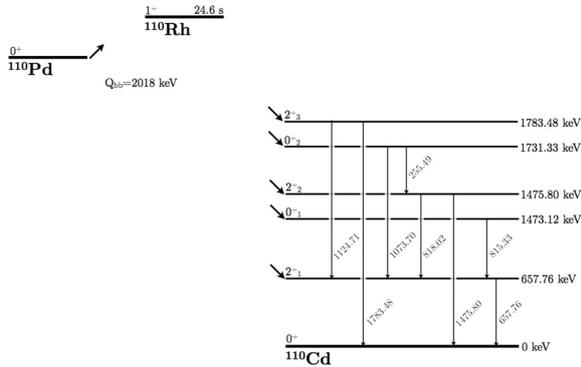| Expt./Th. model	Lower limit $T_{1/2}$(yr)	Reference	Year of publication
^{102}Pd 2_1^+ excited-state transition @ 475.10 keV			
Expt.	2.68×10^{18} (95% CL)	[25]	2011
^{102}Pd 0_1^+ excited-state transition @ 943.69 keV			
Expt.	7.64×10^{18} (95% CL)	[25]	2011

FIG. 1. ^{110}Pd level scheme of investigated decay modes. Nuclear data are from Ref. [35].

located at a depth of 225 m inside the Boom clay formation and has a flat overburden that amounts to roughly 500 m water equivalent [36].

The detector setup consists of two high-purity germanium (HPGe) detectors in a sandwich configuration with integrated muon veto panels on the top [37]. It is shown in Fig. 3. The sample is placed between the top (Ge-7) and bottom (Ge-6) detector. The distance between the two can be adjusted to maximize the solid angle acceptance and the detection efficiency. Ge-6 is a p-type HPGe detector with 80% efficiency and 0.9-mm dead layer in a 102-mm cryostat with a Cu endcap, whereas Ge-7 is an extended range p-type HPGe detector with 90% efficiency and a 0.3-μm dead layer in an Al cryostat. The characteristics of the Ge-7 detector makes it suitable for the detection of low-energetic x rays while the configuration of the Ge-6 detector has the advantage of reducing the background and x-ray coincidences. The shielding consists of an outer layer of 14.5-cm 20 Bq/kg (^{210}Pb) lead, an intermediate layer of 4.0-cm 2.4 Bq/kg (^{210}Pb) low-activity lead, and an inner layer of 3.5-cm electrolytic copper with less than 15 μBq/kg ^{60}Co and less than 20 μBq/kg ^{228}Th [37].

The data acquisition (DAQ) is twofold. The main DAQ, the DAQ2000 multi parameter system, is self-fabricated by the Institute for Reference Materials and Measurements (IRMM) and is recording events in list mode from the two
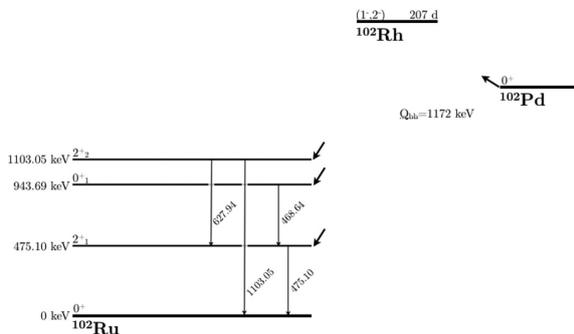

FIG. 2. ^{102}Pd level scheme of investigated decay modes. Nuclear data are from Ref. [35].
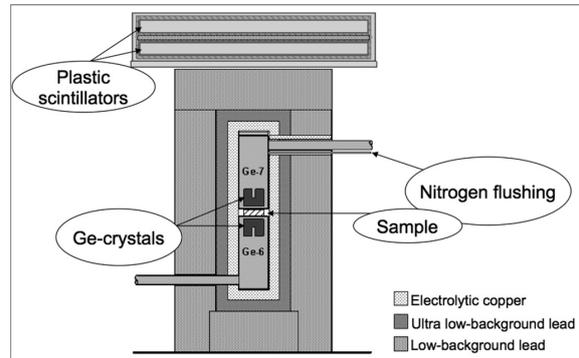

FIG. 3. IRMM germanium detector sandwich setup.

HPGe detectors as well as from the two muon panels which enables coincidence analysis in the ROOT framework [38]. Additionally, a standard GENIE DAQ system is used in histogram mode for each HPGe detector redundantly. The DAQ2000 was only operative for a reduced measuring time with limited sample exposure; thus the analysis in this work is performed with the GENIE DAQ and without muon veto or detector coincidence.

The total background rate in the germanium detectors was previously measured with 992 cts/d in an energy range of 40–2400 keV of which 124 cts/d were identified as muon events [37].

B. Palladium sample

Irregular shaped 1 mm $\times$ 1 cm^2 plates of palladium (802.35 g) were placed inside a measuring container of 70 mm in diameter and 50 mm in height. The plates were piled inside the container as dense as possible and an effective density of 10.2 g/cm^3 was calculated. The palladium was approximated with a homogeneous distribution and the effective density in the simulations for determining the detection efficiency. Recently, the sample was purified by C. HAFNER GmbH + Co. KG in 2010 to a certified purity of >99.95%, which lowered the continuous background in the peak regions by approximately 20% [25]. To avoid radionuclides produced by cosmic ray spallation, the palladium was kept underground and exposed only 18 d during purification in 2010 and 3 d for transport in the fall of 2011. A picture of the palladium sample before and after purification is shown in Fig. 4.
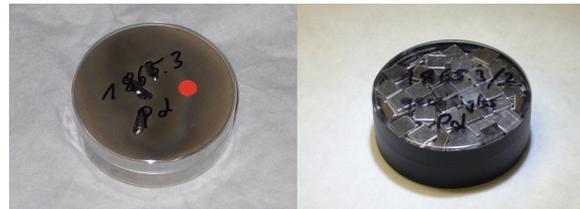

FIG. 4. (Color online) Palladium sample before (left panel) and after (right panel) purification inside the measuring container.

IV. ANALYSIS

A. Stability check

The histogram data of the GENIE DAQ was separated into individual runs of roughly 24 h for each of the two detectors Ge-6 and Ge-7. This enabled the stability check of the DAQ system over the extended period of measurement and the removal of individual runs.

The stability was checked by plotting the count rate and the peak centroid of the background peaks at 609 and 2614 keV as a function of time (spectrum number). Although counting statistics prevented detailed analysis of the short-term stability, it was clear that there was no measurable energy drift during the measurement period. In addition, quality controls with a point source containing ^{60}Co, ^{137}Cs, and ^{241}Am were carried out before, after, and once in-between the measurement. The average ^{222}Rn activity concentration in the laboratory during the data taking was measured to 9.5 Bq/m^3 and at no point higher than 25 Bq/m^3. No correlation to the background count rate was observed mainly due to effective Rn removal by minimizing empty space inside the shield and flushing with N$_2$. The count rate remained stable over the 32 runs with one exception; in the first two runs an increase in total counts and counts from ^{208}Tl was observed, however not from ^{214}Bi. This behavior was cross-checked with additional visible γ lines from 583.19-keV ^{208}Tl and 239.63-keV ^{212}Pb, and 1764.49-keV ^{214}Bi representing the ^{232}Th and ^{238}U decay chains, respectively. The increased count rate of the ^{232}Th chain in the first days is only seen in the lower Ge-6 detector with a Cu endcap and not in the upper Ge-7 detector with an Al endcap. One possible explanation is that the short half-life of ^{220}Rn (55.6 s) implies that it is not flushed out by boil-off nitrogen and that its daughters preferentially stick to the copper surface of the lower detector (Ge-6) rather than to the aluminum surface of the upper detector (Ge-7). ^{222}Rn with a longer half-life (3.8 d) will be flushed out of the shield before a significant number of daughters are produced. Consequently, the first two runs are removed from the analysis resulting in a total of 30 runs with 44.77 d of good data out of 32 runs with 46.49 d total data, which translates into a total exposure of 35.92 kg/d.

B. Data processing

For the final analysis a single energy spectrum is used in which all individual runs are summed: In a first step, all selected runs of one detector are combined with the same energy calibration. In a second step, the single detector spectra are rebinned into a common binning of 0.5 keV/bin and a common energy range from 20 to 2720 keV. Additionally, the Ge-6 spectrum is scaled to the lifetime of the Ge-7 spectrum, which becomes the common lifetime of the sum spectrum. The commonly binned and scaled spectra are added. These steps result in a noninteger sum spectrum that denotes the count per bin in the lifetime of Ge-7. The difference in lifetime between the two detectors is less than 0.5% for the selected runs. The combined spectrum of Ge-6 and Ge-7 together with a background spectrum of 13.62 d is shown in Fig. 5.
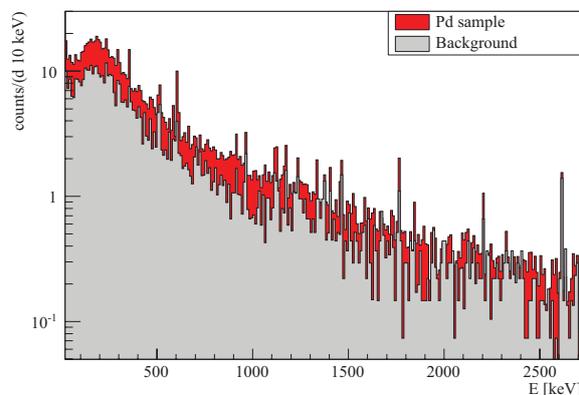

FIG. 5. (Color online) Sum spectrum of Ge-6 and Ge-7 detectors for a selected data set (44.77 d) in red and a background spectrum (13.62 d) in gray. The spectra are shown in common 10-keV bins between 20 and 2720 keV.

C. Background investigation

The radiopurity of the palladium sample was assessed during the γ-spectrometry measurement performed at HADES. In the measured spectrum, the major γ lines emitted by natural radionuclides belonging to the ^{238}U and ^{232}Th chains and to ^{40}K as well as the ^{60}Co lines are visible. The palladium spectrum is compared to the background spectrum measured without a sample. The background peak count rate is subtracted from that of the palladium sample. The result, if positive, is then used for the evaluation of the activity due to the impurities in the sample. In case of a negative result, a decision threshold is calculated according to Ref. [39]. The results are reported in Table III. Decision thresholds are also calculated for the following radionuclides: ^{102}Rh ($T_{\frac{1}{2}} = 207.3$ d), ^{102m}Rh ($T_{1/2} = 3.742$ yr), and ^{110m}Ag ($T_{1/2} = 249.76$ d). The reason is the possible interference with the search for ^{110}Pd and ^{102}Pd isotopes, because of the emission of γ lines from the same excited daughter states. No presence of these radionuclides is found, as reported in Table IV.

D. Peak finding

The analysis is a peak search on the detector sum spectrum and either retrieves the number of counts in a respective peak or states an upper limit of counts according to a level of confidence. In an experiment with non-negligible background, the background can fluctuate upwards or downwards. The sensitivity of an experiment is then defined as a resulting signal which originates from a 1 σ upward fluctuation of the background. This can be calculated before performing the experiment if the background is known. In the case of the observation of a downward fluctuation, which formally results in negative signal counts, the signal is usually set to zero and the sensitivity is quoted as an upper limit of the counts. On the other hand, when using classical uncertainties on the observed downward fluctuated counts, it is possible that in some cases even the upper limit is negative. In these cases it results in a poor coverage of the quoted confidence level at best and in

TABLE III. Massic activities (in mBq/kg) of radioimpurities detected in the Pd sample.

| Nuclide	E (keV)	Massic activity (mBq/kg)	Decision threshold ($\alpha = 95\%$) (mBq/kg)	Weighted mean massic activity (mBq/kg)
[214]Pb	295.22	1.9 ± 1.0	1.4	1.4 ± 0.4
	351.93	1.3 ± 0.5	0.6	
[214]Bi	609.32	1.9 ± 0.4	0.4	1.9 ± 0.4
	1120.29	2.0 ± 0.8	0.9	
	1238.11	—	2.2	
	1377.67	—	2.7	
	1764.54	—	3.2	
[210]Pb	46.54	—	414.3	
[228]Ac	911.20	—	0.5	
	968.97	—	0.9	
[212]Pb	238.63	—	0.7	
[208]Tl	583.19	—	0.6	
	2614.51	—	0.3	
[40]K	1460.82	—	1.0	
[137]Cs	661.66	—	0.2	
[60]Co	1173.23	—	0.2	
	1332.49	—	0.1	

an unphysical negative result at worst. Additionally there is a discontinuity in the coverage when crossing from a two-sided confidence interval definition to a one-sided one.

All these problems are addressed by the method of Feldman and Cousins in their paper [40]. They use a Neyman construction of a confident belt and an ordering principle based on likelihood ratios. The advantages are a physical yield in all background situations, i.e., a positive upper count limit and avoiding discontinuities in the coverage while crossing the statistical interpretation from a nonobservation to an observation, i.e., from a one-sided to a two-sided confidence interval. The confidence intervals of the Feldman-Cousins method are believed to have a better coverage for small numbers than Gaussian ones [40].

No prominent peak structures are observed in the signal region and the results of the analysis are upper limits only for the peak counts. To obtain a numerical value, all bins within a peak are combined into a single analysis bin that covers at least the full width at half maxium of the peak. The real

TABLE IV. Decision thresholds for direct γ background of double-β-decay intermediate nuclei.

Nuclide	E (keV)	Decision threshold ($\alpha = 95\%$) (mBq/kg)
[110m]Ag	1384.30	0.5
	1505.04	1.0
[102]Rh	475.05	0.4
[102m]Rh	631.28	0.3
	697.49	0.3
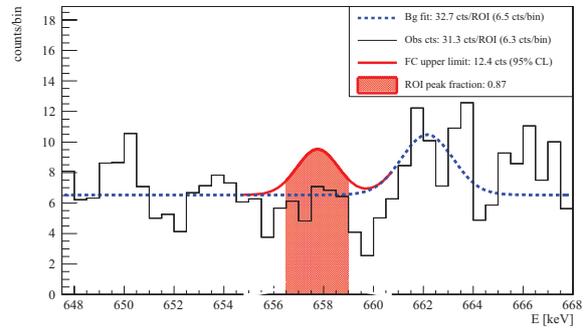
FIG. 6. (Color online) The peak region around the 657.76-keV γ line from [110]Pd and the 661.66-keV γ line from [137]Cs.

signal fraction coverage is calculated as the Gaussian peak area in the analysis bin and depends on the actual binning of the spectrum. The peak background is fitted with a constant function defined ± 30 keV around the peak energy excluding a window of ± 5 keV around the peak. In the case of prominent background peaks in the side bands, they are included in the background function as Gaussians. This was done for the background peaks at 609.31, 1120.29, and 1764.49 keV from [214]Bi, at 238.63 keV from [212]Pb, at 1461.83 keV from [40]K, and at 661.66 keV from [137]Cs. In the case of the 661.66-keV peak which is close to the 657.76-keV peak in the [110]Pd system, the flat background function was defined closer than ± 5 keV into the signal region to improve the background estimation.

The observed counts in the analysis bin are compared to the expected background with the ROOT class TFeldmanCousins, which returns the lower and upper bound of the signal confidence interval according to a specified confidence level that is set to 95% in this work. All investigated peaks show a lower count limit of zero; this is in agreement with a nonobservation of the peak. To account for the incomplete coverage of the peak area by the analysis bin, the upper count limit is divided by the fraction of coverage and thus adjusts the upper count limit in a conservative way.

An illustration of the technique is shown in Figs. 6 to 9 with the energy spectrum in the solid black line, the background function in the dashed blue line, the peak fraction marked as
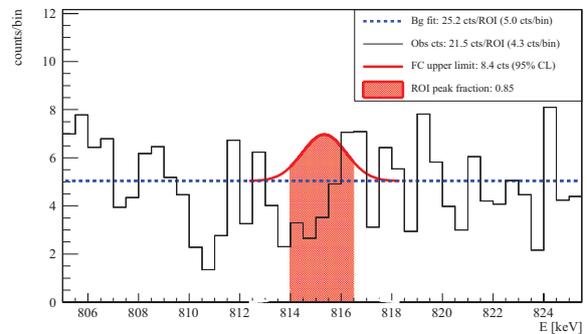
FIG. 7. (Color online) The peak region around the 815.33-keV γ line from [110]Pd 0_1^+.
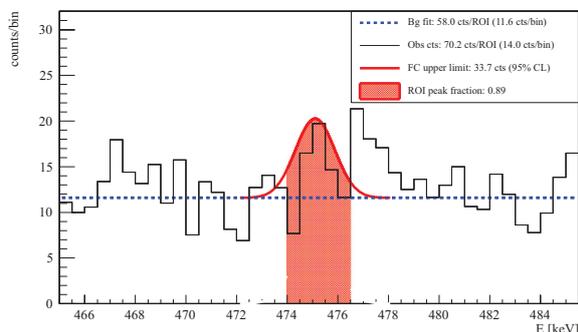
FIG. 8. (Color online) The peak region around the 475.10-keV γ line from ^{102}Pd 2^+_1.
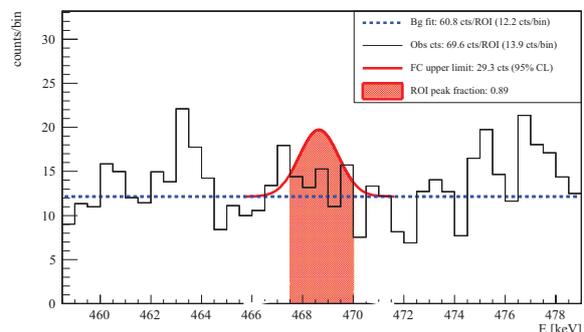

FIG. 9. (Color online) The peak region around the 468.64-keV γ line from ^{102}Pd 0^+_1.

the solid red area and the gaussian signal peak as it appears with the Feldman Cousins upper limit as the red solid line. The Feldman and Cousins limits are cross-checked with the International Organization for Standardization (ISO) standard methods [39] and agree better than within a factor of 2 with each other; this can be explained by the different treatment of statistical background fluctuations.

E. Monte Carlo simulation for γ line efficiencies

The full-energy peak (FEP) efficiencies were determined using Monte Carlo simulations with the EGS4 software. The

models of the detectors were first determined from manufacturer data and using information from radiography. Thereafter the dead layer thicknesses were adjusted in the model to agree with measured FEP efficiencies from point sources within 3%. The final model was validated using volume sources of a size similar to that of the Pd source in this study. Each decay branch was simulated separately with information from Ref. [35] and the calculations involved all the cascading γ rays of each branch so that the resulting FEP efficiency was inherently corrected for the coincidence summing effect. X-ray coincidences and the angular correlations were neglected in

TABLE V. Experimental results for each decay mode and γ line. The columns from left to right denote the decay mode, the γ line energy, the emission probability in %, and the detection efficiency in %. The last two columns show the upper signal count limit and the deduced lower half-life limit at 95% CL.

Decay mode	γ line energy (keV)	Emission probability	Detection efficiency	Signal count limit	$T_{1/2}$ limit (yr)
^{110}Pd 2^+_1 657.76 keV	657.76 keV	100%	4.70%	12.4	1.72×10^{20}
^{110}Pd 0^+_1 1473.12 keV	815.33 keV	100%	3.84%	8.4	1.98×10^{20}
	657.76 keV	100%	3.94%	12.4	1.44×10^{20}
^{110}Pd 2^+_2 1475.80 keV	1475.80 keV	35.25%	1.32%	11.5	5.17×10^{19}
	818.02 keV	64.75%	2.40%	16.3	6.67×10^{19}
	657.76 keV	64.75%	2.53%	12.4	9.26×10^{19}
^{110}Pd 0^+_2 1731.33 keV	1073.7 keV	86.73%	1.89%	10.1	8.50×10^{19}
	657.76 keV[a]	95.32%	3.78%	12.4	1.38×10^{20}
	255.49 keV	13.27%	0.36%	25.3	6.46×10^{18}
	1475.80 keV	4.68%	0.12%	11.5	4.87×10^{18}
	818.02 keV	8.59%	0.24%	16.3	6.63×10^{18}
^{110}Pd 2^+_3 1783.48 keV	1783.48 keV	21.57%	0.88%	6.2	6.45×10^{19}
	1125.71 keV	78.43%	2.48%	12.0	9.41×10^{19}
	657.76 keV	78.43%	2.99%	12.4	1.09×10^{20}
^{102}Pd 2^+_1 475.10 keV	475.10 keV	100%	5.09%	33.7	5.95×10^{18}
^{102}Pd 0^+_1 943.69 keV	468.64 keV	100%	4.32%	29.3	5.81×10^{18}
	475.10 keV	100%	4.31 %	33.7	5.04×10^{18}
^{102}Pd 2^+_2 1103.05 keV	1103.05 keV	37.11%	1.60%	13.5	4.66×10^{18}
	627.94 keV	62.90%	2.54%	11.7	8.55×10^{18}
	475.10 keV	62.90%	2.67%	33.7	3.13×10^{18}

[a]This γ line is part of two sub-branches starting from the same excited state.

NEW HALF-LIFE LIMITS ON DOUBLE-β DECAYS . . .

TABLE VI. Summary of measured half-life limits for all ^{110}Pd and ^{102}Pd double-β-decay excited-state transitions.

Decay mode	$T_{1/2}$ limit (yr) (95%)
^{110}Pd 2_1^+ 657.76 keV	1.72×10^{20}
^{110}Pd 0_1^+ 1473.12 keV	1.98×10^{20}
^{110}Pd 2_2^+ 1475.80 keV	9.26×10^{19}
^{110}Pd 0_2^+ 1731.33 keV	1.38×10^{20}
^{110}Pd 2_3^+ 1783.48 keV	1.09×10^{20}
^{102}Pd 2_1^+ 475.10 keV	5.95×10^{18}
^{102}Pd 0_1^+ 943.69 keV	5.81×10^{18}
^{102}Pd 2_2^+ 1103.05 keV	8.55×10^{18}

the simulations and it was assumed that the activity was homogeneously distributed in the whole volume of the sample.

V. RESULTS

All γ lines participating in a γ cascade were investigated and a half-life was calculated for each. Intrinsically, the calculation of limits is influenced by statistical fluctuations in the experimental spectrum; hence the largest calculated limit for an excited-state transition is quoted as the half-life limit of this transition. A summary of all investigated γ lines can be found in Table V: Quoted are the emission probability, the detection efficiency including summation effects, the upper count limit in the spectrum, and the calculated half-life. The selected half-life for each transition is listed in Table VI. The peak regions for the γ lines originating from the favored 0_1^+ transitions are shown in Figs. 6 and 7 for ^{110}Pd and in Figs. 8 and 9 for ^{102}Pd.

VI. CONCLUSION

A palladium sample has been investigated for double-β-decay transitions into excited states at the low background laboratory HADES. Lower half-life limits could be improved for the 0_1^+ and 2_1^+ transitions in ^{110}Pd and ^{102}Pd and first limits were established for all possible higher-energetic excited-state transitions. The best limit could be set for the ^{110}Pd 0_1^+ transition with a half-life larger than 1.98×10^{20} yr. The largest improvement compared to previous results was archived for the ^{110}Pd 2_1^+ transition with 1.72×10^{20} yr, which is an improvement by a factor of 3.9. For the ^{102}Pd system, the improvements were smaller due to upward fluctuations of the background in the peak region of the 475.10- and 468.64-keV γ lines.

Possible improvement of the search of double-β decays in palladium could be achieved by the consideration of x rays. This would require a different geometric assembly of the palladium plates, e.g., in a layer around an n-type HPGe detector with a thin dead layer. Further improvement could be achieved by considering γ coincidences using the multi-parameter DAQ system. This would also reduce the muonic background. The intrinsic massic activity of the palladium sample was determined to be 1.7 mBq/kg for the ^{238}U chain and below the detection threshold for the ^{232}Th chain. Further purifications are not expected to yield significant improvement. However, accumulating storage underground will reduce the general background from cosmic-activated radio isotopes in the palladium sample and the measuring system.

ACKNOWLEDGMENT

[1] K. Abe *et al.* (Super-Kamiokande Collaboration), Phys. Rev. D **83**, 052010 (2011).

[2] B. Aharmim *et al.* (SNO Collaboration), arXiv:1109.0763.

[3] G. Alimonti *et al.* (BOREXINO Collaboration), Nucl. Instrum. Methods Phys. Rese., Sect. A **600**, 568 (2009).

[4] S. Hatakeyama *et al.*, Phys. Rev. Lett. **81**, 2016 (1998).

[5] J. K. Ahn *et al.* (RENO Collaboration), Phys. Rev. Lett. **108**, 191802 (2012).

[6] F. P. An *et al.* (Daya Bay Collaboration), Phys. Rev. Lett. **108**, 171803 (2012).

[7] S. Abe *et al.* (KamLAND Collaboration), Phys. Rev. Lett. **100**, 221803 (2008).

[8] F. Ardellier *et al.* (Double Chooz Collaboration), arXiv:hep-ex/0606025.

[9] P. Adamson *et al.* (MINOS Collaboration), Phys. Rev. Lett. **101**, 131802 (2008).

[10] K. Abe *et al.* (T2K Collaboration), Nuclear Instrum. Methods Phys Res., Sect. A **659**, 106 (2011).

[11] N. Agafonova *et al.* (OPERA Collaboration), New J. Phys. **14**, 033017 (2012).

[12] G. Mathews *et al.*, Phys. Rev. D **85**, 105023 (2012).

[13] J. Wolf, Nucl. Instrum. Methods Phys. Res., Sect. A **623**, 442 (2010).

[14] A. Monfardini *et al.* (MARE Collaboration), Nucl. Instrum. Methods Phys. Res., Sect. A **559**, 346 (2006).

[15] N. Jarosik *et al.*, Astrophys. J. Suppl. Ser. **192**, 14 (2011).

[16] H. Klapdor-Kleingrothaus, A. Dietz, H. Harney, and I. Krivosheina, Mod. Phys. Lett. A **16**, 2409 (2001).

[17] H. Klapdor-Kleingrothaus and I. Krivosheina, Mod. Phys. Lett. A **21**, 1547 (2006).

[18] V. I. Tretyak and Y. G. Zdesenko, At. Data Nucl. Data Tables **80**, 83 (2002).

[19] N. Ackerman *et al.* (EXO Collaboration), Phys. Rev. Lett. **107**, 212501 (2011).

[20] F. Avignone, S. Elliott, and J. Engel, Rev. Mod. Phys. **80**, 481 (2008).

[21] A. Barabash *et al.*, Phys. Lett. B **345**, 408 (1995).

[22] A. Barabash, F. Hubert, P. Hubert, and V. I. Umatov, Phys. At. Nucl. **67**, 1216 (2004).

[23] D. Fink *et al.*, Phys. Rev. Lett. **108**, 062502 (2012).

[24] R. Winter, Phys. Rev. **85**, 687 (1952).

[25] B. Lehnert and K. Zuber, Phys. Lett. B **705**, 47 (2011).
[26] R. Chandra *et al.*, Eur. Phys. J. A **23**, 223 (2005).
[27] S. V. Semenov, F. Šimkovic, V. V. Khruschev, and P. Domin, Phys. At. Nucl. **63**, 1196 (2000).
[28] O. Civitarese and J. Suhonen, Phys. Rev. C **58**, 1535 (1998).
[29] S. Stoica, Phys. Rev. C **49**, 2240 (1994).
[30] M. Hirsch, X. Wu, H. Klapdor-Kleingrothaus, C. Cheng-rui, and H. Tso-hsiu, Phys. Rep. **242**, 403 (1994).
[31] A. Staudt, K. Muto, and H. V. Klapdor-Kleingrothaus, Europhys. Lett. **13**, 31 (1990).
[32] P. Domin, S. Kovalenko, F. Šimkovic, and S. Semenov, Nucl. Phys. A **753**, 337 (2005).
[33] J. Suhonen, Nucl. Phys. A **864**, 63 (2011).

[34] A. Raduta and C. Raduta, Phys. Lett. B **647**, 265 (2007).
[35] ENSDF database, http://www.nndc.bnl.gov/ensdf (July 10, 2012).
[36] E. Andreotti *et al.*, in *the Proceedings of the 3rd International Conference on Current Problems in Nuclear Physics and Atomic Energy* (KINR, Kyiv, Ukraine, 2010).
[37] J. S. E. Wieslander *et al.*, Appl. Radiat. Isot. **67**, 731 (2009).
[38] I. Antcheva *et al.*, Comput. Phys. Commun. **180**, 2499 (2009).
[39] International Organization for Standardization, ISO 11929:2010 (2010).
[40] G. J. Feldman and R. D. Cousins, Phys. Rev. D **57**, 3873 (1998).

Appendix H

List of Acronyms

This is a list of frequently used acronyms throughout this work. Note that some definitions are unique for this work or may differ from other literature.

$0\nu\beta\beta$	-	neutrinoless double beta decay
$2\nu\beta\beta$	-	two-neutrino double beta decay
$0\nu\beta^-\beta^-$	-	neutrinoless double beta minus decay
$2\nu\beta^-\beta^-$	-	two-neutrino double beta minus decay
$0\nu\beta^+\beta^+$	-	neutrinoless double beta plus decay
$2\nu\beta^+\beta^+$	-	two-neutrino double beta plus decay
0νECEC	-	neutrinoless double electron capture
2νECEC	-	two-neutrino double electron capture
0νECβ^+	-	neutrinoless electron capture beta plus decay
2νECβ^+	-	two-neutrino electron capture beta plus decay
AC	-	anti-coincidence
ADC	-	analog-to-digital converter
ADL	-	AGATA Detector Library
ANG	-	German: ANGereichert. Enriched GERDA detectors from the HdM experiment
APD	-	avalanche photo diode
AV	-	active volume
BAO	-	baryonic acoustic oscillations
BAT	-	Bayesian Analysis Toolkit
BBN	-	big bang nucleosynthesis
BEGe	-	Broad Energy Germanium
BI	-	background index
c.d.f.	-	commutative distribution function
C.I.	-	credibility interval
C.L.	-	confidence level
CCE	-	charge collection efficiency
CKM	-	Cabibbo-Kobayashi-Maskawa mixing matrix for the quark sector

CMB	-	cosmic microwave background
CP	-	charge conjugation parity
CSDA	-	continuous-slowing-down approximation
DAQ	-	data acquisition
DBD	-	double beta decay
DDR	-	drift dominated region
DEP	-	double escape peak
DL	-	dead layer
DLF	-	dead layer fraction
DLPP	-	dead layer post processing
DLT	-	dead layer thickness
DOF	-	degrees of freedom
EDF	-	Energy Density Functional
FADC	-	fast ADC
FAV	-	fully active volume
FCCD	-	full charge collection depth
FEP	-	full energy peak
FWHM	-	full width at half maximum
GAr	-	gaseous argon
GCM	-	Generating Coordinate Method
GELATIO	-	GErda LAyouT for Input/Output: Data processing software
GERDA	-	GERmanium Detector Array
GPS	-	General Particle Source
GTF	-	Genius Test Facility. Natural GERDA detectors from the GENIUS experiment
HADES	-	High Activity Disposal Experimental Site
HdM	-	Heidelberg-Moscow
HDPE	-	high density polyethylene
HEROICA	-	HADES Experimental Research Of Intrinsic Crystal Appliances

HFB	-	Hartree-Fock Bogoljubov
HPGe	-	High Purity Germanium
HV	-	high voltage
IBM-2	-	Interactive Boson Model 2
IGEX	-	International Germanium Experiment
INFN	-	Instituto Nazionale di Fisica Nucleare
IRMM	-	Institute for Reference Material and Measurements
JFET	-	junction gate field-effect transistor
LAr	-	liquid argon
LC	-	leakage current
LET	-	linear energy transfer
LHC	-	Large Hadron Collider
LNGS	-	Laboratori Nazionali del Gran Sasso
LNV	-	lepton number violation
LSS	-	large scale structures
LXe	-	liquid xenon
MaGe	-	Majorana GERDA: MC framework
MC	-	Monte Carlo
MCA	-	multi channel analyzer
MGDO	-	Majorana Gerda Data Objects: Data processing software
MS	-	Mini-Shroud
MSE	-	multi-site event
MSW	-	MikheyevSmirnovWolfenstein effect
MWA	-	moving window average
NME	-	nuclear matrix element
p.d.f.	-	probability density function
PE	-	polyethylene
PMNS	-	Pontecorvo-Maki-Nakagawa-Sakata mixing matrix for the lepton sector
PMT	-	photomultiplier tube
PPC	-	p$^+$ point contact
PSD	-	pulse shape discrimination

PSF	-	phase space factor
PVC	-	polyvinyl chloride
PWS	-	peak window size
QRPA	-	Quasi Random Phase Approximation
RDR	-	recombination dominated region
RG	-	Italian: Ricco Grande. Enriched GERDA detectors from the IGEX experiment
ROI	-	region of interest
SB	-	side band
SDT	-	single detector threshold
SEL	-	sum energy limit
SEP	-	singe escape peak
SF	-	suppression factor
ShM	-	Shell Model
SiPM	-	silicon photomultiplier
SM	-	Standard Model
SN	-	supernova
SPB	-	slow pulse band
SSB	-	single-site band
SSE	-	single-site event
SUSY	-	supersymmetry
TL	-	transition layer
TLF	-	transition layer fraction
TLT	-	transition layer thickness
TPB	-	tetraphenyl butadiene
TPC	-	time projection chamber
TOF	-	time of flight
UV	-	ultraviolet
VKTA	-	Verein für Kernverfahrenstechnik und Analytik
WLS	-	wavelength shifter
XUV	-	extreme ultraviolet

Bibliography

[1] C. L. Cowan et al., "Detection of the Free Neutrino: a Confirmation", *Science*, 124 (1956), 1–2.

[2] F. Reines and C. L. Cowan, "The Neutrino", *Nature*, 178, 4531 (1956), 446–449.

[3] E. Fermi, "Versuch einer Theory der β-Strahlen", *Z. für Phys.* 88 (1934), 161–177.

[4] M. Goldhaber, L. Grodzins, and A. W. Sunyar, "Helicity of Neutrinos", *Phys. Rev.* 109 (1957), 1015–1018.

[5] C. S. Wu et al., "Experimental Test of Parity Conservation in Beta Decay", *Phys. Rev.* 105 (1957), 1414–1417.

[6] D. R. Hamilton, W. P. Alford, and L. Gross, "Upper limits on the neutrino mass from the tritium beta spectrum", *Phys. Rev.* 92, 6 (1953), 1521–1525.

[7] S. L. Glashow, "Partial-Symmetries of Weak Interactions", *Nuc. Phys.* 22, 4 (1961), 579.

[8] *Particle Data Group @ONLINE*, 2015, URL: http://pdg.lbl.gov.

[9] . ALEPH, DELPHI, L3, OPAL Collaboration and LEP Electroweak Working Group, "Precision electroweak measurements on the Z resonance", *Phys. Rep.* 427, 5-6 (2006), 257–454.

[10] Z. Maki, M. Nakagawa, and S. Sakata, "Remarks on the Unified Model of Elementary Particles", *Prog. Theor. Phys.* 28, 5 (1962), 870–880.

[11] V. N. Gribov and B. Pontecorvo, "Neutrino astronomy and lepton charge", *Phys. Lett.* B28, 7 (1969), 493–496.

[12] A. Strumia and F. Vissani, "Neutrino masses and mixings and...", 25 (2006), eprint: 0607317v1 (hep-ph).

[13] L. Wolfenstein, "Neutrino oscillations in matter", *Phys. Rev. D*, 17, 9 (1978), 2369–2374.

[14] N. Schmitz, "Neutrinophysik", Teubner Verlag, 1997.

[15] C. Kraus et al., "Final results from phase II of the Mainz neutrino mass searching tritium β decay", *Eur. Phys. J. C*, 40, 4 (2005), 447–468.

[16] V. N. Aseev et al., "Upper limit on the electron antineutrino mass from the Troitsk experiment", *Phys. Rev. D*, 84, 11 (2011), 112003.

[17] G. Drexlin, V. Hannen, S. Mertens, and C. Weinheimer, "Current Direct Neutrino Mass Experiments", *Adv. High Energ. Phys.* 2013 (2013), 1–39.

[18] G. Drexlin, "KATRIN - direct measurement of a sub-eV neutrino mass", *Nucl. Phys. B (Proc. Suppl.)* 145 (2005), 263–267.

[19] K. Blaum et al., "The Electron Capture ^{163}Ho Experiment ECHo" (2013), eprint: 1306.2655v1 (physics.ins-det).

[20] A. Nucciotti, "Statistical sensitivity of 163-Ho electron capture neutrino mass experiments" (2014), eprint: 1405.5060v2 (physics.ins-det).

[21] P. J. Doe et al., "Project 8: Determining neutrino mass from tritium beta decay using a frequency-based method" (2013), eprint: 1309.7093 (nucl-ex).

[22] A. Faessler, R. Hodak, S. Kovalenko, and F. Simkovic, "Beta Decay and the Cosmic Neutrino Background", *EPJ Web of Conferences*, 71 (2014), 00044.

[23] G. Pagliaroli, F. Rossi-Torres, and F. Vissani, "Neutrino mass bound in the standard scenario for supernova electronic antineutrino emission", *Astrop. Phys.* 33, 5-6 (2010), 287–291.

[24] T. Loredo and D. Lamb, "Bayesian analysis of neutrinos observed from supernova SN 1987A", *Phys. Rev. D*, 65, 6 (2002), 063002.

[25] P. A. R. Ade et al., "Planck 2013 results. XVI. Cosmological parameters" (2013), eprint: 1303.5076v3 (astro-ph.CO).

[26] S. Dell'Oro, S. Marcocci, and F. Vissani, "New expectations and uncertainties on Neutrinoless Double Beta Decay" (2014), eprint: 1404.2616 (hep-ph).

[27] M. Agostini et al., "Results on Neutrinoless Double-β Decay of ^{76}Ge from Phase I of the GERDA Experiment", *Phys. Rev. Lett.* 111 (2013), 122503.

[28] J. B. Albert et al., "Search for Majorana neutrinos with the first two years of EXO-200 data", *Nature*, 510, 7504 (2014), 229–234.

[29] W. Maneschg, A. Merle, and W. Rodejohann, "Statistical analysis of future neutrino mass experiments including neutrino-less double beta decay", *Europhys. Lett.* 85, 5 (2009), 51002.

[30] R. B. Firestone, C. M. Baglin, and S. Y. F. Chu, "Table of Isotopes", 8th ed., Wiley-Interscience, 1999.

[31] V. I. Tretyak, F. A. Danevich, S. S. Nagorny, and Y. G. Zdesenko, "On the possibility to search for double beta decay of initially unstable (alpha/beta radioactive) nuclei", *Europhys. Lett.* 69, 1 (2004), 41–47.

[32] K. Zuber, "Neutrino Physics", 1st ed., Series in High Energy Physics, Cosmology and Gravitation, Taylor & Francis, 2003.

[33] *Nuclear Physics Yale @ONLINE*, 2015, URL: http://nucleartheory.yale.edu.

[34] J. Kotila and F. Iachello, "Phase-space factors for double-β decay", *Phys. Rev. C*, 85, 3 (2012), 034316.

[35] V. I. Tretyak and Y. G. Zdesenko, "Tables of double beta decay data - an update", *Atom. Data Nucl. Data Tabl.* 80 (2002), 83–116.

[36] N. Ackerman et al., "Observation of Two-Neutrino Double-Beta Decay in ^{136}Xe with the EXO-200 Detector", *Phys. Rev. Lett.* 107 (2011), 212501.

[37] J. Kotila, J. Barea, and F. Iachello, "Neutrinoless double-electron capture", *Phys. Rev. C*, 89, 6 (2014), 064319.

[38] A. Faessler et al., "Uncovering multiple CP-nonconserving mechanisms of $(\beta\beta)_{0\nu}$ decay", *Phys. Rev. D*, 83, 11 (2011), 113003.

[39] J. C. Helo, S. G. Kovalenko, M. Hirsch, and H. Päs, "Neutrinoless double beta decay and lepton number violation at the LHC", *Phys. Rev. D*, 88, 1 (2013), 011901.

[40] W. Rodejohann, "Neutrinoless double beta decay and particle physics", *Int. J. Mod. Phys. E*, 20, 09 (2011), 1833–1930.

[41] M. Duerr, M. Lindner, and A. Merle, "On the quantitative impact of the Schechter-Valle theorem", *J. High Energ. Phys.* 2011, 6 (2011), 91–19.

[42] K. Amos, A. Faessler, and V. Rodin, "Charge-exchange reaction cross sections and the Gamow-Teller strength for double β decay", *Phys. Rev. C*, 76, 1 (2007), 014604.

[43] O. Cremonesi and M. Pavan, "Challenges in Double Beta Decay", *Adv. High Energ. Phys.* 2014, 4 (2014), 1–40.

[44] J. Barea, J. Kotila, and F. Iachello, "$0\nu\beta\beta$ and $2\nu\beta\beta$ nuclear matrix elements in the interacting boson model with isospin restoration", *Phys. Rev. C*, 91, 3 (2015), 034304–11.

[45] A. S. Barabash et al., "Two neutrino double-beta decay of ^{100}Mo to the first excited 0^+ state in ^{100}Ru", *Phys. Lett. B*, 345 (1995), 408–413.

[46] A. S. Barabash, F. Hubert, P. Hubert, and V. I. Umatov, "Double beta decay of ^{150}Nd to the first 0^+ excited state of ^{150}Sm", *JETP Lett.* 79 (2004), 10–12.

[47] R. Arnold et al., "Investigation of double beta decay of ^{100}Mo to excited states of ^{100}Ru", *Nucl. Phys. A* (2014).

[48] A. Barabash, P. Hubert, A. Nachab, and V. Umatov, "Investigation of $\beta\beta$ decay in ^{150}Nd and ^{148}Nd to the excited states of daughter nuclei", *Phys. Rev. C*, 79, 4 (2009), 045501.

[49] J. Barea, J. Kotila, and F. Iachello, "Nuclear matrix elements for double β decay", *Phys. Rev. C*, 87, 1 (2013), 014315.

[50] A. S. Barabash, "Precise half-life values for two-neutrino double-β decay", *Phys. Rev. C*, 81 (2010), 035501.

[51] A. Bakalyarov et al., "Improved limits on β^- and $\beta^-\beta^-$ decays of ^{48}Ca", *JETP Lett.* 76, 9 (2002), 545–547.

[52] M. Agostini et al., "Results on $\beta\beta$ decay with emission of two neutrinos or Majorons in ^{76}Ge from GERDA Phase I", *Eur. Phys. J. C*, 75, 9 (2015), 416–12.

[53] S. I. Vasilev, A. A. Klimenko, S. B. Osetrov, and A. A. Smolnikov, "New bound to the probability of ^{76}Ge $\beta\beta$ decay to the 0_1^+ ^{76}Se Level", *JETP Lett.* 72 (2000), 279–281.

[54] M. Aunola and J. Suhonen, "Systematic study of beta and double beta decay to excited final states", *Nucl. Phys. A*, 602 (1996), 133–166.

[55] J. Toivanen and J. Suhonen, "Study of several double-beta-decaying nuclei using the renormalized proton-neutron quasiparticle random-phase approximation", *Phys. Rev. C*, 55 (1997), 2314–2323.

[56] S. Stoica and I. Mihut, "Nuclear structure calculations of two-neutrino double-beta decay transitions to excited final states", *Nucl. Phys. A*, A602, 2 (1996), 197–210.

[57] J. Suhonen et al., "Renormalized proton- neutron QRPA and double beta decay of ^{82}Se to excited states in ^{82}Kr", *Z Phys A - Particles and Fields*, 358, 3 (1997), 297–301.

[58] A. S. Barabash et al., "Investigation of the decay of to excited states in bb decay of ^{96}Zr to excited states in ^{96}Mo", *J. Phys. G: Nucl. Part. Phys.* 22, 4 (1996), 487–496.

[59] J. Hirsch, O. Castanos, P. Hess, and O. Civitarese, "Double-beta decay of ^{100}Mo: The deformed limit", *Phys. Rev. C*, 51, 4 (1995), 2252–2255.

[60] R. Winter, "A Search for Double Beta-Decay in Palladium", *Phys. Rev.* 85, 4 (1952), 687–687.

[61] B. Lehnert, K. Zuber, E. Andreotti, and M. Hult, "New half-life limits on double-β decays of ^{110}Pd and ^{102}Pd into excited states", *Phys. Rev. C*, 87 (2013), 034312.

[62] J. Suhonen, "On the double-beta decays of ^{70}Zn, ^{86}Kr, ^{94}Zr, ^{104}Ru, ^{110}Pd, ^{124}Sn", *Nucl. Phys. A*, 864, 1 (2011), 63–90.

[63] A. Piepke et al., "Investigation of the $\beta\beta$ decay of ^{116}Cd into excited states of ^{116}Sn", *Nucl. Phys. A*, 577, 3-4 (1994), 493–510.

[64] E. Andreotti et al., "Search for double-β decay of ^{130}Te to the first 0^+ excited state of ^{130}Xe with the CUORICINO experiment bolometer array", *Phys. Rev. C*, 85, 4 (2012), 045503.

[65] Y.-R. Yen, "A Search for the Double-Beta Decay of ^{136}Xe to an Excited State of ^{136}Ba with EXO-200 ", PhD thesis, 2013.

[66] A. S. Barabash, F. Hubert, P. Hubert, and V. I. Umatov, "New limits on the $\beta\beta$ decay of ^{130}Te to excited states of ^{130}Xe", *Eur. Phys. J. A*, 11, 2 (2001), 143–145.

[67] J. Beller et al., "Constraint on $0\nu\beta\beta$ Matrix Elements from a Novel Decay Channel of the Scissors Mode: The Case of ^{154}Gd", *Phys. Rev. Lett.* 111, 17 (2013), 172501.

[68] A. Gando et al., "Limit on Neutrinoless $\beta\beta$ Decay of ^{130}Xe from the First Phase of KamLAND-Zen and Comparison with the Positive Claim in ^{76}Ge", *Phys. Rev. Lett.* 110, 6 (2013), 062502.

[69] H. V. Klapdor-Kleingrothaus, A. Dietz, H. L. Harney, and I. V. Krivosheina, "Evidence for Neutrinoless Double Beta Decay", *Mod. Phys. Lett. A*, 16 (2002), 2409–2420. 14 p.

[70] H. V. Klapdor-Kleingrothaus, I. V. Krivosheina, A. Dietz, and O. Chkvorets, "Search for neutrinoless double beta decay with enriched ^{76}Ge in Gran Sasso 1990–2003", *Phys. Lett. B*, 586, 3-4 (2004), 198–212.

[71] H. V. Klapdor-Kleingrothaus and I. V. Krivosheina, "The Evidence For The Observation Of $0\nu\beta\beta$ Decay", *Mod. Phys. Lett. A* (2006).

[72] B. Schwingenheuer, "Status and prospects of searches for neutrinoless double beta decay", *Ann. Phys.* 525, 4 (2013), 269–280.

[73] A. Gando et al., "Measurement of the double-β decay half-life of ^{136}Xe with the KamLAND-Zen experiment", *Phys. Rev. C*, 85, 4 (2012), 045504.

[74] M. Auger et al., "Search for Neutrinoless Double-Beta Decay in ^{136}Xe with EXO-200", *Phys. Rev. Lett.* 109, 3 (2012), 032505.

[75] J. B. Albert et al., "Improved measurement of the $2\nu\beta\beta$ half-life of ^{136}Xe with the EXO-200 detector", *Phys. Rev. C*, 89, 1 (2014), 015502.

[76] T. R. Rodríguez and G. Martínez-Pinedo, "Energy Density Functional Study of Nuclear Matrix Elements for Neutrinoless $\beta\beta$ Decay", *Phys. Rev. Lett.* 105, 25 (2010), 252503.

[77] J. Menéndez, A. Poves, E. Caurier, and F. Nowacki, "Disassembling the nuclear matrix elements of the neutrinoless $\beta\beta$ decay", *Nucl. Phys. A*, 818, 3-4 (2009), 139–151.

[78] J. Suhonen and O. Civitarese, "Effects of orbital occupancies and spin–orbit partners on $0\nu\beta\beta$-decay rates", *Nucl. Phys. A*, 847, 3-4 (2010), 207–232.

[79] F. Simkovic, V. Rodin, A. Faessler, and P. Vogel, "0$\nu\beta\beta$ and 2$\nu\beta\beta$ nuclear matrix elements, quasiparticle random-phase approximation, and isospin symmetry restoration", *Phys. Rev. C*, 87, 4 (2013), 045501.

[80] M. T. Mustonen and J. Engel, "Large-scale calculations of the double-β decay of ^{76}Ge,^{130}Te,^{136}Xe, and ^{150}Nd in the deformed self-consistent Skyrme quasiparticle random-phase approximation", *Phys. Rev. C*, 87, 6 (2013), 064302.

[81] M. Agostini et al., "Limit on Neutrinoless Double Beta Decay of ^{76}Ge by GERDA", *Phys. Proc.* 61 (2015), 828–837.

[82] N. F. de Barros and K. Zuber, "Solar neutrino–electron scattering as background limitation for double-beta decay", *J. Phys. G: Nucl. Part. Phys.* 38, 10 (2011), 105201–18.

[83] M. G. Inghram and J. H. Reynolds, "Double Beta-Decay of ^{130}Te", *Phys. Rev.* 78, 6 (1950), 822–823.

[84] J. J. Gomez-Cadenas et al., "Sense and sensitivity of double beta decay experiments" (2010), eprint: 1010.5112 (hep-ex).

[85] H. Bhang, R. S. Boiko, and D. M. Chernyak, "AMoRE experiment: a search for neutrinoless double beta decay of ^{100}Mo isotope with ^{40}Ca^{100}MoO$_4$ cryogenic scintillation detector", *J. Phys.: Conf. Ser.* (2012).

[86] L. Cardani, "LUCIFER: A scintillating bolometer array for the search of neutrinoless double beta decay", *J. Phys.: Conf. Ser.* (2012).

[87] *XCOM: Photon Cross Sections Database @ONLINE*, 2015, URL: http://www.nist.gov/pml/data/xcom/.

[88] O. Klein and Y. Nishina, "Über die Streuung von Strahlung durch freie Elektronen nach der neuen relativistischen Quantendynamik von Dirac", *Z. für Phys.* 52, 11-12 (1929), 853–868.

[89] G. F. Knoll, "Radiation Detection and Measurement", Third Edition, Library of Congress, 2000.

[90] *Stopping-Power and Range Tables for Electrons, Protons, and Helium Ions @ONLINE*, 2015, URL: http://www.nist.gov/pml/data/star/.

[91] G. Gilmore, "Practical Gamma-ray Spectroscopy", John Wiley & Sons, 2011.

[92] M. Agostini et al., "Signal modeling of high-purity Ge detectors with a small readout electrode and application to neutrinoless double beta decay search in Ge-76", *J. Inst.* 6, 03 (2011), P03005–P03005.

[93] S. Ramo, "Currents induced by electron motion", *Proc. I.R.E* (1939), 584.

[94] W. Shockley, "Currents to Conductors Induced by a Moving Point Charge", *J. Appl. Phys.* 9, 10 (1938), 635.

[95] K. H. Ackermann et al., "The GERDA experiment for the search of 0$\nu\beta\beta$ decay in ^{76}Ge", *Eur. Phys. J. C*, 73 (2013), 2330.

[96] M. Agostini et al., "Improvement of the energy resolution via an optimized digital signal processing in GERDA Phase I", *Eur. Phys. J. C*, 75, 6 (2015), 255.

[97] M. Agostini et al., "Pulse shape discrimination for GERDA Phase I data", *Eur. Phys. J. C*, 73 (2013), 2583.

[98] T. Doke et al., "Absolute Scintillation Yields in Liquid Argon and Xenon for Various Particles", *Jpn. J. Appl. Phys.* 41, 3R (2002), 1538–1545.

[99]   C. Amsler et al., "Luminescence quenching of the triplet excimer state by air traces in gaseous argon", *J. Inst.* 3 (2008), P02001.

[100] R. Acciarri, M. Antonello, and B. Baibussinov, "Effects of Nitrogen contamination in liquid Argon", *J. Inst.* (2010).

[101] A. Hitachi et al., "Effect of ionization density on the time dependence of luminescence from liquid argon and xenon", *Phys. Rev.* B27 (1983), 5279–5285.

[102] E. Morikawa et al., "Argon, krypton, and xenon excimer luminescence: From the dilute gas to the condensed phase", *J. Chem. Phys.* 91, 3 (1989), 1469.

[103] W. H. Lippincott et al., "Scintillation time dependence and pulse shape discrimination in liquid argon", *Phys. Rev. C*, C78 (2008), 035801.

[104] A. Neumeier et al., "Attenuation of vacuum ultraviolet light in liquid argon", *Eur. Phys. J. C*, 72, 10 (2012), 2190–9.

[105] G. M. Seidel, R. E. Lanou, and W. Yao, "Rayleigh scattering in rare-gas liquids", *Nucl. Inst. a. Meth. A*, 489 (2002), 189–194.

[106] N. Ishida et al., "Attenuation length measurements of scintillation light in liquid rare gases and their mixtures using an improved reflection suppresser", *Nucl. Inst. a. Meth. A*, 384, 2-3 (1997), 380–386.

[107] B. J. P. Jones et al., "A measurement of the absorption of liquid argon scintillation light by dissolved nitrogen at the part-per-million level", *J. Inst.* 8, 07 (2013), P07011–P07011.

[108] R. Acciarri, M. Antonello, and B. Baibussinov, "Oxygen contamination in liquid Argon: combined effects on ionization electron charge and scintillation light", *J. Inst.* 5, 05 (2010), P05003–P05003.

[109] G. Alimonti et al., "The Borexino detector at the Laboratori Nazionali del Gran Sasso", *Nucl. Instr. Meth. A*, 600, 3 (2009), 568–593.

[110] G. Bellini et al., "Final results of Borexino Phase-I on low-energy solar neutrino spectroscopy", *Phys. Rev. D*, 89, 11 (2014), 112007.

[111] G. Heusser, "Low-radioactivity background techniques", *Annu. Rev. Nucl. Part. Sci.* 45, 1 (1995), 543–590.

[112] J. F. Ziegler, "Terrestrial cosmic ray intensities", *IBM J. of Res. a. Dev.* 42, 1 (1998), 117–140.

[113] P. K. F. Grieder, "Cosmic Rays at Earth", Researcher's Reference Manual and Data Book, ELSEVIER, 2001.

[114] M. Agostini et al., "Production, characterization and operation of ^{76}Ge enriched BEGe detectors in GERDA", *Eur. Phys. J. C*, 75, 2 (2015), 39.

[115] M. Agostini et al., "The background in the $0\nu\beta\beta$ experiment GERDA", *Eur. Phys. J. C*, 74 (2014), 2764.

[116] A. Bettini, "The world underground scientific facilities. A compendium", *arXiv* (2007), eprint: 0712.1051 (hep-ex).

[117] V. D. Ashitkov, A. S. Barabash, and S. G. Belogurov, "New experimental limit on the 42 Ar content in the Earth's atmosphere", *Nucl. Inst. a. Meth. A*, 416, 1 (1998), 179–181.

[118] *LNGS @ONLINE*, 2015, URL: https://www.lngs.infn.it.

[119] *EIG EURIDICE (European Underground Research Infrastructure for Disposal of nuclear waste in Clay Environment) @ONLINE*, 2015, URL: http://www.euridice.be.

[120] E. Andreotti et al., "Status Of Underground Radioactive Measurements In HADES", *Proc. of Int. Conf. on Current Prob. in Nucl. Phys. a. Atom. Energy Kyev Ukrain* (2011), P601.

[121] E. Andreotti et al., "HEROICA: an underground facility for the fast screening of germanium detectors", *J. Inst.* 8, 06 (2013), P06012–P06012.

[122] M. Köhler et al., "A new low-level γ-ray spectrometry system for environmental radioactivity at the underground laboratory Felsenkeller", *Appl. Rad. Isot.* 67, 5 (2009), 736–740.

[123] I. Abt et al., *GERDA - Letter of Intent*, tech. rep., 2004.

[124] K. Freund, P. Grabmayr, and C. Schmitt, *GSTR-13-014: Investigation of muon-vetoed germanium signals*, tech. rep., 2013.

[125] H. V. Klapdor-Kleingrothaus et al., "Latest results from the Heidelberg-Moscow double beta decay experiment", *Eur. Phys. J. A*, 12 (2001), 147–154.

[126] C. Aalseth et al., "IGEX ^{76}Ge neutrinoless double-beta decay experiment: Prospects for next generation experiments", *Phys. Rev. D*, 65, 9 (2002), 092007.

[127] H. V. Klapdor-Kleingrothaus, L. Baudis, and A. Dietz, "GENIUS-TF: a test facility for the GENIUS project", *Nucl. Inst. a. Meth. A*, 481 (2002), 149–159.

[128] M. Agostini, L. Pandola, P. Zavarise, and O. Volynets, "GELATIO: a general framework for modular digital analysis of high-purity Ge detector signals", *J. Inst.* 6 (2011), P08013.

[129] M. Agostini et al., "The MGDO software library for data analysis in Ge neutrinoless double-beta decay experiments", *J. Phys.: Conf. Ser.* 375 (2012), 042027.

[130] M. Boswell et al., "MaGe - a Geant4-Based Monte Carlo Application Framework for Low-Background Germanium Experiments", *IEEE Trans. Nucl. Sci.* 58, 3 (2011), 1212–1220.

[131] J. Allison et al., "Geant4 developments and applications", *IEEE Trans. Nucl. Sci.* 53, 1 (2006), 270–278.

[132] S. Agostinelli et al., "Geant4 - a simulation toolkit", *Nucl. Instr. Meth. A*, 506, 3 (2003), 250–303.

[133] B. Lehnert, "Commissioning of the GERDA experiment", *Proc. Int. Sch. Phys. Fermi*, 182 (2012), 309–313.

[134] D. Budjáš et al., "Isotopically modified Ge detectors for GERDA: from production to operation", *J. Inst.* 8, 04 (2013), P04018–P04018.

[135] M. Agostini et al., "Characterization of a broad energy germanium detector and application to neutrinoless double beta decay search in ^{76}Ge", *J. Inst.* 6, 04 (2011), P04005–P04005.

[136] M. Salathe, "Personal Communication", 2015.

[137] E. Aguayo et al., "Nuclear Instruments and Methods in Physics Research A", *Nucl. Instr. Meth. A*, 701, C (2013), 176–185.

[138] *NuDat 2: National Nuclear Data Center @ONLINE*, 2015, URL: http://www.nndc.bnl.gov/nudat2/.

[139] A. G. Schubert, "Personal Communication", 2012.

[140] A. G. Schubert, *Geant4 bug report @ONLINE*, 2013, URL: http://bugzilla-geant4.kek.jp/show_bug.cgi?id=1340.

[141] O. A. Ponkratenko, V. I. Tretyak, and Y. G. Zdesenko, "Event generator DECAY4 for simulating double-beta processes and decays of radioactive nuclei", *Phys. Atom. Nuc.* 63, 7 (2000), 1282–1287.

[142] *ORTEC GammaVision v7 User Manual*, tech. rep., 2013.

[143] S. Hauf et al., "Validation of Geant4-based Radioactive Decay Simulation" (2013), eprint: 1306.5129v1 (physics.comp-ph).

[144] G. A. P. Cirrone et al., "Validation of the Geant4 electromagnetic photon cross-sections for elements and compounds", *Nucl. Instr. Meth. A*, 618, 1-3 (2010), 315–322.

[145] L. Pandola, "Personal Communication", 2013.

[146] W. Fransen, "Personal Communication", 2013.

[147] M. Agostini et al., "Measurement of the half-life of the two-neutrino double beta decay of ^{76}Ge with the GERDA experiment", *J. Phys. G: Nucl. Part. Phys.* 40 (2013), 035110.

[148] P. S. Finnerty, "A Direct Dark Matter Search with the Low-Background Broad Energy Germanium Detector", PhD thesis, 2014.

[149] B. Pratt, "Diffusion of Lithium into Ge and Si", *J. Appl. Phys.* 37, 4 (1966), 1893.

[150] G. Kegel, B. D. Bhardwaj, and R. J. Laramee, "Precipitation of lithium in germanium", *J. of Solid State Chem.* 3, 2 (1971), 161–171.

[151] F. A. Trumbore, "Solid Solubilities of Impurity Elements in Germanium and Silicon", *Bell Syst. Techn. J.* 39, 1 (1960), 205–233.

[152] M. Salathe, "Study on modified point contact germanium detectors for low background applications", PhD thesis, 2015.

[153] B. Bruyneel, P. Reiter, and G. Pascovici, "Characterization of large volume HPGe detectors. Part I: Electron and hole mobility parameterization", *Nucl. Instr. Meth. A*, 569, 3 (2006), 764–773.

[154] L. J. Harkness-Brennan et al., "An experimental characterisation of a Broad Energy Germanium detector", *Nucl. Inst. a. Meth. A*, 760, C (2014), 28–39.

[155] B. Bruyneel, P. Reiter, and G. Pascovici, "Characterization of large volume HPGe detectors. Part II: Experimental results", *Nucl. Instr. Meth. A*, 569, 3 (2006), 774–789.

[156] M. Heisel, "LArGe - A liquid argon scintillation veto for Gerda", PhD thesis, 2012.

[157] B. Scholz, "A design study to determine the ideal setup for an in-situ measurement of the attenuation length of liquid argon in GERDA", MA thesis, 2012.

[158] B. Schneider, "Development of a setup for an in-situ measurement of the light attenuation of liquid argon for the GERDA experiment", MA thesis, 2014.

[159] A. Bideau-Mehu, Y. Guern, and R. Abjean, "Measurement of refractive indices of neon, argon, krypton and xenon in the 253.7–140.4 nm wavelength range. Dispersion relations and estimated oscillator strengths of the resonance lines", *J. Quant. Spectrosc. Radiat. Transfer*, 25, 5 (1981), 395–402.

[160]   A. Lubashevskiy, "Personal Communication", 2014.

[161]   M. Walter, "Personal Communication", 2014.

[162]   N. Barros, "Personal Communication", 2014.

[163]   C. Wiesinger, "Personal Communication", 2015.

[164]   M. Agostini et al., "$2\nu\beta\beta$ decay of ^{76}Ge into excited states with Gerda phase I", *J. Phys. G: Nucl. Part. Phys.* 42, 11 (2015), 1–18.

[165]   B. J. Mount, M. Redshaw, and E. G. Myers, "Double-β-decay Q values of ^{74}Se and ^{76}Ge", *Phys. Rev. C*, 81 (2010), 032501.

[166]   G. Schatz and A. Weidinger, "Nukleare Festkörperphysik", Teubner, 1997.

[167]   J. Suhonen, "Effects of orbital occupancies and spin–orbit partners II: $0\nu\beta\beta$ decays of ^{76}Ge, ^{82}Se and ^{136}Xe to first excited 0^+ states", *Nucl. Phys. A*, 853 (2011), 36–60.

[168]   J. Suhonen, "Personal communication", 2014.

[169]   F. Iachello, "Personal communication", 2014.

[170]   J. Menéndez, "Personal communication", 2015.

[171]   E. Caurier, F. Nowacki, and A. Poves, "Shell Model description of the $\beta\beta$ decay of ^{136}Xe", *Phys. Lett. B*, 711, 1 (2012), 62–64.

[172]   M. Beck et al., "New half life limits for the $\beta\beta_{2\nu+0_\nu}$ decay of ^{76}Ge to the excited states of ^{76}Se from the Heidelberg-Moscow $\beta\beta$ experiment", *Z. Phys. A*, 342, 4 (1992), 397–400.

[173]   A. S. Barabash, A. V. Derbin, and L. A. Popeko, "Search for $\beta\beta$ decay of ^{76}Ge to the excited states in ^{76}Se", *Z. Phys. A*, 352 (1995), 231–233.

[174]   W. C. Haxton and G. J. Stephenson Jr, "DOUBLE BETA DECAY", *Prog. Part. Nucl. Phys.* 12 (1984), 409–479.

[175]   S. Dhiman and P. Raina, "Two-neutrino double-beta decay matrix elements for ground and excited states of ^{76}Ge and ^{82}Se nuclei", *Phys. Rev. C*, 50 (1994), R2660–R2663.

[176]   O. Civitarese and J. Suhonen, "Two-neutrino double-beta decay to excited one- and two-phonon states", *Nucl. Phys. A*, 575 (1994), 251–268.

[177]   J. Schwieger, F. Šimkovic, A. Faessler, and W. Kamiński, "Double β decay to excited states of several medium-heavy nuclei within the renormalized quasiparticle random phase approximation", *Phys. Rev. C*, 57 (1998), 1738–1743.

[178]   S. Unlu, "Quasi Random Phase Approximation Predictions on Two-Neutrino Double Beta Decay Half-Lives to the First 2^+ State", *Chin. Phys. Lett.* 31, 4 (2014), 042101.

[179]   W. A. Rolke, A. M. López, and J. Conrad, "Limits and confidence intervals in the presence of nuisance parameters", *Nucl. Instr. Meth. A*, 551, 2-3 (2005), 493–503.

[180]   A. Caldwell, D. Kollár, and K. Kröninger, "BAT – The Bayesian analysis toolkit", *Comp. Phys. Comm.* 180, 11 (2009), 2197–2209.

[181]   D. Fink et al., "Q Value and Half-Lives for the Double-β-Decay Nuclide ^{110}Pd", *Phys. Rev. Lett.* 108, 6 (2012), 062502.

[182]   B. Lehnert and K. Zuber, "A first search of excited states double beta and double electron capture decays of ^{110}Pd and ^{102}Pd ", *Phys. Lett. B*, 705, 1-2 (2011), 47–51.

[183] A. Staudt, K. Muto, and H. V. Klapdor-Kleingrothaus, "Calculation of 2ν and 0ν Double-Beta Decay Rates", *Europhys. Lett.* 13, 1 (1990), 31–36.

[184] S. Stoica, "Half-lives for two neutrino double-beta-decay transitions to first 2^+ excited states", *Phys. Rev. C*, 49, 4 (1994), 2240–2243.

[185] M. Hirsch et al., "Operator expansion method and nuclear $\beta\beta$ decay", *Phys. Rep.* 242, 4-6 (1994), 403–422.

[186] O. Civitarese and J. Suhonen, "Is the single-state dominance realized in double-β-decay transitions?", *Phys. Rev. C*, 58, 3 (1998), 1535–1538.

[187] S. V. Semenov, F. Šimkovic, V. V. Khruschev, and P. Domin, "Contribution of the lowest 1^+ intermediate state to the $2\nu\beta\beta$-decay amplitude", *Phys. Atom. Nuc.* 63, 7 (2000), 1196–1199.

[188] P. Domin, S. Kovalenko, F. Šimkovic, and S. V. Semenov, "Neutrino accompanied $\beta^\pm\beta^\pm$, $\beta\beta^+/EC$ and EC/EC and processes within single state dominance hypothesis", *Nucl. Phys. A*, 753 (2005), 337–363.

[189] R. Chandra et al., "Two-neutrino double-β decay of $94 \le A \le 110$ nuclei for the 0^+ - 0^+ transition", *Eur. Phys. J. A*, 23, 2 (2005), 223–234.

[190] A. A. Raduta and C. M. Raduta, "Double beta decay to the first state within a boson expansion formalism with a projected spherical single particle basis", *Phys. Lett. B*, 647, 4 (2007), 265–270.

[191] C. M. Cattadori et al., "Observation of β decay of ^{115}In to the first excited level of ^{115}Sn", *Nucl. Phys. A*, 748, 1-2 (2005), 333–347.

[192] . International Organization for Standardization, *ISO_11929_2010*, tech. rep., 2010.

[193] *Lund/LBNL Nuclear Data Search @ONLINE*, 2015, URL: http://nucleardata.nuclear.lu.se/toi/.

[194] M. Redshaw, B. Mount, E. Myers, and F. Avignone, "Masses of ^{130}Te and ^{130}Xe and Double-β-Decay Q Value of ^{130}Te", *Phys. Rev. Lett.* 102, 21 (2009), 212502.

[195] M. Redshaw et al., "Atomic mass and double-β-decay Q value of ^{48}Ca", *Phys. Rev. C*, 86, 4 (2012), 041306.

[196] P. M. McCowan and R. C. Barber, "Q value for the double-β decay of ^{136}Xe", *Phys. Rev. C*, 82 (2010), 024603.

[197] M. Redshaw, E. Wingfield, J. McDaniel, and E. Myers, "Mass and Double-Beta-Decay Q Value of ^{136}Xe", *Phys. Rev. Lett.* 98, 5 (2007), 053003.

[198] G. Douysset et al., "Determination of the ^{76}Ge Double Beta Decay Q Value", *Phys. Rev. Lett.* 86, 19 (2001), 4259–4262.

[199] D. L. Lincoln et al., "First Direct Double-β Decay Q-Value Measurement of ^{82}Se in Support of Understanding the Nature of the Neutrino", *Phys. Rev. Lett.* 110, 1 (2013), 012501.

[200] V. S. Kolhinen et al., "Double-β decay Q value of ^{150}Nd", *Phys. Rev. C*, 82, 2 (2010), 022501.

[201] G. Audia, A. H. Wapstrab, and C. Thibaulta, "The AME2003 atomic mass evaluation", *Nucl. Phys. A*, 729 (2003), 337–676.

[202] S. Rahaman et al., "Q values of the ^{76}Ge and ^{100}Mo double-beta decays", *Phys. Lett. B*, 662, 2 (2008), 111–116.

[203]   D. A. Nesterenko et al., "Double-β transformations in isobaric triplets with mass numbers A=124, 130, and 136", *Phys. Rev. C*, 86, 4 (2012), 044313.

[204]   S. Rahaman et al., "Double-beta decay Q values of ^{116}Cd and ^{130}Te", *Phys. Lett. B*, 703, 4 (2011), 412–416.

[205]   J. L. Campbell and H. H. Jorch, "On the analytic fitting of full energy peaks from Ge (Li) and Si (Li) photon detectors. II", *Nucl. Inst. a. Meth.* 159, 1 (1979), 163–170.

[206]   E. Andreotti et al., *GSTR-13-020: Intercomparison of activities of ^{241}Am and ^{60}Co sources used within the GERDA Phase II BEGe acceptance tests*, tech. rep., 2013.

Acknowledgments

First and foremost I want to thank Kai Zuber as my supervisor and mentor for the last years who gave me inspiration, guidance, support and all the possibilities to pursue my ideas. He had a big influence on my life and simply said, without him I would not be where I am. I also warmly thank Stefan Schönert for accepting the effort of reading and refereeing my thesis. I feel very grateful for the genuine interest in my work and for his council and his career advice.

I want to give personal thanks to Nuno Barros as my Postdoc from whom I learned so much. I will never forget our heated discussions where everybody else thought we were fighting and his nasty comments about my badly written early drafts which I secretly collected in a blooper file. I am glad we shared so much time together and hope this will continue in the future. I also want to give personal thanks to Bernhard Schwingenheuer who always had an open ear and a helping hand especially during my time at Gran Sasso. I could always count on his honest and valuable opinion and I treasure his upright and candid personality as a role model for a physicist. I would also like to give personal thanks to Luciano Pandola who helped me to get started with simulations and analyses in the beginning of my time in GERDA. With his quick email responses he always felt available when I had questions and doubts. These are the people who taught me the most during my PhD. I will be eternally grateful for this.

I could not have done the work in this thesis without help. Every project was done in collaboration with other people which I would like to thank and acknowledge here:

The characterization of the BEGe detectors was a large effort shared by many people. I would like to give a very personal thank to Katharina von Sturm for the help with the surface and active volume characterization. It was an excellent teamwork and made the often tedious work so much more enjoyable. I also thank Marco Salathe and Victoria Wagner for the help with the surface scans and I would like to acknowledge Werner Maneschg and Erica Andreotti for the difficult task of organizing the characterization campaign.

The upside down BEGe measurement at LNGS would not have been possible without the hardware work of Konstantin Gusev, Tobias Bode and Dušan Budjáš and the support from Stefan Schönert. I would like to thank the TU Munich group for this hardware experience and the possibility for the measurements. I would also like to thank Bernhard Schwingenheuer and Victoria Wagner for helping with the data taking.

For the investigation of the n^+ surface pulses I would like to strongly and personally thank Dušan Budjáš - with an exclamation point. Long after leaving GERDA he was still open for every discussion and improved this study with his friendly pedantic poking at every little

detail. I am proud having this chapter finally endorsed by him. I would also like to thank Marco Salathe for our very efficient and helpful code exchanges and the possibility to use ADL. Furthermore, I thank Matteo Agostini, Andrea Lazzaro and Alexander Hegai as well as David Radford and Susanne Mertens from the Majorana Collaboration for discussions on this subject.

For the LAr veto simulations I would like to thank Nuno Barros for his fundamental work of bringing light into the simulations (pun intended). I would also like to thank everyone involve in the construction of the veto to be finally able to put the simulations to the test. In addition I would like to thank Christoph Wiesinger for providing the initial data for the comparison.

I was starting to prepare the excited state analysis in GERDA a long time ago but I could not have finished it without Thomas Wester. I am very grateful for his invaluable contribution for bringing this project to a successful end. I would also like to thank Bernhard Schwingenheuer and Allen Caldwell for the statistical discussions, Peter Grabmayr for his tireless correcting and editing of the paper draft, as well as many others for the useful comments.

For the excited states analysis in the palladium isotopes I would like to thank everyone involved in the three experiments. Detlev Degering for the measurement in the Felsenkeller and Dora Sommer for the initial MC simulations; Mikael Hult and Erica Andreotti for the measurement in HADES, the help with the analysis and the friendly accommodation at IRMM; and finally Matthias Laubenstein for the measurement at LNGS. I would also like to thank Thomas Wester and Alexander Domula for the help and discussion with this analysis.

In addition, I would like to thank everyone who helped me to improve this document with comments and corrections. I am extremely grateful to Kai Zuber who read and corrected the entire thesis. I also warmly thank Nuno Barros, Dušan Budjáš, Valentina Lozza, Luciano Pandola and Thomas Wester whose comments strongly improved individual chapters.

I cannot enough emphasize my gratitude to Kai Zuber and my graduate school (Mass, Spectrum, Symmetry GK 1504) for giving me the opportunity to live and work for 14 month at Gran Sasso in Italy. Apart from the chance to work directly with the GERDA experiment and experience a different institute at the worldwide center of low background physics, it also gave me the opportunity to get to know many interesting people from different experiments. There is not enough space to mention everyone but I am very much looking forward to see many of them again at future conferences. Besides the professional experience at LNGS, I am even more grateful to have experienced the Italian culture with all its vices and virtues. The experience at Gran Sasso became a part of myself for the rest of my life.

I would like to thank the ZIH computing cluster in Dresden for providing the foundation of all simulations in this work and apologize for the many times in which I exceeded my quotas. I would also like to thank the secretaries and administrators of the IKTP whose work in the background saves a tremendous amount of time and too often is taken for granted.

During the last years, my life was dominated by work which I would not have enjoyed with-

out the people I worked with and shared an office. In a sense they contributed as much to this thesis as everyone else. I want to thank my (office) friends Arnd Sörensen for our climbing adventures, Thomas Wester for loosing so many times at the soccer table, Alexander Domula for our office parties and cigaret breaks, Carla Maccolino and Giovanni Benato for teaching me Italian and for our adventures at Gran Sasso, Belina von Krosigk for giving me trusted advice when writing difficult emails and Valentina Lozza for the late night office sessions, the crucial support in the last days and for bringing a little bit of Italy to Dresden.

In the GERDA collaboration I would like to thank Nuno, Alex, Kai, Katharina, Béla, Nesli, Fabiana, Dimitris, Chris and Chris, Heng-Ye, Dušan, Marik, Matteo, Konstantin, Tobias, Andrea, Giovanni, Manuel, Francis, Tarka, Vici, Alexey, Mark, Carla, Ana, Paolo and many more for the unforgettable fun part of the meetings.

In the IKTP in Dresden I would like to thank Valentina, Nuno, Arnd, Belina, Alex, Thomas, Stefan, Birgit, Heinrich, Jan as well as everyone from the institute who made this workplace more enjoyable with the soccer table, birthday cakes and institute parties.

Ich möchte hier auch ganz besonders meinen Eltern danken - denen ich sonst leider viel zu selten dafür danke dass sie immer bedingungslos für mich da waren und mich unterstützt haben.

E infine voglio dare un ringraziamento speciale a Francesca per essermi stata sempre vicino anche se purtroppo era spesso lontana.

Erklärung

Hiermit versichere ich, dass ich die vorliegende Arbeit ohne unzulssige Hilfe Dritter und ohne Benutzung anderer als der angegebenen Hilfsmittel angefertigt habe; die aus fremden Quellen direkt oder indirekt übernommenen Gedanken sind als solche kenntlich gemacht. Die Arbeit wurde bisher weder im Inland noch im Ausland in gleicher oder ähnlicher Form einer anderen Prüfungsbehörde vorgelegt.

Die Promotion wurde an der Technischen Universität Dresden, am Institut für Kern- und Teilchenphysik unter der wissenschaftlichen Betreuung von Prof. Dr. Kai Zuber durchgeführt.

Ich erkenne die Promotionsordnung der Fakultät Mathematik und Naturwissenschaften vom 23.02.2011 an.

Dresden, den 21. Oktober 2015

Björn Lehnert